Weifei Hu *Editor*

Advanced Wind Turbine Technology

Advanced Wind Turbine Technology

Weifei Hu

Editor

Advanced Wind Turbine Technology

Editor
Weifei Hu
Sibley School of Mechanical and Aerospace
Engineering and Department of Earth
and Atmospheric Sciences
Cornell University
Ithaca, New York, USA

Introduction

Introduction

Wind energy has been significantly growing as one of clean, abundant, and affordable renewable energies worldwide during the past decades. More than 314,000 wind turbines (WT) are now operating around the world and supplied more than 4.3% of 2015 global electricity demand. The levelized cost of energy from WT has decreased substantially in recent years making wind energy now the lowest cost, non-hydropower renewable electricity source. A recent expert elicitation on future wind energy costs projected reductions of levelized total annual operating expenditures (which closely equate to operation and maintenance costs) of 9% over the period 2015–2030. Meanwhile, WT have evolved rapidly with the rated power increased from 100 kW in the early 1980s to 8 MW-plus today. Advanced WT technology emerges to support these ever-increasing titans to improve efficiency, increase reliability, reduce cost, and provide more power than their counterparts before, eventually making wind power a better choice for power generation.

There are plenty of books addressing the fundamentals of WT technology but very few providing in-depth and easy-to-follow discussion on the emerging advanced technology in wind turbine analysis, design, and development. New technology in wind energy is continuing on being developed. Thus, it is necessary to update the WT technology portfolio which holds the latest technology. In addition, specific technology has been researched and developed in the separate subfields of wind energy, for example, WT structural dynamics and WT condition monitoring. Actually, understanding the WT load and structural analysis could benefit the better interpretation of the monitoring data. With these considerations, it is of critical importance to put different aspects of advanced WT technology into one book and provide a big picture of the current development.

Some unique features of this book are briefly explained as follows: (1) The theories, analysis procedures, software codes, results are originally developed by each chapter authors. (2) The current results presented in each chapter are accurately calculated by using high-fidelity simulation models and/or comparing experimental

test results. As a strong support for the accuracy, large amount of high impact journal papers related to each chapter have been published by chapter authors. (3) The book provides unique technologies that are innovative and intelligent contributions in wind energy fields. Many of the provided technologies are ongoing and cutting edge research work in chapter authors' groups. (4) The underlying methods are clearly introduced using graphics, tables, appendixes, simulation models, and experimental instrumentation. One of the key goals of this book is to put the most critical challenges, the latest methodologies, discussions, and results together, and prepare the readers a comprehensive understanding of the current status and future direction of the selected cutting edge WT technology.

Scope

This book introduces the current challenges in modern WT analysis, design, and development and provides a comprehensive examination of state-of-the-art technologies from both academia and industry. The following 12 information-rich chapters cover a wide range of topics for WT including reliability-based design, computational fluid dynamics, gearbox and bearing analysis, lightning analysis, structural dynamics, health condition monitoring, WT repairing, offshore floating WT modeling and analysis, control and grid integration, as well as introduction of some emerging technologies. Each chapter begins with the current status of technology in a lucid, easy-to-follow treatment, and then elaborates on the corresponding advanced technology using detailed methodologies, mathematical models, numerical examples, and graphs. Relevant to a broad audience from students and faculty to researchers, manufacturers, and wind energy engineers and designers, the book is ideal for both educational and research needs.

A brief introduction of each chapter is provided as follows:

- Chapter 1 elaborates a reliability-based design optimization (RBDO) approach for designing reliable and cost-effective WT systems particularly considering wind load uncertainty and manufacturing variability.
- Chapter 2 provides a review of computational fluid dynamics (CFD) techniques that use numerical algorithms to solve and analyze WT fluid analysis.
- Chapter 3 explains an efficient numerical method to simulate gear dynamics of complex multibody gear system and applies the numerical method into deterministic design optimization (DDO) and RBDO of a WT gearbox.
- Chapter 4 proposes a hierarchical multiscale method to study the rolling contact fatigue in WT bearing with the consideration of lubrication effects.
- Chapter 5 provides the basic physics of WT lightning strike and lightning interaction and evaluates the lightning strike damage that counts for one of the greatest number of losses for WT.
- Chapter 6 presents the geometrically exact beam theory based on the Legendre-spectral-finite-element method, which is used for efficient and accurate WT

blade dynamic analysis and is implemented in the National Renewable Energy Laboratory (NREL)'s FAST code.

- Chapter 7 offers a novel condition monitoring strategy for WT drive train and the associated signal processing method, namely wavelet-transform-based energy tracking technique (WETT), which utilizes readily available generator power signal to evaluate the health condition of the whole WT drivetrain system through extracting and assessing the energy of WT power signals at fault characteristic frequencies.
- Chapter 8 provides a detailed survey of conventional and state-of-the-art repairing techniques for WT blades and summarizes the current machining processes of hardened steels for WT bearing and gearbox, followed by an overview of future applications.
- Chapter 9 first explains sophisticated dynamics of the mooring system used in offshore floating wind turbines, and then introduces state-of-the-art dynamic analyses including dynamic responses, design standards, and fault conditions of offshore floating wind turbines.
- Chapter 10 reviews advanced control techniques for wind turbine fatigue load alleviation and power enhancement and discusses two combined feedforward and feedback control designs for use with the 600 kW controls advanced research turbine at the NREL National Wind Technology Center.
- Chapter 11 surveys different models for short-term wind forecasting and ramp forecasting including individual and ensemble machine learning models and a recently developed optimized swinging door algorithm.
- Finally, Chap. 12 provides a comprehensive literature review and a concise summary for four emerging technologies: WT with permanent magnetic direct-drive, 3D printing used for WT, WT anti-icing and de-icing techniques, and data-mining techniques for wind energy.

Ithaca, NY, USA   Weifei Hu

Contents

Chapter 1
Reliability-Based Design Optimization of Wind Turbine Systems

Weifei Hu

1.1 Introduction

1.1.1 Reliability-Based Design Optimization

Reliability-based design optimization (RBDO) has been well developed to obtain reliable and cost-effective designs of many engineering problems under various uncertainties. One of the applications is RBDO of fatigue-sensitive structures for which engineers would like to evaluate an accurate fatigue lifespan. By applying RBDO to the fatigue-sensitive structures, their design could then be fine-tuned to reduce needless costs while satisfying the target reliability of fatigue performance. Therefore, as an expensive energy harvest machine, designing a reliable wind turbine is one of the most necessary tasks in wind energy business. A cost-effective design of wind turbine systems reduces the initial investment, while a reliable design saves maintenance cost of the wind turbine systems. Hence, RBDO can achieve both the reduction of initial investment and maintenance cost.

Reliability-based design optimization is an optimization method based on reliability analysis. In each design iteration, RBDO requires reliability analysis of performance measures. Reliability analysis methods can be classified into two groups: (1) sensitivity-based methods and (2) sampling-based methods. The representative sensitivity-based methods include the first-order reliability method (FORM) (Hasofer and Lind 1974; Tu et al. 1999, 2001), the second-order reliability method (SORM) (Hohenbichler and Rackwitz 1988; Breitung 1984), and the dimension reduction method (DRM) (Rahman and Wei 2006; Lee et al. 2010).

W. Hu (✉)
Sibley School of Mechanical and Aerospace Engineering and Department of Earth and Atmospheric Sciences, Cornell University, Ithaca, NY, USA
e-mail: wh348@cornell.edu

The FORM and SORM approximate a performance measure at the most probable point (MPP) using first- and second-order Taylor series expansion, respectively, and the DRM approximates a multidimensional performance function with a sum of lower-dimensional functions to calculate the probability of failure. In order to find the MPP, the sensitivity (gradient) of performance function needs to be calculated. However, for many engineering applications, e.g., fatigue of wind turbine blades, accurate sensitivities of performance functions are not available. Therefore, in such applications, the sensitivity-based methods, which require the sensitivities of performance functions to find the MPP, cannot be directly used. On the other hand, the sampling-based methods do not require the sensitivity of performance function to calculate the probability of failure (Lee et al. 2011a, b). Instead, the sampling-based methods directly calculate the probability of failure using Monte Carlo simulation (MCS). However, the sampling-based methods could be computationally inefficient because the MCS may require thousands of analyses of a performance function. In order to handle the computational issue using MCS, surrogate models are often used to reduce computational cost. A challenge when using sampling-based RBDO in complex engineering problems (e.g., wind turbine design) is developing an accurate surrogate model to replace complicated, nonlinear, and implicit performance functions (e.g., fatigue, deflection, extreme stress and strain, dynamic frequencies, and buckling loads of wind turbine systems).

1.1.2   Wind Load Uncertainty

It is difficult to accurately predict reliability for wind turbine systems due to various uncertainties from material properties, manufacturing process, and external loads. Among those uncertainties, wind load uncertainty is one of the most significant sources of uncertainty affecting the reliability of wind turbine systems, e.g., blade and drivetrain. Hence, a better understanding of the wind load uncertainty could facilitate the designs that are more reliable than those designed without correctly considering the wind load uncertainty.

In order to consider the wind load uncertainty, partial safety factors have been introduced in wind turbine standards (International Electrotechnical Commission 2005; Germanischer Lloyd 2010). Researchers applied the partial safety factors on wind load for design of wind turbine blades (Ronold et al. 1999; Ronold and Christensen 2001; Kong et al. 2005, 2006), wind turbine drivetrain (Derks 2008; Guo et al. 2015), wind turbine tower and foundation (Nicholson 2011), and other wind turbine systems (Bansal et al. 2002). Although using the partial safety factors to account for the wind load uncertainty is convenient, the spatial and temporal wind load variation cannot be represented accurately. Another disadvantage of using the partial safety is that the produced design may be too conservative if unnecessary large safety factors are used.

A number of studies have also applied probabilistic models for mean wind speed to characterize the annual wind load variation (Ronold et al. 1999; Ronold and Christensen 2001; Shokrieh and Rafiee 2006; Griffith and Ashwill 2011; Manwell et al. 2010; Burton et al. 2011; Manuel et al. 2001; Messac et al. 2011; Carta et al. 2009). One of the most widely used models is the two-parameter Weibull distribution, which is based on annual wind speed data. This distribution has been used to determine the percentage of time that the wind turbine experiences different mean wind speeds during its life cycle. Using this time percentage, the wind loads are calculated under each mean wind speed, and the long-term turbine performances (e.g., wind power and fatigue damage) can then be accumulated using the specified mean wind speed distribution. However, by applying a fixed Weibull distribution, only deterministic turbine performances can be obtained because the assumed Weibull distribution is constant in different years. The fixed Weibull distribution based either on wind turbine standards (International Electrotechnical Commission 2005; Germanischer Lloyd 2010) or measured wind data at a specific location cannot truly render the wind load uncertainty over a large spatiotemporal range, for instance, at different locations and in different years.

Besides the mean wind speed, the fluctuations in the wind speed about the short-term mean naturally have a major impact on the design loadings, as they are the source of extreme gust loads and a large part of the blade fatigue loading (Burton et al. 2011; Manwell et al. 2010). However, very few turbulence intensities are used in reliability analysis and design optimization of wind turbines. Only three deterministic turbulence intensities are used to classify different wind turbine designs in the International Electrotechnical Commission (IEC) standard (International Electrotechnical Commission 2005). Noda and Flay applied a single turbulence intensity when simulating the wind turbine blade fatigue damage in a typical New Zealand site, by which different sites are classified as either low- or high-intensity turbulence sites (Noda and Flay 1999). In reality, the turbulence intensity should follow a certain distribution at a specific site. For example, Ronold et al. assumed the turbulence intensity followed a lognormal distribution (Ronold et al. 1999). Consequently, in order to facilitate new wind turbine design surviving under realistic uncertain wind load, both variations of wind speed and turbulence intensity have to be involved. Hu et al. identified the distribution of 10-min turbulence intensity to be a log-logistic distribution and applied both the distributions of 10-min mean wind speed and 10-min turbulence intensity in reliability analysis of wind turbine blades for fatigue life (Hu et al. 2012).

As the wind load varies over a large spatiotemporal range, the wind turbines are expected to survive the uncertain wind load at different locations and in different years. However, this level of wind load uncertainty has not been found in existing research or wind energy standards (International Electrotechnical Commission 2005; Germanischer Lloyd 2010). Fixed distribution for mean wind speed is still widely applied for wind turbine designs (e.g., (Ronold et al. 1999; Shokrieh and Rafiee 2006; Do et al. 2014)), which assumes that the same mean wind speed distribution continues for the entire lifespan.

1.1.3 Current Reliability-Based Design of Wind Turbines

As a modern MW-scale wind turbine involving complex subassemblies, the current reliability-based design of wind turbines often targets to design specific subassembly, for example, rotor blade, gearbox, bearing, and tower. One of the very beginning works is investigated by Ronold et al. who studied reliability-based design of wind turbine blades against fatigue failure using a probabilistic model with measured bending moments at the blade root of a site-specific wind turbine (Ronold et al. 1999). Even though no optimization procedure is involved, this work has developed reliability-based safety factor calibration to calibrate site- and wind turbine-specific safety factors applicable to flapwise bending of rotor blades (Ronold et al. 1999). A probabilistic framework for designing wind turbine blades is presented in Toft and Sørensen (2011), which requires tests with the basic composite materials and full-scale blades during the design process. Reliability-based design of wind turbine blades against failure under extreme conditions was studied by Ronold and Larsen (2000) and Cheng (2002). However, fatigue failure under wind load uncertainty was not included in their reliability-based design. Reliability-based design has also been implemented in designing offshore wind turbine systems. For example, Lee et al. investigated RBDO of a monopole transition piece in an offshore wind turbine system (Lee et al. 2014). In the thesis (Firouzianbandpey 2016), reliability-based design facilitates the development of a low-cost foundation for future offshore wind farms by focusing on the geotechnical site assessment. Cheng et al. applied statistical methods to determine the distribution of the extreme response of offshore wind turbines (Cheng et al. 2003). However, none of the aforementioned works have specifically involved load uncertainty into a design optimization process. In addition, it is more challenging to accurately and efficiently integrate a realistic wind load uncertainty into RBDO. A recent endeavor has been carried out by Hu et al. who implemented a dynamic wind load uncertainty model into a reliability-based design optimization procedure to obtain an optimal 5-MW wind turbine blade satisfying the target probability of failure of 2.275% (Hu et al. 2016b).

   This chapter aims to present reliability-based design optimization methods which could design reliable and cost-effective wind turbine systems to reduce the cost of wind energy. In order to achieve this goal, several challenges have been taken on, including development of a realistic wind load uncertainty model and development of an RBDO procedure that can be easily adopted for various wind turbine systems to minimize their cost and satisfy the reliability requirement under uncertain wind load. The reminder of this chapter is outlined as follows: The dynamic wind load uncertainty model is explained in detail in Sect. 1.2 followed by the elaboration of a reliability analysis method for wind turbine systems in Sect. 1.3. Finally, Sect. 1.4 presents a sampling-based RBDO method and its application in composite wind turbine blades.

1.2 Dynamic Wind Load Uncertainty

A dynamic wind load uncertainty model has been developed based on measured wind data. The wind load uncertainty model involves both the annual wind load variation and the wind load variation in a large spatiotemporal range, for example, in different years and at different locations. The annual wind load variation is represented by the joint probability density function (PDF) of 10-min mean wind speed V_{10} and 10-min turbulence intensity I_{10}. The wind load variation in a large spatiotemporal range is represented by the distributions of five marginal distribution and correlation parameters C, k, a, b, and τ, which determine the joint PDF of V_{10} and I_{10} as described in this section. The basic structure of the dynamic wind load uncertainty model is shown in Fig. 1.1.

1.2.1 Annual Wind Load Variation

1.2.1.1 Marginal Distributions of Random Parameters for Wind Speed

The annual wind load variation means that the wind load under different wind conditions, which are often determined by mean wind speed and turbulence intensity during a short period (e.g., 10 min or 1 h), is varying due to the frequency of occurrence of the individual wind conditions in 1 year and at one location. The variable wind load is often represented by the variation of 10-min mean wind speed,
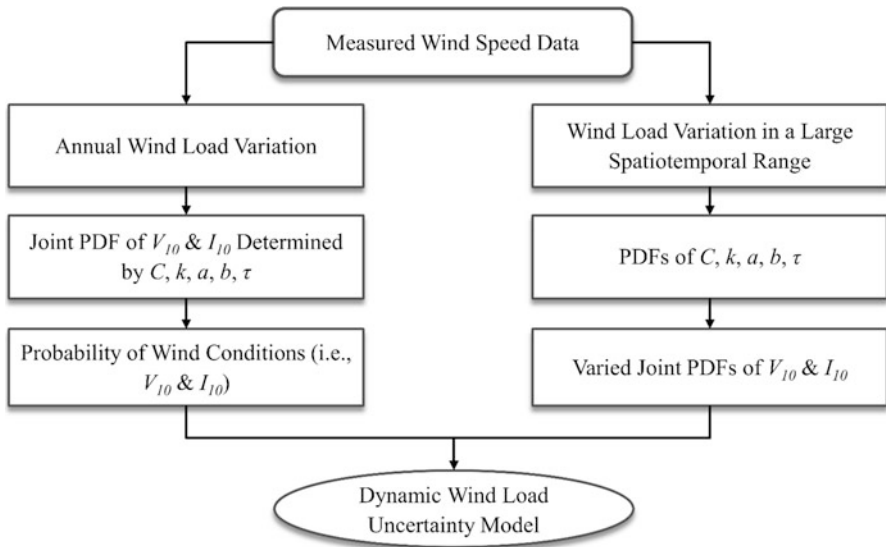

Fig. 1.1 Dynamic wind load uncertainty model

V_{10}, in the state-of-the-art wind energy standards (International Electrotechnical Commission 2005; Germanischer Lloyd 2010). In this chapter, another factor, 10-min turbulence intensity, I_{10}, which also affects both dynamic response and fatigue damage during 10 min, is considered. Thus, the annual wind load variation is represented by the joint probability density function (PDF) of V_{10} and I_{10}. In addition, it is found that there is a correlation between V_{10} and I_{10} based on measured wind data. In order to properly consider this correlation in the joint PDF of V_{10} and I_{10}, the 10-min standard deviation Σ_{10} of wind speed is used. This section will first provide the marginal distributions of the three random parameters for wind speed, i.e., V_{10}, I_{10}, and Σ_{10}. The correlation between these parameters is then studied by using copula (Noh et al. 2009, 2010; Lee et al. 2011a). The joint distribution of V_{10} and I_{10} is derived using the copula for V_{10} and Σ_{10} and marginal distributions of V_{10} and Σ_{10}.

Before identifying the marginal distributions, the wind speed data is first transformed to the same hub height from different measured heights, since the wind speed is inherently different at different heights. The hub height wind speed is calculated by a normal wind profile model (International Electrotechnical Commission 2005; Germanischer Lloyd 2010) using the measured wind speed at other heights as

$$V_{hub} = \frac{V_z}{(z/z_{hub})^{\alpha}} \tag{1.1}$$

where z is the measured height above the ground, z_{hub} is the hub height, and V_{z} is the measured wind speed at the height z. The power law exponent α is assumed to be 0.2 according to the standards (International Electrotechnical Commission 2005; Germanischer Lloyd 2010). The following distribution-identifying procedure is based on adjusted wind data at the wind turbine hub height.

The probability distributions of V_{10}, I_{10}, and Σ_{10} are fitted using seven different positive-valued distribution types, gamma, Weibull, log-logistic, lognormal, Nakagami, Rayleigh, and Rician (Hu et al. 2016a). The maximum likelihood estimation (MLE) is implemented to find parameters for fitting the candidate distributions (Hoog et al. 2005). The likelihood function $L(\theta)$ and its natural logarithm $l(\theta)$ are, respectively, given by

$$L(\boldsymbol{\theta}) = \prod_{i=1}^{n} f(x_i; \boldsymbol{\theta}) \tag{1.2}$$

$$l(\boldsymbol{\theta}) = \sum_{i=1}^{n} \ln f(x_i; \boldsymbol{\theta}) \tag{1.3}$$

where $f(x_i;\boldsymbol{\theta})$ is the PDF value of a candidate distribution calculated at data x_i given the vector of distribution parameter $\boldsymbol{\theta}$. For each group of wind data, the distribution
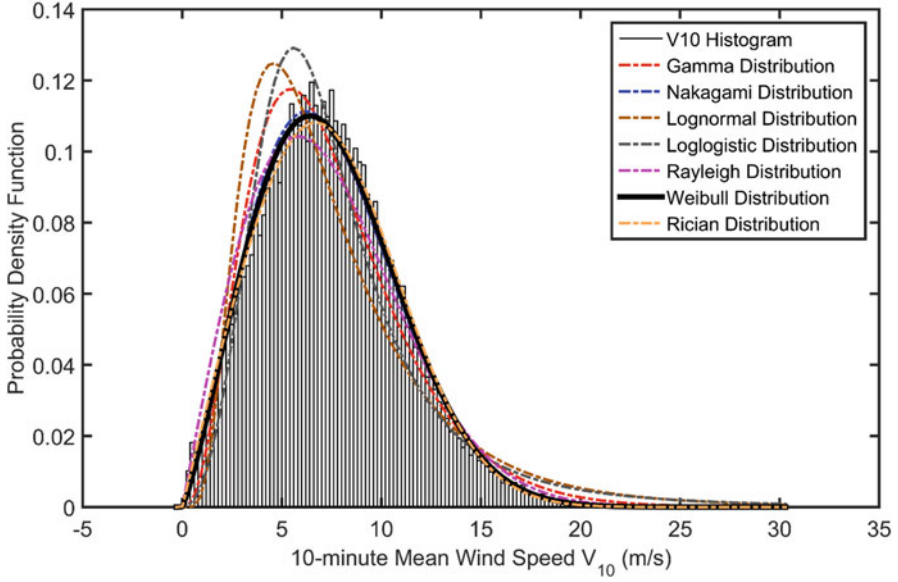
Fig. 1.2 Distribution fit of V_{10}

type corresponding to the largest log-likelihood value is viewed as the best fit distribution. One example marginal distribution fit for V_{10} is shown in Fig. 1.2, in which the Weibull distribution corresponds to the largest log-likelihood value among the seven candidate distribution types. Thus the Weibull distribution is selected for the annual V_{10} distribution, which is consistent with the fact that the Weibull distribution has been widely accepted for representing the annual mean wind speed distribution. Similarly, using the MLE, the best marginal distribution types of I_{10} and Σ_{10} have been identified as a log-logistic distribution type and a gamma distribution type, respectively (Hu et al. 2016a, b). Examples of marginal distribution fits for I_{10} and Σ_{10} are shown in Figs. 1.3 and 1.4, respectively. The PDF of the Weibull distribution of V_{10} is given by

$$f_{V10}(v_{10}; C, k) = \frac{k}{C}\left(\frac{v_{10}}{C}\right)^{k-1} \exp\left[-\left(\frac{v_{10}}{C}\right)^k\right] \tag{1.4}$$

where v_{10} is a realization of V_{10} and C and k are the scale parameter and shape parameter, respectively. The PDF of the log-logistic distribution of I_{10} is given by

$$f_{I10}(i_{10}; \gamma, \delta) = \frac{\exp\left(\frac{\ln i_{10} - \gamma}{\delta}\right)}{\delta i_{10}\left[1 + \exp\left(\frac{\ln i_{10} - \gamma}{\delta}\right)\right]^2} \tag{1.5}$$
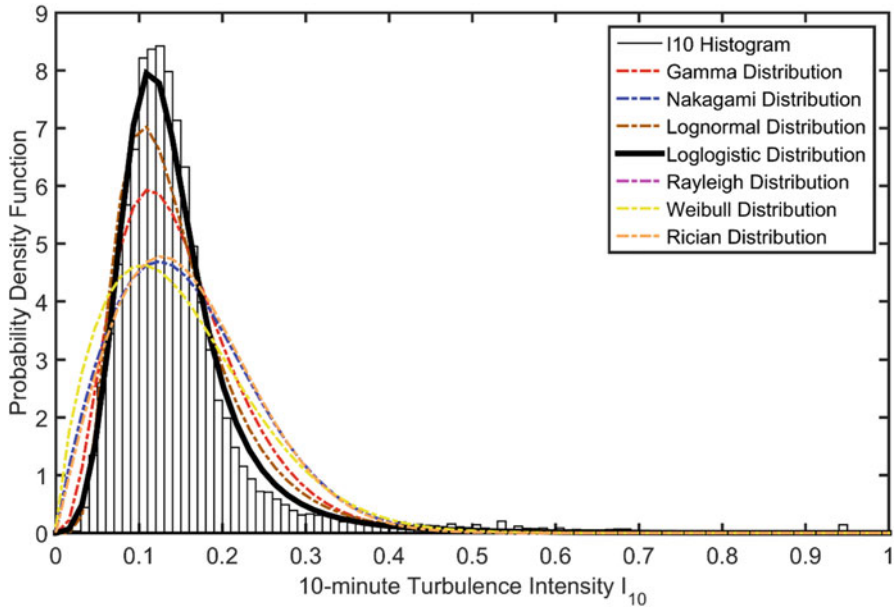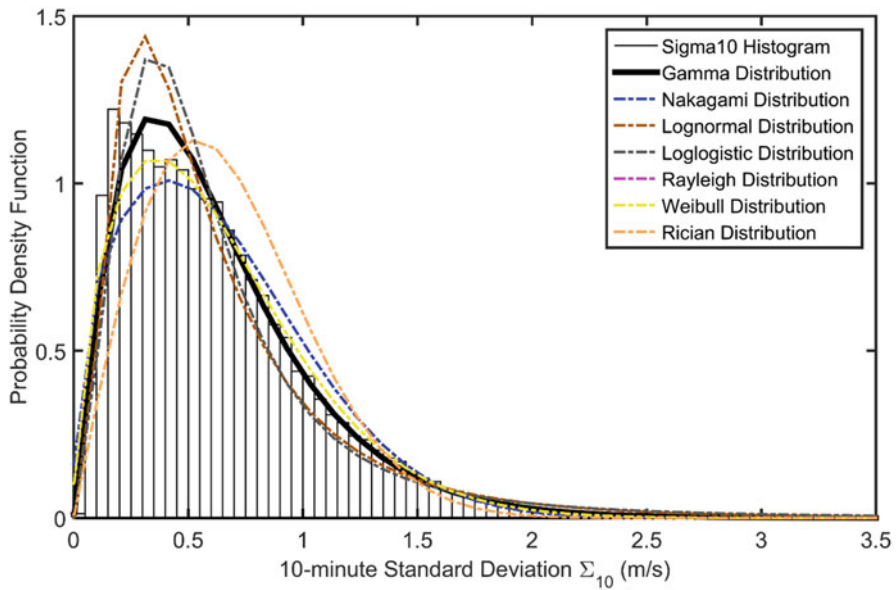
Fig. 1.3 Distribution fit of I_{10}

Fig. 1.4 Distribution fit of Σ_{10}

where i_{10} is a realization of I_{10} and γ and δ are the log-location parameter and log-scale parameter, respectively. $\ln i_{10}$ is the natural logarithm of i_{10}. The PDF of the gamma distribution of Σ_{10} is given by

$$f_{\Sigma 10}(\sigma_{10}; a, b) = \frac{1}{b^a \Gamma(a)} \sigma_{10}^{a-1} \exp\left(-\frac{\sigma_{10}}{b}\right) \tag{1.6}$$

where σ_{10} is a realization of Σ_{10} and a and b are the shape parameter and scale parameter, respectively. $\Gamma(a)$ is the gamma function of a.

The Weibull distribution of V_{10} characterizes the 10-min mean wind speed variation during the year, while the log-logistic distribution of I_{10} and the gamma distribution of Σ_{10} represent the variation of fluctuation in wind speed in 10 min. It is useful to think of the wind as consisting of a mean wind speed with turbulent fluctuations superimposed. The mean wind speed and turbulence intensity are often used to represent the wind load strength/level by wind turbine design standards (International Electrotechnical Commission 2005; Germanischer Lloyd 2010). It is found that using V_{10} and Σ_{10} could better represent the correlated joint PDF of V_{10} and I_{10}. The correlation between V_{10} and I_{10} and the correlation between V_{10} and Σ_{10} are discussed as follows.

1.2.1.2 Correlation Between Random Parameters for Wind Speed

In order to calculate the probability of a certain wind condition, i.e., V_{10} and I_{10}, in 1 year, the joint PDF of V_{10} and I_{10} is necessary. If the random variables V_{10} and I_{10} are assumed to be independent, the joint PDF of V_{10} and I_{10} can be simply calculated as

$$f_{VI} = f_{V10} \cdot f_{I10} \tag{1.7}$$

where f_{VI0} and f_{I10} are the marginal PDFs of V_{10} and I_{10}, respectively. However, the scatter plots of (V_{10}, I_{10}) and (V_{10}, Σ_{10}) in Fig. 1.5 clearly show that there are strong correlations among these three random parameters.

For bivariate correlated input random variables $\mathbf{X} = [X_i, X_j]^T$, the joint PDF of $\mathbf{X}$ can be expressed using copula as (Noh et al. 2009, 2010; Lee et al. 2011a)

$$f_{\mathbf{X}}(\mathbf{x}; \boldsymbol{\mu}) = \frac{\partial^2 C(u, v; \theta)}{\partial u \partial v} f_{X_i}(x_i; \mu_i) f_{X_j}(x_j; \mu_j)$$
$$= C_{,uv}(u, v; \theta) f_{X_i}(x_i; \mu_i) f_{X_j}(x_j; \mu_j) \tag{1.8}$$

where C is the copula function; f_{Xi} and f_{Xj} are the marginal PDFs for X_i and X_j, respectively; $u = F_{Xi}(x_i; \mu_i)$ and $v = F_{Xj}(x_j; \mu_j)$ are marginal CDFs for X_i and X_j, respectively; and θ is the correlation coefficient between X_i and X_j. The partial derivative of the copula function with respect to u and v is called the copula density function and is written as
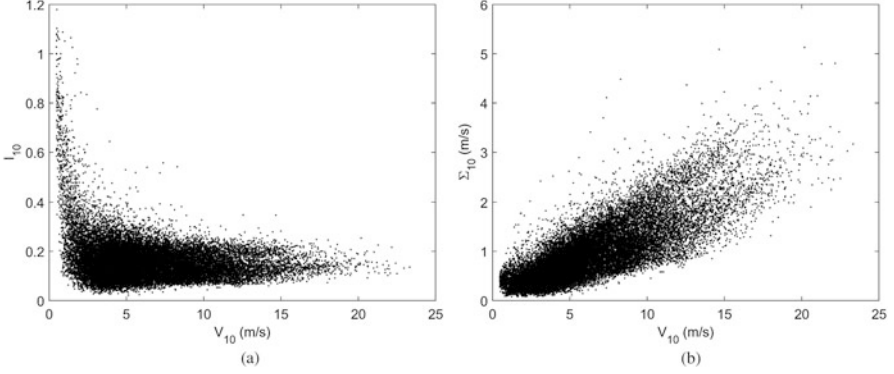
Fig. 1.5 (**a**) Scatter plot of one group of measured (V_{10}, I_{10}) and (**b**) scatter plot of one group of measured (V_{10}, Σ_{10})

$$c\left(u, v; \theta\right) \equiv \frac{\partial^2 C\left(u, v; \theta\right)}{\partial u \partial v} = C_{,uv}\left(u, v; \theta\right) \tag{1.9}$$

It might be straightforward to derive the joint PDF of V_{10} and I_{10} by using the marginal PDF of V_{10} and I_{10} as well as identify the copula between V_{10} and I_{10}. However, there is a mathematical correlation between V_{10} and I_{10} because I_{10} is calculated by Σ_{10}/V_{10}. In contrast, the V_{10} and Σ_{10} data are directly obtained from the measured wind data. To exclude the mathematical correlation and consider statistical correlation between V_{10} and I_{10}, the joint PDF of V_{10} and Σ_{10} is obtained first and then transferred to the joint PDF of V_{10} and I_{10} (Hu et al. 2016b).

The statistical correlation between V_{10} and Σ_{10} is represented using copula density function for V_{10} and Σ_{10}. Among eight candidate copula types, the best copula type for V_{10} and Σ_{10} is found to be the Gumbel copula using 249 groups of V_{10} and Σ_{10} data (Hu et al. 2016b). The Gumbel copula function $C_{V\Sigma}$ and copula density function $c_{V\Sigma}$ for V_{10} and Σ_{10} are expressed, respectively, as

$$C_{V\Sigma}\left(u, v; \tau\right) = \exp\left(-w^{1-\tau}\right) \tag{1.10}$$

$$c_{V\Sigma}\left(u, v; \tau\right) = \frac{(-\ln u)^{\frac{\tau}{1-\tau}}(-\ln v)^{\frac{\tau}{1-\tau}}\left(\frac{1}{1-\tau} + w^{1-\tau} - 1\right)w^{-1-\tau}\exp\left(-w^{1-\tau}\right)}{uv} \tag{1.11}$$

where u and v are marginal CDFs of V_{10} and Σ_{10}, respectively. The parameter w is calculated as

$$w = (-\ln u)^{\frac{1}{1-\tau}} + (-\ln v)^{\frac{1}{1-\tau}} \tag{1.12}$$

where τ is Kendall's tau (Noh et al. 2010) for V_{10} and Σ_{10}.

$$\theta = 1 / (1 - \tau) \tag{1.13}$$

By substituting Eqs (1.4), (1.6), and (1.11) into Eq. (1.8), the joint PDF of V_{10} and Σ_{10} is expressed as

$$f_{V\Sigma}(v_{10}, \sigma_{10}; C, k, a, b, \tau) = c_{V\Sigma}(v_{10}, \sigma_{10}; \tau) f_{V10}(v_{10}; C, k) f_{\Sigma10}(\sigma_{10}; a, b) \tag{1.14}$$

The joint PDF of V_{10} and I_{10} could be derived using the joint PDF of V_{10} and Σ_{10} based on the one-to-one transformation from the random vector (V_{10}, Σ_{10}) to the random vector (V_{10}, I_{10}) with the Jacobian of the transformation $J = v_{10}$. Thus, the joint PDF of V_{10} and I_{10} is expressed as

$$\begin{aligned} f_{VI}(v_{10}, i_{10}; C, k, a, b, \tau) &= f_{V\Sigma}(v_{10}, \sigma_{10}; C, k, a, b, \tau) |J| \\ &= f_{V\Sigma}(v_{10}, v_{10} \cdot i_{10}; C, k, a, b, \tau) v_{10} \end{aligned} \tag{1.15}$$

where v_{10}, i_{10}, and σ_{10} are realizations of random variables V_{10}, I_{10}, and Σ_{10}, respectively; $i_{10} = \sigma_{10} / v_{10}$; C and k are the scale parameter and shape parameter, respectively, of the Weibull distribution of V_{10}; a and b are the shape parameter and scale parameter, respectively, of the gamma distribution of Σ_{10}; and τ is Kendall's tau for V_{10} and Σ_{10}.

Applying the derived joint PDF of V_{10} and σ_{10}, the 1-year fatigue damage can be calculated as

$$\begin{aligned} D_{1year}(\mathbf{d}, C, k, a, b, \tau) &= 52560 \int_{V_{low}}^{V_{upp}} \int_{I_{low}}^{I_{upp}} f_{VI}(v_{10}, i_{10}; C, k, a, b, \tau) \\ &\quad D_{10}(\mathbf{d}, v_{10}, i_{10}) \, dv_{10} di_{10} \\ &= 52560 \int_{V_{low}}^{V_{upp}} \int_{I_{low}}^{I_{upp}} c_{V\Sigma}(v_{10}, v_{10} \cdot i_{10}; \tau) f_{V10}(v_{10}; C, k) \\ &\quad f_{\Sigma10}(v_{10} \cdot i_{10}; a, b) v_{10} D_{10}(\mathbf{d}, v_{10}, i_{10}) \, dv_{10} di_{10} \end{aligned} \tag{1.16}$$

where $\mathbf{d}$ is a design vector of a wind turbine subassembly (e.g., composite laminate thickness of wind turbine blades); $c_{V\Sigma}$ is the Gumbel copula for V_{10} and Σ_{10}; f_{V10} and $f_{\Sigma10}$ are the Weibull PDF and gamma PDF of V_{10} and Σ_{10}, respectively; V_{low} and V_{upp} are the lower and upper bounds of V_{10}, respectively; and I_{low} and I_{upp} are the lower and upper bounds of I_{10}, respectively. D_{10} is the 10-min fatigue damage which is determined by the design $\mathbf{d}$ of a wind turbine subassembly under the specified wind condition (v_{10}, i_{10}).

1.2.2 Wind Load Variation in a Large Spatiotemporal Range

The joint PDF of V_{10} and I_{10} accounts for the wind load variation during 1 year at a specific location. However, the wind load is also varying year to year for a specific location. In addition, the wind load could be different at different locations for various reasons, e.g., the nonuniformity of the earth's surface or the thermal effect due to differences in altitude. Even though the variation of wind load in a large spatiotemporal range seems unpredictable, the distributions and correlation type of the random wind parameters, V_{10}, I_{10}, and Σ_{10}, are assumed to be the same. For example, significant amount of literatures use a Weibull distribution to represent the mean wind speed distribution, disregarding when or where their research investigation has been carried out (Burton et al. 2011; Germanischer Lloyd 2010; Griffith and Ashwill 2011; International Electrotechnical Commission 2005; Manwell et al. 2010; Ronold et al. 1999; Shokrieh and Rafiee 2006). In this study, the wind load variation in a large spatiotemporal range is represented by the distributions of the marginal distribution and correlation parameters, i.e., C, k, a, b, and τ, which determine the joint PDF of V_{10} and I_{10} in Eq. (1.15).

Previous study has used 249 groups of wind data measured from different years and at different locations to obtain 249 sets of (C, k, a, b, τ) values (Hu et al. 2016a, b). Then marginal distribution types of C, k, a, b, and τ can be identified using the same MLE method as explained in Sect. 1.2.1. The log-likelihood function values for each candidate marginal distribution type for C, k, a, b, and τ can be calculated similarly. Based on the 249 sets of (C, k, a, b, τ) values, it is found that the largest log-likelihood values for C, k, a, b, and τ correspond to log-logistic distribution, normal distribution, generalized extreme value distribution, Weibull distribution, and extreme value distribution, respectively. Consequently, the specific PDFs of random parameters C, k, a, b, and τ, as listed in Table 1.1, are obtained after calculating the distribution parameters using MLE. The best fit distributions for C, k, a, b, and τ are shown in Fig. 1.6.

Table 1.1 Identified PDFs of C, k, a, b, and τ using 249 groups of wind data (Hu et al. 2016a)

Parametere	Distribution type	PDF
C	Log-logistic	$f_C(x) = \dfrac{\exp\left[\frac{\ln(x)-2.0701}{0.1024}\right]}{0.1024x\left[1+\exp\left(\frac{\ln(x)-2.0701}{0.1024}\right)\right]^2}$
k	Normal	$f_k(x) = \dfrac{1}{0.2532\sqrt{2\pi}} \exp\left[\dfrac{-(x-2.1913)^2}{0.1282}\right]$
a	Generalized extreme value	$f_a(x) = 1.1888 \dfrac{(0.7429+0.0827x)^{-15.3746}}{\exp\left[(0.7429+0.0827x)^{-14.3746}\right]}$
b	Weibull	$f_b(x) = \dfrac{4.1254}{0.3470}\left(\dfrac{x}{0.3470}\right)^{3.1254} \exp\left[-\left(\dfrac{x}{0.3470}\right)^{4.1254}\right]$
τ	Extreme value	$f_\tau(x) = 0.0986^{-1} \exp\left(\dfrac{x-0.5696}{0.0986}\right) \exp\left[-\exp\left(\dfrac{x-0.5696}{0.0986}\right)\right]$
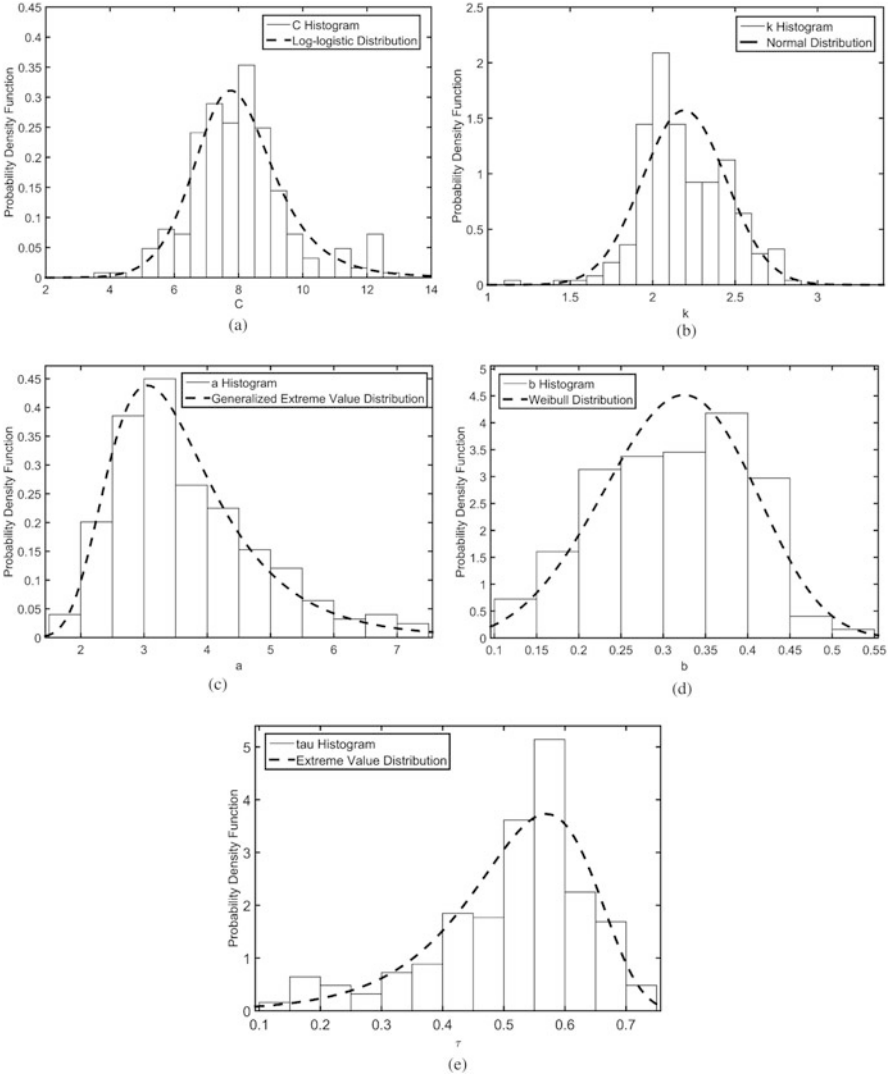
Fig. 1.6 Best fit distributions for C, k, a, b, and τ (**a**) Log-logistic distribution fit for C data (**b**) Normal distribution fit for k data (**c**) Generalized extreme value distribution fit for a data (**d**) Weibull distribution fit for b data (**e**) Extreme value distribution fit for τ data

1.2.3 Wind Load Probability Table

As explained at the end of Sect. 1.2.1, the 1-year fatigue damage is determined by the design vector **d** and random parameters C, k, a, b, and τ. However, the theoretical equation to calculate the 1-year fatigue damage, as shown in Eq. (1.16), cannot be

explicitly expressed as a function of **d**, C, k, a, b, and τ, due to the complexity of the joint PDF and 10-min fatigue damage calculation for wind turbine systems. Thus, in real damage calculation, the double integration in Eq. (1.16) is numerically calculated using the Riemann integral as

$$
\begin{aligned}
D_{1year}\,&(\mathbf{d}, C, k, a, b, \tau) \\
&\approx 52560 \sum_{i=1}^{m} \sum_{j=1}^{n} P_{VI}^{i,j}\left(v_{10}^{i}, i_{10}^{j}; C, k, a, b, \tau\right) D_{10}^{i,j}\left(\mathbf{d}, v_{10}^{i}, i_{10}^{j}\right)
\end{aligned} \tag{1.17}
$$

where the probability of V_{10} and I_{10} being in a small cell can be calculated as

$$
P_{VI}^{i,j}\left(v_{10}^{i}, i_{10}^{j}; C, k, a, b, \tau\right) = f_{VI}\left(v_{10}^{i}, i_{10}^{j}; C, k, a, b, \tau\right) \Delta v_{10} \Delta i_{10} \tag{1.18}
$$

Here, Δv_{10} and Δi_{10} are the intervals discretizing ranges of V_{10} and I_{10}, respectively. In this study, the ranges of V_{10} and I_{10} are evenly discretized. The numbers of selected V_{10} and I_{10} are m and n, respectively. v_{10}^{i} is the value of V_{10} at the center of ith interval in the V_{10} direction. Therefore, $v_{10}^{i} = v_{10}^{1} + (i - 1)\,\Delta v_{10}$. Similarly, i_{10}^{j} is the value of I_{10} at the center of the jth interval in the I_{10} direction. Hence, $i_{10}^{j} = i_{10}^{1} + (j - 1)\,\Delta i_{10}$. f_{VI} is the joint probability density function (PDF) of V_{10} and I_{10}.

In this study, a large range of V_{10} and I_{10} has been considered to examine the fatigue damage considering all probable wind conditions. Moriarty et al. applied the cut-in wind speed and the cut-out wind speed as the lower bound and upper bound, respectively, of 10-min segments in 1-year fatigue simulation, and the calculated fatigue load cycles agreed well with those obtained by a long-term extrapolation method in their work (Moriarty et al. 2004). The turbines were assumed to operate 100% of the time between cut-in and cut-out wind speed with 100% availability (Moriarty et al. 2004). Even though the unsteadiness when wind speed is larger than cut-out wind speed can cause large fluctuating loads, the probability of occurrence of such extreme wind conditions is very small, which makes little fatigue contribution in long term. The damage due to extreme wind condition may be better addressed by wind turbine extreme analysis, which is beyond the scope of this study. In this study, the lower bound and upper bound of V_{10} are set to be the cut-in wind speed of 3 m/s and cut-out wind speed of 25 m/s, respectively (Jonkman et al. 2009). The lower bound and upper bound of I_{10} are set to be 0.02 and 1, respectively. The 10-min fatigue analyses for a wind turbine system, e.g., blade and gearbox, are run over the range of V_{10} between 3 m/s and 25 m/s in 2 m/s increments and the range of I_{10} between 0.02 and 1 in 0.02 increments. Therefore, the number of V_{10} and I_{10} are 12 and 50, respectively (i.e., m = 12 and n = 50 in Eq. (1.17)). There are 600 different wind conditions in total. All the wind conditions are listed in Table 1.2.

At each wind condition, a wind load probability $P_{VI}^{i,j}$ is calculated using Eq. (1.18), and a 10-min fatigue damage $D_{10}^{i,j}$ is calculated using a fatigue analysis procedure for a wind turbine system. In this way, a 12-by-50 wind load probability

Table 1.2 Selected 600 wind conditions

V_{10} (m/s) \ I_{10}	0.02	0.04	0.06	...	0.96	0.98	1
3	3, 0.02	3, 0.04	3, 0.06	...	3, 0.96	3, 0.98	3, 1
5	5, 0.02	5, 0.04	5, 0.06	...	5, 0.96	5, 0.98	5, 1
7	7, 0.02	7, 0.04	7, 0.06	...	7, 0.96	7, 0.98	7, 1
⋮	⋮	⋮	⋮	⋱	⋮	⋮	⋮
21	21, 0.02	21, 0.04	21, 0.06	...	21, 0.96	21, 0.98	21, 1
23	23, 0.02	23, 0.04	23, 0.06	...	23, 0.96	23, 0.98	23, 1
25	25, 0.02	25, 0.04	25, 0.06	...	25, 0.96	25, 0.98	25, 1

Table 1.3 Wind load probability table

V_{10} \ I_{10}	i_{10}^1	i_{10}^2	...	i_{10}^{50}
v_{10}^1	$P_{VI}^{1,1}$	$P_{VI}^{1,2}$	...	$P_{VI}^{1,50}$
v_{10}^2	$P_{VI}^{2,1}$	$P_{VI}^{2,2}$	...	$P_{VI}^{2,50}$
⋮	⋮	⋮	⋱	⋮
v_{10}^{12}	$P_{VI}^{12,1}$	$P_{VI}^{12,2}$	...	$P_{VI}^{12,50}$

Table 1.4 Ten-minute fatigue damage table

V_{10} \ I_{10}	i_{10}^1	i_{10}^2	...	i_{10}^{50}
v_{10}^1	$D_{VI}^{1,1}$	$D_{VI}^{1,2}$	...	$D_{VI}^{1,50}$
v_{10}^2	$D_{VI}^{2,1}$	$D_{VI}^{2,2}$	...	$D_{VI}^{2,50}$
⋮	⋮	⋮	⋱	⋮
v_{10}^{12}	$D_{VI}^{12,1}$	$D_{VI}^{12,2}$	...	$D_{VI}^{12,50}$

table and a 12-by-50 10-min fatigue damage table can be constructed. For brevity, the wind load probability table and the 10-min fatigue damage table are symbolically shown in Tables 1.3 and 1.4, respectively.

To facilitate understanding of the two types of tables, a typical wind load probability table and a typical 10-min fatigue damage table are illustrated by 3-D bar charts in Figs. 1.7 and 1.8, respectively. In Fig. 1.7, the C, k, a, b, and τ used to generate the illustrated wind load probability table are C = 6.5856, k = 2.5178, a = 3.1570, b = 0.4123, and τ = 0.6826. Figure 1.8 uses 10-min fatigue damages calculated at a node-section point randomly selected from the blade model (Hu et al. 2016b). As shown in Fig. 1.7, the large probabilities are concentrated at mild wind conditions, e.g., V_{10} < 11 m/s, I_{10} < 0.3. For extreme wind conditions, the probabilities are much smaller than those corresponding to mild wind load conditions. The reason these extreme wind conditions are also considered is that the 10-min fatigue damages under extreme wind conditions are often much larger than those under mild wind conditions. As shown in Fig. 1.8, the 10-min fatigue damage increases exponentially as V_{10} and I_{10} increase. Hence, it is necessary to include all
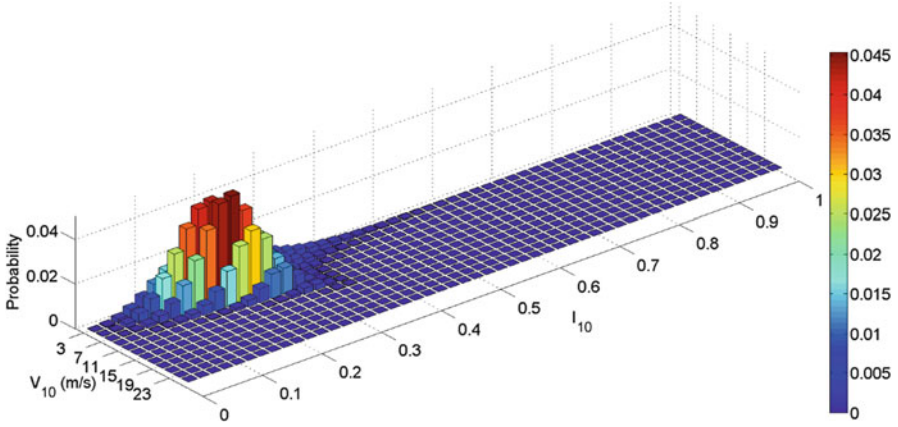
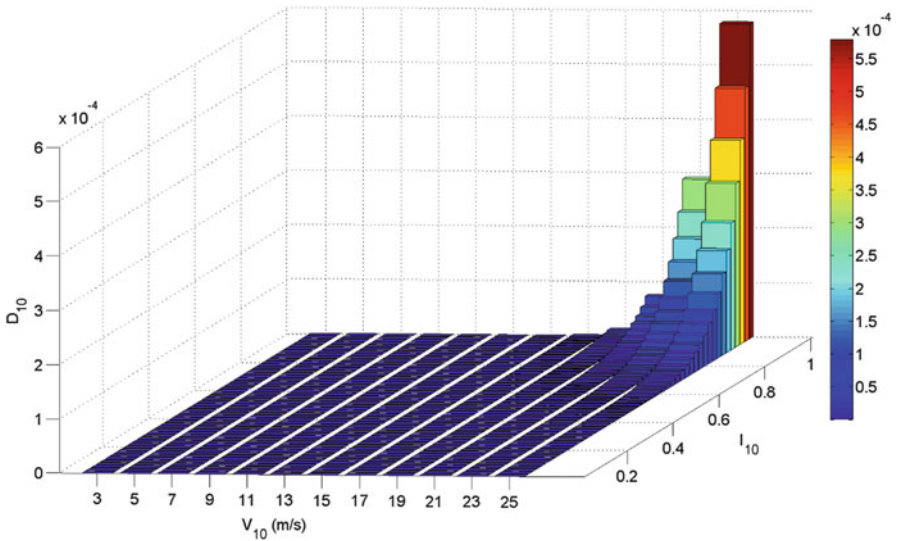**Fig. 1.7** A 3-D bar chart of a wind load probability table

Fig. 1.8 A 3-D bar chart of a 10-min fatigue damage table

the wind conditions when calculating the 1-year fatigue damage. A 3-D bar chart of the multiplication of the wind load probability table (Fig. 1.7) and the 10-min fatigue damage table (Fig. 1.8) are shown in Fig. 1.9. As shown in Fig. 1.9, in this case the distribution of the multiplication is more close to that of the wind load probability table. The large multiplication values are clustered at the mild wind conditions. The reason is that the magnitude of probability at the extreme wind conditions is much smaller than that at the mild wind conditions. For example, $P_{VI} = 0.0453$ when $V_{10} = 7$ m/s, $I_{10} = 0.22$, while $P_{VI} = 2.27E - 36$ when $V_{10} = 17$ m/s, $I_{10} = 1$
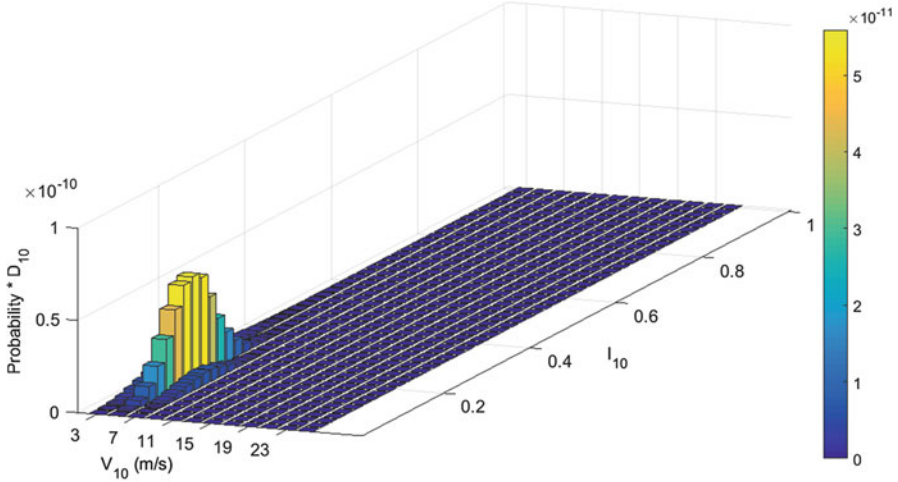
Fig. 1.9 A 3-D bar chart of the multiplication of a wind load probability table and a 10-min fatigue damage table

in Fig. 1.7. Even though the D_{10} is relatively large at the extreme wind conditions, the multiplication of the probability and the D_{10} is smaller at the extreme wind conditions than that at the mild wind conditions in this case.

In cases that wind load variation in a large spatiotemporal range is not considered, e.g., deterministic design optimization (DDO) only considering the average wind load effect, a mean wind load probability table is generated using the Monte Carlo simulation (MCS) method. The main procedure to calculate the mean wind load probability table is listed below.

1. Generate one million MCS sample sets of (C, k, a, b, τ) based on the identified distributions in Table 1.1. Assume C, k, a, b, and τ are independent.
2. Create one million joint PDFs of V_{10} and I_{10} based on the MCS samples of (C, k, a, b, τ). The joint PDF of V_{10} and I_{10} is shown in Eq. (1.15).
3. Create a wind load probability table based on each joint PDF of V_{10} and I_{10}. The probability value $P_{VI}^{i,j}$ in each cell (corresponding to each combination of v_{10}^i and i_{10}^j in the probability table) is calculated using Eq. (1.18). Thus, one million wind load probability tables can be created using one million joint PDFs of V_{10} and I_{10}.
4. Calculate an average value $\overline{P}_{VI}^{i,j}$ of one million probability values corresponding to the same wind condition v_{10}^i and i_{10}^j. Then use the average value as the probability value in the cell of the mean wind load probability table. Similarly, the mean probability values corresponding to other wind conditions can be obtained. Finally, the mean wind load probability table using one million MCS samples of (C, k, a, b, τ) is obtained.
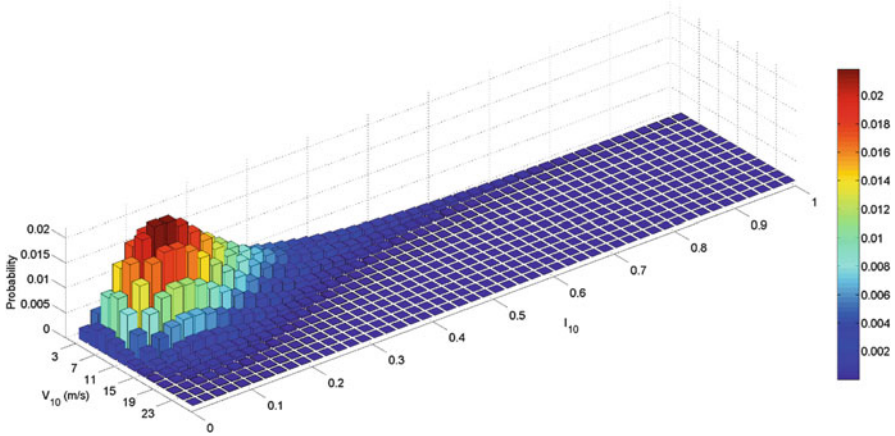
Fig. 1.10 3-D bar chart of the mean wind load probability table

The generated mean wind load probability table based on the identified distributions of (C, k, a, b, τ) in Table 1.1 is schematically shown in Fig. 1.10. As shown in Fig. 1.10, the largest probability value 0.0218 corresponds to $V_{10} = 7$ m/s and $I_{10} = 0.1$. Each cell in the mean wind load probability table contains an averaged probability of one wind load considering the wind load variation in a large spatiotemporal range. The mean wind load probability table essentially represents the average wind load distribution of the variable wind load at large spatiotemporal range.

1.3   Reliability Analysis of Wind Turbine Systems

This section describes the reliability analysis method for wind turbine systems under dynamic wind load uncertainty. The Monte Carlo simulation (MCS) method is used to simulate uncertain wind load based on the developed dynamic wind load uncertainty model. The reliability analysis method using MCS can estimate the probability that a wind turbine could survive 20 years of target lifespan. The reliability analyses at an initial design and a deterministic optimal design have been demonstrated. In addition, results and discussion are provided in this section. The overall procedure to carry out reliability analysis for a given design under wind load uncertainty is shown in Fig. 1.11.
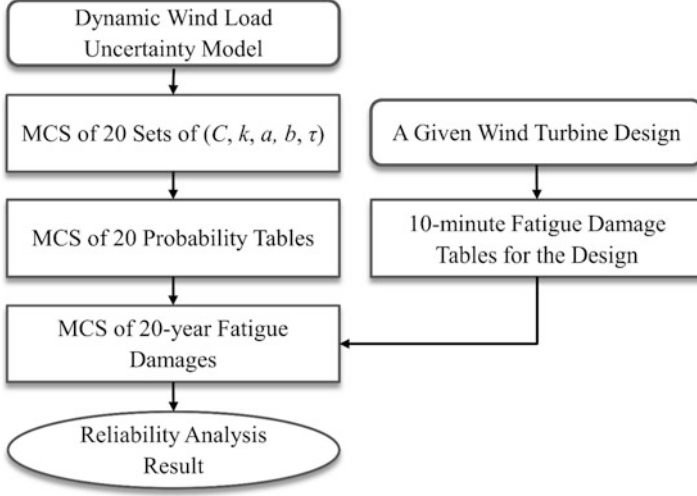
Fig. 1.11 Flowchart of reliability analysis of a wind turbine design under dynamic wind load uncertainty

1.3.1 Reliability Analysis Using Monte Carlo Simulation

In this study, the wind load condition table includes 600 wind load conditions and does not change, as shown in Table 1.2. Thus, the 1-year fatigue damage calculation (Eq. (1.17)) depends only on the wind load probability table and the 10-min fatigue damage table. Furthermore, the wind load probability table is determined by (C, k, a, b, τ), and the 10-min fatigue damage table is determined only by design **d**. Therefore, for a given design **d**, the 1-year fatigue damage is a function of (C, k, a, b, τ) only. Finally, considering the wind load variation in a 20-year range, 20-year fatigue damage at a given design **d** can be calculated as

$$D_{20year}\left(\mathbf{d}; \mathbf{C}, \mathbf{k}, \mathbf{a}, \mathbf{b}, \boldsymbol{\tau}\right) = \sum_{t=1}^{20} D_{1year}^{t}\left(\mathbf{d}, C^{t}, k^{t}, a^{t}, b^{t}, \tau^{t}\right)$$

$$= 52560 \sum_{t=1}^{20} \sum_{i=1}^{12} \sum_{j=1}^{50} P_{VI}^{i,j}\left(v_{10}^{i}, i_{10}^{j}; C^{t}, k^{t}, a^{t}, b^{t}, \tau^{t}\right) D_{10}^{i,j}\left(\mathbf{d}, v_{10}^{i}, i_{10}^{j}\right)$$

$$(1.19)$$

where random vectors **C**, **k**, **a**, **b**, and **τ** contain 20 sets of (C, k, a, b, τ) as $\mathbf{C} = [C^{1}, C^{2}, \ldots, C^{20}]$, $\mathbf{k} = [k^{1}, k^{2}, \ldots, k^{20}]$, $\mathbf{a} = [a^{1}, a^{2}, \ldots, a^{20}]$, $\mathbf{b} = [b^{1}, b^{2}, \ldots, b^{20}]$, and $\boldsymbol{\tau} = [\tau^{1}, \tau^{2}, \ldots, \tau^{20}]$. Hence, there are 100 random parameters in Eq. (1.19). In this study, the random vectors are assumed to be independent. The 20 random parameters in one random vector are also assumed to be independent, which means last year's wind load is independent from this year's.

In Eq. (1.19), the 20-year fatigue damage D_{20year} is also random because the random vectors $\mathbf{C}$, $\mathbf{k}$, $\mathbf{a}$, $\mathbf{b}$, and $\boldsymbol{\tau}$ are random. Consequently, a fatigue failure ($D_{20year} > 1$) in 20 years can be measured with its probability. The probability of fatigue failure cannot be calculated using a sensitivity-based reliability method such as the first-order reliability method (FORM) or the second-order reliability method (SORM) because the sensitivity (gradient) of D_{20year} is not available due to its implicit feature. In this study, the probability of fatigue failure is calculated using a sampling-based reliability method that uses MCS. Using Eq. (1.19) and MCS, the probability of fatigue failure is calculated as

$$
\begin{aligned}
P \left(\text{Fatigue Life} < 20 \text{ years} \right) &= P \left(D_{20year} \left(\mathbf{d}; \mathbf{X} \right) > 1 \right) \\
&= \int_{D_{20year}(\mathbf{d},\mathbf{X})>1} f_{\mathbf{X}} \left(\mathbf{x} \right) d\mathbf{x} \\
&= \int_{\mathbb{R}^N} I_{\Omega_F} \left(\mathbf{x} \right) f_{\mathbf{X}} \left(\mathbf{x} \right) d\mathbf{x} \\
&\cong \frac{1}{NMCS} \sum_{i=1}^{NMCS} I_{\Omega_F} \left[\mathbf{x}^{(i)} \right]
\end{aligned}
\tag{1.20}
$$

where $\mathbf{X} = [\mathbf{C}, \mathbf{k}, \mathbf{a}, \mathbf{b}, \boldsymbol{\tau}]$ and $\mathbf{x}^{(i)}$ is the ith realization of $\mathbf{X}$. It is worth noting that the realization $\mathbf{x}^{(i)}$ is randomly generated based on the PDFs of (C, k, a, b, τ) in Table 1.1. Each realization includes 20 sets of (C, k, a, b, τ). *NMCS* is the number of realizations for MCS. Ω_F is the failure domain such that $D_{20year}(\mathbf{d}; \mathbf{X}) > 1$, and $I_{\Omega_F} (\cdot)$ is an indicator function defined as

$$
I_{\Omega_F} \left(\mathbf{x} \right) = \begin{cases} 1, & \text{for } \mathbf{x} \in \Omega_F \\ 0, & \text{otherwise} \end{cases} .
\tag{1.21}
$$

Though the reliability analysis calculation is straightforward, there are two points that need to be noted. One is that the uncertainty of design variables (e.g., laminate thicknesses of wind turbine blades) due to manufacturing has not been considered in the following reliability analysis examples. Instead, the design variable uncertainty will be discussed in Sect. 1.4. The other is that each MCS realization, which includes 20 sets of (C, k, a, b, τ), represents the wind load variation in 20 years.

1.3.2 Reliability Analysis Examples, Results, and Discussion

The reliability analyses of fatigue in a wind turbine blade at an initial design and an optimal design obtained from the deterministic design optimization (DDO) (Hu et al. 2016a) have been carried out in this section. The blade model at the DDO optimum design, which is used for the reliability analysis, has the same laminate

schedule as the initial design. The detailed laminate schedule, composite material distribution, and blade part composition of the initial and DDO optimum designs are seen in (Hu et al. 2016a, b).

The basic procedure of reliability analysis is explained briefly as follows. The reliability analyses are carried out for all the 60,954 node-section points (Hu et al. 2016a). Fifty thousand realizations of **C**, **k**, **a**, **b**, and **τ** have been generated for reliability analysis. As explained earlier, each realization is 20 sets of (C, k, a, b, τ). Then, 50,000 20-year fatigue damages have been calculated using Eq. (1.19) at each node-section point. The probability of fatigue life smaller than 20 years is then calculated by Eq. (1.20). The largest probability of failure among node-section points associated with one finite element (FE) node is selected as the probability of failure for that FE node. It is noted that all the 10-min fatigue damage tables for 60,954 node-section points have already been obtained in the DDO procedure (Hu et al. 2016a). In this example, the probability tables for 50,000 realizations are generated, and the generation requires only small computational cost. Therefore, the reliability analysis considering only wind load uncertainty is computationally affordable.

The reliability analysis has been carried out on the Linux machine (Dell PowerEdge R720 single server, 8 quad-core Xeon E5–2690 CPUs-32 cores, 2.9 GHz, 256 GB of RAM). Ten cores were used in parallel. Given the 10-min fatigue damage tables of all 60,954 node-section points, the computational time for reliability analyses is about 7 h. It is worth noting that the computational time for generating the 10-min fatigue damage tables of all the node-section points using the same machine is about 14 h. Thus, the total computational time would be about 21 h for a given blade design using the machine.

The probability of fatigue failure contours of the initial design and the DDO optimum design is shown in Fig. 1.12. As shown in Fig. 1.12a, the probability of failure of the initial design is 100%, especially at the rear parts of the aft shear web, forward shear web, and spar cap. The reason for the high probability of failure may be that the initial design of these parts is too small, as these parts often endure much larger aerodynamic wind loads than the root part. After the DDO procedure, the design variables associated with the rear parts of the aft shear web, forward shear web, and spar cap are increased by 62.8%, 76.5%, and 54%, respectively (Hu et al. 2016a). The maximum probability of failure of the DDO optimum design is reduced to 49.9%, which occurs at the leading edge. Other areas with high probability of failure are isolated on the root of the blade as shown in Fig. 1.12b.

The reliability analysis results show that there is a significant reduction of the probability of fatigue failure from 100% at the initial design to 49.9% at the DDO optimum design. This indicates that the DDO procedure indeed reduces the probability of failure. However, the probability of failure of the DDO optimum design is still up to 49.9%, which obviously does not satisfy the target reliability requirement. Thus, the reliability-based design optimization (RBDO) is necessary to further improve the fatigue reliability of the wind turbine systems as explained in the following section.
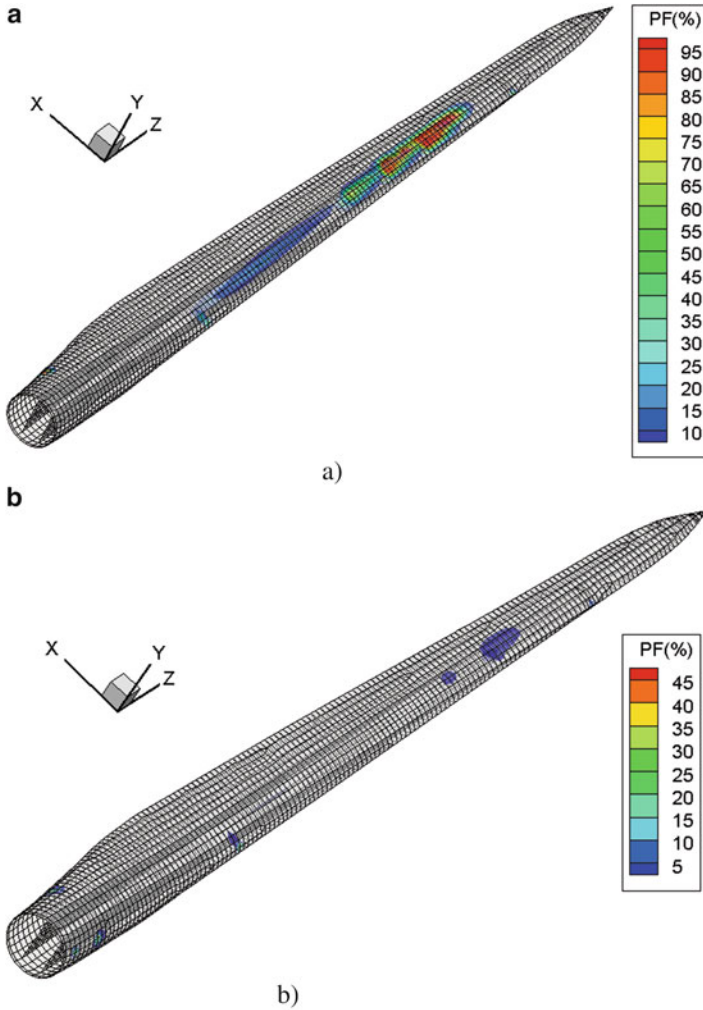
Fig. 1.12 Probability of failure contour of (**a**) the initial design and (**b**) the DDO optimum design

1.4 Reliability-Based Design Optimization of Wind Turbine Systems

The fundamental theory of a sampling-based RBDO method provided in this section lays the foundation to design reliable and economic wind turbine systems in which design sensitivities are often complicated, nonlinear, and implicit. One wind turbine system, rotor blade, is implemented into the RBDO procedure to assure the target reliability under dynamic wind load uncertainty and manufacturing uncertainty. The RBDO case study is elaborated in detail including random design variables,

objective function, probabilistic constraints, and RBDO formulation. The RBDO optimum design obtained using the developed procedure can achieve the target 97.725% reliability for a designed lifespan of 20 years.

1.4.1 Sampling-Based RBDO Theory

1.4.1.1 Reliability Analysis

Reliability analysis is a procedure to calculate the probability of failure of a performance measure. The probability of failure, denoted by P_F, can be calculated using a multidimensional integral as (Madsen et al. 2006)

$$P_F \equiv P\left[G\left(\mathbf{X}\right) > 0\right] = \int_{G(\mathbf{X})>0} f_{\mathbf{X}}\left(\mathbf{x}\right) d\mathbf{x} \qquad (1.22)$$

where $P[\bullet]$ represents a probability measure, $\mathbf{X} = [X_1, X_2, \ldots, X_N]^T$ is an N-dimensional vector of input random variables X_i, $G(\mathbf{X})$ is a performance measure function such that $G(\mathbf{X}) > 0$ is defined as failure, and $f_{\mathbf{X}}(\mathbf{x})$ is a joint probability density function (PDF) of the input random variables. For real engineering problems, it is very difficult to evaluate Eq. (1.22) analytically, because the type of joint PDF is usually not Gaussian (multivariate normal distribution), and the performance measure $G(\mathbf{X})$ is nonlinear and implicit. To solve this kind of problem, there are two approaches: sensitivity-based reliability analysis and sampling-based reliability analysis. The sensitivity-based reliability analysis needs to transform the random variable vector $\mathbf{X}$, which follows a non-Gaussian PDF, into independent standard normal space (U-space) and approximate the nonlinear performance measure by Taylor series expansion in the U-space. The Taylor series expansion requires the sensitivity (gradient) of the performance measure $G(\mathbf{X})$, while the wind turbine performance is a complicated, nonlinear, and implicit function. Thus, it is not suitable to use the sensitivity-based reliability analysis method for the reliability analysis of wind turbine systems. In contrast, the sampling-based reliability analysis does not require the sensitivity of the performance. Instead, it directly uses the Monte Carlo simulation (MCS) method, which applies samples drawn from the input joint PDF $f_{\mathbf{X}}(\mathbf{x})$. Thus, sampling-based reliability analysis is used for the reliability analysis method of wind turbine systems and is explained as follows.

1.4.1.2 Sampling-Based Reliability Analysis

The sampling-based reliability analysis calculates the probability of failure in Eq. (1.22) by applying the MCS method as (Lee et al. 2011a, b)

$$P_F = \int_{G(\mathbf{X})>0} f_{\mathbf{X}}(\mathbf{x}) \, d\mathbf{x} = \int_{\mathbb{R}^N} I_{\Omega_F}(\mathbf{x}) \, f_{\mathbf{X}}(\mathbf{x}) \, d\mathbf{x}$$

$$\cong \frac{1}{NMCS} \sum_{i=1}^{NMCS} I_{\Omega_F}\left[\mathbf{x}^{(i)}\right] \tag{1.23}$$

where $\mathbf{x}^{(i)}$ is the ith realization of $\mathbf{X}$ (ith MCS sample), $NMCS$ is the number of MCS samples, Ω_F is the failure domain such that G($\mathbf{X}$) > 0, and $I_{\Omega_F}(\cdot)$ is an indicator function defined as Eq. (1.21).

Although sampling-based reliability analysis does not require the sensitivity of the performance measure, the accuracy of the calculated probability of failure depends on the number of MCS samples $NMCS$. To calculate an accurate probability of failure, a large number of MCS samples are required. Based on the 95% confidence interval of the estimated probability of failure, the percentage error can be defined as (Haldar and Mahadevan 2000)

$$\varepsilon\% = \sqrt{\frac{\left(1 - P_F^{Tar}\right)}{NMCS \times P_F^{Tar}}} \times 200\% \tag{1.24}$$

where $NMCS$ is the number of MCS samples and P_F^{Tar} is the target probability of failure. Equation (1.24) shows that $NMCS$ should be increased to maintain the accuracy as the target probability of failure reduces. Because real engineering problems may involve expensive computational time, a large number of MCS samples could be unaffordable. In order to solve the computational issue, surrogate models are often used for sampling-based reliability analysis, as well as sampling-based RBDO.

1.4.1.3 Sampling-Based RBDO

The general formulation of an RBDO problem can be expressed as

$$\begin{aligned} \text{minimize} \quad & \text{Cost}(\mathbf{d}) \\ \text{subject to} \quad & P\left[G_j(\mathbf{X}) > 0\right] \leq P_{F_j}^{Tar}, \, j = 1, \ldots, NC \\ & \mathbf{d}^L \leq \mathbf{d} \leq \mathbf{d}^U, \quad \mathbf{d} \in \mathbb{R}^{NDV} \text{ and } \mathbf{X} \in \mathbb{R}^N \end{aligned} \tag{1.25}$$

where $\mathbf{X}$ is the N-dimensional random variable vector, $\mathbf{d}$ is the NDV-dimensional random design variable vector, G_j is the jth constraint function, $P[G_j(\mathbf{X}) > 0]$ is the probability of failure of the jth constraint, $P_{F_j}^{Tar}$ is the target probability of failure of the jth constraint, and NC is the number of constraints. The different dimensionalities of the design variable vector $\mathbf{d}$ and $\mathbf{X}$ is due to the fact that $\mathbf{X}$ contains random parameters, such as C, k, a, b, and τ, in addition to the random design variables. It is noted that a random design variable d_i is the mean μ_j of

the corresponding random variable X_j. Also, standard deviation σ_j of X_j is linearly changing as random design variable d_i changes in this study.

In sampling-based RBDO, the probability of failure used in a probabilistic constraint is directly calculated using Eq. (1.23). The design sensitivity of the probabilistic constraint is derived using the score function and the MCS method (Lee et al. 2011a, b). The design sensitivity is calculated during estimation of the probability of failure using the same MCS samples and constraint function evaluations. Thus, no extra MCS samples are required for calculating the design sensitivity.

Before derivation of the design sensitivity, the following four regularity conditions should be satisfied (Rubinstein and Shapiro 1993; Rahman 2009).

1. The joint PDF $f_{\mathbf{X}}(\mathbf{x};\boldsymbol{\mu},\boldsymbol{\sigma})$ is continuous.
2. The mean $\mu_i \in M_i \subset \mathbb{R}$, $i = 1, \ldots, N$, where M_i is an open interval on $\mathbb{R}$.
3. The partial derivative $\partial f_{\mathbf{X}}(\mathbf{x}; \boldsymbol{\mu}, \boldsymbol{\sigma})/\partial \mu_i$ exists and is finite for all $\mathbf{x}$ and μ_i. In addition, $P_F(\boldsymbol{\mu})$ is a differentiable function of $\boldsymbol{\mu}$.
4. There exists a Lebesgue integrable dominating function $r(\mathbf{x})$ for all $\boldsymbol{\mu}$ such that

$$\left| h(\mathbf{x}) \frac{\partial f_{\mathbf{X}}(\mathbf{x}; \boldsymbol{\mu}, \boldsymbol{\sigma})}{\partial \mu_i} \right| \leq r(\mathbf{x}) \tag{1.26}$$

where $h(\mathbf{x})$ is a general function and can be $I_{\Omega_F}(\mathbf{x})$.

With the four conditions satisfied, taking the partial derivative of Eq. (1.23) with respect to d_i yields

$$
\begin{aligned}
\frac{\partial P_F(\boldsymbol{\mu})}{\partial d_i} &= \frac{\partial}{\partial d_i} \int_{\mathbb{R}^N} I_{\Omega_F}(\mathbf{x}) f_{\mathbf{X}}(\mathbf{x}; \boldsymbol{\mu}, \boldsymbol{\sigma}) \, d\mathbf{x} \\
&= \int_{\mathbb{R}^N} I_{\Omega_F}(\mathbf{x}) \frac{\partial f_{\mathbf{X}}(\mathbf{x}; \boldsymbol{\mu}, \boldsymbol{\sigma})}{\partial d_i} d\mathbf{x} \\
&= \int_{\mathbb{R}^N} I_{\Omega_F}(\mathbf{x}) \frac{\partial \ln f_{\mathbf{X}}(\mathbf{x}; \boldsymbol{\mu}, \boldsymbol{\sigma})}{\partial d_i} f_{\mathbf{X}}(\mathbf{x}; \boldsymbol{\mu}) \, d\mathbf{x} \\
&= E\left[I_{\Omega_F}(\mathbf{x}) \frac{\partial \ln f_{\mathbf{X}}(\mathbf{x}; \boldsymbol{\mu}, \boldsymbol{\sigma})}{\partial d_i} \right]
\end{aligned}
\tag{1.27}
$$

The partial derivative of the log function of the joint PDF in Eq. (1.27) with respect to d_i is called the first-order score function for d_i and is denoted as

$$s_{d_i}^{(1)}(\mathbf{x}; \boldsymbol{\mu}, \boldsymbol{\sigma}) \equiv \frac{\partial \ln f_{\mathbf{X}}(\mathbf{x}; \boldsymbol{\mu}, \boldsymbol{\sigma})}{\partial d_i} \tag{1.28}$$

As shown in Eq. (1.27), the design sensitivity using the first-order score function does not depend on the sensitivity of the constraint function G(**X**). Instead, it can be analytically obtained using the score function in Eq. (1.28). The reason is well

Fig. 1.13 Design sensitivity
for sampling-based RBDO
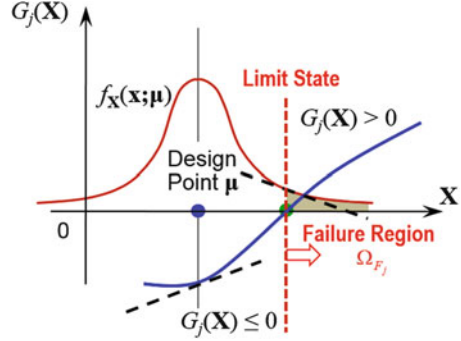
illustrated in Fig. 1.13. As shown in Fig. 1.13, the horizontal axis is the random
vector, and the vertical axis represents the jth constraint $G_j(\mathbf{X})$. The failure region
of the constraint is set as $G_j(\mathbf{X}) > 0$, and the gray area in Fig. 1.13 represents
the probability of failure. When the random design variable $\mathbf{d}$ changes in the
optimization process, the constraint function $G_j(\mathbf{X})$ holds its position, whereas the
joint PDF $f_{\mathbf{X}}(\mathbf{x}; \boldsymbol{\mu}, \boldsymbol{\sigma})$ moves along with the random design variable. Consequently,
the gray area, i.e., the probability of failure, changes as the random design variable
changes. The rate of the probability of failure change is the same as the rate of the
gray area change, which depends on the shape (slope) of the PDF on the limit state.
The shape (slope) of the PDF on the limit state is related to the score function. This
is the reason that the design sensitivity of the probabilistic constraint with respect
to random design variable is related to the score function, not the sensitivity of the
constraint function in Eq. (1.27).

In this study, the random design variables and random parameters are assumed
to be independent. For statistically independent random variables, the first-order
score function for d_i in Eq. (1.28) can be expressed with the marginal PDF as
$f_{X_j}\left(x_j; \mu_j, \sigma_j\right)$ as

$$s_{d_i}^{(1)}\left(\mathbf{x}; \boldsymbol{\mu}, \boldsymbol{\sigma}\right) \equiv \frac{\partial \ln f_{\mathbf{X}}\left(\mathbf{x}; \boldsymbol{\mu}, \boldsymbol{\sigma}\right)}{\partial d_i} = \frac{\partial \ln f_{X_j}\left(x_j; \mu_j, \sigma_j\right)}{\partial \mu_j} + \frac{\partial \sigma_j}{\partial \mu_j} \frac{\partial \ln f_{X_j}\left(x_j; \mu_j, \sigma_j\right)}{\partial \sigma_j}$$

$$(1.29)$$

where the random design variable d_i corresponds to the random variable X_j. If the
random variables are statistically correlated, the score function needs to consider
the correction between random variables. Noh et al. used a copula to consider the
correlation between two random variables in RBDO problems (Noh et al. 2009),
and Lee et al. derived the first-order score function of mean μ_j for both independent
and correlated random variables (Lee et al. 2011a). Cho et al. developed the first-
order score functions for fixed coefficient of variation (CoV) problems for both
independent and correlated random variables (Cho et al. 2015).

1.4.2   RBDO of Composite Wind Turbine Blades

1.4.2.1   Random Design Variables

In RBDO, the uncertainty of composite laminate thickness due to the manufacturing process has been considered. Three assumptions are made for uncertainty of laminate thickness due to the manufacturing variability, as explained below.

1. The variability of laminate thickness is assumed to follow normal distribution.
2. The coefficient of variation (CoV) of the laminate thickness is assumed to be the same at different designs. Therefore, standard deviation of the laminate thickness changes linearly as design (thickness) changes. The CoV of the two composite materials used in the blade, QQ1 and P2B, are referred from the SNL/MSU/DOE composite material fatigue database (Mandell and Smaborsky 2014).
3. The randomness of laminate thickness in seven parts of the blade is assumed to be independent. Thus the laminate thicknesses in seven parts are represented by seven independent random variables, respectively.

The current RBDO process starts from a DDO optimum design obtained previously (Hu et al. 2016a). Based on the third assumption above, seven random design variables are used in RBDO. As we consider the manufacturing variability, the laminate thickness becomes random. A random variable transformation is used to bridge the seven RBDO random design variables and the twelve random thickness variables (Hu et al. 2016a). In summary, the properties of random design variables for RBDO are listed in Table 1.5, where μ^L, μ^O, and μ^U are the normalized lower bound, mean, and upper bound of the random design variables in RBDO, respectively. μ^i, $i = 1, 2, \ldots, 7$ are RBDO design variables, each of which is the mean of random design variables.

Table 1.5 Properties of random design variables (Hu et al. 2016a)

Random design variable	Distribution	μ^L	μ^O	μ^U	CoV	Corresponding part	Composite material
μ_1	Normal	0.5010	1	2.0039	0.0323	Root	QQ1
μ_2	Normal	0.5707	1	1.7988	0.0323	Forward shear web	QQ1
μ_3	Normal	1.0000	1	1.8184	0.0323	Aft shear web	QQ1
μ_4	Normal	1.0000	1	4.0000	0.0323	Tip	QQ1
μ_5	Normal	0.4230	1	1.6919	0.0323	Leading edge	QQ1
μ_6	Normal	0.3764	1	1.5057	0.0323	Trailing edge	QQ1
μ_7	Normal	0.3898	1	1.1695	0.0203	Spar cap	P2B

1.4.2.2 Objective Function

The normalized total cost of composite materials that are used in the blade is set as the objective function, which is expressed as

$$
C\left(\boldsymbol{\mu}\right) = \left(4.18 \times 1000 \times \sum_{i}^{6} M_i^0 \frac{\mu_i}{\mu_i^0} + 11.70 \times 1000 \times M_7^0 \frac{\mu_7}{\mu_7^0}\right) \Big/ Cost^{DDO}
$$

(1.30)

where M_i^0 (unit, ton) is the mass of the ith part at the RBDO initial design, i.e., the DDO optimum design; μ_i^0 is the normalized RBDO initial design corresponding to the ith part; μ_i is the current design corresponding to the ith part; $i = 1, 2, \ldots, 7$; and $Cost^{DDO}$ is the RBDO initial cost, i.e., the cost of the DDO optimum design, which is \$125,605 obtained in DDO. According to (TPI Composites 2003), the material costs of QQ1 and P2B are \$4.18/kg and \$11.70/kg, respectively. It is worth noting that the cost of the carbon/glass-hybrid-fiber-reinforced laminate P2B is 2.8 times more expensive than that of QQ1, which is a glass-fiber-reinforced laminate. The objective function in Eq. (1.30) is minimized in the RBDO process.

1.4.2.3 Probabilistic Constraints

The probabilistic constraint is the probability of fatigue failure (fatigue life smaller than 20 years) at a selected hotspot being smaller than a target probability of failure $P_F^{tar} = 2.275\%$. The hotspots for RBDO are the node-section points where probability of fatigue failure is considered as the RBDO constraints. In this study, the event that fatigue life is smaller than 20 years fatigue damage is larger than 1. Thus, the 20-year fatigue damage is calculated first. Considering the manufacturing variability and wind load uncertainty, the 20-year fatigue damage can be calculated as

$$
D_{20year}\left(\mathbf{X}, \mathbf{C}, \mathbf{k}, \mathbf{a}, \mathbf{b}, \boldsymbol{\tau}\right) = \sum_{t=1}^{20} D_{1year}^t \left(\mathbf{X}, C^t, k^t, a^t, b^t, \tau^t\right)
$$

$$
= 52560 \sum_{t=1}^{20} \sum_{i=1}^{12} \sum_{j=1}^{50} P_{VI}^{i,j} \left(v_{10}^i, i_{10}^j; C^t, k^t, a^t, b^t, \tau^t\right)
$$

$$
D_{10}^{i,j}\left(\mathbf{X}, v_{10}^i, i_{10}^j\right)
$$

(1.31)

where $\mathbf{X}$ is a random thickness vector and random vectors $\mathbf{C}$, $\mathbf{k}$, $\mathbf{a}$, $\mathbf{b}$, and $\boldsymbol{\tau}$ contain 20 sets of (C, k, a, b, τ) as $\mathbf{C} = [C^1, C^2, \ldots, C^{20}]$, $\mathbf{k} = [k^1, k^2, \ldots, k^{20}]$, $\mathbf{a} = [a^1, a^2, \ldots, a^{20}]$, $\mathbf{b} = [b^1, b^2, \ldots, b^{20}]$, and $\boldsymbol{\tau} = [\tau^1, \tau^2, \ldots, \tau^{20}]$. The realizations of

random vectors can be randomly drawn from the obtained PDFs of C, k, a, b, and τ (Table 1.1 in Sect. 1.2.2).

In this study, the probability of fatigue failure is calculated using a sampling-based reliability analysis introduced in Sect. 1.4.1. Using Eq. (1.31) and MCS, the probability of fatigue failure is calculated as

$$P \text{ (Fatigue Life} < 20 \text{ years)} = P\left(D_{20year}(\mathbf{Y}) > 1\right) = \int_{D_{20year}(\mathbf{Y})>1} f_{\mathbf{Y}}(\mathbf{y})\, d\mathbf{y}$$

$$= \int_{\mathbb{R}^N} I_{\Omega_F}(\mathbf{y})\, f_{\mathbf{Y}}(\mathbf{y})\, d\mathbf{y} \cong \frac{1}{NMCS} \sum_{i=1}^{NMCS} I_{\Omega_F}\left[\mathbf{y}^{(i)}\right] \tag{1.32}$$

where $\mathbf{Y} = [\mathbf{X}, \mathbf{C}, \mathbf{k}, \mathbf{a}, \mathbf{b}, \tau]$ and $\mathbf{y}^{(i)}$ is the ith realization of $\mathbf{Y}$. It is worth noting that the realization $\mathbf{y}^{(i)}$ is randomly generated based on the PDF of a random thickness vector $\mathbf{X}$ and the PDFs of random parameters (C, k, a, b, τ) in the dynamic wind load uncertainty model. The mean of the random thickness vector $\mathbf{X}$ is the random design vector $\boldsymbol{\mu}$ in RBDO. Each realization $\mathbf{y}^{(i)}$ includes 20 sets of (C, k, a, b, τ), which represent the wind load variation in 20 years. $NMCS$ is the number of realizations for MCS. Ω_F is the failure domain such that $D_{20year}(\mathbf{Y}) > 1$, and I_{Ω_F} is an indicator function defined as

$$I_{\Omega_F}(\mathbf{y}) = \begin{cases} 1, & \text{for } \mathbf{y} \in \Omega_F \\ 0, & \text{otherwise} \end{cases} \tag{1.33}$$

By using Eqs. (1.31) and (1.32), the probabilistic constraints can be expressed as

$$P\left(D_{20year}^j(\mathbf{Y}) > 1\right) \leq P_{F_j}^{\text{tar}} = 2.275\%, \qquad j = 1, \ldots, NC \tag{1.34}$$

where NC is the number of probabilistic constraints.

In order to accurately carry out RBDO with affordable computational time, two issues need to be addressed. The first issue is that the hotspots for RBDO probabilistic constraints need to be carefully selected. By using enough hotspots, the RBDO optimum design obtained in the future could guarantee that all the node-section points in the blade model satisfy the 2.275% target probability of failure requirement. However, too many hotspots increase the computational cost. The second issue is that the 20-year fatigue damage in Eq. (1.31) needs to be accurately and efficiently calculated, so that the probability of failure calculation in Eq. (1.32) will be accurate and efficient. Three hotspot selection criteria are developed to resolve the first issue, and the second issue that the 20-year fatigue damage needs to be accurately and efficiently calculated is well addressed by using local surrogate models of 10-min fatigue damages (Hu et al. 2016b).

1.4.2.4 RBDO Formulation

In summary, the RBDO problem can be formulated as

$$
\begin{aligned}
&\text{minimize} && C(\boldsymbol{\mu}) \\
&\text{subject to} && P\left(D_{20year}^{j}(\mathbf{Y}) > 1\right) \le P_{F_j}^{\text{tar}} = 2.275\%, \qquad j = 1, \ldots, n \quad (1.35) \\
& && \boldsymbol{\mu}^{L} \le \boldsymbol{\mu} \le \boldsymbol{\mu}^{U}, \quad \boldsymbol{\mu} \in \mathbb{R}^{7} \text{ and } \mathbf{Y} \in \mathbb{R}^{107}
\end{aligned}
$$

where $\mathbf{Y}$ is the 107-dimensional random vector including seven random thickness variables and 20 sets of (C, k, a, b, τ), $\boldsymbol{\mu}$ is the seven-dimensional random design variable vector, $C(\boldsymbol{\mu})$ is the normalized cost as shown in Eq. (1.30), and D_{20year}^{j} is the 20-year fatigue damage for the jth probabilistic constraint $P(D_{20year}^{j}(\mathbf{Y}) > 1) \le P_{F_j}^{tar}$. Figure 1.14 shows a schematic picture of the RBDO process of composite wind turbine blades.

1.4.2.5 RBDO Results and Discussion

The RBDO process has been carried out on the Linux machine (Dell PowerEdge R720 single server, 8 quad-core Xeon E5–2690 CPUs-32 cores, 2.9 GHz, 256 GB of RAM). Fifteen cores were used in parallel. The entire RBDO process has 12 design iterations, 12 line searches, and 4 episodes of hotspot checking. Each design iteration or line search requires one set of local surrogate models and one reliability analysis. Thus, 25 sets of local surrogate models have been generated, including one set for the RBDO initial design. Accordingly, there are 25 reliability analyses for the RBDO initial design and designs at 12 iterations and 12 line searches. It takes about 16 h to generate one set of local surrogate model and 3 h for one reliability analysis. The computational time is about 15 h for checking hotspots at one design. The total computational time for the entire RBDO process is about 535 h (22.3 days).

Table 1.6 provides detailed histories of random design variables, normalized cost (objective function), true cost, mass, and the maximum probability of failure. As shown in Table 1.6, the maximum probability of fatigue failure has been reduced from 50.06% at the RBDO initial design to 2.28% at the RBDO optimum design, while the cost is only increased by 3.01%. In spite of the little cost increase, the mass of the RBDO optimum design is increased by 10.95% compared to that of the RBDO initial design. The reason for the large increase in mass is that more cheap but heavy composite material, QQ1, is applied at the RBDO optimum design than at the RBDO initial design. Meanwhile, the expensive composite material, which is P2B corresponding to the random design variable μ_7, at the RBDO optimum design is used 13.33% less than at the RBDO initial design. The hotspots are checked at four designs, which correspond to iterations 0, 4, 8, and 12 highlighted in bold in Table 1.6.
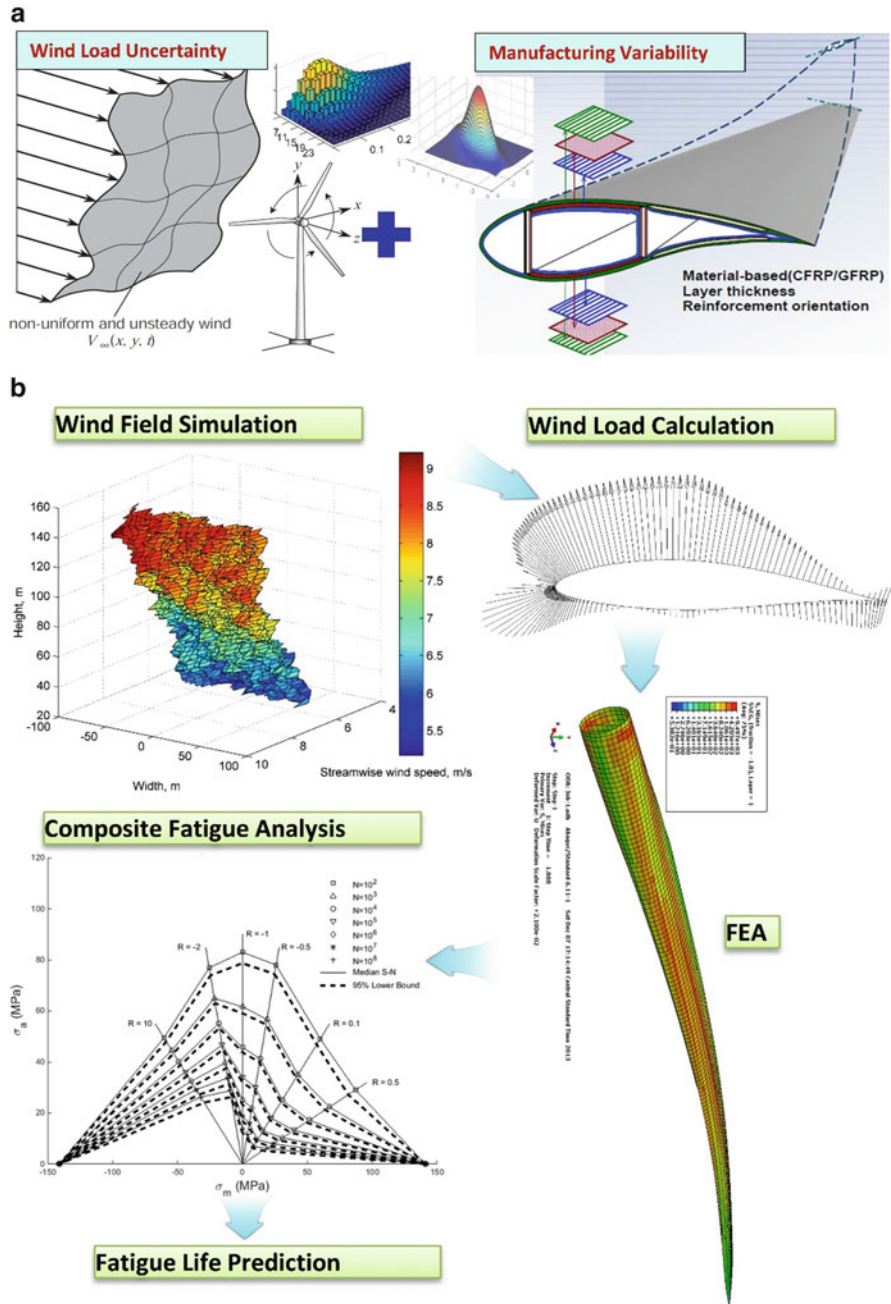
Fig. 1.14 RBDO of composite wind turbine blades for fatigue life under dynamic wind load uncertainty. (**a**) Dynamic wind load uncertainty and manufacturing variability modeling; (**b**) Deterministic blade fatigue analysis procedure; (**c**) RBDO procedure (see next page)
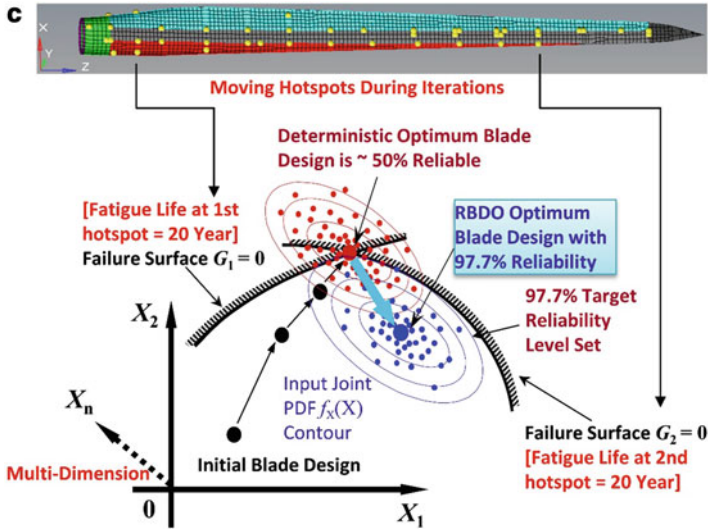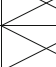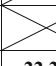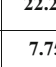
Fig. 1.14 (continued)

Table 1.7 provides the history of probability of failure of each probabilistic constraint. The maximum probability of failure at each iteration is highlighted in bold. As shown in Table 1.7, the probabilistic constraint with the maximum probability of failure is changing as the design iteration proceeds, which indicates the most probable fatigue failure location is changing as the design changes. The probabilistic constraint 9 has no results of probability of failure at iterations 0, 1, 2, and 3 because the corresponding hotspot was not identified until checking the hotspots at the fourth design iteration. The largest probability of failure at the RBDO optimum design occurs at the probabilistic constraint 3. In order to distinguish the probabilities of failure at the last iteration, three decimal places are used for the probabilities of failure at the last iteration.

Table 1.8 compares the laminate thickness, true cost, mass, and probability of failure of three designs: the initial design, the DDO optimum design, and the RBDO optimum design. As shown in Table 1.8, at the RBDO optimum design, the laminate thicknesses t_4, t_7, and t_8 corresponding to forward shear panels 10–13, aft shear web panels 9–12, and aft shear web panels 13–16, respectively, are significantly increased by 155.75%, 221%, and 100%, respectively, compared to those at the initial design. Along the direction from root to tip, the blade becomes thinner and thinner, which makes the two shear webs inside the blade shell decrease the height significantly close to the blade tip. Thus, a much thicker rear part of the two shear webs is necessary in order to keep the shear webs stiff, which makes the blade more fatigue reliable. This explains why the laminate thicknesses t_4, t_7, and t_8 are significantly increased. Table 1.8 also shows that the laminate thicknesses, for example, t_5 and t_6, are decreased from the initial design to the DDO optimum design

Table 1.6 RBDO histories of random design variables, normalized cost, true cost, mass, and the maximum probability of failure

Iteration	Random design variables							Normalized cost	True cost ($)	Mass (ton)	Maximum probability of failure (%)
	μ_1	μ_2	μ_3	μ_4	μ_5	μ_6	μ_7				
0	1.0000	1.0000	1.0000	1.0000	1.0000	1.0000	1.0000	1.0000	125605.49	21.8050	50.06
1	1.0644	1.1397	1.0414	1.0000	1.0455	1.0288	1.0163	1.0316	129576.55	22.5735	12.78
2	1.0933	1.3309	1.1619	1.0000	1.0498	1.0410	0.9986	1.0424	130935.77	23.0962	5.86
3	1.1060	1.4853	1.3095	1.0205	1.0485	1.0455	0.9650	1.0407	130721.00	23.4183	3.29
4	1.1162	1.5568	1.4252	1.0645	1.0566	1.0472	0.9508	1.0440	131130.63	23.6742	22.22
5	1.1175	1.5434	1.4483	1.0783	1.0601	1.0718	0.9399	1.0430	131011.32	23.7669	7.75
6	1.1195	1.5430	1.5127	1.1182	1.0644	1.0862	0.9252	1.0410	130750.47	23.8683	3.67
7	1.1231	1.5462	1.7120	1.2414	1.0770	1.1130	0.8850	1.0344	129926.80	24.1181	2.93
8	1.1305	1.5827	1.8184	1.3069	1.1027	1.1067	0.8588	1.0280	129127.31	24.2184	2.51
9	1.1296	1.5885	1.8184	1.3001	1.0986	1.0977	0.8620	1.0281	129139.96	24.1862	2.40
10	1.1313	1.5850	1.8184	1.3021	1.1035	1.0931	0.8650	1.0293	129284.61	24.1869	2.31
11	1.1328	1.5741	1.8184	1.2983	1.1124	1.0914	0.8662	1.0298	129346.03	24.1883	2.30
12	1.1333	1.5708	1.8184	1.2990	1.1148	1.0913	0.8667	1.0301	129384.14	24.1917	2.28

Table 1.7 History of probability of failure of each probabilistic constraint

Probability of Failure (%)		Probabilistic Constraints									
		1	2	3	4	5	6	7	8	9	10
Iterations	0	0	0.36	5.18	0	**50.06**	49.10	18.75	49.37		48.74
	1	0	0.22	3.05	0	1.52	**12.78**	7.97	12.47		12.38
	2	0	0.17	2.55	0	0.02	**5.86**	4.02	4.76		4.91
	3	0	0.18	2.52	0	0.00	**3.29**	2.81	2.80		2.99
	4	0	0.15	2.19	0	0.00	2.39	2.22	2.40	**22.22**	2.41
	5	0	0.16	2.25	0	0.01	2.30	2.27	0.56	**7.75**	2.42
	6	0	0.16	2.26	0	0.02	2.29	2.27	0.21	**3.67**	2.45
	7	0	0.14	2.25	0	1.62	2.37	2.25	0.03	0.66	**2.93**
	8	0	0.15	**2.51**	0	2.39	0.52	2.30	0.02	0.81	2.28
	9	0	0.15	**2.40**	0	2.39	0.66	2.24	0.05	1.58	2.37
	10	0	0.15	**2.31**	0	2.30	0.53	2.23	0.07	2.15	2.29
	11	0	0.15	**2.30**	0	2.25	0.34	2.27	0.08	2.27	2.28
	12	0	0.144	**2.281**	0	2.262	0.304	2.279	0.076	2.265	2.277

but increased from the DDO optimum design to the RBDO optimum design, in order to satisfy the target 2.275% probability of failure requirement. The laminate thickness in spar cap, which is made of expensive composite material P2B, is decreased by 13.51% from the DDO optimum design to the RBDO optimum design in order to minimize the cost.

The mass distributions of the initial design, the DDO optimum design, and the RBDO optimum design have been studied. Table 1.9 compares the mass of each part in the blade model. As shown in Table 1.9, the DDO procedure significantly increases the mass of the trailing edge and the spar cap by 24.31% and 53.91%, respectively, in order to satisfy the 20-year fatigue life constraint. The RBDO procedure significantly increases the mass of the forward shear web and the aft shear web by 46.38% and 62.20%, respectively, while the mass of the spar cap is reduced by 13.33% through the RBDO procedure. This finding indicates that the two shear webs play important role in fatigue reliability of the blade. By enhancing the two shear webs, the thickness of the spar cap, which is made of expensive composite material P2B, can be reduced in order to decrease the total cost. The total mass of the DDO optimum design and the RBDO are increased by 17.88% and 30.78%, respectively, comparing that of the initial design. The reasons of the significant increment of the total mass may be that:

Table 1.8 Comparison of the initial design, the DDO optimum design, and the RBDO optimum design

Laminate thickness (mm)	Corresponding panel	Initial design	DDO optimum design	RBDO optimum design
t_1	Root	4	3.99	4.52
t_2	Forward shear panels 1–5	4	3.50	5.50
t_3	Forward shear panels 6–9	4	4.45	6.99
t_4	Forward shear panels 10–13	4	6.51	**10.23**
t_5	Aft shear web panels 1–4	4	2.00	3.64
t_6	Aft shear web panels 5–8	4	2.00	3.64
t_7	Aft shear web panels 9–12	4	7.06	**12.84**
t_8	Aft shear web panels 13–16	4	4.40	**8.00**
t_9	Tip	4	2.00	2.60
t_{10}	Leading edge	4	4.73	5.27
t_{11}	Trailing edge	4	5.31	5.80
t_{12}	Spar cap	2.5	3.85	3.33
True cost ($)		95494.42	125605.49	129384.14
Mass (ton)		18.4981	21.8048	24.1918
Probability of failure (%)		100	50.06	2.28

Table 1.9 Comparison of part mass of the initial design, the DDO optimum design, and the RBDO optimum design

	Part mass (ton)		
Part name	Initial design	DDO optimum design	RBDO optimum design
Root	1.5246	1.5217	1.7245
Forward shear web	2.1122	2.1400	**3.1326**
Aft shear web	2.4529	1.9422	**3.1503**
Tip	0.2230	0.1115	0.1448
Leading edge	2.4673	2.8191	3.0814
Trailing edge	5.7002	**7.0862**	7.5984
Spar cap	4.0180	**6.1840**	**5.3598**
Total mass (ton)	18.4981	21.8048	24.1918

1. The composite material QQ1 is too heavy to be used in the blade model.
2. The defined laminate schedule in the blade model may not be an optimal laminate schedule.
3. The assumed constant life diagram (CLD) in shear direction may be too conservative comparing to the true CLD in shear direction.
4. The objective function of both DDO and RBDO only considers the total cost of composite materials. The optimization procedure tends to apply more heavy but cheap material QQ1, instead of light but expensive material P2B, in order to minimize the cost.

The total mass is an important factor when designing wind turbine blades. It is not only related to the material cost but also affects the blade transportation, energy generation, and blade control. For designing a cost-effective, reliable, and light wind turbine blade, optimization problem could use a multi-objective function including both the mass and the cost and subject to probabilistic constraints. This work may be carried out in the future.

Table 1.10 compares section mass in the spanwise direction of the initial design, the DDO optimum design, and the RBDO optimum design. Figure 1.15 clearly shows the distributed section mass in the spanwise direction of the above three designs, as well as the 5-MW NREL reference wind turbine blade (Jonkman et al. 2009). The larger section mass of the DDO optimum design and the RBDO optimum design comparing that of the 5-MW NREL reference wind turbine blade could also be because of the above four points.

One question about the obtained RBDO optimum design is that are all the node-section points at the RBDO optimum design satisfying the target reliability requirement when considering both wind load uncertainty and manufacturing variability? The difficulty to solve this question is that it is very computationally expensive to carry out reliability analysis for all node-section points considering both wind load uncertainty and manufacturing variability. On the other side, it is affordable to check the probability of failure only considering wind load uncertainty and to calculate 1-year fatigue damage under the mean wind load for all node-section pints, as explained in Sect. 1.3. Moreover, by studying the results of the probability of failure considering only wind load uncertainty and the results of the 1-year fatigue damage under the mean wind load, it is possible to see if there are any missing node-section points which may violate the target reliability requirement when considering both wind load uncertainty and manufacturing variability. Details are explained as follows.

Both the probability of failure considering only wind load uncertainty and the 1-year fatigue damage under the mean wind load for all node-section points at the RBDO optimum design have been calculated. Table 1.11 provides the probability of failure PF_{wind} considering only wind load uncertainty, the probability of failure $PF_{wind + manu}$ considering both wind load uncertainty and manufacturing variability (surrogate models for 10-min fatigue damage are used), and the 1-year fatigue damage under the mean wind load at the selected ten hotspots. In order to study the fatigue effect due to different load types, i.e., wind load, gravity load, and

Table 1.10 Comparison of blade section mass of the initial design, the DDO optimum design, and the RBDO optimum design

Section ID	Section width (m)	Blade span	Section Mass (ton)			Section Mass Density (kg/m)		
			Initial design	DDO optimum design	RBDO optimum design	Initial design	DDO optimum design	RBDO optimum design
1	2.7333	0.022	2.0380	1.9013	2.2922	745.6291	695.6097	838.6171
2	2.7333	0.067	1.6483	1.7733	2.0501	603.0344	648.7656	750.0545
3	2.7333	0.111	1.5611	1.7082	1.9556	571.1488	624.9563	715.4619
4	4.1000	0.167	2.4718	2.8557	3.1502	602.8756	696.5107	768.3363
5	4.1000	0.233	2.0328	2.4036	2.6069	495.7976	586.2532	635.8205
6	4.1000	0.300	1.4220	1.7081	1.8367	346.8200	416.6032	447.9715
7	4.1000	0.367	1.2988	1.5844	1.6791	316.7907	386.4347	409.5285
8	4.1000	0.433	1.1972	1.4790	1.5480	292.0105	360.7259	377.5529
9	4.1000	0.500	1.0975	1.4973	1.6432	267.6793	365.1954	400.7856
10	4.1000	0.567	0.9171	1.2806	1.4239	223.6918	312.3376	347.2886
11	4.1000	0.633	0.7514	1.0430	1.1696	183.2579	254.4022	285.2758
12	4.1000	0.700	0.5874	0.8082	0.9190	143.2674	197.1119	224.1487
13	4.1000	0.767	0.5221	0.6889	0.7494	127.3410	168.0162	182.7750
14	4.1000	0.833	0.4365	0.5793	0.6043	106.4681	141.2854	147.3954
15	2.7333	0.889	0.2622	0.3490	0.3628	95.9165	127.6862	132.7236
16	2.7333	0.933	0.1950	0.1155	0.1626	71.3273	42.2498	59.4857
17	2.7333	0.978	0.0590	0.0295	0.0383	21.5856	10.7928	14.0193
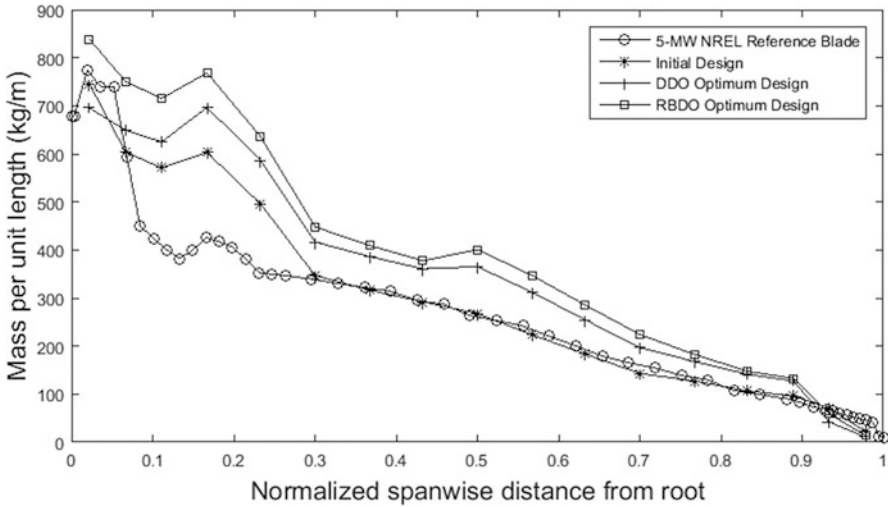
Fig. 1.15 Comparison of sectional mass distribution

centrifugal load, the 1-year fatigue damage due to wind load, gravity load, and centrifugal load is also calculated. In Table 1.11, the $D_{1year\text{-}wind}$, $D_{1year\text{-}gravity}$, and $D_{1year\text{-}centrifugal}$ indicate that only aerodynamic wind load, gravity load, and centrifugal load, respectively, are applied when calculating 10-min fatigue damage. The D_{1year} in Table 1.11 indicates that all three kinds of load are applied when calculating 10-min fatigue damage. For each case, the mean wind load probability table is used to calculate the 1-year fatigue damage. Some interesting findings extracted from Table 1.11 are listed below.

1. The probability of failure considering both wind load uncertainty and manu-facturing variability is either larger than or equal to the probability of failure considering only wind load uncertainty. The larger probability of failure con-sidering both wind load uncertainty and manufacturing variability is due to that the manufacturing variability introduces design uncertainty, which increases the probability of failure. The equal probability of failure occurs at two hotspots, node 61-section point 15 and at node 1167-section point 3, which have 0 probability of failure due to very small fatigue damage as indicated in Table 1.11. For these two hotspots, the RBDO optimum design is in a very safe region, and the introduction of manufacturing variability does not increase the probability of failure at all.
2. The node-section points, for which the wind load dominates the overall fatigue damage, have probability of failure considering both wind load uncertainty and manufacturing variability close to that considering only wind load uncertainty.

Table 1.11 Probability of failure and 1-year fatigue damage of the ten hotspots at the RBDO optimum design

Probabilistic constraint	Nodal ID	Section point ID	PF_{wind} (%)	$PF_{wind + manu.}$ (%)	D_{1year}	$D_{1year\text{-}wind}$	$D_{1year\text{-}gravity}$	$D_{1year\text{-}centrifugal}$
1	61	15	0	0	$1.5069E-04$	$8.1900E-09$	$1.2625E-06$	0
2	1074	9	0.142	0.144	$1.7648E-03$	$1.7060E-03$	$6.2187E-14$	0
3	1099	9	2.030	2.281	$2.2703E-02$	$2.0688E-02$	$7.9918E-32$	0
4	1167	3	0	0	$2.8135E-09$	$2.8780E-09$	$2.5181E-18$	0
5	**1582**	**9**	0.032	2.262	$4.2083E-02$	$3.3417E-06$	$3.8250E-04$	0
6	1988	15	0	0.304	$3.2140E-02$	$1.1997E-08$	$8.4981E-04$	0
7	2297	1	2.190	2.279	$9.2256E-03$	$1.0096E-02$	$3.6445E-14$	0
8	2644	1	0	0.076	$3.2918E-02$	$3.4867E-13$	$1.9853E-03$	0
9	**2657**	**15**	0.010	2.265	$3.6132E-02$	$7.2627E-10$	$3.1032E-04$	0
10	**2887**	**1**	0	2.277	$2.9686E-02$	$2.2233E-09$	$1.0124E-03$	0

For example, the wind load dominates the fatigue damage at node 1074-section point 9 as shown in Table 1.11. The $PF_{\text{wind} + \text{manu}}$ is close to PF_{wind} at this hotspot. The reason of the closed probability of failure is that the introduction of manufacturing variability has nonsignificant influence on the probability of failure calculation since the wind load dominates the overall fatigue damage. This finding also holds true for node 1099-section point 9 and node 2297-section point 1 as shown in Table 1.11.

3. The node-section points, for which the gravity load dominates the overall fatigue damage, may have much larger probability of failure considering both wind load uncertainty and manufacturing variability than that considering only wind load uncertainty. The reason is that manufacturing variability is directly related to the gravity load uncertainty. By introducing the manufacturing variability for gravity load-dominated node-section points, the probability of failure may increase significantly due to the gravity load uncertainty. For example, the gravity load-dominated hotspots, node 1582-section point 9, node 2657-section point 15, and node 2881-section point 1 in Table 1.11, have much larger $PF_{\text{wind} + \text{manu}}$ than PF_{wind}.

Among the probabilities of failure of all node-section points considering only wind load uncertainty, the largest probability of failure is 2.19% and occurs at node 2297-section point 1. Thus, there is no node-section point at the RBDO optimum design violating the target probability of failure if only wind load uncertainty is considered. It is also found that node 1582-section point 9, node 2657-section point 15, node 2644-section point 1, and node 1988-section point 15 are top four gravity load-dominated node-section points among all node-section points by ordering 1-year fatigue damage. These four node-section points have already been selected as hotspots. In addition, another four node-section points are selected at the RBDO optimum design to calculate the probability of failure considering both wind load uncertainty and manufacturing variability. The four node-section points are not close to any selected hotspots. The 1-year fatigue damages corresponding to the four node-section points are among the top 50 large 1-year fatigue damages of all node-section points. In order to calculate the probability of failure, the surrogate models for 10-min fatigue damages of the four node-section points are generated first. Then, the probability of failure considering both wind load uncertainty and manufacturing variability is calculated using the surrogate models. The probability of failure and 1-year fatigue damage of the additional four node-section points are shown in Table 1.12. As shown in Table 1.12, all of the additional tested four node-section points satisfy the target 2.275% probability of failure considering both wind load uncertainty and manufacturing variability.

In summary, all of the node-section points at the RBDO optimum design satisfying the target reliability requirement when considering both wind load uncertainty and manufacturing variability.

Table 1.12 Probability of failure and 1-year fatigue damage of the four selected node-section points at the RBDO optimum design

Nodal ID	Section point ID	PF_{wind} (%)	$PF_{wind + manu.}$ (%)	D_{1year}	$D_{1year-wind}$	$D_{1year-gravity}$	$D_{1year-centrifugal}$
1572	9	0	0.0005	$1.7646E - 02$	$1.2086E - 05$	$1.2990E - 04$	0
1961	12	0	0.0055	$2.5300E - 02$	$2.3344E - 08$	$1.2439E - 03$	0
2527	3	0	0	$2.7234E - 02$	$5.6960E - 11$	$2.4691E - 04$	0
2872	1	0	0.0045	$1.7703E - 02$	$3.1586E - 10$	$1.4755E - 04$	0

1.5   Conclusions and Future Recommendations

1.5.1   Conclusions

A dynamic wind load uncertainty model has been developed using 249 groups of measured wind data. The wind load uncertainty model involves both the annual wind load variation and the wind load variation in a large spatiotemporal range. The annual wind load variation is represented by the joint probability density function (PDF) of V_{10} and I_{10}. In order to properly represent the joint PDF of V_{10} and I_{10}, the marginal distributions and copula types (correlation) for V_{10} and 10-min standard deviation of wind speed Σ_{10} have been studied. Based on the 249 groups of measured wind data, the best fit marginal distribution types of V_{10} and Σ_{10} are identified to be Weibull distribution and gamma distribution, respectively. The best copula type for V_{10} and Σ_{10} is also identified as Gumbel. The joint PDF of V_{10} and I_{10} is derived from the joint PDF of V_{10} and Σ_{10}. The wind load variation in a large spatiotemporal range is represented by the PDFs of five parameters C, k, a, b, and τ, which determine the joint PDF of V_{10} and I_{10}. Using the 249 sets of (C, k, a, b, τ), the best fit PDFs of C, k, a, b, and τ are identified to be log-logistic distribution, normal distribution, generalized extreme value distribution, Weibull distribution, and extreme value distribution, respectively. Using two different sets of (C, k, a, b, τ), a case study has been carried out to predict the fatigue damage of the developed composite wind turbine blade. One case study result shows that the calculated maximum 1-year fatigue damage using one set of (C, k, a, b, τ) is 5.32 times larger than that when the other set is used. This finding confirms that the wind load variation in the lifespan of wind turbine blades plays a critical role in blade fatigue analysis and that the uncertain wind load must be considered in the fatigue reliability analysis of wind turbines.

The reliability analysis method under wind load uncertainty is then proposed using the sampling-based reliability analysis method. The MCS method simulates uncertain wind load using the proposed wind load uncertainty model. The reliability analysis estimates the probability that a wind turbine could survive 20 years of target lifespan. The reliability analyses of the initial wind turbine blade design and the DDO optimum design are taken as examples. The reliability analysis has been carried out for all 60,954 node-section points of the blade. Thus the probability of failure of each node-section point is obtained. Detailed probability of failure contours have been obtained for both the initial design and the DDO optimum design. Using the probability of failure contour, the largest probability of failure can be located. The reliability analysis results show that the probability of failure considering only wind load uncertainty is reduced from 100% at the initial design to 49.9% at the DDO optimum design, which indicates that the DDO procedure indeed reduces the probability of failure. However, the high probability of failure (49.9%) at the DDO optimum design also indicates that RBDO is necessary to further improve the fatigue reliability of the composite wind turbine blade.

Finally, the RBDO procedure for composite wind turbine blades considering both wind load uncertainty and manufacturing variability is developed. The wind load uncertainty model could provide realistic uncertain wind load through the designed 20-year lifespan. The fundamental theories of sampling-based RBDO with fixed coefficient of variation (CoV) are reviewed. The 12 random thickness variables are linked to seven random design variables by using the DDO optimum design result. The RBDO objective function is normalized cost based on true cost at the DDO optimum design. The probabilistic constraints are probability of fatigue failure at the selected hotspots. During the RBDO iterations, local surrogate models of 10-min fatigue damages are created to calculate 20-year fatigue damage efficiently and accurately. Using the surrogate models, probability of fatigue failure is calculated considering both wind load uncertainty and manufacturing variability. The obtained RBDO optimum design reduces the maximum probability of failure from 50.06% at the RBDO initial design to 2.28% at the RBDO optimum design. This research demonstrates that applying RBDO methods to wind turbine blades could provide reliable and yet economical designs considering wind load uncertainty. The developed wind load uncertainty, the reliability analysis method, and the RBDO methods could be applicable to other wind turbine components, such as rotor hub, gears, and bearings.

1.5.2   Future Recommendations

The proposed wind load uncertainty model utilizes 249 groups of measured wind data. If more wind data is available, the developed dynamic wind load uncertainty model could generate more realistic uncertainty wind load for reliability analysis and RBDO. At the current state, due to lack of wind data over 20 years, the random variables of C, k, a, b, and τ are assumed to be independent. In other words, the wind load variation over years is assumed to be independent. In reality, the wind load distribution in 1 year at a location is probably close to the wind load distribution in the following years at the same location. That means there is a correlation between the wind loads in years. In the future, the correlation among random variables of C, k, a, b, and τ may be studied. For example, by adding the correlation into the wind load uncertainty model, the correlation between wind loads generated from sequential years may be considered.

References

Bansal R, Bhatti T, Kothari D (2002) On some of the design aspects of wind energy conversion systems. Energy Convers Manag 43(16):2175–2187

Breitung K (1984) Asymptotic approximations for multinormal integrals. J Eng Mech 110(3):357–366

Burton T, Sharpe D, Bossanyi E, Jenkins N (2011) Wind energy handbook. Wiley, Hoboken

Carta JA, Ramirez P, Velazquez S (2009) A review of wind speed probability distributions used in wind energy analysis: case studies in the Canary Islands. Renew Sust Energ Rev 13(5):933–955

Cheng PW (2002) A reliability based design methodology for extreme responses of offshore wind turbines. DUWIND Delft University Wind Energy Research Institute

Cheng PW, van Bussel G, van Kuik G, Vugts J (2003) Reliability-based design methods to determine the extreme response distribution of offshore wind turbines. Wind Energy 6(1):1–22

Cho H, Choi K, Lee I, Lamb D (2015) Design sensitivity method for sampling-based RBDO with fixed COV. In: ASME 2015 international design engineering technical conferences and computers and information in engineering conference, 2015. American Society of Mechanical Engineers, pp V02BT03A059–V002BT003A059

Derks A (2008) Development of a wind turbine drive train engineering model. Faculty of Aerospace Engineering. Delft University of Technology, Delft

Do TQ, Mahmoud H, van de Lindt JW (2014) Fatigue life of wind turbine tower bases throughout Colorado. J Perform Constr Facil 29(4):04014109

Firouzianbandpey S (2016) Reliability-based design of wind turbine foundations: geotechnical site assessment. PhD thesis, Aalborg University, Aalborg

Germanischer Lloyd (2010) Guideline for the certification of wind turbines. Hamburg, Germany

Griffith DT, Ashwill TD (2011) The Sandia 100-meter all-glass baseline wind turbine blade: SNL100–00. Sandia National Laboratories, Albuquerque, Report No SAND2011–3779

Guo Y, Bergua R, Dam J, Jove J, Campbell J (2015) Improving wind turbine drivetrain designs to minimize the impacts of non-torque loads. Wind Energy 18(12):2199–2222

Haldar A, Mahadevan S (2000) Probability, reliability, and statistical methods in engineering design. Wiley, New York

Hasofer AM, Lind NC (1974) Exact and invariant second-moment code format. J Eng Mech Div 100(1):111–121

Hohenbichler M, Rackwitz R (1988) Improvement of second-order reliability estimates by importance sampling. J Eng Mech 114(12):2195–2199

Hoog RV, McKean JW, Craig AT (2005) Introduction to mathematical statistics, 6th edn. Pearso Prentice Hall, Upper Saddle River

Hu W, Choi K, Gaul N, Hardee E (2012) Reliability analysis of wind turbine blades for fatigue life under wind load uncertainty. In: 12th AIAA Aviation Technology, Integration, and Operations (ATIO) conference and 14th AIAA/ISSMO multidisciplinary analysis and optimization conference, 2012, p 5601

Hu W, Choi K, Cho H (2016a) Reliability-based design optimization of wind turbine blades for fatigue life under dynamic wind load uncertainty. Struct Multidiscip Optim 54(4):953–970

Hu W, Choi K, Zhupanska O, Buchholz JH (2016b) Integrating variable wind load, aerodynamic, and structural analyses towards accurate fatigue life prediction in composite wind turbine blades. Struct Multidiscip Optim 53(3):375–394

International Electrotechnical Commission (2005) Wind turbines part 1: design requirements, IEC 61400-1, 3rd edn. IEC, Geneva

Jonkman J, Butterfield S, Musial W, Scott G (2009) Definition of a 5-MW reference wind turbine for offshore system development. National Renewable Energy Laboratory, Golden, Technical report no NREL/TP-500-38060

Kong C, Bang J, Sugiyama Y (2005) Structural investigation of composite wind turbine blade considering various load cases and fatigue life. Energy 30(11):2101–2114

Kong C, Kim T, Han D, Sugiyama Y (2006) Investigation of fatigue life for a medium scale composite wind turbine blade. Int J Fatigue 28(10):1382–1388

Lee I, Choi KK, Gorsich D (2010) System reliability-based design optimization using the MPP-based dimension reduction method. Struct Multidiscip Optim 41(6):823–839

Lee I, Choi KK, Noh Y, Zhao L, Gorsich D (2011a) Sampling-based stochastic sensitivity analysis using score functions for RBDO problems with correlated random variables. J Mech Des 133(2):021003

Lee I, Choi KK, Zhao L (2011b) Sampling-based RBDO using the stochastic sensitivity analysis and Dynamic Kriging method. Struct Multidiscip Optim 44(3):299–317

Lee Y-S, Choi B-L, Lee JH, Kim SY, Han S (2014) Reliability-based design optimization of monopile transition piece for offshore wind turbine system. Renew Energy 71:729–741

Madsen HO, Krenk S, Lind NC (2006) Methods of structural safety. Courier Corporation, Mineola

Manuel L, Veers P, Winterstein S (2001) Parametric models for estimating wind turbine fatigue loads for design. In: 20th 2001 ASME wind energy symposium, p 47

Mandell JF, Samborsky DD (2014) SNL/MSU/DOE Composite material fatigue database mechanical properties of composite materials for wind turbine blades version 23.0. Montana State University, Bozeman

Manwell JF, McGowan JG, Rogers AL (2010) Wind energy explained: theory, design and application. Wiley, Chichester

Messac A, Chowdhury S, Zhang J (2011) Modeling the uncertainty in farm performance introduced by the Ill-predictability of the wind resource. In: 6th AIAA theoretical fluid mechanics conference, 2011, p 3302

Moriarty PJ, Holley W, Butterfield CP (2004) Extrapolation of extreme and fatigue loads using probabilistic methods. National Renewable Energy Laboratory, Golden

Nicholson JC (2011) Design of wind turbine tower and foundation systems: optimization approach. MS (Master of Science) Thesis, University of Iowa, Iowa City

Noda M, Flay R (1999) A simulation model for wind turbine blade fatigue loads. J Wind Eng Ind Aerodyn 83(1):527–540

Noh Y, Choi K, Du L (2009) Reliability-based design optimization of problems with correlated input variables using a Gaussian Copula. Struct Multidiscip Optim 38(1):1–16

Noh Y, Choi K, Lee I (2010) Identification of marginal and joint CDFs using Bayesian method for RBDO. Struct Multidiscip Optim 40(1–6):35

Rahman S (2009) Stochastic sensitivity analysis by dimensional decomposition and score functions. Probab Eng Mech 24(3):278–287

Rahman S, Wei D (2006) A univariate approximation at most probable point for higher-order reliability analysis. Int J Solids Struct 43(9):2820–2839

Ronold KO, Christensen CJ (2001) Optimization of a design code for wind-turbine rotor blades in fatigue. Eng Struct 23(8):993–1004

Ronold KO, Larsen GC (2000) Reliability-based design of wind-turbine rotor blades against failure in ultimate loading. Eng Struct 22(6):565–574

Ronold KO, Wedel-Heinen J, Christensen CJ (1999) Reliability-based fatigue design of wind-turbine rotor blades. Eng Struct 21(12):1101–1114

Rubinstein RY, Shapiro A (1993) Discrete event systems: sensitivity analysis and stochastic optimization by the score function method. Wiley, New York

Shokrieh MM, Rafiee R (2006) Simulation of fatigue failure in a full composite wind turbine blade. Compos Struct 74(3):332–342

Toft HS, Sørensen JD (2011) Reliability-based design of wind turbine blades. Struct Saf 33(6):333–342

TPI Composites (2003) Innovative design approaches for large wind turbine blades. Sandia report SAND 2003–0723. SAND 2003–0723, Sandia National Laboratory, Albuquerque. Available from: http://prod.sandia.gov/techlib/access-control.cgi/2003/030723.pdf. Accessed in Nov 2016

Tu J, Choi KK, Park YH (1999) A new study on reliability-based design optimization. J Mech Des 121:557–564

Tu J, Choi KK, Park YH (2001) Design potential method for robust system parameter design. AIAA J 39(4):667–677

Chapter 2
Computational Fluid Dynamics Methods for Wind Turbines Performance Analysis

Navid Goudarzi

2.1 Introduction

2.1.1 Wind Turbines

The importance of reducing greenhouse gases leads to developing sustainable and efficient technologies. Wind power as a free, abundant, and globally available energy source is one of the most promising energy resources for green electricity generation. Figure 2.1 shows the world's total cumulative installed wind power capacity between 1991 and 2016 (Goudarzi and Zhu 2013). The average annual growth in the total installed wind power capacity in the last 10 years is more than 25% per year; it is anticipated that 12% of the world's electricity consumption will be provided by wind power by 2020 (Goudarzi and Zhu 2013).

A wind turbine converts the captured kinetic energy in the wind to electrical energy. Rankine-Froude momentum or actuator disk model is known as the first estimation for wind turbine efficiency (Mikkelsen 2003). Betz law shows the maximum ideal captured power by a horizontal axis turbine cannot exceed 59.3% of the kinetic energy in wind (Manwell et al. 2010). Current commercial wind turbines work at 75–80% of the Betz limit (Mikkelsen 2003). While more wind turbines are installed in large wind farms, reduced power production (8% for onshore farms and 12% for offshore farms) due to wake velocity deficits and increased dynamic loads on turbine blades due to higher turbulent flow levels should be studied for determining wind turbines aerodynamic characteristics. Understanding the aerodynamic performance of wind turbines and in particular turbine blades

N. Goudarzi (✉)

Mechanical Engineering (ETCM) Program, University of North Carolina at Charlotte, Charlotte, NC, USA

e-mail: navid.goudarzi@uncc.edu
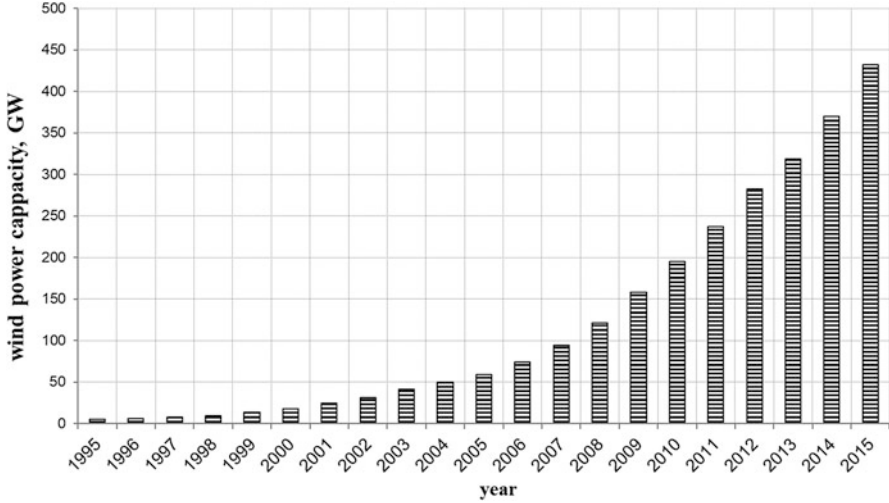
Fig. 2.1 World's cumulative installed wind power capacity during 1995–2015

at different wind speeds can help to improve the accuracy in the prediction of wind turbine performance and facilitate an optimized design of turbine blades for a desired performance goal.

There has been a significant number of researchers studying aerodynamic performance of turbine blades (Martinez Tossas and Leonardi 2013; Lee and Wu 2011). They have developed computational methods to analyze the global flow field around the turbine blades. These methods got further improved to reduce the numerical results uncertainties by comparing them with experimental tests. This chapter provides a brief review on the developed numerical techniques with emphasis on computational fluid dynamics (CFD) methods used for wind turbine applications: airfoil design, blade design, and load calculations.

2.1.2 Aerodynamics Characteristics of Wind Turbines

The turbine blade efficiency, power coefficient C_P, is an important factor in determining the aerodynamic performance of a wind turbine:

$$C_p = \frac{P_m}{P_w} = \frac{T_m * \omega}{1/2\rho A_r V^3} \tag{2.1}$$

where P_m is the mechanical power, P_w is the wind power, T_m is the mechanical torque, ω is the rotational speed, ρ is the air density, A_r is the rotor area, and V is the wind speed. The fraction of the year the turbine generator is operating at rated
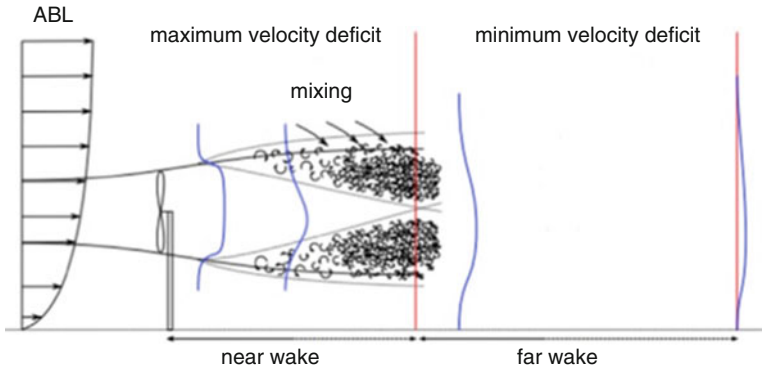
Fig. 2.2 Velocity profile behind the wind turbine (Shakoor et al. 2016)

power is defined by the capacity factor (CF). It is based on both turbine and site characteristics. Aerodynamic characteristics of wind turbines are directly related to the airfoil designs used in turbine blades.

Airfoils such as NACA44xx, NACA230xx, and NACA63xxx with high maximum lift coefficient, low minimum drag, and low pitching moment are among popular airfoils used for wind turbine blades. Flow separation and stall phenomenon are among the main concerns in designing airfoils. Stall phenomenon occurs either at high angles of attack (generally at angles more than 15°) or at low tip-speed ratios (TSR) at a given wind speed. During stall, the airfoil lift decreases significantly, and the draft force increases.

The wake flow behind the wind turbine (near wake or far wake) can have a significant impact on the turbine blade performance (Fig. 2.2). The near wake is within 1–2 rotor diameters downstream behind the turbine rotor which is affected directly by the turbine geometry, the presence of tip vortices, and mixing flows. Hence, the wake analysis should include both axial- and tangential-induced velocities from formed vortices and the blade shear layers. The far wake is affected indirectly by the turbine geometry; it has a reduced axial velocity and an increased turbulence intensity. The far wake analysis would be needed in the case of wind farm design. Generally, three types of turbulence exist in the far wake: atmospheric turbulence due to surface roughness and thermal effects, mechanical turbulences due to the wind turbine, and wake turbulence from vortex breakdown. The wake flow applies a swirl velocity component to the air in the opposite direction to the turning of the blades. This wake behind the turbine slows down the airflow going through the rotor and changes the local angle of attack of blades which directly impacts the aerodynamic forces. Far downstream, a Gaussian and axisymmetric velocity field is observed (Hu 2016).

The future trends for wind turbine technology developments include performance improvements and cost reductions. Wind turbines with novel designs, higher towers, larger blades, and an improved reliability and availability, at a reduced weight and an expanded installation in offshore sites, can further reduce the cost of

energy from wind and make it more competitive on the energy market. While airfoil aerodynamics characteristics are well-known (Abbot and Doenhoff 1949), understanding and accurate estimation of turbine blade interactions due to different forces in a rotating frame such as centrifugal forces as well as the wake behind the turbine and modifying the blade aerodynamic characteristics facilitate achieving the future goals of this industry.

2.2   Numerical Techniques

Blade element momentum (BEM) theory and CFD methods are widely used to predict wind turbine performance. BEM methods predict the aerodynamic performance and obtain the optimal blade design by integrating linear and angular air mass momentum changes with the toque and axial forces acting on blades. CFD methods provide visualization capabilities of flow behavior on the blade surface and in the wake region. Hence, BEM is used for designing the wind turbine rotor geometry, and CFD is used for validating and evaluating the design and its performance.

2.2.1   Blade Element Method (BEM)

BEM predicts the turbine blade aerodynamic characteristics based on linear momentum theory. It assumes that (1) the flow is steady state and incompressible, (2) there are an infinite number of blades, (3) there is no rotating wake behind the turbine blade, (4) there is a uniform thrust over the actuator disk, and (5) there is no frictional drag. It only considers the 2D lift and drag forces on airfoils that do not have aerodynamic interactions with each other. Basic BEM methods underpredict torque, as they compute the aerodynamics of each airfoil section along the blades independently of neighboring sections. It will result in neglecting spanwise flow and other potential 3D effects. Such effects might be significantly important especially near wind turbine blade roots. Correction equations such as the Prandtl tip loss factor (Manwell et al. 2010), the stall delay model (Martinez Tossas and Leonardi 2013), the Viterna-Corrigan stall model (Lee and Wu 2011), and the Spera's correction (Spera 2009) are used to improve the prediction accuracy and consider the 3D effects in basic BEM methods.

2.2.2   Computational Fluid Dynamics (CFD)

CFD is a powerful tool to estimate the aerodynamic performance characteristics and to visualize the flow behavior around wind turbine components. In recent years, commercial CFD software products such as ANSYS Fluent, COMSOL, Star
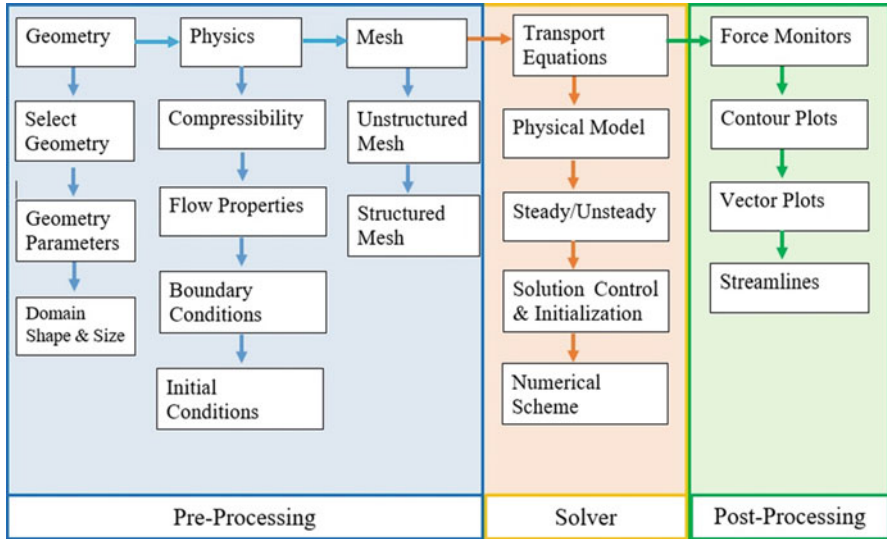
Fig. 2.3 Three main steps in CFD

CCM+, EllipSys3D, Open Foam, etc. are widely used by engineers. Figure 2.3 illustrates three common main steps in all of these tools: preprocessing, solver, and post-processing. The geometry creation, mesh generation, and boundary conditions definitions are conducted in the preprocessing step. A very important step in solving the partial differential Navier-Stokes (NS) equations is to use and develop stable, consistent, and accurate algebraic replacements for the NS equations, called discretization, where the physics and inherent structure of the problem are retained. Generally, three types of numerical discretization schemes including finite volume method (FVM), finite element method (FEM), and finite difference method (FDM) are currently in use. These schemes transform the infinite-dimensional NS equations into finite-dimensional algebraic equations. The FVM methods are flux conserving construction based on the approximation of conservation laws. Compared to the FVM methods, FEMs have a more flexible discretization but with fewer quality constraints. FDMs use a completely different approach compared to the preceding two and are limited to structured grids. Within the solver step, the NS equations are solved for a time-dependent velocity field, appropriate turbulence models are selected, and the solver settings such as solution control and initialization are performed. Finally, the post-processing will obtain the forces (such as normal force, thrust, and torque) and visualization of flow using contour plots, vector plots, and streamlines.

CFD techniques (turbulence models are more elaborated in Sect. 2.2.2.2) can be classified in four broad categories:

1. Actuator blade methods that provide physics-based characterization of wind turbine wakes at a reduced computational cost

2. Hybrid Reynolds-averaged Navier-Stokes (RANS)/large eddy simulation (LES) methods that provide an improved estimation of unsteady and separated flows
3. The overset methods (Chimera methods) to treat the relative motion between rotor and its support structures
4. Combined CFD-computational structure dynamics (CSD) methods to model the aeroelastic response of the rotor blades

A combination of level of understanding of the problem (flow physics), computational cost, and ease of using a specific CFD technique, range of applicability, and the level of required accuracy will determine the desired CFD technique for an application.

2.2.2.1   Mesh and Boundary Conditions

Design and construction of a quality grid are crucial to the success of the CFD analysis. There are three general approaches that can be used to simulate the turbine blade rotation (Cabezon et al. 2009):

1. Moving reference frame (MRF): it simulates the aerodynamic performance of a single turbine blade using a periodic boundary condition in steady-state flow conditions.
2. Sliding mesh model: it simulates the aerodynamic performance of a full-scale model in transient flow with two distinct domains that have a relative motion and a nonmatching grid.
3. Dynamic mesh model: it has a high computational cost and is useful for modeling relative motions between different components.

A trade-off between accuracy, computational time, and the objective of the problem can determine the most appropriate discretization. The structured and unstructured grid generation can be conducted in a number of mesh tools such as Gambit, Pointwise, and ICEM CFD. The structured grids are widely used along the blade boundary layer. Based on the geometry complexity, flow field, and solver-supported cell types, other computational domains including upstream and downstream of the boundary can be meshed with either structured or unstructured grids. The grid quality can be determined based on three measures: skewness (zero is the best, and one is the worst), smoothness (change in size), and aspect ratio (one is the ideal value for an equilateral triangle or a square). Accurate and fast converging solutions require a high grid quality: skewness does not exceed 0.85–0.90, local cell size variations have to be gradual (the maximum change in grid spacing should be less than 20%), and the aspect ratio has to be defined based on the pertinent flow features. While more cells can offer higher accuracy, it significantly increases the computational cost. Cell counts in the order of 10^4–10^7 are common for small- to large-size problems. Higher cell counts should be avoided if possible; otherwise, different techniques such as using multiple CPUs should be employed.

In order to ensure adequate grid resolution on turbine blades, solution-based grid adoptions can be employed based on gradients of flow, boundary cells, volume changes, and adjacent to wall cells (nondimensional wall distant y^+). The near-wall region is generally modeled by either the wall function or the near-wall function (viscous sub-layer and buffer layer). The wall function approach solves the attached flow on turbine blade surface at a large initial y^+ value with a low computational cost. However, an accurate prediction of the stall point for separation flows requires a fine mesh along the inboard blade section. In recent years, near-wall functions use standard or modified turbulence models (based on the y^+) to obtain accurate solutions for the laminar sub-layer region.

One of the ongoing challenges in CFD simulation techniques is the boundary condition definition, especially when comparing with experimental data and when the model solves for the wind turbine wakes. While uniform and laminar inflow profiles have been widely used in early CFD simulations, the LES simulations showed the presence of both shear inflow profile and turbulence in the incoming flow; these have significant impact on the flow field behind the rotor. To address velocity components and turbulence quantities independent of time, Monin-Obukhov similarity theory can be used for RANS simulations (Martinez Tossas and Leonardi 2013).

2.2.2.2 Turbulence Model

Inherent turbulent characteristics of the atmospheric airflow make wind turbine rotors' operation impacted by the turbulent fluctuations. There are a number of approaches such as RANS, LES, and detached eddy simulation (DES) for modeling turbulent flows and determining the velocity fluctuations on turbine blades. The focus of this section is on RANS models. Solving the RANS equations for the flow field around a turbine blade requires a proper turbulent model. RANS models provide a statistical description of the flow and describe the turbulent flow as a random variation around a mean value. The RANS equations can be written as

$$\rho \frac{\partial U_i}{\partial t} + \rho U_j \frac{\partial U_i}{\partial x_j} = -\frac{\partial P}{\partial x_j} + \frac{\partial}{\partial x_j} \left(2\mu S_{ij} - \rho \overline{u_j' u_i'} \right) \tag{2.2}$$

with the time-averaged mass conservation to be as

$$\frac{\partial U_i}{\partial x_i} = 0 \tag{2.3}$$

where U_i is the time-averaged velocity, u_i' is the fluctuating velocity, μ is the molecular viscosity, and S_{ij} is the deformation tensor. Note that the $\rho \overline{u_j' u_i'} = \rho \tau_{ij}$ is known as the Reynolds stress tensor and two main approaches of either turbulent-viscosity models or Reynolds stress models (RSM) are used to model it. The turbulent-viscosity models are more suitable for simple turbulent shear flows such

as boundary layers, channel flows, and mixing flows. The RMS models solve transport equations for individual Reynolds stress terms and for the dissipation rate ε or specific dissipation rate ω. They are advantageous to more complex turbulent flows such as swirling flows and the effects of large streamlines curvature. In RANS equations, there are 10 unknowns (pressure, 1; velocity components, 3; and Reynolds stress tensor components, 6) and four equations. Hence, more equations should be introduced to solve for the unknowns. There are different models introduced such as (Sanderse et al. 2011):

1. One-equation models (Spalart-Allmaras turbulence model): they solve transport equations for the turbulent viscosity ($\mu = f(\tilde{\upsilon})$). They are less sensitive in the near wall and used mainly for aerodynamic applications with mild separation.
2. Two-equation models (k-ε and k-ω turbulence models): they solve transport equations for two turbulence quantities, turbulent kinetic energy k, and turbulent dissipation rate ε. Two-equation eddy k-ε models ($\mu = f(\rho k^2/\varepsilon)$) are rarely used in wind turbine studies, as they do not offer good results for flows with large pressure gradients and strong separation. For such flows, the renormalization group k-ε models and realizable k-ε models offer better and superior performance, respectively (Jones and Launder 1972). Two-equation eddy viscosity k-ω models ($\mu = f(\rho k/\omega)$ where $\omega = k/\varepsilon$ is the specific dissipation rate) are currently popular for turbine blades aerodynamic forces simulation analysis (Wilcox 1988). The transition k-ω SST turbulence models conduct 3D aerodynamic analysis of turbine blades and show strong agreements with the experimental results (Menter 1994).
3. Hybrid turbulence models: these models address multiple different flow behaviors. For example, DES combines the accuracy of LES within separation region (solving for smallest, subgrid-scale (SGS) eddies) and efficiency of RANS inside a boundary layer to address high-level separation flows with high-level transient properties and vortex shedding. There are a number of successful RANS-LES hybrid models such as very large eddy simulation (VLES), detached eddy simulation (DES), and partially averaged Navier-Stokes (PANS).

Note that there is literature on alternative numerical methods to solve complex CFD problem. One example (Pasquali 2016) is the implication of lattice Boltzmann method for computational domain discretization (grid generation) and near-wall turbulent flow analysis (boundary treatment for turbulent flows).

2.3   Numerical Simulation of Wind Turbine Wakes

RANS and LES methods are largely used for studying the influences of atmospheric and wake turbulence around wind turbines. The LES methods with abilities such as handling unsteady, anisotropic turbulent flows have drawing more attention in recent years. However, the LES computational cost is much higher than RANS models. The actuator disk model (ADM) and actuator line model (ALM) predict blade forces
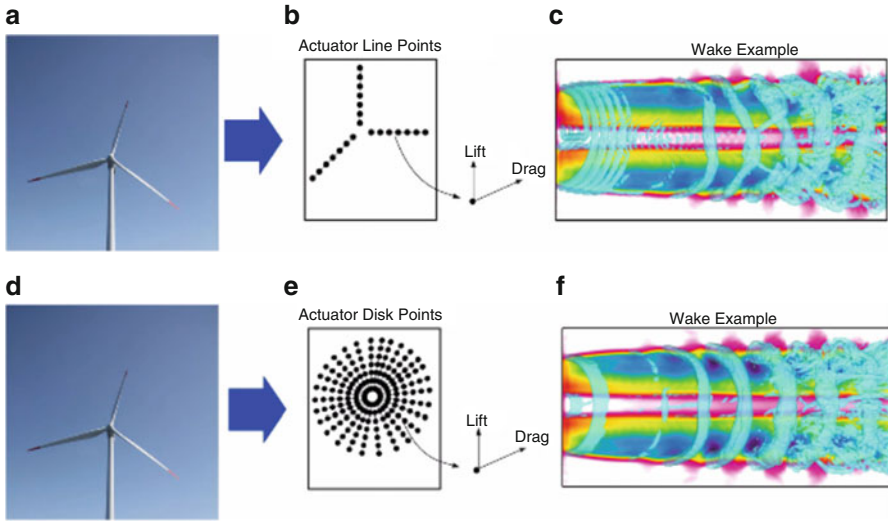
Fig. 2.4 ADM/ALM for a real turbine wake flow visualization (Martinez Tossas et al. 2014). (**a**) Commercial scale turbine. (**b**) Actuator line representation. (**c**) Flow visualization. (**d**) Commercial scale turbine. (**e**) Actuator disk representation. (**f**) Flow visualization

(as body forces) based on the local fluid velocity at each actuator element, without taking care of the full blade geometry (Fig. 2.4). The ADM simulates a wind turbine as a distributed force (both axial and tangential forces) on the rotor disk. The ALM simulates the turbine blade by a distributed force from the hub to the blade tip. It can predict the vortex structures and instabilities formation for both near and far wake. Several computational and experimental works have shown that both ADM and ALM can successfully simulate the wind turbine aerodynamic characteristics as well as the effects of local and regional turbulent fluxes of momentum and heat in wind farms (Martinez Tossas and Leonardi 2013).

The CFD-BEM approach uses the flow simulation around a wind turbine to estimate power curves, forces, and moments. There are a number of literature comparing the use of either of those methods or a combined approach (Lynch 2011). It is shown that this approach offers a lower computational cost at a high degree of accuracy. The accuracy of numerical approaches requires a good understanding about the physics of the problem. The BEM does not provide a reliable aerodynamic load simulation on the turbine blade especially at stall flow conditions. Different corrections such as hub loss correction, tip loss correction, Glauert, skewed wake correction, buhl empirical corrections, and 3D corrections can improve the BEM results. Most RANS methods have a stable and robust approach with using second-order accurate finite volume schemes on structured grids, with upwind discretization of convective terms and central discretization of diffusive terms. In LES methods,

spatial convective terms require more careful discretization; central and spectral schemes are preferred to upwind schemes as the latter one introduces numerical dissipation in spatial discretization.

2.4 Conclusions and Future Recommendations

This chapter provided numerical approaches with focus on CFD methods used in studying the aerodynamic performance of wind turbine blades. Some conclusions include:

- BEM methods provide a rapid aerodynamic characteristics and performance of a turbine blade, using 2D airfoil data. Correction methods should be used to address the stall and 3D effects and improving the prediction accuracy.
- CFD methods provide flow visualization capabilities and accurate aerodynamic characteristic estimations for turbine blades. Turbulence model selection and discretization techniques play key roles in simulation accuracy. It showed that the LES with ADM and ALM models provide reliable estimations in turbine blades wake. However, more work should be done to study the impact of wind turbine tower and nacelle on estimated turbine performance and wake profiles.
- The CFD-BEM approach offers an accurate prediction model at a low computational cost.
- Further research can focus on quantifying computational uncertainties from discretization, from turbulence modeling, as well as from the inflow description, terrain geometry, and rotor geometry. This improves CFD results for comparing with experimental data that can further enhance the accuracy of wind turbine aerodynamic characteristics estimations. In a bigger picture, a combination of CFD analysis together with experimental methods such as field measurements, wind tunnel measurements, and particle image velocimetry (PIV) techniques improves the development and evaluation of wind harnessing machines. For instance, the most comprehensive wake measurements are determined experimentally, using PIV systems. Hence, the added value of combining experimental methods in addressing the fundamental and practical gaps in wind energy development should be further explored.

References

Abbot IH, Doenhoff AE (1949) Theory of wings sections including a summary of airfoil data. McGraw-Hill, New York

Cabezón D, Sanz J, Marti I (2009) Crespo A CFD modeling of the interaction between the surface boundary layer and rotor wake. Comparison of results obtained with different turbulence models and mesh strategies. In: European wind energy conference and exhibition, Marseille

Goudarzi N, Zhu W (2013) A review of wind turbine generators across the world. Int J Dyn Control 1:192–202

Hu B (2016) Design of a simple wake model for the wind farm layout optimization considering the wake meandering effect. MSc Dissertation, TuDelft University

Jones W, Launder B (1972) The prediction of laminarization with a two-equation model of turbulence. Int J Heat Mass Transf 15(2):301–314

Lee HM, Wu Y (2011) An experimental study of stall delay on the blade of a horizontal axis wind turbine using tomographic particle image velocimetry. J Wind Eng Ind Aerodyn 123(A):56–68

Lynch E (2011) Advanced CFD methods for wind turbine analysis. Aerospace Engineering Department, Georgia Institute of Technology, Atlanta

Manwell JF, McGowan JG, Rogers AL (2010) Wind energy explained: theory, design, and application. Wiley, New York

Martinez Tossas LA, Leonardi S (2013) Wind turbine modeling for computational fluid dynamics. National Renewable Energy Laboratory, Golden, Technical report no NREL/SR-5000-55-54

Martinez Tossas LA, Churchfield MJ, Leonardi S (2014) Large eddy simulation of the flow past wind turbines: actuator line and disk modeling. Wind Energy J 18:1047–1060

Menter FR (1994) Two-equation eddy-viscosity turbulence models for engineering applications. AIAA J 32(8):1598–1605

Mikkelsen R (2003) Actuator disc methods applied to wind turbines. Mechanical Engineering, Technical University of Denmark, Copenhagen

Pasquali A (2016) Enabling the cumulant lattice Boltzmann method for complex CFD engineering problems. In: Architecture, civil engineering and environmental sciences. Technical University of Braunschweig, Braunschweig

Sanderse B, Pijl SP, Koren B (2011) Review of computational fluid dynamics for wind turbine wake aerodynamics. Wind Energy J 14:799–819

Shakoor R, Hassan MY, Raheem A, Wu YK (2016) Wake effect modeling: a review of wind farm layout optimization using Jensen's model. Renew Sustain Energy Rev J 58:1048–1059

Spera DA (2009) Wind turbine technology: fundamental concepts in wind turbine engineering. American Society of Mechanical Engineers (ASME), New York

Wilcox D (1988) Reassessment of the scale determining equation for advanced turbulent models. AIAA J 19(2):248–819

Chapter 3
Gearbox of Wind Turbine

Huaxia Li

3.1 Introduction

3.1.1 Wind Turbine Gearbox Failure

An accurate prediction of the product life of drivetrains is crucial for safe and reliable operation of wind turbines. It is reported that the failure rate of gearboxes is higher than other wind turbine components (Aydin 2013; Sheng et al. 2011; Errichello and Muller 2012a). Failures of gear components stop wind turbine operation and cause pecuniary loss due to turbine downtime and increased maintenance, resulting in wind energy being less competitive when compared to existing fossil fuels (Sheng et al. 2011). For this reason, developing a reliable and cost-effective design procedure for wind turbine components is of crucial importance.

According to the National Renewable Energy Laboratory (NREL) report (Errichello 2000), wind turbine drivetrain failure modes are classified as follows: (a) bending fatigue, (b) contact fatigue, (c) wear, (d) scuffing, (e) grinding cracks, and (f) case-core separation cracks. The main cause of bending fatigue is an inadequate material cleanliness or incomplete hardening on the tooth root. Wear is due to the tearing of asperities, and it can be alleviated by sufficient lubrication on tooth surfaces. Scuffing also called as severe adhesion occurs when lubricant dries out accidently. Grinding cracks and case-core separation cracks are caused by improper heat treatment of gear materials. These failures can be prevented by the use of appropriate materials and careful surface treatments. On the other hand, more careful consideration needs to be given to rolling contact fatigue in gear design (Tallian 1983). Since a gear tooth experiences severe cyclic rolling and sliding

H. Li (✉)
The University of Iowa, Iowa City, IA, USA
e-mail: huaxia-li@uiowa.edu

contact resulting from highly variable wind loads which are stochastic in nature, prediction of fatigue failure is not straightforward, thus contact fatigue becomes one of the major causes of unintended gearbox failure that would prevent wind turbines from achieving the expected service life (Errichello and Muller 2012b; Milburn 2011).

The gear tooth contact fatigue is caused by either surface-initiated cracking or subsurface-initiated cracking (Choi and Liu 2006a). Overheating of tooth surfaces due to insufficient lubrication leads to the surface-initiated failure, but for properly lubricated gears, the subsurface crack happens in most cases. Furthermore, it is widely agreed that the contact fatigue failure process due to the subsurface-initiated crack can be divided into two stages (Keer and Bryant 1983; Glodez et al. 1997): (1) crack initiation period and (2) crack propagation period. Contact fatigue life is estimated by the sum of the total number of load cycles required for the crack initiation and that required for the crack to propagate to the surface (Choi and Liu 2006a). The crack initiation process can be modeled by the multiaxial high cycle fatigue criteria (Crossland 1970; Liu and Zenner 2003; Dang 1973), which is influenced by contact stress and material fatigue parameters. The crack propagation process is modeled by the Paris equation using mode II stress intensity factor (Choi and Liu 2006b; Osman and Velex 2011). For case-hardened materials, it is observed that the crack propagation under rolling contact is influenced by the ratio of the maximum shear stress to the material hardness (Choi and Liu 2006c; Jiang et al. 1993). In other words, to estimate the contact fatigue life of wind turbine gear teeth, the maximum shear stress needs to be predicted accurately under various dynamic load conditions. The use of a deterministic single domain simulation may, however, lead to an unrealistic load prediction due to high variability of wind loads, thereby resulting in underestimation or overestimation of the gear tooth fatigue life. The dynamic wind load uncertainty model described in Chap. 1 is implemented for wind turbine gearbox dynamics simulation to consider wide spatiotemporal wind uncertainty (i.e., wind load uncertainty for different locations and in different years), so that a wide range of probabilistic wind loads can be truly accounted in the gear contact fatigue life prediction.

3.1.2 Multibody Dynamics Simulation of Geared Systems

Multibody dynamics simulation is widely used to predict the dynamic mesh force variation as well as transmission error of complex gear trains. Lumped torsional mass-spring models that account for the effect of variable stiffness associated with the gear tooth contact are widely used in the vibration analysis of gear systems (Ozguven and Houser 1988; Wang et al. 2003; Kahraman 1994). While the lumped vibration models are computationally efficient and provide an important insight into the dynamic response of gear trains, they are in general used for the analysis of steady-state response in the frequency domain. In addition, the three-dimensional gear tooth geometry is not fully considered in the models.

To perform the time-domain transient analysis of gear systems, multibody dynamics models have been used for various engineering applications (Haug 1989; Shabana 2010; Cardona 1997; Palermo et al. 2013). The tangential and bending deformation of the gear tooth can be considered by introducing discrete translational and rotational springs defined between the rigid tooth and rigid gear body (Ebrahimi and Eberhard 2006; Lee et al. 2012). The flexibility of the entire gear body can be incorporated into multibody dynamics simulation using the floating frame of reference formulation with modal reduction techniques, allowing for prediction of accurate tooth impact force influenced by the tooth and gear wheel deformation (Ziegler and Eberhard 2009). Since flexible multibody models, in general, lead to large dimensionality to ensure accuracy, the computational cost is high, and application to the gear train dynamics simulation would be impractical. To reduce the computational cost for the full finite element gear model, the surface integral solution for the tooth contact is integrated into the finite element model, thereby allowing for the use of coarse finite element meshes while retaining the precise gear tooth contact calculation (Vijayakar 1991; Parker et al. 2000). For wind turbine applications, various gearbox models are developed using either rigid or flexible multibody dynamics approaches (Peeters et al. 2005; Oyague 2009; Qin et al. 2009; Helsen et al. 2011), some of which are validated against test bench results (Vanhollebeke et al. 2015). Furthermore, the probabilistic flexible multibody gear dynamics simulation has been advocated for wind turbine gearboxes to account for uncertainties associated with wind loads and manufacturing errors (Alemayehu and Osire 2015).

In gear dynamics simulation, precise tooth surface geometry description and accurate prediction of the location of the contact point are crucial to the mesh force and transmission error evaluation of gear trains (Litvin and Fuentes 2004). In particular, contact search for the tooth surface geometry obtained by computer-aided design (CAD) and/or direct tooth measurement leads to extensive computation efforts in the dynamic simulation. In the constraint contact formulation, the non-conformal contact condition between tooth surfaces in contact is imposed on the equations of motion as constraint equations, and the normal contact forces are evaluated by Lagrange multipliers associated with the contact constraint. This formulation leads to an accurate and efficient prediction of the contact point on the continuous smooth surface (Shabana et al. 2008).

However, intermittent contact of multiple gear teeth is involved in the time-domain dynamic analysis; thus, use of the constraint contact formulation necessitates ad hoc numerical procedures for modeling the gear tooth impact as well as loss of contact due to changes in the system degrees of freedom. Furthermore, a rigid contact assumption used in the formulation prevents consideration of the effect of variable mesh stiffness. For this reason, the elastic (penalty) contact approach has been widely used in the analysis of multibody gear contact dynamics in which the normal contact force is defined as a compliant force function of the penetration between two surfaces in contact. The contact point can be determined during the gear dynamics simulation by either solving nonlinear contact search equations iteratively to ensure the tangency condition or searching a pair of nodes that have

the maximum penetration on the discretized surfaces. The nodal search method, however, is not recommended due to the discrete surface representation which causes numerical noise in mesh forces. In the use of contact search equations, on the other hand, nonlinear equations need to be solved iteratively at every time step, leading to extensive computational time for the entire gear train model. Furthermore, a special technique is required for treating a discontinuous contact event such as impact, loss, or jump in contact point that can occur when gear geometry imperfections are involved. To address these fundamental and essential issues in the contact search algorithm for gear tooth surfaces with geometric imperfection, a combined nodal and non-conformal contact search algorithm which can determine contact before gear dynamics simulation is introduced and generalized to the gear tooth contact problem in this study.

3.1.3 Gear Design Optimization

Gear design is a complicated iterative process, involving many design variables, requirements, and constraints (Vanderplaats et al. 1988). Many gear design optimizations have been carried out using deterministic design variables and loads. In most literature, optimizations of the contact ratio, face width, and tooth tip and root profiles are explored to meet the fatigue life constraint associated with gear tooth bending and surface pitting failures (Spitas and Spitas 2007; Sansalvador and Jauregui 1993; Kapelevich and Shekhtman 2009). Minimization of gear transmission error, which is the main source of gearbox noise and vibration, is also investigated by modifying the gear tooth profile through lead crowning and tip/root relief (Barbieri et al. 2008; Maatar and Velex 1997; Velex et al. 2011). Since tooth profile modification is on an order of microns and it is in the same order of manufacturing variance, a robust design optimization using Taguchi Method is adopted in the literature (Sundaresan et al. 1991; Yu 1998; Ghribi et al. 2012) to make the gear profile design insensitive to the manufacturing variance.

It is suggested that a gear tooth profile optimization process consists of two steps: (1) generation of a candidate design that meets design requirements (e.g., the center distance, gear ratio, etc.) and constraints (e.g., maximum bending and contact stresses, etc.) and (2) tooth profile optimization (Sundaresan et al. 1991). That is, the candidate design is found at the first stage, and then further refinement is made by the profile modification at the second stage such that the transmission error can be minimized and insensitive to the manufacturing variance.

It is also shown that the maximum contact pressure due to the cyclical contact loading can be lowered by tooth profile modification (tip relief) (Osman and Velex 2011), therefore allowing for the lowering of the maximum shear stress beneath the contact surface, which is a major driving force for the crack growth due to pitting fatigue. It is important to notice here that, for the evaluation of the effect of profile modification on the contact fatigue life, precise gear tooth contact geometry as well

as the mesh stiffness variation needs to be incorporated into the multibody gear dynamics simulation model to account for the contact pressure variation associated with the gear tooth microgeometry.

Furthermore, to meet a target reliability for gear tooth contact failure, reliability-based design optimization (RBDO) of an automobile gearbox is discussed in the literature (Madhusekhar and Madhava Reddy 2014), in which gear face width is selected as design variable.

3.2 Gear Dynamics Simulation

In this section, a numerical procedure for gear dynamics simulation of multibody systems is developed using the tabular contact search method. Existing online contact search algorithms, which are widely used in multibody dynamics simulation, lead to a computational intensive procedure if detailed tooth surface geometry described by CAD or measured data points are considered with geometric imperfections. In the numerical procedure developed in this section, the contact geometry analysis based on the non-conformal contact condition is performed using the detailed tooth surface description prior to the dynamic simulation, and then the contact point and the tooth geometry at the contact point stored in the look-up contact tables are used to determine mesh forces in the multibody gear dynamics simulation. This allows for detecting multi-point contact without any iterative procedures and the contact point on the backside of the tooth can also be considered by switching look-up contact tables in a straightforward manner.

3.2.1 Parameterization of Gear Tooth Surface

As shown in Fig. 3.1, the global position vector of a contact point on the tooth k of rigid gear body i can be expressed as

$$\mathbf{r}^{ik} = \mathbf{R}^i + \mathbf{A}^i \overline{\mathbf{u}}^{ik} \tag{3.1}$$

where $\mathbf{R}^i = \begin{bmatrix} R_X^i & R_Y^i & R_Z^i \end{bmatrix}^T$ is the global position vector of the origin of the body coordinate system attached to the center of gear body, $\mathbf{A}^i$ is the orientation matrix parameterized by the three Euler angles $\boldsymbol{\theta}^i = \begin{bmatrix} \psi^i & \phi^i & \theta^i \end{bmatrix}^T$ (successive rotations about the Z^i-, X^i-, and Y^i-axes of the body coordinate system), and $\overline{\mathbf{u}}^{ik}$ defines the location of the contact point defined with respect to the body coordinate system. The gear tooth geometry is parameterized by two surface parameters s_1^{ik} and s_2^{ik}, and the local position vector $\overline{\mathbf{u}}^{ik}$ can be expressed as

$$\overline{\mathbf{u}}^{ik} \left(s_1^{ik}, s_2^{ik} \right) = \overline{\mathbf{u}}_0^{ik} + \mathbf{A}_0^{ik} \overline{\mathbf{u}}_p^{ik} \left(s_1^{ik}, s_2^{ik} \right) \tag{3.2}$$
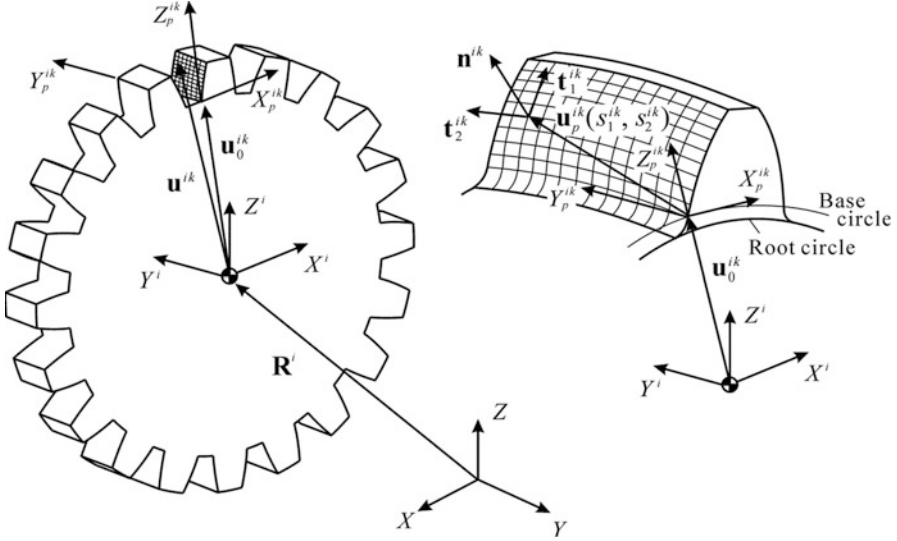
Fig. 3.1 Gear coordinate systems

In the preceding equation, $\bar{\mathbf{u}}_0^{ik}$ and $\mathbf{A}_0^{ik}$ define the location and orientation of the tooth profile coordinate system with respect to the body coordinate system, respectively. The location of the contact point on the tooth profile is defined by $\bar{\mathbf{u}}_p^{ik}\left(s_1^{ik}, s_2^{ik}\right)$ with respect to the profile coordinate system using the surface parameters in either analytical (Litvin and Fuentes 2004) or numerical form (Piegl and Tiller 1996; Shikin and Plis 1995). In the B-spline computational surface geometry representation, the tooth surface can be described with respect to the profile coordinate system as follows (Piegl and Tiller 1996):

$$\bar{\mathbf{u}}_p\left(s_1, s_2\right) = \sum_{a=1}^{n}\sum_{b=1}^{m} N_{a,p}\left(s_1\right) M_{b,q}\left(s_2\right) \mathbf{P}_{a,b} \tag{3.3}$$

For simplicity, the superscripts *ik* that denote the body and contact numbers are omitted. In the preceding equation; p and q are orders of polynomials, n and m are the numbers of basis functions $N_{a,p}(s_1)$ and $M_{b,q}(s_2)$, respectively; and $\mathbf{P}_{a,b}$ $(a = 1, \cdots, n; \quad b = 1, \cdots, m)$ is a vector of control points. The surface parameters in Eq. 3.3 are defined as knots in the entire parametric B-spline domain.

On the other hand, in the case of tooth surface obtained from the direct measurement, smoothing of the original data points $\left(\bar{\mathbf{u}}_p\right)_{ij} = \left[\, x_i \; y_j \; z_{ij} \,\right]^T$ $(i = 1, \ldots, n_x;$ $j = 1, \ldots, n_y)$ needs to be performed to remove undesirable irregularities associated with the measurement noise that causes numerical convergence problems in the contact analysis. To this end, smoothing spline function $f(x, y)$ is generated from the data points such that the following function J can be minimized (Shikin and Plis 1995):

$$J(f) = \int_{y_a}^{y_b} \int_{x_a}^{x_a} \left(\frac{\partial^4 f(x,y)}{\partial x^2 \partial y^2}\right)^2 dxdy + \sum_{i=1}^{n_x} \frac{1}{\rho_i} \int_{y_a}^{y_a} \left(\frac{\partial^2 f(x_i,y)}{\partial y^2}\right)^2 dy$$
$$+ \sum_{j=1}^{n_y} \frac{1}{\sigma_j} \int_{x_a}^{x_b} \left(\frac{\partial^2 f(x,y_j)}{\partial x^2}\right)^2 dx + \sum_{i=1}^{n_x} \sum_{j=1}^{n_y} \frac{1}{\rho_i \sigma_j} \left(f\left(x_i, y_j\right) - z_{ij}\right)^2 \tag{3.4}$$

where $[x_a, \ x_b]$ and $[y_a, \ y_b]$ are the data domain and $\rho_i \geq 0$ and $\sigma_j \geq 0$ are weight coefficients for smoothing. Furthermore, to ensure the continuity of the derivatives of the generated surface, the three-layer smoothing spline technique is employed (Shabana et al. 2008). If the tooth profile is assumed to be constant along the width, the smoothing spline curve can be used instead to parameterize the tooth surface.

Using the local position vector defined by Eq. 3.3, a unit normal vector to the tangent plane can be defined in the profile coordinate system as

$$\bar{\mathbf{n}}^{ik} = \frac{\bar{\mathbf{t}}_1^{ik} \times \bar{\mathbf{t}}_2^{ik}}{\left|\bar{\mathbf{t}}_1^{ik} \times \bar{\mathbf{t}}_2^{ik}\right|} \tag{3.5}$$

where $\bar{\mathbf{t}}_1^{ik} = \partial \bar{\mathbf{u}}_p^{ik}/\partial s_1^{ik}$ and $\bar{\mathbf{t}}_2^{ik} = \partial \bar{\mathbf{u}}_p^{ik}/\partial s_2^{ik}$ are the tangent vectors. The principal curvature κ_l^{ik} can then be obtained as the eigenvalues from the following generalized eigenvalue problem (Litvin and Fuentes 2004):

$$\left(\mathbf{B}^{ik} - \kappa_l^{ik}\mathbf{A}^{ik}\right)\mathbf{X}_l^{ik} = \mathbf{0} \ , \quad l = 1, \ 2 \tag{3.6}$$

where

$$\mathbf{A}^{ik} = \begin{bmatrix} E^{ik} & F^{ik} \\ F^{ik} & G^{ik} \end{bmatrix} \ \text{and} \ \mathbf{B}^{ik} = \begin{bmatrix} L^{ik} & M^{ik} \\ M^{ik} & N^{ik} \end{bmatrix} \tag{3.7}$$

In the preceding matrices, E^{ik}, F^{ik}, and G^{ik} are coefficients of the first fundamental form defined by

$$E^{ik} = \bar{\mathbf{t}}_1^{ik} \cdot \bar{\mathbf{t}}_1^{ik}, \quad F^{ik} = \bar{\mathbf{t}}_1^{ik} \cdot \bar{\mathbf{t}}_2^{ik}, \quad G^{ik} = \bar{\mathbf{t}}_2^{ik} \cdot \bar{\mathbf{t}}_2^{ik} \tag{3.8}$$

and L^{ik}, M^{ik}, and N^{ik} are coefficients of the second fundamental form defined as follows:

$$\left. \begin{aligned} L^{ik} &= -\bar{\mathbf{t}}_1^{ik} \cdot \left(\frac{\partial \bar{\mathbf{n}}^{ik}}{\partial s_1^{ik}}\right) \\ M^{ik} &= -\frac{1}{2}\left(\bar{\mathbf{t}}_1^{ik} \cdot \left(\frac{\partial \bar{\mathbf{n}}^{ik}}{\partial s_2^{ik}}\right) + \bar{\mathbf{t}}_2^{ik} \cdot \left(\frac{\partial \bar{\mathbf{n}}^{ik}}{\partial s_1^{ik}}\right)\right) \\ N^{ik} &= -\bar{\mathbf{t}}_2^{ik} \cdot \left(\frac{\partial \bar{\mathbf{n}}^{ik}}{\partial s_2^{ik}}\right) \end{aligned} \right\} \tag{3.9}$$

The principal directions of the principal curvatures κ_1^{ik} and κ_2^{ik} can be defined by the eigenvectors associated with them, and they are used to evaluate the Hertzian contact patch between the tooth surfaces in contact.

3.2.2 Gear Contact Formulation

3.2.2.1 Tabular Contact Search for Gear Tooth Contact

With the detailed tooth surface description discussed in the previous section, the contact search is performed in the multibody dynamics simulation. Use of online contact search algorithms, which are widely used in general multibody dynamics computer formulations, leads to extensive computational time if general CAD or measured tooth profiles (Kin 1994; Zhang et al. 1994) are considered together with various gear geometry imperfections. For this reason, a contact search algorithm based on look-up contact tables is generalized in this study to the gear dynamics simulation of multibody systems.

Since the gear tooth contact is periodic, solution to the contact geometry problem of a one-tooth contact model can be repeatedly used for detecting the contact of all the teeth in the gear body. In other words, the contact geometry analysis for a one-tooth model is performed a priori for various rotation angles and the contact point as well as the tooth geometry at the contact point, which includes tangents, normal, and principal curvatures, is stored at various configurations in the look-up table. The look-up table obtained for the one-tooth model is then interpolated as a function of rotation of gear bodies to determine the location of the contact point online. One can also include the in-plane and out-of-plane relative displacement between centers of the gear bodies as an input to the look-up contact tables to consider the effect of the shaft deflection and the bearing compliance on the change in the contact point on the tooth surfaces. Furthermore, use of look-up contact tables allows for the detection of a jump in contact point in a straightforward manner for measured tooth profiles with tooth surface imperfections (Li et al. 2015). While look-up contact tables of all pairs of gears in the gear train under consideration need to be prepared in advance, the gear tooth contact search can be performed efficiently without any iterative solution procedures in the dynamic simulation while retaining the detailed gear contact geometry in calculation of the mesh forces.

3.2.2.2 Contact Geometry Analysis Using Non-conformal Contact Constraints

In order to generate the look-up contact tables, the contact geometry analysis of a one-tooth model is carried out. The method is based on the non-conformal contact condition imposed on gear teeth in contact. That is, two points on the two surfaces must coincide, and the two surfaces must have the same tangent planes at the contact

point. These two conditions are described by the following five constraint equations for contact k between surface i and j (Shabana et al. 2008):

$$\mathbf{C}^{ijk}\left(\mathbf{q}^i, \mathbf{q}^j, \mathbf{s}^{ik}, \mathbf{s}^{jk}\right) = \begin{bmatrix} \mathbf{t}_1^{jk} \cdot \left(\mathbf{r}^{ik} - \mathbf{r}^{jk}\right) \\ \mathbf{t}_2^{jk} \cdot \left(\mathbf{r}^{ik} - \mathbf{r}^{jk}\right) \\ \mathbf{n}^{jk} \cdot \left(\mathbf{r}^{ik} - \mathbf{r}^{jk}\right) \\ \mathbf{t}_1^{ik} \cdot \mathbf{n}^{jk} \\ \mathbf{t}_2^{ik} \cdot \mathbf{n}^{jk} \end{bmatrix} = \mathbf{0} \qquad (3.10)$$

The preceding equations are defined for 16 unknowns (i.e., 6 generalized coordinates $\mathbf{q}^i = \left[\left(\mathbf{R}^i\right)^T \left(\boldsymbol{\theta}^i\right)^T\right]^T$ and 2 surface parameters $\mathbf{s}^{ik} = \left[s_1^{ik}\ s_2^{ik}\right]^T$ for each body). To determine all the sixteen unknowns, the three translational coordinates and two rotations about the axes perpendicular to the gear rotation axis of gear j are constrained first. This leads to the following five constraint equations:

$$\mathbf{R}^j - \mathbf{R}_0^j = \mathbf{0}, \quad \psi^j - \psi_0^j = 0, \quad \phi^j - \phi_0^j = 0 \qquad (3.11)$$

where the gear spin axis is defined by the Y^j-axis of the body coordinate system as shown in Figs. 3.1 and 3.2; ψ^j and ϕ^j are Euler angles about the Z^j- and X^j-axes of the body coordinate system, respectively. The subscript 0 in the preceding equations denotes coordinates at the initial configuration. By imposing the non-conformal contact constraint equations given by Eq. 3.10, the location of the contact point (i.e., surface parameters $\mathbf{s}^i$ and $\mathbf{s}^j$) and the spin angle θ^j of gear j are determined for prescribed position and orientation of gear i. In the simplest case, only spin rotation angle θ^i is selected as a variable, and it leads to the following six equations:

$$\mathbf{R}^i - \mathbf{R}_0^i = \mathbf{0}, \quad \psi^i - \psi_0^i = 0, \quad \phi^i - \phi_0^i = 0, \quad \theta^i - \delta_\theta^{i(n)} = 0 \qquad (3.12)$$

where $\delta_\theta^{i(n)}$ defines the prescribed spin angle at incremental step n and the spin angle is defined in the range that the two teeth are in contact. The effect of the axial, radial, and angular misalignments of gear shaft can also be considered by prescribing the relative deviations between gear body i and j. A total of 16 equations given by Eqs. 3.10, 3.11, and 3.12 are solved iteratively using Newton-Raphson method for 16 unknowns at every step n, and the results are stored in the look-up contact table. The look-up table contains not only the generalized coordinates and surface parameters of both bodies at each configuration but also the tangent vectors ($\bar{\mathbf{t}}_1^{ik}$ and $\bar{\mathbf{t}}_2^{ik}$), unit normal ($\bar{\mathbf{n}}^{ik}$), and principal curvatures (κ_1^{ik} and κ_2^{ik}) at the contact point evaluated by Eqs. 3.5 and 3.6.

3.2.2.3   Combined Nodal and Non-conformal Contact Search

For ideal involute profiles, use of the non-conformal equations leads to efficient solutions in the contact geometry analysis of gear teeth. On the other hand, in
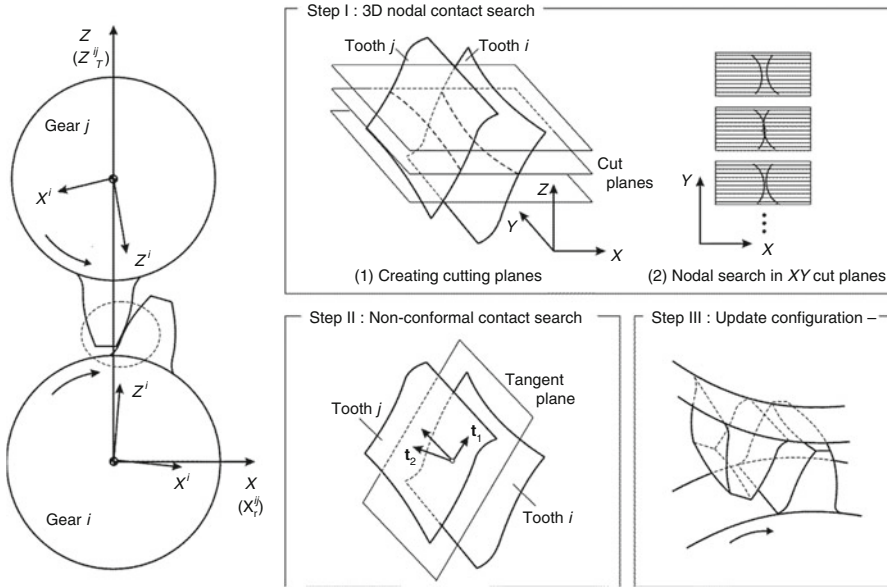
Fig. 3.2 Combined nodal and non-conformal contact search for gear tooth contact

the case of measured tooth profiles with tooth surface imperfections (Kin 1994; Zhang et al. 1994), undesirable jumps in the contact point occur on the surface, and the use of the non-conformal contact search leads to a difficulty in finding the correct contact point. Since the solution of the iterative solution procedure is obtained around the initial estimate provided, it fails to detect the discontinuous jump in contact point if the initial estimate is far from the solution sought. For this reason, in this study, the nodal search is employed as a global search to provide a rough estimate of the contact point (i.e., surface parameters), and then the contact point obtained is used as the initial estimate for the non-conformal contact search equations as shown in Fig. 3.2. Such a two-stage procedure leads to a robust algorithm, which allows for detecting an appropriate initial estimate for non-conformal contact search for tooth surfaces with tooth surface imperfections.

To determine the contact point between two arbitrary surfaces in the three-dimensional space using the nodal search method, each tooth surface is discretized into nodal points first, and the nodal coordinates, defined with respect to its profile coordinate system, are stored in a tabular form together with the surface parameters associated with them. For a given configuration of two gear teeth, the global position of the discretized nodal points is evaluated using Eq. 3.1. The gear surfaces in the three-dimensional space are then sliced into a number of two-dimensional plane along the Z-axis as shown in Fig. 3.2.

The cut planes that contain both tooth profile curves are extracted for further consideration. Having obtained the multiple two-dimensional profile curves discretized by a number of nodal points in the XY cut planes, the relative distances

between the two curves along the X-axis are calculated, and the minimum distance is identified for each plane. If the distance is negative, the two surfaces at the nodal points are penetrated. If none of the minimum distances is negative, the pitch angle θ^j of gear j is incremented until the contact nodes with penetration are detected. Recall here that the pitch angle θ^i of gear i is prescribed by Eq. 3.12 at every step. Having determined the contact point (i.e., a pair of nodes in contact on body i and j), the surface parameters associated with these nodes are obtained and used as initial estimates for the interactive solution procedure for the non-conformal contact search equations given by Eqs. 3.10, 3.11, and 3.12. The accuracy of the contact point and the computational effort in the nodal search stage depend on the resolution of the nodal surface discretization. However, the contact point obtained by the nodal search is not used as the final solution but rather used as the initial estimates for the iterative solution procedure; thus, one can use relatively coarse mesh.

3.2.3   Numerical Procedure in Dynamic Simulation

3.2.3.1   Tabular Contact Search in Dynamic Simulation

In the contact geometry analysis discussed in the previous section, the global coordinate system is defined such that: (1) the origin of the coordinate system is attached to the center of the gear body i; (2) the global Y-axis is parallel to the axis of spin rotation of gear body i; and (3) the global Z-axis passes through the center of gear body j as shown in Fig. 3.2. In other words, the generalized coordinates stored in the look-up contact tables are defined with respect to this coordinate system introduced in the contact geometry analysis. For this reason, the generalized coordinates of gear bodies defined in the dynamic simulation need to be transformed to those consistent with the contact geometry analysis, and then the look-up contact table needs to be utilized with the transformed generalized coordinates. Hereinafter, this coordinate system is called the look-up table coordinate system. The orientation of the look-up table coordinate system $\mathbf{A}_T^{ij} = \begin{bmatrix} \mathbf{i}_T^{ij} & \mathbf{j}_T^{ij} & \mathbf{k}_T^{ij} \end{bmatrix}$ for gear body i and j is defined by the following three unit vectors:

$$\mathbf{i}_T^{ij} = \mathbf{j}_T^{ij} \times \mathbf{k}_T^{ij}, \quad \mathbf{j}_T^{ij} = \mathbf{j}^i, \quad \mathbf{k}_T^{ij} = \frac{\mathbf{R}^j - \mathbf{R}^i}{\left| \mathbf{R}^j - \mathbf{R}^i \right|} \tag{3.13}$$

where $\mathbf{j}^i$ is the unit vector along the Y-axis (spin axis) of the body coordinate system of gear body i. The orientation matrices of gear i and j defined with respect to the look-up table coordinate system are defined as

$$\widehat{\mathbf{A}}^i = \left(\mathbf{A}_T^{ij} \right)^T \mathbf{A}^i \text{ and } \widehat{\mathbf{A}}^j = \left(\mathbf{A}_T^{ij} \right)^T \mathbf{A}^j \tag{3.14}$$
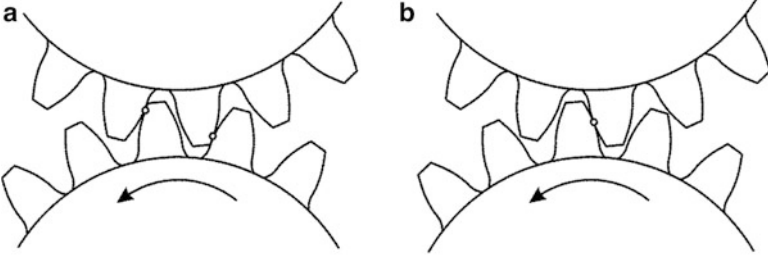
Fig. 3.3 Contact scenario (**a**) Multi-point contact (**b**) Backside contact

from which, one can extract Euler angles $\widehat{\boldsymbol{\theta}}^i = \left[\widehat{\psi}^i \ \widehat{\phi}^i \ \widehat{\theta}^i \right]^T$ and $\widehat{\boldsymbol{\theta}}^j = \left[\widehat{\psi}^j \ \widehat{\phi}^j \ \widehat{\theta}^j \right]^T$ defined with respect to the table coordinate system used for the tabular interpolation. The three translational coordinates that defines the origin of the body coordinate system can also be defined in the look-up table coordinate system as follows:

$$\widehat{\mathbf{R}}^i = \mathbf{0} \text{ and } \widehat{\mathbf{R}}^j = \mathbf{R}^j - \mathbf{R}^i \tag{3.15}$$

from which, the six coordinates of gear body i and j used for the tabular contact search in the dynamic simulation are defined as follows:

$$\widehat{\mathbf{q}}^i = \left[\left(\widehat{\mathbf{R}}^i \right)^T \ \left(\widehat{\boldsymbol{\theta}}^i \right)^T \right]^T \text{ and } \widehat{\mathbf{q}}^j = \left[\left(\widehat{\mathbf{R}}^j \right)^T \ \left(\widehat{\boldsymbol{\theta}}^j \right)^T \right]^T \tag{3.16}$$

The preceding sets of coordinates are consistent with the generalized coordinates stored in the look-up contact tables. The tabular contact search is then carried out for all the gear teeth positioned in the searching range given in the look-up table tooth by tooth. This allows for detecting multi-point contact as shown in Fig. 3.3a without ad hoc procedures. The contact point on the backside of the tooth as shown in Fig. 3.3b can also be considered by switching the look-up table with that of the backside contact in a straightforward manner.

3.2.3.2 Numerical Procedure for Planetary Gear System

To demonstrate the use of the tabular contact search method for complex geared systems, the numerical procedure for a planetary gear model that consists of three planet gears (bodies 1 through 3), one ring gear (body 4), one sun gear (body 5), and one carrier (body 6) shown in Fig. 2.4 is discussed in this subsection. The ring gear is fixed to the ground, and the carrier is connected to the centers of the three planet gears by revolute joints. The carrier is assumed to rotate at a constant speed by imposing a driving constraint.

In this planetary gear model, look-up tables for (1) the ring and planet gear teeth; and (2) the planet and sun gear teeth are prepared prior to the dynamic simulation.
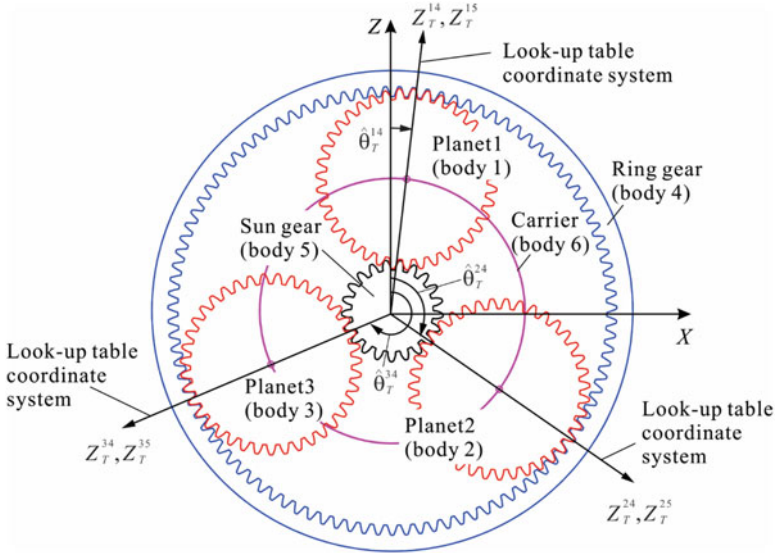
Fig. 3.4 Look-up table coordinate systems of planetary gear contact

For each gear tooth contact, a contact table for the backside tooth surface contact is also prepared if the backlash effect is considered in the dynamic simulation. To determine contact points using look-up contact tables at every time step, the look-up table coordinate system is defined as shown in Fig. 3.4 for each pair of gears in a way described in Sect. 3.2.3.1. As shown in Fig. 3.4, the look-up table coordinate systems defined for the planet and ring gears and the planet and sun gears coincide since centers of the ring and sun gears coincide. The look-up table coordinate system rotates about its Y-axis as the planet gear rotates around the sun gear.

In what follows, the numerical procedure in the dynamic simulation is summarized.

Step 1: For each pair of gears, the look-up table coordinate system is defined at the current configuration, and the generalized coordinates of gear bodies defined with respect to the look-up table coordinate system $\widehat{\mathbf{q}}$ are calculated.

Step 2: Using the rotational coordinates defined with respect to the look-up table coordinate system, the angular position of the gear tooth profile coordinate system positioned in the tabular search range is determined with respect to the look-up table coordinate system at the current configuration. In Fig. 3.5, the three teeth, k, k + 1, and k + 2 are positioned in the tabular search range, and the rotation angles $\theta_p^{14,k}$, $\theta_p^{14,k+1}$, and $\theta_p^{14,k+2}$ of the tooth profile coordinate systems are defined, where the superscript 1 indicates the body number of the planet gear, while superscript 4 indicates that of the ring gear.

Step 3: Using the rotation angle of the tooth profile coordinate system k defined with respect to the look-up table coordinate system, the tabular contact search is

Fig. 3.5 Tooth profile coordinate system of planet and ring gears
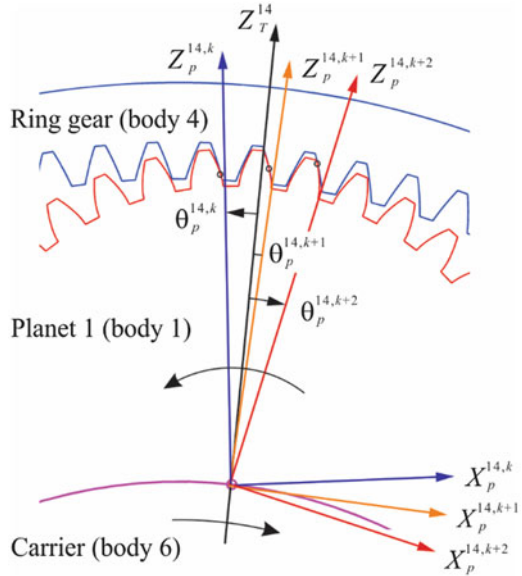
performed to determine the location of the contact point (i.e., surface parameters) and the geometric properties at the contact point. The same procedure is repeated for all the teeth in the tabular search range (i.e., tooth $k + 1$ and $k + 2$ in the model shown in Fig. 3.5).

Step 4: If the tooth under consideration has a tooth geometry imperfection, the look-up table is switched to that accounts for the tooth geometry imperfection.

Step 5: If the backside tooth surface contact is considered, the angular position of the backside tooth profile coordinate systems positioned in the tabular search range is determined (i.e., $\theta_{pb}^{14,k}$, $\theta_{pb}^{14,k+1}$, and $\theta_{pb}^{14,k+2}$ in the model shown in Fig. 3.6). These rotation angles are used to determine whether the backside tooth surface contact occurs or not. The look-up contact tables for the backside contact are used to determine the location of the contact point and the geometric properties at the contact point. That is, the backlash effect can be considered by simply switching the look-up contact tables.

Step 6: The normal and tangential contact forces are calculated using the procedure presented in Sect. 3.2.4 with the variable mesh stiffness model, and then the generalized mesh force vectors are evaluated.

Step 7: The same procedure from Step 1–6 is repeated for all the other pairs of gears in the system.

Step 8: The generalized mesh force vectors of all of the gear bodies under consideration are added to the generalized external force vector $\mathbf{Q}_e$ in the equations of motion of the multibody gear system defined as

Fig. 3.6 Backside tooth profile coordinate system of planet and ring gears
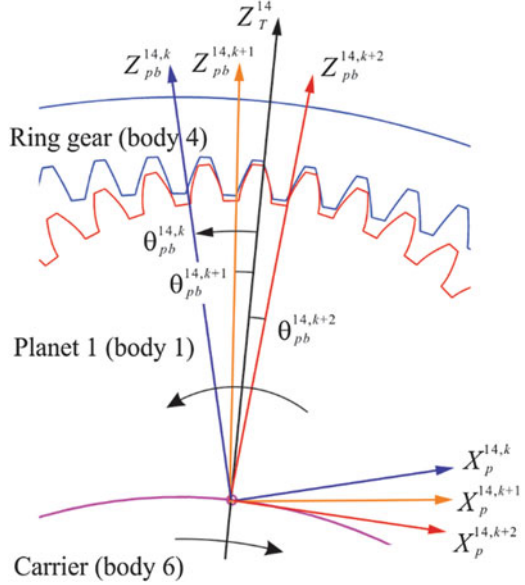
$$\mathbf{M\ddot{q}} + \mathbf{C_q}^T \boldsymbol{\lambda} = \mathbf{Q}_v + \mathbf{Q}_e \atop \mathbf{C}\left(\mathbf{q}, t\right) = \mathbf{0} \Bigg\} \tag{3.17}$$

where $\mathbf{C}$ is the vector of the system constraint equations that describe mechanical joints and/or specified motion trajectories, q is the vector of the system generalized coordinates, $\mathbf{M}$ is the system mass matrix, $\mathbf{Q}_v$ is the vector of inertia forces that are quadratic in velocity, $\mathbf{Q}_e$ is the vector of the generalized external forces, $\mathbf{C_q}$ is the Jacobian matrix of the constraint equations, and $\boldsymbol{\lambda}$ is the vector of Lagrange multipliers that are used to define the generalized constraint forces.

Step 9: The system equations of motion are integrated forward in time to determine the generalized coordinates and velocities using a time integration scheme for differential algebraic equations. Steps 1–9 are repeated until the simulation time is exceeded.

3.2.4 Gear Mesh Stiffness and Contact Force

The normal contact force between two tooth surfaces is defined as

$$F_N^{ijk} = -k_N^{ijk} \delta^{ijk} - c_N^{ijk} \dot{\delta}^{ijk} \left| \delta^{ijk} \right| \tag{3.18}$$

where k_N^{ijk} is the mesh stiffness; c_N^{ijk} is the damping coefficient; δ^{ijk} is the penetration defined by $\delta^{ijk} = (\mathbf{r}^{ik} - \mathbf{r}^{jk}) \cdot \mathbf{n}^{jk}$; $\dot{\delta}^{ijk}$ is its velocity; and $\mathbf{n}^{jk}$ is the unit normal at the contact point defined in the global coordinate system. For an accurate prediction of the transmission error, which is the main source of noise and vibration of gear trains, the mesh stiffness needs to account for the effect of the contact stiffness, tooth bending stiffness, and gear body (foundation) stiffness (Cornell 1981). Due to the nonuniform gear tooth thickness, tooth bending stiffness varies as the contact point move along its length. The compliance of gear tooth i can be modeled with the following series spring model:

$$\frac{1}{k_N^{ik}} = \frac{1}{k_{N1}^{ik}} + \frac{1}{k_{N2}^{ik}} + \frac{1}{k_{N3}^{ik}} \tag{3.19}$$

In the preceding equation, the contact compliance is defined based on the semiempirical Hertz contact model as (Hu et al. 2016b).

$$\frac{1}{k_{N1}} = \frac{1.37}{\left(E_{eff}\right)^{0.9} \left(b_{eff}\right)^{0.8} (F_N)^{0.1}} \tag{3.20}$$

For simplicity, the superscripts ik that denote the body and contact numbers are omitted. In the preceding equation, b_{eff} is the effective face width; F_N is the normal load acting on the tooth face, E_{eff} is the effective Young's modulus determined by Young's modulus and the tooth width to thickness ratio (Tavakoli 1986).

The tooth bending stiffness is approximated by the nonuniform cantilevered beam of an effective length L_e discretized by transverse segments of rectangular cross section as shown in Fig. 3.7. The tooth bending compliance is expressed as (Tavakoli 1986).

$$\frac{1}{k_{N2}} = \sum_{i=1}^{Ns} (Q_{ti} + Q_{si} + Q_{mi}) \cos \beta \tag{3.21}$$

where Ns is the number of the discretized segments and β is the pressure angle at the contact point. The tooth stiffness associated with the transverse normal, transverse shear, and bending deformations is considered in the preceding expression by the compliance Q_{ti}, Q_{si}, and Q_{mi} for segment i, respectively. These compliances are defined as (Tavakoli 1986)

$$Q_{ti} = \frac{\cos \beta}{6 E_{eff} \overline{I}_i} \left(2(L_i)^3 + 3(L_i)^2 S_i\right) \tag{3.22}$$

$$Q_{si} = \frac{1.2 L_i \cos \beta}{G \overline{A}_i} \tag{3.23}$$

Fig. 3.7 Tooth compliance
model

Root circle
Base circle
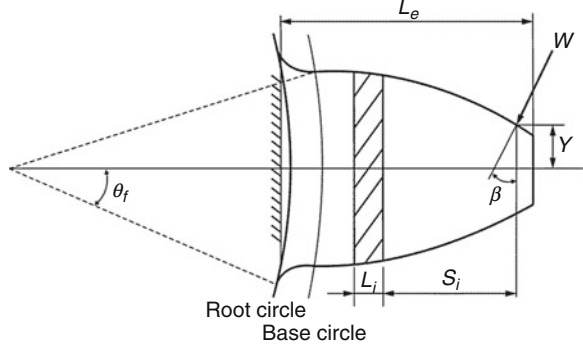
$$Q_{mi} = \frac{(S_i \cos \beta - Y \sin \beta)}{2 E_{eff} \overline{I}_i} \left((L_i)^2 + 2 L_i S_i \right) \tag{3.24}$$

where L_i, $\overline{I}_i$, and $\overline{A}_i$ are the thickness, the mean second moment of area, and the
mean cross-sectional area of segment i, respectively, S_i is the distance between the
segment i and the contact point, and G is the shear modulus of rigidity.

The third factor that contributes to the mesh stiffness is the foundation stiffness
of the gear tooth. The foundation compliance is defined as follows (Cornell 1981):

$$\frac{1}{k_{N3}} = \frac{\cos^2 \beta}{b\,E} \left(L \left(\frac{L_f}{H_f} \right)^2 + M \left(\frac{L_f}{H_f} \right) + P \left(1 + Q \tan^2 \beta \right) \right) \tag{3.25}$$

where b is the tooth face width, E is Young's modulus, L_f is the effective tooth
length, and H_f is the effective tooth thickness. The coefficients L, M, P, and Q in the
preceding equation, based on the semi-infinite elastic plane assumption, are given in
Table 3.1 (Cornell 1981). The semi-analytical formula for the gear body rotational
stiffness for an elastic ring model, on the other hand, is derived in the literature
(Sainsot and Velex 2004). In this case, the four coefficients L, M, P, and Q in Eq.
3.25 are defined by the following polynomial in terms of angle θ_f as shown in Fig.
3.7:

$$X \left(\theta_f, h_f \right) = a_1 \frac{1}{(\theta_f)^2} + a_2 (h_f)^2 + a_3 \frac{h_f}{\theta_f} + a_4 \frac{1}{\theta_f} + a_5 h_f + a_6 \tag{3.26}$$

where the polynomial coefficients a_i ($i = 1, \cdots, 6$) defined for L, M, P, and Q are
given in Table 3.2 (Sainsot and Velex 2004) and h_f is the ratio of the radius of the
root circle to the inside radius of the gear body.

Using Eqs. 3.20, 3.21, and 3.25, one can define the tooth compliance, and then
the total mesh stiffness at contact k between tooth i and j is defined as

$$k_N^{ijk} = \frac{k_N^{ik} k_N^{jk}}{k_N^{ik} + k_N^{jk}} \tag{3.27}$$

Table 3.1 Coefficients L, M, P, and Q for semi-infinite elastic plane assumption model (Cornell 1981)

	Narrow tooth ($R > 5$)	Wide tooth ($R < 5$)
L	5.306	$5.306(1-v^2)$
M	$2(1-v)$	$2(1-v-2v^2)$
P	1.534	$1.534(1-v^2)$
Q	$0.4167/(1 + v)$	$0.4167/(1 + v)$

$R = b/H_p$ (b tooth width, H_p tooth thickness at the pitch point)

Table 3.2 Polynomial coefficients L, M, P, and Q for an elastic ring model (Sainsot and Velex 2004)

	a_1	a_2	a_3	a_4	a_5	a_6
L	-5.574×10^{-5}	-1.9986×10^{-3}	-2.3015×10^{-4}	4.7702×10^{-3}	0.0271	6.8045
M	60.111×10^{-5}	28.100×10^{-3}	-83.431×10^{-4}	-9.9256×10^{-3}	0.1624	0.9086
P	-50.952×10^{-5}	185.50×10^{-3}	0.0538×10^{-4}	53.300×10^{-3}	0.2895	0.9236
Q	-6.2042×10^{-5}	9.0889×10^{-3}	-4.0964×10^{-4}	7.829×10^{-3}	-0.1472	0.6904

from which, the normal contact force vector defined by Eq. 3.18 is expressed in the global coordinate system as follows:

$$\mathbf{F}_N^{ijk} = F_N^{ijk} \mathbf{n}^{jk} \tag{3.28}$$

In order to account for the effect of friction, the unit relative velocity vector along the tangent plane of contact can be determined as

$$\mathbf{v}_T^{ijk} = \frac{\dot{\mathbf{r}}^{ijk} - \left(\dot{\mathbf{r}}^{ijk} \cdot \mathbf{n}^{jk}\right) \mathbf{n}^{jk}}{\left|\dot{\mathbf{r}}^{ijk} - \left(\dot{\mathbf{r}}^{ijk} \cdot \mathbf{n}^{jk}\right) \mathbf{n}^{jk}\right|} \tag{3.29}$$

where $\dot{\mathbf{r}}^{ijk}$ is the relative velocity vector at the contact point. Using an assumption of Coulomb friction, the friction force vector at the contact point can be defined as

$$\mathbf{F}_F^{ijk} = -\, \text{sign}\left(\mathbf{v}_T^{ijk}\right)\ \mu^{ijk} F_N^{ijk}\ \mathbf{v}_T^{ijk} \tag{3.30}$$

where μ^{ijk} is a coefficient of friction. For a more accurate prediction of tangential contact forces on lubricated tooth surfaces, one can use models based on elasto-hydrodynamic lubrication theory (Mohammadpour et al. 2014; Karagiannis et al. 2012).

3.3   Numerical Examples of Gear Dynamics Simulation

In this section, several numerical examples are presented in order to evaluate the accuracy and validity of the numerical procedure proposed for the gear dynamics

Table 3.3 Specification of
the spur gear model

	Gear	Pinion
Number of teeth	82	23
Module (mm)	8.5	
Tooth width (mm)	170	186
Inside diameter (mm)	240	100
Root diameter (mm)	675.75	174.25
Applied torque (Nm)	3500	

simulation of multibody systems. In particular, an accuracy of mesh stiffness model and transmission error of a gear tooth with tip relief is discussed first. A planetary gear model is then introduced to discuss the effect of tooth surface irregularity on mesh force variation. A wind turbine gearbox model is presented in the last example and is validated against test data provided in the literature.

3.3.1 Mesh Stiffness Model

In the first numerical example, the accuracy of the mesh stiffness model presented in Sect. 3.2.4 is discussed. The specification of the spur gear and pinion models considered in this example is summarized in Table 3.3 (Sheng 2012). The tooth and mesh stiffness evaluated using Eqs. 3.18 and 3.26 are presented in Fig. 3.8 as a function of the pinion rotation angle. In this figure, the rotational gear body stiffness based on the semi-infinite elastic plane assumption, defined as Model 1 (see Table 3.1), and the elastic ring model, defined as Model 2 (see Table 3.2), are used for comparison. The tooth and mesh stiffness obtained using the finite element model created by ANSYS™ are also presented in this figure. The eight-node hexahedral and six-node pentahedron elements are used with the augmented Lagrangian method for modeling gear tooth contact. The element is carefully refined around the contact region to ensure the accuracy as shown in Fig. 3.9. The external torque of 3500 Nm is assumed.

It is observed from Fig. 3.8 that the use of the elastic ring rotational stiffness model (Model 2) leads to good agreement with the finite element solution while Model 1 with the semi-infinite elastic plane assumption overestimates the tooth stiffness. In particular, error in the gear tooth is larger than that of the pinion gear due to the larger ratio of the root circle to the inside radii of the gear body.

3.3.2 Transmission Error of Spur Gear Teeth with Tip Relief

In this example, the transmission error of the gear tooth with tip relief is evaluated using the procedure developed in this study. The transmission error is defined by the deviation of the theoretical angular position of a pair of gears from its actual position
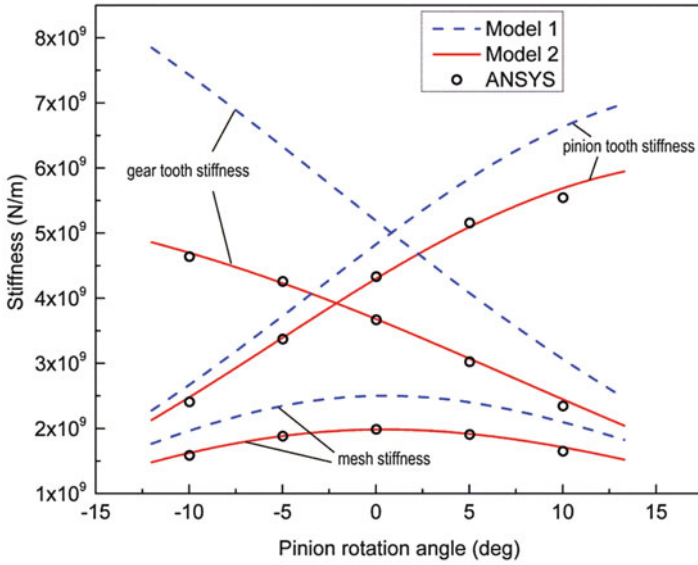
Fig. 3.8 Tooth and mesh stiffness
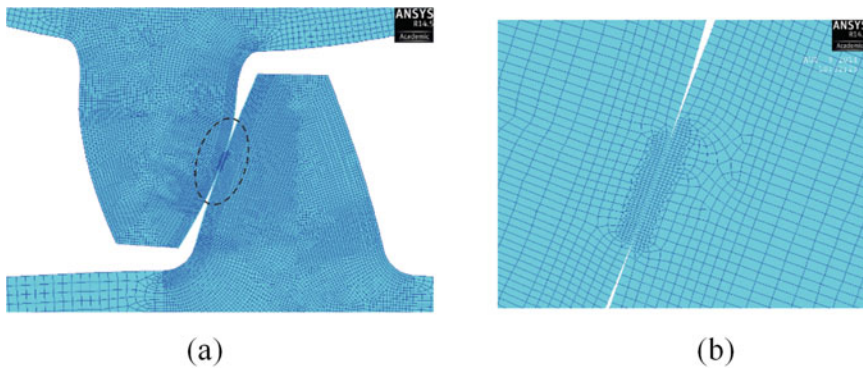
Fig. 3.9 Finite element tooth contact model (**a**) Gear tooth mesh (**b**) Mesh around contact region

at a constant steady rotation and is the main source of gear noise and vibration. To reduce the transmission error at an operating torque, the tip relief is introduced. The linear tip relief, as shown in Fig. 3.10, is defined by the following equation:

$$\delta(r) = \delta_a \frac{r - r_s}{r_a - r_s} \tag{3.31}$$

where r_s is the point that the tip relief starts and its end point is defined by r_a. The amount of tip relief at the end point is defined by δ_a.

Fig. 3.10 Tooth tip relief
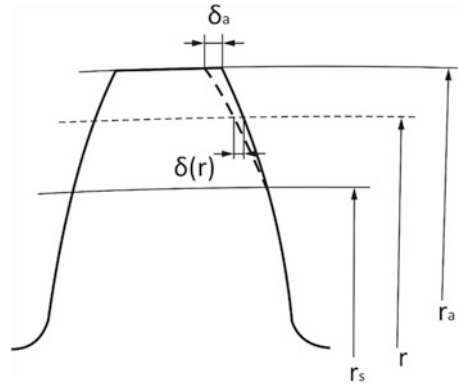
Table 3.4 Specification of the spur gear model with tip relief

Number of teeth	50	Outside diameter	156 mm
Gear ratio	1:1	Root diameter	141 mm
Center distance	150 mm	Pitch diameter	150 mm
Module	3 mm	Pinion tip relief[a]	12.7 μm
Pressure angle	20 deg	Gear tip relief[a]	10.16 μm

[a]The tip relief starts at the tooth pitch point ($r = 75$ mm)

To evaluate the transmission error with the linear tip relief, the specification of the spur gear and pinion in Houser et al. (1996) is used in this study and summarized in Table 3.4, where the linear tip reliefs of the pinion and gear are assumed to be 12.7 μm and 10.16 μm, starting at the pitch point (Houser et al. 1996). The peak to peak transmission errors (PPTEs) with and without the tip relief are compared in the Fig. 3.11. It is observed from this figure that V-pattern of the transmission error versus torque curve is predicted as presented in Houser et al. (1996). If the tip relief is not considered, the PPTE increases as the torque increases. In Fig. 3.11, the lowest PPTE of 36.07 μin (0.9163 μm) is obtained for the external torque of 1550 lbs-in (175 Nm), which are in good agreement with that of Houser et al. (1996).

3.3.3   Dynamic Simulation for Planetary Gear with Tooth Surface Imperfection

In this example, a planetary gear model, which consists of three planet gears, is considered as shown in Fig. 3.12, and the specification is given in Table 3.5. In this model, a small tooth surface imperfection is considered in one of the planet gear teeth with H = 0.288 mm and W = 1.492 mm. All the look-up contact tables for the planet/ring gear teeth contact and planet/sun gear teeth contact are generated first using the procedure discussed in Sect. 3.2.3, and these contact tables are used to predict the contact points in the planetary gear in the dynamic simulation. The change in the location of contact point between the planet gear tooth with the
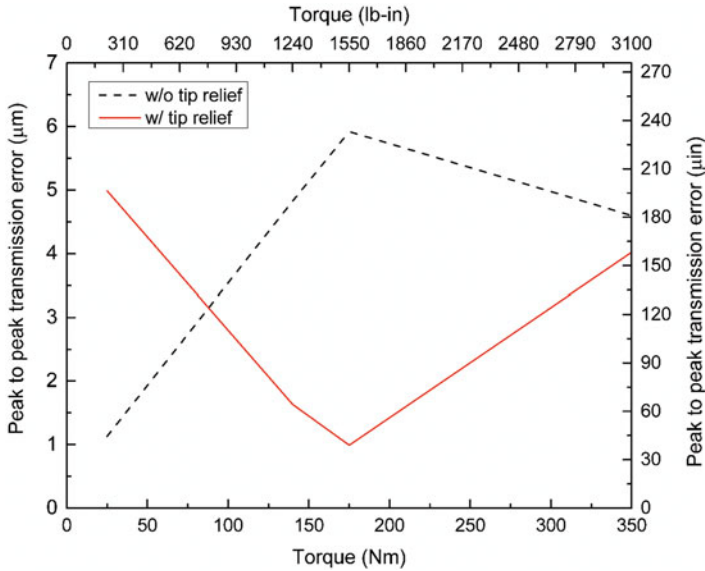
Fig. 3.11 Peak to peak transmission error with and without tip relief
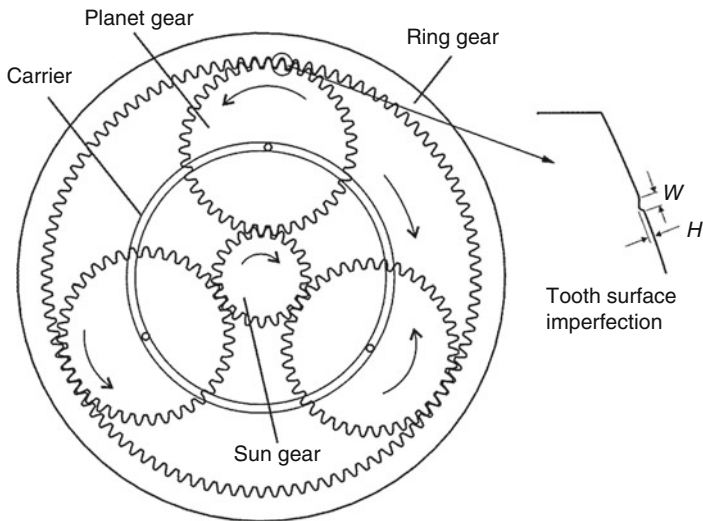
Fig. 3.12 Planetary gear model with tooth surface imperfection

imperfection and the internal ring gear tooth is shown in Figs. 3.13 and 3.14. It is observed from these figures that the contact point moves along the line of action, and then it deviates from the line of action after the contact point reaches the edge of the groove. A jump in contact point occurs from one edge to the other (see points

Table 3.5 Specification of the planetary gear model

Component	# of teeth	Pressure angle(deg)	Pitch diameter (mm)	Tooth width (mm)	Circular crowning (mm)
Sun	21	20	214.2	220	0.5
Planet	39	20	397.8	227.5	0.5
Ring	99	20	1009.8	230	0.5
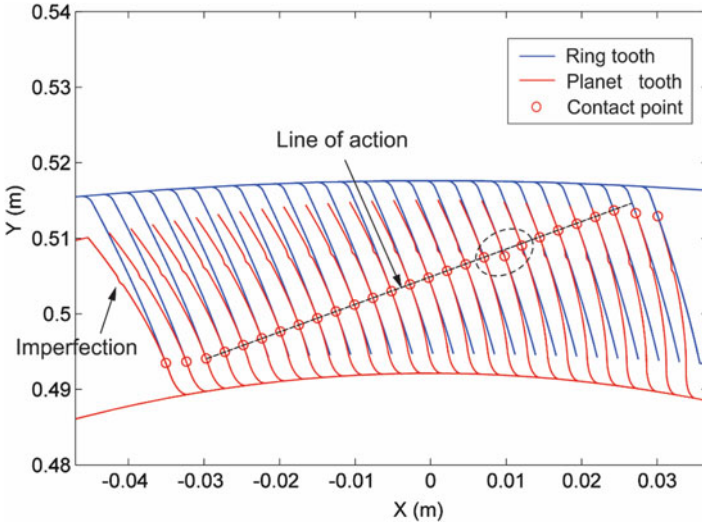
Fig. 3.13 Location of contact point

A and B). This behavior is clearly observed in the surface parameter presented in Fig. 3.15 as a function of the planet gear rotation.

In order to discuss the performance of different contact search methods used in the contact geometry analysis, the accuracy and CPU time are compared and summarized in Table 3.6. The accuracy is measured by the norm of the non-conformal contact constraint violation for solutions obtained by each method and is defined by the following equation:

$$e = \left| \mathbf{C}^{ijk} \left(\mathbf{q}^i, \mathbf{q}^j, \mathbf{s}^{ik}, \mathbf{s}^{jk} \right) \right| \tag{3.32}$$

It is observed from this table that the use of the nodal search method leads to extensive computational burden, and violation of the non-conformal contact condition is noticeable, despite the fact that a very fine nodal discretization (10 μm) is used. Furthermore, the use of the nodal search method leads to discontinuous change in the contact point on the entire surface as shown in Fig. 3.15 and is not suited for an accurate prediction of mesh forces. On the other hand, the non-conformal contact search method failed to reach the convergent solution in the
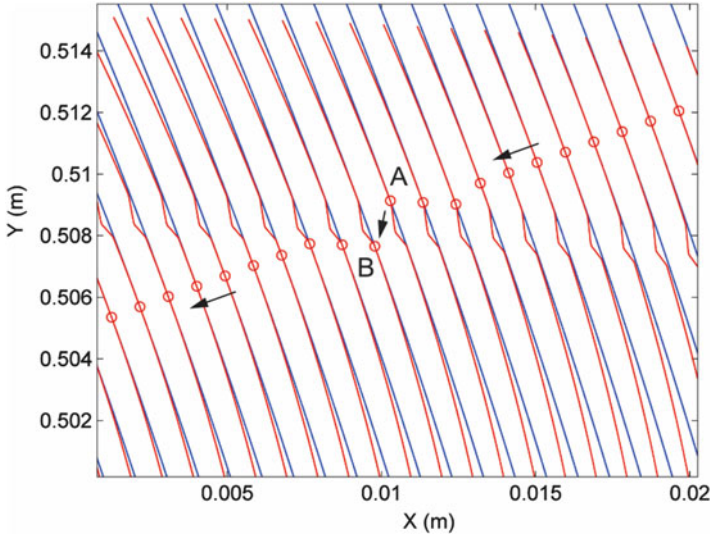
Fig. 3.14 Jump in contact point around the surface imperfection
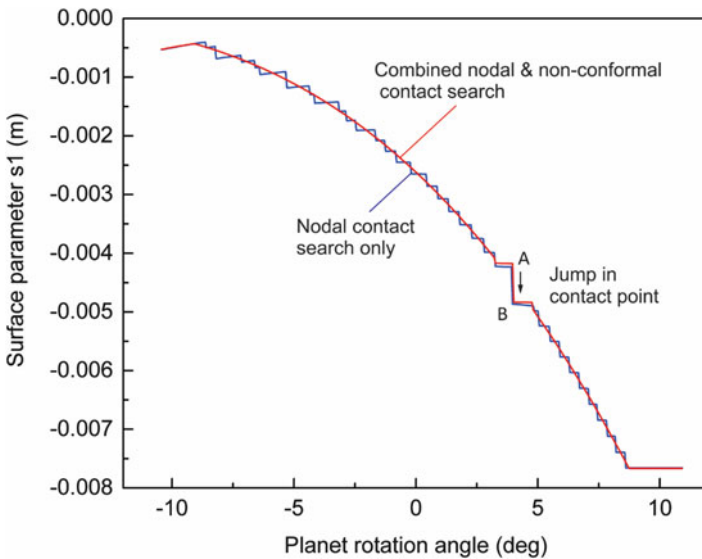
Fig. 3.15 Location of contact point (s1) as a function of rotation angle

vicinity of the groove on the gear tooth surface, where a jump in contact point is supposed to occur.

The combined nodal and non-conformal contact search proposed in this study leads to accurate solutions with significantly less CPU time. This is attributed to the

Table 3.6 Comparison of contact search methods

Contact search method	Nodal search	Non-conformal contact search	Combined nodal and non-conformal contact search (proposed)	
Distance between nodes (m)	1.00×10^{-5}	–	1.00×10^{-5}	2.50×10^{-4}
Maximum error (m)	5.85×10^{-4}	Not converged	4.36×10^{-12}	5.65×10^{-12}
CPU time (s)	20,520	Not converged	2222	97

fact that the nodal search used in the vicinity of the groove allows for detecting the discontinuous change in the contact point, while the non-conformal contact search used in the region where the tooth surface is smooth and continuous leads to fast and accurate solutions. The contact point estimated by the nodal search method is refined using the non-conformal contact equation, thereby enforcing the non-conformal contact condition strictly at every configuration considered in the simulation scenario. It is important to notice here that the use of relatively coarse nodal discretization (250 μm) leads to less CPU time while keeping the same order of accuracy, leading to a robust contact detection algorithm which allows for not only detecting the discontinuous change in the contact point but also the smooth change in the contact point before/after the jump in contact point as shown in Fig. 3.15.

Using the multiple look-up contact tables prepared prior to the dynamic simulation that includes the one considering the planet/ring teeth contact with the imperfection, the dynamic simulation is performed. The look-up table needs to be switched when the nonideal planet tooth enters into the contact search region to consider the effect of the tooth surface imperfection in the mesh force calculation. It is important to notice here that the nonideal planet gear tooth surface shown in Fig. 3.12 does not come into contact with the sun gear since the other side of the ideal tooth surface comes into contact with the sun gear. The carrier is rotated at a constant angular speed of 25 deg./s, and the mesh forces of all the planet/ring teeth contact as well as the planet/sun teeth contact are shown in Figs. 3.16, 3.17, and 3.18. The results in Fig. 3.16 involve the tooth with the imperfection in one of the planet gear teeth. It is observed from Fig. 3.16 that the impulsive change in the mesh force occurs in the planet/ring gear teeth contact when the tooth with the surface imperfection comes into contact.

In particular, a loss of the contact force is observed when the jump in contact point occurs, and it leads to an increase in the mesh force of the tooth next to the one with imperfection. The similar result is observed in the dynamic transmission error (DTE) presented in Fig. 3.19. In this figure, the dynamic transmission errors between the ring and planet gears with and without the tooth surface imperfection are compared. It is observed from this figure that the transmission error increases, and its magnitude becomes same as that of the single point contact when the loss of contact due to the imperfection occurs. This is attributed to the fact that the double tooth contact is changed to the single tooth contact while the contact is lost. Furthermore, the change in the transmission error due to the mesh stiffness variation is also captured in both results. It is also important to notice here that the
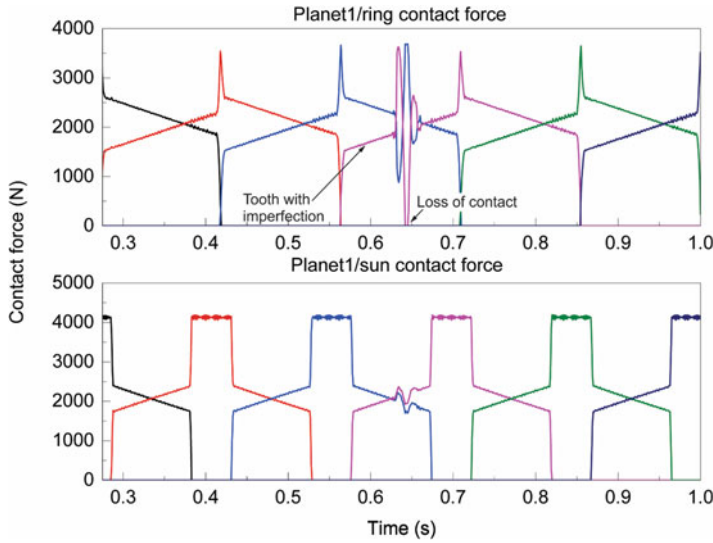
Fig. 3.16 Mesh forces of planet-1/ring and planet-1/sun teeth contact with surface imperfection
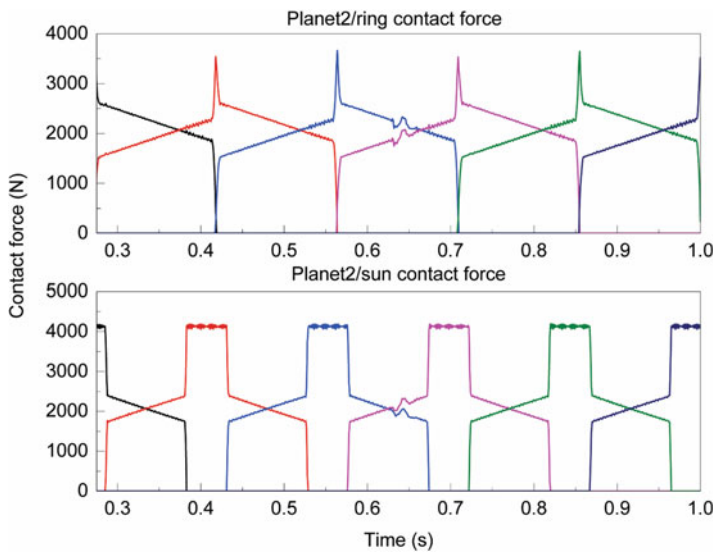
Fig. 3.17 Mesh forces of planet-2/ring and planet-2/sun teeth contact

abrupt change in mesh force caused by the tooth surface imperfection influences the mesh force with the sun gear, and a change in the mesh force is transmitted to the other two planet gears without tooth surface imperfections through the contact with sun gear as observed in Figs. 3.17 and 3.18.
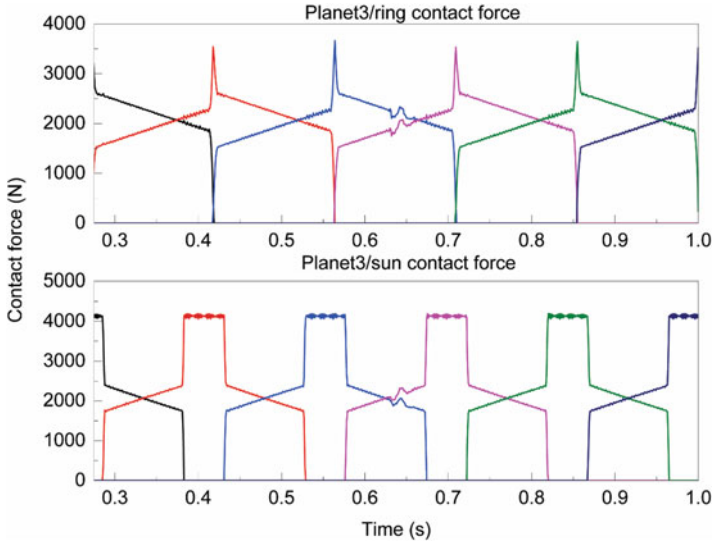
Fig. 3.18 Mesh forces of planet-3/ring and planet-3/sun teeth contact
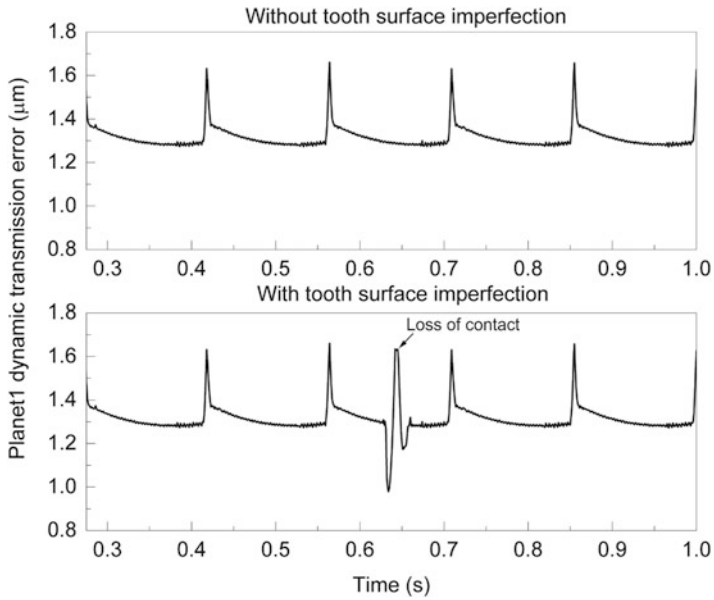
Fig. 3.19 Dynamic transmission error of planet-1/ring teeth contact

Fig. 3.20 Sliced helical gear tooth
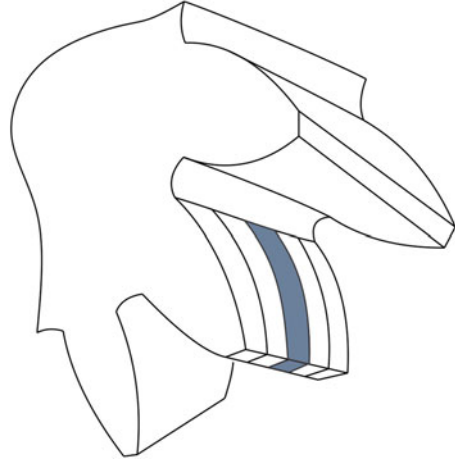
3.3.4   Helical Gear Modeling and Verification

To model helical gear tooth contact in the gear dynamics simulation, the gear tooth is cut into a number of slices across the face width to describe the helix curve as shown in Fig. 3.20, and a point contact is defined on each sliced surface of a helical gear. By doing so, the load distribution across the face width of helical gears can be described as a collection of forces acting on the sliced tooth surfaces in a straightforward manner using a look-up contact table. The transverse module and transverse pressure angle for a helical gear are considered. Since the tooth surface is cut into a number of slices, tabular contact search is repeated for all the slices for one tooth surface in a way described in Sect. 3.2.3.2. It is important to notice here that the look-up coordinate system defined on sliced tooth needs to be rotated by $\Delta\theta$ from the one side to the other incrementally to account for the helix curve, and $\Delta\theta$ is given by

$$\Delta\theta = \frac{B \cdot \cos\alpha_t \cdot \tan\beta_h}{n_s \cdot r_b} \tag{3.33}$$

where B is the face width, α_t is the transverse pressure angle, β_h is the helix angle, r_b is the base radius, and ns is the number of slices. The helical gear mesh force distribution obtained using 21 slices is shown in Fig. 3.21.

To verify the helical gear mesh model in the gear dynamics simulation, the mesh forces obtained using the present approach and the finite element model using ABAQUS are compared. The gear geometry parameters and material properties of the model under consideration are shown in Tables 3.7 and 3.8, respectively. The CAD model of four-tooth gear and pinion is generated and imported into ABAQUS
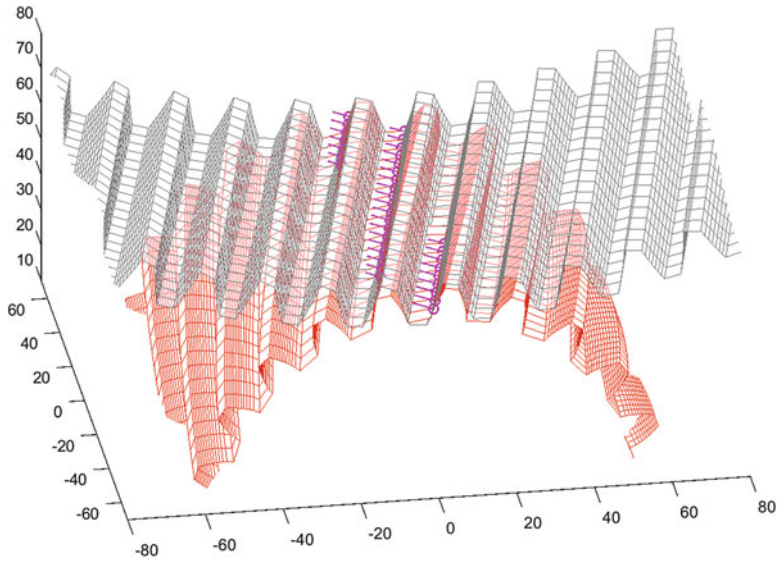
Fig. 3.21 Example of helical gear tooth mesh force distribution with 21 slices

Table 3.7 Basic gear geometry parameters

	No. of teeth	Normal module	Root diameter	Pressure angle	Helix angle	Face width	Center distance
Gear	39	10	372 mm	20°	7.5° L	220 mm	308 mm
Pinion	21	10	186 mm	20°	7.5° R	220 mm	

Table 3.8 Gear material properties

Young's modulus	210 GPa
Poisson ratio	0.3
Density	7850 kg/m^3

for the quasi-static contact analysis between the gear and pinon for various angular positions. The center of the pinion is rigidly fixed to the ground for a given pinion angle in each analysis, while the gear is allowed to rotate about the spin axis, about which a constant torque of 5122 Nm is applied to evaluate the mesh forces on the gear and pinion tooth surfaces. The mesh size of the finite element model is approximately 2.6 mm. The pinion rotational angle is incrementally changed from −16 deg. to 16 deg. with 2 deg. increment as shown in Fig. 3.22. The resultant mesh force of one of the teeth in the pinion at each configuration is presented in Fig. 3.23 and compared with the result obtained using the sliced helical gear model implemented in the gear dynamics simulation code. In the gear dynamics simulation, the pinion is rotated very slowly with the same driving torque as the finite element model. The gear and pinion teeth are cut into 21 slices.
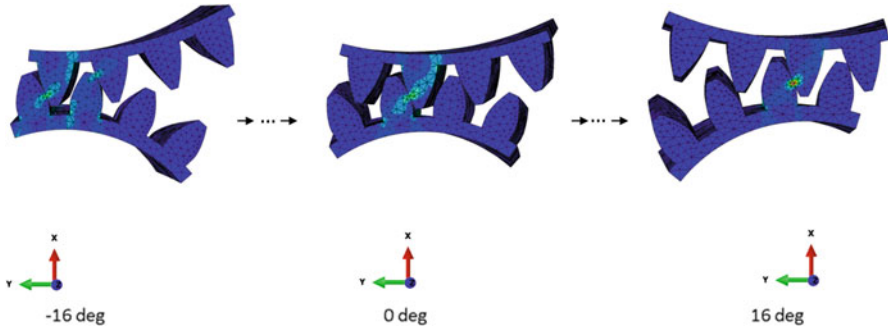
Fig. 3.22 ABAQUS FE model in different configurations
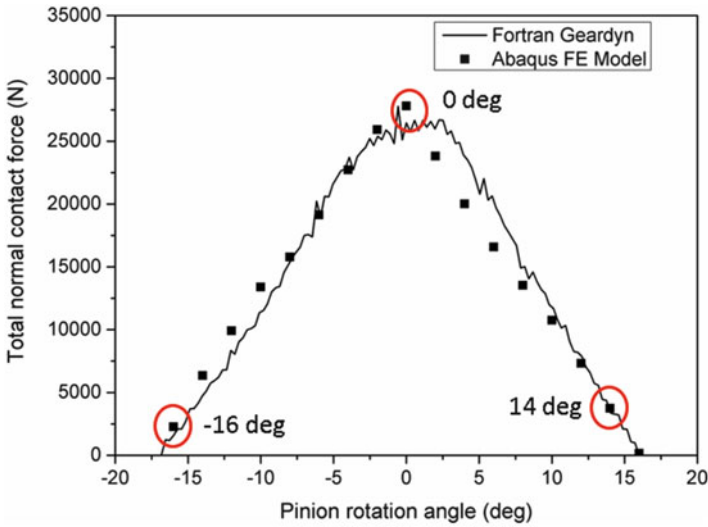
Fig. 3.23 Total contact force variation on pinion second tooth

It is observed from Fig. 3.23 that the gear dynamics simulation results agree well with those of the ABAQUS model for various pinion angles. In order to compare the contact force distribution for different pinion angels, the mesh force distribution at −16, 0, and +14 degrees is compared with ABAQUS results in Figs. 3.24, 3.25, and 3.26, respectively. While only a single tooth is in contact at the pinion angle of 0 degree, two teeth are in contact at the pinion angle of −16 and +14 degrees. The similar mesh force distributions are obtained in both models for the three pinion angels.
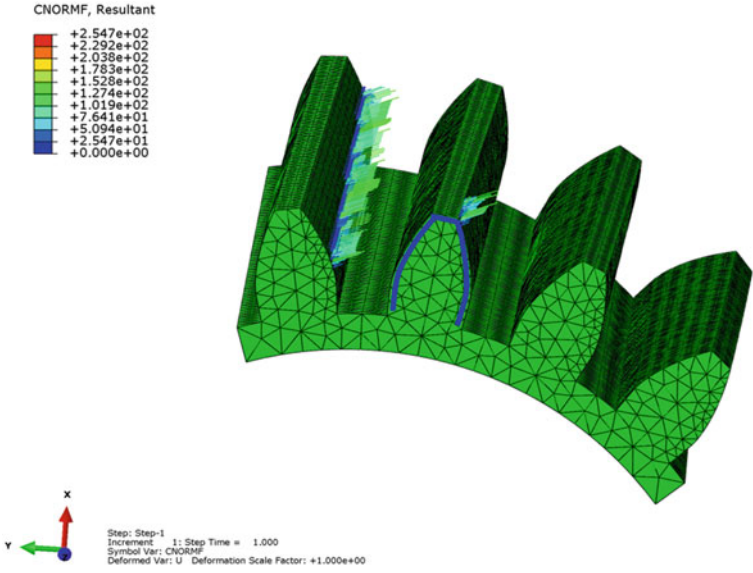
(a)
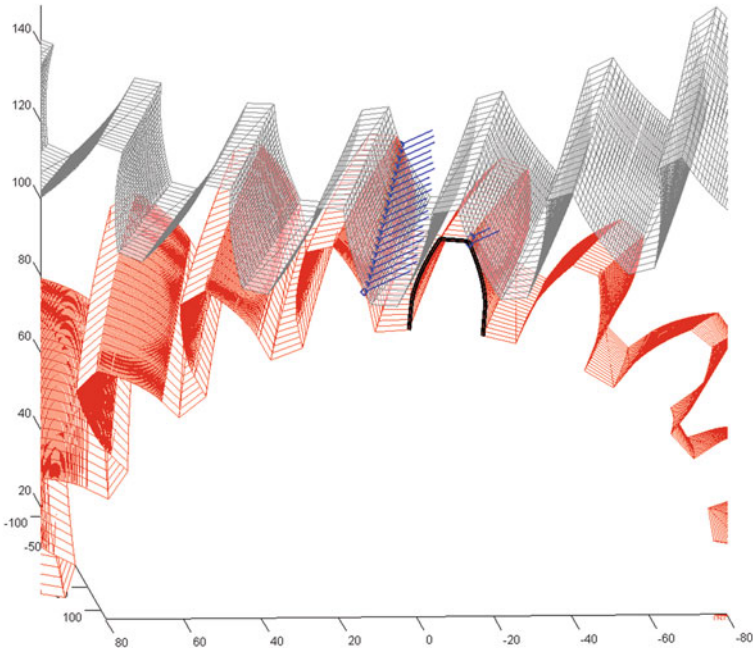
(b)

Fig. 3.24 Contact force distribution at pinion configuration: −16 deg. (**a**) ABAQUS FE model result (**b**) FORTRAN Geardyn model result

(a)

(b)
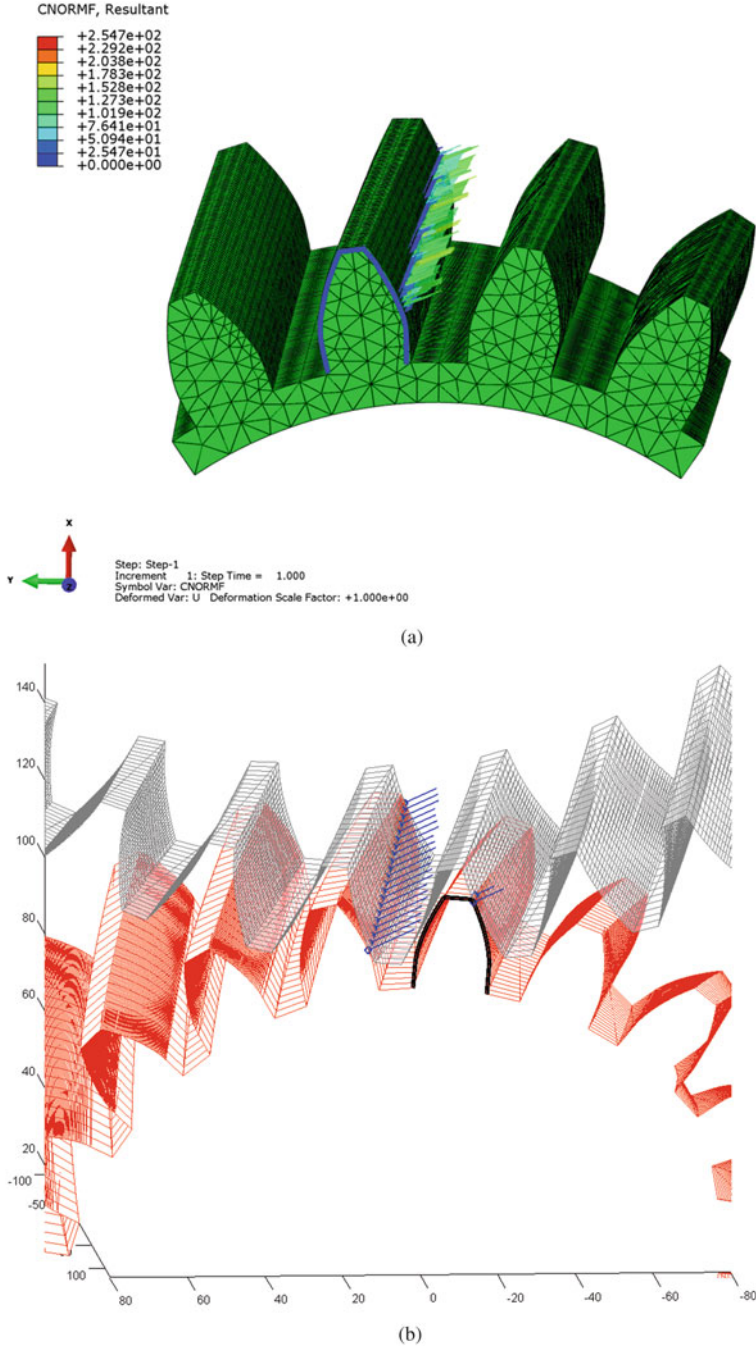
Fig. 3.25 Contact force distribution at pinion configuration: 0 deg. (**a**) ABAQUS FE model result (**b**) FORTRAN Geardyn model result

CNORMF, Resultant

+2.547e+02
+2.292e+02
+2.038e+02
+1.783e+02
+1.528e+02
+1.273e+02
+1.019e+02
+7.641e+01
+5.094e+01
+2.547e+01
+0.000e+00

Step: Step-1
Increment   1: Step Time =   1.000
Symbol Var: CNORMF
Deformed Var: U   Deformation Scale Factor: +1.000e+00

(a)

(b)
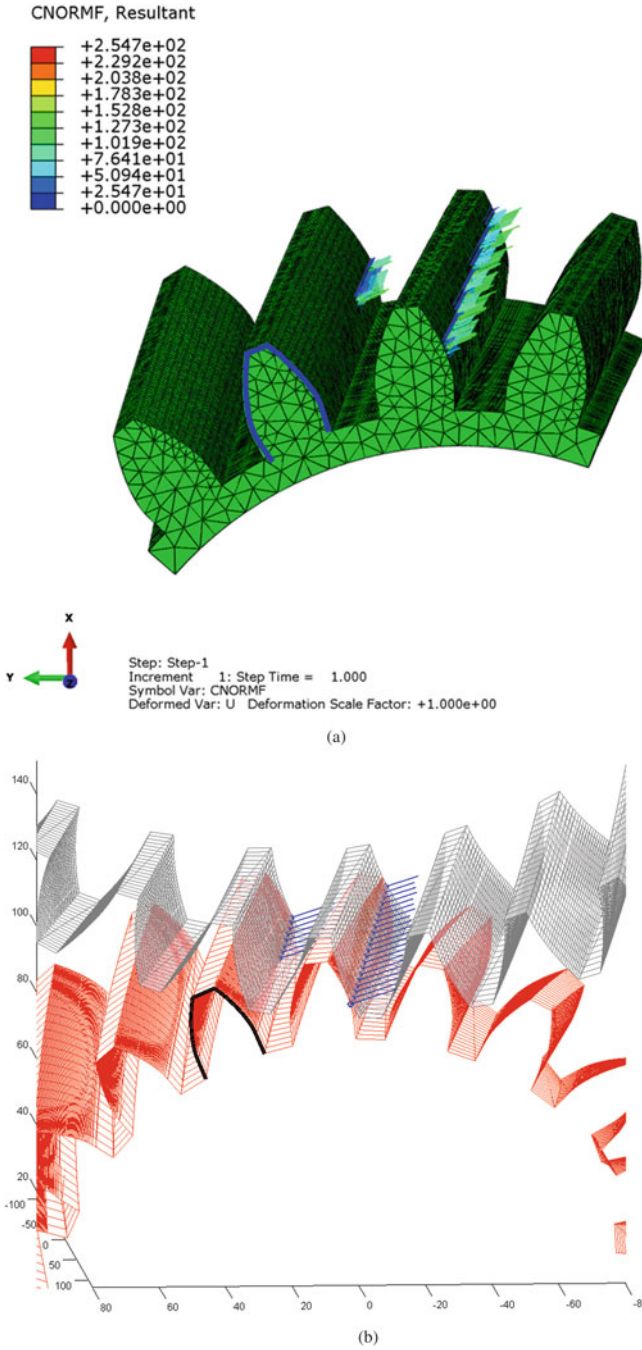
Fig. 3.26 Contact force distribution at pinion configuration: 14 deg. (**a**) ABAQUS FE model result (**b**) FORTRAN Geardyn model resul

Table 3.9 General
description of the wind
turbine (Sheng 2012)

Type	Three blade up wind
Power rating	750 KW
Rotor diameter	48.2 m
Rated rotor speed	22 rpm
Nominal hub height	55 m
Blade length	23.5 m
Gearbox ratio	1:81.491
Rated wind speed	16 m/s
Design life	20 years

3.3.5 Wind Turbine Gearbox Model and Dynamic Simulation

3.3.5.1 Gearbox Model and Specification

In the 750 kW GRC wind turbine as summarized in Table 3.9 (Sheng 2012), the gearbox consists of one planetary gear at the low-speed stage and two parallel axis gears at the intermediate and high-speed stages as shown in Fig. 3.27. Planetary gear systems are commonly used in wind turbine to provide high power density that can be achieved by sharing the large input torque by multiple planet-ring and planet-sun gear contact loads. In the low-speed stage of the GRC gearbox, there are three planet gears framed on the carrier, which carries the input load from wind turbine rotor. The ring gear is fixed to the gear train housing. The sun gear is connected to the input shaft of the intermediate-speed stage parallel axis gear. Considering a lubricated gear toot surface condition, the coefficient of friction is assumed to be 0.04. Gear geometry parameters, mass and inertia properties, and the bearing stiffness can be found in literature (Sheng 2012; Guo et al. 2012a).

NREL conducted field and dynamometer tests for the GRC wind turbine drivetrain (Guo et al. 2012b), and the test data was used to evaluate the accuracy and computation efficiency of the gear train numerical models with different levels of fidelity. In the experimental test setup, the proximity and strain measurement sensors are placed on the planet rim and planet bearings to measure the planet gear motion and its bearing loads, respectively. More details on the test instrumentation can be found in the literature (Guo et al. 2012b). The test data was compared with simulation results obtained using gearbox models with different fidelity. Those computational models include P1 and P2 models created by NREL's partners in industry and academia as well as M1A, M1B, and M3B models created by NREL. The P1 model is a planetary stage multibody model, and the gear face width is divided into nine force elements. The planet carrier and pins are modeled as flexible bodies. The P2 model is a quasi-static fully flexible model created using a software called RomaxWIND. The M1A and M1B models are rigid gear train models created by SIMPACK, where bearing clearance is considered in M1B model. The M3B model is a fully flexible multibody gearbox model, and the housing and carrier deformations are modeled using finite element software ABAQUS, and then the reduced order modal models are imported into SIMPACK. Further details on the model description can be found in literature (Guo et al. 2012b).
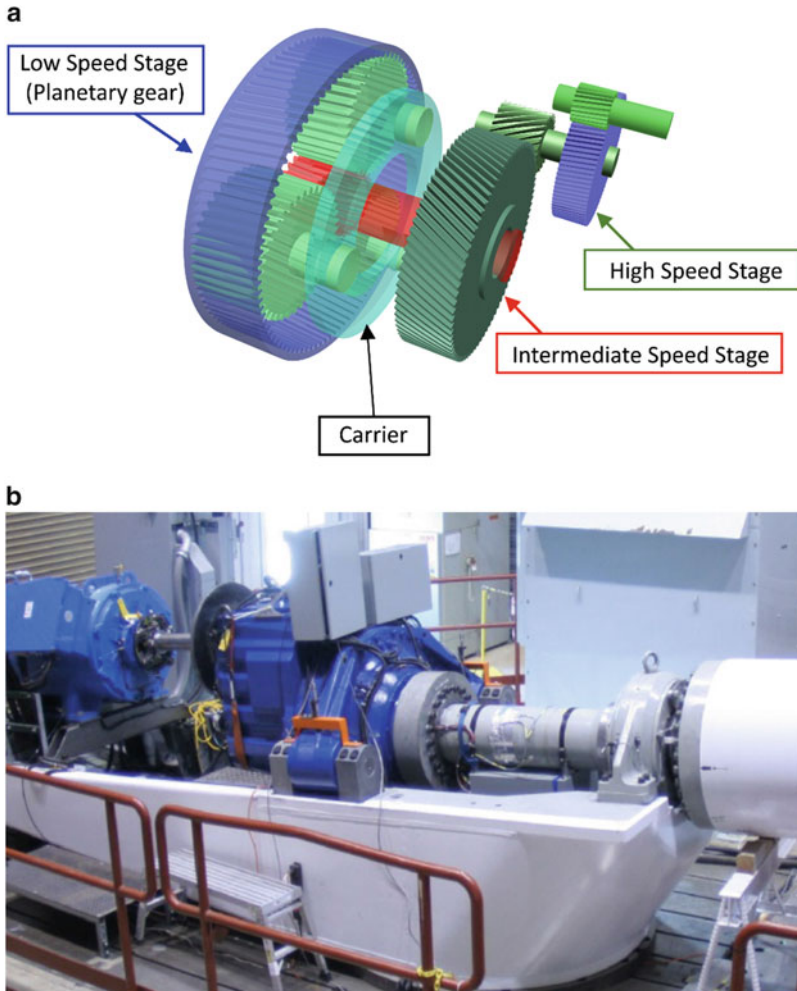
Fig. 3.27 GRC wind turbine drivetrain (**a**) Drivetrain components (**b**) Drivetrain for dynamometer testing (Guo et al. 2012b)

3.3.5.2   Numerical Result and Validation Against Test Data

To demonstrate the capability of the gear dynamics simulation program developed in this study using the tabular contact search method for complex geared systems, two numerical examples are presented. To describe contact geometry of gear teeth in contact in the GRC gearbox model, the following four look-up tables are generated prior to the gear dynamics simulation using the contact geometry analysis described in Sect. 3.2.2:
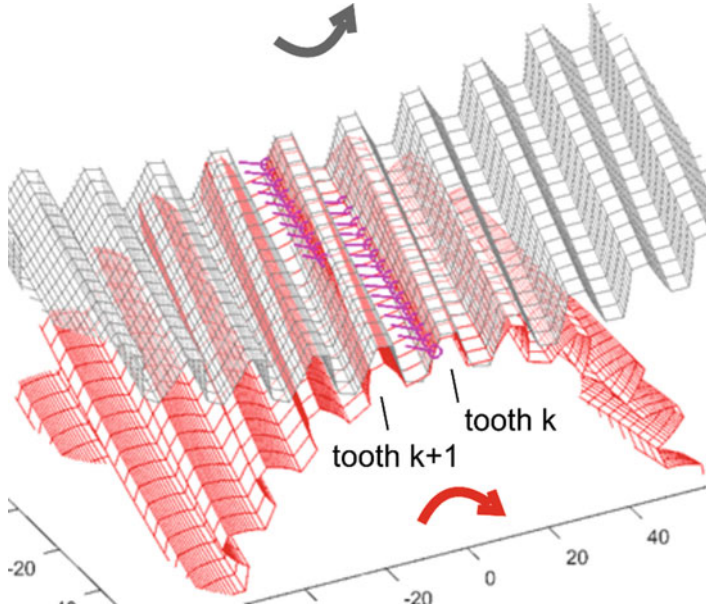
Fig. 3.28 Helical gear mesh force distribution

1. Ring-planet gear tooth contact
2. Planet-sun gear tooth contact
3. Pinion-gear tooth contact at the intermediate-speed stage
4. Pinion-gear tooth contact at the high-speed stage

In the first numerical example for the GRC gearbox, a rated constant angular velocity of 22 rpm is applied to the carrier of planetary gear at the low-speed stage, and the rotational resistance of the output shaft connected to the generator is modeled by a torsional damping (16.92 Nm/rad) at the high-speed stage. There is no gear tooth profile modification (i.e., tip relief). A 2-second simulation is carried out to discuss the mesh force variation. The contact forces between the planet and sun gears at time 0.99 s are shown in Fig. 3.28, where the length and direction of the arrow indicate the magnitude and direction of each contact force on the sliced tooth surface, respectively. The gear tooth is cut into 21 slices in this example. It is observed from this figure that the contact forces are distributed along the straight contact line across the face width and the angle between the contact line and spin axis corresponds to the helix angle.

Since the tooth surface is sliced to model gradual engagement between helical gears, the number of contact points on a tooth surface increases gradually from zero to the maximum number of slices, and then gradually decreases to zero for one mesh cycle. The total contact forces on the planet and sun gear tooth contact are shown in Fig. 3.29. Since the sun-planet gear contact ratio is 2.15, two or three pairs of teeth are always in contact as demonstrated in Fig. 3.29.

Fig. 3.29 Total contact force on planet and sun gear teeth
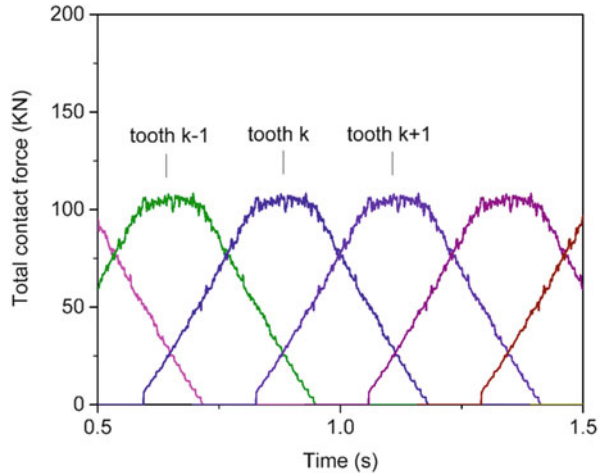
To validate the drivetrain model developed in this study against test data, the planet gear bearing loads calculated in the multibody gearbox dynamic simulation are compared with test data of NREL dynamometer test (Guo et al. 2012b). The sinusoidal torque as shown in Fig. 3.30a is applied to the carrier of the drivetrain simulation model to describe the input torque data of NREL dynamometer test. There are two bearings mounted on each side of the planet gear shaft. The one on the front side is called upwind bearing while that on the rear side is called downwind bearing. The bearing stiffness listed in Guo et al. (2012b) is used for the spring/damper force element. The gravitational force is applied to the geometrical center of each drivetrain component. The upwind bearing forces are compared with NREL test results in Fig. 3.30b, c, showing good agreement in magnitude and frequency with the NREL test results. Furthermore, it is also observed that the simulation results are close to the NREL M1A simulation model results (Guo et al. 2012b), which is a rigid multibody drivetrain model developed using SIMPACK.

It is important to notice there that the non-torque loads caused by the wind turbine rotor overhang weight and aerodynamic forces are not considered in the bench test. In the original GRC wind turbine design, as shown in Fig. 3.27b, the widely used three-point suspension (one main bearing on the rotor shaft and two mounts for the gearbox trunnion) can transfer significant bending loads of the main shaft to the drivetrain, which is approximately 60% of wind turbine rated torque. This main shaft deflection can cause the carrier angular misalignment in the planetary stage of the drivetrain. Despite the micron level deflection of main shaft, the contact stress distribution, the planetary gear load sharing factor, and the gear teeth mesh phasing can be altered. The resulting unequal loads have an adverse impact on the drivetrain contact fatigue life. The non-torque loads are the combination of rotor weight and complex aerodynamic loads which have uncertainty. Thus, the non-torque loads raise a reliability issue for the three-point suspension drivetrains.
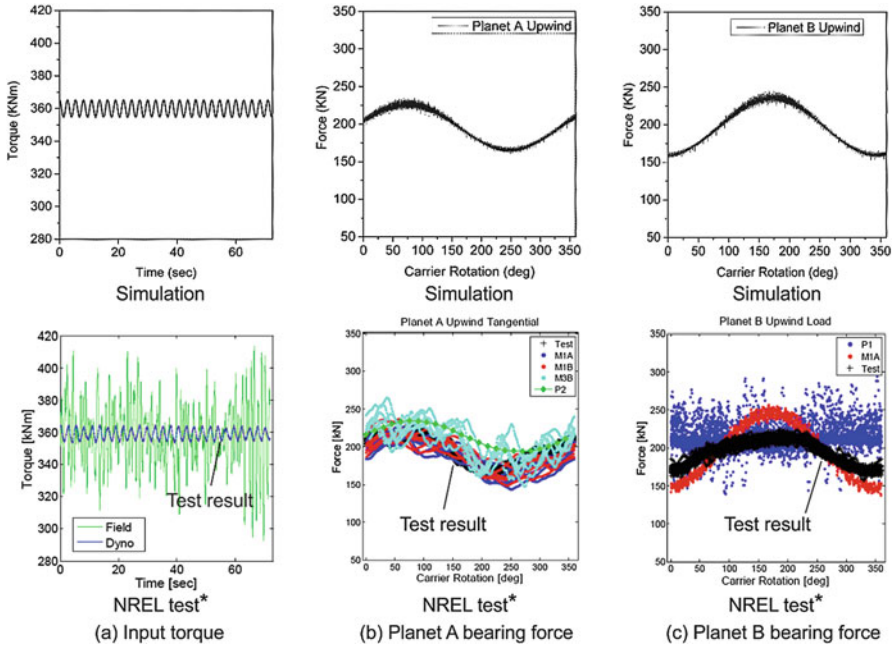
Fig. 3.30 Planetary gear bearing load comparison between simulation results and NREL test results (Guo et al. 2012b)

To address this issue, Alstom designed a new hub support configuration (Guo et al. 2015). In this design, the non-torque loads are transferred directly to the tower rather than through gearbox in original design. It's called Alstom's Pure Torque drivetrain. A significant reduction of carrier misalignment as well as main shaft bending load is demonstrated using the newly designed drivetrain (Guo et al. 2015).

3.4 Contact Fatigue Prediction Using Multibody Gear Dynamics Simulation

3.4.1 Pitting Contact Fatigue Model

Using the dynamic wind load uncertainty model introduced in Chap. 1, a numerical procedure for predicting the pitting fatigue life is discussed in this section. The pitting fatigue is a typical failure mode exhibited in lubricated gears and is classified as the subsurface-initiated failure (Choi and Liu 2006a). That is, the total fatigue life is defined by the sum of the number of load cycles required to initiate the subsurface crack N_i and that required for the crack to propagate to the surface N_p as (Osman and Velex 2011)

$$N = N_i + N_p \tag{3.34}$$

Using the Dang Van's assumption that the fatigue micro-crack appears when the monocrystal reaches the elastic shakedown due to shearing, the number of cycles for crack initiation is defined by (Osman and Velex 2011)

$$N_i = \frac{1}{2} \left(\frac{\tau_{\max} + 3 \left(\tau_f'/\sigma_f' - 0.5 \right) p_H}{\tau_f'} \right)^{1/c} \tag{3.35}$$

where $\tau_{\max}$ and p_H are, respectively, the maximum shear stress and hydrostatic stress in the subsurface; σ_f' and τ_f' are fatigue strength coefficients for tension/compression and shearing, respectively; and c is a fatigue strength exponent. It is assumed that the crack is initiated at a point where the ratio of the maximum shear contact stress to the hardness is maximal and the initial crack is parallel to the surface (Choi and Liu 2006a).

Assuming the Hertzian contact between two cylinders has the radius of curvature of R_1 and R_2, the maximum contact pressure is obtained by $p_{\max} = 2\overline{F}/\pi b_0$ as shown in Fig. 3.31a (Budynas and Nisbett 2008), where $\overline{F}$ is the contact force per unit length along the cylinder axis and b_0 is the half width of the contact patch defined by $b_0 = 2\sqrt{FR/\pi\overline{E}}$. Note that $\overline{E}$ is an equivalent Young's modulus of two materials in contact defined by $1/\overline{E} = \left(1 - v_1^2\right)/E_1 + \left(1 - v_2^2\right)/E_2$; and $\overline{R}$ is an equivalent radius evaluated by the principal radii of curvature at the contact point on surfaces in contact and is defined by $1/\overline{R} = 1/R_1 + 1/R_2$. The greatest value of the maximum shear stress occurs at $z_0 = 0.786\,b_0$ measured from the contact surface with a value of $\tau_{\max} = 0.3p_{\max}$ (Budynas and Nisbett 2008), and it is assumed that the subsurface crack parallel to the surface is initiated at this point when the number of load cycles reaches N_i as illustrated in Fig. 3.31a.

After the subsurface crack is initiated, the crack propagates under cyclical contact loads to the surface. Using the Paris equation, the crack propagation is modeled by (Liu and Zenner 2003)

$$\frac{da_p}{dN} = C_p \left((\Delta K)^m - (\Delta K_0)^m \right) \tag{3.36}$$

where a_p is the half length of the crack; N is the number of load cycles; C_p and m are constants; and ΔK is the model II stress intensity factor range. ΔK_0 is the threshold for the crack growth given by the empirical formula $\Delta K_0 = 2.45 + 3.41 \times 10^{-3}HV$ for the Vickers hardness HV (Kato et al. 1993). That is, the crack grows only if ΔK is greater than ΔK_0. The stress intensity factor ΔK is defined by Choi and Liu (2006a) and Osman and Velex (2011).

$$\Delta K = s\sqrt{\pi a_p}\, U\left(a_p\right) \tag{3.37}$$

where $U(a_p)$ is a factor considering the crack closure given by the empirical formula of Newman $U(a_p) = 0.89(1 + 0.11 \exp{(-0.1a_p)})$ (1992), while s is the crack
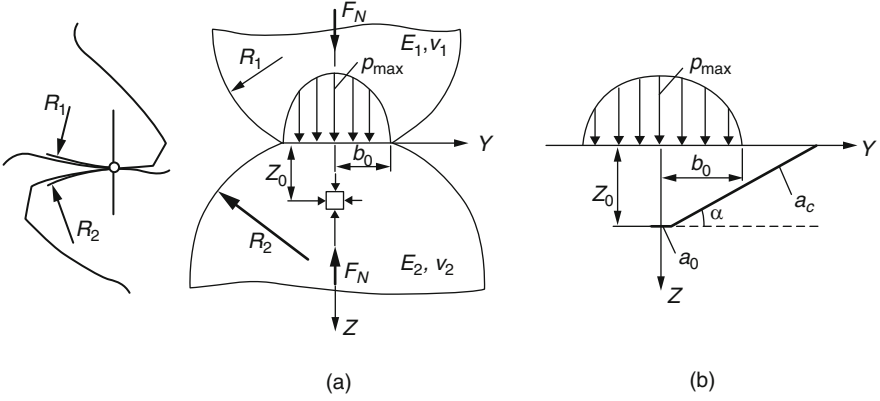
Fig. 3.31 Contact stresses and crack and subsurface-initiated crack (**a**) Contact stresses (**b**) Subsurface-initiated crack

growth driving force. It is shown in the literature (Jiang et al. 1993) that the growth of the subsurface crack under rolling contact loads is driven by the value defined by a ratio of the maximum shear stress to the hardness, and the following expression for s is suggested by considering the effect of porosity and notch effects (Osman and Velex 2011; Jiang et al. 1993):

$$s = \left(\frac{\tau_{\max}\delta_K}{\psi}\right)^2 \frac{1}{HV} \tag{3.38}$$

where $\delta_K = (K_t - 1)\eta + 1$ and $\psi = e^{-4.3\varepsilon}$ for empirically identified parameters K_t, η, and ε (Straffelini et al. 2000). Using Eq. 3.36, the number of cycles that causes the initial crack, parallel to the surface, to reach the surface is calculated as

$$N_p = \int_{a_0}^{a_c} \frac{1}{C_p\left((\Delta K)^m - (\Delta K_0)^m\right)} da_p \tag{3.39}$$

where a_0 is the half length of the initial crack assumed by (Osman and Velex 2011)

$$a_0 = \frac{1}{8\pi}\left(\frac{\Delta K_0}{0.475 S_u}\right)^2 \tag{3.40}$$

and S_u is the ultimate tensile strength. a_c in Eq. 3.39 is a half of the critical crack length and is defined by $a_c = z_0/\sin\alpha$ as shown in Fig. 3.31b, where α defines the direction that the subsurface crack grows and z_0 is the depth from the surface at which the crack is initiated, i.e., a point where the maximum shear stress occurs. Accordingly, the total number of load cycles to pitting failure can be predicted by a sum of Eqs. 3.35 and 3.39 as a function of the maximum shear stress under a cyclic rolling contact load.

3.4.2 Use of Gear Dynamics Simulation for Prediction of Maximum Contact Pressure

As shown in the previous subsection, the crack growth is driven by the maximum shear contact stress τ_{max} due to the contact load, and, therefore, an accurate prediction of the maximum contact pressure p_{max} during gear meshing is of crucial importance in predicting the pitting fatigue life. Furthermore, to account for the wind load uncertainty characterized by the averaged joint PDF of the 10-minute mean wind speed (v_{10}) and turbulence intensity (i_{10}) introduced in Chap. 1, multiple 10-minute gearbox dynamics simulations need to be performed for various choices of v_{10} and i_{10}; thus, use of general multibody dynamics simulation becomes a computational burden in the entire design optimization process. In addition, since the tooth contact pressure is sensitive to the gear tooth profile, an accurate description of the tooth profile geometry and precise contact geometry calculation are required, and use of a simplified gear contact dynamics model is not suited. For example, profile modification called tip relief is widely used to lower the transmission error that is a cause of gear noise and vibration (Litvin and Fuentes 2004; Tavakoli 1986) and a slight modification of the tooth profile geometry on the order of microns alters the contact pressure on the profile surface, thereby influencing the pitting fatigue damage (i.e., crack growth). For this reason, the amount of tip relief is one of the important design parameters, together with the tooth face width (Sundaresan et al. 1991), and the effect of microgeometry needs to be precisely evaluated using the gear dynamics simulation.

For this reason, a numerical procedure for the multibody gear dynamics simulation based on the tabular contact search algorithm presented in Sect. 3.2 is introduced and integrated into the gear design optimization procedure considering the wind load uncertainty. This procedure allows for the detection of the gear tooth contact in an efficient manner by introducing the look-up contact tables while retaining the precise contact geometry and mesh stiffness variation in the evaluation of mesh forces, thereby leading to a computationally efficient gear dynamics simulation suited for the design optimization procedure considering wind load uncertainty.

3.4.3 Probabilistic Contact Fatigue Damage

For evaluation of fatigue life of wind turbine systems, 10-minute wind data is widely used to characterize the short-term wind load variability at a specific location (Veers and Winterstein 1998; Li et al. 2016). As described in Chap. 1, the joint probability density function (PDF) of 10-minute mean wind speed (v_{10}) and 10-minute turbulence intensity (i_{10}) $f_{VI}(v_{10}, i_{10})$ is introduced to characterize the wind load uncertainty. For gear deterministic design optimization, the averaged wind load probability model is developed using Monte Carlo simulation of the joint PDFs for

v_{10} and i_{10} considering the spatiotemporal wind load variability. To this end, one million joint PDFs defined by one million sets of $\mathbf{y}^l = \begin{bmatrix} C^l & k^l & a^l & b^l & \tau^l \end{bmatrix}^T$ ($l = 1, \cdots, N_{VI}$) are described as (Hu et al. 2016a)

$$f_{VI}^{ijl}\left(v_{10}^i, i_{10}^j; \mathbf{y}^l\right) = c_{V\Sigma}\left(v_{10}^i, \sigma_{10}^{ij}; \tau^l\right) \cdot f_{V10}\left(v_{10}^i; C^l, k^l\right) \cdot f_{\Sigma 10}\left(\sigma_{10}^{ij}; a^l, b^l\right) \cdot v_{10}^i \tag{3.41}$$

where $N_{VI} = 1 \times 10^6$ and the PDF are evaluated for v_{10}^i and i_{10}^j. Using the resulting one million joint PDFs, the mean of the PDF evaluated for each v_{10}^i and i_{10}^j is calculated to develop the averaged wind load PDF model used for the design optimization as

$$\overline{f}_{VI}^{ij}\left(v_{10}^i, i_{10}^j\right) = \frac{\sum\limits_{l=1}^{N_{VI}} f_{VI}^{ijl}\left(v_{10}^i, i_{10}^j; \mathbf{y}^l\right)}{N_{VI}} \tag{3.42}$$

where the lower bound of the mean wind speed is selected as the cut-in wind speed, while the upper bound is the cut-out wind speed for the wind turbine under consideration.

In this chapter, the speed range is defined from 5 m/s to 25 m/s with an increment of 2 m/s (i.e., $i = 1, \cdots, 12$), while the turbulence intensity range is assumed from 0.02 (2%) to 1 (100%) with 0.02 (2%) increment (i.e., $j = 1, \cdots, 50$). The averaged joint PDF obtained for the measured wind data is presented in Fig. 3.32. The volume of each bar gives an averaged probability for one scenario defined for v_{10} and i_{10} considering the wind load variation in a wide spatiotemporal range.

Then the 10-minute fatigue damage can be defined as follows:

$$D_{10\,\mathrm{min}}(\mathbf{d}) = \int_{I_L}^{I_U} \int_{V_L}^{V_U} \overline{f}_{VI}(v_{10}, i_{10}) D_{10\,\mathrm{min}}(\mathbf{d}, v_{10}, i_{10}) \, dv_{10} di_{10} \tag{3.43}$$

where $D_{10\mathrm{min}}(\mathbf{d}, v_{10}, i_{10})$ is the 10-minute fatigue damage evaluated for v_{10} and i_{10}; V_L and V_U indicate the lower and upper bounds of the mean wind speed under consideration, and I_L and I_U are those of the turbulence intensity. By numerically integrating Eq. 3.43 using Riemann integral, 1-year fatigue damage can be obtained as

$$D_{1\mathrm{year}} = 6 \times 3000 \sum_{i=1}^{n_v} \sum_{j=1}^{n_i} \overline{f}_{VI}^{ij}\left(v_{10}^i, i_{10}^j\right) D_{10\,\mathrm{min}}^{ij}\left(\mathbf{d}, v_{10}^i, i_{10}^j\right) \Delta v_{10} \Delta i_{10} \tag{3.44}$$

where $D_{10\,\mathrm{min}}^{ij}\left(\mathbf{d}, v_{10}^i, i_{10}^j\right)$ is evaluated for $i = 1, \cdots, n_v$ and $j = 1, \cdots, n_i$. It is assumed that a wind turbine is operated for 3000 h per year (Lesmerises and Crowley 2013), and the gear teeth do not experience cyclical loading during the
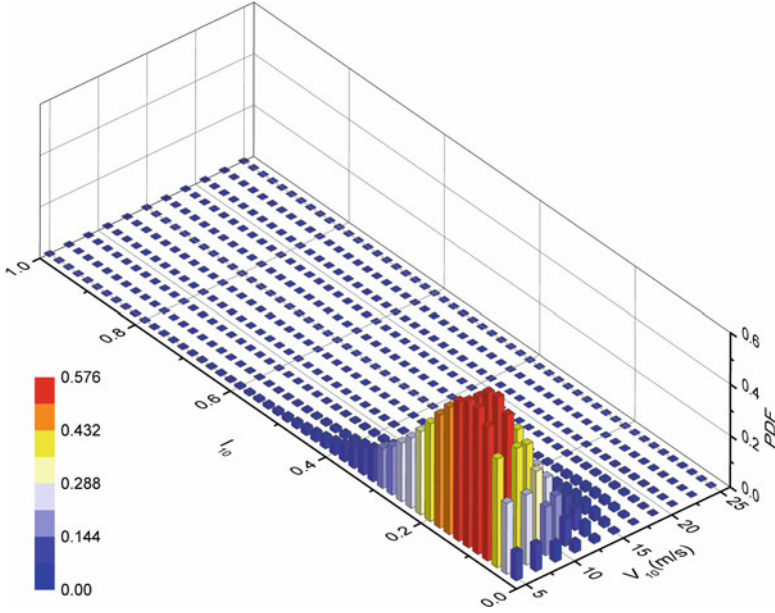
Fig. 3.32 Averaged joint probability density function for v_{10} and i_{10}

maintenance period and when the wind speed is lower than the cut-in wind speed or higher than the cut-out speed. To evaluate the 1-year fatigue damage for given design variable $\mathbf{d}$, the 10-minute damage $D^{ij}_{10\,\mathrm{min}}\left(\mathbf{d}, v^i_{10}, i^j_{10}\right)$ needs to be calculated at $n_v \times n_i$ sampling points for v^i_{10} $(i = 1, \cdots, n_v)$ and i^j_{10} $(j = 1, \cdots, n_i)$ using the 10-minute gearbox dynamics simulation. It is important to notice here that the input rotational speed varies as a function of time; thus, the maximum contact pressure used for the pitting fatigue life calculation varies at each load cycle.

To account for the contact load variation, the pitting fatigue damage is evaluated by Miner's rule as (Melchers 1999)

$$D^{ij}_{10\,\mathrm{min}}\left(\mathbf{d}, v^i_{10}, i^j_{10}\right) = \sum_{k=1}^{n^{ij}_{10}} \frac{1}{N^{ijk}\left(p^{ijk}_{\max}\right)} \tag{3.45}$$

where N^{ijk} is the number of load cycles to failure for each meshing cycle k and n^{ij}_{10} is the number of load cycles of the gear tooth under consideration in the 10-minute simulation. That is, N^{ijk} is defined using the maximum contact pressure $p^{ijk}_{\max}$ at load cycle k for the wind scenario defined by v^i_{10} and i^j_{10}. As an alternative to Miner's rule, one can determine the 10-minute damage as

$$D_{10\,\min}^{ij}\left(\mathbf{d}, v_{10}^i, i_{10}^j\right) = \frac{n_{10}^{ij}}{N^{ij}\left(\overline{p}_{\max}^{ij}\right)} \tag{3.46}$$

where $\overline{p}_{\max}^{ij}$ is the equivalent maximum contact pressure for the 10-minute wind load scenario as (Dong et al. 2013)

$$\overline{p}_{\max}^{ij} = \left(\int_0^\infty \left(p_{\max}^{ij}\right)^n f_{p_{\max}}^{ij}\left(p_{\max}^{ij}\right) dp_{\max}^{ij}\right)^{1/n} \tag{3.47}$$

where $f_{p_{\max}}^{ij}\left(p_{\max}^{ij}\right)$ is a probability density function of the maximum contact pressure for the 10-minute simulation for v_{10}^i and i_{10}^j. The exponent n is selected to be the exponent of the Paris equation given in Eq. 3.36, i.e., $n = m$ (Dong et al. 2013), while $n = 1$ leads to a mean value of the maximum contact pressures in the 10-minute simulation.

The 10-minute fatigue damage $D_{10\min}(\mathbf{d}, v_{10}, i_{10})$ at the recess point on the most critical tooth of the wind turbine sun gear is calculated for each wind load scenario defined by v_{10} and i_{10} as shown in Fig. 3.33. Each length of the bar in this figure indicates the magnitude of 10-minute fatigue damage. It is observed from this figure that the fatigue damage increases with an increase of the mean wind speed since the number of load cycles and contact loads increase as the rotor speed increases. However, the fatigue damage plateaus when the wind speed gets higher than the rated speed of 16 m/s. This is attributed to the fact that the blade pitch control is activated at the rated speed (16 m/s) to maintain constant power generation at a constant rotor speed (Muljadi and Butterfield 2000).

In general, the fatigue damage increases as the turbulence intensity increases for the same mean wind speed. However, the opposite trend is observed when the blade pitch control is active. This is explained by change in rotor angular velocity of the wind turbine shown in Fig. 3.34. In this figure, mean wind speed of 11 m/s is assumed as an example, and time histories of rotor angular velocity for different turbulence intensities from 0.06 to 1 are compared. As observed from this figure, the rotor velocity amplitude increases as the turbulence intensity increases. However, since the pitch control is activated when the wind speed exceed rated speed, maximum rotor speed is bounded, whereas minimum rotor speed is not bounded. For this reason, a larger turbulence intensity wind scenario has smaller minimum rotor speed value, resulting in smaller damage evaluated by the contact fatigue model. If pitch control is off, the maximum rotor speed is not bounded; larger turbulence intensity leads to larger damage value.

The integrand of Eq. 3.43 is calculated as a product of averaged joint PDF of random wind load $\overline{f}_{VI}^{ij}\left(v_{10}^i, i_{10}^j\right)$ and 10-minute fatigue damage distribution $D_{10\min}(\mathbf{d}, v_{10}, i_{10})$ as shown in Fig. 3.35. The volume of each bar gives a probabilistic 10-minute fatigue damage with certain design $\mathbf{d}$ for one wind load range defined for v_{10} and i_{10}. It is observed that probabilistic damage value for wind condition
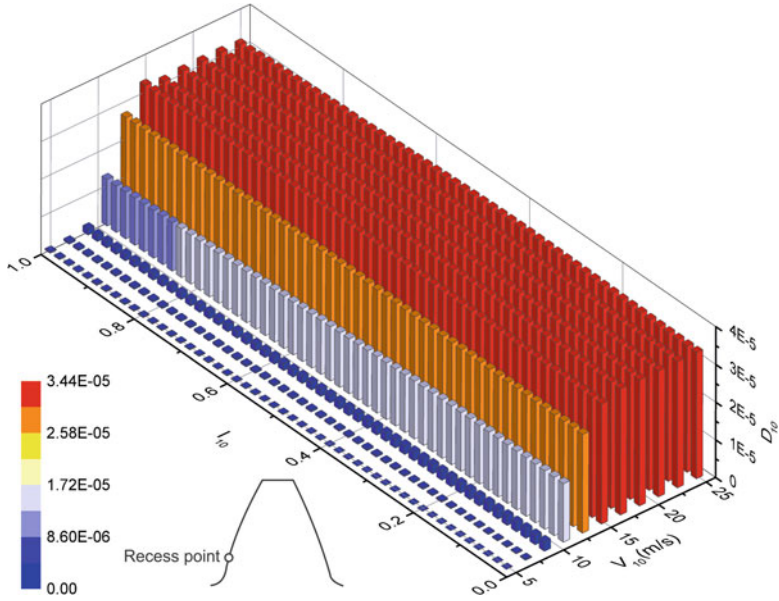
Fig. 3.33 10-minute fatigue damage at recess point of sun gear
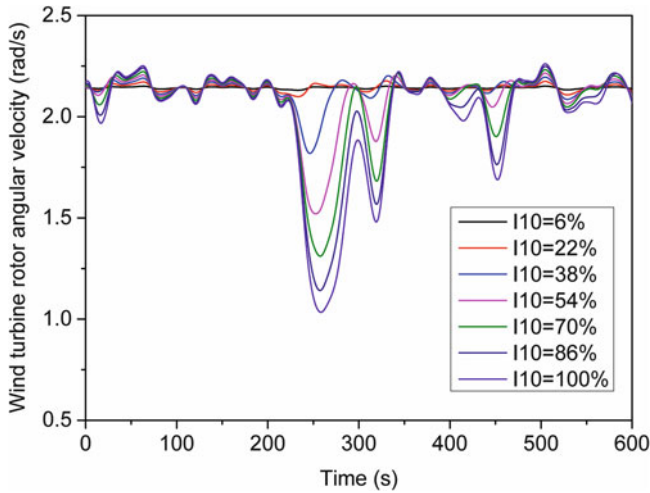
Fig. 3.34 10-minute rotor angular velocity under 11 m/s mean wind speed and different turbulence intensity

in the range of 10 m/s $< v_{10} <$ 15 m/s and 0.05 $< i_{10} <$ 0.2 is relatively high, while the probabilistic damage value of the extreme wind condition given in the range of 20 m/s $< v_{10} <$ 25 m/s and 0.4 $< i_{10} <$ 1 is low. Furthermore, the highest probability density of 3.69 $\times$ 10^{-6} occurs at $v_{10} =$ 11 m/s and $i_{10} =$ 0.1, which
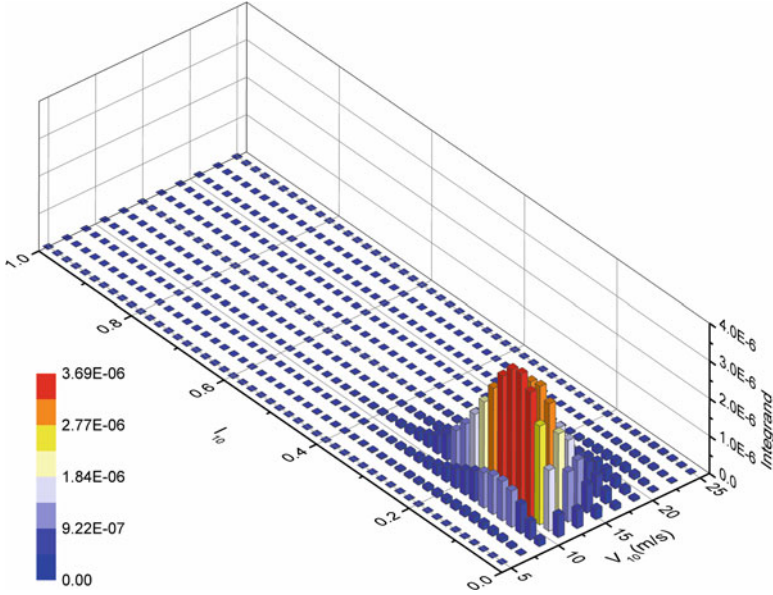
Fig. 3.35 The product of averaged joint PDF of wind load and 10-minute fatigue damage distribution

is different from those of averaged wind load ($v_{10} = 7$ m/s and=0.1) as shown in Fig. 3.32. It means that the v_{10} and i_{10} giving the highest probability density depend on not only the distribution of averaged wind load joint PDF $\overline{f}_{VI}^{ij}\left(v_{10}^i, i_{10}^j\right)$ but also the 10-minute fatigue damage distribution $D_{10\text{min}}(\mathbf{d}, v_{10}, i_{10})$. Furthermore, the wind load distribution changes at different years, and contact fatigue damages will differ significantly. Thus, other than repeatedly using the averaged joint PDF of wind load for different years, consideration of different wind load distributions for different years is crucial to realistic prediction of the gear tooth contact fatigue life for RBDO of wind turbine gearbox.

3.5   Wind Turbine Gearbox Design Optimization

For gear design optimization to ensure the expected service life under the wind load uncertainty, an integrated numerical procedure (Li et al. 2016) is developed using the wind uncertainty model, the pitting fatigue prediction model, and multibody gear dynamics simulation procedure discussed in the previous sections.
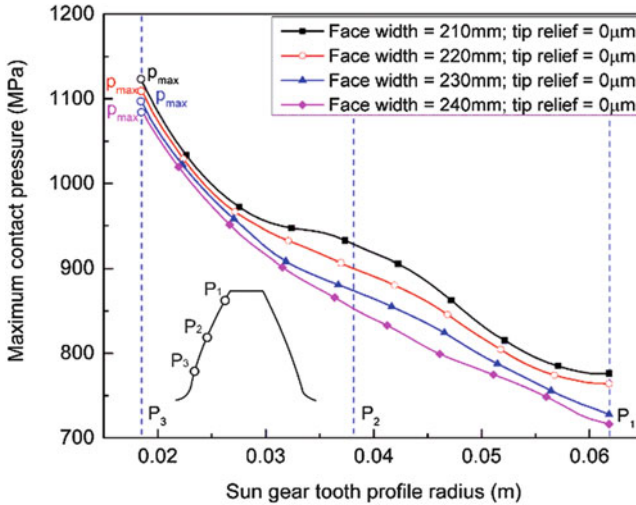
Fig. 3.36 Effect of face width on maximum contact pressure

3.5.1   Selection of Design Variables

To improve the pitting fatigue life under the wind load uncertainty, the face width
and the amount of the tip relief are defined as design variables for the sun gear. For
example, in the initial (reference) design, the face width is 220 mm, and no tip relief
(i.e., involute profile) is used (Sheng 2012). To demonstrate the effect of those two
design variables on the pitting fatigue life, the maximum contact pressure evaluated
at various points on the gear tooth for one mesh cycle is shown in Fig. 3.36 for four
different face widths without tip relief. In this figure, the rated mean wind speed of
16 m/s and turbulence intensity of 0.14 categorized in the medium range based on
ISO standard (International Organization for Standardization 2005) are assumed as
a wind load. It is observed from this figure that the maximum pressure at the recess
point P_3 is largest regardless the face width selected, and it is clear that larger face
width leads to smaller maximum contact pressure over the tooth surface, resulting
in smaller damage as shown in Fig. 3.37.

However, the increase in face width makes the weight of the gear larger, and it
also has an impact on the increase of cost. The other way of altering the contact
pressure on the tooth surface is the profile modification. The linear tip relief defined
by Eq. 3.31 is considered, and the maximum contact pressure for different tip relief
amount is shown in Fig. 3.38. In this figure, the face width of 220 mm is assumed,
and the tip relief start point is the pitch point. It is observed from this figure that the
maximum contact pressure over the tooth surface changes in a different way as the
tip relief increases and the greatest maximum contact pressure is shifted to the pitch
point as the tip relief amount increases.
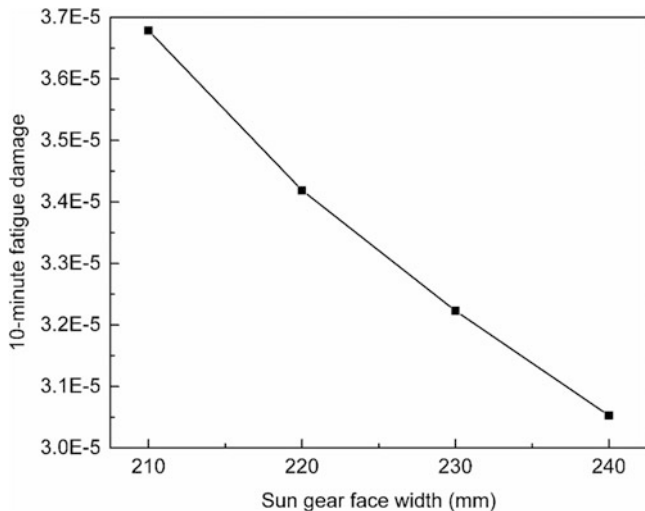
Fig. 3.37 Effect of face width on 10-minute fatigue damage
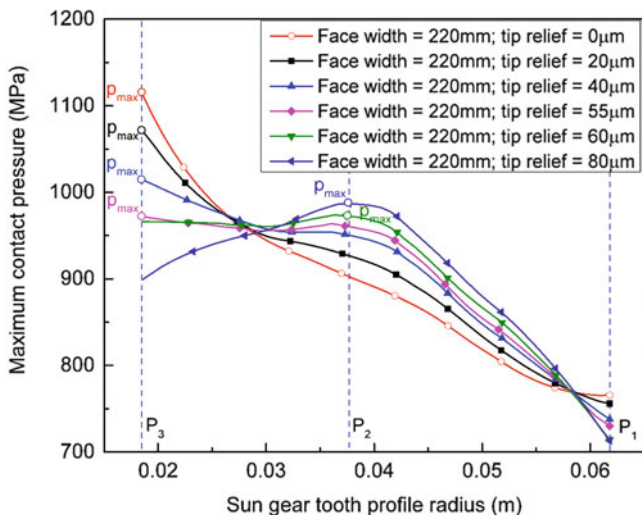
Fig. 3.38 Effect of tip relief on maximum contact pressure

It is also observed that the greatest maximum contact pressure can be minimized at a tip relief amount of 55 μm. That is, there exists an optimum tip relief amount that can minimize the greatest maximum contact pressure over the tooth profile as shown in Fig. 3.39 summarizing the 10-minute fatigue damage for different tip relief amount. It is important to emphasize at this point that the optimum value depends on the wind condition defined by the mean wind speed and turbulence intensity. Furthermore, the material removed is in the order of microns; thus, the tip relief has
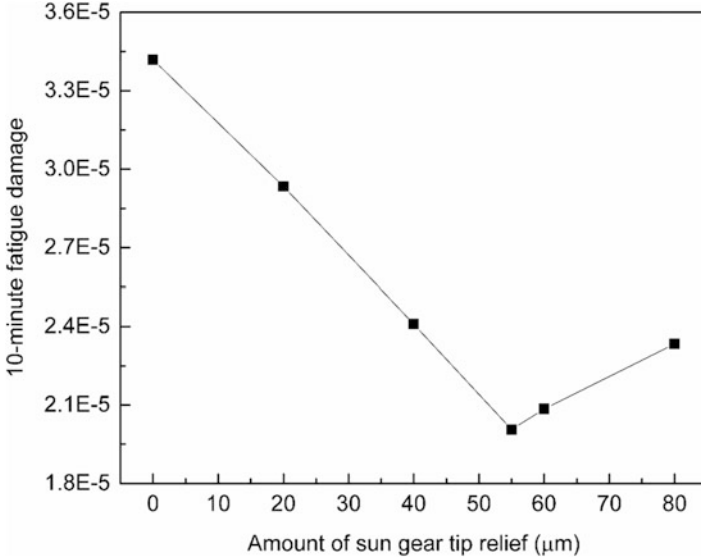
Fig. 3.39 Effect of tip relief on 10-minute fatigue damage

almost no effect on the gear weight but has major impact on the fatigue life defined as a constraint.

For this reason, in what follows, design optimization is discussed to find an optimum face width and tip relief that leads to minimization of the total weight of the gear train under the wind load uncertainty while ensuring the 20-year fatigue life.

3.5.2 Wind Turbine Gearbox Deterministic Design Optimization

The expected service life of wind turbines is 20 years, thus the constraint for the optimization problem is defined by $G(\mathbf{d}) = 20D_{1\text{year}} - 1 < 0$ for $\mathbf{d}^L < \mathbf{d} < \mathbf{d}^U$, where $\mathbf{d}^L$ and $\mathbf{d}^U$ are lower and upper bounds of the design variable $\mathbf{d}$. Accordingly, the following optimization problem is posed (Li et al. 2016):

$$
\begin{aligned}
&\text{Minimize } J(B) \\
&\text{Subject to } G(B, \delta_a) = 20D_{1\text{year}} - 1 \leq 0 \\
&\qquad\text{for} \quad B^L \leq B \leq B^U \quad \text{and} \quad \delta_a^L \leq \delta_a \leq \delta_a^U
\end{aligned}
\tag{3.48}
$$

where design variables include the face width B and the tip relief amount δ_a of the sun gear defined by $\mathbf{d} = \begin{bmatrix} B & \delta_a \end{bmatrix}^T$; the cost function $J(B)$ is defined as the total mass

of the planetary stage gears consisting of a ring gear, a sun gear, and three planet gears. The constraint is imposed to ensure that the pitting fatigue life is longer than 20 years (i.e., the 20-year fatigue damage is less than 1).

In what follows, the entire numerical procedure is summarized as shown in Fig. 3.40.

Step 1: For given measured wind data at different locations (i.e., wind farms) in different years, the joint probability density functions for v_{10} and i_{10} are identified as $f_{VI}(v_{10}, i_{10}; \mathbf{y})$, and then PDFs of $\mathbf{y} = \begin{bmatrix} C & k & a & b & \tau \end{bmatrix}^T$ are identified to account for the wide spatiotemporal wind load uncertainty (Hu et al. 2016b). The averaged joint PDF $\overline{f}_{VI}^{ij}\left(v_{10}^i, i_{10}^j\right)$ is generated using the 10^6 samples for $n_v \times n_i$ points of v_{10}^i $(i = 1, \cdots, n_v)$ and i_{10}^j $(j = 1, \cdots, n_i)$.

Step 2: For $n_v \times n_i$ points of v_{10}^i and i_{10}^j in the range of the averaged joint PDF, the time-domain 10-minute random wind data $\mathbf{U}^{ij}\left(v_{10}^i, i_{10}^j\right) = \begin{bmatrix} u^{ij}(t) & v^{ij}(t) & w^{ij}(t) \end{bmatrix}^T$ is generated using the wind field simulation software TurbSim (Jonkman 2009).

Step 3: Using the 10-minute wind data obtained at Step 2, the time-domain coupled nonlinear aero-hydro-servo-elastic simulation of a wind turbine is performed using FAST software (Jonkman and Buhl 2005) to predict rotor angular velocity variation for each wind scenario v_{10}^i and i_{10}^j. The elastic deformation of rotor blades and its interaction with aerodynamics are considered with a simplified pitch control algorithm.

Step 4: For all the pairs of gears in the gearbox under consideration for design variables $\mathbf{d}$, the contact geometry analysis for a one-tooth model considering profile modification is performed using the combined non-conformal and nodal contact search method for various rotation angles, and then the contact point as well as the tooth geometry at each contact point including the tangents, normal, and principal curvatures is stored in the look-up contact tables.

Step 5: Using the multiple look-up contact tables generated for design variable $\mathbf{d}$, multibody gearbox dynamics simulation is performed for the 10-minute input rotor angular velocity data obtained at Step 3 for each wind scenario v_{10}^i and i_{10}^j. The tabular contact search is performed to determine the contact point for all the pair of gears using multiple look-up contact tables, and the contact forces are calculated using the variable mesh stiffness model that accounts for the effect of the contact stiffness, tooth bending stiffness, and gear body (foundation) stiffness. The mesh force time-history data for each tooth are stored as output for contact fatigue prediction. Notice that the 10-minute multibody gearbox simulation is performed for all the $n_v \times n_i$ wind scenarios, and the simulation for each scenario runs in parallel using parallel computing technique.

Step 6: Using the mesh force time-history data obtained at Step 5, the 10-minute damage $D_{10\,\mathrm{min}}^{ij}\left(\mathbf{d}, v_{10}^i, i_{10}^j\right)$ is calculated, and then the critical tooth with the largest damage is selected. The $D_{10\,\mathrm{min}}^{ij}$ is evaluated by either Miner's rule
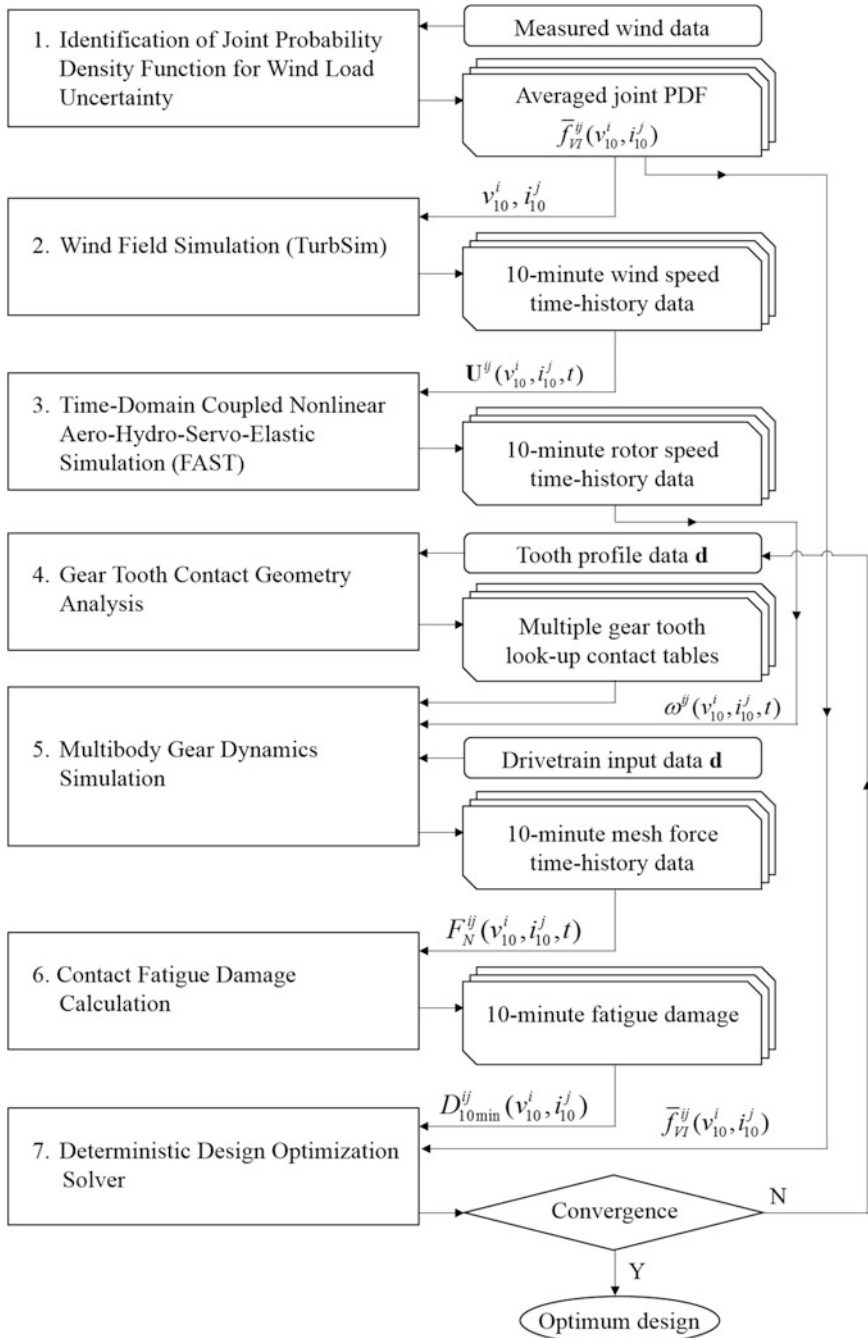
Fig. 3.40 Flowchart of DDO process

(Eq. 3.45) or the equivalent maximum contact pressure method (Eq. 3.46) for all the $n_v \times n_i$ wind scenarios, and then the 1-year fatigue damage $D_{1\text{year}}$ for the current design **d** is evaluated by Riemann integral as Eq. 3.44.

Step 7: Using the 1-year fatigue damage evaluated, the constraint is defined such that contact fatigue life is longer than 20 years as given by Eq. 3.48, and the cost function is evaluated for the current design **d**.

Step 8: Step 4 through 7 are repeated by updating the design variables **d** until the cost function is minimized while meeting the fatigue failure constraint using the deterministic design optimization solver.

3.5.3 Wind Turbine Gearbox Reliability Based Design Optimization

RBDO of the wind turbine gearbox is formulated as follows (Li et al. 2017):

$$
\begin{aligned}
&\text{Minimize} \quad J\left(\mu_B\right) \\
&\text{Subject to} \quad P\left[D_{20year}\left(B, \delta_a; \mathbf{Y}\right) > 1\right] \leq P_F^{Tar} \\
&\qquad\qquad \text{for} \;\; \mu_B^L \leq \mu_B \leq \mu_B^U \;\text{and}\; \mu_{\delta_a}^L \leq \mu_{\delta_a} \leq \mu_{\delta_a}^U
\end{aligned}
\tag{3.49}
$$

where μ_B and μ_{δ_a} are means of the random face width B and the random tip relief amount δ_a of the sun gear, respectively; the lower and upper bounds of the design variables are the same as the deterministic design optimization; the cost function $J(\mu_B)$ is defined as the total mass of the planetary stage gears consisting of a ring gear, a sun gear, and three planet gears; $\mathbf{Y}$ is the random wind load vector including 20 sets of (C, k, a, b, τ) (Hu et al. 2016b); and $D_{20year}(B, \delta_a; \mathbf{Y})$ is the 20-year contact fatigue damage of the sun gear. For each of the MCS design point, D_{20year} is evaluated as follows:

$$
\begin{aligned}
D_{20year}\left(\widehat{B}^h, \widehat{\delta}_a^h; \widehat{\mathbf{y}}^h\right) = 6 \times 3000 \sum_{l=1}^{20} \sum_{i=1}^{n_v} \sum_{j=1}^{n_i} f_{VI}^{ijlh}\left(v_{10}^i, i_{10}^j; C^{lh}, k^{lh}, a^{lh}, b^{lh}, \tau^{lh}\right) \\
D_{10\,\min}^{ij}\left(\widehat{B}^h, \widehat{\delta}_a^h; v_{10}^i, i_{10}^j\right) \Delta v_{10} \Delta i_{10}
\end{aligned}
\tag{3.50}
$$

(for $h = 1, \ldots, NMCS$) where $\widehat{B}^h$ and $\widehat{\delta}_a^h$ are realizations of random face width B and tip relief amount δ_a, respectively; and $\widehat{\mathbf{y}}^h$ is the realization vector of random wind load parameters. The probabilistic constraint $P[D_{20year}(B, \delta_a; \mathbf{Y}) > 1]$ is imposed to ensure that the probability of contact fatigue life being shorter than 20 years is smaller than the target probability of failure P_F^{Tar}.

A numerical procedure of wind turbine gearbox RBDO using the surrogate model is summarized as follows:

Step 1: As shown in Fig. 3.41, using the DDO optimum design obtained in above section, 50 DOE points are randomly generated using the truncated Gaussian sampling (TGS) method with hypercube window in the twelve sigma range. The intermediate surrogate models of the sun gear 10-minute contact fatigue damages are generated using the dynamic kriging method. For each DOE point, the 10-minute fatigue damages for all the wind load conditions (35 scenarios) under consideration are calculated, and the obtained 10-minute fatigue damages are used to generate 35 surrogate models associated with 35 wind load conditions using the dynamic kriging method.

Step 2: The RBDO process starts from the DDO optimum design. At every RBDO design, NMCS realizations of designs are created considering the design variable manufacturing variability. The NMCS realizations are inputted to the 35 surrogate models to obtain the NMCS 10-minute fatigue damage tables containing 35 10-minute fatigue damages under 35 wind load conditions.

Step 3: The NMCS realizations of 20 sets of (C, k, a, b, τ) are defined using the PDFs, and NMCS × 20 wind load probability tables are created. Each table contains the probabilities of 35 wind load conditions.

Step 4: The NMCS 20-year fatigue damages are calculated using Eq. 3.50, and then the probabilistic constraint is evaluated at the current design. If the convergence criteria are met, the RBDO iteration stops, and an optimum design is obtained. Otherwise, the design is updated and then continues the RBDO process by repeating steps 2–4 until the RBDO optimum design is achieved.

3.5.4 Case Study of Wind Turbine Gearbox Design Optimization

In this Section, the 750 KW GRC wind turbine (Sheng 2012), as shown in Fig. 3.27, is used to conduct gearbox design optimization considering wind load uncertainty and manufacturing uncertainties. The wind turbine properties are shown in Table 3.9. The gearbox consists of planetary helical gears (a ring gear, a sun gear, and three planetary gears) at the low-speed stage and two parallel axis helical gears at the intermediate and high-speed stages as shown in Fig. 3.27. The detail gearbox properties can be found in literature (Sheng 2012; Guo et al. 2012a). The face width and tip relief of sun gear are selected as design variables. Face width of 220 mm and tip relief of 0 μm are set as baseline design.

First, the deterministic design optimization (DDO) of the gearbox is conducted using the procedure described in Sect. 3.5.2. The design optimization results are shown in Table 3.10. In this table, the optimum solution obtained without considering the tip relief as design variable is also included. As it can be seen from this table, face width of the sun gear is increased to 231 mm from 220 mm in the initial design to satisfy 20-year fatigue life when only face width is included in the design variable. This leads to 4.7% increase in the normalized mass. On
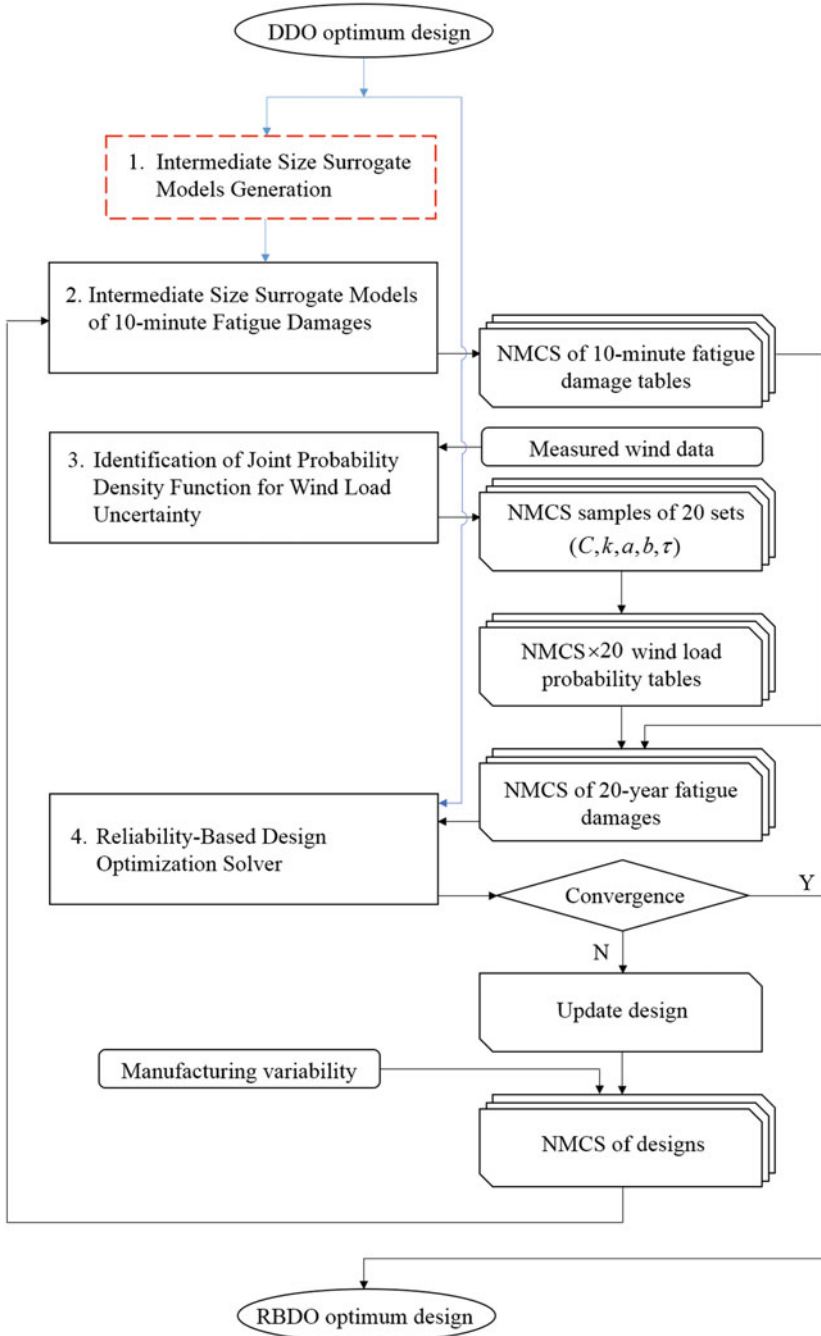
Fig. 3.41 Flowchart of the RBDO process

Table 3.10 Deterministic design optimization results

	Baseline design	Optimum design w/o tip relief	Optimum design w/ tip relief
Face width (mm)	220	231	202
Tip relief (μm)	0	0	41
Pitting fatigue life	15 years	20 years	20 years
Normalized mass	1.000	1.047	0.916

Table 3.11 Standard deviations and tolerances of the design variables

	Standard deviation	Tolerance
Face width (mm)	1.2	3.6
Tip relief (μm)	1.5	4.5

other hand, if the tip relief is introduced to the design variables, the optimum face width becomes 202 mm with a tip relief amount of 41 μm. This optimum tip relief allows for minimization of the greatest maximum shear stress on the gear tooth surface without relying heavily on face width widening to meet the 20-year fatigue life constraint, and it leads to mass reduction by 8.4%, leading to a more cost-effective design. For this DDO optimum design, the probability of failure under the spatiotemporal wind load uncertainty as well as the gear design variable uncertainties turned out to be approximately 50% (Li et al. 2017).

Then, based on the DDO optimum design (face with 202 mm, tip relief 41 μm), reliability-based design optimization (RBDO) of the 750 KW GRC wind turbine gearbox, under large spatiotemporal wind load and gear design variable uncertainties, is carried out to achieve an optimum gear design that meets 20-year service life with a target reliability (2.275%) while minimizing the cost (weight). The standard deviation and manufacturing tolerance of the design variables are shown in Table 3.11. The RBDO procedure described in Sect. 3.5.3 is conducted, and the Monte Carlo simulation size for this RBDO is set as 50,000 (Li et al. 2017). And the RBDO optimum design is presented in Table 3.12 and compared with the baseline design as well as the DDO optimum design. It is observed from this table that the face width and tip relief amount increase from the DDO design to meet the target probability of failure. This leads to an increase in weight. However, as compared to the baseline design exhibiting 91.7% probability of failure (8.3% reliability), the weight is increased by only 1.4%, while the probability of failure is improved significantly from 91.7% to 2.275% (i.e., 97.725% reliability) in the case of $P_F^{Tar} = 2.275$ % (two sigma quality level). These results clearly indicate the importance of incorporating the tip relief as a design variable and justify needs for the gear dynamics simulation capability that accounts for microgeometry of gear tooth contact for wind turbine gearbox RBDO. This, however, does not mean that a larger tip relief is always preferred since an optimum tip relief amount depends on stochastic wind loads, and an optimum tip relief cannot be found deterministically, which indicates the needs of RBDO for wind turbine gearbox design.

Table 3.12 Reliability-based design optimization results

	Baseline design	DDO design	RBDO design
Face width (mm)	220	202	223
Tip relief (μm)	0	41	54
Fatigue life	15 years	20 years	20 years
Probability of failure	91.7%	47.7%	2.275%
Normalized mass	1.000	0.916	1.014

3.6 Summary

Gears in wind turbine are subjected to severe cyclical loading due to variable wind loads that are stochastic in nature, and the failure rate of drivetrain systems is reported to be relatively higher than the other wind turbine components. For this reason, improving reliability of gearbox design is one of the key issues to make wind energy more competitive to fossil fuels. However, limited studies have been carried out regarding deterministic and reliability-based design optimization (DDO and RBDO) of wind turbine gearbox considering wind load as well as manufacturing uncertainties. It requires an extensive numerical procedure involving uncertainty quantification of wind loads as well as manufacturing errors of gears, the contact dynamics of multibody geared systems, probabilistic contact fatigue prediction of gear teeth, and design optimization procedures to meet 20-year service life with high reliability while minimizing the cost (weight) of drivetrains.

To this end, a numerical procedure for gear dynamics simulation of multibody geared systems is developed first using the tabular contact search method. Since 10-minute wind data is widely used to characterize the short-term wind speed variability in wind energy industry, 10-minute wind turbine gear dynamics simulations under different wind load conditions are required to evaluate probabilistic contact fatigue life under random wind load. Furthermore, since the tooth contact pressure is sensitive to the gear tooth profile, an accurate description of the tooth profile geometry and precise contact geometry calculation are required, and the use of a simplified gear contact dynamics model is not suited.

To improve computational efficiency associated with the gear contact dynamics simulation considering precise contact geometry as well as mesh stiffness variations, a tabular contact search algorithm using the combined nodal and non-conformal contact search approach is generalized to gear tooth contact in this chapter. By doing so, a robust contact search algorithm which allows for detecting an appropriate initial estimate for non-conformal contact search for tooth surfaces with gear geometry imperfections can be achieved.

In the dynamics simulation, the tabular contact search is performed for all the gear teeth positioned in the searching range defined in the look-up table tooth by tooth. This allows for detecting multi-point contact without any iterative procedures. Furthermore, the coordinate transformation between the generalized coordinates

and those defined in the look-up table coordinate system introduced in the contact geometry analysis are established. With this transformation, the look-up contact table can be directly applied to any pair of gears in the dynamic simulation. Several numerical examples are presented in Sect. 3.3 in order to demonstrate the use of this developed numerical procedure. In particular, an accuracy of the mesh stiffness model introduced in this study and the transmission error of gear tooth with tip relief are discussed. A planetary gear model is then introduced to discuss the effect of tooth surface irregularity on mesh force variation. A wind turbine drivetrain model is presented in the last example and is validated against test data.

The pitting fatigue model based on the Paris equation is then used to predict the contact fatigue life of gear tooth using the maximum contact pressure obtained using the multibody gearbox dynamics simulation under various 10-minute wind scenarios. Numerical results indicate that the wind load variation plays an important role to realistic estimation of contact fatigue life of wind turbine gearbox.

An integrated numerical procedure for design optimization of wind turbine drivetrains is described in Sect. 3.5 using the gear dynamics simulation procedure based on the multivariable tabular contact search algorithm considering wind load uncertainty. The joint probability density function (PDF) of the 10-minute mean wind speed (v_{10}) and 10-minute turbulence intensity (i_{10}) is introduced to characterize the short-term wind speed variability at a specific location and time. Since the wind load distribution varies at different locations in different years, a wide spatiotemporal variability is considered by identifying PDF of all the joint PDF parameters (C, k, a, b, τ), and these PDFs are used in the reliability-based design optimization (RBDO). The averaged joint PDF obtained using Monte Carlo simulation (MCS) is used in the deterministic design optimization (DDO). The random time-domain wind speed data is generated using NREL TurbSim and then inputted into NREL FAST to perform the aero-hydro-servo-elastic simulation of rotor blades under pitch control to predict the transmitted torque and speed of the main shaft of the drivetrain, which are sent to the multibody gear dynamics simulation for contact fatigue prediction.

Using the optimization procedure developed in this chapter, DDO and RBDO of a 750 kW GRC wind turbine gearbox have been successfully carried out. The obtained optimum tip relief allows for lowering the greatest maximum shear stresses on the tooth surface without relying heavily on face width widening to meet the 20-year fatigue life constraint, and it leads to weight reduction, which means a more cost-effective and reliable design.

References

Alemayehu FM, Osire SE (2015) Probabilistic performance of helical compound planetary system in wind turbine. ASME J Comput Nonlinear Dyn 10:1–12

Aydin E (2013) Determination of best drive train technology for future onshore wind turbines as a function of the output power. Master Thesis, Eindhoven Technical University

Barbieri M, Scagliarini G, Bonori G, Pellicano F, Bertccchi G (2008) Optimization methods for spur gear dynamics. In: Proceedings of EUROMECH nonlinear dynamics conference, Saint Petersburg

Budynas R, Nisbett K (2008) Shigley's mechanical engineering design, 9th edn. McGraw-Hill, New York

Cardona A (1997) Three-dimensional gears modeling in multibody systems analysis. Int J Numer Methods Eng 40:357–381

Choi Y, Liu CR (2006a) Rolling contact fatigue life of finish hard machined surfaces, part 1. Model development. Wear 261:485–491

Choi Y, Liu CR (2006b) Rolling contact fatigue life of finish hard machined surfaces, part 2. Experimental verification. Wear 261:492–499

Choi Y, Liu CR (2006c) Rolling contact fatigue life of finish hard machined surfaces. Wear 261:485–491

Cornell RW (1981) Compliance and stress sensitivity of spur gear teeth. ASME J Mech Des 103:447–459

Crossland B (1970) The effect of pressure on the fatigue of metals. In: Pugh H (ed) Mechanical Behaviour of Materials Under Pressure. Elsevier, London, pp 299–354

Dang VK (1973) Sur La Resistance a La Fatigue des Metaux. Sci Tech Armem 47:647–722

Dong W, Xing Y, Moan T, Gao Z (2013) Time domain-based gear contact fatigue analysis of a wind turbine drivetrain under dynamic conditions. Int J Fatigue 48:133–146

Ebrahimi S, Eberhard P (2006) Rigid-elastic modeling of meshing gear wheels in multibody systems. Multibody Sys Dyn 16:55–71

Errichello R (2000) Wind turbine gearbox failures. GEARTECH. Townsend, Montana, USA

Errichello R, Muller J (2012a) Gearbox reliability collaborative gearbox 1 failure analysis report. NREL/SR-5000-53062

Errichello R, Muller J (2012b) Gearbox reliability collaborative gearbox 1 failure analysis report. NREL/SR-500-53062

Ghribi D, Bruyere J, Velex P, Octrue M, Mohamed H (2012) Robust optimization of gear tooth modifications using a genetic algorithm. In: Condition monitoring of machinery in non-stationary operations. Springer, Berlin, pp 589–597

Glodez G, Flasker J, Ren Z (1997) A new model for the numerical determination of pitting resistance of gear teeth flanks. Fatigue Fract Eng Mater Struct 20(1):71–83

Guo Y, Keller J, LaCava W (2012a) Combined effects of gravity, bending moment, bearing clearance, and input torque on wind turbine planetary gear load sharing. NREL/CP-5000-55968

Guo Y, LaCava W, Xing Y, Moan T (2012b) Determining wind turbine gearbox model complexity using measurement validation and cost comparison. NREL/CP-5000-54545

Guo Y, Bergua R, Dam JV, Jove J, Campbell J (2015) Improving wind turbine drivetrain designs to minimize the impacts of non-torque loads. Wind Energy 18:2199–2222

Haug EJ (1989) Computer aided kinematics and dynamics of mechanical systems. Ally and Bacon, Boston

Helsen J, Vanhollebeke F, Marrantb B, Vandepitte D, Desmet W (2011) Multibody modelling of varying complexity for modal behaviour analysis of wind turbine gearboxes. Renew Energy 36:3098–3113

Houser DR, Bolze VM, Graber JM (1996) A comparison of predicted and measured dynamic and static transmission error for spur and helical gear sets. In: SEM 14th international modal analysis conference, Dearborn

Hu W, Choi KK, Zhupanska O, Buchholz J (2016a) Integrating variable wind load, aerodynamic, and structural analyses towards accurate fatigue life prediction in composite wind turbine blades. Struct Multidiscip Optim 53:375–394

Hu W, Choi KK, Cho H (2016b) Reliability-based design optimization of wind turbine blades for fatigue life under dynamic wind load uncertainty. Struct Multidiscip Optim 54:953–970

International Organization for Standardization (2005) Wind turbines part 1: design requirements, IEC 61400-1:2005. ISO, Geneva

Jiang B, Zheng X, Wang M (1993) Calculation for rolling contact fatigue life and strength of case-hardened gear materials by computer. J Test Eval 21:9–13

Jonkman BJ (2009) TurbSim user's guide. Technical Report NREL/TP-500-46198

Jonkman JM, Buhl ML (2005) FAST user's guide. Technical Report NREL/TP-500-38230

Kahraman A (1994) Planetary gear train dynamics. ASME J Mech Des 116:71–720

Kapelevich A, Shekhtman Y (2009) Gear tooth fillet profile optimization. Gear Solut 9:63–69

Karagiannis I, Theodossiades S, Rahnejat H (2012) On the dynamics of lubricated hypoid gears. Mech Mach Theory 48:94–120

Kato M, Deng G, Inoue K, Takatsu N (1993) Evaluation of the strength of carburized spur gear teeth based on fracture mechanics. Bull Japan Soc Mech Eng Ser C 36:233–234

Keer LM, Bryant MD (1983) A pitting model for rolling contact fatigue. ASME Tribol 105:198–205

Kin V (1994) Computerized analysis of gear meshing based on coordinate measurement data. ASME J Mech Des 116:738–744

Lee CH, Bae DS, Song JS (2012) Multibody approach of gear transmission error dynamics. In: Proceedings of Asian conference on multibody dynamics, Shanghai

Lesmerises A, Crowley D (2013) Effect of different Workscope strategies on wind turbine gearbox life cycle repair costs. Int J Prognos Health Manag 17:1–7

Li H, Terao A, Sugiyama H (2015) Application of tabular contact search method to multibody gear dynamics simulation with tooth surface imperfections. IMechE J Multibody Dyn 229:274–290

Li H, Sugiyama H, Cho H, Choi KK, Gaul NJ (2016) Numerical procedure for design optimization of wind turbine drivetrain using multibody gear dynamics simulation considering wind load uncertainty. In: Proceedings of the ASME 2016 IDETC & CIE conference, Charlotte, DETC2016-59654

Li H, Cho H, Sugiyama H, Choi KK, Gaul NJ (2017) Reliability-based design optimization of wind turbine drivetrain with integrated multibody gear dynamics simulation considering wind load uncertainty. Struct Multidiscip Optim 56:183–201

Litvin FL, Fuentes A (2004) Gear geometry and applied theory, 2nd edn. Cambridge University Press, Cambridge

Liu J, Zenner H (2003) Fatigue limit of ductile metals under multiaxial loading. Biaxial Multiaxial Fatigue Fract 31:147–164

Maatar M, Velex P (1997) Quasi-static and dynamic analysis of narrow-faced helical gears with profile and lead modifications. ASME Mech Des 119:474–480

Madhusekhar D, Madhava Reddy K (2014) Reliability based optimum design of a gear box. Int J Eng Res Appl 4(10):1–8

Melchers RE (1999) Structural reliability analysis and prediction. Wiley, Chichester

Milburn A (2011) Wind turbine gearbox wear and failure modes and detection methods. NREL Wind Turbine Condition Monitoring Workshop

Mohammadpour M, Theodossiades S, Rahnejat H (2014) Multiphysics investigations on the dynamics of differential hypoid gears. ASME J Vib Acoust 136:1–3

Muljadi E, Butterfield CP (2000) Pitch-controlled variable-speed wind turbine generation. Technical Report NREL/CP-500-27143

Newman CJ (1992) Small-crack test method. ASTM STP 1149:6–33

Osman T, Velex P (2011) A model for the simulation of the interactions between dynamic tooth loads and contact fatigue in spur gears. Tribol Int 46:84–96

Oyague F (2009) Gearbox modeling and load simulation of a baseline 750-kW wind turbine using State-of-the-Art simulation code. NREL/TP-500-41160

Ozguven HN, Houser DR (1988) Mathematical models used in gear dynamics – a review. J Sound Vib 121:383–411

Palermo A, Mundo D, Hadjit R, Desmet W (2013) Multibody element for spur and helical gear meshing based on detailed three-dimensional contact calculations. Mech Mach Theory 62:13–30

Parker RG, Agashe V, Vijayakar SM (2000) Dynamic response of a planetary gear system using a finite element/contact mechanics model. ASME J Mech Des 122:305–311

Peeters JLM, Vandepitte D, Sas P (2005) Analysis of internal drive train dynamics in a wind turbine. Wind Energy 9:141–161

Piegl LA, Tiller W (1996) The NURBS book. Springer, New York

Qin D, Wang J, Lin TC (2009) Flexible multibody dynamics modeling of a horizontal wind turbine drivetrain system. ASME J Comput Nonlinear Dyn 131:1–8

Sainsot P, Velex P (2004) Contribution of gear body to tooth deflections- a new bi-dimensional analytical formula. ASME J Mech Des 126:748–752

Sansalvador RL, Jauregui JC (1993) Practical optimization of helical gears using computer software. Gear Technol 10:16–21

Shabana AA (2010) Computational dynamics, 3rd edn. Wiley, Chichester

Shabana AA, Zaazaa KE, Sugiyama H (2008) Railroad vehicle dynamics: computational approach. CRC Press, Boca Raton

Sheng S (2012) Wind turbine gearbox condition monitoring round robin study. NREL/TP-5000-54530

Sheng S, McDade M, Errichello R (2011) Wind turbine gearbox failure modes-a brief. In: Proceedings of ASME/STLE 2011 international joint tribology conference, Los Angeles

Shikin EV, Plis AI (1995) Handbook on splines for the user. CRC Press, Boca Raton

Spitas V, Spitas C (2007) Optimizing involute gear design for maximum bending strength and equivalent pitting resistance. Proc IMechE 221:479–488

Straffelini G, Molinari A, Marcupuscas T (2000) Identification of rolling-sliding damage mechanisms in porous alloys. Metall Mater Trans A 31:3091–3099

Sundaresan S, Ishii K, Houser DR (1991) A procedure using manufacturing variance to design gears with minimum transmission error. ASME J Mech Des 113:318–324

Tallian TE (1983) Rolling contact fatigue. SKF Ball Bear J 217:5–13

Tavakoli MS, Houser DR (1986) Optimum profile modifications for the minimization of static transmission errors of spur gears. ASME J Mech Trans Auto Des 108:86–94

Vanderplaats GN, Chen X, Zhang N-T (1988) Gear optimization. NASA CR-4201, pp 1–60

Vanhollebeke F, Peeters P, Helsen J, Lorenzo ED, Manzato S, Peeters J, Vandepitte D, Desmet W (2015) Large scale validation of a flexible multibody wind turbine gearbox model. ASME J Comput Nonlinear Dyn 10:1–12

Veers PS, Winterstein SR (1998) Application of measured loads to wind turbine fatigue and reliability analysis. ASME J Solar Energy Eng 120:233–239

Velex P, Bruyere J, Houser DR (2011) Some analytical results on transmission errors in narrow-faced spur and helical gears: influence of profile modifications. ASME J Mech Des 133:1–11

Vijayakar S (1991) A combined surface integral and finite element solution for a three-dimensional contact problem. Int J Numer Methods Eng 31:525–545

Wang J, Li R, Peng X (2003) Survey of nonlinear vibration of gear transmission systems. ASME Appl Mech Rev 56:309–329

Yu CJ (1998) Design optimization for robustness using quadrature factorial models. Eng Optim 30:203–225

Zhang Y, Litvin FL, Maruyama N, Takeda R, Sugimoto M (1994) Computerized analysis of meshing and contact of gear real tooth surfaces. ASME J Mech Des 116:738–744

Ziegler P, Eberhard P (2009) An elastic multibody model for the simulation of impacts on gear wheels. In: Proceedings of ECCOMAS thematic conference on multibody dynamics, Warsaw

Chapter 4
A New Multiscale Modeling and Simulation of Rolling Contact Fatigue for Wind Turbine Bearings

Mir Ali Ghaffari and Shaoping Xiao

4.1 Introduction

Gearbox failure is one of the largest sources of unplanned maintenance costs in wind industries because repairing or replacing a failed gearbox in wind turbine in particular is an extremely expensive undertaking. Therefore, when a failure occurs, it is important to correctly identify the failure mode so that the appropriate actions can be taken to reduce the likelihood of a reoccurrence of the same type of failure.

Gearbox failures can be caused by fundamental design issues, manufacturing defects, deficiencies in the lubricant or lubrication system, excessive time at standstill, large loading, and many other reasons. A correct failure mode diagnosis is the first step in identifying the actions that can be taken to prevent additional failures. As one of the key elementary mechanical components, ball and roller bearings are used to allow rotary motion and support significant loads. The rotational motion and dynamics of rollers, i.e., rolling elements, in a bearing give rise to alternate contact between the bearing inner race and the rolling elements. High pressures caused by these contacts are developed between the load-carrying elements. Due to alternate contact, the contacting elements are subjected to cyclic stressing. This cyclic nature of stress makes the contacting elements susceptible to failure due to fatigue. It is one of the leading causes of failure in bearings, and this phenomenon is known as rolling contact fatigue (RCF). RCF is also commonly observed in gears, cam-follower mechanisms, and rail-wheel contacts. Therefore, it is crucial to understand the mechanisms of RCF and predict fatigue life during machinery design.

M. A. Ghaffari (✉)
General Motors Co., 48092 Warren, MI, USA
e-mail: ali.ghaffari@gm.com

S. Xiao
Department of Mechanical and Industrial Engineering, The University of Iowa, 52242 Iowa City, IA, USA
e-mail: shoaping-xiao@uiowa.edu

There have been several numerical approaches to study RCF of bearings or other mechanical components (Sadeghi et al. 2009). These models can be classified into either probabilistic engineering models or deterministic research models. The probabilistic engineering models include the formulas to predict RCF life, and the formula parameters were obtained from extensive experimental testing. Lundberg and Palmgren (1947, 1952) proposed the first engineering model, the L-P model, to predict the bearing life based on the assumption of crack initiating at a subsurface weak point in the material. The Weibull statistical strength theory was applied in their model. In order to overcome the limitations of the L-P model, Ioannides and Harris (1985) modified the principles of crack initiation and proposed another new model, the I-H model, to predict the bearing lives. Based on the given defect's severity distribution, Tallian (1992) proposed a statistical model to compute fatigue crack propagation life. Then, Kudish and Burris (2000) modified Tallian's theory by considering more material and loading parameters. However, this model didn't include the fatigue crack initiation life.

The deterministic research models were developed to estimate the fatigue crack initiation life or the crack fatigue propagation life based on mechanics of the failure process. Keer and Bryant (1983) developed the first deterministic research model to calculate the fatigue lives for rolling Hertzian contacts. They used two-dimensional fracture mechanics and only considered the fatigue crack propagation life. Considering both the crack initiation life and the crack propagation life, Zhou and coworkers (Zhou et al. 1989; Zhou 1993) proposed a new life prediction model taking into account the accumulated damage. Another fatigue life prediction model was presented by Bhargava et al. Bhargava et al. (1990) based on plastic strain accumulation under the cyclic contact stress. Other similar prediction models can be found in Vincent et al. (1998), Xu and Sadeghi (1996), and Lormand et al. (1998). However, the assumption of homogeneous materials in the contact region was employed in most deterministic research models. To overcome this limitation, a few models, including finite element models, were developed to take into account the micromechanical material behavior in the contact region. A so-called Voronoi finite element method (VFEM) was proposed by Jalalahmadi and Sadeghi (2009). With the implementation of a fatigue life criterion (Raje et al. 2008), VFEM can be used to study the effect of material micromechanical behavior on rolling contact fatigue. When using the above models to study RCF, the mechanical components, i.e., rolling elements in bearings, were assumed to be well lubricated. On the other hand, the friction force was prescribed on the contact surface to calculate the RCF lives. Consequently, the lubrication effect was neglected. It has been known that partially lubricated mechanical components and the debris in the lubrication would dramatically reduce the mechanical component's RCF lives because of the large friction force on the contact surface. Therefore, it is necessary to consider the lubrication effects when predicting the RCF lives of bearings or other lubricated mechanical elements.

Lubricant is used to reduce wear, to lower friction, and to release heat. The behavior of sliding surfaces is affected and modified by the lubrication between them. The scientific study of lubrication, in tribology community, started when Reynolds in 1886 discussed the feasibility of a theoretical treatment of film lubrication. A recapitulative friction diagram was first proposed by Stribeck in 1902 after extensive experiments have been conducted on lubricated bearings to distinguish different lubrication regimes. The diagram indicates how the friction force or the coefficient of friction is changed due to various pressures.

Although the lubrication approximation originated from thin film studies, there is a limitation due to its continuum mechanics assumptions. When two separating surfaces are sliding under the contacting load, the lubricant between surfaces has the thickness comparable to the molecular scale. Therefore, the continuum assumption becomes invalid. For example, one of the common assumptions in the fluid mechanics is the no-slip boundary condition which has been proved to be invalid in thin film lubrication at nanoscale. In addition, surface roughness may be considered when the length scale is down to the nanoscale. In the case of boundary lubrication, some surface regions are separated by lubricant, while the others are under direct contact due to the existing asperities. Generally, the surface roughness, lubricant, and adhesion force together determine the contact mechanism between two surfaces. Therefore, a fully understanding of the fundamental mechanism of friction and lubrication between contact surfaces at nanoscale becomes very important to predict RCF lives.

Among many powerful numerical methods to elucidate nanoscale phenomena, molecular dynamics (MD) has outstanding advantages to provide the steady state of a system as well as simulate the nonequilibrium process under various conditions. It can help to investigate the unobservable tribological aspects, including the lubricant behavior between contact surfaces at nanoscale. A review of the molecular mechanisms of tribology in thin films and at surfaces was brought forward in Bhushan et al. (1995). Zhang (Zhang and Tanaka 1998) employed MD to conduct friction analyses and wearability evaluation. In addition, MD was adopted to simulate heat transfer at the interface of contacting solids (Chantrenne et al. 2000) and to examine the effects of surface roughness on friction (Harrison et al. 1993; Zheng et al. 2013a,b, 2014; Zheng 2014).

With the development in nano-engineering and nano-material science, nanoparticles have been introduced into lubricants. The nanoscale additives were reported to be capable of improving the friction performance of lubricants in anti-wear and friction-reduction properties (Tao et al. 1996; Tarasova et al. 2002; Ghaednia et al. 2015). Some nanoparticles were shown to play a favorable role as solid lubricants under severe conditions (Chhowalla and Amaratunga 2000; Rapoport et al. 2005). Ghaednia and coworkers (Ghaednia et al. 2013) conducted MD simulations to explore the interactions between the nanoparticles and the lubricant or the contact surfaces. They found that the presence of nanoparticles reduced friction. The friction-reduction mechanism indicated that nanoparticles in the thin film elastohydrodynamic lubricant regime restrict only a few layers of lubricant

molecules to slide (shearing) on each other. It should be noted that nanotubes also showed promising properties for the lubrication (Rosentsveig et al. 2009; Maharaj and Bhushan 2013).

A new multiscale model for studying rolling contact systems is proposed in this study. The molecular model of lubricants is carried to study the friction phenomenon between rolling contact surfaces. The calculated friction coefficient is then passed to a continuum FEM model to predict rolling contact fatigue life. The outline of this chapter is as below. The molecular model of lubricant between the contact surfaces is described in Sect. 4.2. In Sect. 4.3, MD simulations are conducted to calculate the friction coefficient. Then, a continuum FEM model is discussed in Sect. 4.4, to predict the rolling contact fatigue life. Results and discussions are given in Sect. 4.5 followed by the conclusion.

4.2 Molecular Modeling of Lubricant

4.2.1 Molecular Dynamics

MD simulation, which is a numerical technique used to calculate the equilibrium and transport properties of a classical many-body system, is adopted to study hydrodynamic lubrication in this chapter. In the MD simulation, the atoms or molecules in the simulated system follow the laws of classical mechanics. The motion of an atom, e.g., atom i, with mass m_i, is due to its interaction with other atoms in the system according to Newton's second law:

$$m_i \vec{a}_i = \vec{f}_i = -\Delta u(\vec{r}_i) \tag{4.1}$$

where $\vec{a}_i$ is the acceleration of atom i and the interatomic force, $\vec{f}_i$, applied on atom i, is derived from the total potential energy due to its interaction with other atoms

$$u(\vec{r}_i) = \sum_j u_{ij}(\vec{r}_i, \vec{r}_j) \tag{4.2}$$

where $\vec{r}_i$ and $\vec{r}_j$ are the atomic positions of atoms i and j, respectively. u_{ij} is the potential function to describe the interaction between atoms i and j.

MD simulation requires solving the equations of motion, i.e., Eq. (4.1), to obtain the atomic trajectories. In this study, the velocity Verlet algorithm is employed as the time integration algorithm since it achieves a considerable accuracy (Omelyan et al. 2002).

The atomic position, $\vec{r}_i(t)$; velocity, $\vec{v}_i(t)$; and acceleration, $\vec{a}_i(t)$, at the time $t + \delta t$ (here δt is the time step) can be obtained from the equivalents at the time t as below:

$$\vec{r}_i(t + \delta t) = \vec{r}_i(t) + \vec{v}_i(t).\delta t + \frac{1}{2}\vec{a}_i(t) \cdot (\delta t)^2 \tag{4.3}$$

$$\vec{v}_i(t + \frac{1}{2}\delta t) = \vec{v}_i(t) + \frac{1}{2}\vec{a}_i(t) \cdot \delta t \tag{4.4}$$

$$\vec{a}_i(t + \delta t) = -\frac{\partial u(\vec{r}_i)}{\partial \vec{r}_i} \cdot \frac{1}{m_i} \tag{4.5}$$

$$\vec{v}_i(t + \delta t) = \vec{v}_i(t + \frac{1}{2}\delta t) + \frac{1}{2}\vec{a}_i(t + \delta t) \cdot \delta t \tag{4.6}$$

At each iteration, the atomic position for the next time step is updated first, and then the velocity at the half time step is obtained through the acceleration at the previous time step. Afterward, the acceleration at the next time step is calculated from Newton's second law. At last, the velocity at the next time step is updated by adding the velocity increment with the consideration of the updated acceleration. The choice of time step δt is essential. Its value should be at least an order of magnitude less than the typical time of the system that is defined by the phonon frequencies or the ratio of velocity to acceleration.

One of key issues in MD simulation of tribological phenomena is the temperature regulation because the work done during two walls sliding from each other is ultimately converted into a random thermal motion at the nanoscale. The temperature of the simulated system would increase infinitely if only modeling the simulated system as an isolated one. To model the heat dissipation from the simulated system to the surrounding media, a numerical heat bath is implemented in MD simulations. A classic approach to adding or subtracting kinetic energy to the system is multiplying the velocities of all particles with the same global factor. In this simplest version of velocity rescaling, the factor is chosen to keep the kinetic energy constant at each time step, so that the temperature can be maintained. However, there might be fluctuations in the kinetic energy in a true constant temperature ensemble. Alternatively, the equations of motion can be modified to gradually scale the velocities so that the average kinetic energy can be maintained over a longer time scale. The Nose-Hoover method (Nose 1984; Hoover 1985) is one of these methods, and it is used in this study to conduct MD simulations of hydrodynamic lubricants at a constant temperature.

The Nose-Hoover method couples the simulated system with a heat bath, and the heat will be transferred back and forth between the system and heat bath in order to keep the system temperature relatively constant. In this method, Newton's second law of motion is modified with an additional term related to the heat bath:

$$\vec{a}_i(t) = \frac{\vec{f}_i(t)}{m_i} - \zeta(t)\vec{v}_i(t) \tag{4.7}$$

The coefficient ζ is defined as

$$\frac{d}{dt}\zeta(t) = \frac{N_F}{Q}(k_B T(t) - k_B T_0) \tag{4.8}$$

in which N_F is the degrees of freedom and equals to $3N + 1$, with N as the number of particles in the simulated system, $T(t)$ is the instantaneous temperature, T_0 is the heat bath temperature or the desired temperature, and k_B is the Boltzmann constant. The heat transfer rate is determined by the fictitious mass parameter Q.

4.2.2 Molecular Model of Lubricant System

The MD simulations in this study are carried out with the Larger-Scale Atomic Molecular Massively Parallel Simulator (LAMMPS) code Plimpton (1995). The schematic view of the simulated system is depicted in Fig. 4.1. The MD model of lubricant system includes the lubricant chains that are confined between upper and lower Fe walls. The solid walls are divided into six layers, including upper and lower rigid layers, thermostat layers, and free layers. Linear alkanes with the chain length of C_8 are considered as the fluid film of lubrication, as shown in Fig. 4.2, in this chapter. There are a total of 1950 chains in the simulated model. Most industrial applications indicate a thin lubricant thickness of only several nanometers (Berro et al. 2010; Savio et al. 2012) under a high normal pressure. In this study, the initial film thickness of about 5 nm is used to model the rheological and frictional behavior of the lubricant. Periodic boundary conditions are used in other two directions.

The whole MD simulation process includes three main stages named relaxing, compressing, and shearing. In the relaxing stage, the upper and lower walls are fixed to keep the system height constant, and the randomly distributed lubricant alkane chains can move freely. It is essential to have lubricant chains becoming fully relax. In other words, the system will be at thermodynamic equilibrium state. In the compressing stage, a uniformly distributed external load is applied onto the upper rigid layer, while the lower rigid layer remains fixed. To investigate tribological phenomena of the system subject to external loadings, it is generally desirable to keep the interface as undisturbed by the external force as possible. Therefore, it is crucial to apply any external forces and constraints to the outmost layers, i.e., rigid layers shown in Fig. 4.1. The temperature regulation is usually applied on the middle region of the upper or lower solid layer, named the thermostat layers. Therefore, the contacting solids are undisturbed by regulating the thermostat regions. The lubricant is compressed in the second stage until the system reaches to the thermodynamic equilibrium state again. At the last stage, shearing, a constant velocity of 10 m/s is applied onto the upper and lower rigid layers along the longitudinal direction, as indicated in Fig. 4.1a, so that the lubricant is sheared. This sliding velocity
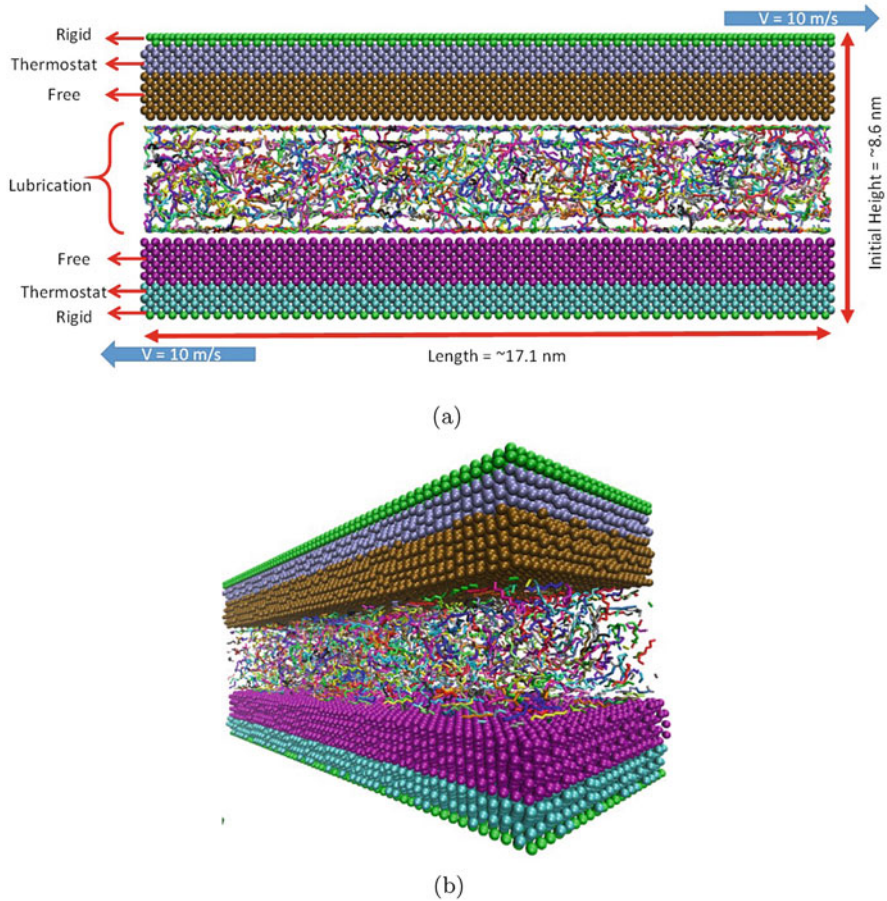
Fig. 4.1 The molecular model of thin film lubrication between two contact surfaces: (**a**) schematic view and (**b**) three-dimensional view
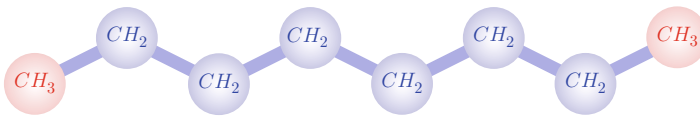
Fig. 4.2 Schematic view of an alkane with eight chains used as the lubricant. The red atom is the united atom of CH_3 and the blue atom stands for that of CH_2

conduction has been widely used in MD simulations of thin film lubrication as it enables the simulation to obtain a required sliding distance within a reasonable calculation time (Zheng et al. 2013a,b; Spijker et al. 2011; Berro et al. 2010). In addition, the constant velocity mode makes it easy to record the friction forces.

4.2.3   Potential Functions

In the MD simulation, the selection of proper potential functions is important to describe interaction between molecules. In the molecular model of lubricant system, the alkane molecules are represented via an optimized united-atom (UA) potential TraPPE-UA, and the Fe atoms in solid walls are modeled by the embedded atom method (EAM) potential. The non-bonded interactions among alkane molecules as well as the liquid-solid interaction are modeled through the Lennard-Jones (L-J) potential with the Lorentz-Berthelot combination rules.

4.2.3.1   Bonded Interaction in a Single Alkane Chain

A liquid lubricant, such as n-alkanes, has two unique properties compared to solids such as Fe, Al, Au, etc. At first, unlike a solid with a well-ordered crystalline structure, the liquid by nature has no ordered internal structure. The lubricant can flow, and the lubricant molecules can pass one another during the motion. Secondly, the lubricant molecules are typically made of flexible chains and branches which include bonded, angular, and torsional interactions.

Linear alkane chains are used in this chapter to model the lubricant, and the molecular architecture includes bond stretching, angle bending, and torsion. The TraPPE-UA potential has been well developed to simulate both linear and branched alkanes (Martin and Siepmann 1998; Wick et al. 2000). It was extended to simulate molecules in short chains (Stubbs et al. 2004; Ketko et al. 2008) which has been widely used to model surfactants and lubricants. Generally, the UA potential is a sum of the covalent bond stretching, angle bending, and torsion presented as

$$E_{bond} = \frac{K_b}{2} (r - r_0)^2 \tag{4.9}$$

$$E_{bend} = \frac{K_\theta}{2} (\theta - \theta_0)^2 \tag{4.10}$$

$$E_{torsion} = c_0 + c_1 \left[1 + cos(\alpha)\right] + c_2 \left[1 - cos(2\alpha)\right] + c_3 \left[1 + cos(3\alpha)\right] \tag{4.11}$$

The potential parameters for the alkane chains are listed in Table 4.1.

4.2.3.2   Liquid-Solid Interactions and Other Non-bonded Interactions

The interfacial interaction between surfaces and lubricant determines how surfaces influence the structure of confined lubricants and interfacial sliding (Thompson and Robbins 1990a,b). A wide range of potentials have been adopted in MD simulations in tribology community. For example, the simple ideal springs (Zheng 2014; Berro et al. 2010) and sine-wave potentials are often used. Another

Table 4.1 Potential parameters for alkanes

Bond	$K_b(\text{eV/Å}^2)$	$r_0(\text{Å})$		
$C - C$	39.0279464	1.54		
Angle	$K_\theta(\text{eV/rad}^2)$	$\theta_0(\text{deg})$		
$C - C - C$	5.3858393	114		
Dihedral	$c_0(\text{eV})$	$c_1(\text{eV})$	$c_2(\text{eV})$	$c_3(\text{eV})$
$C - C - C - C$	0	0.030594	-0.005876	0.068190

Table 4.2 Potential parameters for interatomic interactions

L-J 12-6 potentials	$\sigma(\text{Å})$	$\varepsilon(\text{eV})$	Mass (g/mol)
CH_3	3.75	0.008444	15.0351
CH_2	3.95	0.003963	14.0272
CH	4.68	0.000861	13.0191
Fe	2.321	0.04097	55.8450

potential function, the L-J potential (Spijker et al. 2011, 2012), gives a realistic representation of typical interatomic interactions. The L-J potential is a two-body potential commonly used for non-bonded interactions between atoms or molecules. In a molecular model of lubricant, an L-J particle may present a single atom on the chain (explicit atom model), a CH_3 segment (united-atom model), or even a segment consisting of several CH_2 units in a coarse-grained model. Here, the L-J potential is used to describe the interactions between a pair of CH_3 and CH_2 segments, which are on two different alkane chains or separated by more than four segments along a single alkane chain. In addition, the liquid-solid interaction, i.e., the interaction between a CH_3 or CH_2 segment and an Fe atom, is also modeled via the L-J potential.

The commonly used 12-6 L-J potential has the following form:

$$U(r_{ij}) = 4\varepsilon \left[\left(\frac{\sigma}{r_{ij}} \right)^{12} - \left(\frac{\sigma}{r_{ij}} \right)^{6} \right] \tag{4.12}$$

where r_{ij} is the distance between particles i and j, ε is the L-J interaction energy, and σ is the L-J interaction diameter. The parameters of dissimilar interactions can be computed by the Lorentz-Berthelot combining rules:

$$\begin{cases} \sigma_{ij} = \frac{1}{2} \left(\sigma_{ii} + \sigma_{jj} \right) \\ \varepsilon_{ij} = \sqrt{\varepsilon_{ii}\varepsilon_{jj}} \end{cases} \tag{4.13}$$

The potential parameters for the alkanes are listed in Table 4.2. As Eq. (4.12) shows, the well-depth determines the strength of the interaction between the surface and the lubricant. The L-J parameters for liquid-solid interaction are guided by the mixing rule in Eq. (4.13), so the liquid-solid interaction can be controlled by using a range of well-depth parameters of the L-J potential of the surface (Fe).

It shall be noted that the selection of potential functions depends on the studied physical phenomenon. A simple spring model can be used for thin film lubrication, and the wall atoms are attached to their lattice position with a spring in the molecular model. However, it is more common to use the L-J potential in modeling thin film lubrication or surface sliding. In studying thin film lubrication, the main interest is to investigate the behavior of the lubricant between two sliding walls. The L-J potential for the interaction between the wall atoms and the lubricant molecules is acceptable as long as the parameters are chosen properly. Moreover, reasonable results can be gained by using the L-J potential for the atoms of surfaces when two surfaces are sliding against each other (Spijker et al. 2011). Another significant advantage of using this potential is the computational efficiency.

4.2.3.3 Solid (Fe)

In the embedded atom method (EAM) (Daw and Baskes 1984) for Fe, the total potential energy has a pairwise part and a local density part:

$$E = \sum_{i=1}^{N-1} \sum_{j=i+1}^{N} \varphi(r_{ij}) + \sum_{i=1}^{N} (\Phi(\rho_i)) \tag{4.14}$$

where the subscripts i and j label distinct atoms, N is the number of atoms in the system, r_{ij} is the distance between atoms i and j

$$\rho_i = \sum_j \Psi(r_{ij}) \tag{4.15}$$

All functions above are represented as sums of basis functions:

$$\varphi(r) = \sum_{k=1}^{n^\varphi} a_k^\varphi \varphi_k(r) \tag{4.16}$$

$$\Psi(r) = \sum_{k=1}^{n^\Psi} a_k^\Psi \Psi_k(\rho) \tag{4.17}$$

$$\Phi(r) = \sum_{k=1}^{n^\Phi} a_k^\Phi \Phi_k(\rho) \tag{4.18}$$

where φ_k, Ψ_k, and Φ_k are the basis functions and a_k are coefficients to be fitted to material properties. Those coefficients in the EAM for Fe can be found in Daw and Baskes (1984).

4.3 MD Simulation Results

In the MD simulations, the normal pressure is applied onto the upper wall atoms. The tribological phenomena of the system subject to different normal loads are investigated first. Figure 4.3 indicates the variation in the system height, i.e., the film thickness, due to different normal loads. The system has a transient response at the beginning of compression, and the film thickness oscillates and tends to be stable as the system reaches a state of equilibrium. As the normal load increases, the film thickness gets thinner. It can be seen that the film thickness gets stable after 0.6 ns.

The film density profiles are shown in Fig. 4.4, which give a clear layering structure. The lubricant in the middle seems to remain in its bulk state. It suggests that the confining effect decays toward the inner layers. In addition, the density profile exhibits an asymmetry. This is due to the normal motion of the upper boundary layer, while the lower boundary layer is fixed in the vertical direction. As it is mentioned before, the united atoms include CH_3 and CH_2 which have corresponding atom mass and the volume confined between the walls to calculate the average density. Figure 4.4 also shows that the density profile structure becomes larger near the walls and its thickness shrinks. It is predictable that the film thickness is smaller under a larger normal load, and the density profile has to be denser in some areas.
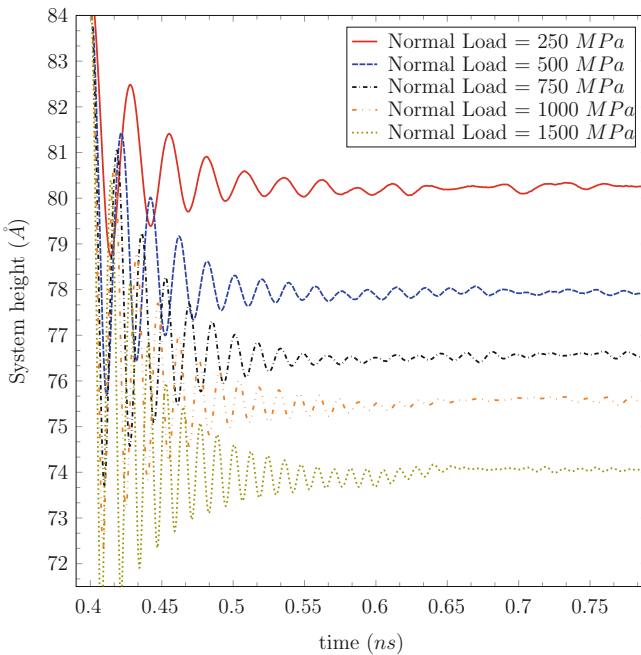
Fig. 4.3 System height, i.e., the film thickness, under various normal loads
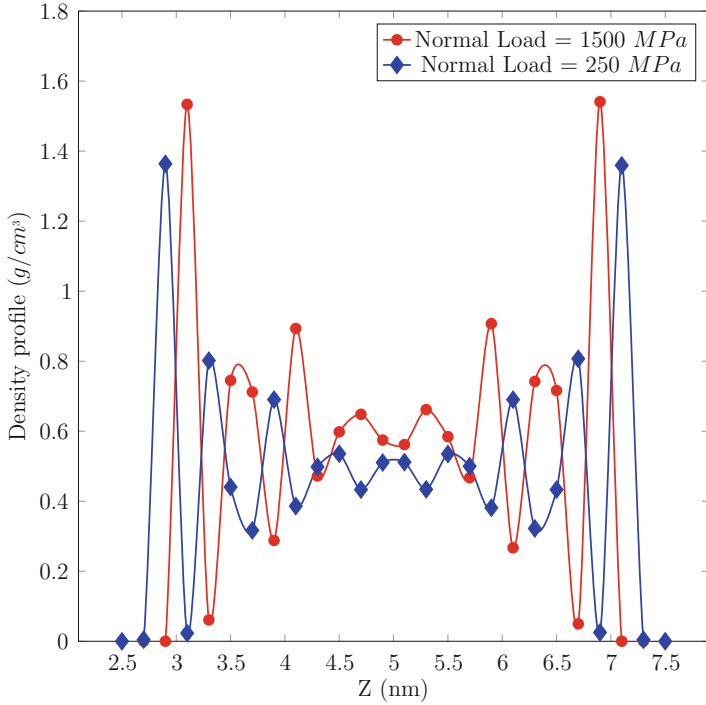
Fig. 4.4 Density profile of the linear alkane confined by surfaces

The friction force under each normal load can be obtained in the MD simulation by summing the forces exerted on the atoms of the rigid and thermostat layers in the longitudinal direction. The friction forces under different normal loads are shown in Fig. 4.5.

Generally, the friction coefficient can be calculated by

$$\mu = \frac{F}{P} \tag{4.19}$$

where F is the friction force and P is the externally applied load.

A linear function is used to fit the data in Fig. 4.5 to determine the coefficient of friction. The slope of the linear function indicates that the coefficient of friction equals to 0.0483. The calculated coefficient of friction is similar to the typical friction coefficients for many hydrodynamic lubricant applications. The friction coefficient calculated from the molecular model will then be passed to the fatigue life prediction model at the continuum level in next section.
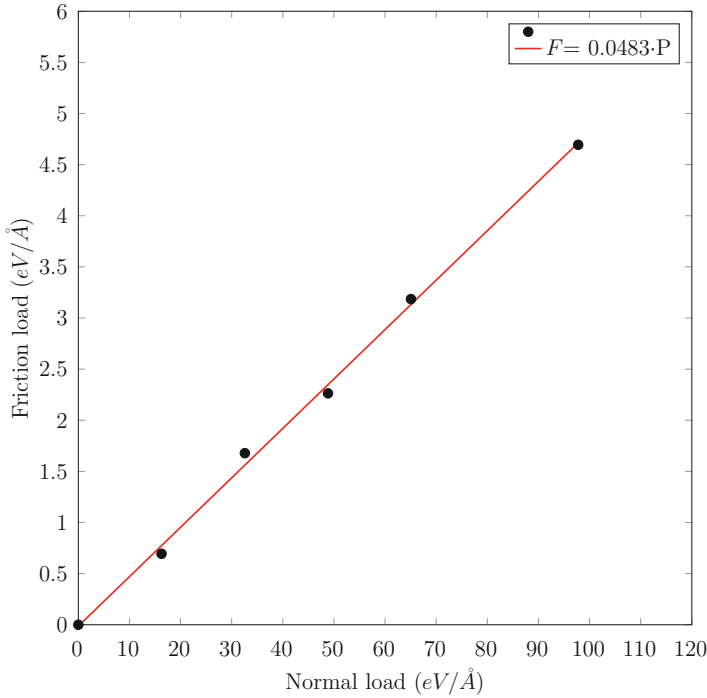
Fig. 4.5 Friction forces vs. normal loads

4.4   Continuum Modeling of Rolling Contact Fatigue

In this study, the fatigue life at crack initiation is predicted via the continuum mechanics approach. The contact pair, e.g., bearing, in the rolling contact model includes the rolling element and the bearing inner race. The rolling element is modeled as a rigid body, while the material of bearing inner race is assumed to be homogeneous and isotropic. The stress analysis of the rolling contact model is conducted in the FEM framework through ANSYS parametric design language with the default contact algorithm, as shown in Fig. 4.6. The application of rolling element as the rigid body in our model is identical to applying Hertzian contact load (Ghaffari et al. 2015). The boundary conditions are shown in Fig. 4.6 as well. In addition, the bearing is assumed to be free of imperfections. Since the curvature of the bearing inner race is much smaller than the one of the rolling element, the bearing inner race is considered having flat surface in our model. The stress analysis of the rolling contact model is conducted in the FEM framework through ANSYS parametric language for moving Hertzian contact load (Ghaffari et al. 2015), as shown in Fig. 4.6. Two-dimensional model is used here, and the simulation includes two steps. Firstly, the normal load is applied to achieve the contact between the roller and the surface. Then, the roller moves in X-direction while the contact load
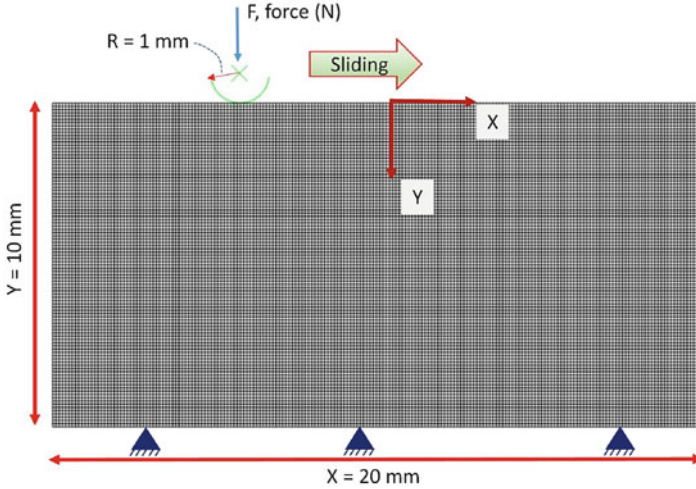
Fig. 4.6 Schematic finite element model and cyclic Hertzian contact load through analytical rigid body on the surface

is applied. It shall be noted that the prescribed friction coefficient of 0.0483 was obtained via MD modeling and simulation discussed in previous section. During the simulation, the stress state at each node is calculated per step of the moving Hertzian contact loading. Then, the stress history, i.e., the stress loading cycle, for each node in one Hertzian contact loading cycle is obtained. The stress loading cycle is calculated using the critical plane damage method (Ghaffari et al. 2015) based upon the analysis of stresses or strains as they experienced at a particular plane of the material. The critical plane approach was widely used for fatigue analysis (Socie 1993; Fatemi and Socie 1988), and it is the plane with the most predicted fatigue failure and fracture. Critical plane approach was used to identify the location where the fatigue failure starts and it gradually developed from considering how cracks initiate and propagate. Socie's research (Socie 1993) supports the idea that cracks initiate and propagate on critical planes and based on the material, critical planes may be either tensile strain planes or shear strain.

The extreme damage occurs at the critical plane where the fatigue crack initiates. Therefore, it is essential to calculate the stress loading cycle at the critical plane during the rolling contact fatigue life analyses (Podrug et al. 2008). The emergence of different fracture modes generally depends on the material type, strain amplitude, and state of stresses. If the shear stress is the dominant stress in the material, the following shear-based damage model will be used to predict the fatigue crack initiation life of the material (Podrug et al. 2008):

$$d_s = \gamma_a \left(1 + k \frac{\sigma_{max}}{\sigma_{ys}}\right) = \frac{\tau'_f}{S}(2N_i)^{b_{0i}} + \gamma'_f(2N_i)^{c_{0i}} \tag{4.20}$$

Table 4.3 Material properties (Boardman 1982)

Description	Symbol	
Yield strength (MPa)	Y	447
Ultimate tensile strength (MPa)	U	836
Elastic modulus (MPa)	E	2.07×10^5
Fatigue strength coeff. (MPa)	σ_{max}	1278
Fatigue strength exponent	b_i	-0.11
Fatigue ductility exponent	c_i	-0.54
Fatigue ductility coeff.	ε_a	0.53
Cyclic strain hardening exponent	n'	0.19
Cyclic strength coeff.	K'	1448

where d_s is shear damage parameter, γ_a is the largest shear strain amplitude for any plane, S was the shear modulus, and τ'_f is shear fatigue strength coefficient. Yield stress and maximum normal stress on the same plane as largest normal strain amplitude are demonstrated by σ_{ys} and σ_{max}, respectively. Material parameters of b_{0i}, c_{0i}, and k are shear fatigue strength exponent, shear fatigue ductility exponent, and empirical material constant, respectively. The shear damage parameter is calculated for both the plane strain and plane stress conditions as follows:

$$d_s = \gamma_a \left(1 + k \frac{\sigma_{max}}{\sigma_{ys}}\right) = \frac{1+\upsilon}{2E} \sigma_n \left(1 + k \frac{\sigma_n}{\sigma_{ys}}\right) \tag{4.21}$$

where σ_n is the normal stress at the plane normal to the surface.

4.5 Results and Discussions

A quasi-static simulation is conducted to model moving Hertzian contact (Ghaffari et al. 2015). C-Mn Steel SAE1561 is used as the material of the bearing inner race. The material properties are shown in Table 4.3. The fatigue-related parameters are obtained from the E-N fatigue data of this material shown in Fig. 4.7.

Based on the above material fatigue data and the E-N fatigue calculation approach, fatigue life cycles for the different load cases are analyzed via Eq. 4.20, and the results are shown in Fig. 4.8. For the Hertzian load lower than 3000 MPa, there is no fatigue observed. In other words, fatigue only occurs under the loads equal to and larger than 3000 MPa. It is also shown in Fig. 4.8 that the fatigue life decreases as the normal load increases and the behavior is almost logarithmic.

In the continuum model, the stress histories at various points during one contact loading cycle are calculated first. Then, the fatigue lives are evaluated at those points to find the critical location where fatigue occurs. Since the stress is only various along the vertical direction in the two-dimensional model, the locations at x=0 are considered to calculate the stress histories. One point on the contact surface and other six points under the surface are chosen. The distances between those points
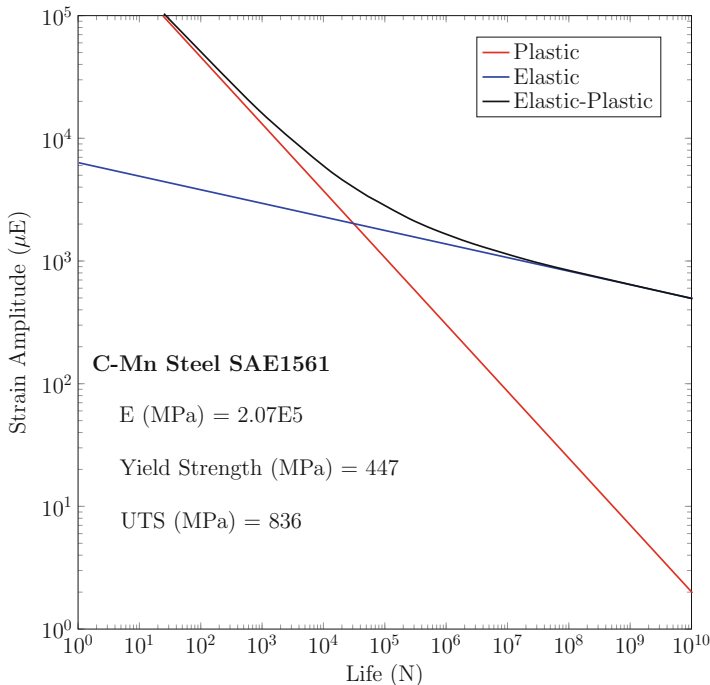
Fig. 4.7 Strain-life data for C-Mn Steel SAE1561

and the contact surface are 0.000, 0.027, 0.055, 0.083, 0.111, 0139, and 0.167 mm. The shear and von Mises stress profiles at those seven points during one contact loading cycle are shown in Fig. 4.9. It shall be noted that the stress profiles under various contact loads are pretty similar and only the stress magnitudes are different. Therefore, a single load case of Hertzian contact load with $P_{max} = 6000$ MPa is considered first. Figure 4.9 shows that as it goes deeper from the contact surface, the shear stress increases until to the point at $y = -0.139$ mm and then decreases. However, the von Mises stress keeps decreasing.

Using the relationship between the deformation and the number of loading cycles for the fatigue crack initiation, i.e., Eq. (4.20), the position of initial fatigue fracture and the corresponding number of stress cycles can be determined, as shown in Fig. 4.10. The number of loading cycles required for initial fatigue crack occurring is 6.01E4 cycles. In addition, the initial fatigue crack occurs at $y = 0.08$ mm under the contact surface.

Various normal loads are also considered here as 3000, 4000, and 5000 Mpa. The fatigue lives at the points below the contact surface are shown in Fig. 4.11. It indicates that the fatigue life scatters are almost the same at all the loads, and the difference is only in its value. The locations of the initial crack are the same under all the normal loads. Figure 4.11 also demonstrates that as the normal load increases, the fatigue life decreases and the crack initiation occurs after 5.2×10^6,
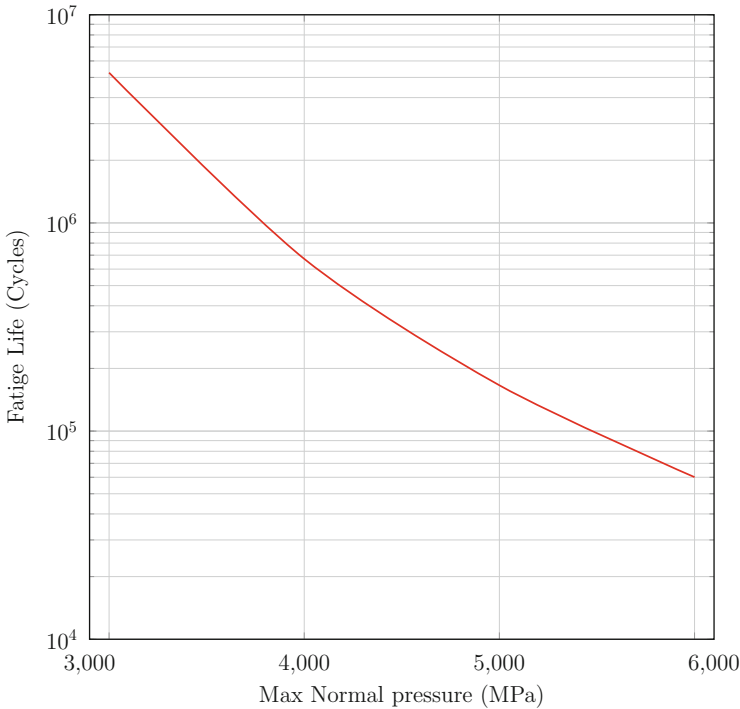
Fig. 4.8 Fatigue life versus different Hertzian normal pressures

6.7×10^5, and 1.6×10^5 cycles when the normal loads are 3000, 4000, and 5000 MPa, respectively. It shall be noted that the crack initiates below the surface and it will start to propagate in different angles and then to reach the surface eventually. This phenomenon is so-called spallation.

In the application of wind turbine, the wind turbine blades rotate due to wind's forces, including two primary aerodynamic forces: lift and drag. Mostly, the wind flow is not steady so that the wind turbine blades exhibit vibrations during rotation. Consequently, the torque and the bending moment transferred to the wind turbine gearbox through the speed shaft have some fluctuations, i.e., noises, as well as the resulted normal load on the bearings in the gearbox. Therefore, it is crucial to consider the load fluctuation when predicting bearing fatigue life in wind turbine gear box. To study rolling contact fatigue life under fluctuating loads, the continuum model, described in the above, is implemented in the software of nCode Designlife. The nCode Designlife utilizes the frequency domain fatigue analysis in which the random loading and response are categorized using power spectral density (PSD) functions (Halfpenny and Bishop 1997).

Three fluctuating normal loads, shown in Fig. 4.12, due to random vibrations are considered here to calculate rolling contact fatigue lives. Although those three fluctuating loads have the same mean value of 3000 MPa, they have different
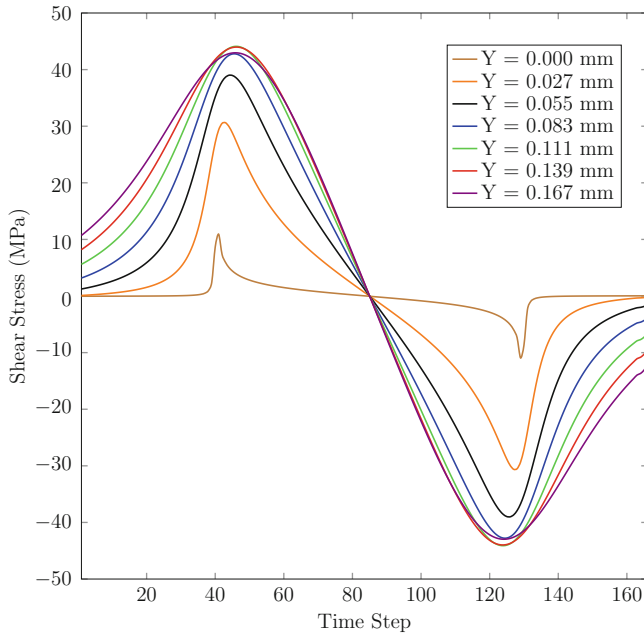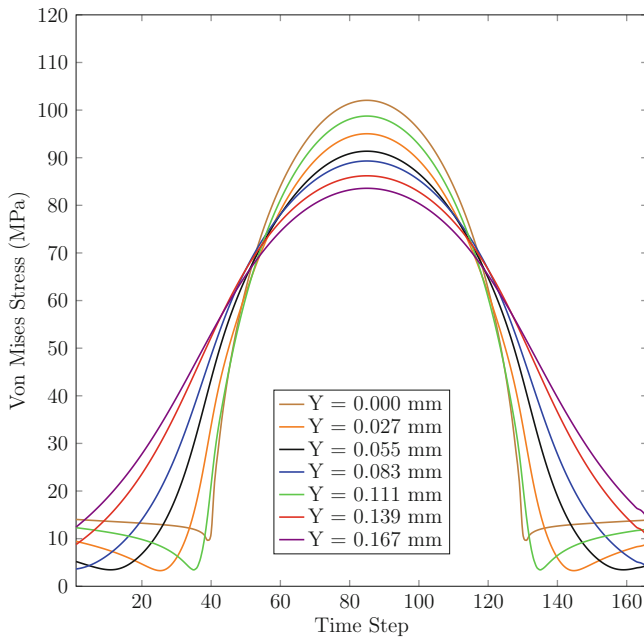
Fig. 4.9 Stress histories under the contact surface when Hertzian contact load of P_{max} = 6000 MPa; (**a**) shear stress; (**b**) von Mises stress
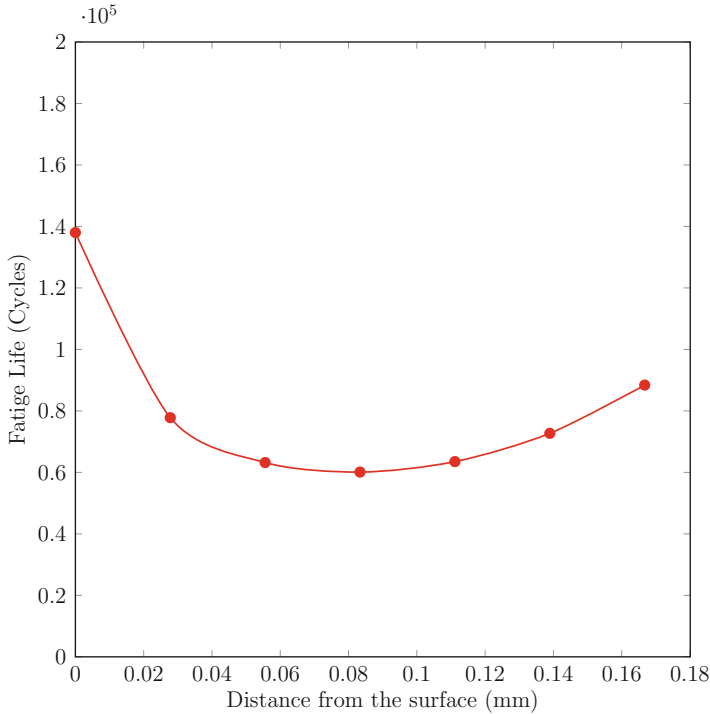
Fig. 4.10 The number of loading cycles till the initial crack occurs at the observed material points when $P_{max} = 6000$ Mpa

amplitudes. The minimum and maximum loads of those three fluctuating loads are [0.7, 1.3], [0.8, 1.2], and [0.9, 1.1] of the mean load which is represented as the dot line in Fig. 4.12. The prescribed friction with the friction coefficient of 0.0483 is applied here. It shall be noted that the friction coefficient under fluctuating loads can be calculated via the same molecular model as described in Sect. 4.2.

The time histories of the von Mises stress at a node on the contact surface are shown in Fig. 4.13. It shows that for the fluctuating load with larger amplitude, the resulted von Mises stress has larger fluctuation. It shall be noted that the difference of noise levels between various random loads is significant, especially the noise peaks.

The predicted rolling contact fatigue lives under various fluctuating normal loads are shown in Table 4.4, compared with the result due to a constant normal load of 3000 MPa. As shown in this table, the fatigue life for the case under a constant normal load is much higher than the others. This demonstrates that if the system was subject to a fluctuating cyclic load, the fatigue life would be dramatically reduced. In addition, as the amplitude of the fluctuating load becomes smaller, the fatigue life increases.
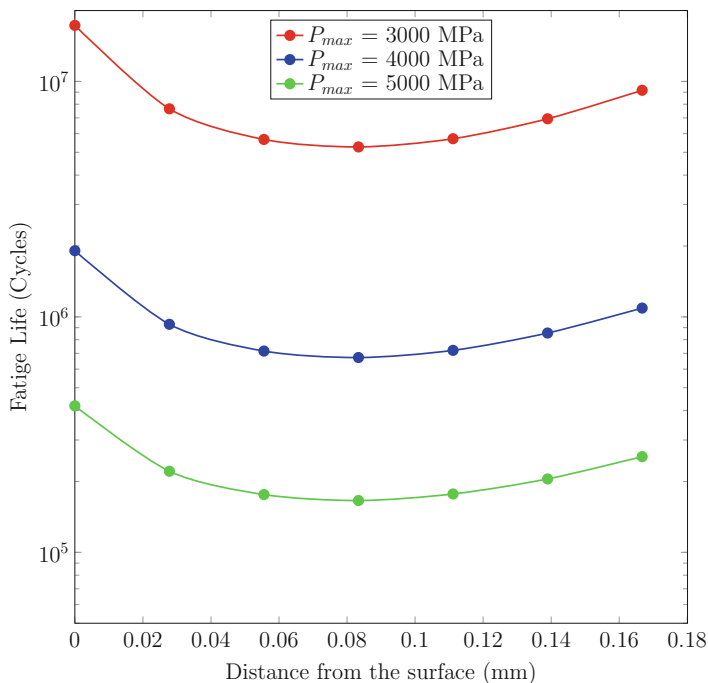
Fig. 4.11 Number of loading cycles till the initial crack occurs at the observed material points when $P_{max} = 3000$ MPa, $P_{max} = 4000$ MPa, and $P_{max} = 5000$ MPa

4.6   Conclusion

In this study, a new multiscale modeling is proposed to study rolling contact fatigue with the consideration of lubricant effects. Since the thickness of the lubricant is very small, molecular model is a proper method to simulate the lubricant so that the friction phenomena can be studied between two contact surfaces. The calculated friction coefficient is then passed to the continuum model of the rolling contact component to calculate its fatigue life. The fluctuating load is also considered, and the fatigue life is significantly reduced. The proposed multiscale method belongs to the family of hierarchical or sequential multiscale methods due to its one-way message passing from the molecular model to the continuum model. Although only smooth contact surfaces were considered in this study, rough contact surfaces and the lubricant with nanoparticles can be easily modeled and studied via the molecular model in the framework of the proposed multiscale model.
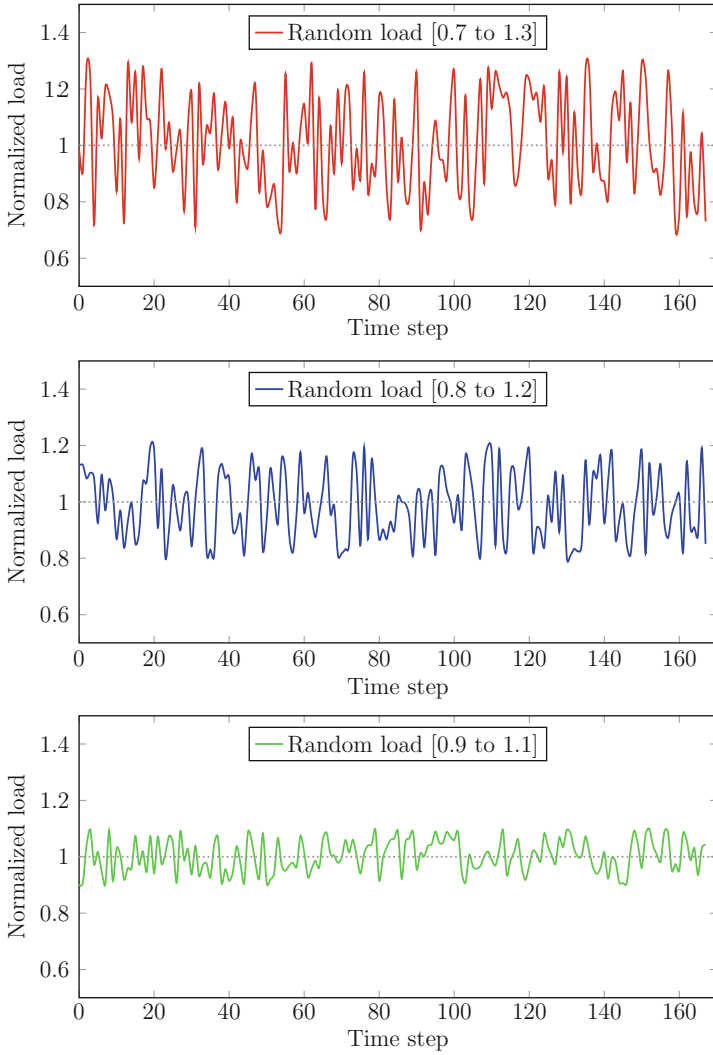
Fig. 4.12 Three different normalized fluctuating normal loads during one Hertzian contact cycle
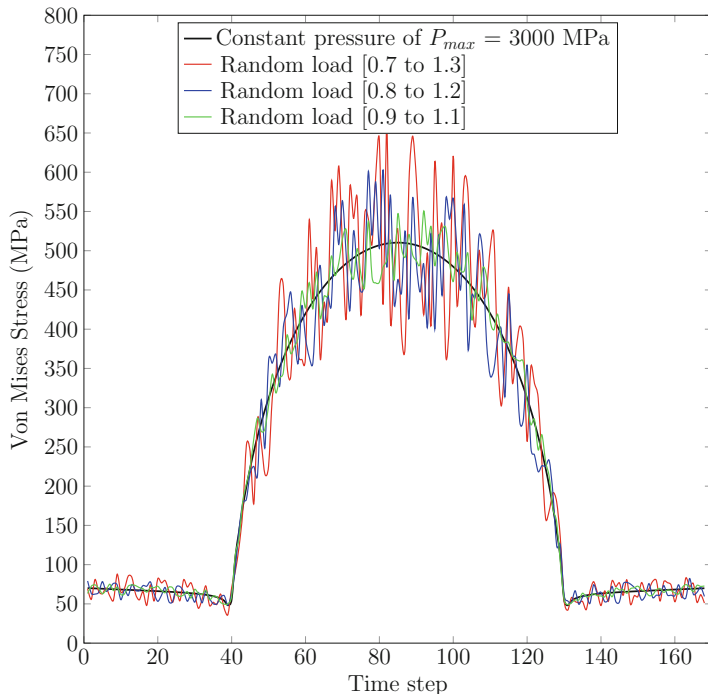
Fig. 4.13 Von Mises time history for different random loads at a node on the contact surface

Table 4.4 Rolling contact fatigue lives under a constant load of $P_{max} = 3000$ MPa and various fluctuating loads with the mean value of 3000 MPa

Case study	Fatigue life
Constant pressure of P_{max}	5.2×10^6
Random load [0.9, 1.1]	2.4×10^6
Random load [0.8, 1.2]	1.3×10^6
Random load [0.7, 1.3]	0.8×10^6

References

Berro H, Fillot N, Vergne P (2010) Molecular dynamics simulation of surface energy and ZDDP effects on friction in nano-scale lubricated contacts. Tribol Int 43:1811–1822

Bhargava V, Hahn GT, Rubin CA (1990) Rolling contact deformation, etching effects and failure of high strength steels. Metall Trans A 21:1921–1931

Bhushan B, Israelachvili JN, Landman U (1995) Nanotribology: friction, wear and lubrication at the atomic scale. Nature 374:607–616

Boardman B (1982) Crack initiation fatigue – data, analysis, trends and estimation, SAE Technical Paper 820682

Chantrenne P, Raynaud M, Clapp PC, Rifkin J, Becquart CS (2000) Molecular dynamics simulations of friction. Heat Technol 18:49–56

Chhowalla M, Amaratunga GA (2000) Thin films of fullerene-like MoS2 nanoparticles with ultra low friction and wear. Nature 407:164–167

Daw M, Baskes M (1984) Embedded-atom method: derivation and application to impurities, surfaces, and other defects in metals. Phys Rev B 29:6443–6453

Fatemi A, Socie DF (1988) A critical plane approach to multiaxial fatigue damage including out-of-phase loading. Fatigue Fract Eng Mater Struct 11:149–165

Ghaednia H, Babaei H, Jackson R, Bozack M, Khodadadi JM (2013) The effect of nanoparticles on thin film elasto-hydrodynamic lubrication. Appl Phys Lett 103:263111

Ghaednia H, Jacksona RL, Khodadadi JM (2015) Experimental analysis of stable CuO nanoparticle enhanced lubricants. J Exp Nanosci 10:1–18

Ghaffari MA, Pahl E, Xiao S (2015) Three dimensional fatigue crack initiation and propagation analysis of a gear tooth under various load conditions and fatigue life extension with boron/epoxy patches. Eng Fract Mech 135:126–146

Halfpenny A, Bishop NWM (1997) Vibration fatigue, nCode International Ltd. 230 Woodbourn Road, Sheffield, S9 3LQ. UK

Harrison JA, Colton RJ, Whit CT, Brenner DW (1993) Effect of atomic-scale surface roughness on friction: a molecular dynamics study of diamond surfaces. Wear 168:127–133

Hoover W (1985) Canonical dynamics: equilibrium phase-space distributions. Phys Rev A 31:1695–1697

Ioannides E, Harris T (1985) A new fatigue life model for rolling bearings. ASME J Tribol 107:367–378

Jalalahmadi B, Sadeghi F (2009) A voronoi finite element study of fatigue life scatter in rolling contacts. ASME J Tribol 131:022203

Keer LM, Bryant MD (1983) A pitting model for rolling contact fatigue. ASME J Lubr Tech 105:198–205

Ketko M, Rafferty J, Siepmann J, Potoff J (2008) Development of the TraPPE-UA force field for ethylene oxide. Fluid Phase Equilibr 274:44–49

Kudish II, Burris KW (2000) Modern state of experimentation and modeling in contact fatigue phenomenon: part II – analysis of the existing statistical mathematical models of bearing and gear fatigue life. New statistical model of contact fatigue. Tribol Trans 43:293–201

Lormand G, Meynaud G, Vincent A, Baudry G, Girodin D, Dudragne G (1998) From cleanliness to rolling fatigue life of bearings – a new approach. In: Hoo J, Green W (eds) Bearing steels: into the 21st century, ASTM STP No. 1327. ASTM Special Technical Publication, West Conshohocken, pp 55–69

Lundberg G, Palmgren A (1947) Dynamic capacity of rolling bearings. Acta Polytech Scand Mech Eng Ser 1:1–52

Lundberg G, Palmgren A (1952) Dynamic capacity of roller bearings. Acta Polytech Scand Mech Eng Ser 2:96–127

Maharaj D, Bhushan B (2013) Effect of mos_2 and ws_2 nanotubes on nanofriction and wear reduction in dry and liquid environments. Tribol Lett 49:323–339

Martin M, Siepmann J (1998) Transferable potentials for phase equilibria. 1. United-atom description. J Phys Chem 1012:2569–2577

Nose S (1984) A unified formulation of the constant temperature molecular dynamics methods. J Chem Phys 81:511–519

Omelyan I, Mryglod I, Folk R (2002) Optimized verlet-like algorithms for molecular dynamics simulations. Phys Rev E 65:056706

Plimpton S (1995) Fast parallel algorithms for short-range molecular dynamics. J Comp Phys 117:1–19

Podrug S, Jelaska D, Glodez S (2008) Influence of different load models on gear crack path shapes and fatigue lives. Fatigue Fract Eng 31:327–339

Raje NN, Sadeghi F, Rateick RGJ, Hoeprich MR (2008) A numerical model for life scatter in rolling element bearings. ASME J Tribol 130:011011

Rapoport L, Fleisher N, Tenne R (2005) Applications of WS_2 (MoS_2) inorganic nanotubes and fullerene-like nanoparticles for solid lubrication and for structural nanocomposites. J Mater Chem 15:1782–1788

Rosentsveig R, Gorodnev A, Feuerstein N, Friedman H, Zak A, Fleischer N, Tannous J, Dassenoy F, Tenne R (2009) Fullerene-like mos_2 nanoparticles and their tribological behavior. Tribol Lett 36:175–182

Sadeghi F, Jalalahmadi B, Slack TS, Raje N, Arakere NK (2009) A review of rolling contact fatigue. J Tribol 131:041403

Savio D, Fillot N, Vergne P, Zaccheddu M (2012) A model for wall slip prediction of confined n-alkanes: effect of wall-fluid interaction versus fluid resistance. Tribol Lett 46:11–22

Socie D (1993) Critical plane approaches for multiaxial fatigue damage assessment. Advances in Multiaxial Fatigue, ASTM STP 1191

Spijker P, Anciaux G, Molinari JF (2011) Dry sliding contact between rough surfaces at the atomistic scale. Tribol Lett 44:279–285

Spijker P, Anciaux G, Molinari JF (2012) The effect of loading on surface roughness at the atomistic level. Comput Mech 50:273–283

Stubbs J, Potoff J, Siepmann J (2004) Transferable potentials for phase equilibria. 6. United-atom description for ethers, glycols, ketones, and aldehydes. J Phys Chem 108:17596–17605

Tallian T (1992) Simplified contact fatigue life prediction model – part II: new model. ASME J Tribol 114:214–222

Tao X, Jiazheng Z, Kang X (1996) The ball-bearing effect of diamond nanoparticles as an oil additive. J Phys D: Appl Phys 29:2932

Tarasova S, Kolubaeva A, Belyaeva S, Lernerb M, Tepperc F (2002) Study of friction reduction by nanocopper additives to motor oil. Wear 252:63–69

Thompson P, Robbins M (1990a) Origin of stick-slip motion in boundary lubrication. Science 250:792–794

Thompson P, Robbins M (1990b) Shear flow near solids: epitaxial order and flow boundary conditions. Phys Rev A 41:6830–6837

Vincent A, Lormand G, Lamagnere P, Gosset L, Girodin D, Dudragne G, Fougeres R (1998) From white etching areas formed around inclusions to crack nucleation in bearing steels under rolling contact. In: Hoo J, Green W (eds) Bearing steels: into the 21st century, ASTM STP No. 1327. ASTM Special Technical Publication, West Conshohocken, pp 109–123

Wick C, Martin M, Siepmann J (2000) Transferable potentials for phase equilibria. 4. United-atom description of linear and branched alkanes and of alkylbenzenes. J Phys Chem 104:8008–8016

Xu G, Sadeghi F (1996) Spall initiation and propagation due to debris denting. Wear 201:106–116

Zhang L, Tanaka H (1998) Atomic scale deformation in silicon monocrystals induced by two-body and three-body contact sliding. Tribol Int 31:425–433

Zheng X, Zhun H, Tieu AK, Kosasih B (2013a) A molecular dynamics simulation of 3D rough lubricated contact. Tribol Int 67:217–221

Zhou RS (1993) Surface topography and failure life of rolling contact bearings. Tribol Trans 36:329–340

Zhou RS, Cheng HS, Mura T (1989) Micropitting in rolling and sliding contact under mixed lubrication. ASME J Tribol 111:605–613

Zheng X, Zhu H, Kosash B, Tieu A (2013b) A molecular dynamics simulation of boundary lubrication: the effect of n-alkanes chain length and normal load. Wear 301:62–69

Zheng X, Zhun H, Tieu AK, Kosasih B (2014) Roughness and lubricant effect on 3D atomic asperity contact. Tribol Lett 53:215–223

Zheng X (2014) Molecular dynamics simulation of boundary lubricant contacts. Ph.D. thesis, University of Wollongong

Chapter 5
Lightning Analysis of Wind Turbines

Yeqing Wang

5.1 Introduction

5.1.1 Basic Physics of Lightning Strikes

Lightning discharge is essentially the dielectric breakdown of the air. It occurs when the strength of the electric field between the cloud and the earth or between two clouds exceeds the dielectric breakdown strength of the air (i.e., 3 MV/m). Due to the large intensity of the electric field, the air molecules are ripped apart, leaving free electrons and positive ions. Meanwhile, the electric field between the cloud and the earth or between two clouds accelerates these charges causing a rapid motion of the electric charge, which heats the surrounding air molecules up to 50,000 °F (i.e., almost five times the temperature of the Sun's surface) (Oard 2015). The extreme heat leads to a rapid volume expansion of the air and, thus, emanates sound waves (i.e., the thunder). In addition to the sound waves, the lightning plasma channel also emits light, radio waves, x-rays, and even gamma rays (Rupke 2002).

The luminous lightning flash (i.e., can be visually observed in the air) is not instantly formed after the dielectric breakdown of the air. Instead, a few steps with durations of several milliseconds are completed prior to the formation of the luminous lightning flash. Taking the negative polarity downward initiated cloud-to-ground (CG) lightning flash for example, in the beginning of the lightning flash, the positive charge in the cloud travels in the speed of light through the air

Y. Wang (✉)
Department of Mechanical and Aerospace Engineering, University of Florida,
Gainesville, FL, USA
e-mail: yeqwang@reef.ufl.edu

propagating toward the ground. The propagating channel, known as the lightning stepped leader, is a weakly luminous channel that can be visually observed in the air and only lasts for several milliseconds. As the lightning stepped leader approaches the ground, the intensified electric field between the tip of the lightning stepped leader and the ground structures triggers the ground structures to emit answering leaders. Once the lightning stepped leader connects with the answering leader, the first luminous lightning channel, known as the lightning return stroke (i.e., the channel with negative charge that travels from the ground to the cloud), is then formed. Common structures that can emit answering leaders are normally electrically conductive such as transmission towers and TV towers. Moreover, the electrically non-conductive structures (e.g., glass fiber-reinforced polymer-matrix (GFRP) composite wind turbine blades) are also able to emit answering leaders if conductive components (receptors and down conductors, etc.) or conductive contamination (salt, dirt, moisture, etc.) is included (Madsen 2006).

Furthermore, a typical lightning discharge includes one or more intermittent partial discharges; each component discharge is called a stroke. Figure 5.1 shows a standard waveform of the lightning strike electric current used for common lightning strike analysis, where the waveform components A, B, C, and D denote the initial return stroke, intermediate stroke, continuing stroke, and restrike stroke, respectively. The initial return stroke current has a pulsed profile with a peak reaching up to hundreds kiloamperes. The electric current return stroke wave heats and pressurizes the lightning plasma channel which leads to the rapid channel expansion, optical radiation, and shock wave propagation in the outward direction. The initial return stroke with high-intensity short-duration pulsed current is typically followed by a continuing stroke with almost constant current, which is about two orders of magnitude lower and three orders of magnitude longer than that of the pulsed current of the initial return stroke.
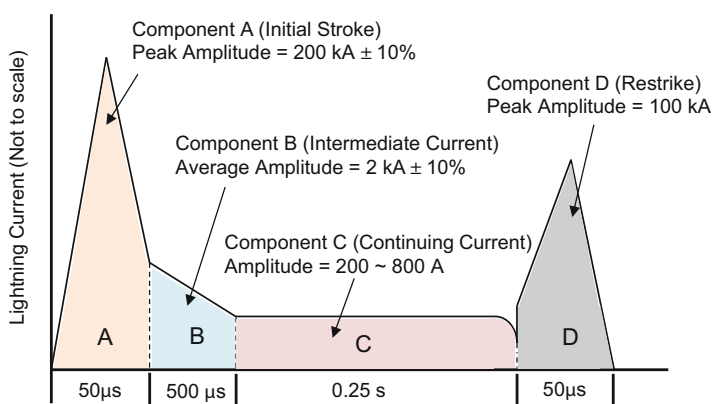
Fig. 5.1 Standard lightning current waveform suggested by MIL-464-A (1997)

5.1.2 Direct Effects of Lightning Strikes on Wind Turbines

5.1.2.1 Dielectric Breakdown

Lightning strikes cause frequent structure damage to the wind turbines, especially to the wind turbine blades which are typically made of the sandwiched composite laminated panels. The most widely used type of composite materials on the wind turbine blades are the electrically non-conductive glass fiber-reinforced polymer-matrix (GFRP) composite laminates. During a lightning strike event, the electric field strength in the vicinity of the composite wind turbine blades significantly intensifies. If it exceeds the dielectric breakdown strength of the composite wind turbine blade, the dielectric breakdown occurs and, thus, may result in pin holes or punctures in the blades. Typically, the electrical field required to puncture a given thickness of glass fiber or aramid fiber composite is greater than that required to ionize a similar thickness of air due to the high porosity and inhomogeneity of the composite structure (Rupke 2002). The dielectric breakdown strength of the solid composite material is highly dependent on the thickness, temperature, humidity, and pressure. A detailed discussion of the dielectric breakdown strength of the composite wind turbine blade is provided in Sect. 5.2.4.

5.1.2.2 Surface Flashover

In the case when the electric field strength on the composite wind turbine blade is lower than its dielectric breakdown strength, the lightning arc automatically searches for the weakest spots (i.e., least resistant) to conduct the lightning electric current once it attaches to the surface of the non-conductive composite wind turbine blade. If the electric field strength exceeds the surface flashover field strength (i.e., lower than the dielectric breakdown strength), the conduction of the lightning current on the surface can be visually observed in a form of surface flashover (also known as streamers). Figure 5.2 shows an example of a surface flashover on a composite wind turbine blade surface caused by the lightning arc. The surface flashover produces extensive heat along the conducting path and, thus, may lead to appreciable thermal damage, such as skin peeling, burning, melting, and material vaporization.

5.1.2.3 Lightning Strike-Induced Localized Damage on Composite Wind Turbine Blades

The direct injection of the lightning arc channel onto the surface of the composite wind turbine blade produces extensive localized damage, such as melting or burning on the lightning attachment points, and mechanical damage due to magnetic force and acoustic shock wave. If the blade is made of electrically conductive material (e.g., carbon fiber polymer-matrix composite laminates), the conduction of the
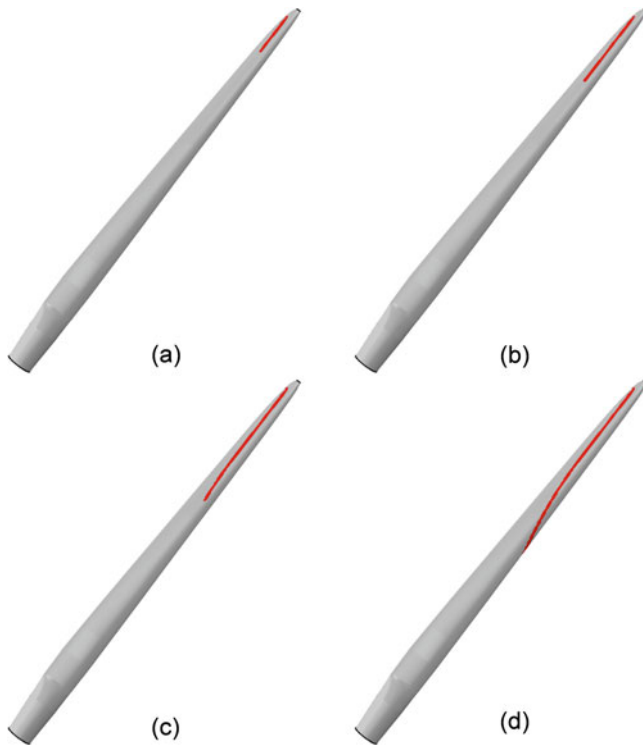
Fig. 5.2 Example of the evolution of the surface flashover on a wind turbine blade at 1 (**a**), 2 (**b**), 3 (**c**), and 4 milliseconds (**d**) (where the gray denotes room temperature and red denotes high temperatures)

lightning current through the interior of the conductive blade also produces extreme high Joule heating, which may lead to more extensive thermal damage. Generally, if a lightning arc attaches to the surface of the solid material, the direct heat flux injection leads to a rapid temperature rise on the surface of the composite wind turbine blade. With the increasing temperature, the resin component (i.e., the polymer matrix) of the composite material starts to decompose at around 300 °C and is fully consumed as the temperature reaches 800 °C. The decomposition of the resin leads to the fluctuations in the overall density and material properties of the material, the degradations in the material strength, and the liberation of the pyrolysis gases. The decomposition of the interlaminar resin will also lead to the delamination of the composite laminates. At temperatures around 1100 °C (or higher), the glass fiber quickly melts and vaporizes (or experiences rapid melt expulsion).

In addition, the pyrolysis gases may be trapped in between the laminate layers as the interlaminar resin decomposes. With the accumulation of the trapped pyrolysis gases, the volume of the pyrolysis gases expands, and if the stress caused by the internal pressure of the pyrolysis gases exceeds the rupture strength of the
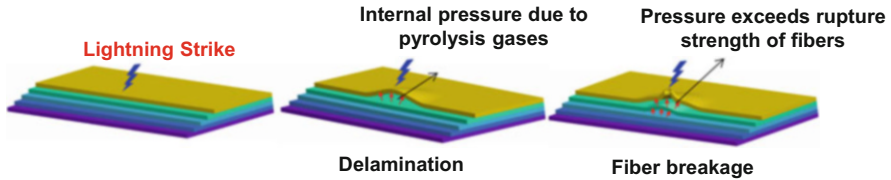
Fig. 5.3 Lightning-induced delamination and fiber breakage in polymer-matrix composite structures
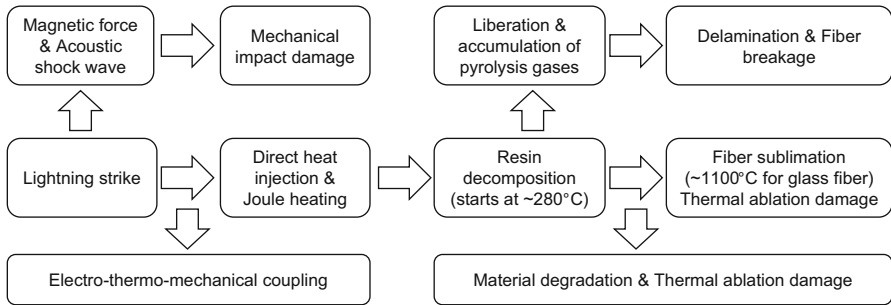
Fig. 5.4 Lightning strike direct effects on polymer-matrix composite laminated structures

fibers, fiber breakage develops and results in surface cracks (see Fig. 5.3). Inoue et al. (2004) studied the relationship between the pressure rise inside a laminated composite panel and the energy of a spark arc that is enforced on the composite blade surface. It was reported that the internal pressure between the laminate layers is proportional to the arc energy. Furthermore, the induced magnetic force and acoustic shock wave as the lightning arc attaches to the surface of the composite wind turbine blade may also result in minor mechanical impact damage (Chemartin et al. 2012; Muñoz et al. 2014). An overview of the lightning strike direct effects on polymer-matrix composite laminates is provided in Fig. 5.4.

5.1.3 Common Lightning Strike Protections (LSP) for Wind Turbines

As described in Sect. 5.1.1, the approaching of the lightning stepped leader toward the ground intensifies the electric field between the tip of the lightning stepped leader and the ground structures. When the tip of the lightning stepped leader arrives within a certain distance (i.e., the lightning striking distance) to a ground structure, answering leaders will be emitted from the structure and attempt to arrest the lightning stepped leader. Once they are connected, the first lightning return stroke is formed. Normally, structures such as metallic conductors are able to emit answering

leaders (as conductors allow electric charges to move freely under lightning electric field). As described earlier, non-conductive structures such as the GFRP composite wind turbine blades are also able to emit answering leaders due to the presence of internal down conductors, receptors, and surface contaminations (e.g., moisture, dirt, and rain drops).

To intercept the lightning stepped leader and conduct the high-intensity lightning current safely to the ground, the wind turbine blades are normally designed with lightning strike protections (LSP). The most commonly used LSP system is to embed conductive (e.g., special tungsten alloy) receptors on the surfaces of wind turbine blades (IEC-61400-24 2002). These receptors are connected to down conductors (e.g., unshielded high-voltage cables) which are installed inside the blade shell extending from the root to the tip of the blade. The receptors are designed to intercept the lightning strokes and safely conduct the lightning current through the down conductors to the earth. The efficiency of LSP is expressed as a product of interception efficiency and sizing efficiency, where the interception efficiency refers to the ability of the receptors to intercept a lightning stroke, and the sizing efficiency refers to the ability of the LSP system to conduct the lightning current (IEC-61400-24 2002). The sizing efficiency can be increased by increasing the diameter of the down conductors, while the interception efficiency may be increased by using multiple receptors. The receptors often undergo partial evaporation with repeated lightning strikes. They need to be replaced after every several lightning strikes. Figure 5.5 shows an example of embedding multiple receptors on the surface of a 100-meter long wind turbine blade. Recently, Wang and Hu investigated the effects of five different configurations of receptors on the lightning strike protection of wind turbine blades (Wang and Hu 2017).
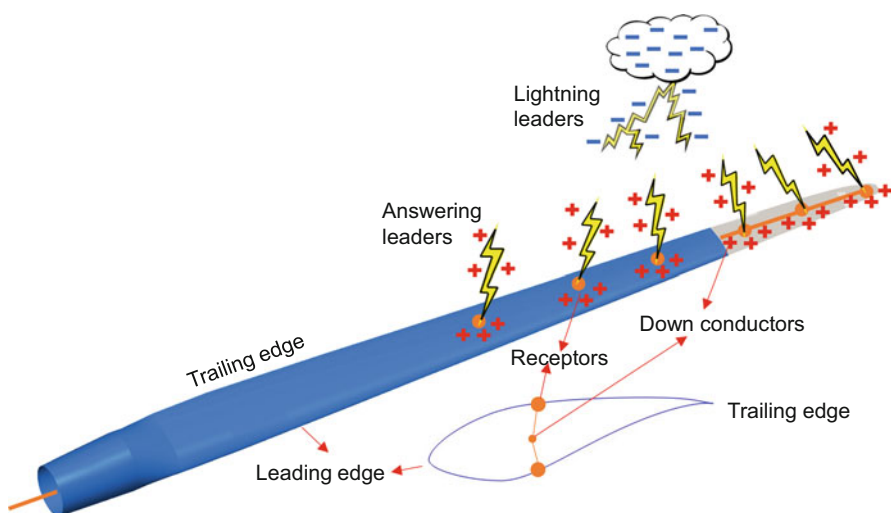
Fig. 5.5 A schematic of the formation of lightning leaders and answering leaders emitting from the receptors of a wind turbine blade

5.1.4 Lightning Current Conduction on Electrically Non-conductive Composite Wind Turbine Blades

Although LSP is widely used on wind turbines, lightning strike damage is still not completely avoidable. It has been reported that many electrically non-conductive wind turbine blades with the receptor and down conductor system are still subjected to lightning strike damage (Madsen 2006 and Madsen et al. 2006). This is because the answering leaders will not be only emitted from the receptors but will also be emitted from the non-conductive regions other than the receptors. If the emitted answering leaders from those non-conductive regions arrest the lightning stepped leader, appreciable thermal damage can occur due to the direct injection of the lightning arc. One prevalent hypothesis that explains the possible reason for the non-conductive regions on the blade surface to emit answering leaders is illustrated in the schematic diagram (see Fig. 5.6). It can be seen from Fig. 5.6, the large electric field due to the approaching of lightning stepped leader ionizes the molecules on the down conductor. Then, the ionized positive charges flow upward and deposit on the interior surface of the blade, which also induces negative charges on the exterior surface (see Fig. 5.6a). At the same time, the positive charges flow to the surface of the receptors and search for and neutralize those negative charges. The searching path through the electrically non-conductive blade regions can also emit multiple answering leaders (see Fig. 5.6b). If one of them arrests the approaching lightning stepped leader, the lightning arc channel is directly attached to the surface of the non-conductive blade region (see Fig. 5.6c), leading to a significant temperature increase and appreciable thermal damage on the attached spot. Moreover, severe damage, such as puncture through, can develop if the induced electric field strength at the attached spot exceeds the dielectric breakdown strength of the composite wind turbine blade (see Fig. 5.6d) (Madsen et al. 2006).

In general, if the lightning strike-induced electric field strength is lower than the dielectric breakdown strength of the GFRP composite wind turbine blade, the damage is predominately attributed to the direct heat conduction due to the lightning channel attachment on the surface of the structure. In contrast, if the electric field strength exceeds the dielectric breakdown strength of the GFRP composite wind turbine blade, the non-conductive blade becomes instantly conductive in the through-the-thickness direction, and a considerable amount of Joule heating will be produced along the conducting path. Once dielectric breakdown occurs, the Joule heating must be considered in the damage predictive models in addition to the direct heat conduction (i.e., radiative heat exchange between the lightning arc and the wind turbine blade). Therefore, an estimation of dielectric breakdown of the GFRP composite wind turbine blade subjected to a lightning stepped leader is essential and inevitable prior to any predictive lightning strike damage models of the non-conductive GFRP wind turbine blades. Section 5.2 introduces methods to predict the lightning strike-induced electric field strength and, hence, to estimate the dielectric breakdown of the GFRP composite wind turbine blade subjected to a lightning stepped leader.
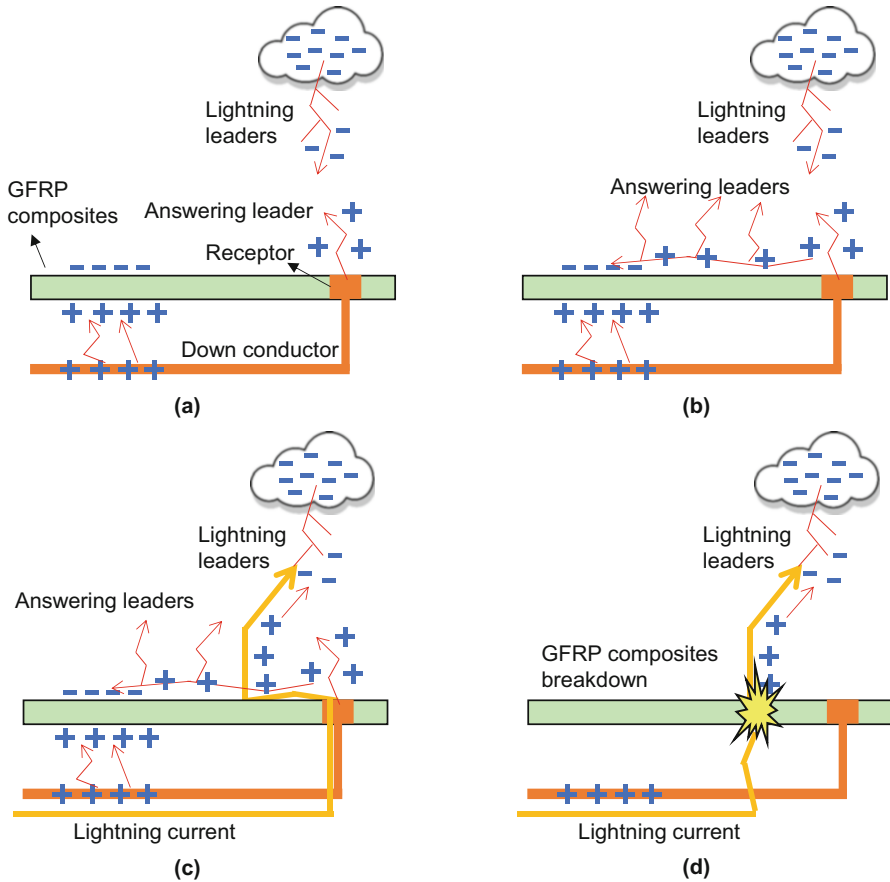
Fig. 5.6 Lightning attachment on a non-conductive surface: (**a**) free positive charges flow upward and deposit on the interior blade surface, inducing negative charges on the exterior blade surface; (**b**) positive charges on the receptor surface search for and neutralize negative charges on the exterior blade surface. Searching path and receptor emit answering leaders; (**c**) one of the answering leader emitted from the searching path captures the lightning stepped leader; (**d**) dielectric breakdown occurs when the electric field exceeds the dielectric breakdown strength of the blade

5.2 Analysis of Lightning Strike-Induced Electric Field at Wind Turbines

5.2.1 Lightning Striking Distance

As described in Sect. 5.1.1, the distance between the tip of the lightning stepped leader (i.e., the weakly luminous leader which propagates from the cloud to the ground) and the ground structure at the particular moment when the answering

Fig. 5.7 Lightning striking distance from stepped leader tip to a ground structure characterized using the rolling sphere method
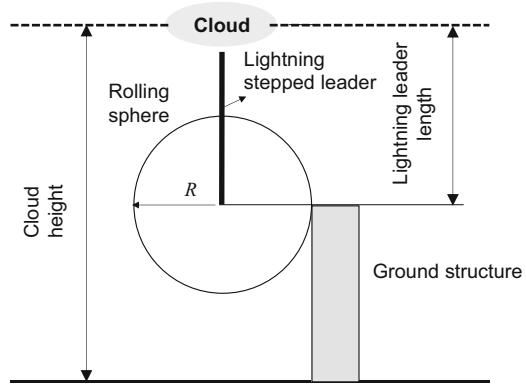
leaders are triggered from the ground structure is called the lightning striking distance. According to the IEC 61400–24 standard (IEC-61400-24 2002), for the wind turbine blades longer than 20 m, the lightning striking distance can be defined using the rolling sphere method, where the radius of the rolling sphere attached to the ground structure can be considered equal to the lightning striking distance (see Fig. 5.7).

The rolling sphere radius is a function of the peak current of the lightning return stroke. A traditional expression to calculate the sphere radius (and, therefore, the lightning striking distance) is given by Uman (2001):

$$R = 10 \cdot I_{\text{peak}}^{0.65}, \tag{5.1}$$

where I_{peak} is the peak current of the lightning return stroke (in kA), and R is the rolling sphere radius (in m).

Recently, Cooray et al. (2007) suggested another expression for the radius of the rolling sphere, which agrees better with the recorded physical measurement data on the lightning striking distances:

$$R = 1.9 \cdot I_{\text{peak}}^{0.90}, \tag{5.2}$$

where the rolling sphere radius R is in m and the unit of peak current I_{peak} is in kA. However, it should be noted that the above equation yields the lightning striking distance to a flat ground and not to an object protruding above the ground. Therefore, Eq. (5.2) may not be appropriate to be used to calculate the lightning striking distance to a wind turbine.

Another widely used equation for calculating the lightning striking distance is proposed by Eriksson (1979):

$$R = 0.6 \cdot I_{\text{peak}}^{1.46}, \tag{5.3}$$

Here, Eq. (5.3) is applicable for calculating the lightning striking distance to a wind turbine (Eriksson 1979).

Table 5.1 Lightning striking distance for the lightning stepped leader

		Lightning striking distance (m)	
LPL	Peak current, I_{peak} (kA)	From Eq. (5.1)	From Eq. (5.3)
I	200	313.09	1372.95
II	150	259.69	902.08
III	100	199.53	499.06

Table 5.1 shows the lightning striking distance calculated using Eqs. (5.1 and 5.3) for three lightning protection levels (LPLs). The LPLs represent three different lightning severity levels as identified by the IEC-61400-24 (2002). The peak current of the initial return strokes (see Fig. 5.1) is 200, 150, and 100 kA for LPL I, LPL II, and LPL III, respectively.

Table 5.1 shows that the lightning striking distances calculated by Eq. (5.3) are around 2.5 to 4 times larger than those calculated by Eq. (5.1). Therefore, using Eq. (5.3) may result in lower predictions of electric field strength at a ground structure, when compared to the predictions using Eq. (5.1).

As a side note, below we discuss the difference between the lightning striking distance and the lightning attractive radius, which are both widely used in the modeling of lightning attachment to structures.

The attractive radius can be calculated as (D'Alessandro and Petrov 2006):

$$R_a = 0.84 \cdot I_{peak}^{0.74} h_a^{0.6}, \tag{5.4}$$

where R_a is the attractive radius (in m), I_{peak} is the peak current (in kA), and h_a is the structure height (in m). There is a significant difference between lightning striking distance, R, as defined by Eqs. (5.1, 5.2 and 5.3), and the lightning attractive radius, R_a, as defined by Eq. (5.4). It can be noticed that the lightning striking distance depends on the charge transfer only, whereas the lightning attractive radius takes into account the size of the structure. Figure 5.8 shows the ratio R/R_a as a function of the structure height h_a for $I_{peak} = 100$ kA. For tall structures (i.e., $h_a > 35$ m), the lightning striking distance is smaller than the lightning attractive radius. Therefore, one needs to be cautious when choosing between the lightning striking distance and the lightning attractive radius for a conservative prediction of the lightning strike-induced electric field, since the results could be quite sensitive to the choice between the two.

5.2.2 Lightning Electric Charge Transfer

5.2.2.1 Charge Transfer of a Lightning Return Stroke

According to Cooray et al. (2007), as the lightning stepped leader approaches the ground, the charge density of the lightning stepped leader is determined by both

Fig. 5.8 Ratio of striking distance to the attractive radius as a function of the structure height ($I_{peak} = 100$ kA)
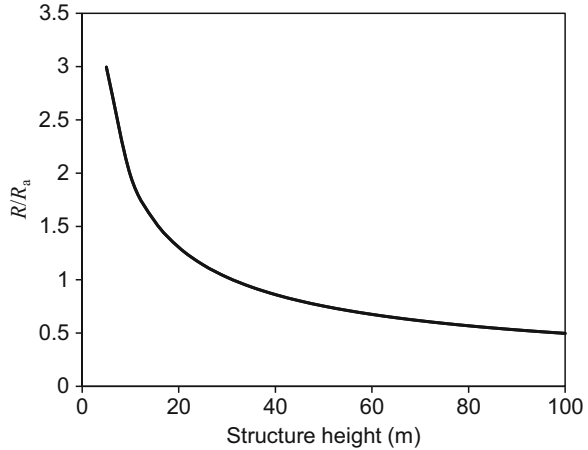
Fig. 5.9 Simplified lightning stepped leader model proposed by Cooray et al. (2007) (**a**) Real stepped leader (**b**) Simplified stepped leader (**c**) Negative charges on the stepped leader (**d**) Positive charges on the return stroke channel induced by the cloud voltage
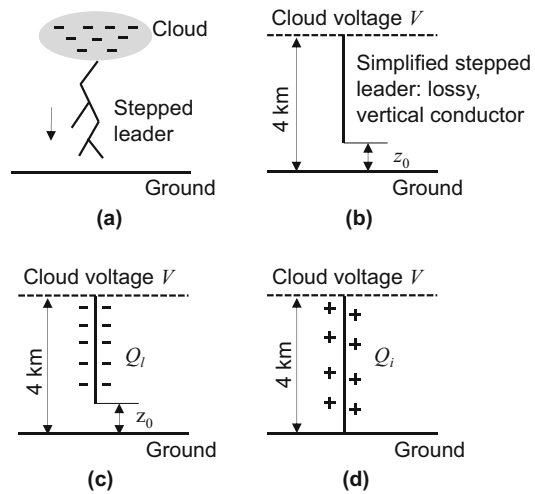
the electric field due to the cloud charge and the electric field enhancement due to the presence of the ground. Figure 5.9 shows a simple lightning stepped leader model: a cloud is represented by a conductive plane at potential V, the ground is represented by a perfect conductor, and the lightning stepped leader is assumed to be a vertical line charge (where, in real situations, branched leaders may develop, and the weakly luminous paths of those leaders often form an inverted tree shape). Figure 5.9a shows a real lightning stepped leader approaching the ground with branched channels; Fig. 5.9b shows an idealized vertical lightning stepped leader; Fig. 5.9c shows a negative charge Q_l along the lightning stepped leader prior to the formation of the return stroke; Fig. 5.9d shows a positive charge Q_i flowing upward along the lightning channel that is induced by the cloud voltage after the initial return stroke is formed. The total positive charge, $Q_{t, 100\mu s}$, entering from the

ground to the fully developed return stroke channel during the first 100 μs equals the sum of the positive charges that neutralize the negative charges Q_l stored along the lightning stepped leader and the positive charges Q_i due to the cloud voltage:

$$Q_{t,100 \ \mu s} = |Q_l| + Q_i = 0.61 \cdot I_{peak}, \tag{5.5}$$

where $Q_{t,100 \mu s}$ is in C, and I_{peak} is the peak current, in kA.

5.2.2.2   Charge Density of a Lightning Stepped Leader

Typically, the charge density of the lightning stepped leader is nonuniform (Becerra 2008; Cooray et al. 2007; Golde 1945, 1977; Lewke et al. 2007). Golde (1945, 1977) assumed that the charge density decreased exponentially along the lightning stepped leader from the tip to the origin of the leader in the cloud:

$$\lambda(\eta) = \lambda_0 e^{-\eta/\xi}, \ 0 \le \eta \le L, \tag{5.6}$$

where λ is the charge density distribution (in C/m) along the leader; λ_0 is the charge density at the leader tip; ξ is the decay height constant, $\xi = 1000$ m; and L is the length of the leader (in m). In addition, $\eta = z\text{-}z_0$ (in m), where z is the vertical distance from the ground ($z = 0$ at the ground) and z_0 is the distance from the ground to the leader tip.

The total charge deposited on the leader is obtained by taking the integral of the charge density Eq. (5.6) over the leader length:

$$Q_l = \int_0^L \lambda(\eta) \, d\eta = \lambda_0 \xi \left[1 - e^{-L/\xi} \right], \tag{5.7}$$

where Q_l is the total charge (in C) (Golde 1945, 1977).

Meanwhile, the relationship between the peak current of the lightning return stroke and the charge density at the leader tip is

$$\lambda_0 = 4.36 \cdot 10^{-5} I_{peak}, \tag{5.8}$$

where I_{peak} is the peak current (in kA).

Using the charge simulation method, Cooray et al. (2007) derived a different nonuniform distribution for the charge density along the lightning stepped leader:

$$\lambda(\eta) = a_0 \cdot \left(1 - \frac{\eta}{H-z_0} \right) \cdot G(z_0) \cdot I_{peak} + \frac{I_{peak} \cdot (a+b \cdot \eta)}{1+c \cdot \eta + d \cdot \eta^2} \cdot F(z_0),$$
$$0 \le \eta \le L, \ z_0 \ge 10, \tag{5.9}$$

where η, in m, is the distance along the leader, $\eta = 0$ is at the leader tip, $\eta = z\text{-}z_0$, $\lambda(\eta)$ is the line charge density (in C/m), H is the height of the cloud (typically

Fig. 5.10 Charge density of the lightning stepped leader for the LPL III (i.e., $I_{peak} = 100$ kA) (when $z_0 = 250$ m)
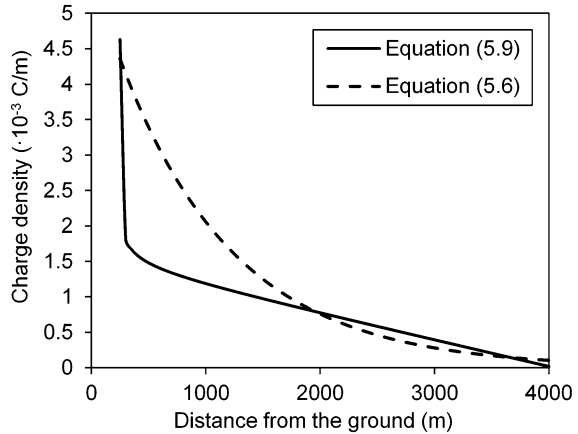
Table 5.2 Total charge entering from the ground to the lightning channel, $Q_{t, 100\ \mu s}$, and the total charge deposited on the lightning stepped leader, Q_l

| LPL | $Q_{t, 100\ \mu s}$ (C) | | Q_l (C) | |
	From IEC-61400-24	From Eq. (5.5)	From Eq. (5.6)	Integral of Eq. (5.9)
I	300	183	8.51493	5.70252
II	225	91.5	6.38619	4.27689
III	150	61	4.25746	2.85126

$H = 4000$ m), z_0 is the distance from the ground to the leader tip (in m), I_{peak} is the peak current of the return stroke (in kA), and $G(z_0) = 1\text{-}(z_0/H)$, $F(z_0) = 0.3\alpha + 0.7\beta$, $\beta = 1\text{-}(z_0/H)$, $a_0 = 1.476 \times 10^{-5}$, $a = 4.857 \times 10^{-5}$, $b = 3.9097 \times 10^{-6}$, $c = 0.522$, and $d = 3.73 \times 10^{-3}$. It is assumed that $z_0 > 10$ m. Cooray et al. (2007) found that the distribution Eq. (5.9) was in a better agreement with the physical measurements than the distribution Eq. (5.6) proposed by Golde (1945, 1977). The total charge deposited on the leader is obtained by numerically taking the integral of the charge density Eq. (5.9) over the length of the leader.

Figure 5.10 shows the charge density as a function of the height z (i.e., distance from the ground). Calculations are performed using Eqs. (5.6 and 5.9) for the LPL III (i.e., $I_{peak} = 100$ kA). The distance from the stepped leader tip to the ground is $z_0 = 250$ m, and the length of the lightning stepped leader is $L = 3750$ m. As one can see, at the leader tip and at the vicinity of the cloud, the charge densities calculated by Eqs. (5.6 and 5.9) are similar, but they are quite different in between. Table 5.2 shows the total charge entering from the ground to the lightning channel, $Q_{t,100\ \mu s}$, within the first 100 μs, calculated using Eq. (5.5) and provided by the IEC 61400–24 standard (IEC-61400-24 2002), and the total charge on the leader, Q_l, in the case of uniform (5.6) and nonuniform (5.9) charge density distributions. As one can see, the total charge is larger if charge density is uniform. However, the charge density near the lightning stepped leader tip (i.e., the distance from the ground is around 250 m, see Fig. 5.10) is larger, if calculated using the charge density distribution (5.9).

5.2.3 Prediction of Lightning Strike-Induced Electric Field in the Vicinity of a Wind Turbine: Analytical and Finite Element Methods

In this section, we present two methods, the analytical and finite element methods (FEM), to predict the static electric field (i.e., the effects of the lightning stepped leader propagation are not considered) in the vicinity of a wind turbine induced by a lightning stepped leader. The first simple method provides a qualitative estimation of the electric field by using an analytical approach, while the second method incorporates the charge density (i.e., Eqs. (5.6 and 5.9)) into a finite element model with COMSOL, which provides more accurate predictions of the electric field.

5.2.3.1 Analytical Model

In this section, we assume the charge density of a lightning stepped leader to be uniform and calculate the induced electric field at the vertically positioned blade (i.e., blade *OA*, see Fig. 5.11). To simplify the problem, here, we make a few more assumptions: (i) the ground (i.e., zero electric potential) is at the infinity, (ii) the electric potential between a cloud and the ground is ignored, and (iii) the effects of the wind turbine receptors and down conductors on the electric fields are disregarded. With these assumptions, the problem of calculating the electric field due to a vertical lightning stepped leader becomes similar to calculations of the electric field due to a charged lines and rods (Tipler and Mosca 2007; Uman 2001).

Fig. 5.11 Electric field calculation at point *p* of the blade *OA* due to a uniformly charged lightning stepped leader
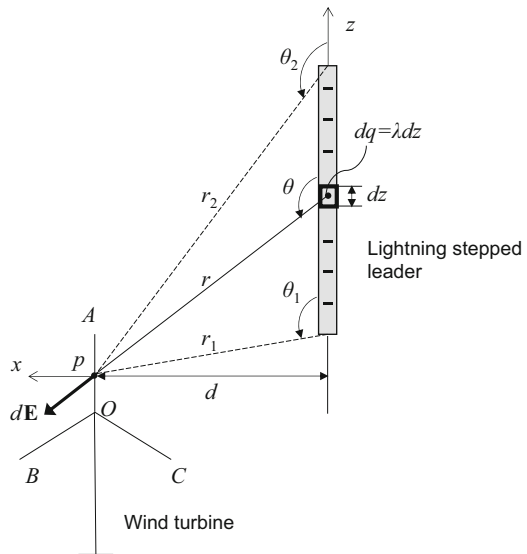
As described in Sect. 5.2.2, the lightning stepped leader is assumed to be a vertical line charge with uniform charge density:

$$\lambda = \frac{Q_l}{L}.$$ (5.10)

where λ is the line charge density (in C/m), Q_l is the total charge (in C) deposited on the lightning stepped leader calculated by taking the integral of the nonuniform charge density Eq. (5.9), and L is the length of the lightning stepped leader (in m). The electric field due to a line charge can be calculated using the Coulomb's law based on the assumption that the field due to an infinitesimal line charge element dq is the same as the field due to a point charge. Therefore, the electric field at an arbitrary point p of the blade OA due to the charge dq within dz can be calculated as:

$$dE = \frac{kdq}{r^2} = \frac{k\lambda dz}{r^2} = \frac{k\lambda d\theta}{d},$$ (5.11)

where r is the distance from the element charge dq to the point p at the blade, $k = 9 \times 10^9$ N·m²·C^{-2} is Coulomb's constant, and $d = r \cdot \sin\theta$ is the lightning striking distance, which is equal to the rolling sphere radius (see discussions in Sect. 5.2.1). The x and z components of the electric field E from all the charge in the leader are

$$E_x = \int_{\theta_1}^{\theta_2} \sin\theta \frac{k\lambda d\theta}{d} = -\frac{k\lambda}{d}(\cos\theta_2 - \cos\theta_1),$$

$$E_z = \int_{\theta_1}^{\theta_2} \cos\theta \frac{k\lambda d\theta}{d} = \frac{k\lambda}{d}(\sin\theta_2 - \sin\theta_1).$$ (5.12)

Finally, the magnitude (i.e., strength) of the electric field at a particular point p along the blade OA due to the lightning stepped leader is

$$|E| = \sqrt{E_x^2 + E_z^2} = \frac{2k\lambda}{d}\sin\frac{\theta_2 - \theta_1}{2}.$$ (5.13)

Here $|E|$ denotes the magnitude of the electric field (in V/m).

5.2.3.2 Finite Element Model

In this section, we present a finite element model to predict the electric field in the vicinity of a wind turbine due to a lightning stepped leader. The finite element analysis (FEA) is performed using the COMSOL Multiphysics®. This finite element model enables us to account for the effects of the nonuniform charge density distribution Eq. (5.9), the effects of the receptors and down conductors, and the finite ground that were not included in the analytical model considered in Sect. 5.2.3.1, which, therefore, provides us more accurate predictions.

Fig. 5.12 Interaction of a
lightning stepped leader and a
wind turbine: problem
formulation
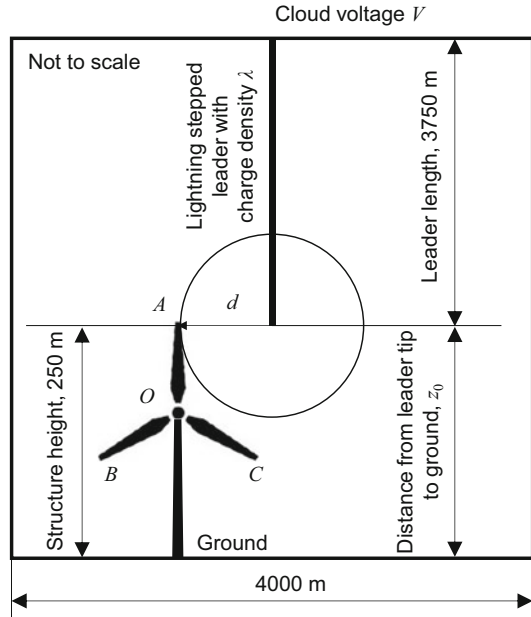
In particular, we consider a horizontal axis wind turbine blade (see Fig. 5.12), the
three blades of which are placed on top of a 150-m wind turbine tower, representing
the Sandia 100-meter all-glass baseline wind turbine blades (SNL 100–00) (Griffith
and Ashwill 2011). The length of each blade is 100 m, the overall structure height
(when one blade is resting at its top vertical position, see Fig. 5.12) is 250 m, and
the distance from the leader tip to the ground is $z_0 = 250$ m. The length of the
lightning stepped leader is 3750 m. The distance from the ground to the cloud is
4000 m. Moreover, a typical 100 m non-conductive wind turbine blade is equipped
with multiple receptors, which are evenly embedded on each side of the blade
surface and are connected to the internal down conductor (e.g., unshielded high-
voltage cables that are installed inside the blade shell extending from the blade
tip to the root buildup, see Fig. 5.5). In this finite element model, the effects of
the receptors and the down conductors are taken into account through applying
ground potential boundary conditions to the surface of the wind turbine blades. In
addition, it is assumed that the lightning stepped leader is a vertical line charge that is
perpendicular to the turbine axis and is located in the same plane with the blades (see
Fig. 5.12). Moreover, since blades are 100-meter long, the rolling sphere method is
used to obtain the lightning strike distance (i.e., d in Fig. 5.12). It is assumed that
the rolling sphere is tangentially attached to the tip of the blade OA. The lightning
striking distance between the leader and blade OA is equal to the rolling sphere
radius Eq. (5.1). Here, the attachment to the tip is chosen because the tip region
of the blade has the highest probability (>98%) to emit answering leaders (Madsen
2006).
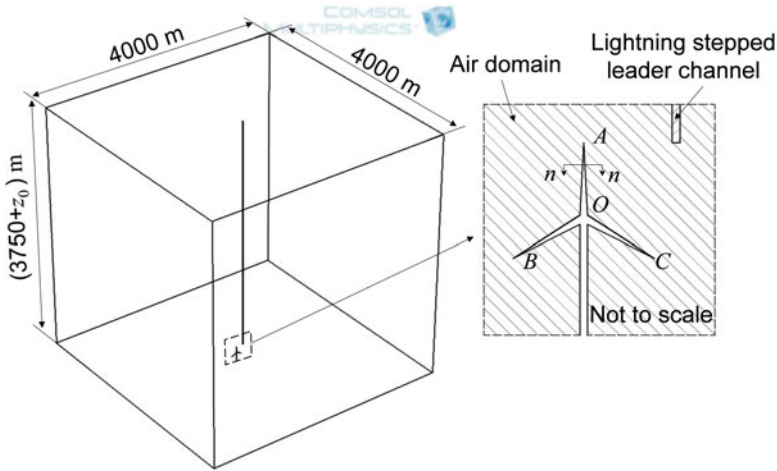
Fig. 5.13 Problem setup in COMSOL

The computational domain is a 3D parallelepiped containing a cutout in the shape of a wind turbine as shown in Fig. 5.13. The dimensions of the cutout are determined by the dimensions of the wind turbine. To simplify the problem, the wind turbine blades are assumed to be beams of square cross section, 2.5 m by 2.5 m. The computational domain represents the air between a cloud and the ground. The length and width of the parallelepiped are 4000 m. The depth is $L + z_0$, where $L = 3750$ m is the length of the lightning stepped leader and $z_0 = 250$ m is the distance from the tip of the leader to the ground. The lightning stepped leader is assumed to be a vertical cylindrical channel of length $L = 3750$ m and radius $R_l = 5$ m. The cylindrical leader channel is placed in the center of the 3D parallelepiped extending from the top surface to the bottom surface (see Fig. 5.13). A volume charge density, $\rho_v = \lambda/\pi R l^2$, where λ is the line charge density Eq. (5.9), is applied to the leader channel. The lightning striking distance, d, as shown in Fig. 5.12, is calculated using the rolling sphere radius Eq. (5.1).

In addition, an electric potential, $V = 40$ MV (Becerra 2008), representing the cloud voltage, is applied to the top surface of the parallelepiped. Ground potential is applied to the bottom surface of the parallelepiped and to the exterior surface of the wind turbine (i.e., hub, nacelle, and the tower) and the surface of the three wind turbine blades (i.e., to account for the effects of multiple receptors and down conductors). Open boundary conditions are assumed at all four vertical sides of the parallelepiped. Moreover, the domain (including the leader) is assigned with an "air material" defined in the COMSOL Material Library. The domain is meshed with 815,112 free tetrahedral elements. The average duration of each simulation is 128 s on a four-core laptop PC.

Next, FEA was performed to predict the electric fields along the wind turbine blades *OA*, *OB*, and *OC* (see Fig. 5.13). FEA results are shown in Table 5.3 and

Table 5.3 The magnitude of the electric field at the wind turbine blade tips and the stepped leader tip (nonuniform charged lightning stepped leader, $z_0 = 250$ m)

Magnitude of the electric field (V/m)			
Blade *OA* tip	Blade *OB* tip	Blade *OC* tip	Lightning stepped leader tip
$1.60 \cdot 10^7$	$5.30 \cdot 10^6$	$6.05 \cdot 10^6$	$2.09 \cdot 10^7$
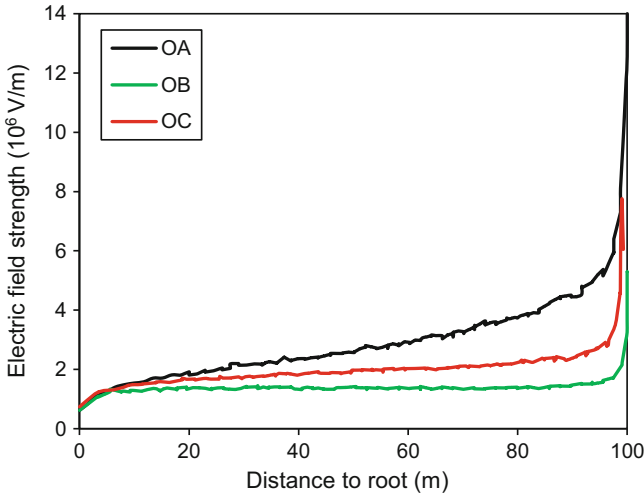
Fig. 5.14 The magnitude of the electric field at blades *OA*, *OB*, *OC*, LPL I

Figs. 5.14 and 5.15. Figure 5.14 shows the electric field strength along the blades *OA*, *OB*, and *OC* at LPL I (i.e., $I_{peak} = 200$ kA). It can be seen that the electric field at blade *OA* is larger than that at blades *OB* and *OC*. However, although the peak current corresponding to LPL I is the highest comparing to the less severe conditions (i.e., LPL II and LPL III), the electric field strength at the tip of blade *OA* could be considerably lower than those obtained under LPL II and LPL III conditions (Wang and Zhupanska 2014). Lastly, Fig. 5.15 shows a contour plot of the electric field strength distribution in the vicinity of the wind turbine.

It is worth emphasizing again that the effect of the dynamic propagation of the lightning stepped leader was not taken into account in the above calculations. In other words, only the static electric field was predicted at the particular moment when the lightning stepped leader arrived within the lightning striking distance. Future simulations are suggested to incorporate the effect of dynamic propagation of the lightning stepped leader for a more accurate prediction of electric field and therefore a more accurate estimation of dielectric breakdown in the composite structures (see discussion in Sect. 5.2.4).
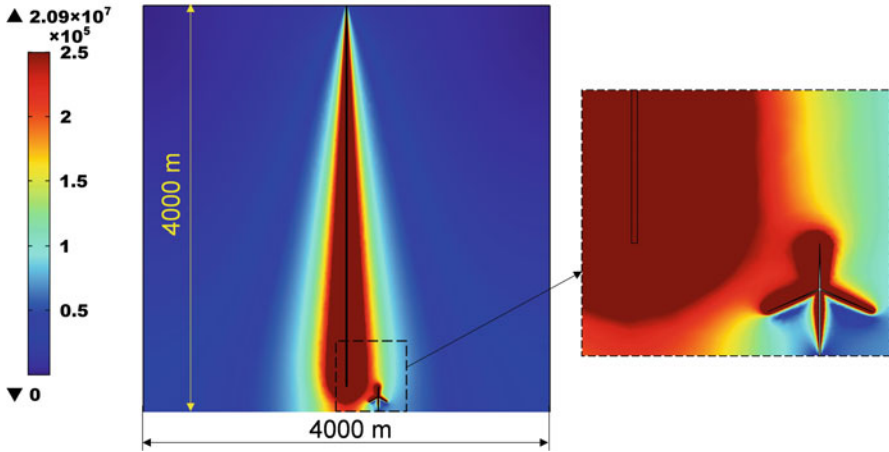
Fig. 5.15 Electric field magnitude distribution in the vicinity of the wind turbine at LPL I

5.2.4 Estimation of Dielectric Breakdown of Non-conductive Composite Wind Turbine Blades

As described in Sect. 5.1.2, severe lightning strikes may cause the dielectric breakdown of the non-conductive composite wind turbine blade, which could lead to punctures through the thickness direction of the blade and even more extensive structural damage. Therefore, it is quite crucial to evaluate the conservativeness of the blade design against the lightning strike-induced dielectric breakdown. A straightforward method for such evaluation is to compare the predicted electric field strength (see Sect. 5.2.3) with the dielectric breakdown strength of the wind turbine blade. If the dielectric breakdown strength of the blade is lower than the predicted electric field strength on the blade induced by the lightning strike, the blade is very likely to experience dielectric breakdown. The previous section (Sect. 5.2.3) describes the methods to predict the electric field strength in the vicinity of the wind turbines due to lightning strikes. In this section, we provide some discussions on the dielectric breakdown strength of composite wind turbine blades.

Experimental investigations (Madsen et al. 2004, 2006) on the dielectric breakdown strength of the glass fiber polymer-matrix (GFRP) composite laminates used on the wind turbine blades revealed that the dielectric breakdown strength is a function of both the thickness and the surface tracking resistance of the composites and is expressed by

$$E_b = a/t + b \cdot TI, \tag{5.14}$$

where E_b is the average dielectric breakdown strength (V/m), a and b are the coefficients, t is the thickness of the composite laminate (m), and TI is the tracking

Fig. 5.16 Dielectric
breakdown strength of the
GFRP composite laminate
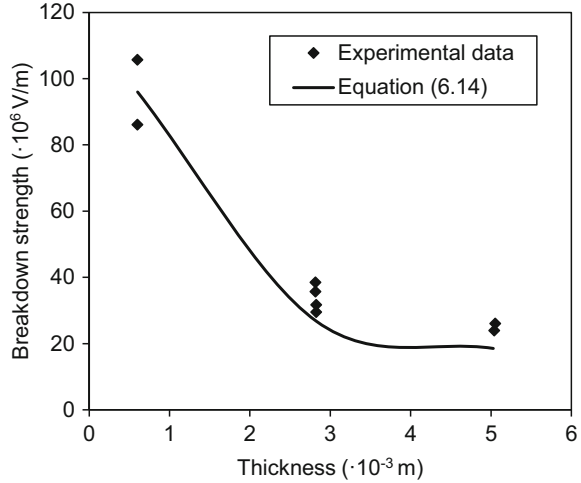
index, which is highly dependent on the fiber orientation, fiber and matrix properties, surface defects, and wide erosions. Generally, the values of the tracking index are stochastic due to uncertainties involved in manufacturing and handling (Madsen 2006; Madsen et al. 2004, 2006). Here, the product of the coefficient b and the tracking index is assumed to be a constant, i.e., $b \cdot TI = 8.0 \cdot 10^6$. The coefficient a is $5.3 \cdot 10^4$. These parameters were chosen by fitting the experimental data reported by (Madsen 2006, Madsen et al. 2004, 2006). Figure 5.16 shows the comparison between the dielectric breakdown strength that is predicted using Eq. (5.14) and the dielectric breakdown strength obtained from experimental tests (Madsen 2006; Madsen et al. 2004, 2006). It should be mentioned that the dielectric breakdown strength of the GFRP composite laminate reported by Madsen (2006), Madsen et al. (2004, 2006) is for laminates with thicknesses within 2~6 mm. However, in practical situations, the laminate thickness of the real blades can reach to ~100 mm. The applicability of Eq. (5.14) to describe the dependence of dielectric breakdown on the thickness may be questioned and needs further investigation.

Meanwhile, according to the ASTM standard (ASTM 1994), the breakdown strength for solid can be expressed by

$$E_b = 4.2/t + 63/\varepsilon_s, \tag{5.15}$$

where ε_s is the permittivity of the solid. From Eq. (5.15), it can be seen that, in cases of large thickness and low permittivity (~4 for GFRP according to (Madsen 2006; Madsen et al. 2004, 2006) specimens, the term containing t becomes relatively insignificant, and the product of permittivity and the breakdown strength are approximately a constant. In other words, the dielectric breakdown strength approximately becomes a constant (~15 MV/m) when the thickness increases. The same can be captured by Eq. (5.14). Therefore, here, we assume that Eq. (5.14) can be extrapolated to describe the thickness dependence on the dielectric breakdown of the wind turbine blade along the entire spanwise, for which the thickness may

Fig. 5.17 Planform of Sandia 100-m baseline blade with laminated designations (Blue, spar cap; orange, trailing edge reinforcement; red, additional shear web) (Griffith and Ashwill 2011)

Fig. 5.18 Sandia 100-meter all-glass baseline wind turbine blade (SNL 100–00) planform
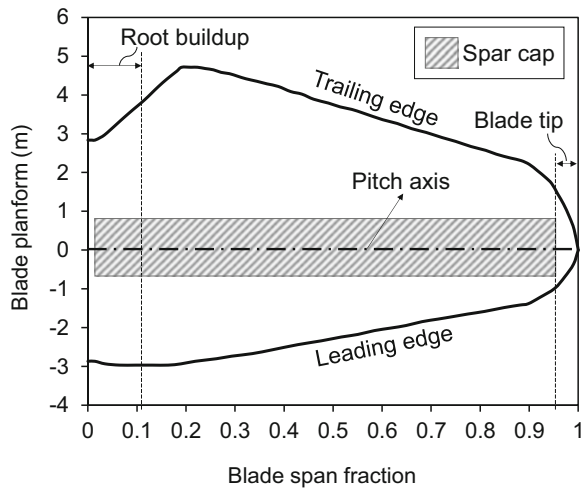
be larger than 6 mm. Note that this extrapolation may not be rigorous due to the lack of experimental data. If more experimental data are available, a more accurate expression to describe the thickness dependence on the dielectric breakdown can be found.

Now we present an example to estimate the dielectric breakdown strength of a wind turbine blade. This particular blade considered here is the Sandia 100-meter all-glass baseline wind turbine blade (SNL 100–00) (Griffith and Ashwill 2011). The planform of the blade is shown in Figs. 5.17 and 5.18.

The root buildup and spar cap of the blade are made of GFRP composites. The other parts of the blade are made of sandwich panels with foam core and GFRP composite facesheets. The experimental data on the dielectric breakdown strength of the sandwich composites are not available, so only the root buildup and spar cap sections are considered. Moreover, the blade is divided into 34 sections along the spanwise direction. Thicknesses of the root buildup and spar cap at various sections along the spanwise direction are shown in Table 5.4. The dielectric breakdown strengths of the root buildup and spar cap along the spanwise direction are calculated using Eq. (5.14) and shown in Fig. 5.19. Then, they are compared to the magnitudes of the predicted electric fields along the blade *OA* obtained using FEA (see Sect. 5.2.3). The ratios of the dielectric breakdown strength to the magnitude of the predicted electric field (referred to "safety factor" hereinafter) are shown in Fig. 5.20. As one can see, the root buildup design is generally conservative against the dielectric breakdown, for which the safety factor is far above 1, whereas

Table 5.4 Composite laminate thickness at various sections of the wind turbine blade (Griffith and Ashwill 2011)

Section number	Blade span fraction	Overall thickness (mm)	
		Root buildup	Spar cap
1	0.000	170	
2	0.005	150	1
3	0.007	130	2
4	0.009	110	3
5	0.011	90	4
6	0.013	80	10
7	0.024	73	13
8	0.026	65	13
9	0.047	50	20
10	0.068	35	30
11	0.089	25	51
12	0.114	15	68
13	0.146		94
14	0.163		111
15	0.179		119
16	0.195		136
17	0.222		136
18	0.249		136
19	0.277		128
20	0.358		119
21	0.439		111
22	0.521		102
23	0.602		85
24	0.667		68
25	0.683		64
26	0.732		47
27	0.765		34
28	0.846		17
29	0.895		9
30	0.944		5
31	0.957		5
32	0.972		5
33	0.986		5
34	1.000		

the tip region is comparatively less conservative, for which the safety factor is only 1.55. This low safety factor 1.55 indicates that the tip of blade *OA* has the highest risk of experiencing dielectric breakdown. Recall that electric fields along blades *OB* and *OC* are generally weaker than those along blade *OA*. Overall, blade *OA* is the most vulnerable one to the dielectric breakdown.

Fig. 5.19 Dielectric
breakdown strength of the
Sandia 100-meter all-glass
baseline wind turbine blade
(SNL 100–00) at both root
buildup region and spar cap
region. Distance at 0 denotes
the blade root and distance at
100 m denotes the blade tip
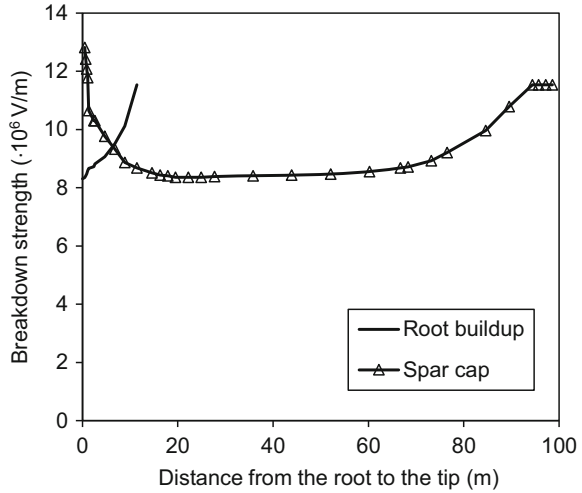
Fig. 5.20 Safety factor (ratio
between estimated dielectric
breakdown strength and
electric field predicted) at
LPL I for wind turbine blade
OA root buildup region and
spar cap region
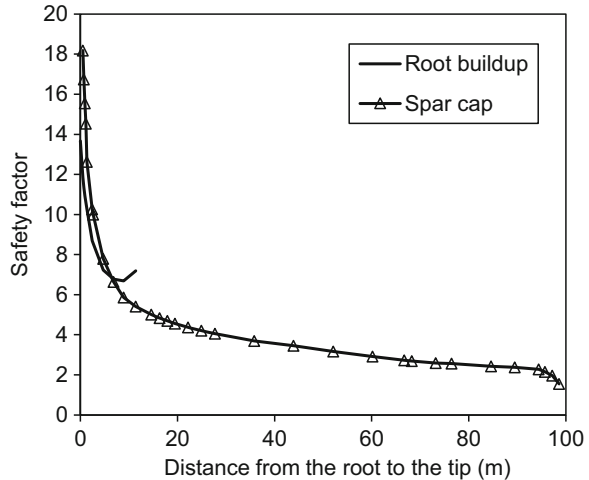
It is worth mentioning that the dielectric breakdown strength of the composite
materials may deteriorate during the service lifetime of wind turbine blades due
to the presence of moisture, defect accumulation, etc. Although experimental data
specific to composite wind turbine blades are not available, laboratory studies of
glass-reinforced composites may be useful to assess the extent of deterioration
in properties. For instance, experimental results reported by Morgan et al. (2009)
indicate that cyanate ester/S2 glass composite retains 90% of its dielectric strength
after 6-month exposure to 99% humidity. Hong et al. (2009) observed that the
breakdown strength of the specimens underwent a 67% reduction when the dry
specimen was immersed in water until their weight was increased by 1.5%.

5.3 Current Predictive Models of Lightning Strike-Induced Thermal and Ablative Damage in Non-conductive Composite Wind Turbine Blades

In the case when the dielectric breakdown does not occur in composite laminated blades, lightning strike attachments will come as a direct heat injection into the surface of the non-conductive blades. The direct heat injection can produce a considerable damage that includes thermal ablation, internal explosion, and delamination.

As a part of damage prediction due to lightning-induced heat injection, a heat transfer problem needs to be solved (Wang and Zhupanska 2015). A heat transfer problem formulation for non-conductive structures (e.g., GFRP composite wind turbine blades) is different from the one for conductive structures (e.g., carbon fiber-reinforced polymer-matrix (CFRP) composite wind turbine blades). For the conductive structures, a heat transfer equation has to be solved simultaneously with electrodynamics equations to determine the distribution of the electric current and associated Joule heat densities. In the following sections, the formulation of such heat transfer problem is provided, along with brief descriptions on the estimation of different structural damage (i.e., delamination and thermal ablation) using the obtained heat distributions.

5.3.1 Heat Transfer Due to Lightning Strike Current

The attachment of the lightning arc onto the surface of the wind turbine blade (i.e., laminated and sandwiched composite structures with possible coatings) produces considerable heat. The heat conduction in the material is governed by the energy balance equation. To account for the electric-thermal coupling effects (if the composite material is electrically conductive, such as the CFRP composites), the energy balance equation is written as (Abdelal and Murphy 2014; Muñoz et al. 2014; Ogasawara et al. 2010; Wang et al. 2014; Wang and Zhupanska 2014, 2016)

$$\rho C_p \left(\frac{\partial T}{\partial t} - \dot{s} \frac{\partial T}{\partial z} \right) = \nabla \cdot (\mathbf{k} \nabla T) + Q_J + Q_L, \qquad (5.16)$$

where ρ, C_p, and $\mathbf{k}$ are, respectively, the instant density, specific heat, and directional thermal conductivity of the composite material, all of which are temperature dependent, $\dot{s}$ is the surface recession rate due to progressive material removal (e.g., rapid vaporization), z is the coordinate normal to the material surface, Q_J is internal Joule heating generation, $Q_J = \mathbf{J} \cdot \mathbf{E}$ (where $\mathbf{J}$ is the lightning current density and $\mathbf{E}$ is the electric field), and Q_L is the energy loss due to the resin decomposition (i.e., liberation of pyrolysis gases).

Meanwhile, the current density is governed by the Ohm's law:

$$\mathbf{J} = \boldsymbol{\sigma} \cdot \mathbf{E}, \tag{5.17}$$

where $\boldsymbol{\sigma}$ is the temperature-dependent electrical conductivity tensor.

The energy loss, Q_L, is mainly due to the liberation of the pyrolysis gases, for which the induced pyrolysis gases percolate through the material to the surface and bring part of the heat away. The energy loss is highly dependent on the density variation of the material during the heating process, the enthalpy of the material, and the enthalpy of the pyrolysis gases. Parameters such as the density variation of the material during the heating process are usually determined using thermogravimetric (TGA) tests. However, such tests are normally conducted under the laboratory conditions for which the heating rates applied to the materials were normally lower than 50 °C/min (Feih and Mouritz 2012; Negarestani et al. 2010; Ogasawara et al. 2002). Such low heating rate cannot represent the lightning strike conditions, since the heating rate under lightning strike conditions can reach $\sim 10^{10}$ °C/min. Many experimental evidences (Feih and Mouritz 2012; Negarestani et al. 2010; Ogasawara et al. 2002) have shown that the mass loss under high heating rate is much lower than that under low heating rate when temperature rises to the same magnitude. Therefore, under lightning strike conditions, it is expected that the mass loss rate is significantly lower than the mass loss rates obtained in those traditional TGA tests. To the author's knowledge, TGA experimental tests under lightning strike conditions have not been reported. The author hereby suggests the experimentalists to develop techniques to enable future TGA tests with the capability of applying extreme high heating rates or to develop alternative experimental tests.

In addition to the difficulties in determining the density variations during the lightning strike heating process, the accurate determination of the material parameters (i.e., directional thermal/electric conductivity, specific heat) from room temperature to the sublimation temperature of the glass/carbon fiber is still quite a challenging task to date.

5.3.2   Thermal Ablation

The ablation mechanism of the fiber-reinforced polymer-matrix composite material (i.e., the material used for wind turbine blades) due to lightning strike is extremely complicated and is still not well understood to date. One should not confuse lightning strike-induced ablation with pulsed laser ablations, although both of them induce rapid heating in the solid materials. The particle composition of lightning arc and the laser beam is quite different (i.e., photons for laser and electrons for lightning arc). Furthermore, materials (e.g., copper, aluminum) are reported to experience phase explosions if subjected to high fluence pulsed laser beam injection (Bulgakova and Bulgakov 2001; Gragossian et al. 2009; Wang et al. 2017). However, phase explosion has never been reported in the literature on lightning strike damage investigations.

The ablation mechanisms of the composite materials are strongly related to the phase transition of the material. For non-conductive GFRP composite materials, the mass loss comes from the decomposition of the resin (300 °C $\sim$ 800 °C) and the rapid vaporization of the melted glass fiber ($\sim$1100 °C) (Dec et al. 2012). For electrically conductive CFRP composites, the ablation mechanism is more complicated. Under elevated temperatures, resin decomposes; meanwhile, carbon atoms in the carbon fibers react with gas species O, C, and H in the air which leads to a rapid mass loss. These reactions include oxidation, nitridation, and sublimation. It appears that the most significant mass loss of CFRP composites is attributed to the sublimation reaction, since the mass loss rates due to oxidation and nitridation reactions are normally much lower. Further experimental investigations are needed to provide more insights into the effects of these reactions on the total mass loss of the composite materials under lightning strike conditions. In addition to these surface-gas reactions, the flow of electric current inside the CFRP composite structure also leads to the generation of internal Joule heating and may lead to additional volumetric mass loss.

5.3.3 Delamination

Delamination is also another commonly reported damage form of the wind turbine blades after lightning strikes. Existing lightning strike experimental studies (Feraboli and Kawakami 2010; Feraboli and Miller 2009; Hirano et al, 2010; Li et al. 2015) examined the damage in the composite material specimens subjected to the artificial pulsed lightning current (components A or D of the standard lightning current waveform (MIL-464-A 1997), see Fig. 5.1) and have identified that delamination (i.e., interlaminar damage) is the most significant damage. Ogasawara et al. (2010) was the first to predict the lightning strike delamination in CFRP composites with a coupled electric-thermal FEA. The material area where the temperature is above the resin decomposition threshold temperature ($\sim$300 °C) was assumed to be the delamination area. However, no actual continuum delamination modeling was accomplished. In addition, the lightning strike-induced shockwave pressure (i.e., acoustic and magnetic), which is the primary cause of delamination, was not taken into account in this model. Muñoz et al. (2014) predicted the stress-induced damage of a CFRP composite panel under the action of the electromagnetic and acoustic pressure. However, continuum delamination was also not captured. Recently, a more sophisticated model was proposed by P. Naghipour et al. (2016), which enabled us to capture the continuum lightning strike delamination using the cohesive zone approach with FEA. In this section, the cohesive zone approach for modeling delamination is briefly reviewed and discussed.

The cohesive zone approach lends itself naturally to the modeling of continuum delamination in laminated composite structures. To use the approach, the laminated composite structure is typically modeled at the ply level, which means the laminate plies are modeled as individual elastic, homogenous transversely isotropic plies, and

the interface of the plies (i.e., resin layers) is modeled with interface elements (i.e., cohesive elements in ABAQUS) with zero thickness.

The damage initiation criterion of the cohesive element used in Naghipour et al. (2016) is the quadratic interfacial traction interaction criterion:

$$\left(\frac{\tau_n}{\tau_n^0(T)}\right)^2 + \left(\frac{\tau_s}{\tau_s^0(T)}\right)^2 + \left(\frac{\tau_t}{\tau_t^0(T)}\right)^2 = 1, \qquad (5.18)$$

where τ is the interfacial traction, τ^0 is the temperature-dependent interfacial elastic traction limits, and subscripts n, s, and t denote the normal direction and two shear directions, respectively. The interfacial traction τ can be calculated using the interfacial constitutive relationship:

$$\tau = \mathbf{D}\delta, \qquad (5.19)$$

where δ is the relative displacement between the upper and bottom nodes of each cohesive element and $\mathbf{D}$ is the interfacial constitutive secant tensor (Naghipour et al. 2011).

At each time increment, the interfacial traction τ is calculated using Eq. (5.19) and is plugged into Eq. (5.18) to check whether damage is initiated. If damage is initiated (δ_m^0 is the relative displacement corresponding to damage initiation in Fig. 5.21), the propagation of the damage follows the Benzeggagh and Kenane (B-K) criterion:

$$G_{IC}(T) + (G_{IIC}(T) - G_{IC}(T))\left(\frac{m^2}{1 + m^2}\right)^\eta = G_C(T), \qquad (5.20)$$

where $G_{IC}(T)$ and $G_{IIC}(T)$ are the temperature-dependent fracture toughness values for mode I and mode II, respectively; m is the mode mixty (Naghipour et al. 2011); and η is a parameter related to the shape of the failure locus in the mixed mode plane.

Fig. 5.21 Schematic of mixed mode traction separation law for cohesive elements
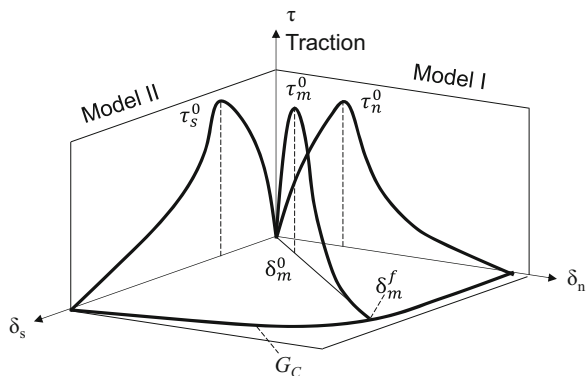
   The implementation of the cohesive zone approach can be achieved in commercial FEA software, such as ABAQUS using the build-in cohesive elements. The parameters of the damage initiation Eq. (5.18) and propagation Eq. (5.20) criterions of the cohesive elements can be defined in the ABAQUS input file. Meanwhile, ABAQUS allows the cohesive elements to be progressively deleted when the final separation point (δ_m^f in Fig. 5.21) is reached; as such, the continuum delamination of the laminated composite structure can be captured.

5.4 Conclusions and Future Recommendations

5.4.1 Conclusions

In this chapter, the basic physics of lightning strike and the interaction between the lightning strike and the wind turbine are discussed. The key mechanisms of the lightning strike damage on the wind turbine blades and the commonly used lightning strike protections are introduced. In addition, the mechanisms of lightning current conduction through the non-conductive GFRP composite wind turbine blade are discussed. Furthermore, the analytical and finite element methods of predicting the lightning strike-induced electric field in the vicinity of a wind turbine are demonstrated. The predicted electric fields are used to compare with the dielectric breakdown strength of the GFRP composite wind turbine blade to estimate the conservativeness of the blade design against lightning strike dielectric breakdown. Moreover, other forms of lightning damage for wind turbine blades are introduced including the thermal ablation and delamination. The corresponding damage mechanisms and their mathematical formulations have been presented.

5.4.2 Future Recommendations

For future study on the lightning strike analysis of wind turbines, there is a need to incorporate the effects of dynamic propagation of the lightning stepped leader into the analysis of the lightning strike-induced electric fields, such that a more accurate estimation of dielectric breakdown in the composite wind turbine blades can be achieved. In addition, there is a need to develop improved lightning thermal and damage models that include the accurate determination of the temperature-dependent thermophysical properties and the mass loss rate of the composite materials under lightning strike conditions, as well as the proper treatment for material phase transitions during the numerical implementation. Furthermore, it should be mentioned that the current lightning damage models in the literature

restrict their analyses to a single type of lightning damage. However, in practical situations, the three lightning damage mechanisms (i.e., ablation, delamination, and dielectric breakdown) may occur at the same time. Hence, the challenge for future research is to develop a fully coupled damage model that concurrently performs all of the three lightning damage analyses.

References

Abdelal G, Murphy A (2014) Nonlinear numerical modelling of lightning strike effect on composite panels with temperature dependent material properties. Compos Struct 109:268–278. Elsevier

ASTM (1994) Standard test method for dielectric breakdown voltage and dielectric strength of solid electrical insulating materials at commercial power frequencies. Retrieved from Technical Report, West Conshohocken

Becerra M (2008) On the attachment of lightning flashes to grounded structures. PhD, Acta Universitatis Upsaliensis

Bulgakova NM, Bulgakov AV (2001) Pulsed laser ablation of solids: transition from normal vaporization to phase explosion. Appl Phys A Mater Sci Process 73(2):199–208

Chemartin L, Lalande P, Peyrou B, Chazottes A, Elias PQ, Delalondre C, Cheron BG, Lago F (2012) Direct effects of lightning on aircraft structure: analysis of the thermal, electrical and mechanical constraints. AerospaceLab 5:1

Cooray V, Rakov V, Theethayi N (2007) The lightning striking distance—revisited. J Electrost 65(5):296–306

D'Alessandro F, Petrov NI (2006) Field study on the interception efficiency of lightning protection systems and comparison with models. In: Proceedings of the Royal Society of London A: Mathematical, Physical and Engineering Sciences. The Royal Society 462(2069): 1365–1386

Dec JA, Braun RD, Lamb B (2012) Ablative thermal response analysis using the finite element method. J Thermophys Heat Transf 26:201–212

Eriksson AJ (1979) The lightning ground flash: an engineering study. PhD, University of KwaZulu-Natal, Durban

Feih S, Mouritz AP (2012) Tensile properties of carbon Fibres and carbon fibre–polymer composites in fire. Compos A: Appl Sci Manuf 43:765–772. Elsevier

Feraboli P, Kawakami H (2010) Damage of carbon/epoxy composite plates subjected to mechanical impact and simulated lightning. J Aircr 47:999–1012

Feraboli P, Miller M (2009) Damage resistance and tolerance of carbon/epoxy composite coupons subjected to simulated lightning strike. Compos A: Appl Sci Manuf 40:954–967. Elsevier

Golde RH (1945) The frequency of occurrence and the distribution of lightning flashes to transmission lines. Electr Eng 64(12):902–910

Golde RH (1977) Lightning. Academic Press, London

Gragossian A, Tavassoli SH, Shokri B (2009) Laser ablation of aluminum from normal evaporation to phase explosion. J Appl Phys 105(10):103304

Griffith DT, Ashwill TD (2011) The Sandia 100-meter all-glass baseline wind turbine blade: SNL100–00. Sandia National Laboratories, Albuquerque. SAND2011–3779

Hirano Y, Katsumata S, Iwahori Y, Todoroki A (2010) Artificial lightning testing on graphite/epoxy composite laminate. Compos A: Appl Sci Manuf 41:1461–1470. Elsevier

Hong TP, Lesaint O, Gonon P (2009) Water absorption in a glass-mica-epoxy composite-[I: influence on electrical properties]. Dielectr Electr Insul IEEE Trans 16(1):1–10

IEC-61400-24 (2002) Wind turbine generator systems–part 24: lightning protection. International Electrotechnical Commission, Geneva

Inoue K, Korematsu Y, Nakamura N, Matsushita T, Murata N, Kuroiwa T, Shibata M, Ueda Y, Arinaga S, Suguro Y (2004) Study on damage-mechanism of wind turbine blades by lightning strike. Paper presented at the international conference on lightning protection, Avignon

Lewke B, Hernández YM, Kindersberger J (2007) A simulation method for the wind turbine's electric field distribution caused by the stepped lightning leader. Paper presented at the European wind energy conference, 9 May

Li Y, Li R, Lu L, Huang X (2015) Experimental study of damage characteristics of carbon woven fabric/epoxy laminates subjected to lightning strike. Compos A: Appl Sci Manuf 79:164–175. Elsevier

Madsen SF (2006) Interaction between electrical discharges and materials for wind turbine blades-particularly related to lightning protection. PhD, Technical University of Denmark

Madsen SF, Holbøll J, Henriksen M, Larsen FM, Hansen LB, Bertelsen K (2004) Breakdown tests of glass fibre reinforced polymers (GFRP) as part of improved lightning protection of wind turbine blades. Paper presented at the IEEE international symposium on electrical insulation, Indianapolis, 19–22 September

Madsen SF, Holboll J, Henriksen M (2006) Direct relationship between breakdown strength and tracking index of composites. Paper presented at the IEEE international symposium on electrical insulation, Toronto, 11–14 June

MIL-464-A (1997) Electromagnetic environmental effects requirements for systems. US Department of Defense, Washington, DC

Morgan B, Madhukar M, Walsh J, Hooker M, Grandlienard S (2009) Moisture degradation of cyanate ester/S2 glass composite insulation systems. J Compos Mater 44:821–837

Muñoz R, Delgado S, González C, López-Romano B, Wang D-Y, Llorca J (2014) Modeling lightning impact thermo-mechanical damage on composite materials. Appl Compos Mater 21:149–164. Springer Netherlands

Naghipour P, Bartsch M, Voggenreiter H (2011) Simulation and experimental validation of mixed mode delamination in multidirectional CF/PEEK laminates under fatigue loading. Int J Solids Struct 48(6):1070–1081

Naghipour P, Pineda EJ, Arnold SM (2016) Simulation of lightning-induced delamination in unprotected CFRP laminates. Applied Composite Materials 23(4):523–535

Negarestani R, Li L, Sezer HK, Whitehead D, Methven J (2010) Nano-second pulsed DPSS Nd: YAG laser cutting of CFRP composites with mixed reactive and inert gases. Int J Adv Manuf Technol 49:553–566. Springer

Oard M (2015) The new weather book. New Leaf Publishing Group, Incorporated, Green Forest

Ogasawara T, Ishikawa T, Yamada T, Yokota R, Itoh M, Nogi S (2002) Thermal response and ablation characteristics of carbon Fiber reinforced composite with novel silicon containing polymer MSP. J Compos Mater 36:143–157. Sage Publications

Ogasawara T, Hirano Y, Yoshimura A (2010) Coupled thermal–electrical analysis for carbon Fiber/epoxy composites exposed to simulated lightning current. Compos A: Appl Sci Manuf 41:973–981. Elsevier

Rupke E (2002) Lightning direct effects handbook. Lightning Technologies Inc. Report No. AGATE-WP3, 1-031027. Retrieved from: http://www.niar.wichita.edu/agate/Documents/Lightning/WP3.1-031027-043.pdf

Tipler PA, Mosca G (2007) Physics for scientists and engineers. Macmillan, New York

Uman MA (2001) The Lightning Discharge, 2nd edn. Dover Publications Inc., New York

Wang Y, Hu W (2017) Investigation of the effects of receptors on the lightning strike protection of wind turbine blades. IEEE Trans Electromagn Compat 59(4):1180–1187

Wang Y, Zhupanska OI (2014) Evaluation of the thermal damage in glass fiber polymer-matrix composites in wind turbine blades subjected to lightning strike. Paper presented at the American Society for Composites 29th annual technical conference, San Diego, 8–10 September

Wang Y, Zhupanska OI (2015) Lightning strike thermal damage model for glass Fiber reinforced polymer matrix composites and its application to wind turbine blades. Compos Struct 132:1182–1191. Elsevier

Wang Y, Zhupanska OI (2016) Thermal ablation in fiber-reinforced composite laminates subjected to continuing lightning current. Paper presented at the 57th AIAA/ASCE/AHS/ASC structures, structural dynamics, and materials conference, San Diego

Wang FS, Ding N, Liu ZQ, Ji YY, Yue ZF (2014) Ablation damage characteristic and residual strength prediction of carbon Fiber/epoxy composite suffered from lightning strike. Compos Struct 117:222–233. Elsevier

Wang Y, Shen N, Befekadu GK, Pasiliao CL (2017) Modeling pulsed laser ablation of aluminum with finite element analysis considering material moving front. Int J Heat Mass Transf 113:1246–1253

Chapter 6
Advanced Wind Turbine Dynamics

Qi Wang

6.1 Efficient High-Fidelity Modeling of Wind Turbine Blade

Beam models are widely used to represent and analyze engineering structures that have one dimension that is much larger than the other two. Many engineering components can be idealized as beams: structural members of buildings and bridges in civil engineering, joists and lever arms in heavy-machine industries, and helicopter rotor blades. The blades, tower, and shaft in a wind turbine system can be analyzed as beams. In the weight-critical applications of beam structures, like high-aspect-ratio wings in aerospace and wind energy applications, composite materials are attractive due to their superior strength-to-weight and stiffness-to-weight ratios. However, analysis of composite-material structures is more difficult than their isotropic counterparts due to elastic coupling effects. Furthermore, wind turbine blades are further complicated by their high flexibility and initial twist/curvatures, which must be treated in the underlying analysis. The geometrically exact beam theory (GEBT) first proposed by Reissner (1973) is a method that has proven powerful for analysis of highly flexible composite beams in the helicopter engineering community. During the past several decades, much effort has been invested in GEBT. Simo (1985) and Simo and Vu-Quoc (1986) extended Reissner's work to deal with 3-D dynamic problems. Jelenić and Crisfield (1999) implemented GEBT using the finite-element method in which a new approach for interpolating the rotation field was proposed that preserves the geometric exactness. Betsch and Steinmann (2002) circumvented the interpolation of rotation by introducing

Q. Wang (✉)
Siemens Wind Energy Inc, Boulder, CO, USA
e-mail: qi.wang2@siemens.com

© Springer International Publishing AG, part of Springer Nature 2018
W. Hu (ed.), *Advanced Wind Turbine Technology*,
https://doi.org/10.1007/978-3-319-78166-2_6

a re-parameterization of the weak form corresponding to the equations of motion of GEBT. Ibrahimbegović (1995) implemented GEBT for static analysis, and Ibrahimbegović and Mikdad (1998) implemented GEBT for dynamic analysis. In contrast to the displacement-based implementations, Hodges (1990) proposed a discretization of the GEBT model with mixed finite elements in which both the primary and dual fields are independently interpolated (Cook et al. 2001). In the mixed formulation, all of the necessary ingredients, including Hamilton's principle and kinematic equations, are combined in a single variational formulation statement. Lagrange multipliers, motion variables, generalized strains, forces and moments, linear and angular momenta, and displacement and rotation variables are considered as independent quantities. Yu and Blair (2012) and Wang et al. (2013) recently presented the implementation of GEBT in a mixed formulation in which various rotation parameters were investigated.

6.2 Geometrically Exact Beam Theory

Figure 6.1 Hodges (1990, 2006) shows a beam in its undeformed and deformed states. A reference frame $\mathbf{b}_i$ is introduced along the beam axis for the undeformed state; a frame $\mathbf{B}_i$ is introduced along each point of the deformed beam axis. Curvilinear coordinate x_1 defines the intrinsic parameterization of the reference line. In this section, we use matrix notation to denote vectorial or vectorial-like
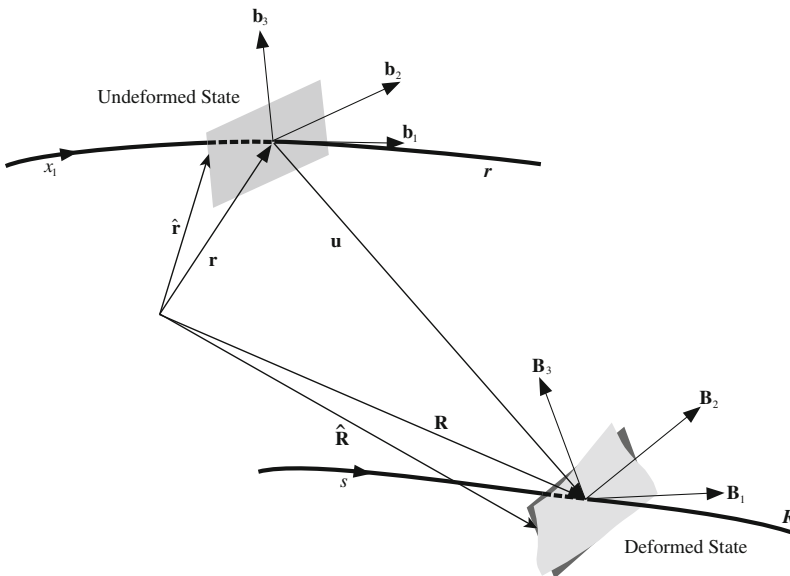
Fig. 6.1 Schematic of the beam in undeformed and deformed states with associated variables

quantities. For example, we use an underline to denote a vector, e.g., $\underline{u}$, a bar to denote unit vector, e.g., $\bar{n}$, and double underline to denote a tensor, e.g., $\underline{\underline{\Delta}}$. Note that sometimes the underlines only denote the dimension of the corresponding matrix. The governing equations of motion for geometric exact beam theory can be written as (Bauchau 2010)

$$\dot{\underline{h}} - \underline{F}' = \underline{f} \tag{6.1}$$

$$\dot{\underline{g}} + \dot{\tilde{u}}\underline{h} - \underline{M}' - (\tilde{x}_0' + \tilde{u}')\underline{F} = \underline{m} \tag{6.2}$$

where $\underline{h}$ and $\underline{g}$ are the linear and angular momenta resolved in the inertial coordinate system, respectively, $\underline{F}$ and $\underline{M}$ are the beam's sectional forces and moments, respectively, $\underline{u}$ is the one-dimensional displacement of the reference line, $\underline{x}_0$ is the initial position vector of a point along the beam's reference line, and $\underline{f}$ and $\underline{m}$ are the distributed force and moment applied to the beam structure, respectively. Notation $(\cdot)'$ indicates a derivative with respect to the beam axis x_1, and $(\dot{\cdot})$ indicates a derivative with respect to time. The tilde operator $(\tilde{\cdot})$ defines a second-order, skew-symmetric tensor corresponding to the given vector. In the literature, it is also termed as "cross-product matrix." For example,

$$\tilde{n} = \begin{bmatrix} 0 & -n_3 & n_2 \\ n_3 & 0 & -n_1 \\ -n_2 & n_1 & 0 \end{bmatrix} \tag{6.3}$$

The constitutive equations relate the velocities to the momenta and the one-dimensional strain measures to the sectional resultants as

$$\left\{ \begin{array}{c} \underline{h} \\ \underline{g} \end{array} \right\} = \underline{\underline{\mathcal{M}}} \left\{ \begin{array}{c} \dot{\underline{u}} \\ \underline{\omega} \end{array} \right\} \tag{6.4}$$

$$\left\{ \begin{array}{c} \underline{F} \\ \underline{M} \end{array} \right\} = \underline{\underline{\mathcal{C}}} \left\{ \begin{array}{c} \underline{\epsilon} \\ \underline{\kappa} \end{array} \right\} \tag{6.5}$$

where $\underline{\underline{\mathcal{M}}}$ and $\underline{\underline{\mathcal{C}}}$ are the 6×6 sectional mass and stiffness matrices, respectively (note that they are not tensors), and $\underline{\epsilon}$ and $\underline{\kappa}$ are the one-dimensional strains and curvatures, respectively. $\underline{\omega}$ is the angular velocity vector that is defined by the rotation tensor $\underline{R}$ as $\underline{\omega} = \text{axial}(\dot{\underline{R}} \, \underline{R})$. For a displacement-based finite-element implementation, there are six degrees of freedom at each node: three displacement components and three rotation components. Here we use $\underline{q}$ to denote the elemental displacement array as $\underline{q} = \begin{bmatrix} \underline{u}^T & \underline{p}^T \end{bmatrix}$, where $\underline{u}$ is the one-dimensional displacement and $\underline{p}$ is the rotation parameter vector. The acceleration array can thus be defined as $\underline{a} = \begin{bmatrix} \ddot{\underline{u}}^T & \dot{\underline{\omega}}^T \end{bmatrix}$. For nonlinear finite-element analysis, the discretized and incremental forms of displacement, velocity, and acceleration are written as

$$\underline{q}(x_1) = \underline{\underline{N}}\,\hat{\underline{q}} \quad \Delta\underline{q}^T = \begin{bmatrix} \Delta\underline{u}^T & \Delta\underline{p}^T \end{bmatrix} \tag{6.6}$$

$$\underline{v}(x_1) = \underline{\underline{N}}\,\hat{\underline{v}} \quad \Delta\underline{v}^T = \begin{bmatrix} \Delta\dot{\underline{u}}^T & \Delta\underline{\omega}^T \end{bmatrix} \tag{6.7}$$

$$\underline{a}(x_1) = \underline{\underline{N}}\,\hat{\underline{a}} \quad \Delta\underline{a}^T = \begin{bmatrix} \Delta\ddot{\underline{u}}^T & \Delta\dot{\underline{\omega}}^T \end{bmatrix} \tag{6.8}$$

where $\underline{\underline{N}}$ is the shape function matrix and $(\hat{\cdot})$ denotes a column matrix of nodal values. The governing equations for beams are highly nonlinear so that a linearization process is needed. According to Bauchau (2010), the linearized governing equations in Eqs. (6.1) and (6.2) are in the form of

$$\hat{\underline{\underline{M}}}\Delta\hat{\underline{a}} + \hat{\underline{\underline{G}}}\Delta\hat{\underline{v}} + \hat{\underline{\underline{K}}}\Delta\hat{\underline{q}} = \hat{\underline{F}}^{ext} - \hat{\underline{F}} \tag{6.9}$$

where $\hat{\underline{\underline{M}}}$, $\hat{\underline{\underline{G}}}$, and $\hat{\underline{\underline{K}}}$ are the elemental mass, gyroscopic, and stiffness matrices, respectively, and $\hat{\underline{F}}$ and $\hat{\underline{F}}^{ext}$ are the elemental forces and externally applied loads, respectively. They are defined as follows

$$\hat{\underline{\underline{M}}} = \int_0^l \underline{\underline{N}}^T\,\underline{\underline{\mathcal{M}}}\,\underline{\underline{N}}dx_1 \tag{6.10}$$

$$\hat{\underline{\underline{G}}} = \int_0^l \underline{\underline{N}}^T\,\underline{\underline{\mathcal{G}}}^I\,\underline{\underline{N}}dx_1 \tag{6.11}$$

$$\hat{\underline{\underline{K}}} = \int_0^l \left[\underline{\underline{N}}^T(\underline{\underline{\mathcal{K}}}^I + \underline{\underline{\mathcal{Q}}})\,\underline{\underline{N}} + \underline{\underline{N}}^T\,\underline{\underline{\mathcal{P}}}\,\underline{\underline{N}}' + \underline{\underline{N}}'^T\,\underline{\underline{\mathcal{C}}}\,\underline{\underline{N}}' + \underline{\underline{N}}'^T\,\underline{\underline{\mathcal{O}}}\,\underline{\underline{N}} \right] dx_1 \tag{6.12}$$

$$\hat{\underline{F}} = \int_0^l (\underline{\underline{N}}^T\,\underline{\mathcal{F}}^I + \underline{\underline{N}}^T\,\underline{\mathcal{F}}^D + \underline{\underline{N}}'^T\,\underline{\mathcal{F}}^C)dx_1 \tag{6.13}$$

$$\hat{\underline{F}}^{ext} = \int_0^l \underline{\underline{N}}^T\,\underline{\mathcal{F}}^{ext}dx_1 \tag{6.14}$$

The new matrix notations in Eqs. (6.10), (6.11), (6.12), (6.13), and (6.14) are briefly introduced here. $\underline{\underline{\mathcal{M}}}$ is the sectional mass matrix resolved in inertial system, $\underline{\mathcal{F}}^C$ and $\underline{\mathcal{F}}^D$ are elastic forces obtained from Eqs. (6.1), and (6.2) as

$$\underline{\mathcal{F}}^C = \left\{ \begin{array}{c} \underline{F} \\ \underline{M} \end{array} \right\} = \underline{\underline{\mathcal{C}}} \left\{ \begin{array}{c} \underline{\epsilon} \\ \underline{\kappa} \end{array} \right\} \tag{6.15}$$

$$\underline{\mathcal{F}}^D = \begin{bmatrix} \underline{\underline{0}} & \underline{\underline{0}} \\ (\tilde{x}_0' + \tilde{u}')^T & \underline{\underline{0}} \end{bmatrix} \underline{\mathcal{F}}^C \equiv \underline{\underline{\Upsilon}}\,\underline{\mathcal{F}}^C \tag{6.16}$$

where $\underline{\underline{0}}$ denotes a 3×3 null matrix. $\underline{\underline{\mathcal{G}}}^I$, $\underline{\underline{\mathcal{K}}}^I$, $\underline{\underline{\mathcal{O}}}$, $\underline{\underline{\mathcal{P}}}$, $\underline{\underline{\mathcal{Q}}}$, and $\underline{\mathcal{F}}^I$ in Eqs. (6.11), (6.12), and (6.13) are defined as

$$\underline{\underline{\mathscr{G}^I}} = \begin{bmatrix} \underline{\underline{0}} & (\tilde{\omega}m\eta)^T + \tilde{\omega}m\tilde{\eta}^T \\ \underline{\underline{0}} & \tilde{\omega}\underline{\underline{\varrho}} - \underline{\underline{\varrho}}\tilde{\omega} \end{bmatrix} \tag{6.17}$$

$$\underline{\underline{\mathscr{K}^I}} = \begin{bmatrix} \underline{\underline{0}} & \dot{\tilde{\omega}}m\tilde{\eta}^T + \tilde{\omega}\tilde{\omega}m\tilde{\eta}^T \\ \underline{\underline{0}} & \ddot{\underline{u}}m\tilde{\eta} + \underline{\underline{\varrho}}\dot{\tilde{\omega}} - \underline{\underline{\varrho}}\dot{\tilde{\omega}} + \tilde{\omega}\underline{\underline{\varrho}}\tilde{\omega} - \tilde{\omega}\underline{\underline{\varrho}}\tilde{\omega} \end{bmatrix} \tag{6.18}$$

$$\underline{\underline{\mathscr{O}}} = \begin{bmatrix} \underline{\underline{0}} & \underline{\underline{C}}_{11}\tilde{E}_1 - \tilde{F} \\ \underline{\underline{0}} & \underline{\underline{C}}_{21}\tilde{E}_1 - \tilde{M} \end{bmatrix} \tag{6.19}$$

$$\underline{\underline{\mathscr{P}}} = \begin{bmatrix} \underline{\underline{0}} & \underline{\underline{0}} \\ \tilde{F} + (\underline{\underline{C}}_{11}\tilde{E}_1)^T & (\underline{\underline{C}}_{21}\tilde{E}_1)^T \end{bmatrix} \tag{6.20}$$

$$\underline{\underline{\mathscr{Q}}} = \underline{\underline{\Upsilon}}\,\underline{\underline{\mathscr{O}}} \tag{6.21}$$

$$\underline{\mathscr{F}^I} = \begin{Bmatrix} m\ddot{\underline{u}} + (\dot{\tilde{\omega}} + \tilde{\omega}\tilde{\omega})m\eta \\ m\tilde{\eta}\ddot{\underline{u}} + \underline{\underline{\varrho}}\dot{\underline{\omega}} + \tilde{\omega}\underline{\underline{\varrho}}\underline{\omega} \end{Bmatrix} \tag{6.22}$$

where m is the mass density per unit length, η is the location of the sectional center of mass, $\underline{\underline{\varrho}}$ is the moment of inertia tensor per unit length, and the following notations were introduced to simplify the writing of the above expressions:

$$\underline{E}_1 = \underline{x}'_0 + \underline{u}' \tag{6.23}$$

$$\underline{\underline{\mathscr{C}}} = \begin{bmatrix} \underline{\underline{C}}_{11} & \underline{\underline{C}}_{12} \\ \underline{\underline{C}}_{21} & \underline{\underline{C}}_{22} \end{bmatrix} \tag{6.24}$$

A viscous damping term is also implemented to account for the structural damping. The damping force is defined as

$$\underline{f}_d = \underline{\underline{\mu}}\,\underline{\underline{\mathscr{C}}} \begin{Bmatrix} \dot{\epsilon} \\ \dot{\kappa} \end{Bmatrix} \tag{6.25}$$

where $\underline{\underline{\mu}}$ is a user-provided damping-coefficient diagonal matrix. The damping force can be recast in two separate parts, like $\underline{\mathscr{F}^C}$ and $\underline{\mathscr{F}^D}$ in the elastic force, as

$$\underline{\mathscr{F}_d^C} = \begin{Bmatrix} \underline{F}_d \\ \underline{M}_d \end{Bmatrix} \tag{6.26}$$

$$\underline{\mathscr{F}_d^D} = \begin{Bmatrix} \underline{0} \\ (\tilde{x}'_0 + \tilde{u}')^T\underline{F}_d \end{Bmatrix} \tag{6.27}$$

More details on the derivation and linearization of governing equations of geometrically exact beam theory can be found in Bauchau (2010).

6.3 Numerical Implementation

6.3.1 Wiener-Milenković Rotation Parameters

The 3-D rotations in BeamDyn are represented as Wiener-Milenković parameters (Wang et al. 2013; Bauchau et al. 2008), which are defined as

$$\underline{p} = 4\tan\left(\frac{\phi}{4}\right)\bar{n} \tag{6.28}$$

where ϕ is the rotation angle and $\bar{n}$ is the unit vector of the rotation axis. It can be observed that the valid range for this parameter is $|\phi| < 2\pi$. The singularities existing at integer multiples of $\pm 2\pi$ can be removed by a rescaling operation at π, as given in Bauchau et al. (2008):

$$\underline{r} = \begin{cases} 4(q_0\underline{p} + p_0\underline{q} + \tilde{p}\underline{q})/(\Delta_1 + \Delta_2), & \text{if}\,\Delta_2 \geq 0 \\ -4(q_0\underline{p} + p_0\underline{q} + \tilde{p}\underline{q})/(\Delta_1 - \Delta_2), & \text{if}\,\Delta_2 < 0 \end{cases} \tag{6.29}$$

where $\underline{p}$, $\underline{q}$, and $\underline{r}$ are the vectorial parameterization of three finite rotations such that $\underline{\underline{R}}(\underline{r}) = \underline{\underline{R}}(\underline{p})\underline{\underline{R}}(\underline{q})$, $p_0 = 2 - \underline{p}^T\underline{p}/8$, $q_0 = 2 - \underline{q}^T\underline{q}/8$, $\Delta_1 = (4-p_0)(4-q_0)$, and $\Delta_2 = p_0q_0 - \underline{p}^T\underline{q}$. It is noted that the rescaling operation could cause a discontinuity of the interpolated rotation field. Therefore, a more robust interpolation algorithm is introduced where the rescaling-independent relative-rotation field is interpolated.

The displacement fields in an element are approximated as

$$\underline{u}(\xi) = \sum_{k=1}^{p+1} h^k(\xi)\underline{\hat{u}}^k \tag{6.30}$$

$$\underline{u}'(\xi) = \sum_{k=1}^{p+1} h^{k\prime}(\xi)\underline{\hat{u}}^k \tag{6.31}$$

where $h^k(\xi)$, a component of shape function matrix $\underline{\underline{N}}$, is the pth-order-polynomial Lagrangian-interpolant shape function of node k, $k = \{1, 2, \ldots, p+1\}$, $\underline{\hat{u}}^k$ is the kth nodal value, and $\xi \in [-1, 1]$ is the element natural coordinate. However, as discussed in Bauchau et al. (2008), the 3-D rotation field cannot simply be interpolated as the displacement field in the form of

$$\underline{c}(\xi) = \sum_{k=1}^{p+1} h^k(\xi)\underline{\hat{c}}^k \tag{6.32}$$

$$\underline{c}'(\xi) = \sum_{k=1}^{p+1} h^{k\prime}(\xi)\underline{\hat{c}}^k \tag{6.33}$$

where $\underline{c}$ is the rotation field in an element and $\underline{\hat{c}}^k$ is the nodal value at the kth node, for three reasons: (1) rotations do not form a linear space so that they must be "composed" rather than added, (2) a rescaling operation is needed to eliminate the singularity existing in the vectorial rotation parameters, and (3) the rotation field lacks objectivity, which, as defined by Jelenić and Crisfield (1999), refers to the invariance of strain measures computed through interpolation to the addition of a rigid-body motion. Therefore, we adopt the more robust interpolation approach proposed by Jelenić and Crisfield (1999) to deal with the finite rotations. Our approach is described as follows.

Step 1: Compute the nodal relative rotations, $\underline{\hat{r}}^k$, by removing the reference rotation, $\underline{\hat{c}}^1$, from the finite rotation at each node, $\underline{\hat{r}}^k = (\underline{\hat{c}}^{1-}) \oplus \underline{\hat{c}}^k$. Note that the minus sign on $\underline{\hat{c}}^1$ denotes that the relative rotation is calculated by removing the reference rotation from each node. The composition in that equation is an equivalent of $\underline{R}(\underline{\hat{r}}^k) = \underline{R}^T(\underline{\hat{c}}^1)\,\underline{R}(\underline{c}^k)$.

Step 2: Interpolate the relative-rotation field: $\underline{r}(\xi) = h^k(\xi)\underline{\hat{r}}^k$ and $\underline{r}'(\xi) = h^{k\prime}(\xi)\underline{\hat{r}}^k$. Find the curvature field $\underline{\kappa}(\xi) = \underline{R}(\underline{\hat{c}}^1)\underline{H}(r)\underline{r}'$, where $\underline{\underline{H}}$ is the tangent tensor that relates the curvature vector $\underline{k}$ and rotation vector $\underline{p}$ as

$$\underline{k} = \underline{\underline{H}}\,\underline{p}' \tag{6.34}$$

Step 3: Restore the rigid-body rotation removed in Step 1: $\underline{c}(\xi) = \underline{\hat{c}}^1 \oplus \underline{r}(\xi)$.

Note that the relative-rotation field can be computed with respect to any of the nodes of the element; we choose node 1 as the reference node for convenience. For the Wiener-Milenković rotation parameter, the tangent vector $\underline{\underline{H}}$ is defined as

$$\underline{\underline{H}}(\underline{c}) = \frac{2}{(4 - c_0)^2}\left[c_0 + \tilde{c} + \frac{1}{4}\underline{c}\underline{c}^T\right] \tag{6.35}$$

where

$$c_0 = 2 - \frac{1}{8}\underline{c}^T\underline{c} \tag{6.36}$$

6.3.2 Legendre Spectral Finite Elements

In the LSFE approach, shape functions (i.e., those composing $\underline{N}$) are pth-order Lagrangian interpolants, where nodes are located at the $p + 1$ GLL points in the $[-1, 1]$ element natural-coordinate domain. Figure 6.2 shows representative LSFE basis functions for fourth- and eighth-order elements. Note that nodes are clustered near element end points.

(a) $p = 4$ (b) $p = 8$
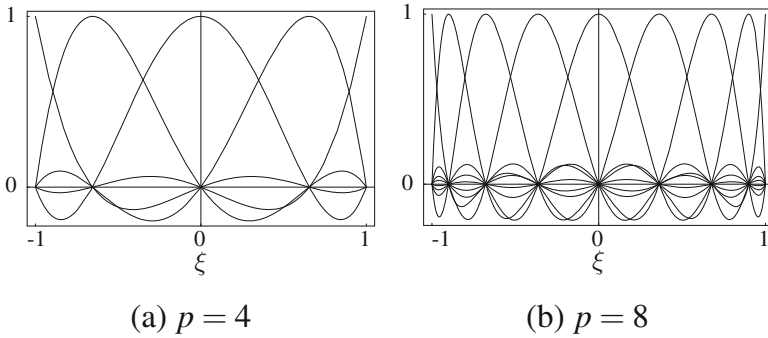
Fig. 6.2 Representative $p + 1$ Lagrangian-interpolant shape functions in the element natural coordinates for (**a**) fourth- and (**b**) eighth-order LSFEs, where nodes are located at the Gauss-Lobatto-Legendre points

6.3.3 Numerical Integration

Numerical integration (quadrature) of the finite-element inner products over an element domain is required in the FE formulation. Typically, the quadrature rule employed in a finite-element implementation is Gauss-Legendre, for which the number of quadrature points is chosen based on the polynomial order of the underlying FE basis functions. In the case in which material properties or applied loads vary significantly over an element domain, the accuracy of the quadrature is degraded, which can affect the overall accuracy of the solution. If the number of quadrature points is fixed to the FE basis-function order, accuracy is increased by either increasing the number of elements (h-refinement) or the order of the elements (p-refinement). However, if the quadrature order is chosen for accurate evaluation of FE inner products, then the choice in FE resolution can be based on overall solution accuracy.

For wind turbine blade analysis, material sectional properties are defined discretely at n_s stations along the beam axis. BeamDyn is equipped with two quadrature options: Gauss-Legendre quadrature and trapezoidal-rule quadrature, where the latter is only enabled when the blade is represented as a *single* element. For Gauss-Legendre quadrature, BeamDyn requires that $n_q = p + 1$, where n_q is the number of quadrature points and p is the order of the LSFE. Material properties are linearly interpolated to quadrature-point locations from the nearest stations. For a modern wind turbine blade, the number of material stations can be large. Further, the values of those material properties can vary dramatically from station to station. As such, an increase in the element order p could instigate a dramatically different solution, because the quadrature points may capture different material properties.

For trapezoidal-rule quadrature, BeamDyn requires that the number of quadrature points be tied to the number of material stations and that, at a minimum, there is a quadrature point associated with each station; additional quadrature points

(if desired) are equally distributed between those stations. Under this structure, $n_q = n_s + (n_s - 1) \times (j - 1) = (n_s - 1) \times j + 1$, where j is a positive integer that is user specified. Trapezoidal-rule quadrature enables a user to model a modern turbine blade defined by many cross-sectional property stations with few node points (i.e., $p \ll n_s$) while capturing all of the provided material properties. For example, the widely used NREL 5-MW reference wind turbine (Jonkman et al. 2009) blade is defined by 49 stations along the blade axis. If one were using first-order FEs with a fixed quadrature scheme, at least 48 elements would be required to accurately capture the material data in the FE inner products. BeamDyn, with the GEBT model and LSFE p-type discretization, is equipped to model a wind turbine blade with a single element. LSFE discretization with trapezoidal-rule quadrature is an effective modeling approach when the beam deformation can be described accurately with relatively few FE nodes, despite the large number of material-property stations. However, for a given element order and $n_q \gg p$, solutions will be more expensive than if $n_q \approx p$ because inner products are evaluated at least once per time step.

6.3.4 Time Integration and Nonlinear-Solution-Stopping Criterion

BeamDyn time integration is performed using the generalized-α scheme, which is an unconditionally stable (for linear systems), second-order accurate algorithm. The scheme allows for users to choose integration parameters that introduce high-frequency numerical dissipation. More details regarding the generalized-α method can be found in Bauchau (2010) and Chung and Hulbert (1993). Generalized-α time integration of the system defined by Eqs. (6.1) and (6.2) (with linearized form in Eq. (6.9)) requires a nonlinear system solve at each time step.

The nonlinear system solve is accomplished with the Newton-Raphson method, for which an energy-like stopping criterion has been chosen, which is calculated as

$$\| \Delta \mathbf{U}^{(i)T} \left({}^{t+\Delta t}\mathbf{R} - {}^{t+\Delta t}\mathbf{F}^{(i-1)} \right) \| \leq \| \epsilon_E \left(\Delta \mathbf{U}^{(1)T} \left({}^{t+\Delta t}\mathbf{R} - {}^{t}\mathbf{F} \right) \right) \| \qquad (6.37)$$

where $\| \cdot \|$ denotes the Euclidean norm, $\Delta \mathbf{U}$ is the incremental displacement vector, $\mathbf{R}$ is the vector of externally applied nodal point loads, $\mathbf{F}$ is the vector of nodal point forces corresponding to the internal element stresses, and ϵ_E is the preset energy tolerance. The superscript on the left side of a variable denotes the time value (in a dynamic analysis), whereas the one on the right side denotes the Newton-Raphson iteration number. As pointed out by Bathe and Cimento (1980), this criterion provides a measure of when the displacements and forces are near their equilibrium values.

6.4   Numerical Example: NREL 5-MW Wind Turbine

This example is an analysis of the NREL 5-MW reference wind turbine (Jonkman et al. 2009), which has straight, 61.5 m blades. We examine simulation results wherein the blades are modeled by BeamDyn or ElastoDyn. The blade structural-dynamics model in the ElastoDyn module of FAST can well be applied to straight isotropic blades dominated by bending. The ElastoDyn model includes two flapwise-bending deformation modes and one edgewise-bending deformation mode, coupled through a structural pre-twist, but neglects axial, shear, and torsional degrees of freedom as well as mass and elastic offsets from the pitch axis. Several geometric and kinematic nonlinearities are accounted for, including radial shortening and centrifugal, Coriolis, and gyroscopic loading.

We examine here the numerical performance of two different BeamDyn quadrature methods, Gauss-Legendre and trapezoidal rule, for this realistic-blade analysis. As described above, the sectional properties for the NREL 5-MW reference turbine blade are defined at 49 evenly spaced stations along its 61.5 m length. First, a cantilevered blade under a uniformly distributed static force of magnitude 10^4 N/m along the flap direction is analyzed. Figure 6.3 shows the tip displacement in the flap direction as a function of the number of nodes. Monotonic convergence of tip displacement is shown for the trapezoidal-quadrature results with an increasing number of nodes. The convergence rate of tip displacements for Gauss-Legendre quadrature, however, is non-monotonic. As described in sect. 6.3.3, the trapezoidal-rule quadrature captures all 49 material-data stations regardless of the number of element nodes, whereas the particular material data incorporated by Gauss-Legendre quadrature varies with the number of element nodes. The advantage of trapezoidal-rule quadrature is also demonstrated in the calculation of total blade mass as shown in Fig. 6.4. The total blade mass as calculated with trapezoidal-rule quadrature is independent of the number of nodes, whereas the mass calculated by Gauss-Legendre quadrature depends on the number of nodes in the element, and a large number of nodes are required for an accurate total-mass calculation. We note that a small scaling factor has been applied to the calculation of blade mass with ElastoDyn and BeamDyn to ensure each is consistent with the target total mass. In all subsequent calculations with BeamDyn, trapezoidal-rule quadrature is employed.

Next, we studied the time step sizes required for stable simulation of BeamDyn in stand-alone and coupled-to-FAST configurations. Figure 6.5 shows the maximum time step size versus the number of nodes for a BeamDyn model composed of a single element. In the stand-alone configuration, we used FAST as the driver but with all coupling options disabled so that the blade rotated at a fixed speed loaded only by gravity. For the coupled-to-FAST case, we conducted an aero-servo-elastic wind turbine analysis under a mean wind speed of 12 m/s with turbulence, which is certification test case #26 in the FAST archive (Jonkman and Jonkman 2016). BeamDyn numerical damping was disabled, and there were no correction iterations in the coupling algorithm. We see that the two-way coupling between BeamDyn and FAST requires significantly smaller time increments for stable solutions.
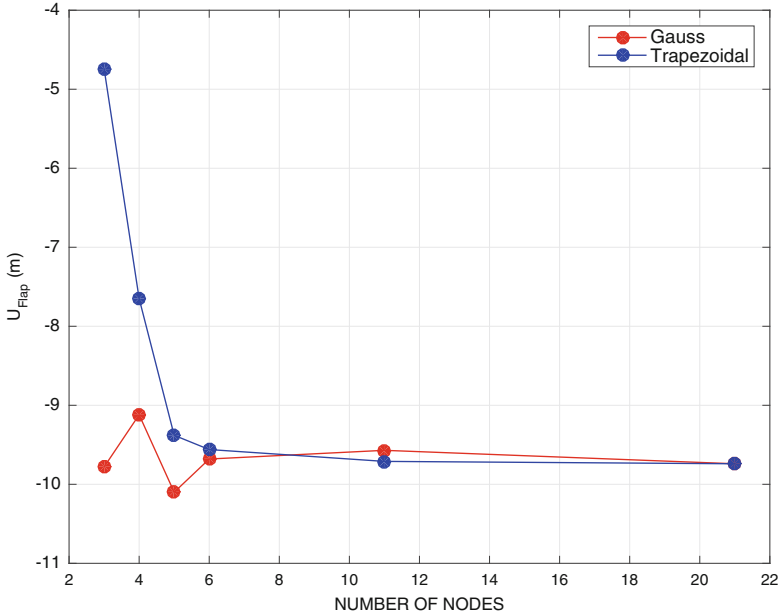
Fig. 6.3 Tip deflections of a cantilevered NREL 5-MW blade under a uniformly distributed load as a function of the number of nodes in a single-element BeamDyn model where finite-element inner products were calculated with Gauss-Legendre or trapezoidal-rule quadrature
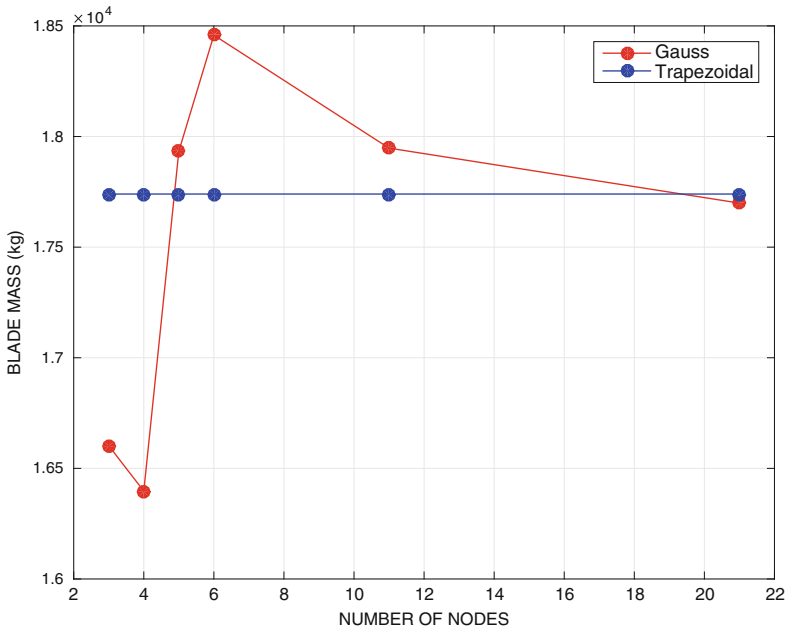
Fig. 6.4 Total blade mass of an NREL 5-MW reference blade as a function of the number of nodes in a single-element BeamDyn model where finite-element inner products were calculated with Gauss-Legendre or trapezoidal-rule quadrature
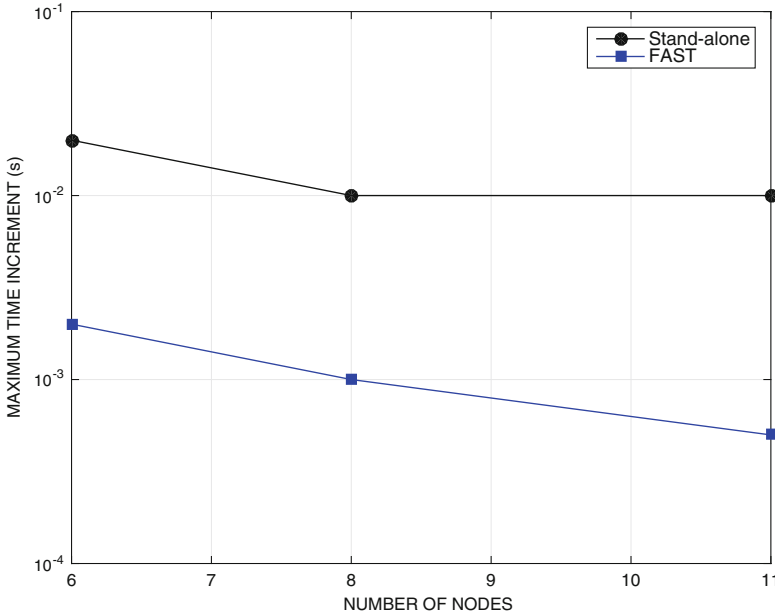
Fig. 6.5 Maximum stable time increments vs. number of FE nodes for an NREL 5-MW blade, wherein the blade is modeled with a single element

Finally, we studied the performance of BeamDyn in the coupled FAST analysis. Figures 6.6 and 6.7 show the tip flap displacement histories under different time and space discretizations. Note that all of the quantities studied here are defined in the body-attached blade reference coordinate system following the International Electrotechnical Commission standard, where the X direction is toward the suction side of the airfoil, the Y direction is toward the trailing edge, and the Z direction is toward the blade tip from the root. These results demonstrate that, for this system, results that are grid independent (in space and time) can be obtained with $\Delta t = 2 \times 10^{-3}$ s and a single fifth-order element for each blade.

We compared the results obtained by BeamDyn with those obtained by ElastoDyn for the coupled analysis (as described earlier). The BeamDyn blades were each modeled with a single fifth-order element (six nodes), and the FAST-BeamDyn system was time integrated with $\Delta t = 2 \times 10^{-3}$ s, which was required for numerical stability. The FAST-ElastoDyn system was time integrated with $\Delta t = 1.25 \times 10^{-2}$ s. The tip displacements of blade 1 are shown in Fig. 6.8. Results for BeamDyn are shown with and without off-diagonal terms in the sectional mass matrices (the latter is for more direct comparison to ElastoDyn). Good agreement can be observed between the ElastoDyn and BeamDyn results. We note that, because of the trapeze effect and elastic stretching considered in BeamDyn, the mean value of the axial tip displacement calculated by BeamDyn is different than that calculated by ElastoDyn. Figures 6.9 and 6.10 show the root reaction forces and moments, respectively, calculated by BeamDyn and ElastoDyn. Again, good agreement is shown. We note
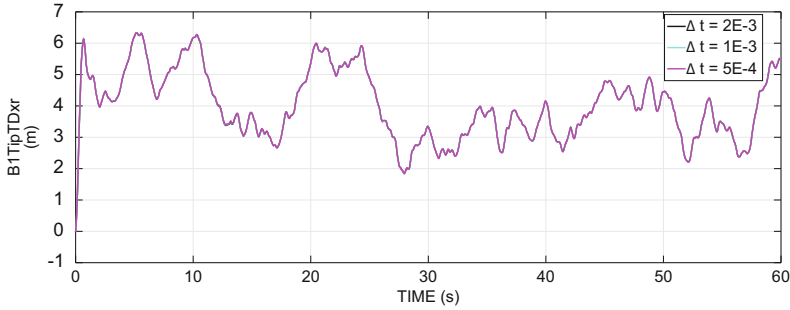
Fig. 6.6 Blade tip deflection histories along flap direction obtained using different time increments, wherein the blade is modeled with a single fifth-order element
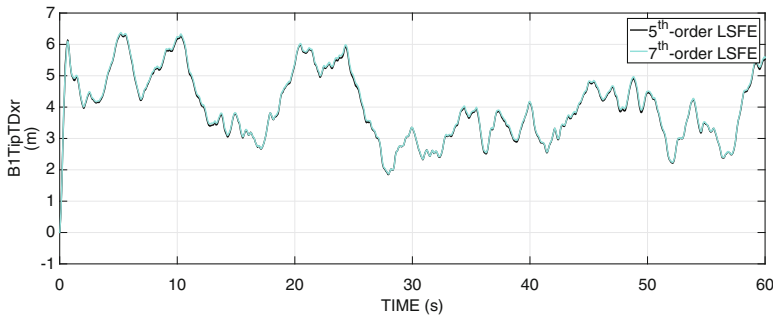
Fig. 6.7 Blade tip deflection histories along flap direction obtained using different BeamDyn refinements, wherein models were time integrated with $\Delta t = 2 \times 10^{-3}$ s

the spurious spikes in the M_{pitch} histories, which will be addressed in a future release of BeamDyn. Although we see noticeable differences in the tip displacement histories, it is interesting to note the excellent agreement between ElastoDyn and BeamDyn results for root reaction forces and moments. This is because the NREL 5-MW blade features are well modeled by the approximations behind the ElastoDyn model. In particular, ElastoDyn is well suited for modeling the NREL 5-MW blade because:

- the blade is naturally straight,
- the lowest modes excited by wind are dominated by bending,
- there are no cross-sectional couplings induced by anisotropic composite laminate layups,
- torsion, extension, and shear effects are mostly negligible (the first torsional mode natural frequency is well above rated rotor speed; the blade aspect ratio is high; and so on),
- the deflections are small enough that they can be accurately captured by the geometric nonlinear terms included in ElastoDyn, and
- the mass-center offsets are small and do not cause a large change in response.
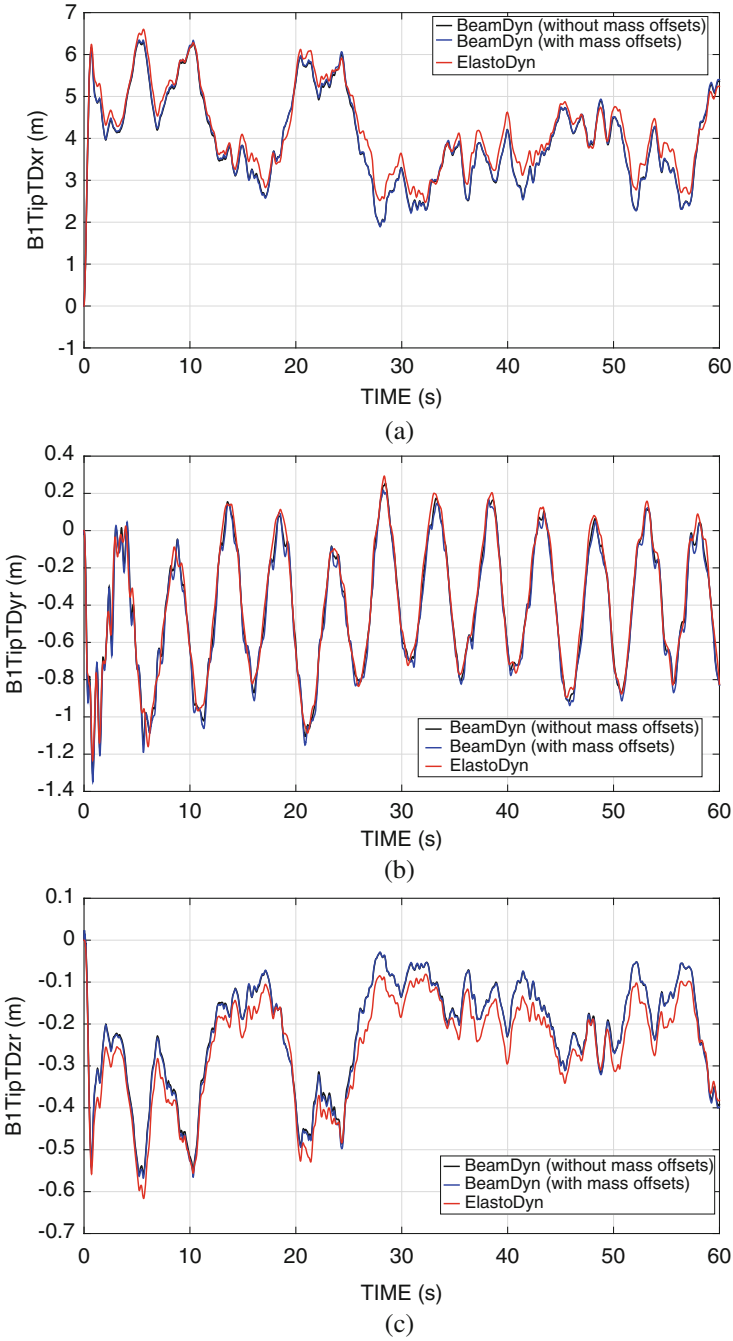
Fig. 6.8 Comparisons of blade tip displacements between ElastoDyn and BeamDyn results. (**a**) Flap direction. (**b**) Edge direction. (**c**) Axial direction
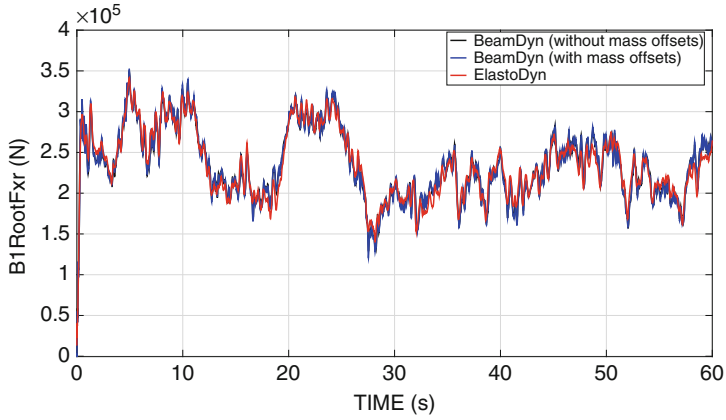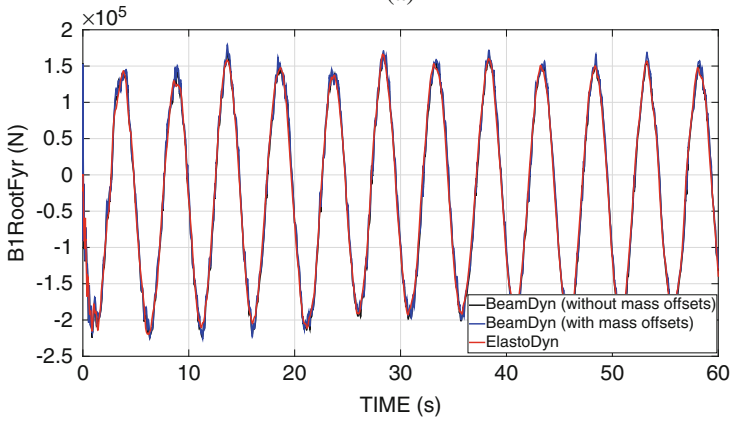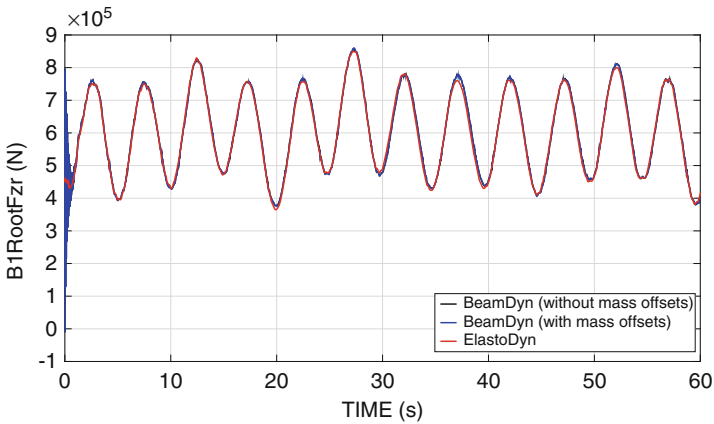
Fig. 6.9 Comparisons of root reaction forces between ElastoDyn and BeamDyn results. (**a**) F_{flap}. (**b**) F_{edge}. (**c**) F_{axial}
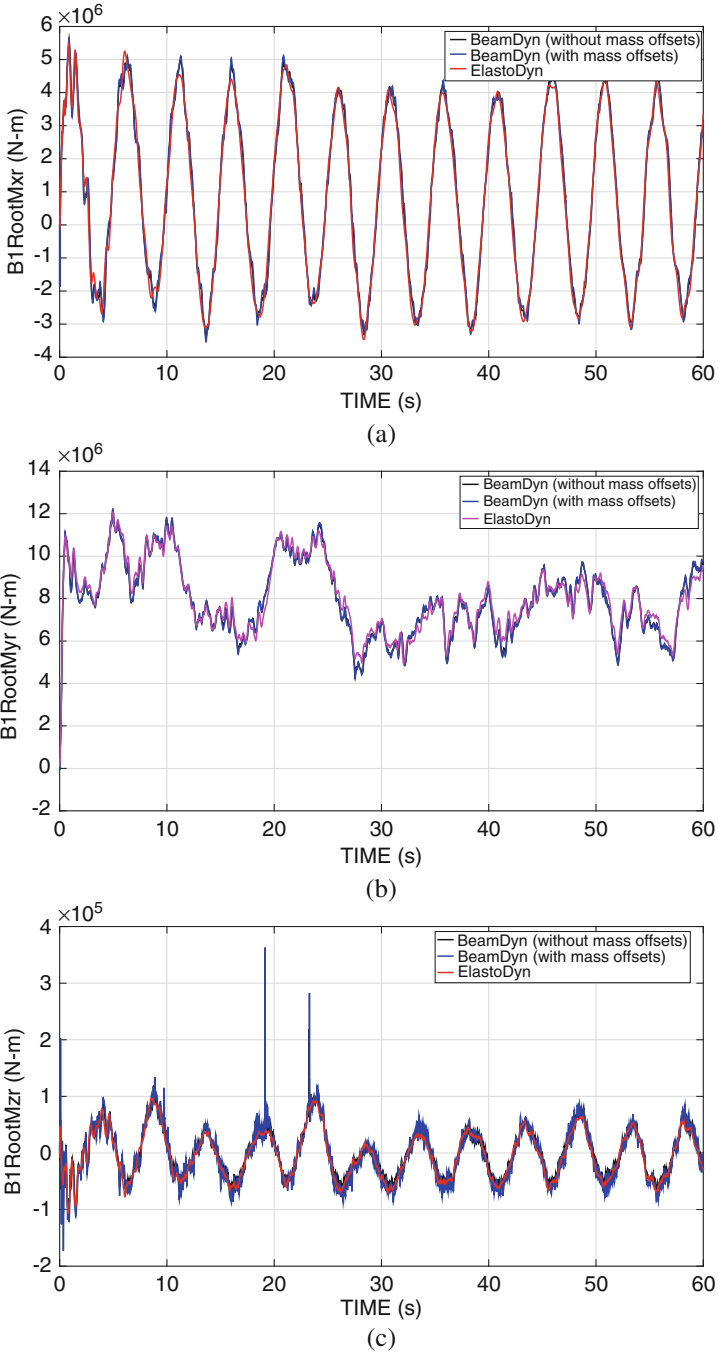
Fig. 6.10 Comparisons of root reaction moments between ElastoDyn and BeamDyn results. (**a**) M_{edge}. (**b**) M_{falp}. (**c**) M_{pitch}

The benefits of moving from an efficient lower-fidelity model like ElastoDyn to a more computationally expensive higher-fidelity model like BeamDyn will be best seen for turbine blades that do not satisfy the above simplifying features, e.g., those with aeroelastically tailored curved blades. For example, Guntur et al. (2016) examined the simulated and field-measured responses of a Siemens 2.3 MW turbine with a 108 m rotor for 1,141 cases with various wind speeds and turbulence intensities. The Siemens turbine had flexible aeroelastically tailored blades with bend-twist coupling. Simulations were performed with the blades modeled in both BeamDyn and ElastoDyn. The BeamDyn models gave results that agreed significantly better, and in some cases dramatically better, with the field measurements for nearly all quantities investigated.

References

Bathe KJ, Cimento AP (1980) Some practical procedures for the solution of nonlinear finite element equations. Comput Methods Appl Mech Eng 22:59–85

Bauchau OA (2010) Flexible multibody dynamics. Springer, New York

Bauchau O, Epple A, Heo S (2008) Interpolation of finite rotations in flexible multibody dynamics simulations. Proc Inst Mech Eng Part K J Multi-body Dyn 222:353–366

Betsch P, Steinmann P (2002) Frame-indifferent beam finite elements based upon the geometrically exact beam theory. Int J Numer Methods Eng 54:1775–1788

Chung J, Hulbert GM (1993) A time integration algorithm for structural dynamics with improved numerical dissipation: the generalized-α method. J Appl Mech 60:371–375

Cook RD, Malkus DS, Plesha ME, Witt RJ (2001) Concepts and applications of finite element analysis, 4th edn. Wiley, New York

Guntur S, Jonkman J, Schreck S, Jonkman B, Wang Q, Sprague MA, Singh M, Hind M, Sievers R (2016) FAST v8 verification and validation for a MW-scale wind turbine with aeroelastically tailored blades. In: Proceedings of the 34th ASME wind energy symposium, San Diego

Hodges D (1990) A mixed variational formulation based on exact intrinsic equations for dynamics of moving beams. Int J Solids Struct 26:1253–1273

Hodges DH (2006) Nonlinear composite beam theory. In: AIAA

Ibrahimbegović A (1995) On finite element implementation of geometrically nonlinear Reissner's beam theory: three-dimensional curved beam elements. Comput Methods Appl Mech Eng 122:11–26

Ibrahimbegović A, Mikdad MA (1998) Finite rotations in dynamics of beams and implicit time-stepping schemes. Int J Numer Methods Eng 41:781–814

Jelenić G, Crisfield MA (1999) Geometrically exact 3D beam theory: implementation of a strain-invariant finite element for statics and dynamics. Comput Methods Appl Mech Eng 171:141–171

Jonkman J, Jonkman B (2016) NWTC Information Portal (FAST v8). https://nwtc.nrel.gov/FAST8

Jonkman J, Butterfield S, Musial W, Scott G (2009) Definition of a 5-MW reference wind turbine for offshore system development. Technical Report NREL/TP-500-38060, National Renewable Energy Laboratory

Reissner E (1973) On one-dimensional large-displacement finite-strain beam theory. Stud Appl Math LII 52:87–95

Simo JC (1985) A finite strain beam formulation. The three-dimensional dynamic problem. Part I. Comput Methods Appl Mech Eng 49:55–70

Simo JC, Vu-Quoc L (1986) A three-dimensional finite-strain rod model. Part II. Comput Methods Appl Mech Eng 58:79–116

Wang Q, Yu W, Sprague MA (2013) Geometric nonlinear analysis of composite beams using Wiener-Milenković parameters. In: Proceedings of the 54th structures, structural dynamics, and materials conference, Boston

Yu W, Blair M (2012) GEBT: a general-purpose nonlinear analysis tool for composite beams. Compos Struct 94:2677–2689

Chapter 7
Advanced Health Condition Monitoring of Wind Turbines

Wenxian Yang, Kexiang Wei, Zhike Peng, and Weifei Hu

7.1 Introduction

Modern maintenance strategies can be broadly classified into corrective maintenance, preventive maintenance, and condition-based maintenance (Dhillon 2002):

- *Corrective maintenance*, also known as run to failure maintenance, is performed only when the machine has totally failed. It is recognized as the least effective maintenance strategy as it is often associated with high maintenance cost due to sudden failure, long downtime, and even catastrophic consequence in the worst case.
- *Preventive maintenance*, also known as periodic maintenance, is carried out on a regular basis. This strategy can help the operator to avoid catastrophic failure of machinery and reduce failure rate. But in the meantime, it also could lead to unnecessary maintenance actions as it is performed regardless of the actual health condition of the machine and thereby increase the overall operating cost;

W. Yang (✉)
School of Engineering, Newcastle University, Newcastle Upon Tyne, UK
e-mail: wenxian.yang@newcastle.ac.uk

K. Wei
Hunan Province Cooperative Innovation Center for Wind Power Equipment and Energy Conversion, Hunan Institute of Engineering, Xiangtan, China

Z. Peng
State Key Laboratory of Mechanical System and Vibration, Shanghai Jiaotong University, Shanghai, China

W. Hu
Sibley School of Mechanical and Aerospace Engineering and Department of Earth and Atmospheric Sciences, Cornell University, Ithaca, NY, USA
e-mail: wh348@cornell.edu

- *Condition-based maintenance*, as the name suggests, is performed based on the actual health condition of machinery. It allows early detection of an impending failure and facilitates the implementation of timely maintenance thus avoiding total machinery breakdown and unnecessary maintenance actions. All these merits can help the operator to reduce the overall O&M costs. However, such kind of maintenance strategy involves high up-front cost, and, particularly, the success of it highly depends on the application of appropriate CM techniques and the accuracy of signal processing.

In contrast to the health monitoring of those machines that operate under constant operational and loading conditions (e.g., steam turbines in coal fire and nuclear power plants, compressors in chemical and oil refinery factories), the CM of WTs is more challenging due to the following issues:

1. *Non-stationary property of CM signals*. Due to the inconsistent wind, WTs are subjected to constantly varying loads over time. As a consequence, the CM signals collected from WTs are usually non-stationary. As the energy of the WT CM signals varies in a large dynamic range, it is difficult to achieve a reliable assessment via simply performing comparison with those thresholds depicted in the currently available international standards, e.g., ISO 10816 and ISO 2372. (Yang and Court 2013);

2. *Contradiction of the efficiency and accuracy of signal processing*. Attributed to the efficient computing algorithm, the fast Fourier transform (FFT) and its extension forms (e.g., envelope analysis (Hatch 2004)) are being widely used in present WT CM systems. However, it is difficult to observe the degradation of WT condition as the tradition signal analysis in frequency domain does not render the degradation trend in time domain. By contrast, time-frequency analysis (e.g., wavelet transform (Torrence and Compo (1998)) is more ideal for analyzing such kind of signals as it presents the information of the signals in both time and frequency domains. However, the conventional time-frequency analyses, for example, the continuous wavelet transform, often involve complex calculations and therefore are not suited to online use (Ferguson and Catterson 2014).

3. *Limited CM capability of vibration analysis*. Currently, the majority of commercial WT CM systems are vibration analysis systems. They are good at detecting faults occurring in mechanical components, such as main shaft, bearing, and gearbox. However, a WT comprises both mechanical and electrical components. Moreover, recent research has shown that online or periodic monitoring of WT electrical components is equally important because WT electrical components are more prone to failure than their mechanical counterparts (Ribrant and Bertling 2007; Tavner et al. 2007). But these electrical component faults can hardly be detected by the approach of vibration analysis because the faulty features of an electrical fault are significantly attenuated in vibration signals.

4. *Limited applicability of commercially available WT CM systems*. Commercially available WT CM systems are originated from other industries and adapted later on for monitoring geared WTs. Their capabilities have not been fully investigated in monitoring gear-less WTs. A survey collected in Germany and Denmark reveals that the gear-less direct-drive WTs show higher failure rate than geared

Table 7.1 Fault-related characteristic frequencies of rolling-element bearings (Tavner et al. 2008)

Type of fault	Characteristic frequency (Hz)	Notes
Inner race fault	$\frac{1}{2}\frac{r}{60}n\left(1+\frac{d}{D}\cos\alpha\right)$	$d-$ball diameter
Outer race fault	$\frac{1}{2}\frac{r}{60}n\left(1-\frac{d}{D}\cos\alpha\right)$	$D-$pitch diameter
Cage fault	$\frac{1}{2}\frac{r}{60}\left(1-\frac{d}{D}\cos\alpha\right)$	$n-$number of balls
Rolling-element fault	$\frac{1}{2}\frac{r}{60}\frac{D}{d}\left(1-\left(\frac{d}{D}\right)^2\cos^2\alpha\right)$	$\alpha-$contact angle
		$r-$revolution per minute

WTs do (Tavner et al. 2006; Qiao and Lu 2015). This requests a more advanced CM technique that can be widely applicable to monitor both concepts of WTs.

In view of these issues, the wind industry requests more advanced strategies and signal processing techniques, which are:

- Applicable to the CM of various concepts of WTs
- Efficient in calculation and thereby applicable to real-time or online WT CM
- Accurate in extracting fault feature from non-stationary WT CM signals
- Capable to detect both mechanical and electrical faults occurring in WTs

The purpose of this chapter is to introduce a newly developed WT CM strategy and the associated signal processing method that can well meet the need of the aforementioned requests. The long-term CM practice (Basak et al. 2006; Li et al. 2010) has shown that fault-related frequency components will appear in the CM signal once an electrical or mechanical fault occurs in a machine. This suggests that the health condition of a WT can be assessed by monitoring the tendencies of the signal energy at these fault-related frequencies. For example, the health condition of a rolling-element bearing and an induction generator can be evaluated by monitoring the variation of the energy at the characteristic frequencies listed in Tables 7.1 and 7.2, respectively.

In order to extract the distinguished signatures at the fault-related frequencies, an energy tracking technique based on wavelet analysis, namely, wavelet-transform-based energy tracking technique (WETT), is proposed here. Before introducing the energy tracking technique, the ideal signals for the energy tracking technique will be discussed first because they are critical for developing a widely applicable WT CM strategy.

7.2 Signals for Globally Monitoring Entire Wind Turbine Drivetrain

In the current WT CM practice, the CM of WT drivetrain is accomplished via a number of transducers that are installed on different drivetrain components, such as main bearing, gearbox, and generator (Yang et al. 2014). However, it is recognized

Table 7.2 Fault-related characteristic frequencies in the power signal of electrical machines (Tavner et al. 2008)

Type of fault	Root cause of fault	Angular frequency of power signal (rad/s)
Mechanical faults	Oil whirl and whip in sleeve bearings	$\omega_{se}\left[1 + \frac{0.43\sim0.48}{p}\right]$
	Unbalanced mass on rotor of a synchronous machine	$\omega_{se}\left[1 + \frac{1}{p}\right]$
	Dynamic eccentricity in a synchronous machine	$\omega_{se}\left[1 + \frac{2}{p}\right]$
	Dynamic displacement of shaft in bearing housing of a synchronous machine	$\omega_{se}\left[1 + \frac{1}{p} + \frac{2}{p} + \cdots\right]$
	Static misalignment of rotor shaft in a synchronous machine	$\omega_{se}\left[1 + \frac{1}{p} + \frac{2}{p} + \cdots\right]$
	Static and dynamic eccentricity in induction machine	$\omega_{se}\left[1 + k_e\frac{1-s}{p} \pm k\right]$
Electrical faults	Broken rotor bar in induction machine	$\frac{2ns\omega_{se}}{p}, \frac{2n(1-s)\omega_{se}}{p}$
	Stator winding faults in a synchronous machine	$\omega_{se}, 3\omega_{se}$

Note: ω_{se} is stator side electrical angular frequency, s indicates asynchronous machine rotor speed slip, p stands for integer pole pair number, n is a positive integer number, k_e represents eccentricity order ($k_e = 0$ for static eccentricity and $k_e = 1, 2, 3, \cdots$ for dynamic eccentricity); and $k = 1,3,5,7,\ldots$ denotes integer stator winding magnetic motive force (MMF) space harmonic number

that the CM signal collected from each individual drivetrain component cannot provide a global view of the health condition of the entire WT drivetrain system. This means that the realization of the overall assessment of the entire WT drivetrain system has to rely on the processing and interpretation of CM signals collected from various drivetrain components. Inevitably, this will make the WT CM system complex in hardware configuration, expensive in capital cost, and inefficient in data processing. Therefore, it is necessary to develop a new CM strategy to mitigate these issues.

In essence, a WT is a device which converts wind energy to electrical power via its drivetrain system. In the energy conversion process, part of energy is consumed and exhibited in thermal and vibratory energy forms, i.e.,

$$T_{\text{shaft}} \times r = P_{\text{electrical}} + E_{\text{vibratory}} + E_{\text{thermal}} \tag{7.1}$$

where T_{shaft} and r indicate the mechanical torque and rotational speed of the main shaft, respectively; $P_{\text{electrical}}$ is the electrical power output from the WT generator; and $E_{\text{vibratory}}$ and E_{thermal} refer to the energy that is consumed by the drivetrain system and present, respectively, in the form of vibratory and thermalenergy. Among

them, the electrical power $P_{\text{electrical}}$ output from a three-phase WT generator can be calculated by

$$P_{\text{electrical}} = \sum_{i=1}^{3} V_i \times I_i \tag{7.2}$$

where V_i ($i = 1, 2, 3$) denote the three-phase voltage and I_i ($i = 1, 2, 3$) the line current measured from the generator.

In Eq. (7.1), $E_{\text{vibratory}}$ and E_{thermal} distribute extensively in the drivetrain system. It is unlikely to assess them accurately via a limited number of transducers installed on drivetrain components. Moreover, different concepts of WTs have different structures, which further increase the difficulty of the assessment. By contrast, T_{shaft} and $P_{\text{electrical}}$ are two parameters that can be easily measured from the main shaft and generator, i.e., the input and output sides of the WT drivetrain system. Moreover, attributed to the mechanical-electrical coupling effect of the drivetrain, T_{shaft} and $P_{\text{electrical}}$ carry the health condition information of both mechanical and electrical drivetrain components. This implies that in contrast to vibration signals that are being adopted by the commercially available WT CM systems, T_{shaft} and $P_{\text{electrical}}$ would be more ideal for the application to WT CM as they provide a global view of the health condition of the whole WT drivetrain system rather than individual components (Tavner 2008).

In order to investigate the potential application of T_{shaft} and $P_{\text{electrical}}$ to overall monitoring of WT drivetrain system, the mechanical unbalance fault and the electrical phase asymmetry fault are emulated in a three-phase induction generator, as shown in Fig. 7.1.

In the experiment, two 0.25 kg masses are attached on the input shaft of the generator to simulate the mechanical unbalance fault, while the electrical phase asymmetry is introduced into the rotor winding of the generator by changing the

Fig. 7.1 The generator for testing T_{shaft} and $P_{\text{electrical}}$
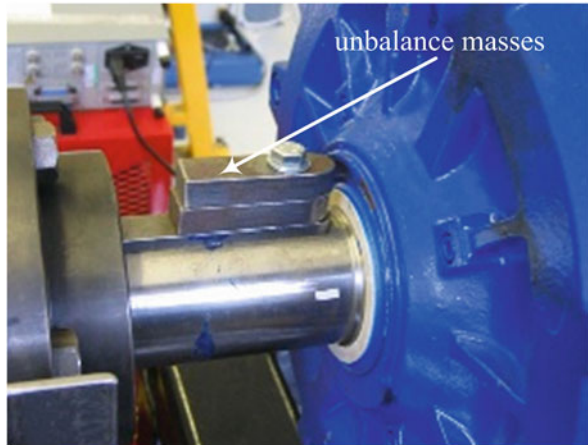
phase resistances of the resistive load bank connected to the generator rotor. When the generator rotated at 1750 rev/min, the shaft torque, vibration displacement, generator stator line current, and electrical power signals are collected before and after the faults are applied. As a demonstration, the time waveforms of the collected signals are shown in Fig. 7.2.

From the time waveforms of the signals shown in Fig. 7.2, it is found that:

- Shaft torque and generator power respond correctly to both the mechanical unbalance and the electrical phase asymmetry faults, although both signals are better in indicating the electrical asymmetry.
- Shaft vibration displacement indicates the presence of the mechanical unbalance fault. However, it fails to respond to the electrical phase asymmetry.
- The amplitude of line current signal is not a good indicator of both the mechanical unbalance and the electrical phase asymmetry faults.

Therefore, T_{shaft} and $P_{electrical}$ are good indicators of the health condition of the entire WT drivetrain system. However, the measurement of torque from WT main shaft is costly, while the generator power signal is readily accessible from all concepts of WTs. For this reason, $P_{electrical}$ is more ideal for the application to WT CM. The advantages of applying the total three-phase power signal to WT CM are summarized as follows:

- *Sensitivity*. Attributed to the absence of mains frequency component (either 50 Hz or 60 Hz depending on area) and their high-order harmonics, the total three-phase power signal is more sensitive to WT failures.
- *Effectiveness*. Both mechanical and electrical faults occurring in the WT drivetrain are detectable from the total power signal. Thus, the total power signal is superior to the vibration signals as the total power signal can provide a global view of the health condition of the entire WT drivetrain system rather than the condition of individual components.
- *Cost*. Since the total power signal is readily available from modern megawatt-scale WTs while the measurement of vibration and torque signals requires additional sensors, the CM based on the total power signal would be more cost-effective than those using vibration and torque signals.
- *Adaptability*. As total power signal is ready to access in all concepts of WTs either geared or direct-drive, the CM technique developed based on the interpretation of power signals will be widely applicable to all concepts of WTs.

7.3   Wavelet-Transform-Based Energy Tracking Technique

Following the identification of the ideal signal for overall assessing the health condition of the entire WT drivetrain system, an advanced signal processing technique, namely, WETT, is introduced in this section in order to provide an efficient tool to accurately process the online or real-time WT CM signals.
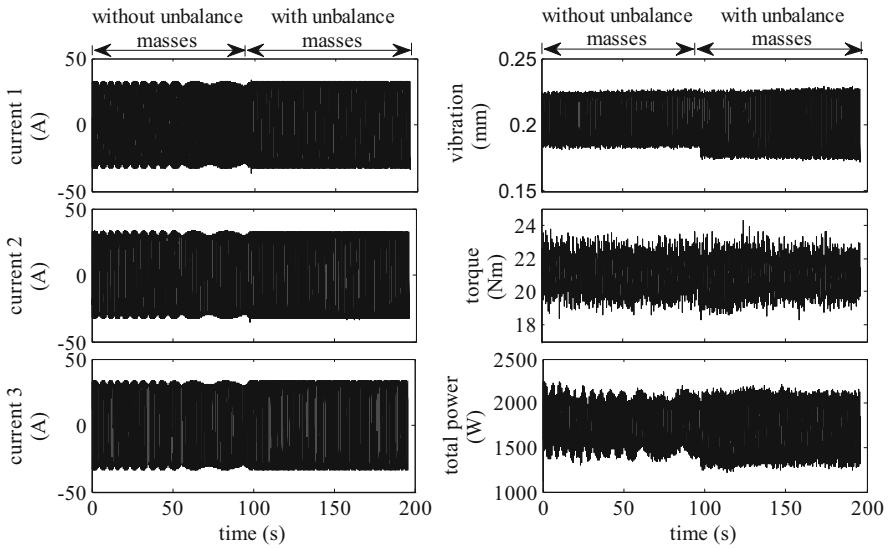
(a)
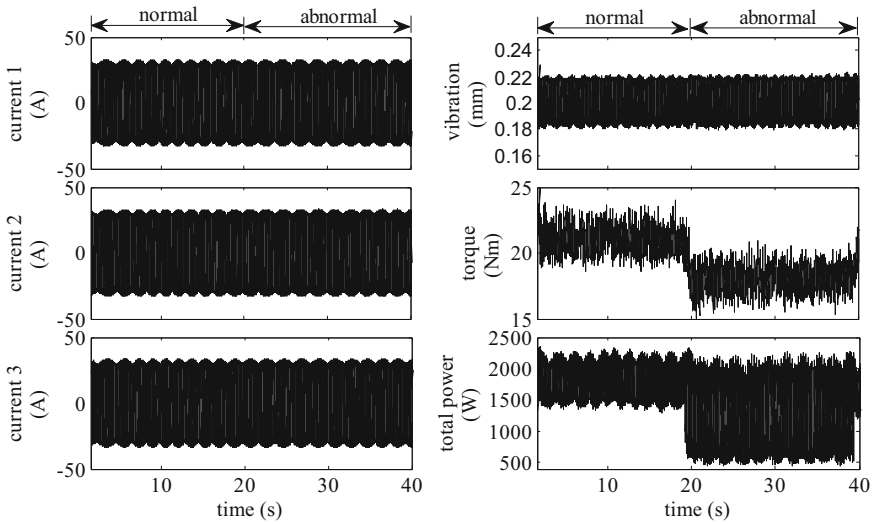
(b)

Fig. 7.2 Experimental results of T_{shaft} and $P_{electrical}$ (**a**) Signals collected before and after the mechanical unbalance fault is applied (**b**) Signals collected before and after the electrical phase asymmetry is applied

The continuous wavelet transform (CWT) of a signal $x(t)$ is defined as (Addison 2002)

$$CWT_x(a, b) = \frac{1}{\sqrt{|a|}} \int_{-\infty}^{\infty} x(t)\psi^*\left(\frac{t-b}{a}\right) dt \tag{7.3}$$

where ψ is a mother wavelet function, the asterisk "*" stands for complex conjugate, and the daughter wavelet function $\psi_{a,b}(t)$ is derived from the mother wavelet function through scale parameter a and time-shift parameter b, i.e.,

$$\psi_{a,b}(t) = \psi\left(\frac{t-b}{a}\right) \tag{7.4}$$

Through changing the value of scale parameter a, the mother wavelet ψ is dilated or compressed. Correspondingly, all frequency components contained in the WT CM signals ranging from frequency 0 to half of the signal sampling frequency (i.e., the Nyquist frequency) can be projected onto an appropriate time scale map (one example is shown in Fig. 7.3) by conducting the convolution calculation of $x(t)$ and the daughter wavelet function $\psi_{a,b}(t)$. In Fig. 7.3, the bottom plot shows the time waveform of a sample CM signal with increasing frequency; and the top plot shows the wavelet coefficients of this signal obtained at different wavelet scales and times. A smaller value of scale parameter a corresponds to a higher frequency; and a larger value of scale parameter a corresponds to a lower frequency. It has no doubt that the CWT of a lengthy WT CM signal will involve complex calculations and take long time. Thus, it is computationally challenging to directly apply the CWT to conduct online CM tasks in spite of its merit in dealing with non-stationary signals.
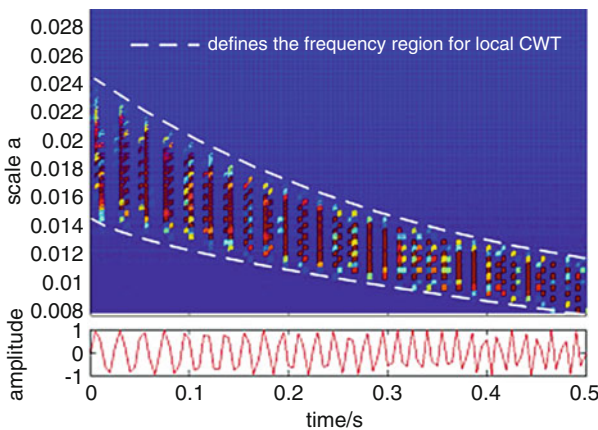
Fig. 7.3 Time scale map derived using the continuous wavelet transform

In addition, Fig. 7.3 suggests that:

1. The time scale map obtained using the CWT cannot be directly used for WT CM as it is hard to identify the fault-related frequencies from a time scale map.
2. Many of the calculations shown in Fig. 7.3 are unnecessary for WT CM because the fault-related frequencies are few in number and the calculation of the wavelet coefficients at non-fault-related frequencies is not helpful for assessing the health condition of the WT.

In order to address the first issue, wavelet scalogram was developed (Auger and Flandrin 1995; Wong and Chen 2001). It defines the relation between the scale parameter a and the central frequency ω_c of a daughter wavelet $\psi_{a,b}(t)$. The wavelet scalogram of a CM signal $x(t)$ can be expressed as

$$SG_x(\omega_c, b) = |CWT_x(a, b)|^2 \tag{7.5}$$

where the central frequency ω_c of the daughter wavelet $\psi_{a,b}(t)$ is approximated by using the following equation

$$\omega_c = \frac{\omega_0}{a} \tag{7.6}$$

where ω_0 is the central frequency of the mother wavelet function ψ.

As the energy distribution in wavelet transform is usually asymmetric, $SG_x(\omega_c, b)$ does not always represent the energy located in the true geometric center (ω_c, b). Therefore, energy reassignment is often conducted for further improving the accuracy of signal processing in practical scalogram calculations. Details of the energy reassignment method are seen in Peng et al. (2002). However, in its application to WT CM, the energy reassignment is not necessary because the fault-related feature is extracted from a local frequency region rather than from a single frequency. Therefore, the WETT can be implemented using the following steps.

Step 1: A time-frequency sliding window is first designed, as shown in Fig. 7.4. Its central frequency ω_c is the mean frequency during the time interval T of the prescribed frequency band. The upper and lower cutoff frequencies ω_{upper} and ω_{lower} are adapted to the fluctuation of the rotational speed ω_r of the WT component being investigated, i.e. (Yang et al. 2009),

$$\begin{cases} \omega_{upper} = \omega_c + \frac{1}{2}\eta\omega_r \\ \omega_{upper} = \omega_c - \frac{1}{2}\eta\omega_r \end{cases} \tag{7.7}$$

where η indicates the fluctuation of the rotational speed ω_r of the WT component. In essence, it is a function of the turbulence of the wind. The fluctuation of the shaft rotational speed is essentially due to the turbulence of the wind speed.
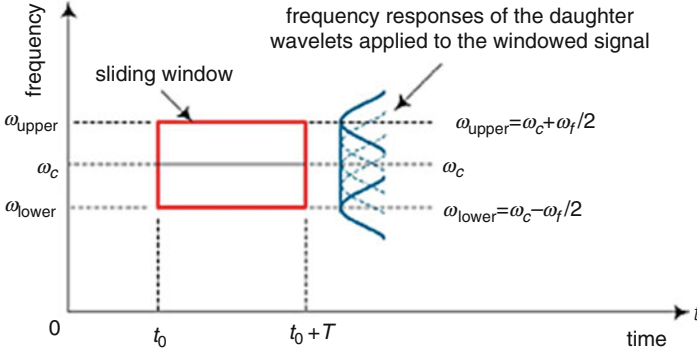
Fig. 7.4 Time-frequency sliding window for performing energy tracking calculation

Correspondingly, the range of the wavelet scales for energy tracking calculation can be determined using Eq. (7.6), i.e.,

$$a \in [a_{\min} \ a_{\max}] \tag{7.8}$$

where $a_{\min} = \frac{\omega_0}{\omega_{\text{upper}}}$ and $a_{\max} = \frac{\omega_0}{\omega_{\text{lower}}}$.

Step 2: Conduct the wavelet scalogram of the windowed signal $\widehat{x}(t)$ locally at all frequencies within the range of $\omega \in [\omega_{\text{lower}} \ \omega_{\text{upper}}]$, i.e.,

$$SG_{\widehat{x}}(\omega, b) = \left| CWT_{\widehat{x}} \left(\frac{\omega_0}{\omega}, b \right) \right|^2 \tag{7.9}$$

Step 3: Estimate the energy A of the CM signal at the fault-related frequency of interest in time interval T by

$$A \left(t_0 + \frac{T}{2} \right) = \max \left(SG_{\widehat{x}}(\omega, b) \right) \tag{7.10}$$

where $\omega \in [\omega_{\text{lower}} \ \omega_{\text{upper}}]$ and $b \in [t_0 \ t_0 + T]$. The frequency of interest can be readily calculated using the equations in Tables 7.1 and 7.2 as long as the rotational speed is known.

Step 4: Move forward the time-frequency sliding window along the signal and redefine the maximum and minimum wavelet scale parameters in Eq. (7.8) according to the average value of ω_r within each time interval T.

Step 5: Repeat the calculations of Eqs. (7.9 and 7.10) to obtain the energy A of the CM signal at the fault-related frequency of interest in the new time interval T.

Step 6: Move forward the time-frequency sliding window along the signal and iterate the aforementioned calculations until the whole WT CM signal has been processed.

The variation of the energy *A* of the CM signal at the fault-related frequency of interest is finally obtained for assessing the health condition of the WT component of interest.

7.4 Test Rig of Wind Turbine Drivetrain

Aiming to verify the WETT described above, a WT drivetrain test rig has been developed (Yang et al. 2009, 2010), as shown in Fig. 7.5. The test rig is driven by a 54 kW DC variable-speed motor first equipped with a 10 kW synchronous permanent magnet generator and then a 20 kW induction generator. A two-stage gearbox is installed on the test rig to decelerate the permanent magnet generator and accelerate the induction generator. The gear ratio is 11.14:1 for driving the permanent magnet generator and 1:5 for driving the induction generator. The three-phase permanent magnet generator has 84 coils on the stator, 108 permanent magnets on the rotor, and a three-phase rectified output. The 20 kW three-phase induction generator has two pole pairs (i.e., $N_p = 2$). The output of both generators is fed to resistive load banks.

The system is instrumented using LabView so that a variety of wind speed inputs can be applied and the relevant CM signals can be collected from the drivetrain and the terminals of the generators. The rotational speed of the DC motor is controlled by an external model incorporating the properties of natural wind at a variety of speeds and turbulences and the mechanical behavior of a 2 MW WT operating under closed-loop control conditions. As shown in Fig. 7.6, a number of transducers are installed on the test rig for data acquisition.
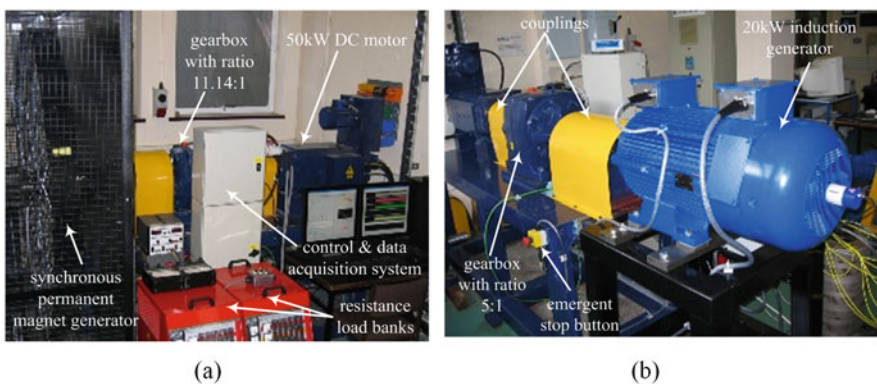
Fig. 7.5 Wind turbine drivetrain test rig (**a**) With a permanent magnet generator (**b**) With an induction generator
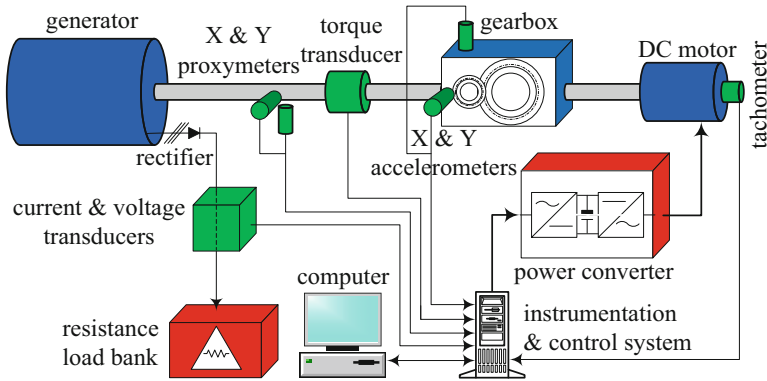
Fig. 7.6 Condition monitoring transducers on the test rig

7.5 Faults Simulated on Test Rig and Fault-Related Characteristic Frequencies

A number of mechanical and electrical faults are emulated on the test rig depicted in Sect. 7.4. As they are not necessarily precise replicas of real WT faults, they have been called "fault-like perturbations" but contain similarities with faults on real WTs. The emulated faults are described in the following.

A. *Electrical fault emulated on rotor of synchronous permanent magnet generator*

The stator winding fault is emulated on the synchronous generator by simultaneously shorting three coils installed on the stator of the generator with the aid of remote relays. The three coils being shorted are shown in Fig. 7.7.

The characteristic frequency f_c corresponding to this kind of fault is the slotting frequency of the synchronous permanent magnet generator, i.e. (Yang et al. 2009),

$$f_c = \frac{r \times M}{60} \tag{7.11}$$

where r is the rotational speed of the rotor of the synchronous generator, the unit of which is revolution per minute (rpm) and M denotes the number of coils on the stator of the generator.

B. *Mechanical fault emulated on rotor of synchronous permanent magnet generator*

Considering rotor imbalance fault often occurs in WTs due to the structural damage or unequal icing/water penetration on the blades, the mechanical rotor unbalance fault is simulated by attaching a 1 kg mass to the generator rotor with an equivalent rotating mass of 290.7 kg, as shown in Fig. 7.8. This represents a balance
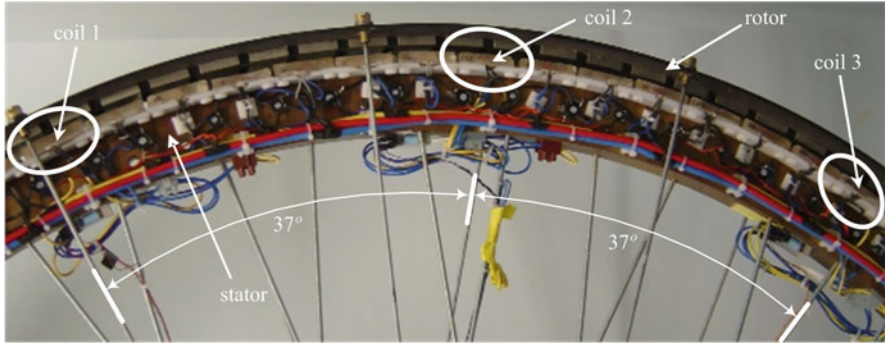
Fig. 7.7 Stator coils being shorted via remote relays (Yang et al. 2009)

Fig. 7.8 Unbalance mass attached on the rotor of synchronous generator
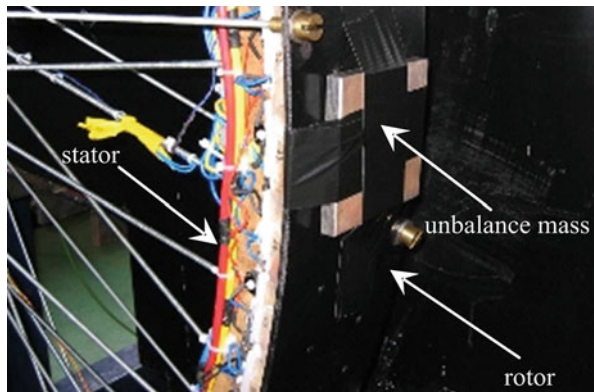
quality grade of G 7.8 (7.8 mm/s), within the limit of G 16 (16 mm/s) prescribed in ISO1940–1:2003 for a low-speed propeller shaft, applicable to a direct-drive WT shaft. The details of this estimation are given below.

Based on BS ISO1940–1:2003, the balance quality grade G may be calculated by

$$G = 2\pi e f_{rm} \tag{7.12}$$

where f_{rm} is the rotational frequency of the generator rotor and e is the specific unbalance that can be estimated by

$$e = \frac{mR}{M_{eq}} \tag{7.13}$$

where m refers to unbalance mass, R the effective radius of the equivalent unbalanced mass, and M_{eq} the equivalent rotating mass of the test rig rotor.

The mechanical unbalance U_m on the generator rotor can be calculated by

$$U_m = \frac{m}{M_{eq}} \times 100\% \qquad (7.14)$$

For the test rig shown in Fig. 7.5a, the unbalance mass $m = 1$kg, the effective radius of the equivalent unbalanced mass $R = 865$mm, and the equivalent rotating mass of the test rig rotor $M_{eq} = 290.7$kg. Thus, when the average rotational speed of the generator rotor is 25 rpm, the calculated balance quality grade and mechanical unbalance is $G = 7.8$ mm/s and $U_m = 0.3\%$, respectively.

The characteristic frequency used to detect the mechanical unbalance fault is

$$f_c = \frac{r}{60} \qquad (7.15)$$

where r indicates the rotational speed of the rotor of synchronous generator (unit: rpm).

C. *Electrical fault emulated on rotor of induction generator*

The electrical winding fault is simulated on the rotor of the induction generator by adjusting the phase resistances in the load bank externally connected to the generator rotor, as shown in Fig. 7.9.

In a healthy three-phase induction generator, the rotating field of the stator and rotor interacts and develops uniform torque. When the rotor resistances in three phases are unequal due to the presence of a winding fault, an opposite filed will be created to the stator that will introduce a twice slip frequency component in the power signal output from the generator. In reality, similar phenomenon can also be observed when the three phases of the power supply to generator stator are not perfectly balanced. But the effect created by an imperfect power supply is ignorable in comparison with that created by a rotor/stator winding fault. Therefore, the

Fig. 7.9 Simulate the electrical winding fault on the rotor of the induction generator
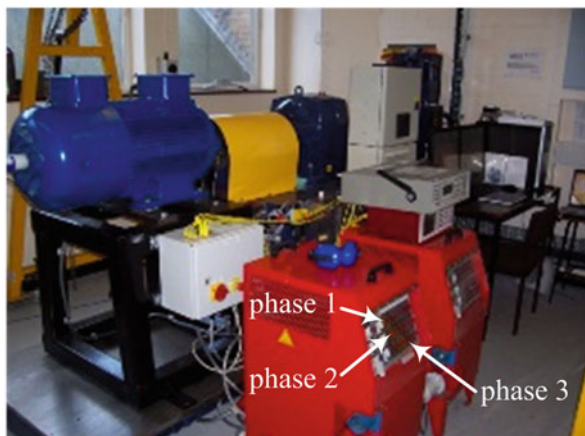
characteristic frequency for detecting the electrical fault is the twice slip frequency of the generator, which can be estimated by.

$$f_c = 2f_s \tag{7.16}$$

where f_s stands for the slip frequency of the induction generator. It can be calculated by (Yang et al. 2010)

$$f_s = \frac{N_p r - \omega_s}{60} \tag{7.17}$$

where ω_s is the synchronous rotational speed of the induction generator in the unit of rpm, r indicates the rotational speed of the rotor of induction generator, and N_p is the number of pole pairs of the induction generator.

In the experiment, the severity of the electrical winding fault is estimated by using an electrical asymmetry criterion U_e. In order to calculate the value of U_e, the details of the generator rotor circuit are shown in Fig. 7.10.

The balanced circuit resistances are given by

$$\begin{cases} R_{AB} = R_{AV} + R_{BV} + R_{AS} + R_{BS} + (R_A + R_B)/2 \\ R_{BC} = R_{BV} + R_{CV} + R_{CS} + R_{BS} + (R_B + R_C)/2 \\ R_{CA} = R_{CV} + R_{AV} + R_{AS} + R_{CS} + (R_C + R_A)/2 \end{cases} \tag{7.18}$$

where the circuits are balanced, giving $R_{AB} = R_{BC} = R_{CA} = \overline{R} = 7.60\ \Omega$, and

$$\overline{R} = (R_{AB} + R_{BC} + R_{CA})/3 \tag{7.19}$$
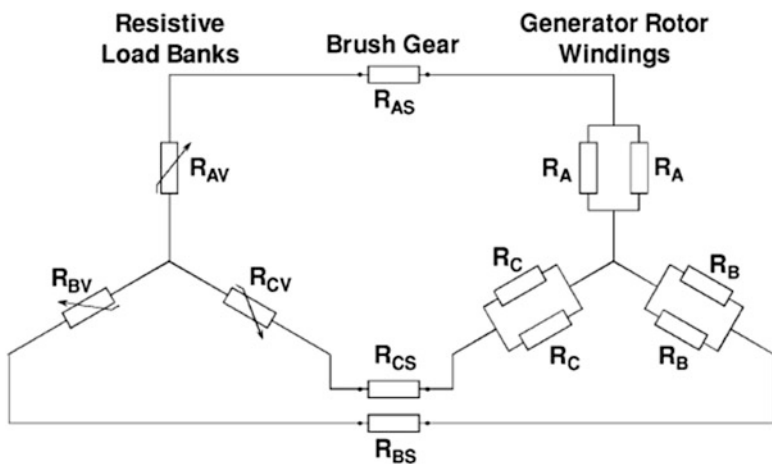
Fig. 7.10 Rotor circuit diagram including a resistive load bank

Then the electrical imbalance can be estimated through calculating the residual circuit resistance δR, i.e.,

$$\delta R = \left| R_{AB} e^{i\theta_1} + R_{BC} e^{i\theta_2} + R_{CA} e^{i\theta_3} \right| \tag{7.20}$$

where $i = \sqrt{-1}$, $\theta_1 = 0$, $\theta_2 = 2\pi/3$, $\theta_3 = 4\pi/3$.

Accordingly, the electrical asymmetry criterion U_e can be obtained by

$$U_e = \frac{\delta R}{R} \times 100\% \tag{7.21}$$

The larger the value of U_e, the more serious the electrical winding fault tends to be.

7.6 Verification Experiments

In this section, the WETT is applied to extracting the energy of total power signal at fault-related frequencies in different fault simulation scenarios. Then, the resultant variation tendency curve will be used to assess the health condition of the WT drivetrain. It is worth noting that in the following calculations, the time interval of the sliding window is $T = 1$s and the cutoff frequencies of the sliding window are adaptive to the rotational speed of the WT generator and calculated by Eq. (7.7).

7.6.1 Detection of the Stator Winding Fault in the Permanent Magnet Generator

When the test rig in Fig. 7.5a is running at variable speeds, the generator speed, shaft torque, and total power signals are collected. During the period of data acquisition, three stator coils indicated in Fig. 7.7 are simultaneously connected and shorted in sequence. The collected signals and the corresponding energy tracking results are shown in Fig. 7.11.

From Fig. 7.11a, it is seen that all collected signals are non-stationary over time and the time waveforms of both shaft torque and total power signals do not give any clear indication to the presence and absence of the fault. For this reason, the slotting frequency f_c is calculated using Eq. (7.11). The extracted energy of the total power signal at the frequency f_c is shown in Fig. 7.11b.

From Fig. 7.11b, it is clearly seen that although the slotting frequency f_c varies over time, the extracted energy curve of the power signal at this frequency gives a correct response to the presence and absence of the fault. In other words, the energy at this frequency increases immediately when the three coils are shorted and decreases to normal level as soon as the coils are re-connected. Apparently, the alteration of coil connection state in a WT can be correctly detected by using the developed WETT.
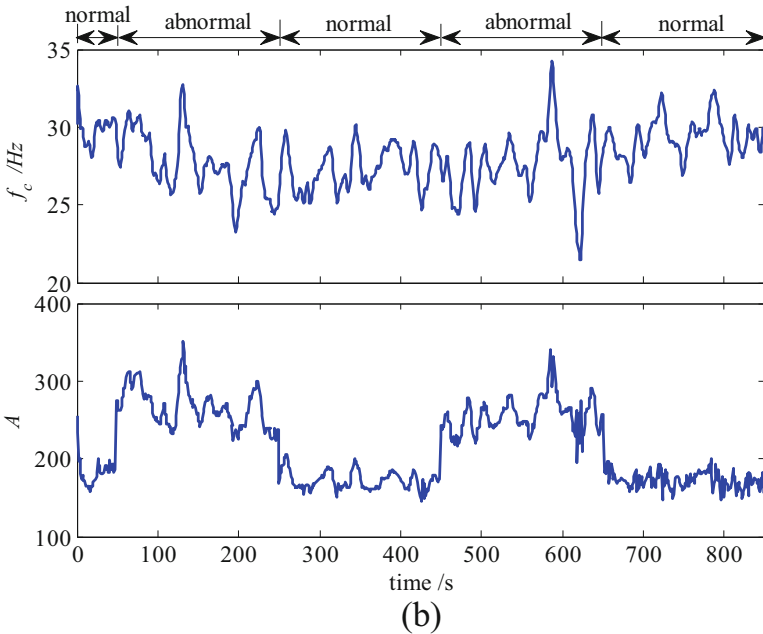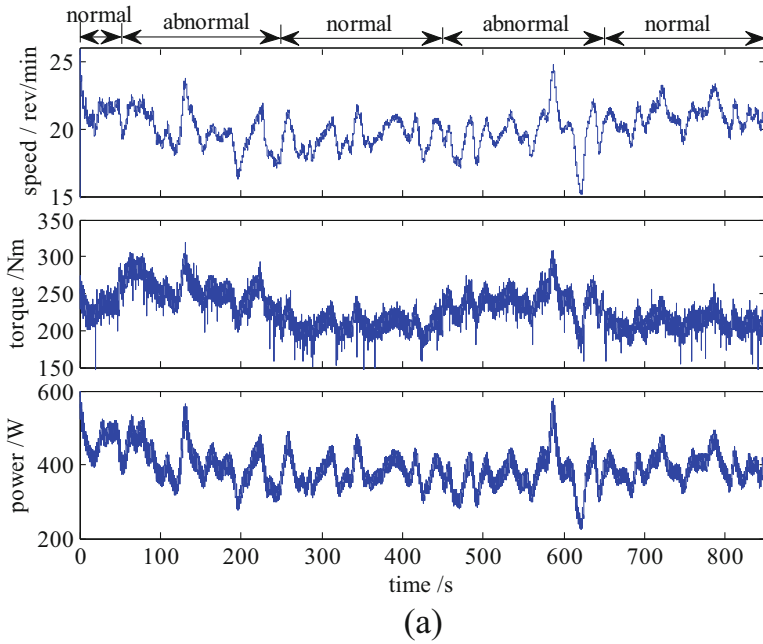
Fig. 7.11 Detection of the stator winding fault in the permanent magnet generator (**a**) Time waveforms of the signals (**b**) Energy A of the power signal extracted at the characteristic frequency f_c

7.6.2 Detection of the Mechanical Unbalance Fault in the Permanent Magnet Generator

As shown in Fig. 7.8, the mechanical unbalance fault is emulated on the permanent magnet generator by attaching an unbalance mass to the generator rotor. When the generator is running at variable speeds, the rotational speed, shaft torque, and total power signals are collected. The signals obtained before and after the unbalance mass are applied, and the corresponding energy tracking results are shown in Fig. 7.12.

From Fig. 7.12a, it is interestingly found that in the presence of the mechanical unbalance fault, the energy of the torque signal measured from the generator shaft fluctuates in a very large range. However, the time waveform of the total power signal seems to not give any indication to the fault. This is because the rotor and stator of the generator are both supported by steel spokes (Spooner et al. 2005). Accordingly, the WETT is applied to extract the energy of the total power signal at the shaft rotating frequency. The energy tracking results are shown in Fig. 7.12b.

As shown in Fig. 7.12b, the energy of the total power signal at shaft rotational speed slightly increases in the presence of the mechanical unbalance fault. Further investigation is necessary to amplify the frequency signatures with the unbalance masses in the permanent magnet generator.

7.6.3 Detection of the Electrical Asymmetry in the Rotor of the Induction Generator

As shown in Fig. 7.9, the electrical asymmetry is emulated on the induction generator by changing the phase resistances of the resistive load bank that is externally connected to the rotor of the induction generator. When the induction generator rotates at constant speed and the phase resistance of the resistive load bank changes periodically, the shaft rotational speed, shaft torque, and three-phase total power signals are collected. The collected signals and the corresponding energy tracking results are shown in Fig. 7.13.

From Fig. 7.13, it is clearly seen that both shaft torque and generator total power signals respond as soon as the fault occurs in the generator at the constant speed. In contrast to the shaft torque, the three-phase total power signal is relatively more sensitive to the electrical asymmetry fault. As shown in Fig. 7.13b, the extracted energy curve at the fault-related characteristic frequency based on the power signal almost concurrently indicates the occurrence of the mechanical unbalance fault.

In order to further demonstrate the capability of the WETT for WT CM, the shaft rotational speed, shaft torque, and three-phase total power signals are also collected when the generator rotates at variable speeds. The signals collected before and after the electrical asymmetry as well as the WETT results are shown in Fig. 7.14.
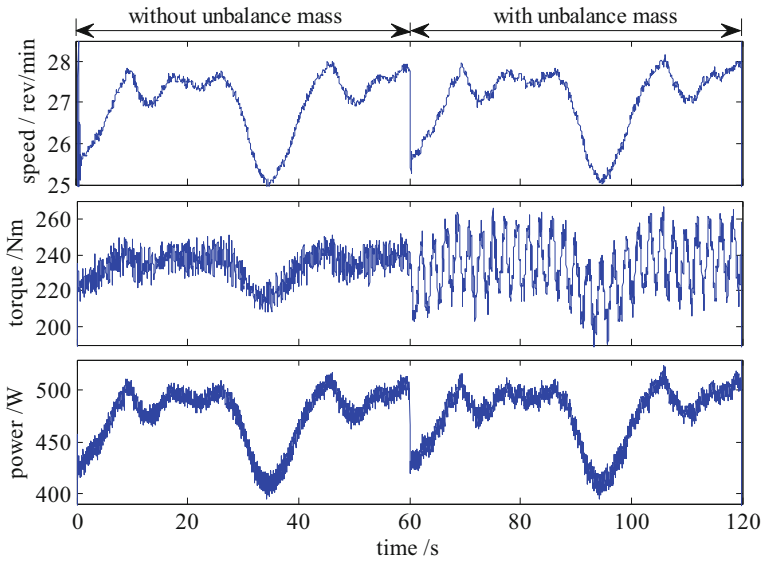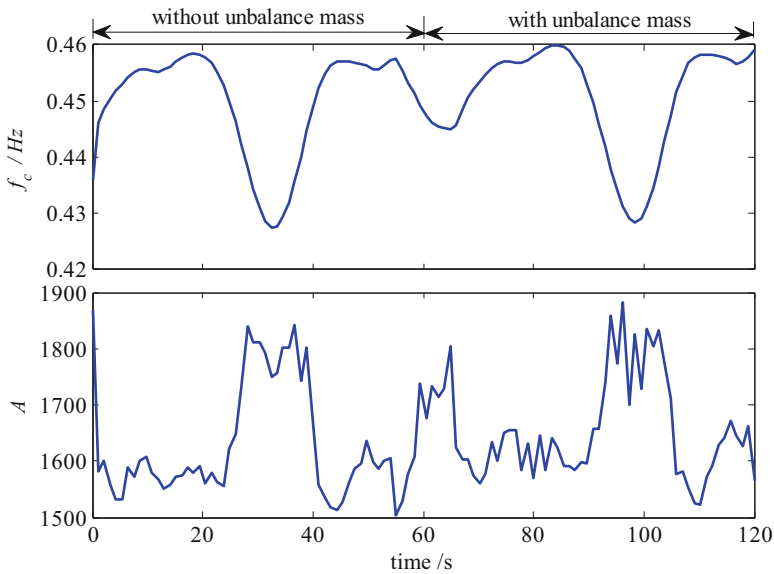
Fig. 7.12 Detection of the mechanical unbalance fault in the permanent magnet generator (**a**) Time waveforms of the signals (**b**) Energy A of the power signal extracted at the characteristic frequency f_c
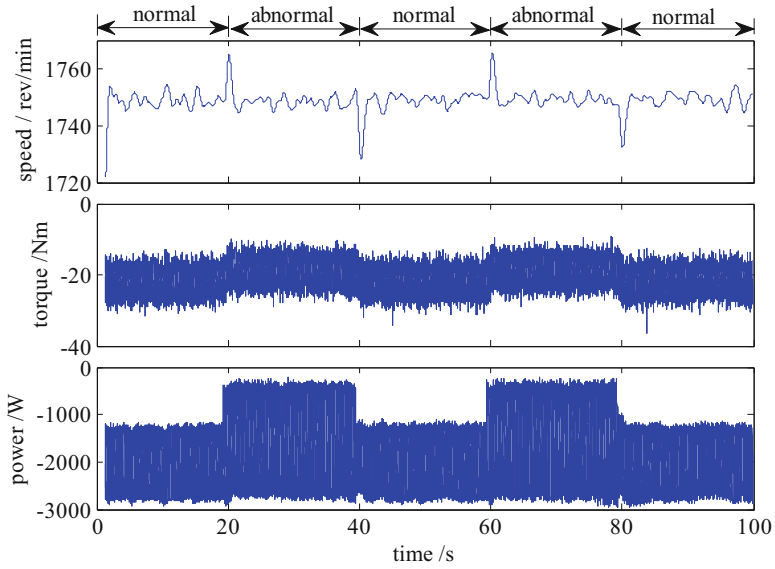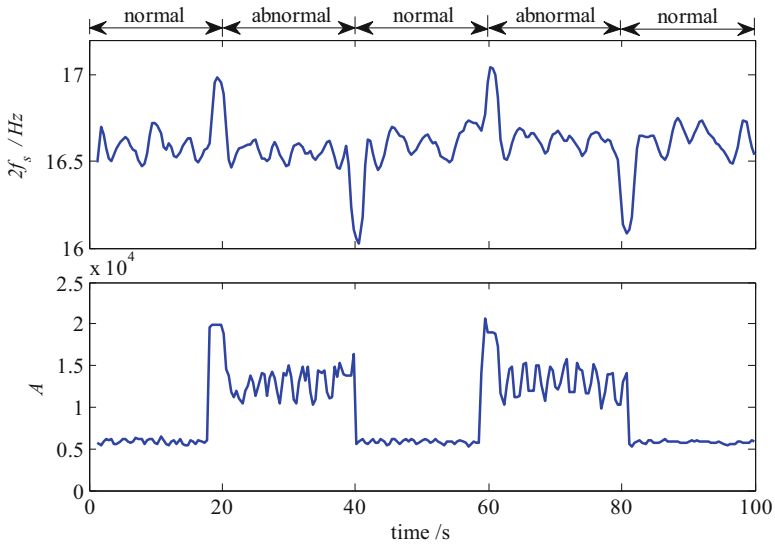
Fig. 7.13 Detection of the electrical asymmetry fault in the constant-speed induction generator (a) Time waveforms of the signals (b) Energy A of the power signal extracted at the characteristic frequency f_c
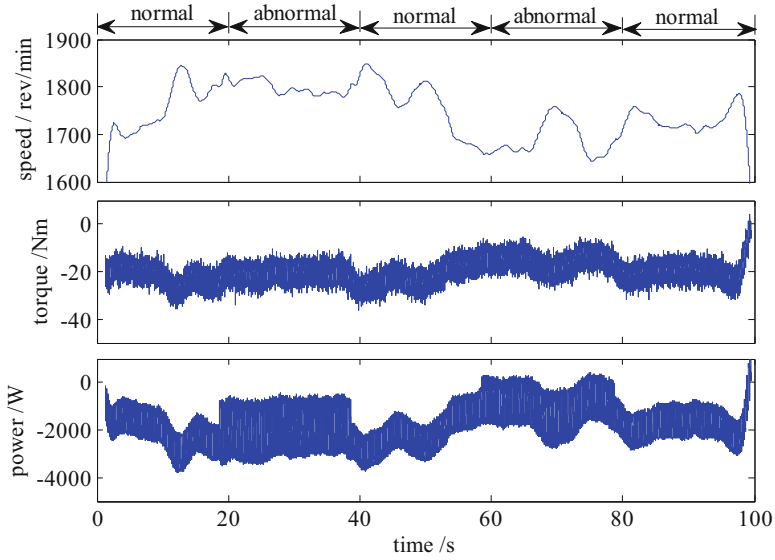
(a)
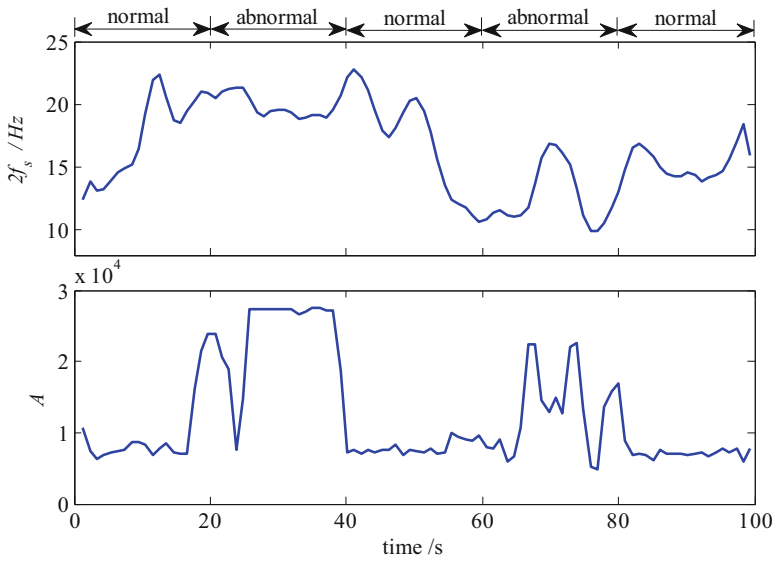
(b)

Fig. 7.14 Detection of the electrical asymmetry fault in the variable speed induction generator (**a**) Time waveforms of the signals (**b**) Energy A of the power signal extracted at the characteristic frequency f_c

From Fig. 7.14a, it is interestingly found that the time waveform of neither shaft torque nor total power signal is able to respond correctly to the presence of electrical asymmetry when the induction generator rotates at variable speeds. Thus, the WETT is applied to extract the energy of the total power signal at the twice slip frequency of the generator. The feature extraction results are shown in Fig. 7.14b.

From Fig. 7.14b, it is found that the extracted energy of the total power signal at the twice slip frequency responds correctly to the presence and absence of the electrical asymmetry in spite of the variation of generator speeds. This suggests that the newly developed energy tracking technique is indeed effective in extracting the fault-related features from non-stationary WT CM signals.

7.6.4 Detection of the Mechanical Unbalance Fault in the Rotor of the Induction Generator

The mechanical unbalance fault in the rotor of the induction generator is simulated by attaching two 0.25 kg unbalance masses on the input shaft of the induction generator, as shown in Fig. 7.1. The collected signals and the corresponding energy tracking results when the generator rotated at the constant and variable speeds are shown in Figs. 7.15 and 7.16, respectively.

From Fig. 7.15a, it is found that both time waveforms of the shaft torque and total power signals fail to indicate the presence of the shaft unbalance fault. However, from Fig. 7.15b, it is seen that the energy of the total power signal at shaft rotating frequency increases significantly as soon as the mechanical unbalance fault is applied to the shaft of the generator. When the generator runs at variable speeds, the fault detection becomes more challenging because the variable speeds will more or less smear the fault features in the CM signals, as shown in Fig. 7.16a. However, Fig. 7.16b shows that the fault-related feature of the total power signal is still successfully detected by the WETT, i.e., the energy of the signal at shaft rotational frequency increases significantly as soon as the mechanical unbalance is present on the shaft.

7.7 Concluding Remarks

A newly developed WT CM technique, i.e., the WETT using generator power signals, is introduced and experimentally verified in the above sections. From the above description and discussion, the chapter is ended with the following comments:

1. In contrast to the vibration signals collected from individual WT drivetrain components, the shaft torque and total power signals carry the health condition information of the entire drivetrain system. Both types of the signals allow
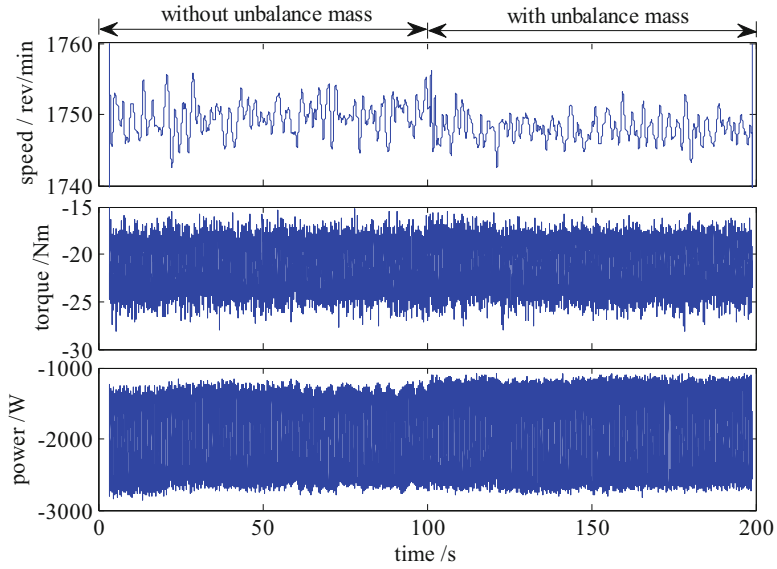
(a)
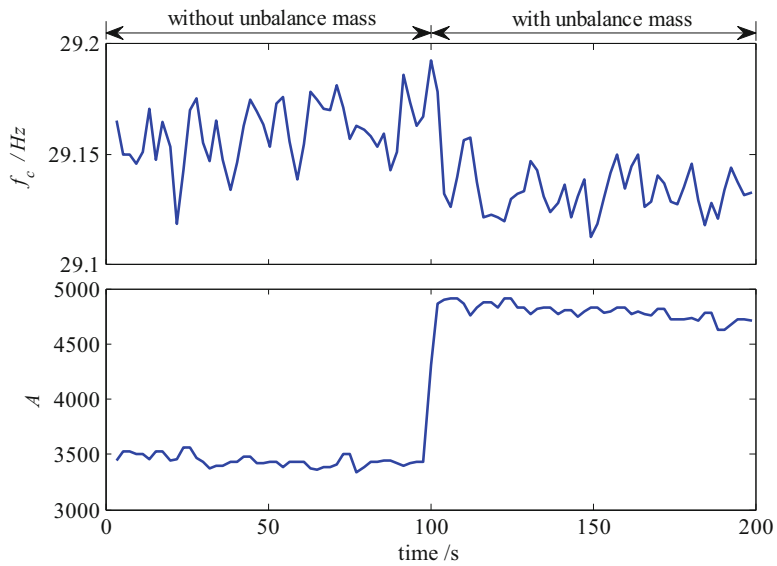
(b)

Fig. 7.15 Detection of the mechanical unbalance fault in constant-speed induction generator (**a**) Time waveforms of the signals (**b**) Energy A of the power signal extracted at the characteristic frequency f_c
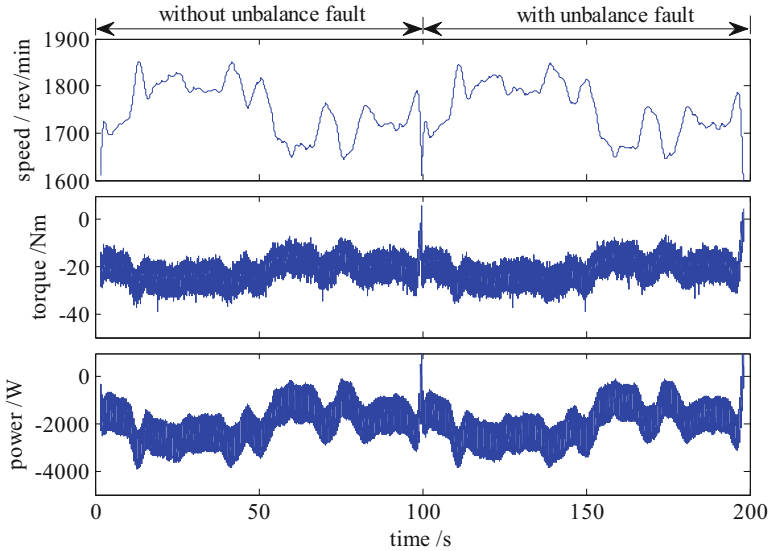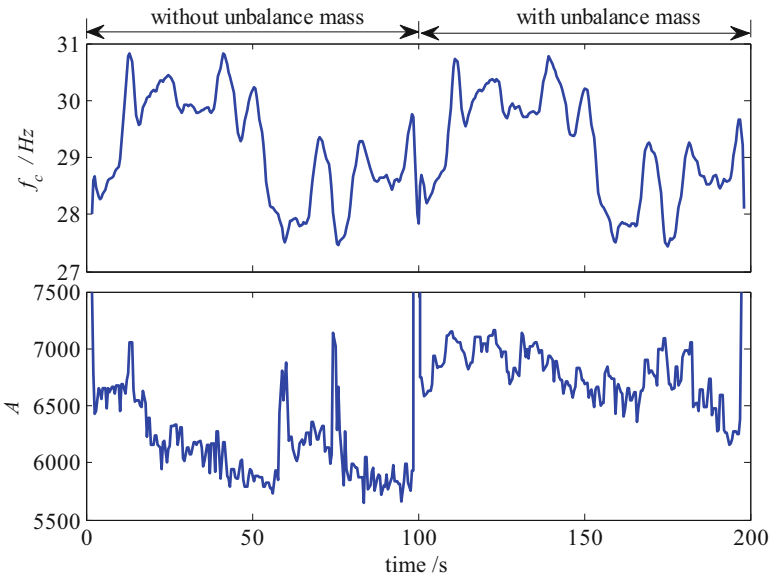
Fig. 7.16 Detection of the mechanical unbalance fault in variable-speed induction generator (a) Time waveforms of the signals (b) Energy A of the power signal extracted at the characteristic frequency f_c

to perform overall assessment of the health condition of the whole drivetrain. However, in the WT CM practice the measurement of shaft torque is not easy. Thus, the total power signal is more suited to the WT CM than the shaft torque signal.

2. The wavelet scalogram provides an effective tool to precisely process non-stationary CM signals. However, it involves complex calculations and cannot be applied to online WT CM. To address this issue, an innovative WETT is developed through introducing a two-dimensional time-frequency sliding window into the conventional wavelet scalogram. The WETT is efficient in calculation thus has a strong potential to be applied to either online or real-time WT CM.

3. Experimental test results validate that the WETT using the generator power signal is able to detect both the mechanical and electrical faults in the WT drivetrain system in both constant-speed and variable-speed scenarios.

References

Addison PS (2002) The illustrated wavelet transform handbook-introduction theory and applications in science, engineering, medicine and fiance. Institute of Physics Publishing, Bristol

Auger F, Flandrin P (1995) Improving the readability of time-frequency and time-scale representations by the reassignment method. IEEE Trans Signal Process 43(5):1068–1089

Basak D, Tiwari A, Das SP (2006) Fault diagnosis and condition monitoring of electrical machines – a review. In: IEEE international conference on industrial technology, 15–17 Dec 2006, pp 3061–3066. https://doi.org/10.1109/ICIT.2006.372719

Dhillon BS (2002) Engineering maintenance: a modern approach. CRC Press, Boca Raton

Ferguson D, Catterson V (2014) Big data techniques for wind turbine condition monitoring. Paper presented at the European Wind Energy Association Annual Event (EWEA 2014), Fira de Barcelona Gran Via, 10–13 Mar 2014

Hatch C (2004) Improved wind turbine condition monitoring using acceleration enveloping. Orbit 61:58–61

Li J, Sumner M, Arellano-Padilla J, Asher G (2010) Condition monitoring for mechanical faults in motor drive systems using the rectifier input currents. In: 5th IET international conference on power electronics, machines and drives (PEMD 2010), 19–21 Apr 2010, pp 1–6. https://doi.org/10.1049/cp.2010.0083

Peng Z, Chu F, He Y (2002) Vibration signal analysis and feature extraction based on reassigned wavelet scalogram. J Sound Vib 253(5):1087–1100

Qiao W, Lu D (2015) A survey on wind turbine condition monitoring and fault diagnosis—part I: components and subsystems. IEEE Trans Ind Electron 62(10):6536–6545

Ribrant J, Bertling L (2007) Survey of failures in wind power systems with focus on Swedish wind power plants during 1997–2005. In: 2007 IEEE power engineering society general meeting, 24–28 June 2007, pp 1–8. https://doi.org/10.1109/PES.2007.386112

Spooner E, Gordon P, Bumby J, French C (2005) Lightweight ironless-stator PM generators for direct-drive wind turbines. IEE Proc-Electr Power Appl 152(1):17–26

Tavner P (2008) Review of condition monitoring of rotating electrical machines. IET Electr Power Appl 2(4):215–247

Tavner P, Van Bussel G, Spinato F (2006) Machine and converter reliabilities in wind turbines. In: 3rd IET international conference on power electronics, machines and drives (PEMD 2006), Dublin, 4–6 Apr 2006, pp 127–130

Tavner P, Xiang J, Spinato F (2007) Reliability analysis for wind turbines. Wind Energy 10(1):1–18

Tavner P, Ran L, Penman J, Sedding H (2008) Condition monitoring of rotating electrical machines. The Institution of Engineering and Technology, London

Torrence C, Compo GP (1998) A practical guide to wavelet analysis. Bull Am Meteorol Soc 79(1):61–78

Wong LA, Chen JC (2001) Nonlinear and chaotic behavior of structural system investigated by wavelet transform techniques. Int J Non-Linear Mech 36(2):221–235

Yang W, Court R (2013) Experimental study on the optimum time for conducting bearing maintenance. Measurement 46(8):2781–2791

Yang W, Tavner P, Wilkinson M (2009) Condition monitoring and fault diagnosis of a wind turbine synchronous generator drive train. IET Renew Power Gener 3(1):1–11

Yang W, Tavner PJ, Crabtree CJ, Wilkinson M (2010) Cost-effective condition monitoring for wind turbines. IEEE Trans Ind Electron 57(1):263–271

Yang W, Tavner PJ, Crabtree CJ, Feng Y, Qiu Y (2014) Wind turbine condition monitoring: technical and commercial challenges. Wind Energy 17(5):673–693

Chapter 8
Advanced Repairing of Composite Wind Turbine Blades and Advanced Manufacturing of Metal Gearbox Components

Ninggang Shen and Hongtao Ding

8.1 Introduction

8.1.1 Composite Wind Turbine Blades

In a wind turbine, composite materials are mainly used in the turbine blades and nacelle as shown in Fig. 8.1. The blades, usually made of glass fiber reinforced polymer (GFRP), represent the largest use of composite material (Tangler 2000). In total, the components made of composite materials make up 25% of the total cost of a wind turbine (Platzer 2012). Each wind turbine must withstand the force of wind and all the debris it brings with it and, thus, must be regularly monitored, maintained, and repaired to remain functional (Lantz 2013). The sources of blade damage include mishandling during delivery and/or installation, lightning strikes, ice, thermal cycling, leading and trailing edge erosion, fatigue, moisture intrusion, and foreign object impact (Cairns et al. 1999, Cairns et al. 2011; Rumsey 2009). Keeping blades in good condition is vital to the ability of the turbine to generate its designed power for a targeted design life of 20 years. In addition, wind turbines have grown larger, which led to large, multistage gearboxes and large bearings. Many require replacement/overhaul at 5–7 years and significantly drive up the cost of ownership.

The wind turbine blades are subject to material fatigue, bird strikes, lightning strikes, and leading edge erosion, especially, toward the tips that can be moving through the air at around 200 mph. In addition, the severe conditions in the surroundings usually accelerate the damage propagation, e.g., ice, thermal cycling,

N. Shen (✉) · H. Ding
Department of Mechanical and Industrial Engineering, The University of Iowa, Iowa City, IA, USA
e-mail: ninggang-shen@uiowa.edu

Component	Cost
Tower	26.30%
Rotor Blades	22.20%
Rotor Hub	1.37%
Rotor Bearings	1.22%
Main Shaft	1.91%
Main Frame	2.80%
Cables	0.96%
Gearbox	12.91%
Generator	3.44%
Yaw System	1.25%
Pitch System	2.66%
Power Converter	5.01%
Transformer	3.59%
Brake System	1.32%
Nacelle Housing	1.35%
Screws	1.04%
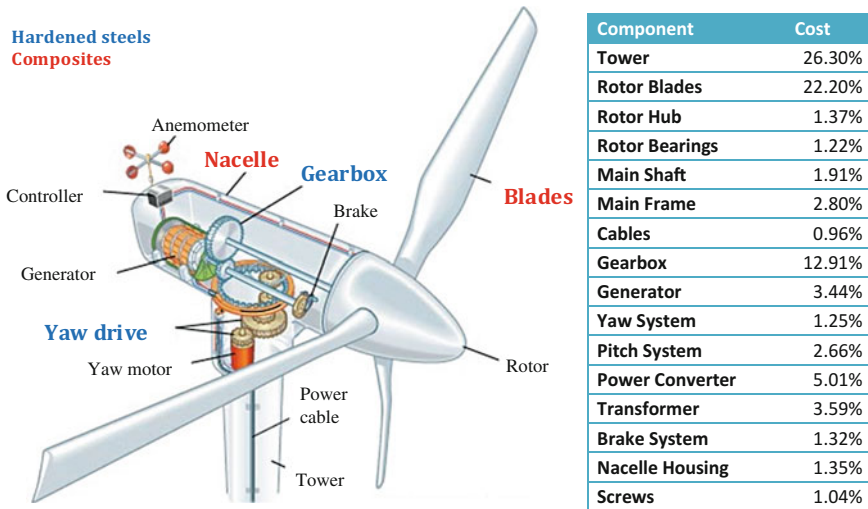
Fig. 8.1 Major wind turbine components and cost (Shen et al. 2013)

moisture intrusion, sand and salt laden, surface erosion from rain, hail, ice and insects. Even relatively small amounts of leading edge erosion can affect the aerodynamic performance of the blade and lead to consequent loss of revenue. If erosion of leading edges is left unrepaired, damage will accumulate and eventually cause catastrophic failure such as the blade edge split or debonding of a section. Figure 8.2a shows some commonly observed damages after only a few years of service: surface cracking, cavity, erosion, near-surface delamination, and severe debonding. Figure 8.2b shows the levels of impact damage observed in the laminates. Even without actual damage, surface roughness caused by minor pitting and particle accretion can spoil the aerodynamic efficiency of the blades, detracting from turbine productivity. With a growing number of blades now in service, many well outside their warranty periods, rotor blade maintenance is becoming a major issue.

Cost-effective onsite repairing of wind turbine blades is very critical for building up the wind energy industry for the next crucial years (Sheng 2013). Repairing the blades is no trivial matter. An average blade repair can cost up to \$30,000, while it can be ramped up to \$350,000 per week if crane is required (Stephenson 2011). In comparison, a new blade costs only about \$200,000 on average. Most rotor blades carry post-installation warranties for only 1–2 years. For structures with an expected service life of 15–20 years, this leaves much of the blade's maintenance outside the warranty window. In fact, as a result of the 2007–2009 wind energy boom, there are now more turbines with expiring warranties than actual turbines being installed (Stephenson 2011). This is putting immense pressure on wind farm managers as they try to optimize turbine uptime.
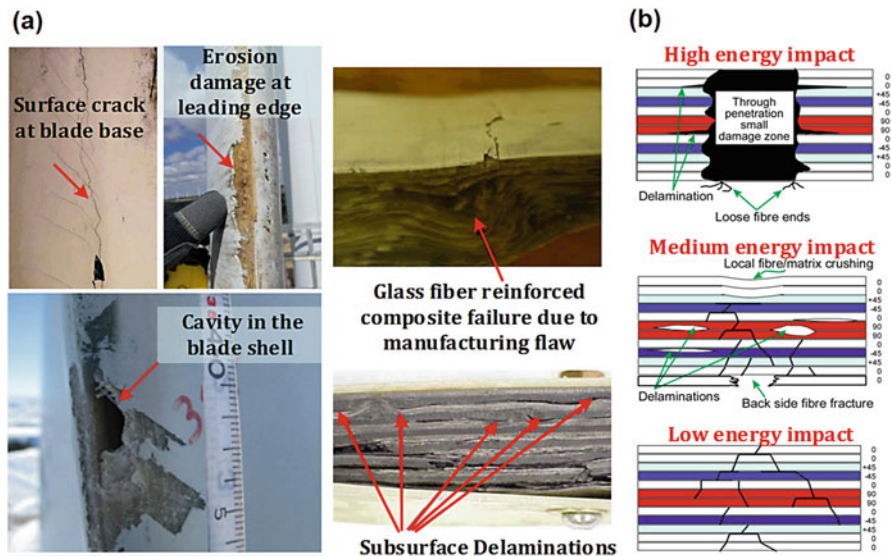
Fig. 8.2 Composite material damage in a wind turbine. (Courtesy of Rumsey (2009), Halliwell (2010), Cairns et al. (2011), MISTRAS Group (2013)) (**a**) Typical damages, (**b**) Damage levels

8.1.2 Metal Gearbox Components

The metal components of wind turbines, e.g., gearboxes, are designed to operate over a calculated service life. As shown in Fig. 8.1, the gearbox and bearing components contributed 15% of the total cost of a wind turbine. Extraordinarily high costs to manufacture and maintain is the main issue to confine the expansion of the share of wind turbine in the energy consumption. For traditional wind turbine, the critical components in the gearbox usually need to be replaced soon. In recent years, size and capacity of wind turbines have increased significantly to meet the ambitious worldwide renewable energy targets, resulting in the use of larger multistage gearboxes (Ribrant and Bertling 2007; Jain and Hunt 2011). Multi-megawatt wind turbine gearboxes usually fail after only a few years due to the demanding environmental conditions, even though they are usually rated for a life span of 20 years (Sroka and Benson 2011). The growing wind turbine size raises the expense even higher.

According to data from the National Renewable Energy Laboratory (NREL) as shown in Fig. 8.3, 70% of wind turbine gearbox failures were caused by bearing failures, e.g., macro-pitting and axial cracks formed on the bearings during high- and intermediate-speed stages (Department of Energy 2015). Gears were identified as the second leading cause of gearbox failures (26%) followed by other components that account for 4% of the failures. Among the other components, lubrication and filtration system problems are dominant (Department of Energy 2015). These
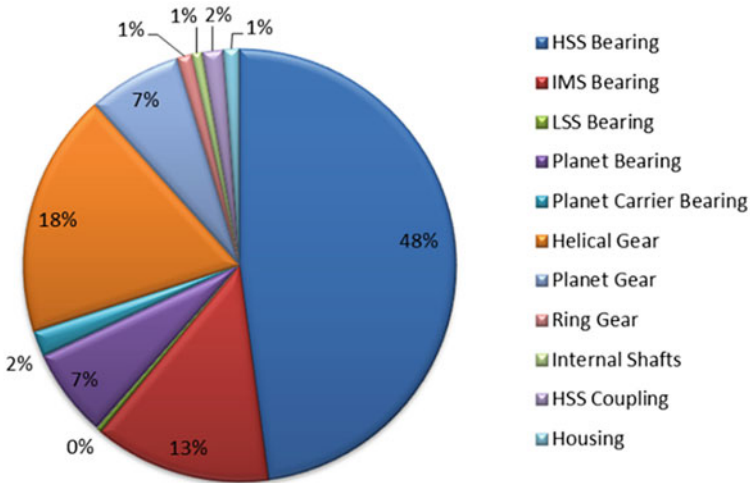
	Damage Records	Bearings	Gears	Others
Planetary	44	23	21	
IMS	N/A	34	47	9
HSS	N/A	123		
Total	257	180	68	9

Fig. 8.3 Statistics of gearbox failures based on 750 confirmable wind turbine gearbox damage records in the USA (Sheng 2014; Department of Energy 2015)

statistics are based on 750 confirmable wind turbine gearbox damage records provided by wind plant owners and operators from 2009 through August 2015. The owners and operators participating in this effort represent 34% of the wind capacity in the USA. Figure 8.4 shows the typical failure of bearings and gears in the wind turbine gearbox, which are usually considered as irreparable.

The failure of bearings and gears in typical bearing steels, e.g., AISI 51200 and 4320, is usually attributed to many reasons, such as inadequate lubrication, deficient sealing, improper mounting, overloading, or other tribological issues (Harris 2001; Errichello et al. 2013; Kang 2014; Šmeļova et al. 2017). Hence, numerous efforts have been performed on tribology and metallurgy over the past decades to determine mitigation strategies for gearbox failures. Moreover, the manufactured components are expected to demonstrate superior quality and enhanced functional performance with properly engineered manufacturing techniques.
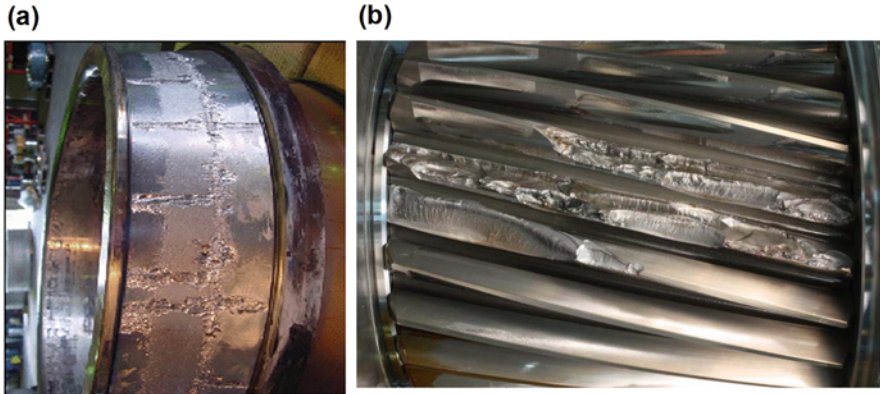
Fig. 8.4 Typical wind turbine gearbox failure: (**a**) Bearing failure; (**b**) Gear failure (Shen et al. 2013; Sheng 2014)

It has been widely acknowledged in the manufacturing community that the functional performance of a manufactured component, especially for machining, can be significantly affected by the quality and reliability of the machined surface, i.e., surface integrity (M'Saoubi et al. 2008). The surface integrity of manufactured components has a critical influence on their functional performance, including corrosion resistance, wear resistance, fatigue life, etc. (Field et al. 1972). The surface integrity attributes usually can be grouped as topography characteristics, mechanical properties, and metallurgical state (Ulutan and Ozel 2011). The alternation of metallurgical state, including microstructure, phase transformation, and grain size, usually results in the change of mechanical properties, such as hardness and residual stress (Field et al. 1989). In the past few decades, many researchers have investigated the nature of the surface and subsurface alterations produced by machining of various materials and their effects on the product's functional performance (Jawahir et al. 2011). The advancement of the knowledge in this field can continually improve the performance, reliability, and durability of manufactured components/parts under severe loading conditions and aggressive environment.

In this chapter, both conventional and state-of-the-art repairing techniques for wind turbine blades (composites) are first introduced in Sect. 8.2. Section 8.3 summarizes current machining process of hardened steels for bearing and gearbox components and current achievements in novel machining process of hardened steel components, such as laser-assisted machining and cryogenic machining. Finally, an overview is provided in Sect. 8.4 on the future applications of the advanced repairing technologies for wind turbines, as well as associated challenges for the future advanced manufacturing technologies for metal gearbox components.

8.2 Wind Turbine Blade Repairing

8.2.1 Conventional Methods

The repair approaches can be broadly divided into non-patch, usually for minor defects, and patch, usually for more major defects and damage. In this chapter, the repair techniques for major defects and damages are mainly discussed. When the damage has weakened the structure through fiber fracture, delamination, or debonding, a structural repair is often needed, which involves replacement of the damaged fiber reinforcement, and core in sandwich structures, to restore the original mechanical properties. The typical structural repair procedures for a wind turbine blade consist of four steps: (1) damage removal and preparation of the damaged site, (2) hand lay-up, (3) post-cure, and (4) leading edge coating application. Figure 8.5 shows an example structural repair work for a lightning blast damage in a wind turbine blade (Performance Composite Inc. 2015).

There are three typical laminate repair styles: (a) patch repair, (b) tapered-scarf repair, and (c) stepped scarf repair. The schematic of these styles is shown in Fig. 8.6. Patch repair is the most common structural repair carried out on wind turbine blades, which is usually applied by wet lay-up techniques. The damage site

Fig. 8.5 An example of current structural repairing. (Courtesy of Performance Composite Inc. (Performance Composite Inc. 2015))
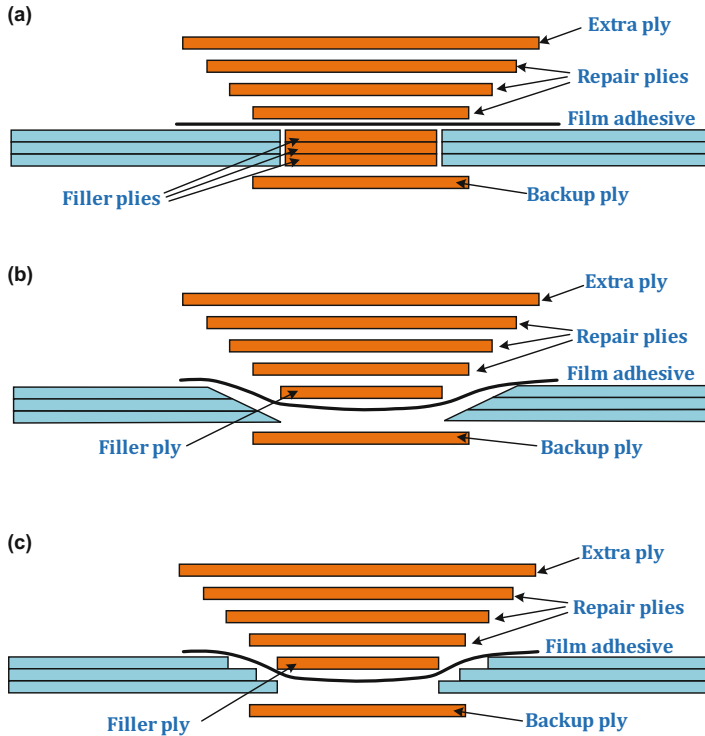
Fig. 8.6 Repair for laminates. (Courtesy of Hexcel Composites (Hexcel Corporation 2015))
(**a**) Patch repair, (**b**) Tapered scarf repair, (**c**) Stepped scarf repair

is not necessarily to be cut cleanly, but the contact surface should be flat, abraded, and degreased (Composites UK 2015). This type of repair is relatively easy to implement and needs the least preparation, which is an ideal option for a fast and urgent "field repairs." Due to its poor appearance and limitation on strength, the repair patches are usually temporary (Halliwell 2010).

The scarf joint repair is favored for strength-critical applications and where it is necessary to restore a surface's aerodynamic or hydrodynamic profile. The scarf joint repair is usually designed to achieve a stronger shear strength than tensile strength of the original material by about 100% (Composites UK 2015). It has been tested that about 90% of the original strength of the undamaged material can be restored by the scarf joint repair for aircraft repair (Arnot-Perrett and Gibson 1998; Smith et al. 1998). Preparation for the scarf repair is usually performed carefully using power tools with routers or abrasive disks to achieve tapered or stepped scarf. Either wet resin lay or prepreg materials can be used, usually based on those with which the blades were originally built. Surroundings of vacuum and specific elevated temperatures are usually required for the repair consolidation. Portable hot bonder devices have been developed and currently available on the market for the
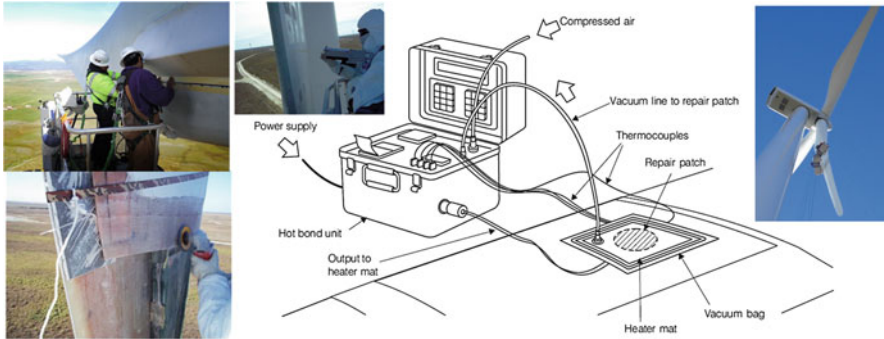
Fig. 8.7 Current structural repair using wet laminating process. (Courtesy of TGM Wind Services LLC; Hexcel Corporation (2015))

on-site repairs as shown in Fig. 8.7. For more complex and higher-quality repairs, an autoclave should be used (Composites UK 2015).

Although scarf joint repair is favored for strength-critical applications, there are significant limitations for this repair style. Scarf repairs often use a high taper ratio (20:1–50:1) for best results, which often poses a great challenge for on-site repair of wind turbines (Halliwell 2010). It is also very difficult avoid the fiber damage in the remaining material around the scarf during routing/abrading, which could cause the initiation of new damage in future. Wet resin systems are used in these repairs, usually based on the ones with which the blades were originally built, so resins must be accurately mixed on the ground just prior to use and hauled up. Hence, the proficiency and attention to details of operators are highly demanded, which make this technique the most expensive to undertake. Furthermore, there is a narrow weather window for these wet resin systems to work (typically at temperatures above 12–15 °C), and they need an elevated temperature post-cure (Cripps 2011). The repair operations are usually performed on a maintenance platform or in a roped position. These situations further increase the difficulty, downtime, and cost of the wind turbine blade repair.

8.2.2 Advanced Methods

Advanced, cost-effective repairing of wind turbines blades is very critical for the wind energy industry. Currently, heat activated curing prepreg has been widely applied to repair wind turbine blades. The curing time can be significantly reduced to about 3 h by using the heat activated curing prepreg, whereas it usually takes 24 h or even days for curing under the ambient environment. However, this approach needs heat and pressure for curing, which could cause a few issues for field-level curing. First, the temperature must be precisely controlled to assure uniform curing, which is challenging for field-level repairing. Second, pressurization of prepreg layers

can be quite complicated when coupled with the heating requirements (Pang et al. 2004). Therefore, advanced repairing techniques should be developed to address these issues.

A breakthrough occurred in polymers when ultraviolet (UV) curing resins were developed in the 1980s. UV curing resins act through photopolymerization by free radicals. Photoinitiators are added to the basic resin chemical constituents of monomers, oligomers, thickeners, and adhesion promoters. Photoinitiators are organic molecules that become excited when exposed to ultraviolet radiation. The excited molecules degrade and produce free radicals, which initiate polymerization of the monomers and oligomers. Curing time can be reduced to 1–30 min, depending on the monomer, photoinitiator, and the light intensity. In general, higher light intensity decreases the overall curing time and oxygen inhibition of polymerization (Pang et al. 2004).

Recently, instead of heat and pressure, a new blade repair system, RENUVO™ multipurpose system (MPS), has been developed by Gurit UK, which uses strong UV light to harden the UV-curable resin in minutes rather than hours (Marsh 2011). The system can be used either as a stand-alone spot repair (small repairs) or in combination with RENUVO™ Prepreg for a structural repair (replace or reinforce the blade laminate) (Gruit UK 2017). For a structural repair, the damage is usually removed by manual blade grinding or routing, and the edges are beveled for a scarfed repair to increase the bonding area. Then, RENUVO™ Prepreg can cut into the desired size to fit the repair site and be applied in single or multiple layers. This prepreg is a biaxial or unidirectional fabric, which has been impregnated with the RENUVO™ resin system already. It can remain uncured for several years if stored in cool and dark conditions (Marsh 2011). Two MPS resin grades are available: a summer grade for the use in temperatures of 15–30 °C and a winter grade for 5–18 °C. The MPS resin acting as the interface to form the bonding to the remaining blade laminates. Full cure can be obtained in about 180 s for repairs up to 3 mm thick, using the large RENUVO™ LED 400F lamp. For large repairs, a specially designed lamp mounting system can be applied to ensure that each part of the patch receives the correct UV dose. Figure 8.8 demonstrates the standard procedure using RENUVO™ system from applying the prepregs to UV curing. It is worth noting that the necessity of a special mounting system, as well as a high requirement for protective precautions, still confined the application of RENUVO™ system for an even larger repair than as shown in Fig. 8.8.

8.2.3 Discussions

The conventional repair techniques have been developed for decades and extensively applied throughout most sectors of industry, including wind energy, and numerous efforts have been made on the improvement or invention of the existing or novel techniques. The advanced technique, e.g., the UV curing repair system like

Using the RENUVO system, a prepreg patch is rolled into position using the MPS paste as a 'wetting' layer to the blade surface.

Excess MPS paste is squeezed out from under the prepreg patch.

MPS paste is also used to provide a smooth, sandable top surface to the prepreg patch.

Peelply is applied as a final layer to ensure an even patch surface.

The RENUVO LED400F lamp is used with the indexing   to ensure the whole repair is evenly cured.

After the UV exposure the patch is completely cured, the peelply can be removed and the repair painted.

Fig. 8.8 The standard procedure of RENUVO™ system (Marsh 2011)

RENUVO™, still adopts the conventional repair design as shown in Fig. 8.6. However, there are a wide range of repair issues to be solved.

For these conventional repair designs, a bonded-on repair constitutes a discontinuity of the original plies, and therefore a stress raiser, structural repair schemes normally require extra plies to be provided in the repair area (Hexcel Corporation 2015). The repair with those extra plies can be unsightly and bulky with much limited strength restoration (Composites UK 2015). The bonding strength of the thermoset resins (or UV curing resin) is of critical importance for structural repairs. However, due to the inherent weakness of the resin matrix, the current joining technology cannot reliably restore the original strength of the composite structure (Halliwell 2010). In fact, the resin-rich region is the major source of delamination (Vizzini and Lee 1995; Sørensen et al. 2004; Giannis et al. 2008). Once initiated, cracks are detrimental to the life of the composite structure, which has been found to be a key failure mechanism of the composite wind turbine blades (Stig 2009; Lomov et al. 2009). It is also well known that complex repairs (i.e., step-lap and tapered-

scarf repairs) possess the higher bonded joint strength comparing with single-lap joints (Soutis and Tong 2003). At the same time, these more complex repairs are time-consuming and difficult to apply. Moreover, a large amount of the undamaged material has to be removed in the process of forming the required taper angle and deviation from the prescribed repair procedure could lead to undesirable stress concentrations and premature structural failure (Baker et al. 2004; Duong and Wang 2010; Khashaba et al. 2010). Additionally, resins must be accurately mixed on the ground just prior to use and hauled up, often subjected to a narrow weather window. Hence, the proficiency and attention to details of operators are highly demanded, which make these techniques expensive to undertake.

During the repair operation, technicians are normally roped up or stand on a platform suspended from the rotor hub. The subject blade is stopped in the down position. Anchor lines may be deployed to the tower or around the blade. Even with a small working space during repair, a variety of tools are needed for the technicians to take or have them hoisted up or lowered down to the working position to carry out structural repair on-site. The essential tools include power router/sander, heater mat, hot bond unit, air-powered tools, repair patches, wet resin systems, power supply, etc. Safety requirement and the low mobility of these tools pose a great challenge for the technicians in air. Therefore, there is still a great need for the development of the next-generation joining method for fiber-reinforced polymers and on-site repairing technology.

8.3 Advanced Manufacturing Technologies for Metal Gearbox Components

8.3.1 Hard Turning

Hardened bearing steels components have been conventionally finished by grinding and hard turning (Poulachon and Moisan 1998; Matsumoto et al. 1999; Klocke and Kratz 2005; Hashimoto et al. 2006). Hard turning is typically defined as the single point turning of post-heat-treated parts with surface hardness ranging from 45 in Rockwell scale (HRC) to 68 HRC or even higher. In comparison to grinding, hard turning can introduce greater flexibility in manufacturing complex geometry and significantly higher material removal rate, while a comparable surface finish still can be achieved. In addition, hard turning process is usually more eco-friendly than grinding, since it can be performed in a dry cutting condition (Bartarya and Choudhury 2012).

Hard turning has been proven to be a worthy alternative to the more expensive and time-consuming grinding process (Ramesh et al. 2005). Process-induced residual stress and its effect on component performance such as fatigue life are key criteria for process selection and optimization. As shown in Fig. 8.9, Guo et al. (2010) summarized that the most significant differences in the characteristics
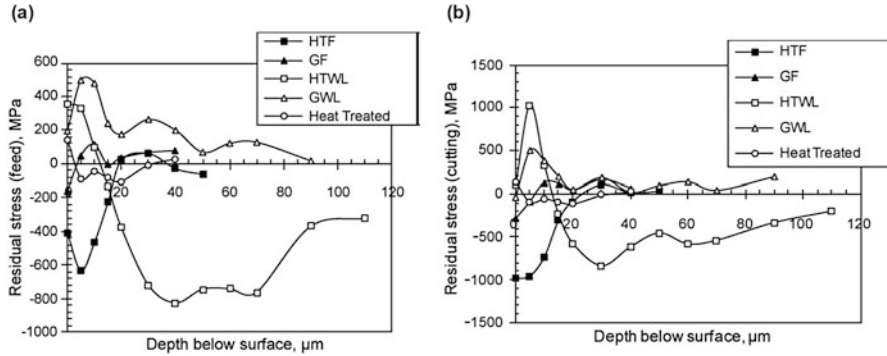
Fig. 8.9 Residual tress profiles in (**a**) Feed direction and (**b**) Cutting direction for hard turned fresh (HTF) surface, ground fresh (GF) surface, hard turned surface with white layer (HTWL), and ground surface with white layer (GWL). "Heat treated" was the original residual stress profile before hard turning or grinding (Guo et al. 2010)

of residual stress profiles by "gentle" hard turning and grinding are manifested in two aspects: (i) hard turning with a sharp cutting-edge geometry (honed or chamfered) generates a "hook"-shaped residual stress profile characterized by compressive residual stress at the surface and maximum compressive residual stress in the subsurface. While gentle grinding only generates maximum compressive residual stress at the surface. (ii) The depth of compressive residual stress in the subsurface by hard turning is much larger than that by grinding. But the magnitude of compressive residual stress at a ground surface is usually higher than that at a turned surface. Due to these residual stress characterizations for hard turned steel surface, without the formation of white layer, a superfinished turned surface may have a roll contact fatigue life twice as long as that of a superfinished ground surface (Hashimoto et al. 2006).

However, there are several issues related to this process for hardened steels that require further investigation, which can strongly affect the surface integrity and the quality of machined products (Umbrello et al. 2012a). The major issues are due to undesired microstructure changes in the machined surface for hardened steels (Chou and Evans 1999; Akcan et al. 2002; Barry and Byrne 2002; Ramesh et al. 2005; Todaka et al. 2005; Li et al. 2007; Han et al. 2008; Burns et al. 2011a, b; Jawahir et al. 2011), which is mainly associated with the high temperatures at the tool-chip and tool-workpiece interfaces in conjunction with the severe plastic deformation (SPD) and dynamic phase transformation.

This undesirable microstructure is often termed as "white etching layer" (WEL) or "white layer" because it appears to be featureless and white when it is viewed under an optical microscope as shown in Fig. 8.10. The formation of WEL has been a great interest in the past decades. Griffiths (1987) attributes white layer formation to one or more of the following possible mechanisms: (1) rapid heating and quenching, which results in dynamic phase transformation; (2) severe plastic

Fig. 8.10 Optical micrograph of a white layer in a sectioned and etched surface of BS 817 M40 steel of 52 HRC. (Figure is adopted from Barry and Byrne (2002))
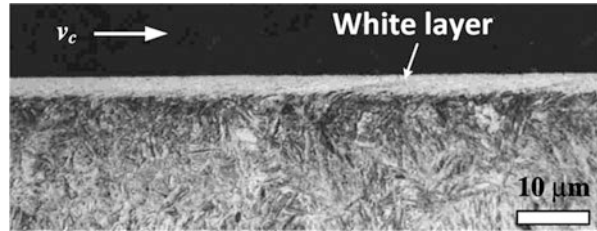
deformation, which produces a refined homogeneous structure; and (3) surface reaction with the environment, e.g., nitriding. Jawahir et al. (2011) argued that metallurgical transformation occurs in the chip or on the workpiece machined surface due to intense, localized, and rapid thermomechanical working during hard turning. Ramesh et al. (2005) suggested that white layers produced by hard turning of bearing steel at low-to-moderate cutting speeds are largely due to the grain refinement induced by SPD, whereas white layer formation at high cutting speeds is mainly due to thermally driven phase transformation. Studies of the drilling of a commercial bearing steel (type SUJ2) in a tempered martensitic structure by Todaka et al. (2005) showed that the white layers formed on the machined surfaces were composed of refined equiaxed nanocrystalline grains. They stipulated that the ultrafine structure layer on the machined surface is produced by both thermally and deformation-driven phase transformation, due to the large strain gradient and high strain rates during the process. Li et al. (2007) showed that both cutting parameters and initial workpiece hardness play vital roles in the white layer formation. Burns et al. (2011a, b) have reported that for carbon steels, e.g., AISI 1045 and 1075 steels, the phase transformation drastically changed the material constitutive behaviors at high temperatures. Hence, the white layer formation in machining of steels should be considered as a coupled effect of dynamic phase transformation and grain refinement process, although there are still different understandings of the mechanism of its formation.

Although the thickness of the white layer is usually only several micrometers, the presence of it causes great concern in the machining industry and academia, which is often very detrimental to component life in roll contact (Schwach and Guo 2006). The white layer has a significantly increased hardness compared with the bulk material, but tensile residual stress is usually associated with the presence of white layer. Samples with white layer showed significantly more cracks in the subsurface domain than those without white layer. As a result, the white layer induced by worn tool in hard turning is very detrimental to the roll contact fatigue (RCF). The RCF life can be decreased as much as eight times with the hard turning-induced white layer as shown in Fig. 8.11. Even shorter RCF life can be caused by thicker white layer.

The white layer formation can usually be facilitated using worn tools under aggressive machining conditions, such as higher cutting speed and greater feed rate. During hard turning, the generated heat mainly remains in the cutting zone and builds up temperature to extreme values, causing softening of the cutting
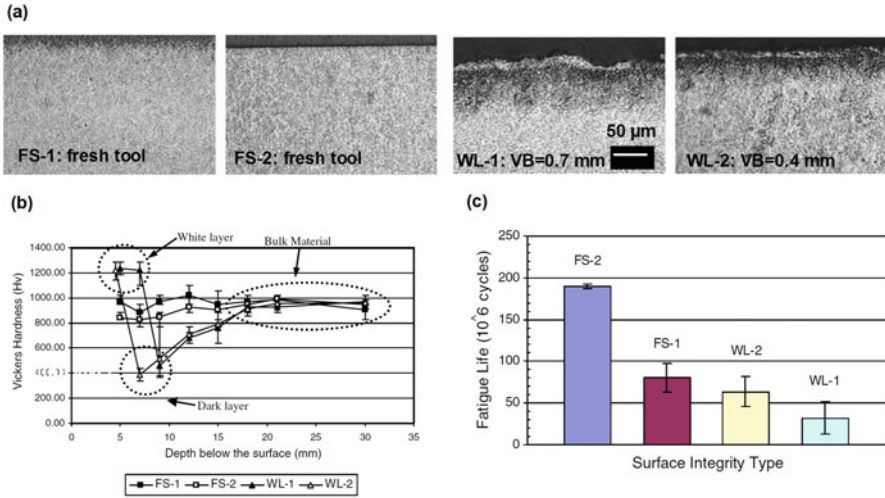
Fig. 8.11 Surface characterization and RCF life comparison for hard turned surface with different surface integrity: (**a**) The subsurface microstructures; (**b**) microhardness profiles below surface; (**c**) RCF life. *Fresh surface (FS), white layer (WL). (Original images and charts are adopt from Schwach and Guo (2006))

tool material and engage aggressive wear mechanisms such as diffusion (Biček et al. 2012). This usually leads to rapid tool wear, especially for flank wear, and consequently shorter cutting tool life. It has been widely acknowledged that a thicker white layer can usually be formed due the greater severe plastic deformation effect induced by the worn tool. Residual stress is difficult to be predicted when white layer is formed, but tensile residual stress is often associated with the presence of white layer, which is detrimental to the surface integrity at the end. In addition, the rapid tool wear rate will significantly increase the cost of manufacturing components in hardened steels for wind turbine gearbox. Hence, novel alternative machining processes, such as laser-assisted machining and cryogenic machining, have been developed to avoid the excessive tool wear and the formation of white layer under aggressive machining conditions, which can also further increase the productivity.

8.3.2 Laser-Assisted Machining (LAM)

LAM implements the concepts of thermally assisted machining using a laser as the heating source. As shown in Fig. 8.12, LAM involves localized, selective laser heating of the workpiece just ahead of the cutting tool in order to reduce the shear strength of the work material in the vicinity of the shear zone. During LAM, the workpiece material is locally heated and softened by a focused laser beam and then removed by a conventional cutting tool. Recently, LAM has been

Photo Credit: Purdue Mechanical Engineering Photo by Michael Black
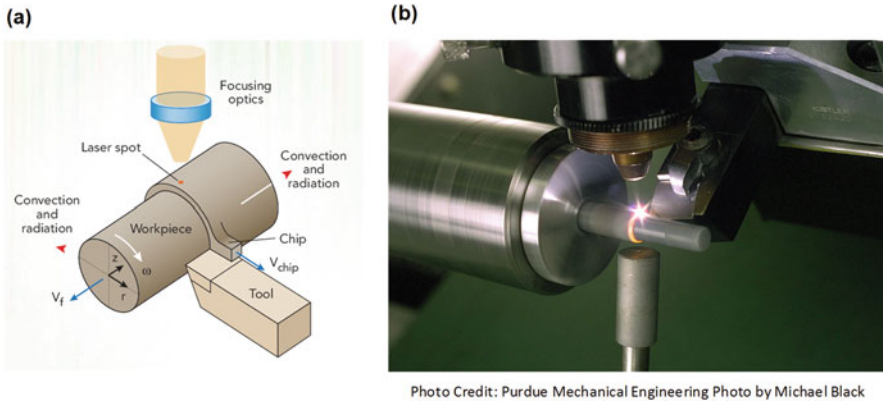
Fig. 8.12 Laser-assisted machining configuration: (**a**) Schematic of LAM; (**b**) Laser-assisted turning operation

considered as an alternative process for machining of high-strength materials like ceramics (Anderson et al. 2006; Dandekar et al. 2010; Sun et al. 2010), metal matrix composites (Skvarenina and Shin 2006), high-temperature alloys (Masood et al. 2011), hardened steels (Lei et al. 2000; Wang et al. 2002; Chang and Kuo 2007; Bejjani et al. 2011), stainless steel (Rebro et al. 2004), and compacted graphite iron (Germain et al. 2005). Extensive experimental investigations conducted so far have shown the feasibility of LAM and its advantages over conventional machining methods in terms of surface finish, tool wear, specific cutting energy, and subsurface integrity (Rebro et al. 2004; Germain et al. 2005; Anderson et al. 2006; Masood et al. 2011).

Focusing on LAM of hardened steels, Germain et al. (2007) showed that the surface roughness of Ra (arithmetic average of the roughness profile) remained stable regardless of the laser power for LAM of AISI 52100 steel, which ranged from 0.6 to 0.75 μm with a small feed rate of 0.1 mm/rev. Dumitrescu et al. (2006) found that machining chatter and saw-tooth chip formation were suppressed in LAM of AISI D2 tool steel with high-power diode laser, and tool life was improved by as much as 100%. Ding and Shin (2010) investigated LAM parameters combination to optimize the relationship between surface integrity of hardened steel parts and process parameters. Currently, as shown in Fig. 8.13, a three-step process is used to produce an automotive transmission shaft after full heat treatment: hard turning, grinding, and polishing. Due to the aforementioned benefit, Ding and Shin (2010) found that LAM process can replace the hard turning and grinding operations and then proposed a one-step LAM process. Without compromising the surface integrity, LAM allows at least a four-time faster material removal rate than the two-step hard turning and grinding operations, and can produce a good surface finish of Ra less than 0.3 μm. The feasibility of precise size control in LAM of hardened steel components has also been demonstrated, which is usually a great concern

Current Method in Prodcution

	Hard Turning	Grinding	Polishing
Hardening (Heat Treatment)			
Material Removal (mm)	0.19	0.17	0.002
Material Removal Rate (mm³/min)	3,100	1,600	0.5 μm/min*
Surface Roughness Ra (μm)	1.6	0.8	0.25

Proposed Method

	LAM	Polishing
Hardening (Heat Treatment)		
Material Removal (mm)	0.36	0.002
Material Removal Rate (mm³/min)	6,400	0.5 μm/min*
Surface Roughness Ra (μm)	0.2~0.4	0.25
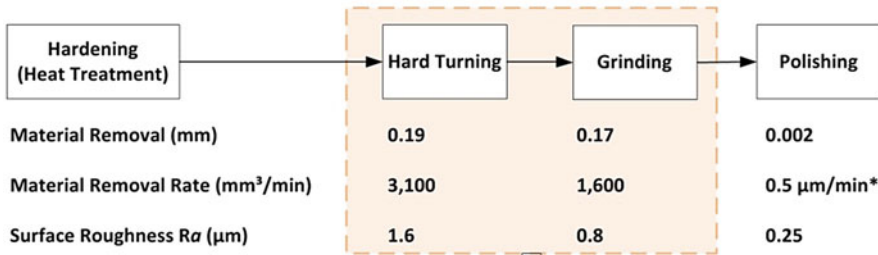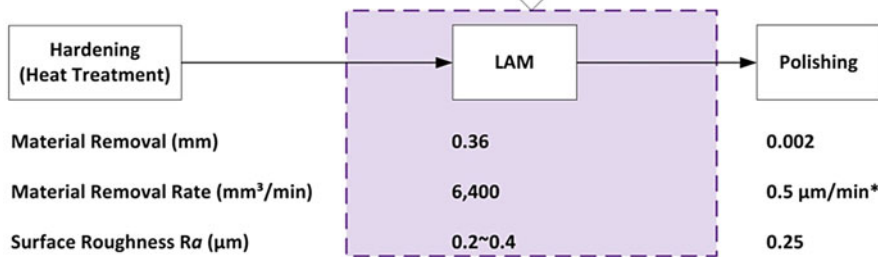
Fig. 8.13 Conventional method and LAM for machining a transmission shaft. *, material removal rate in radius during polishing (Ding and Shin 2010)

for the industrial applications. Compared to conventional hard turning, the specific cutting energy during LAM drops by about 20% as the material removal temperature increased to above 200 °C. The 20% cutting force reduction reduced the workpiece deflection and impeded tool wear progression. The significantly reduced tool wear rate makes the tool wear test difficult to be performed due to the need of a very large number of parts and the associated time and cost. LAM can also achieve a more concentrated surface hardness profile without any softening in the machined subsurface, less variation in the surface hoop residual stress, and more compressive surface axial residual stress. In addition, no detrimental white layer was formed in LAM as shown in Fig. 8.14.

The impact of LAM on the part performance and fatigue life of wind turbine gearbox and bearing components in hardened steels is of great interest for the future study. Compared to hard turning and grinding, more concentration of the martensite near the machined surface will supposedly improve the performance of the hardened steel components under a high-stress state. More compressive residual stresses with less variation over the outer surface are beneficial to improve the fatigue life of these components.

$T_{mr} = 200\ °C$ $T_{mr} = 270\ °C$
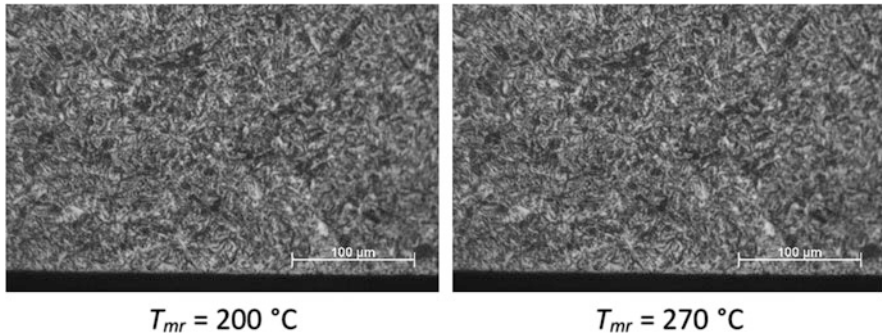
Fig. 8.14 Optical microscopy of microstructures of the subsurface after LAM at speed of 180 m/min and feed of 0.075 mm/rev; various material removal temperature, T_{mr}

8.3.3 Cryogenic Machining

Cryogenic machining firstly has been considered as an eco-friendly and pollution-free machining technology of difficult-to-machine materials, in order to significantly increase the tool life and reduce tool wear due to the reduction of tool-tip temperature (Wang and Rajurkar 2000; Paul et al. 2001). The emergence of cryogenic machining is a result of the sustainability concerns in manufacturing on the use of cutting fluids. During the process, liquid gases, such as nitrogen, carbon dioxide, and helium, are used as alternative coolants to traditional oil- and water-based coolants and lubricants (Jawahir et al. 2016) (Fig. 8.15).

In conventional metal cutting operations, cutting fluids lubricate the cutting zone to control abrasion and improve heat dissipation during the metal cutting process and then reduce the thermal and chemical wear mechanism (El Baradie 1996). However, in the recent two decades, recent studies indicated that exposure to cutting fluids is related to the development of various types of cancers, dermatitis, and respiratory diseases (Brinksmeier et al. 2015). Minimum quantity lubrication (MQL), a near-dry machining technology, has been emerged since the 1990s as a progress and more sustainable solution to significantly reduce the amount of coolants and lubricants in machining operations.

Compared with MQL, cryogenic machining has been shown to be a sustainable alternative to MQL and can generate engineered machined surface with improve surface integrity. The improved surface integrity has been found in the machined surface of Inconel 718, AISI 4140 and 52,100 steels, and Mg alloys (Pusavec et al. 2011; Pu et al. 2012; Umbrello et al. 2012b; Ambrosy et al. 2014). In these studies, an ultrafine-grained (UFG) surface layer is often formed in the machined surface with the increase of surface hardness and compressive residual stresses due to the severe plastic deformation (SPD).
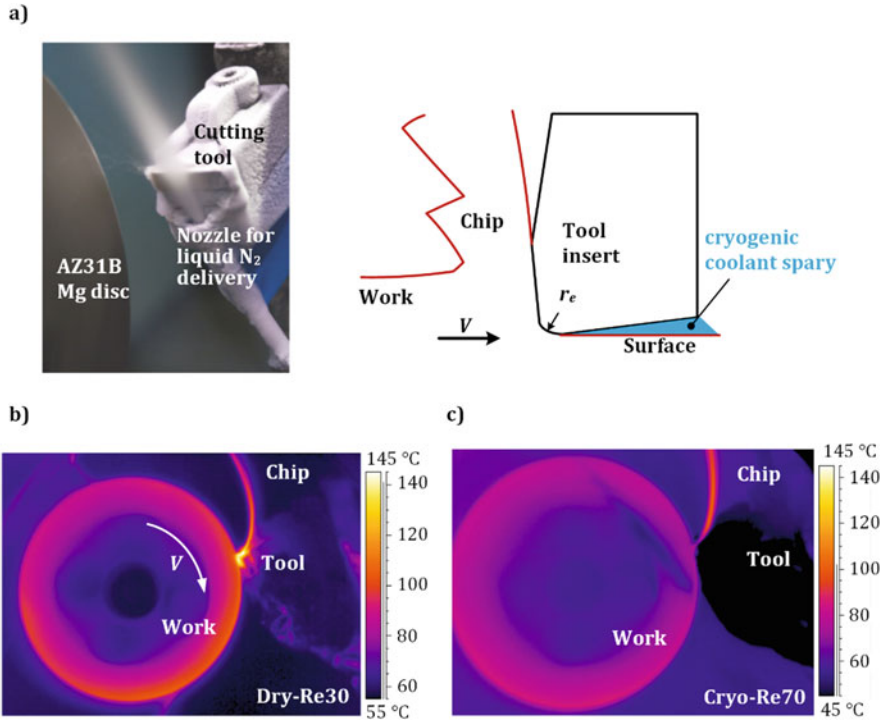
Fig. 8.15 Orthogonal cutting with cryogenic cooling: (**a**) Experimental configuration and process schematic and comparison of IR camera captured temperature distribution during (**b**) IR image for dry cutting and (**c**) IR image for cryogenic cutting. (Original images are adopted from Pu (2012))

Umbrello and his colleagues (Rotella et al. 2012; Umbrello 2013) have performed experimental analysis on the cryogenic machining performance of AISI 52100 steel, focusing on machined surface alterations. Their results show that white layer is either partially reduced or even eliminated under certain cryogenic machining conditions as shown in Fig. 8.16. The formation of white layer was suppressed due to the attenuated martensitic phase transformation induced by the strongly suppressed machining temperature as the cryogenic cooling.

Biček et al. (2012) experimentally compared the surface integrity and tool life for turning of normalized (16 HRC) and hardened (72 HRC) AISI 52100 steel using conventional cutting fluids and cryogenic coolant. Figure 8.17 shows the capability of the machining process to be performed under different cooling and lubrication conditions for both normalized and hardened AISI 52100 steel. Cryogenic turning results show drastic improvements in tool lifetime (up to 370%) for normalized AISI 52100 steel. By comparing both conventional and cryogenic machining, it shows that cutting parameter ranges are expanded toward higher cutting speeds and depths of cut when using cryogenic cooling for both alloy types. Hence, cryogenic machin-
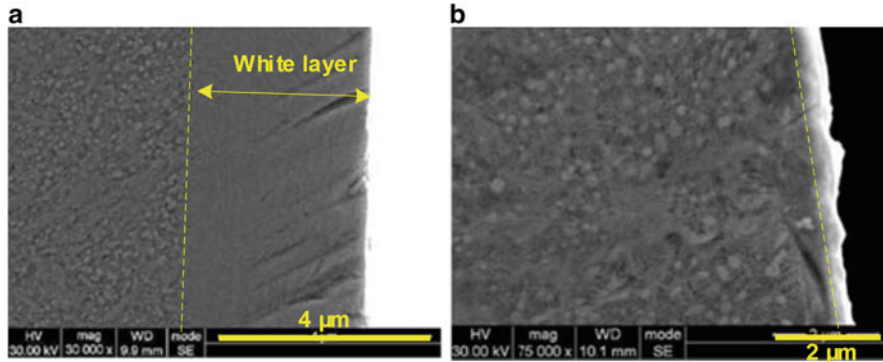
Fig. 8.16 Significantly reduced white layer thickness by cryogenic cutting for 61 HRC AISI 52100 steel with machining speed of 75 m/min and feed rate of 0.125 mm/rev: (**a**) Dry cutting, (**b**) Cryogenic cutting. (Original images are adopted from Umbrello (2013))

ing allows higher productivity and flexibility with maintaining desired machined surface quality. As shown in Fig. 8.18, metallographic analysis showed no white layer was formed in the machined surface after cryogenic turning. Figure 8.19 shows cryogenic machining drastically reduces thermal stress inducements compared to conventional dry machining and has therefore higher compressive stress in the machined surface. Therefore, cryogenic machining improves the machined surface integrity, while it is known that large compressive residual stresses prolong the fatigue life of the final product and are therefore desired.

It can be concluded that cryogenic machining, a novel sustainable process, can offer new opportunities for producing functionally superior products for wind turbine industry.

8.3.4 Discussion

During the machining processes of hardened steels and other difficult-to-machine alloys, machine tools often induce large plastic strains (e.g., a shear strain of 5–10) inside the chip as well as along the machined surface. The chip forms at a high strain rate, characteristically on the order of 10^5 s^{-1}, for typical cutting speeds of 100–300 m/min. A high-temperature gradient also exists in the cutting zone, characterized by a rapid heating rate of 10^5–10^6 °C/s and a fast cooling rate of 10^3–10^4 °C/s. In these processes, mechanical deformation, heat transfer, and metallurgy all inherently couple together, leading to different states of microstructural alterations, which significantly affect the functionality and performance of manufactured products (Field et al. 1972, 1989; Ezugwu 2005; Grzesik and Wanat 2005; Sun et al. 2010; Jawahir et al. 2016). This strong coupling effect is often termed as
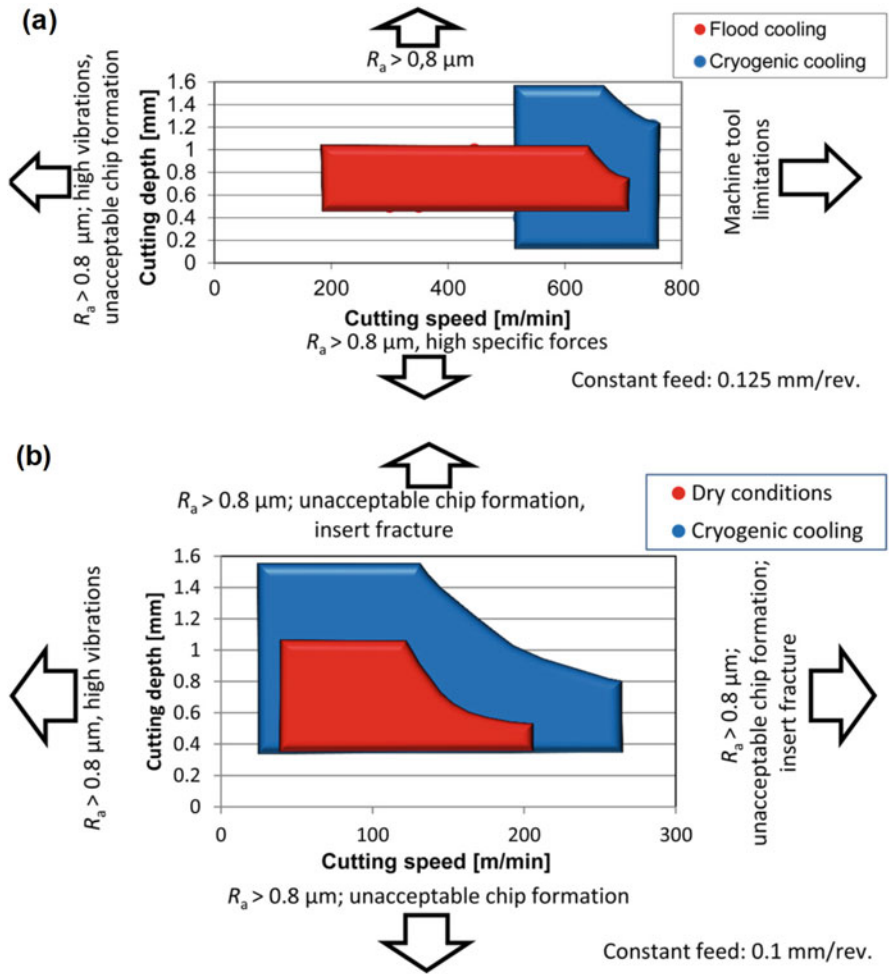
Fig. 8.17 Capability of the machining process to be performed under different cooling and lubrication conditions for (**a**) Normalized AISI 52100 steel and (**b**) Hardened AISI 52100 steel. (Original charts are adopted from Biček et al. (2012))

metallo-thermomechanical (MTM) coupling for manufacturing processes (Inoue 2002; Denis et al. 2002; Bailey et al. 2009), as illustrated in Fig. 8.20 for a hardened steel machining example.

A more comprehensive understanding of the MTM coupling effect will enable the process optimization to maintain a desired microstructure and ensure the requisite functionality of the component (Arrazola et al. 2013). However, the MTM coupling effect is not well understood for hard machining of hardened steels, as well as laser-assisted machining and cryogenic machining. During these processes, complex thermomechanical process loading usually arises at a localized domain
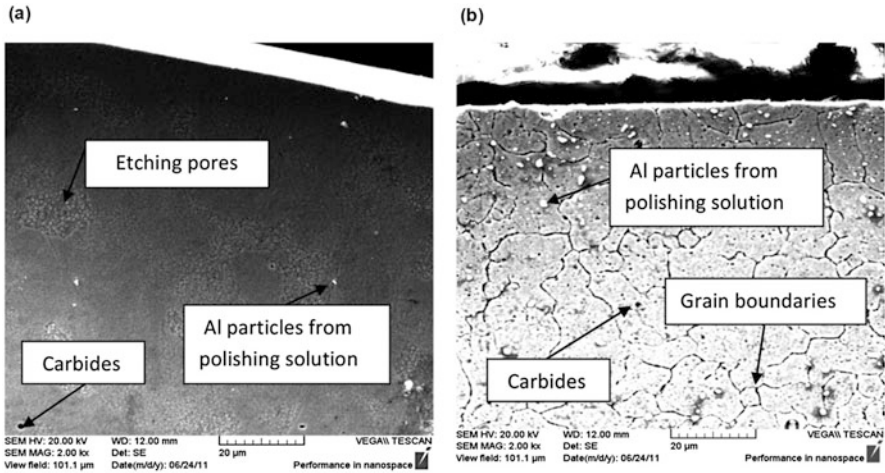
Fig. 8.18 The microstructure below the machined surface for (**a**) Normalized AISI 52100 steel and (**b**) Hardened AISI 52100 steel after cryogenic machining. (Original images are adopted from Biček et al. (2012))
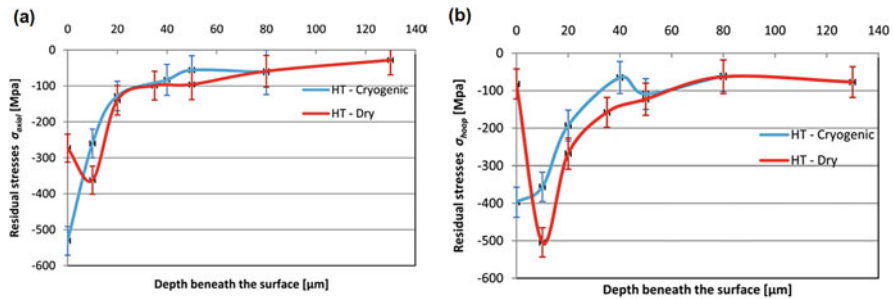
Fig. 8.19 The residual stress for hardened AISI 52100 steel after cryogenic machining: (**a**) Along feed direction; (**b**) Along cutting direction. (Original charts are adopted from Biček et al. (2012))

during a short-time duration. Hence, it remains very difficult to experimentally study the MTM coupling effect for these manufacturing processes.

Future research should aim to eliminate these deficiencies by tightly coupling high-fidelity sub-grid simulations within continuum process simulations to determine the microstructure at each process step using local conditions. Multiple microstructure evolution mechanisms, including mechanical deformation-induced grain refinement, discontinuous dynamic recrystallization, surface nanocrystallization, and white etching layer formation, should be investigated for different metal alloys under various process conditions. Then, numerical models can be developed to simulate the complex coupling of thermomechanical loadings and microstructure evolution during these machining operations. Predictive relationship development between processing parameters, material composition, and resulting microstructure
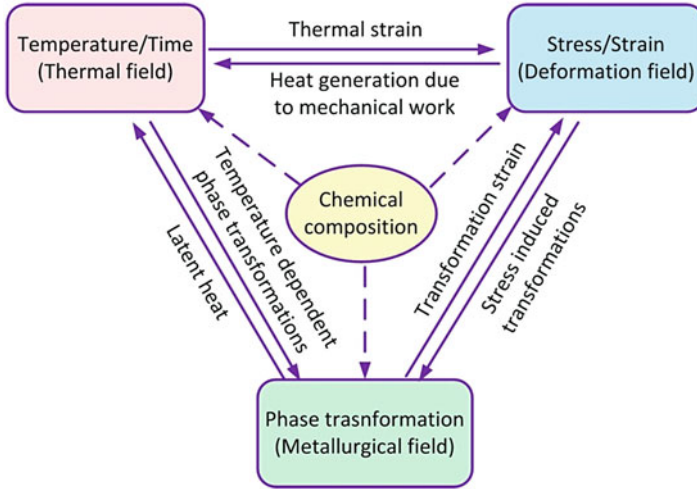
Fig. 8.20 Metallo-thermomechanical coupling in cutting of steels (Ding and Shin 2012)

will greatly reduce experimental iterations and facilitate the design of experiments for optimal microstructure control. The new knowledge will contribute to a better fundamental understanding of manufacturing science, improved knowledge-driven manufacturing process planning, and more accurate prediction of a component's lifetime.

8.4 Outlooks and Conclusions

The conventional composite repair techniques have been developed for decades and extensively applied throughout most sectors of industry, including wind energy, and numerous efforts have been made on the improvement or invention of the existing or novel techniques. Advanced techniques have also been achieved by using UV curing resin, which can significantly reduce the curing time from hours to minutes. There is still a great need for the development of the next generation joining method for FRP and on-site repairing technology to overcome the wide range of repair issues for wind turbine repair.

Current machining process of hardened steels for bearing and gearbox components is summarized. Current achievements in novel machining process of hardened steel components are discussed for laser-assisted machining and cryogenic machining. The relationship between the desired surface integrity and manufacturing process conditions is explained through numerous experimental results in literature. Both laser-assisted machining and cryogenic machining have been demonstrated as ideal alternatives to conventional hard turning, allowing significant improvement

on surface integrity and productivity. More research efforts should be performed in the future to capture the complex metallo-thermomechanical coupling effect during these machining operations for wind turbine bearing and gearbox components.

References

Akcan S, Shah WS, Moylan SP et al (2002) Formation of white layers in steels by machining and their characteristics. Metall Mater Trans A 33:1245–1254

Ambrosy F, Zanger F, Schulze V, Jawahir IS (2014) An experimental study of cryogenic machining on Nanocrystalline surface layer generation. Procedia CIRP 13:169–174. https://doi.org/10.1016/j.procir.2014.04.029

Anderson M, Patwa R, Shin YC (2006) Laser-assisted machining of Inconel 718 with an economic analysis. Int J Mach Tools Manuf 46:1879–1891. https://doi.org/10.1016/j.ijmachtools.2005.11.005

Arnot-Perrett L, Gibson T (1998) CAA regulatory oversight: non-destructive testing. Insight 40(3):166–167

Arrazola PJ, Özel T, Umbrello D et al (2013) Recent advances in modelling of metal machining processes. CIRP Ann Manuf Technol 62:695–718. https://doi.org/10.1016/j.cirp.2013.05.006

Bailey NS, Tan W, Shin YC (2009) Predictive modeling and experimental results for residual stresses in laser hardening of AISI 4140 steel by a high power diode laser. Surf Coat Technol 203:2003–2012

Baker AA, Dutton S, Kelly DW (2004) Composite materials for aircraft structures. AIAA, Reston

Barry J, Byrne G (2002) TEM study on the surface white layer in two turned hardened steels. Mater Sci Eng A 325:356–364. https://doi.org/10.1016/S0921-5093(01)01447-2

Bartarya G, Choudhury SK (2012) State of the art in hard turning. Int J Mach Tools Manuf 53:1–14. https://doi.org/10.1016/j.ijmachtools.2011.08.019

Bejjani R, Shi B, Attia H, Balazinski M (2011) Laser assisted turning of titanium metal matrix composite. CIRP Ann 60:61–64. https://doi.org/10.1016/j.cirp.2011.03.086

Biček M, Dumont F, Courbon C et al (2012) Cryogenic machining as an alternative turning process of normalized and hardened AISI 52100 bearing steel. J Mater Process Technol 212:2609–2618. https://doi.org/10.1016/j.jmatprotec.2012.07.022

Brinksmeier E, Meyer D, Huesmann-Cordes AG, Herrmann C (2015) Metalworking fluids—mechanisms and performance. CIRP Ann 64:605–628. https://doi.org/10.1016/j.cirp.2015.05.003

Burns TJ, Mates SP, Rhorer RL, et al (2011a) Effect on Flow Stress of a Rapid Phase Transition in AISI 1045 Steel. In: ASME 2011 International Manufacturing Science and Engineering Conference, vol 1. ASME, pp 261–266

Burns TJ, Mates SP, Rhorer RL et al (2011b) Dynamic properties for modeling and simulation of machining: effect of pearlite to austenite phase transition on flow stress in AISI 1075 steel. Mach Sci Technol 15:1–20

Cairns D, Mandell J, Scott M, Maccagnano J (1999) Design and manufacturing considerations for ply drops in composite structures. Compos Part B 30:523–534. https://doi.org/10.1016/S1359-8368(98)00043-2

Cairns DS, Riddle T, Nelson J (2011) Wind turbine composite blade manufacturing: the need for understanding defect origins, prevalence, implications and reliability. http://prod.sandia.gov/techlib/access-control.cgi/2011/111094.pdf

Chang C-W, Kuo C-P (2007) Evaluation of surface roughness in laser-assisted machining of aluminum oxide ceramics with Taguchi method. Int J Mach Tools Manuf 47:141–147. https://doi.org/10.1016/j.ijmachtools.2006.02.009

Chou YK, Evans CJ (1999) White layers and thermal modeling of hard turned surfaces. Int J Mach Tools Manuf 39:1863–1881. https://doi.org/10.1016/S0890-6955(99)00036-X

Composites UK (2015) Adhesive bonding of composites. National Composites Network. https://compositesuk.co.uk/system/files/documents/Adhesive%20bonding%20of%20composites_0.pdf

Cripps D (2011) Wind turbine blade repair, Wind Systems. http://www.windsystemsmag.com/media/pdfs/Articles/2011_April/0411_Gurit.pdf

Dandekar CR, Shin YC, Barnes J (2010) Machinability improvement of titanium alloy (Ti-6Al-4V) via LAM and hybrid machining. Int J Mach Tools Manuf 50:174–182. https://doi.org/10.1016/j.ijmachtools.2009.10.013

Denis S, Archambault P, Gautier E et al (2002) Prediction of residual stress and distortion of ferrous and non-ferrous metals: current status and future developments. J Mater Eng Perform 11:92–102. https://doi.org/10.1007/s11665-002-0014-2

Department of Energy (2015) Statistics show bearing problems cause the majority of wind turbine gearbox failures. https://energy.gov/eere/wind/articles/statistics-show-bearing-problems-cause-majority-wind-turbine-gearbox-failures. Accessed 27 Dec 2017

Ding H, Shin YC (2010) Laser-assisted machining of hardened steel parts with surface integrity analysis. Int J Mach Tools Manuf 50:106–114. https://doi.org/10.1016/j.ijmachtools.2009.09.001

Ding H, Shin YC (2012) A Metallo-Thermomechanically coupled analysis of orthogonal cutting of AISI 1045 steel. ASME J Manuf Sci Eng 134:51014. https://doi.org/10.1115/1.4007464

Dumitrescu P, Koshy P, Stenekes J, Elbestawi MA (2006) High-power diode laser assisted hard turning of AISI D2 tool steel. Int J Mach Tools Manuf 46:2009–2016. https://doi.org/10.1016/j.ijmachtools.2006.01.005

Duong CN, Wang CH (2010) Composite repair: theory and design. Elsevier, Oxford

El Baradie MA (1996) Cutting fluids: part I. Characterisation. J Mater Process Technol 56:786–797. https://doi.org/10.1016/0924-0136(95)01892-1

Errichello R, Budny R, Eckert R (2013) Investigations of bearing failures associated with white etching areas (WEAs) in wind turbine gearboxes. Tribol Trans 56:1069–1076. https://doi.org/10.1080/10402004.2013.823531

Ezugwu EO (2005) Key improvements in the machining of difficult-to-cut aerospace superalloys. Int J Mach Tools Manuf 45:1353–1367. https://doi.org/10.1016/j.ijmachtools.2005.02.003

Field R, Kahles JF, Canmett JT (1972) A review of measuring methods for surface integrity. Annals CIRP 21:219–238

Field M, Kahles JF, Koster WP (1989) Surface finish and surface integrity. In: Machining, vol 16, ASM handbook. ASM International, Materials Park, pp 19–36

Germain G, Robert P, Lebrun J-L, Dal Santo P, Poitou A (2005) Experimental and numerical approaches of Laser assisted turning. Int J Form Process 8:347–361

Germain G, Morel F, Lebrun J, Morel A (2007) Machinability and surface integrity for a bearing steel and a titanium alloy in laser assisted machining - (optimisation on LAM on two materials). Lasers in. Engineering 17:329–344

Giannis S, Hansen PL, Martin RH, Jones DT (2008) Mode I quasi–static and fatigue delamination characterisation of polymer composites for wind turbine blade applications. Energy Mater: Mater Sci Eng Energy Systems 3:248–256. https://doi.org/10.1179/174892409x12596773881487

Griffiths BJ (1987) Mechanisms of white layer generation with reference to machining and deformation processes. J Tribol 109:525–530

Gruit UK (2017) RENUVOTM UV Curing Composite Technology Brochure (v10). http://www.gurit.com/-/media/Gurit/Datasheets/renuvo-brochurev8pdf.ashx

Grzesik W, Wanat T (2005) Comparative assessment of surface roughness produced by hard machining with mixed ceramic tools including 2D and 3D analysis. J Mater Process Technol 169:364–371. https://doi.org/10.1016/j.jmatprotec.2005.04.080

Guo YB, Warren AW, Hashimoto F (2010) The basic relationships between residual stress, white layer, and fatigue life of hard turned and ground surfaces in rolling contact. CIRP J Manuf Sci Technol 2:129–134. https://doi.org/10.1016/j.cirpj.2009.12.002

Halliwell S (2010) Repair of fibre reinforced polymer structures, National Composites Network Best Practice Guide. NetComposites, available at http://www.compositesuk.co.uk/LinkClick.aspx?fileticket=rqsK5DrqhU8%3D&tabid=111&mid=550 on May 16, 2014

Han S, Melkote SN, Haluska MS, Watkins TR (2008) White layer formation due to phase transformation in orthogonal machining of AISI 1045 annealed steel. Mater Sci Eng A 488:195–204. https://doi.org/10.1016/j.msea.2007.11.081

Harris TA (2001) Rolling bearing analysis. Wiley, New York

Hashimoto F, Guo YB, Warren AW (2006) Surface integrity difference between hard turned and ground surfaces and its impact on fatigue life. CIRP Ann 55:81–84. https://doi.org/10.1016/S0007-8506(07)60371-0

Hexcel Corporation (2015) Composite repair. http://www.hexcel.com/Resources/DataSheets/Brochure-Data-Sheets/Composite_Repair.pdf

Inoue T (2002) Metallo-thermo-mechanics—application to quenching. In: Totten GE, Howes MAH, Inoue T (eds) Handbook of residual stress and deformation of steel, ASM handbook. ASM International, Materials Park, pp 296–311

Jain S, Hunt H (2011) A dynamic model to predict the occurrence of skidding in wind-turbine bearings. J Phys Conf Ser 305:12027. https://doi.org/10.1088/1742-6596/305/1/012027

Jawahir ISS, Brinksmeier E, M'Saoubi R et al (2011) Surface integrity in material removal processes: recent advances. CIRP Ann Manuf Technol 60:603–626. https://doi.org/10.1016/j.cirp.2011.05.002

Jawahir IS, Attia H, Biermann D et al (2016) Cryogenic manufacturing processes. CIRP Ann Manuf Technol 65:713–736. https://doi.org/10.1016/j.cirp.2016.06.007

Kang J (2014) Mechanisms of microstructural damage during rolling contact fatigue of bearing steels. University of Cambridge

Khashaba UAA, El-Sonbaty IAA, Selmy AII, Megahed AAA (2010) Machinability analysis in drilling woven GFR/epoxy composites: part I - effect of machining parameters. Compos A: Appl Sci Manuf 41:1130–1137. https://doi.org/10.1016/j.compositesa.2010.04.011

Klocke F, Kratz H (2005) Advanced tool edge geometry for high precision hard turning. CIRP Ann 54:47–50. https://doi.org/10.1016/S0007-8506(07)60046-8

Lantz E (2013) Operations expenditures: historical trends and continuing challenges. Congressional Research Service Report for Congress

Lei S, Shin YC, Incropera FP (2000) Deformation mechanisms and constitutive modeling for silicon nitride undergoing laser-assisted machining. Int J Mach Tools Manuf 40:2213–2233. https://doi.org/10.1016/S0890-6955(00)00051-1

Li JG, Umemoto M, Todaka Y, Tsuchiya K (2007) A microstructural investigation of the surface of a drilled hole in carbon steels. Acta Mater 55:1397–1406. https://doi.org/10.1016/j.actamat.2006.09.043

Lomov SV, Bogdanovich AE, Ivanov DS et al (2009) A comparative study of tensile properties of non-crimp 3D orthogonal weave and multi-layer plain weave E-glass composites. Part 1: materials, methods and principal results. Compos A: Appl Sci Manuf 40:1134–1143. https://doi.org/10.1016/j.compositesa.2009.03.012

M'Saoubi; R, Outeiro JC, Chandrasekaran H, et al (2008) A review of surface integrity in machining and its impact on functional performance and life of machined products. Int J Sustain Manuf 1:203. https://doi.org/10.1504/IJSM.2008.019234

Marsh G (2011) Meeting the challenge of wind turbine blade repair. Reinf Plast 55(4):32–36

Masood SH, Armitage K, Brandt M (2011) An experimental study of laser-assisted machining of hard-to-wear white cast iron. Int J Mach Tools Manuf 51:450–456. https://doi.org/10.1016/j.ijmachtools.2011.02.001

Matsumoto Y, Hashimoto F, Lahoti G (1999) Surface integrity generated by precision hard turning. CIRP Ann Manuf Technol 48:59–62. https://doi.org/10.1016/S0007-8506(07)63131-X

MISTRAS Group I (2013) Blade repair and maintenance services. In: MISTRAS Group, Inc. http://www.ropeworks.com/service_wind_blade.htm

Pang S-S, Li G, Jerro HD et al (2004) Fast joining of composite pipes using UV curing FRP composites. Polym Compos 25:298–306. https://doi.org/10.1002/pc.20024

Paul S, Dhar N, Chattopadhyay A (2001) Beneficial effects of cryogenic cooling over dry and wet machining on tool wear and surface finish in turning AISI 1060 steel. J Mater Process Technol 116:44–48. https://doi.org/10.1016/S0924-0136(01)00839-1

Performance Composite Inc. (2015) Wind blade repair, Inspection & expert services. http://www.performancecomposites.com/wind-turbine-service.html

Platzer MD (2012) U.S. wind turbine manufacturing: federal support for an emerging industry. Congressional Research Service Report for Congress

Poulachon G, Moisan A (1998) A contribution to the study of the cutting mechanisms during high speed machining of hardened steel. CIRP Ann 47:73–76. https://doi.org/10.1016/S0007-8506(07)62788-7

Pu Z (2012) Cryogenic machining and burnishing of AZ31B magnesium alloy for enhanced surface integrity and functional performance. University of Kentucky

Pu Z, Outeiro JC, Batista AC et al (2012) Enhanced surface integrity of AZ31B mg alloy by cryogenic machining towards improved functional performance of machined components. Int J Mach Tools Manuf 56:17–27. https://doi.org/10.1016/j.ijmachtools.2011.12.006

Pusavec F, Hamdi H, Kopac J, Jawahir IS (2011) Surface integrity in cryogenic machining of nickel based alloy—Inconel 718. J Mater Process Technol 211:773–783. https://doi.org/10.1016/j.jmatprotec.2010.12.013

Ramesh A, Melkote SN, Allard LF et al (2005) Analysis of white layers formed in hard turning of AISI 52100 steel. Mater Sci Eng A 390:88–97. https://doi.org/10.1016/j.msea.2004.08.052

Rebro PA, Shin YC, Incropera FP (2004) Design of operating conditions for crackfree laser-assisted machining of mullite. Int J Mach Tools Manuf 44:677–694. https://doi.org/10.1016/j.ijmachtools.2004.02.011

Ribrant J, Bertling LM (2007) Survey of failures in wind power systems with focus on Swedish wind power plants during 1997–2005. IEEE Trans Energy Convers 22:167–173. https://doi.org/10.1109/TEC.2006.889614

Rotella G, Umbrello D, Owd J, Jawahir IS (2012) Evaluation of process performance for sustainable hard machining. J Adv Mech Des, Syst, Manuf 6:989–998. https://doi.org/10.1299/jamdsm.6.989

Rumsey MA (2009) NDT, CM and SHM of wind turbine blades at the national labs. 2009 NREL Wind Turbine Condition Monitoring Workshop. http://wind.nrel.gov/public/Wind_Turbine_Condition_Monitoring_Workshop_2009/5.2.Rumsey.NDT_CM_SHM_of_Wind_Turbine_Blades.pdf

Schwach D, Guo Y (2006) A fundamental study on the impact of surface integrity by hard turning on rolling contact fatigue. Int J Fatigue 28:1838–1844. https://doi.org/10.1016/j.ijfatigue.2005.12.002

Shen N, Pence CN, Ding H (2013) Laser assisted machining and hardening of wind turbine components. In: 2013 Iowa EPSCoR annual all-hands meeting, July 22–23. Cedar Falls, Iowa, USA, p 2013

Sheng S (2013) Report on wind turbine subsystem reliability - a survey of various databases, NREL/PR-5000-59111. National Renewable Energy Laboratory

Sheng S (2014) Gearbox typical failure modes, detection and mitigation methods. AWEA Operations & Maintenance and Safety Seminar, NREL/PR-5000-60982

Skvarenina S, Shin YC (2006) Laser-assisted machining of compacted graphite iron. Int J Mach Tools Manuf 46:7–17. https://doi.org/10.1016/j.ijmachtools.2005.04.013

Šmeļova V, Schwedt A, Wang L et al (2017) Microstructural changes in white etching cracks (WECs) and their relationship with those in dark etching region (DER) and white etching bands (WEBs) due to rolling contact fatigue (RCF). Int J Fatigue 100:148–158. https://doi.org/10.1016/j.ijfatigue.2017.03.027

Smith R, Jones LD, Zeqiri B, Hodnett M (1998) Ultrasonic C-scan standardisation for fibre-reinforced polymer composites - minimising the uncertainties in attenuation measurements. Insight - Non-Destr Test Cond Monit 40:34–43

Sørensen BF, Jørgensen E, Debel CP, Jensen FM (2004) Improved design of large wind turbine blade of fibre composites based on studies of scale effects (Phase 1). Summary Report

Soutis C, Tong L (2003) Recent advances in structural joints and repairs for composite materials. Springer, Dordrecht

Sroka GJ, Benson R (2011) Refurbishing wind turbine gears. Gear Solutions 6:28–39

Stephenson S (2011) Wind blade repair: planning, safety, flexibility. Composites Technol

Stig F (2009) An introduction to the mechanics of 3D-woven fibre reinforced composites. Institutionen för Farkost och Flyg. http://urn.kb.se/resolve?urn=urn:nbn:se:kth:diva-10235

Sun S, Brandt M, Dargusch MS (2010) Thermally enhanced machining of hard-to-machine materials—a review. Int J Mach Tools Manuf 50:663–680. https://doi.org/10.1016/j.ijmachtools.2010.04.008

Tangler JL (2000) The evolution of rotor and blade design. Palm Springs, California

TGM wind services LLC blade repairs. In: TGM Wind Services LLC. http://tgmwind.com/bladerepairs.html#bladerepairs

Todaka Y, Umemoto M, Li J, Tsuchiya K (2005) Nanocrystallization of drill hole surface by high speed drilling. J Metastable and Nanocryst Mater 24–25:601–604. https://doi.org/10.4028/www.scientific.net/JMNM. 24-25.601

Ulutan D, Ozel T (2011) Machining induced surface integrity in titanium and nickel alloys: a review. Int J Mach Tools Manuf 51:250–280. https://doi.org/10.1016/j.ijmachtools.2010.11.003

Umbrello D (2013) Analysis of the white layers formed during machining of hardened AISI 52100 steel under dry and cryogenic cooling conditions. Int J Adv Manuf Technol 64:633–642. https://doi.org/10.1007/s00170-012-4073-8

Umbrello D, Micari F, Jawahir IS (2012a) The effects of cryogenic cooling on surface integrity in hard machining: a comparison with dry machining. CIRP Ann 61:103–106. https://doi.org/10.1016/j.cirp.2012.03.052

Umbrello D, Yang S, Dillon OW, Jawahir IS (2012b) Effects of cryogenic cooling on surface layer alterations in machining of AISI 52100 steels. Mater Sci Technol 28:1320–1331. https://doi.org/10.1179/1743284712Y.0000000052

Vizzini AJ, Lee SW (1995) Damage analysis of composite tapered beams. J Am Helicop Soc 40:43–49

Wang ZY, Rajurkar KP (2000) Cryogenic machining of hard-to-cut materials. Wear 239:168–175. https://doi.org/10.1016/S0043-1648(99)00361-0

Wang Y, Yang L, Wang N (2002) An investigation of laser-assisted machining of Al2O3 particle reinforced aluminum matrix composite. J Mater Process Technol 129:268–272. https://doi.org/10.1016/S0924-0136(02)00616-7

Wei Q, Cheng S, Ramesh K, Ma E (2004) Effect of nanocrystalline and ultrafine grain sizes on the strain rate sensitivity and activation volume: fcc versus bcc metals. Mater Sci Eng A 381:71–79. https://doi.org/10.1016/j.msea.2004.03.064

Chapter 9
Modeling and Analysis of Offshore Floating Wind Turbines

Zhiyu Jiang, Xiangqian Zhu, and Weifei Hu

9.1 Introduction

9.1.1 Floating Platform

As of 2016, more than 80 offshore wind farms across 11 European countries have been installed (Wikipedia: Offshore wind power 2016); monopile, gravity, or jacket structures are the main foundation types. Compared to bottom-fixed turbines, floating wind turbine technologies are less mature, and most of the development is still limited by the costs. The Hywind pilot park, the world's first floating wind farm, is expected to produce power in late 2017 (Statoil 2017). This wind farm consists of spar-type floating wind turbines with a total capacity of 30 MW.

Various concepts have been proposed and studied in (Butterfield et al. 2007; Luan et al. 2016; Myhr et al. 2011; Roddier et al. 2010; Sclavounos et al. 2010; Skaare et al. 2015). Figure 9.1 shows four floating wind turbine concepts with different support structures, which have been widely applied by the offshore oil and gas industry. The passive mooring systems are utilized for station-keeping purposes, when wind and wave loads are present. All platforms can be divided into

Z. Jiang
Department of Marine Technology, Norwegian University of Science and Technology, Trondheim, Norway
e-mail: zhiyu.jiang@ntnu.no

X. Zhu (✉)
School of Mechanical Engineering, Pusan National University, Busan, Republic of Korea
e-mail: zhuxiangqian@pusan.ac.kr

W. Hu
Sibley School of Mechanical and Aerospace Engineering and Department of Earth and Atmospheric Sciences, Cornell University, Ithaca, NY, USA
e-mail: wh348@cornell.edu
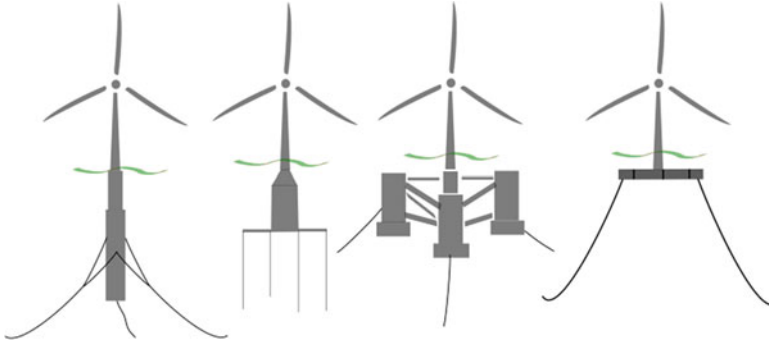
Fig. 9.1 Illustrations of horizontal-axis floating wind turbines supported by a spar buoy, a tension leg platform, a semisubmersible platform, and a barge

three general categories based on the physical principle to achieve static stability: ballast stabilized, buoyancy stabilized, or mooring stabilized. Spar-type wind turbines are intended for deep water and are ballast stabilized with deep draughts. Semisubmersible wind turbines have lower draughts and are under consideration for both immediate water and deep water. Those platforms achieve stability primarily by water plane stiffness; some have active ballast system in addition (Roddier et al. 2010). Compared with spar and semisubmersible turbines, tension leg platform wind turbines are "stiffer" in that the natural periods of the vertical platform motions (heave, roll, and pitch) are placed below the wave period of 4 s rather than above. The tension leg platforms achieve stabilities by mooring line tension. The barge-type turbines have large water plane areas and hydrostatic stiffness, but no attempt has been made to bring the concept to real life, probably because of the large wave-induced motions. In practice, all floating wind turbine concepts are hybrid designs that gain static stability from all three categories.

9.1.2 Mooring System

The marine cables can be classified into three groups: the taut cable, the towed cable, and the mooring cable, respectively, as shown in Fig. 9.2. The floating structure moves within a small range if it was positioned by taut cables (Jonkman and Matha 2010). The TLP (tension leg platform) is a classical facility tethered by the taut cables. The cables are highly tensioned so that the restoring moments are generated when the platform is unbalanced. The towed cables are used to connect two marine vehicles and may transmit the electrical signal. The towed cable moves with the marine vehicles and has obvious motions compared with the surrounding fluid, so the dynamics of the cables are considered in analyses, as done by (Buckham
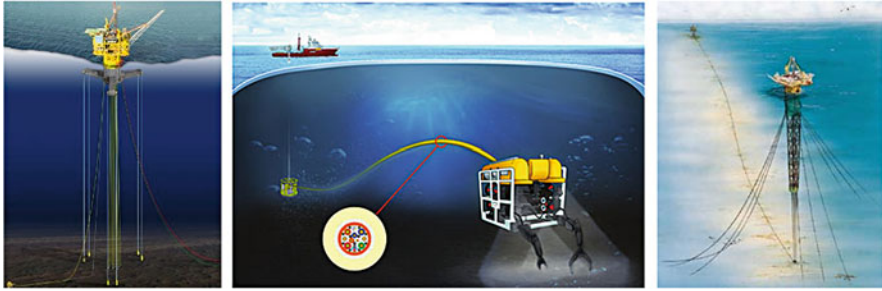
Fig. 9.2 Examples of cables in marine engineering (Engineering 2017), (Nexans 2017), (Offshore 2017)

et al. 2000, 2003; Buckham 2003; Milinazzo et al. 1987). Some towed cables are armored as in (Kim et al. 2012), so the torsion and bending effects are included in the governing equations. Floating structures move with a large range when positioned by mooring cables. Generally, mooring cables are made of heavy chains and move slowly in the fluid, so the inertial effects and the stretching of the cable and the hydrodynamic loads on cables are neglected (Agarwal and Jain 2003; Gobat and Grosenbaugh 2001; Umar and Datta 2003). The system motions are analyzed based on static analysis of the cables.

However, the stretching of the cables dissipates the transient tension (Tahar and Kim 2008; Xu and Chen 2014), and the hydrodynamic loads acting on cables have significant effects on the global motions of the floating facilities (Kim et al. 2013). Additionally, many mooring cables are made up of composite materials, and the inertial effect cannot be ignored. The National Renewable Energy Laboratory (NREL) planned to extend the MAP (Mooring Analysis Program) from the quasi-static analysis to the dynamic analysis (Masciola et al. 2013, 2014) to obtain more accurate results during simulations of floating wind turbines. An established cable model, based on the lumped-mass method, is shown in Fig. 9.3. This model considers the axial stiffness and damping force of the cables, the hydrodynamic drag forces, the apparent weight, and dynamical inertia. These loads are expressed based on the lumped-mass model in which the element reference frame (ERF) is a critical medium to express both the loads acting on cable and motions of cable easily with respect to the inertial reference frame (IRF). A new ERF is generated based on the vectors of the element orientation vector and the relative velocity of the cable (Zhu and Yoo 2017). The advantages of the new ERF are (1) the cable modeling deals with singularity problems that are generated by the Frenet frame and the Euler angle, (2) the hydrodynamic loads are expressed efficiently, and (3) the nonlinear breakup of the drag between the normal and tangential directions are solved, which correctly express the hydrodynamic drag force even for straightly taut cables.

Fig. 9.3 A marine cable modeled by the lumped-mass method
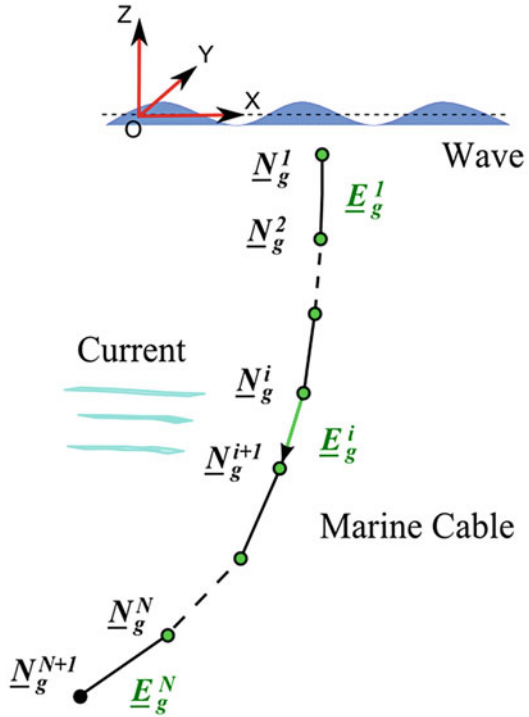
9.1.3 Analysis Tools

The dynamic analysis of the offshore floating wind turbine relates to flexible multibody dynamics, hydrodynamics, aerodynamics, control, mooring loads, and so on. There exist a few commercial software, among which the GH bladed is used to simulate land-based wind turbines (Bossanyi 2009), but it has not been recognized on the simulation of the floating wind turbines. In recent years, NREL has been sponsoring the development, verification, and validation of comprehensive aero-servo-elastic simulators through the national wind technology center. Among the developed simulators, FAST can predict the coupled dynamic response of land- and offshore-based horizontal-axis wind turbines (HAWTs) well. In the following, FAST, together with another state-of-the-art aeroelastic code, HAWC2, will be discussed.

9.1.3.1 FAST

FAST stands for Fatigue, Aerodynamics, Structures, and Turbulence. Developed by NREL, FAST is a nonlinear time-domain simulator that employs a combined
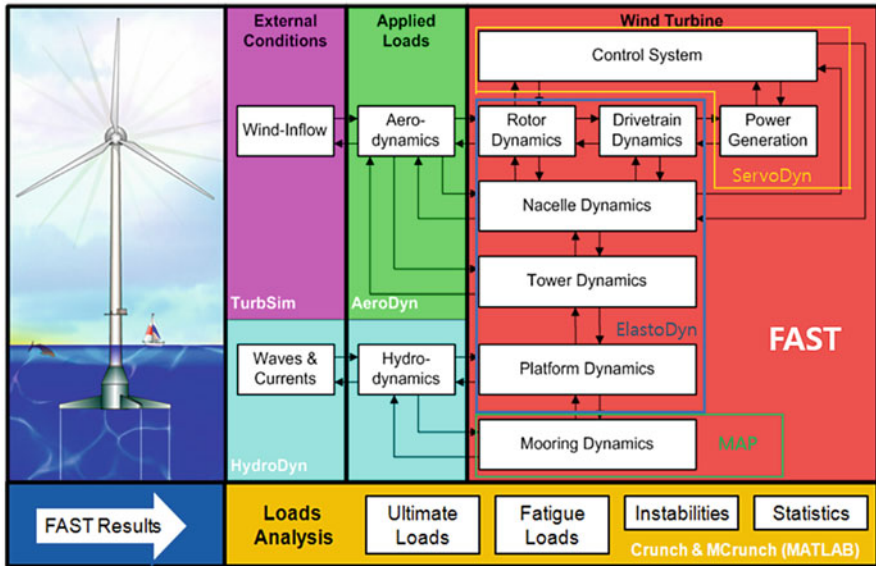
Fig. 9.4 Workflow of the FAST system (Jonkman 2007)

modal and multibody dynamics formulation, considering limited numbers of DOFs. It provides a central platform that combines AeroDyn, HydroDyn, MAP, and other simulation tools, as shown in Fig. 9.4 (Jonkman 2007). AeroDyn uses the blade element momentum (BEM) theory with empirical corrections to calculate the rotor aerodynamics. A more advanced approach, the generalized dynamic wakes (GDW) method, is also available. The tip loss and the turbulent wake state and stall delay are considered by the AeroDyn. HydroDyn is used to analyzed the wave loads, such as the linear hydrostatic restoring, the added mass and damping contributions, the free-surface memory effects, and the nonlinear viscous drag (Jonkman 2007; Matha 2009). Mooring Analysis Program (MAP) is a tool to analyze the multi-segmented quasi-static cable system (Masciola et al. 2013) in which the hydrodynamic loads are ignored. The mooring loads are functions of the six DOFs of the floating platform and act on the center of mass (CM) of the platform for simplicity. However, the quasi-static type is not able to satisfy the accuracy requirement currently due to the application of the new materials in the mooring system. The simulator, MoorDyn, is developed to consider the dynamics of mooring cables (Hall 2015; Wendt et al. 2016). MoorDyn is an open-source dynamic mooring line model. It uses a lumped-mass formulation for modeling axial elasticity, hydrodynamics, and bottom contact.

9.1.3.2 HAWC2

HAWC2 is an aeroelastic code intended for wind turbine calculations in the time domain (Larsen 2009). The structural model of HAWC2 is based on the multibody formulation. The structure is divided into a number of independent bodies with coupling interconnected between them. While large translation and rotation is allowed for the coupling point, small deflections are assumed within each body.

The aerodynamics based on the BEM theory in HAWC2. The BEM model is a steady-state model and should be extended to handle unsteady aeroelastic features such as the dynamic inflow, the dynamic stall, the skew inflow, and the shear effects. The transient aerodynamic loads are generated by time-varying blade loads due to turbulent wind and control actions. They are treated at two levels, unsteady airfoil aerodynamics and the dynamic inflow models. The former deals with the unsteady non-separated effects from shed vorticity and dynamic stall models. The latter accounts for the variations in the inflow velocity, structural vibrations, and tip pitch changes. The MHH Beddoes-Leishman dynamic stall model is employed to calculate the unsteady aerodynamic lift, drag, and pitching moment on an airfoil section undergoing motion in heave, lead-lag, and pitch. The model considers the effects of shed vorticity from the trailing edge and the effects of stall separation caused by an instationary trailing edge separation point (Hansen et al. 2004). The dynamic inflow model in HAWC2 is handled by two first order filters: one for the near wake contribution and one for the far wake. This enables to account for the time lag in update of wake due to load changes. Besides these, other corrections that include the Prandtl tip loss and the skew inflow are also implemented.

Figure 9.5 shows the modularized flowchart procedure. All of the controlled actions, subsystem dynamics, and the hydrodynamic and mooring forces are handled by external dynamic-link libraries (DLL) compiled to a programming language. By doing so, the actual algorithm can be compiled separately from the program. Additional scenarios such as the initiation of fault and subsequent supervisory control behavior are specified here. If the turbine has a subsystem that cannot be modeled directly by the main program, users may also implement the system in a DLL as well. At each time step, the main program feeds the sensor information including the position and velocity of the bodies to the DLL and receives the control actions in return.

9.2   Geometric Configuration and Environmental Conditions

9.2.1   Geometric Configuration

The geometry of the 5 MW offshore floating wind turbine refers to the "OC3-Hywind" system by NERL (Jonkman et al. 2009, 2010). The property of the wind turbine and of the floating spar platform is shown in Table 9.1 and Table 9.2, respectively.

The profile of the blade and wind tower can be found in (Jonkman et al. 2009, 2010).
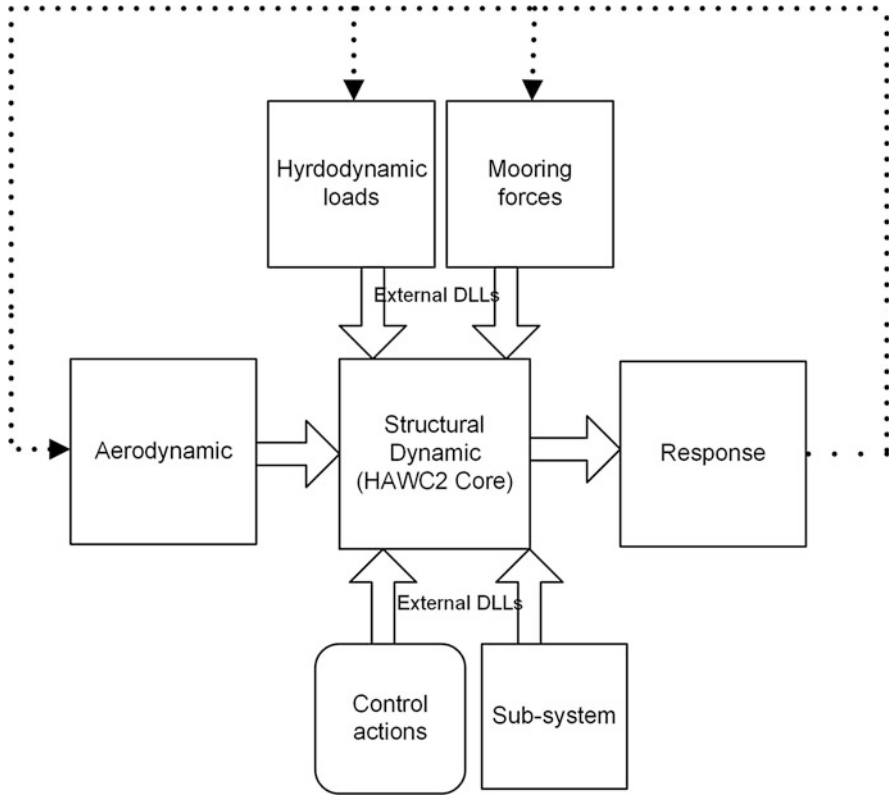
Fig. 9.5 Modularized computational flowchart for floating wind turbines in HAWC2

Table 9.1 Structural properties of the NREL 5 MW wind turbine

Rating	5 MW
Rotor orientation, configuration	Upwind, 3 blades
Control	Variable speed, collective pitch
Drivetrain	High-speed multiple-stage gearbox
Rotor, hub diameter	126 m, 3
Hub height	90 m
Cut-in, rated, cutout wind speed	3 m/s, 11.4 m/s, 25 m/s
Cut-in, rated rotor speed	6.9 rpm, 12.1 rpm
Rated tip speed	80 m/s
Overhang, shaft tilt, precone	5 m, 5°, 2.5°
Rotor mass	110,000 kg
Nacelle mass	240,000 kg
Tower mass	347,460 kg
Coordinate location of overall CM	(−0.2 m, 0.0, 64.0 m)

Table 9.2 Structural properties of the spar platform

Depth of platform base below SWL	120 m
Elevation to platform top above SWL	10 m
Depth to top of taper below SWL	4 m
Depth to bottom of taper below SWL	12 m
Platform diameter above taper	6.5 m
Platform diameter below taper	9.4 m
Cut-in, rated, cutout wind speed	7,466,330 kg
CM location below SWL along platform centerline	89.9155 m
Platform roll inertia about CM	4,229,230,000 kg.m^2
Platform pitch inertia about CM	4,229,230,000 kg.m^2
Platform yaw inertia about platform centerline	164,230,000 kg.m^2

9.2.2 Wind Speed

According to the rated power of the NREL 5 MW offshore wind turbine, the wind speed is around 11.4 m/s. A real-time monitoring data of the wind speed is adopted from a meteorological observation station that is 10 m above the still water level. The wind speed of every height can be obtained through (Journèe and Massie 2001), as shown in Eq. (9.1).

$$V_j = V_r \left(Z_j / Z_r \right)^{0.11} \tag{9.1}$$

where Z_j represents the height of measuring points, which are the time- and position-dependent values, Z_r represents the height of the standard measuring point that is 10 meters above the SWL, V_j represents wind speeds of each measure point, and V_r represents the standard wind speed, which is measured at standard measuring point.

9.2.3 Waves

A surface wave is generated according to the linear wave theory (Journèe and Massie 2001). The elevation of surface wave ζ corresponds with the superposition of waves propagating independently in the X- and Y-directions, as shown in the following equation:

$$\zeta = \zeta_a^x \cos \left(k^x X_g - \omega^x t \right) + \zeta_a^y \cos \left(k^y Y_g - \omega^y t \right) \tag{9.2}$$

The superscripts $()^x$ and $()^y$ indicate the evaluation of $()$ with respect to waves propagating in the X- and Y-directions, respectively. Therefore, ζ_a^x and ζ_a^y denote wave amplitudes, ω^x and ω^y denote circular wave frequencies, k^x and k^y denote wave numbers in the X- and Y-directions, respectively. X_g and Y_g are the position

coordinates in the inertial reference frame. Assuming an infinite water depth, the wave lengths, wave numbers, and circular wave frequencies are given by

$$\lambda^x = \frac{\mid \underline{g} \mid \left(T_a^x\right)^2}{2\pi}, \quad \lambda^y = \frac{\mid \underline{g} \mid \left(T_a^y\right)^2}{2\pi} \tag{9.3}$$

$$k^x = \frac{2\pi}{\lambda^x}, \quad k^y = \frac{2\pi}{\lambda^y} \tag{9.4}$$

$$\left(\omega^x\right)^2 = k^x \mid \underline{g} \mid, \quad \left(\omega^y\right)^2 = k^y \mid \underline{g} \mid \tag{9.5}$$

where $\underline{g}$ denotes the vector of gravitational acceleration and T_a^x and T_a^y denote wave periods in the X- and Y-directions, respectively. u_g^i, v_g^i, and w_g^i are the velocity components of the water particles at the ith node in the X-, Y-, and Z-directions, respectively, where $N_g^{i,1}$, $N_g^{i,2}$, and $N_g^{i,3}$ represent the position components of ith node in the X-, Y-, and Z-directions, respectively.

$$
\begin{aligned}
u_g^i &= \zeta_a^x \cdot \omega^x \cdot e^{k^x N_g^{i,3}} \cos\left(k^x N_g^{i,1} - \omega^x t\right) \\
v_g^i &= \zeta_a^y \cdot \omega^y \cdot e^{k^y N_g^{i,3}} \cos\left(k^y N_g^{i,2} - \omega^y t\right) \\
w_g^i &= \zeta_a^x \cdot \omega^x \cdot e^{k^x N_g^{i,3}} \sin\left(k^x N_g^{i,1} - \omega^x t\right) \\
&\quad + \zeta_a^y \cdot \omega^y \cdot e^{k^y N_g^{i,3}} \sin\left(k^y N_g^{i,2} - \omega^y t\right)
\end{aligned}
\tag{9.6}
$$

Meanwhile, $\dot{u}_g^i$, $\dot{v}_g^i$, and $\dot{w}_g^i$ are the acceleration components of water particles.

$$
\begin{aligned}
\dot{u}_g^i &= \zeta_a^x \cdot (\omega^x) \cdot e^{k^x N_g^{i,3}} \sin\left(k^x N_g^{i,1} - \omega^x t\right) \\
\dot{v}_g^i &= \zeta_a^y \cdot (\omega^y) \cdot e^{k^y N_g^{i,3}} \sin\left(k^y N_g^{i,2} - \omega^y t\right) \\
\dot{w}_g^i &= -\zeta_a^x \cdot (\omega^x) \cdot e^{k^x N_g^{i,3}} \cos\left(k^x N_g^{i,1} - \omega^x t\right) \\
&\quad -\zeta_a^y \cdot (\omega^y) \cdot e^{k^y N_g^{i,3}} \cos\left(k^y N_g^{i,2} - \omega^y t\right)
\end{aligned}
\tag{9.7}
$$

Finally, the velocity of the fluid $\underline{V}_f^i$ is the sum of the wave velocity $\underline{V}_w^i$ and the current velocity $\underline{V}_g^c$, which is given by

$$\underline{V}_f^i = \underline{V}_w^i + \underline{V}_g^c \tag{9.8}$$

where $\underline{V}_w^i = \left[\, u_g^i, \, v_g^i, \, w_g^i \,\right]^T$ and the current is simplified as a constant velocity in this study.

9.3   Numerical Modeling

The numerical modeling of floating wind turbine based on the spar platform is created with respect to the geometric configuration as shown in Sect. 9.2. The loads acting on the floating wind turbine are composed of the aerodynamic loads acting on the blades and tower, the hydrostatic and hydrodynamics loads acting on the spar platform, the inertia characteristics of the system, and the mooring loads acting on the fairlead of the platform. The loads generated by wave and winds are spatial and temporal functions and are distributed on the whole surface of the structural. In here, the modeling of blades, the tower, and spar platform is divided into numbers of small sections, and distributed loads on a section are expressed with a concentrated force acting on the geometry center of the section (Zhu and Yoo 2016a). Finally, all the concentrated forces are summed up according to the strip theory to express the whole loads.

9.3.1   Blade

A blade rotates within a fully enclosed wind, and the aerodynamic loads acting on the blade are divided into the lift forces, L, and the drag forces, D, with respect to the local coordinate, as shown in Eq. (9.9):

$$L = \tfrac{1}{2}\rho W^2 c C_L\,(\alpha)$$
$$D = \tfrac{1}{2}\rho W^2 c C_D\,(\alpha)$$

(9.9)

where ρ is the air density, W is the relative velocity on the blade, c is the cord length of a blade section, α is the angle of attack, is the C_L and C_D are the nondimensional lift and drag coefficients, respectively. An illustration of the lift and drag forces and the attack angle is shown in Fig. 9.6. W includes the effect of induced velocity. BEM is often used to discretize the rotor into many elements and obtain the induced velocity on each annular segment.

9.3.2   Spar

The modeling of spar is divided into several axial elements as shown in Fig. 9.7 (Zhu and Yoo 2015). The origin of the spar frame is located at the geometric center. Initially, the directions of the axes coincide with those of the IRF condition. Initially, the spar is at equilibrium in still water. Because both the acceleration and speed of the water particles vary with the water depth, the total wave loads are the summation of the wave loads acting on all the axial elements.

Fig. 9.6 Schematic of the lift, drag, and angle of attack of a blade airfoil
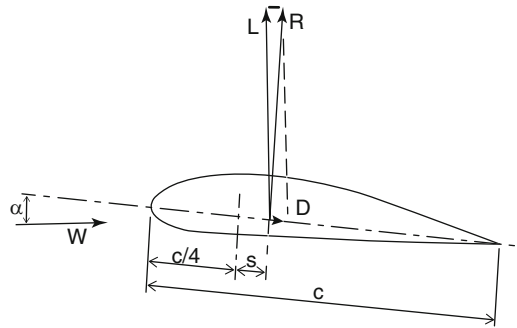
Fig. 9.7 Numerical modeling of a spar platform
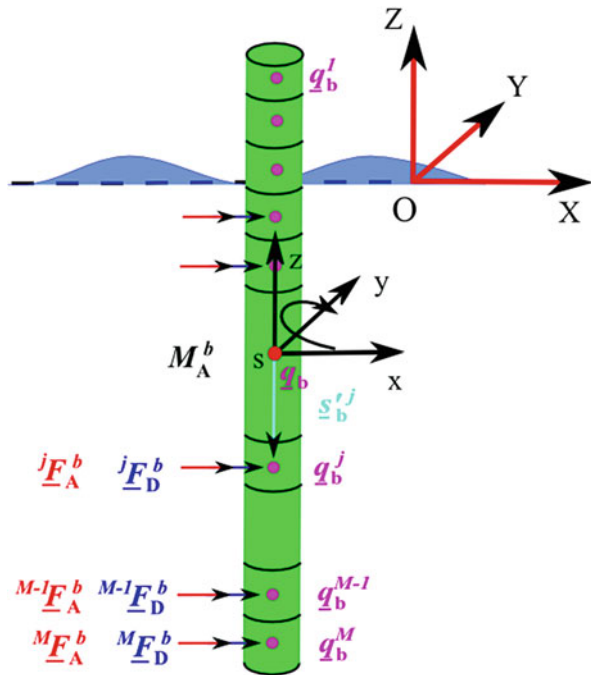
The floating spar survives in a complex environmental condition that can be expressed using several external forces. The external forces acting on the spar platform are denoted by $\underline{F}^b$, which can be found in Eq. (9.10). It is composed of the buoyancy $\underline{F}^b_B$, the effects of the added mass and Froude-Krylov force $\underline{F}^b_A$, the hydrodynamic drag forces $\underline{F}^b_D$, and the associated moments M^b_A generated when the forces acting on the spar elements are translated to the origin of the spar frame.

$$\underline{F}^b = \underline{F}^b_B + \underline{F}^b_A + \underline{F}^b_D + M^b_A \tag{9.10}$$

The buoyancy is equal to the weight of the displaced fluid and directs the inverse direction of the gravity. The restoring moments are generated when the buoyancy is

misaligned with the gravity. Therefore, the buoyancy, the gravity, and the restoring moments are expressed together, as shown in.

$$\underline{F}_B^b = \rho g V_0 \underline{\delta}_{i3} - M^b \underline{g} + \underline{\underline{C}}^b \underline{q}_b \tag{9.11}$$

The first term on the right-hand side of the above equation represents the buoyancy when the spar is in its unmoved position. V_0 is the displaced volume of fluid at that case. The vector $\underline{\delta}_{i3}$ indicates the buoyancy is toward the Z-direction. The second term is the weight of the spar platform. The last term represents the change of the buoyancy and restoring moments as the spar is displaced. In view of the cylinder shape of the platform, matrix $\underline{\underline{C}}^b$ is shown as Eq. (9.12), where A_0 is the cross area of the spar and z_{CB} is the Z-component of the center of buoyancy with respect to the spar frame.

$$\underline{\underline{C}}^b = \begin{bmatrix} 0 & 0 & 0 & 0 & 0 & 0 \\ 0 & 0 & 0 & 0 & 0 & 0 \\ 0 & 0 & \rho_f g A_0 & 0 & 0 & 0 \\ 0 & 0 & 0 & \rho_f g V_0 z_{CB} & 0 & 0 \\ 0 & 0 & 0 & 0 & \rho_f g V_0 z_{CB} & 0 \\ 0 & 0 & 0 & 0 & 0 & 0 \end{bmatrix} \tag{9.12}$$

The Froude-Krylov force is introduced by the unsteady pressure generated by the propagating waves in the horizontal directions. The added mass effects come from the relative acceleration between the wave particles and the spar platform. The added mass and Froude-Krylov effects are expressed as.

$$^j\underline{F}_A^b = (1 + C_A)\, V_s \rho_f \cdot \underline{\dot{V}}_f^j - C_A V_s \rho_f \underline{\ddot{q}}_b^j \tag{9.13}$$

where V_s denotes the volume of the spar element, $\underline{\dot{V}}_f^j$ is the acceleration of the water particles at the jth element, and $\underline{\ddot{q}}_b^j$ represents the acceleration of the jth element of the spar. Because the spar and cable are cylinder shaped, the added mass coefficient C_A is set to be 1 in here (Det Norske Veritas 2010a, b).

According to the Morison equation, the hydrodynamic drag force is a quadratic function of the relative velocity of the fluid. The hydrodynamic drag force is expressed as Eq. (9.14), where C_d is the drag coefficient and A_b is the cross area of the element in the vertical direction. The vector $\underline{V}_f^j$ is the relative velocity of the jth element with respect to the fluid.

$$^j\underline{F}_D^b = -\frac{1}{2} C_d \rho_f A_b \mid \underline{V}_f^j \mid \underline{V}_f^j \tag{9.14}$$

The velocity of the jth element, $\underline{\dot{q}}_b^j$, is defined as Eq. (9.15). $\underline{q}_b$ is the origin of the spar frame with respect to the IRF, and $\underline{\dot{q}}_b$ is the first time derivative of $\underline{q}_b$. $\underline{\underline{A}}_b$ is

the rotational transformation matrix (RTM) of the spar. The vector $\underline{s}'^{j}_{b}$ denotes the position of the spar element with respect to the spar frame, where $\underline{\tilde{s}}'^{j}_{b}$ represents the skew symmetric of the position vector $\underline{s}'^{j}_{b}$.

$$\dot{\underline{q}}^{j}_{b} = \dot{\underline{q}}_{b} - \underline{A}_{b}\underline{\tilde{s}}'^{j}_{b}\omega' \tag{9.15}$$

The strip theory is used to sum up the hydrodynamic loads, the effect of the added mass, and the Froude-Krylov force acting on the submerged spar elements. These forces are expressed with respect to the local frame of the spar and concentrated at the center of each element. The associated moments, as shown by Eq. (9.16), are added while translating the forces acting on the elements to the origin of the spar frame.

$$M^{b}_{A} = \sum_{j=1}^{M}\left({}^{j,1}F^{b}_{A}\cdot s'^{j,3}_{b} + {}^{j,1}F^{b}_{D}\cdot s'^{j,3}_{b}\right) \tag{9.16}$$

where ${}^{j,1}F^{b}_{A}$ is the first value of the jth vector $\underline{F}^{b}_{A}$ and $s'^{j,3}_{b}$ is the Z-directional component of $\underline{s}'^{j}_{b}$, which is the position vector of the jth element of the spar with respect to the spar frame. The added moment M^{b}_{A} is valid only when the jth element is submerged in the fluid.

9.3.3 Mooring Cable

The mooring cable is modeled by the lumped-mass model consisting of nodes and elements. The nodes are the embodiment of the cable modeling and have inertial properties, whereas the cable element is massless and acts as a carrier for both the internal and external loads that are finally carried by cable nodes. Based on researches (Zhu and Yoo 2016a, 2017), the cable is simplified using the lumped-mass-and-spring modeling scheme, wherein the cable is divided into N elements ordered from top to bottom, as shown in Fig. 9.3. The previous paper developed a new ERF by which the formulations of both the rotational transformation matrix and the external forces are effectively expressed. Element position vector $\underline{E}^{i}_{g}$ is expressed by the positions of the terminal nodes, as given by Eq. (9.17). Relative velocity $\underline{V}^{R}_{g}$ is the mean value of the relative velocities acting on the terminal nodes, as given by Eq. (9.18). $\dot{\underline{N}}^{i}_{g}$ is the velocity of the ith node:

$$\underline{E}^{i}_{g} = \underline{N}^{i+1}_{g} - \underline{N}^{i}_{g}, \tag{9.17}$$

Fig. 9.8 Element-fixed
reference frame
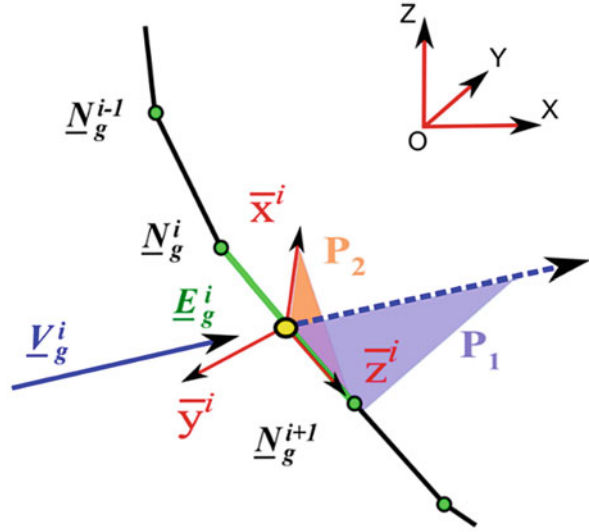
$$\underline{V}_g^R = \frac{\underline{V}_g^{i+1} + \underline{V}_g^i}{2},$$

$$\underline{V}_g^i = \underline{V}_g^f - \underline{\dot{N}}_g^i,$$

(9.18)

$$\bar{z}^i = \frac{\underline{E}_g^i}{\left\| \underline{E}_g^i \right\|},$$

$$\bar{x}^i = \frac{\tilde{z}^i \underline{V}_g^R}{\left\| \tilde{z}^i \underline{V}_g^R \right\|},$$

(9.19)

$$\bar{y}^i = \tilde{z}^i \bar{x}^i.$$

Unit axis $\bar{z}^i$ directs the orientation of the ith element and is obtained by unitizing
the element position vector $\underline{E}_g^i$, as illustrated in Fig. 9.8 (Zhu and Yoo 2016a). Unit
axis $\bar{x}^i$ is perpendicular to plane P_1, which is composed of unit axis $\bar{z}^i$ and relative
velocity, $\underline{V}_g^R$. According to the right-hand principle, unit axis $\bar{y}^i$ is perpendicular to
plane P_2, which is composed of unit axes $\bar{z}^i$ and $\bar{x}^i$. The unit axes of the ith element
are given specifically by Eq. (9.19).

The forces acting on the cable include the stiffness of the cable $\underline{T}_b^i$, damping of
the cable $\underline{D}_b^i$, hydrodynamic drag forces F_z^i and F_y^i, and apparent weight $\underline{F}_W^i$. These
forces are expressed in detail in references (Buckham et al. 2003; Milinazzo et al.
1987; Huang 1994) and are briefly listed in Eq. (9.20):

$$\underline{T}_b^i = \tfrac{\pi d_c^2}{4} E \varepsilon_b^i \bar{z},$$

$$\underline{D}_b^i = C_d \underline{\underline{A}}^{iT} \left(\dot{N}_g^{i+1} - \dot{N}_g^i \right) \bar{z},$$

$$F_z^i = \tfrac{\pi}{2} C_f \rho_f d^i l^i \left\| \underline{V}_g^R \right\| \bar{z}^T \underline{V}_g^R, \tag{9.20}$$

$$F_y^i = -\tfrac{1}{2} C_n \rho_f d^i l^i \left\| \underline{V}_g^R \right\| \bar{x}^T \left(\tilde{z} \underline{V}_g^R \right),$$

$$\underline{F}_W^i = \left(m_c^i - m_f^i \right) \underline{g},$$

where ε_b^i is the axial strain, l^i represents the length of the ith cable element, and the masses of the cable and the displaced fluid for the ith element m_c^i and m_f^i are given by.

$$\varepsilon_b^i = \tfrac{l^i - l_0^i}{l_0^i}$$

$$l^i = \sqrt{\underline{E}_g^{iT} \underline{E}_g^i}$$

$$m_c^i = \tfrac{\pi d_c^2}{4} l_0^i \rho_c \tag{9.21}$$

$$m_f^i = \tfrac{\pi d_c^2}{4} l_0^i \rho_f$$

The mass matrix of the ith element with respect to the ERF is given by Eq. (9.22). The added mass effect along the cable axial is ignored; C_A is the added mass coefficient.

$$M^i = \begin{pmatrix} m_c^i + C_A m_f^i & 0 & 0 \\ 0 & m_c^i + C_A m_f^i & 0 \\ 0 & 0 & m_c^i \end{pmatrix}. \tag{9.22}$$

Mass matrices of the nodes with respect to the IRF are expressed by mass matrices of the elements with respect to local reference frame. Here, the mass matrix of the ith node M_I^i is composed of the element-mass matrices M_b^{i-1} and M_b^i and is given by

$$M_I^i = \tfrac{1}{2} \underline{\underline{A}}^{i-1} M_b^{i-1} \underline{\underline{A}}^{i-1T} + \tfrac{1}{2} \underline{\underline{A}}^i M_b^i \underline{\underline{A}}^{iT}. \tag{9.23}$$
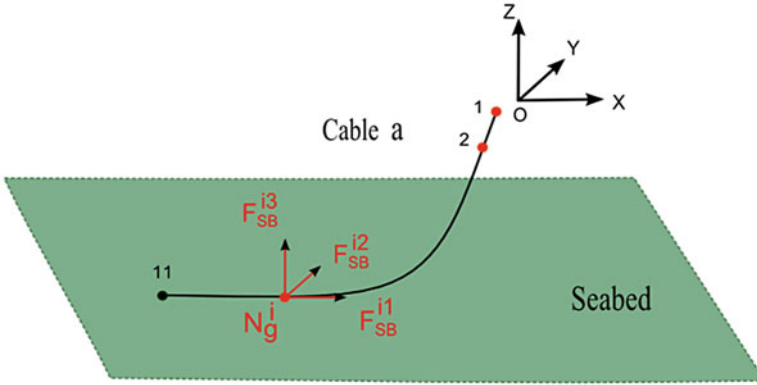
Fig. 9.9 Impact of seabed on mooring cable

Finally, the forces acting on each cable element are shared equally by the element terminal nodes. The governing equation for the ith node is defined by the forces acting on the $(i-1)^{\text{th}}$ and the ith element, as given by Eq. (9.24).

$$
\begin{aligned}
M^i \ddot{N}_g^i &= \underline{\underline{A}}^i \left(T_b^i + D_b^i + \tfrac{1}{2} F_D^i \right) \\
&\quad - \underline{\underline{A}}^{i-1} \left(T_b^{i-1} + D_b^{i-1} - \tfrac{1}{2} F_D^{i-1} \right) + \tfrac{1}{2} \left(F_W^i + F_W^{i-1} \right)
\end{aligned}
\tag{9.24}
$$

The impact of the seabed on the cable is divided into three components with respect to the IRF, as shown in Fig. 9.9. The vertical component, F_{SB}^{i3}, is a function of the relative displacement and velocity of the grounded nodes with respect to the seabed; the X- and Y-components, F_{SB}^{i1} and F_{SB}^{i2}, are functions of the relative velocities and the vertical component of the impact, as shown in Eq. (9.25) where K_{sb}, C_{sb}, and μ denote the stiffness, the damping coefficients, and the friction coefficient of the seabed, respectively:

$$
\begin{aligned}
F_{SB}^{i3} &= K_{sb} \left(D_{sb} - N_g^{i3} \right) - C_{sb} \dot{N}_g^{i3} \\
F_{SB}^{i1} &= \mu\, F_{SB}^{i3}\, \dot{N}_g^{i1} \\
F_{SB}^{i2} &= \mu\, F_{SB}^{i3}\, \dot{N}_g^{i2}
\end{aligned}
\tag{9.25}
$$

9.3.4 Governing Equations

The constraints define the relationship between two independent bodies. A rigid body has six DOFs in three dimensions, while a mass point only has three translational DOFs. Three-dimensional spherical joint modeling was well developed

in references (Nikravesh 1988; Bauchau 2010), but an applicable modification is needed for connecting the spar and cable, because the cable node only has three translational DOFs. The constraint equation $\underline{\Phi}^{sph}$ is expressed by.

$$\underline{\Phi}^{sph} = \underline{q}_b + \underline{\underline{A}}_b \underline{s}_b^{\prime j} - \underline{N}_g^1 \tag{9.26}$$

Because the *first* node of the cable connects to the floating spar, the positon vector of the *first* node, $\underline{N}_g^1$, is used to express the constraint. The Jacobian matrix of the constraint equation is shown in Eq. (9.27).

$$\underline{\underline{\Phi}}_q^{sph} = \left[\underline{\underline{I}} - \underline{\underline{A}}_b \underline{\tilde{s}}_b^{\prime j} \underline{\underline{G}}' - \underline{\underline{I}} \right] \tag{9.27}$$

$$\omega' = G' \dot{\theta}^b \tag{9.28}$$

The rotation angles of the Euler angle set are chosen as the general coordinates. The relationship between the angular velocities of the body and the rotation angles is expressed using $\underline{G}'$, as shown in Eq. (9.28). The Euler angle set, X-Y-Z, expresses the rotation of the spar with respect to the IRF in here. The $\underline{G}'$ for the Z-X-Z set is given by Shabana (Shabana 2013), the $\underline{G}'$ for the X-Y-Z set can be derived according to Greenwood (Greenwood 1988). γ is rest components of the constraint equations and composes of the general coordinates and the first derivation of the general coordinates with respect to the time as given in

$$\gamma = \left(\underline{\underline{A}}_b \underline{\tilde{\omega}}' \underline{\tilde{s}}_b^{\prime j} \underline{\underline{G}}' + \underline{\underline{A}}_b \underline{\tilde{s}}_b^{\prime j} \underline{\dot{\underline{G}}}' \right) \underline{\dot{\theta}}^b \tag{9.29}$$

Finally, the equation of motion for the system of floating spar with mooring cables is expressed in Eq. (9.30). M is the mass matrix of the system, and Q is the external forces modified according to the relationship between the orientation of the structure and the rotation angles. The matrix $\left(\Phi_q^{sph} \right)^T$ denotes the transposed Jacobian matrix.

$$\begin{bmatrix} M & \left(\Phi_q^{sph} \right)^T \\ \Phi_q^{sph} & 0 \end{bmatrix} \begin{bmatrix} \ddot{q} \\ \lambda \end{bmatrix} = \begin{bmatrix} Q \\ \gamma \end{bmatrix} \tag{9.30}$$

9.3.5 Numerical Results

The accuracy of the cable modeling has been verified by both commercial software and experiments (Zhu and Yoo 2016d). A simple numerical model is created to

illustrate the dynamic behavior of the cables of a floating spar platform. The bottom of the spar platform is tethered by one cable, and the bottom of the cable is fixed to the seabed. The properties of the spar and the cable are shown in Table 9.3 and Table 9.4, respectively. This model is subjected to the X-directional waves, the Y-directional waves, and the X-directional current. The sea state parameters are shown in Table 9.5.

The tension in the cable, the three-directional reaction forces of the cable acting on the fairlead of the spar platform, and the apparent weight of the cable in the sea are shown in Fig. 9.10. The results indicate that the Z-directional reaction force is much close to the tension force in the cable. Since the bottom of the cable is fixed to the seabed, both the gravity force and the hydrodynamic force of the cable sink it to the bottom of the sea, but the buoyancy of the spar drags the cable to a dynamic equilibrium position. Because the cable is fully submerged, the apparent weight is constant and is much smaller than the tension in the cable. This indicates that the hydrodynamic force on the cable has a great impact on the fairlead position of the spar. Due to the X-directional current, the X-directional force is larger than the Y-directional force. The relationship of the cable tension with the frequencies of the propagating waves can be found in references (Zhu and Yoo 2016a, b).

Table 9.3 Properties of the spar

Diameter of spar	0.5 m
Mass of spar	500 kg
Length of spar	6 m
Center of mass above bottom	1 m
Drag coefficient	1
Added mass coefficient	1
No. of elements	100

Table 9.4 Properties of the cable

Diameter of cable	0.03 m
Density of cable	3570 kg/m^3
Elastic modulus	2.38 Gpa
Damping coefficient	1000 Ns/m
Transversal drag coefficient	1
Longitudinal drag coefficient	0.01
Added mass coefficient	1
Position of the top node	(0,0,-2.98) m
Position of the bottom node	(0,0,-30) m
No. of elements	20

Table 9.5 Sea state parameters

X-directional wave amplitude	0.6 m
X-directional wave period	6 s
Y-directional wave amplitude	0.6 m
Y-directional wave period	6 s
Current	(0.5,0,0) m/s
Water density	1025 kg/m^3,
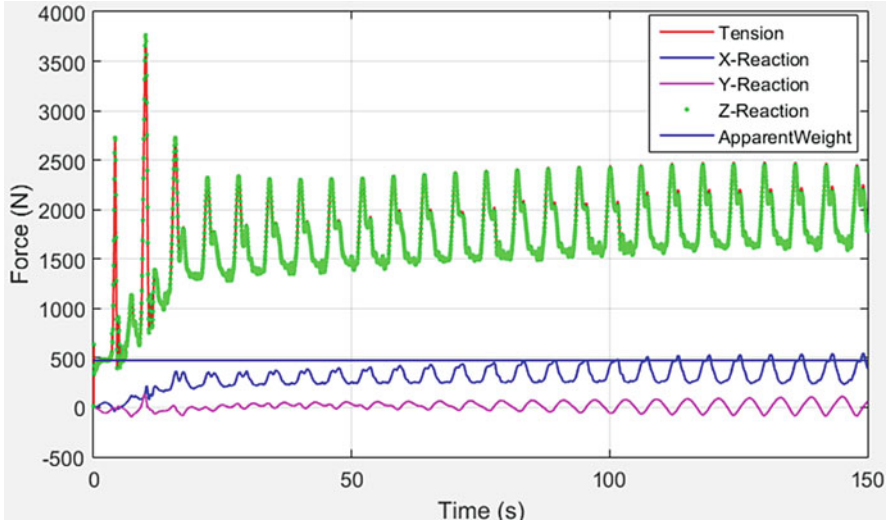
Fig. 9.10 The tension force within the cable, the three-directional reaction forces of the cable acting on the fairlead of spar platform, and the apparent weight of the cable in the sea

9.4 Dynamic Behavior of Floating Wind Turbines

Floating wind turbines are subjected to the combined load effects of wind, waves, control actions, and rarer events such as earthquakes and ship collisions. When it comes to the dynamic behavior of floating wind turbines, there exist disparities among the aforementioned concepts because of their inherent characteristics. We illuminate this point by an example. Figure 9.11 shows a typical relation between rotor thrust characteristics for a pitch-regulated wind turbine with a control frequency of 0.1 Hz. Above the rated wind speed, negative thrust gradient is observed because of the changed blade pitch, which changes the direction of the effective force. This controller, if applied to a spar-type floating wind turbine, will result in instabilities in the platform surge motion, because the traditional controller is faster than the pitch natural frequency of the Hywind Demo (0.035 Hz) (Larsen and Hanson 2007). However, if the same controller is used for a tension leg platform wind turbine with a pitch natural frequency of 0.3 Hz, the instability issue will not appear.

In this section, we direct the readers' attention to the dynamic behavior of spar-type floating wind turbines. The response characteristics of a spar-type turbine are highlighted under fault conditions.
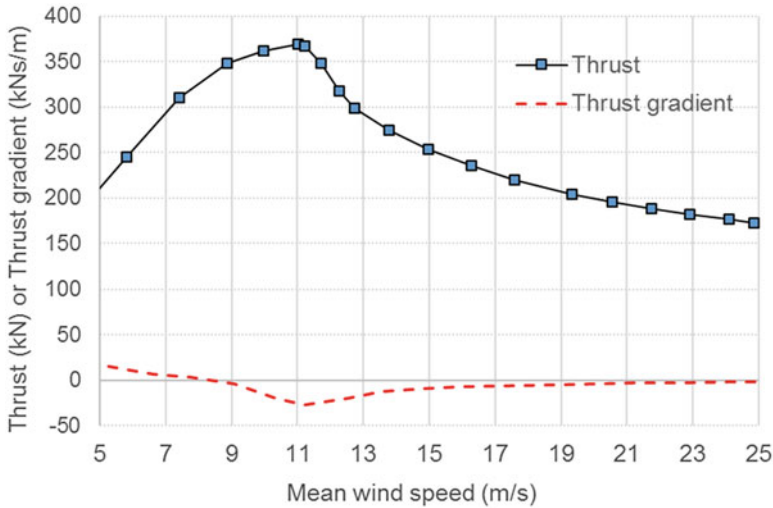
Fig. 9.11 Relation between rotor thrust and wind speed for a typical pitch-regulated wind turbine

Table 9.6 Occurrence evaluation criteria from Ireson et al. (1996)

Probability of faults	Rank	Likely fault rate
Remote: Unlikely fault	1	<0.1% of faults
Low: Rare fault	2	0.1–1% of faults
	3	1–2% of faults
Moderate: Occasional fault	4	2–3% of faults
	5	3–4% of faults
	6	4–5% of faults
High: Repeated fault	7	5–10% of faults
	8	10–15% of faults
Very high: Almost inevitable faults	9	15–20% of faults
	10	>20% of faults

9.4.1 Wind Turbine Faults and Control Remedies

During wind turbines' lifespan, many turbine components are exposed to faults and failures. A fault refers to unpermitted deviation of characteristic properties of the system from the acceptable condition, and failure refers to a permanent interruption of a system's ability to perform a required function under the specified operating conditions. Although faults and failures are different, they are often interchangeably used. Faults can be classified based on their occurrence and the severity of their end-effects. Table 9.6 quantifies the occurrence on a scale from 1 to 10, and these values have only a relative meaning. Table 9.7 provides the severity scale that is applied in the failure mode and effect analysis during product development processes. Severity refers to the harm inflicted on wind turbines or other products.

Table 9.7 Severity evaluation criteria from Stamatis (2003)

Effect	Rank	Criteria
No effect	1	No effect on product or subsequent processes
Very slight effect	2	Very slight effect on product/service performance. Non-vital faults noticed sometimes
Slight effect	3	Slight effect on product/service performance
Minor effect	4	Minor effect on product/service performance. Fault does not require attention. Non-vital faults always noticed
Moderate effect	5	Moderate effect on product/service performance. Fault in non-vital part requires repair
Significant effect	6	Product/process performance degraded, but operable and safe. Non-vital service incomplete
Major effect	7	Major effect on service; rework on service necessary. Product/process performance severely affected but functioning and safe. Subsystem incomplete
Extreme effect	8	Extreme effect on process/service; equipment damaged. Product/service incomplete but safe. System incomplete
Serious effect	9	Potential hazardous effect. Able to stop product/service without mishap. Safety-related. Time-dependent failure. Disruption to subsequent process operations. Compliance with government regulation is in jeopardy
Hazardous effect	10	Hazardous effect. Safety-related sudden failure. Non-compliance with government regulation

Table 9.8 Evaluation of selected wind turbine faults from Mohammed and Aboelyazied (2007), Esbensen and Sloth (2009), Johnson and Fleming (2011)

Fault specification	Component	Effect	Occurrence	Severity
Dirt on blades	Blade surface	Decreased efficiency	10	3
Biased sensor output	Pitch sensor	Unbalanced rotation	3	6
Pump leakage	Pitch actuator	Changed dynamics	3	8
Valve blockage	Pitch actuator	Out of control	3	8
Bearing wear	Drivetrain	Decreased efficiency	3	3

Table 9.8 lists selected wind turbine faults from various sources in the public domain. Sensor faults and actuator faults are the two primary fault types. Many modern wind turbines contain a supervisory control and data acquisition (SCADA) system and a condition monitoring system. The SCADA system handles input and output signals and alarms; this system usually samples signals at 10-min intervals and provides low-resolution monitoring to supervise the operation of wind turbines. Compared with the SCADA system, the condition monitoring system is more costly, but it provides high-resolution monitoring of high-risk subassemblies for diagnosis and prognosis of faults (Tavner 2012). A vast number of sensors are installed on a modern wind turbine, e.g., rotor speed sensors and pitch position sensors. Because of the physical redundancy of the sensors, sensor faults can be harmless if they are detected quickly and the sensor system is reconfigured. Actuator faults can cause severe consequences if not handled in a timely manner.
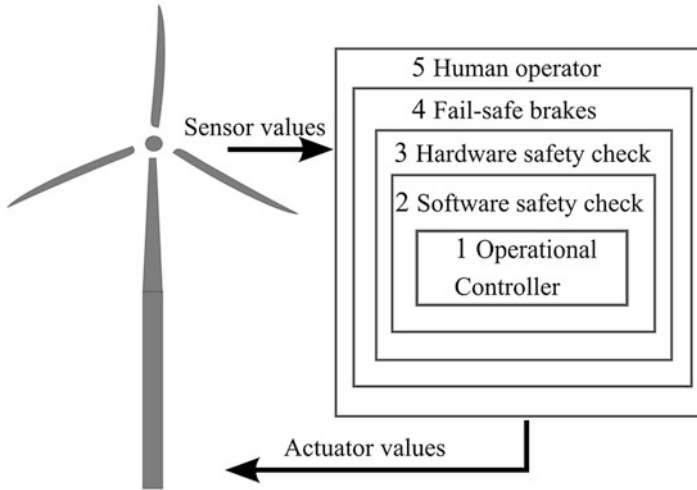
Fig. 9.12 Hierarchy of a wind turbine control system

Figure 9.12 shows a typical hierarchy of the wind turbine control system. For a pitch-regulated wind turbine and under normal conditions, the operational controller regulates the power production of the turbine through control of the blade pitch, generator torque, and yaw. The occurrence of faults changes the system characteristics and alters the signal output from the sensors. The online condition monitoring of all wind turbine components enables the control system to detect, isolate, and accommodate the type, size, and location of the fault at an early stage. A suite of techniques exist for fault detection and isolation, e.g., observer-based schemes (Chen et al. 2011), support vector-based schemes (Laouti et al. 2011), and data-driven approaches (Dong and Verhaegen 2011). These techniques exhibit varying performance in terms of detection time and accuracy. Upon detection of a fault, the supervisory controller selects a remedial action based on existing protection strategies. If the fault is controllable, it will be accommodated using techniques like signal correction and fault-tolerant control. If the situation is severe and the turbine is not in a safe state, the supervisory controller brings the turbine to a halt. Note that the hardware safety system is also capable of performing shutdown independently. In the worst case, if the main control system fails to stop the turbine safely, the safety system takes over. The safety system normally consists of a hard-wired fail-safe circuit linking a number of open relay contacts (Burton et al. 2011). A human operator can override the safety system and execute shutdown under emergency situations.

9.4.2 Response of a Spar-Type Floating Wind Turbine Under Fault Conditions

In the previous section, we have named a few faults, among which the pitch mechanism faults are of particular interest to us, as this fault changes the aerodynamic loading on a turbine.

Since the 1980s, full-span pitching of the blade has been widely employed for wind turbines. Active pitch control was primarily applied for power regulation but offers other advantages. The pitch mechanism can be either electric or hydraulic. There is no clear winner, yet, but maintenance and diagnostics of hydraulic systems are generally easier because fewer components are used. We focus on the hydraulic pitch mechanism, which normally consists of the following subsystems:

- Hydraulic cylinders
- Distributed block with filter
- Leak oil container
- Accumulators
- Hydraulic circuit
- Pitch system brackets
- Rotation unions

A simplified sketch of a hydraulic pitch actuator is provided in Fig. 9.13. Each individual blade can be pitched independently in such a configuration. Pitch maneuverability is dictated by the internal controller, valve characteristics, and capacity of the accumulator. Based on the fail-safe design philosophy, the pitch system of a collective pitch turbine should be able to achieve higher pitch speed (10–15 deg./s) in an emergency situation.
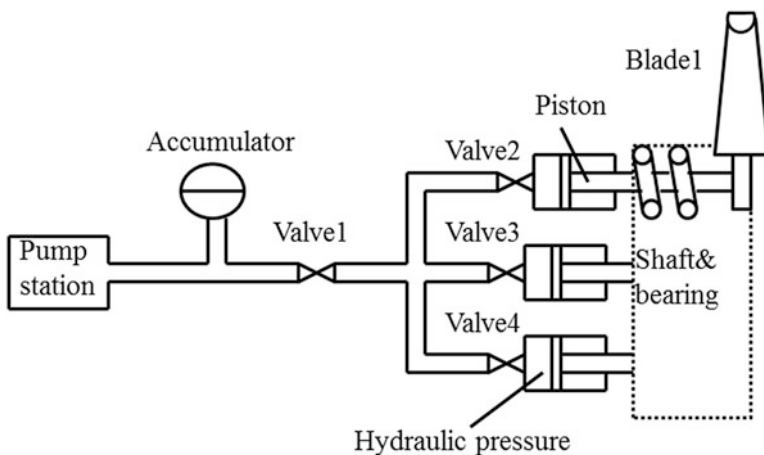
Fig. 9.13 Configuration of a hydraulic pitch actuator for wind turbine

Fig. 9.14 Sequence of the normal operation, fault development, detection, and shutdown
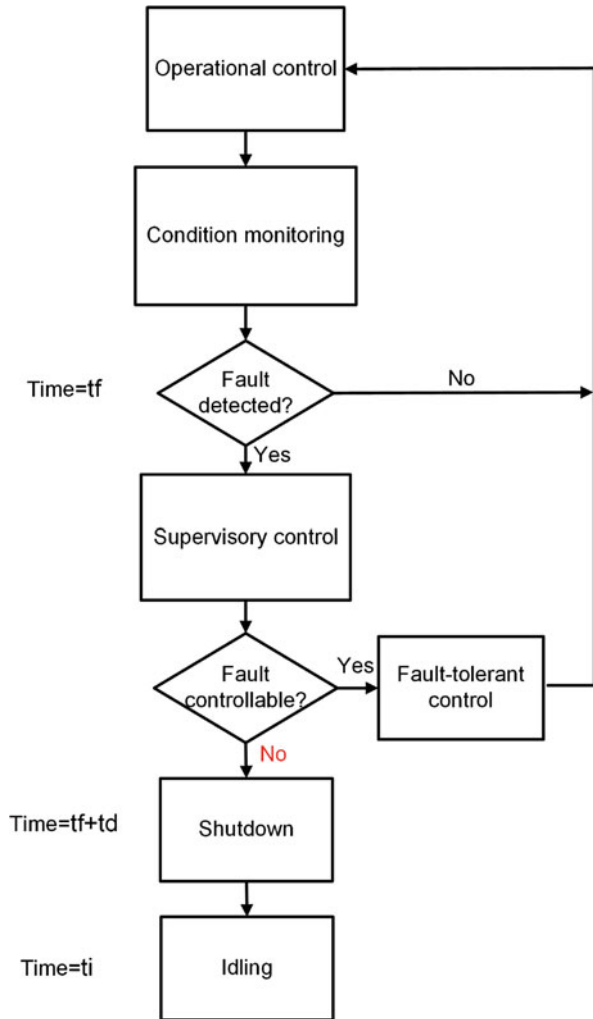
Figure 9.14 shows the operation of a wind turbine which experiences a fault condition. The option of fault-tolerant control applies to less severe faults such as sensor faults. The pitch system fault is deemed severe by the supervisory controller and calls for an immediate shutdown. In the numerical simulations, the time length can be divided into the following four stages:

- Normal operation: Turbine is operational without fault (Time $< tf$).
- Fault occurrence: Fault is initiated, but no remedy measures are applied yet ($tf <$ Time $< tf + td$).
- Shutdown: The normal blades are pitching to feather ($tf + td <$ Time $< ti$) with a rotor speed above 3 RPM.

- Idling: The rotor speed drops below 3 RPM (Time > *ti*).

Here, shutdown refers to the pitch-to-feather activity of the pitch-regulated wind turbines. A mechanical brake may be engaged if necessary. For many utility-scale wind turbines, the mechanical brakes are mainly used during maintenance. The numerical simulations were conducted by implementing the control logic in the DLL, which communicates with the HAWC2 core in discrete time steps. After the occurrence of faults, the user-defined logic supersedes the operational controller and performs desired activities on the turbine.

For floating wind turbines, the change in aerodynamic loads is a key driver of the dynamic responses under the pitch fault and shutdown conditions. Figures 9.15 and 9.16 illustrate the aerodynamic loads on a cross section of a seized and a
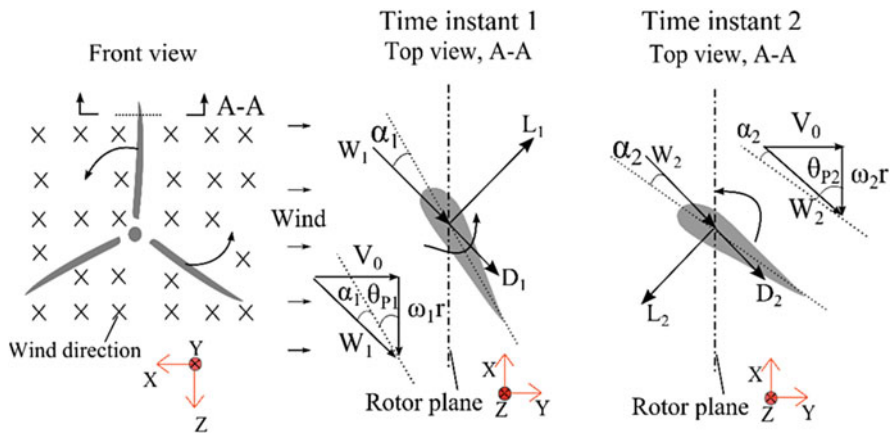
Fig. 9.15 Illustration of the aerodynamic loading on a pitching blade during shutdown
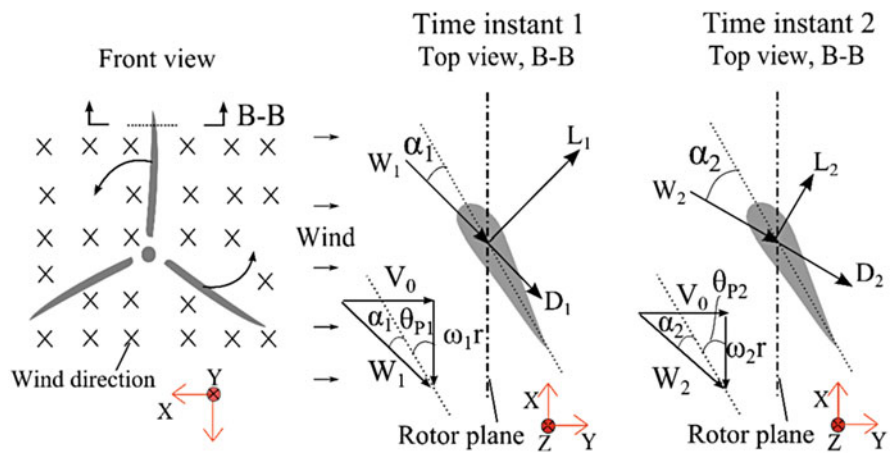
Fig. 9.16 Illustration of the aerodynamic loading on a seized blade during shutdown

Fig. 9.17 Front view of a rotor during shutdown, with two pitching blades and one seized blade
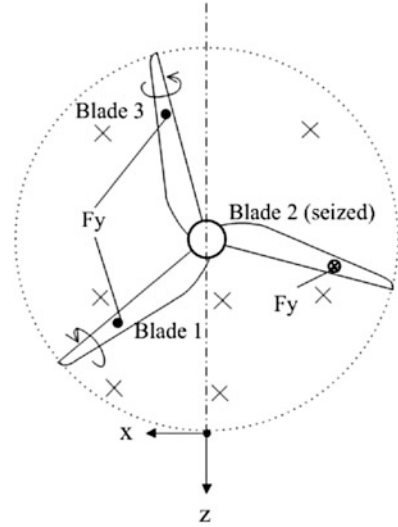
pitching blade at two time instants during the shutdown process. In the figures, α is the aerodynamic angle of attack (AOA), θ_p is the pitch angle, V_0 is the inflow wind velocity, ωr is the velocity at radius r induced by the rotation of the rotor, and W is the relative velocity. As illustrated by Fig. 9.16 during shutdown, a normal blade experiences a drop in AOA due to blade pitching. The rotor slows because of the reversal of direction of the lift force and torque, which is the mechanism of aerodynamic braking. Compared with the pitching blades, a seized blade experiences a rise in AOA during shutdown. Therefore, the directions of the aerodynamic forces do not reverse quickly. The pitching blades create a large aerodynamic force into the wind whereas the seized blade against the wind; see Fig. 9.17. This leads to imbalanced loads on the rotor plane, and other interesting motions and global response phenomena on floating wind turbines.

The layout of a 5 MW floating wind turbine is presented in Fig. 9.18. The floating wind turbine comprises the NREL 5 MW turbine (Jonkman et al. 2009b), a spar platform, and three sets of mooring lines. The delta-line segments form a bridle and provide high yaw stiffness for the platform motion. Details of this turbine can be found in (Jiang et al. 2013a). Note that HAWC2 was used in the following analysis, and a quasi-static mooring line model was considered. The quasi-static model ignores the mooing dynamics, which is discussed in Sect. 9.3.3.

Figure 9.19 illustrates the effect of emergency shutdown on the tower-bottom bending moment. Although one blade is seized and hindered from pitching, the shutdown process with two pitching blades still triggers great aerodynamic excitation that pulls the rotor into the wind. Consequently, negative fore-aft bending moment arises at the interface between the tower structure and the spat platform. Compared with bottom-fixed wind turbines, the spar-type floating system is more compliant, and the induced negative moment is not so prominent.
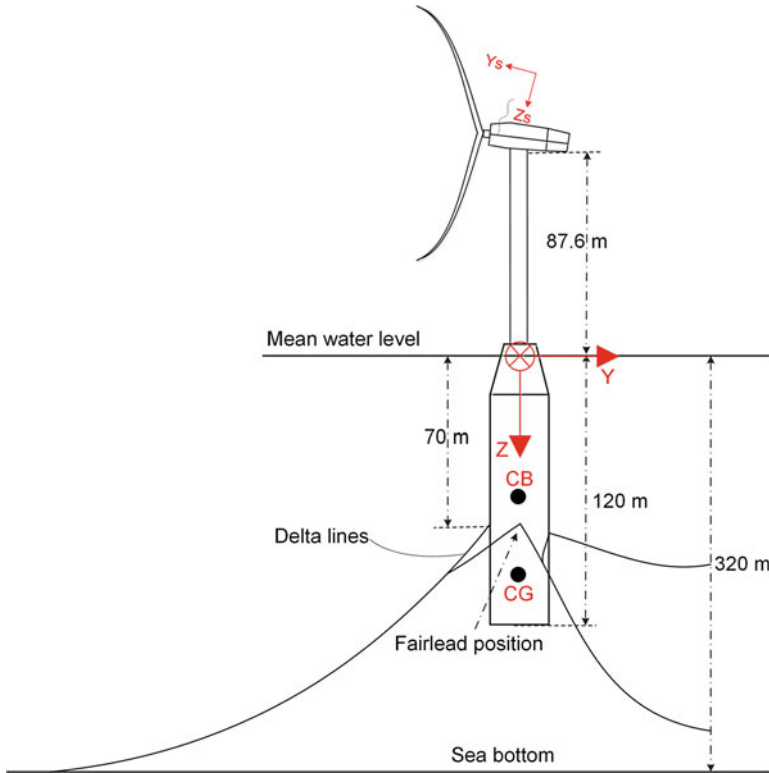
Fig. 9.18 Schematic layout of a spar-type floating wind turbine

Excessive transient responses are observed for the main-shaft equivalent bending moment during shutdown, as shown in Fig. 9.20. Such responses are due to the loads from rotor imbalance and can cause damages on the drivetrain components, e.g., main bearing. This phenomenon has been reported on bottom-fixed wind turbines (Jiang et al. 2013a, b) and is expected for other types of floating wind turbines. For an investigation on the drivetrain, interested readers are referred to (Nejad et al. 2016).

When one blade is seized during shutdown, because of the uneven aerodynamic loads across the rotor plane, large platform motions may occur. For spar-type wind turbines, the yaw motion experiences a significant increase in magnitude, as illustrated by Fig. 9.21. Compared to normal operational conditions, this increase can exceed 400%, which indicates an increase in the mooring line tension (Jiang et al. 2015). During the shutdown phase, strong yaw resonant motion is excited, with a period close to 8 s. For the tension leg platform and semisubmersible wind turbines, there are either greater platform stiffness or larger inertia, and the effects of fault on the platform-yaw motion may not be that severe (Bachynski et al. 2013).
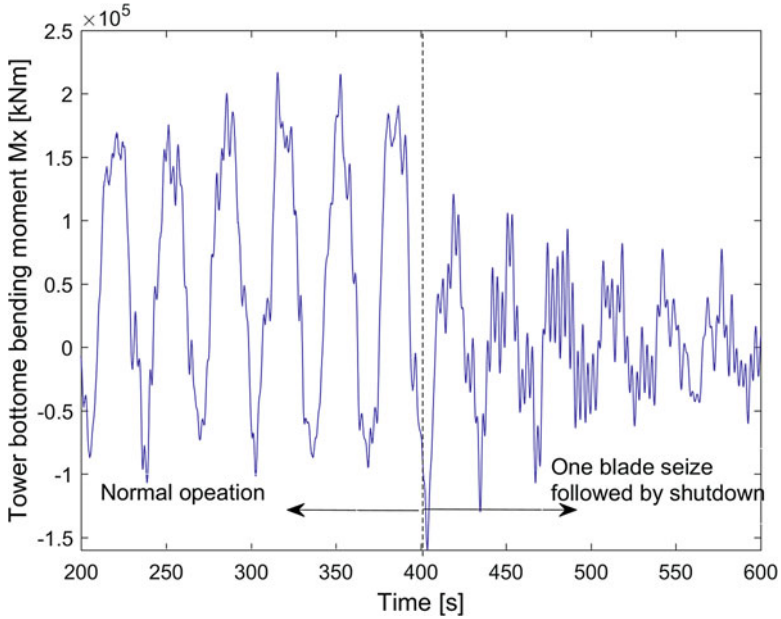
Fig. 9.19 Time series of the tower responses of the spar-type floating wind turbine (mean wind speed, 25 m/s; turbulence intensity, 0.15; significant wave height, 5.9 m; peak period, 11.3 s)
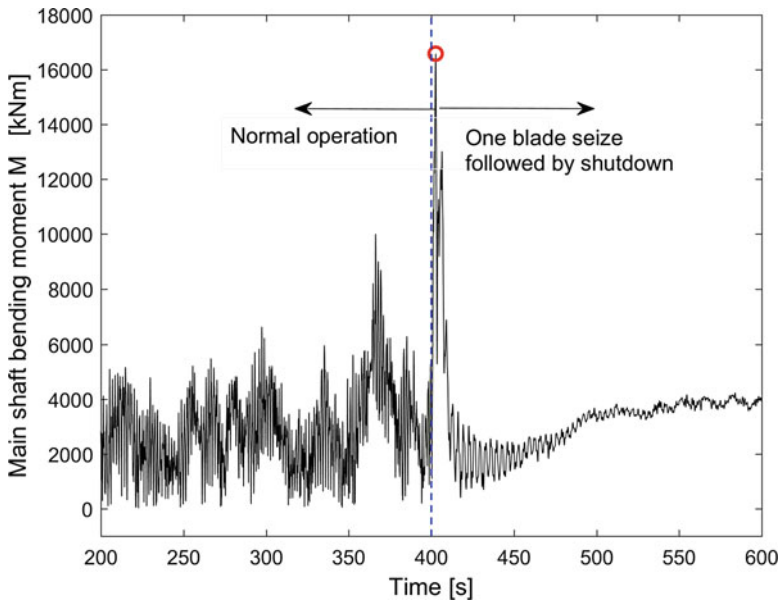
Fig. 9.20 Time series of the main-shaft responses of the spar-type floating wind turbine (mean wind speed, 25 m/s; turbulence intensity, 0.15; significant wave height, 5.9 m; peak period, 11.3 s)
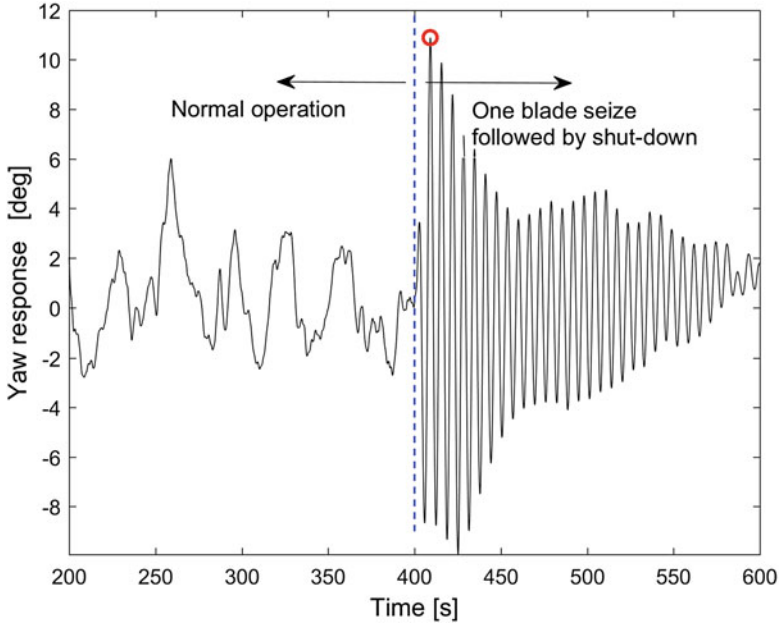
Fig. 9.21 Time series of the platform-yaw motion of the spar-type floating wind turbine (mean wind speed, 25 m/s; turbulence intensity, 0.15; significant wave height, 5.9 m; peak period, 11.3 s)

At the design stage of a floating wind turbine, a number of load cases need to be assessed to ensure that the turbine can survive the worst case during its lifespan. To have an idea of the importance of the fault cases, we will compare them with other extreme load cases recommended by the design standards. Among the load cases (LCs) listed in Table 9.9, LCs 1–3 are fault cases. In LC 1, the grid loss and shutdown case, the generator torque is lost at a specific time, followed by the pitch-to-feather shutdown of the three blades. In LC 2, only blade 2 is assumed to be seized, and its pitch angle is fixed from that specific time. The emergency shutdown ensues by pitching the remaining two blades. In LC 3, the blade runaway and shutdown case, one blade is assumed to be uncontrollably moving to the minimum pitch set (0 deg). A similar shutdown activity follows. In LCs 1–3, a short time delay, td, exists between the time of fault occurrence and the initiation of shutdown. The pitch rate of 8 deg./s is used in the emergency shutdown. LCs 4–5 are reference cases. In LC4 the wind turbines are under normal operation. LC 5 corresponds to the 50-year extreme environmental condition, where significant responses are expected. The acronym "NTM" stands for normal turbulence wind, and "EWM" stands for extreme wind speed model. Only collinear wind and wave conditions are addressed here.

The wind and wave conditions used in the time-domain simulations are listed in Table 9.10. Here, Uw is the 10-min mean wind speed at the hub height, Hs is the significant wave height, Tp is the wave peak period, and TI is the turbulence

Table 9.9 Selected design load cases for ultimate load analysis from International Electrotechnical Commission (2007, 2009)

Load case	Category	Condition	Wind model
1	DLC 2.2	Grid loss and emergency shutdown	NTM
2	DLC 2.2	Blade pitch fault (1-blade seize), grid loss, and emergency shutdown	NTM
3	DLC 2.1	Control system fault (1-blade runaway), grid loss, and emergency shutdown	NTM
4	DLC 1.1	Power production	NTM
5	DLC 6.1	Parked (standstill)	EWM

Table 9.10 Wind and wave conditions for the load cases

LC	U_w (m/s)	H_s (m)	T_p (s)	TI
1, 2, 3, 4	8	2.5	9.9	0.15
	11.2	3.2	10.0	0.15
	14	3.6	10.3	0.15
	17	4.2	10.5	0.15
	20	4.8	10.8	0.15
5	49.4	15.6	15.4	0.10

intensity. For the floating wind turbine, the environmental conditions are selected using the joint probability density distribution of the characteristic parameters of the Statfjord site, located in the northern North Sea (Johannessen et al. 2001).

Figure 9.22 compares the fault cases with the extreme load case in the parked condition. For the floating wind turbine, the studied grid loss case, pitch fault case, and controller fault case are not as critical as the case with extreme wind speed for dimensioning tower structures. For the ultimate load analysis of blades, the controller fault case produces 50% greater flapwise bending moments than the extreme case. The large yaw motion in fault cases indicates the need to perform a design check on the mooring line extreme loads. Most important, the main-shaft bending moment under the fault conditions can more than double the reference case and should catch attention for drivetrain design.

9.5 Conclusions and Future Recommendations

9.5.1 Conclusions

Continuous research activities have contributed to more accurate modeling and analysis of floating wind turbines. Compared to land-based wind turbines, floating platforms have more complicated dynamics, because of the station-keeping system and the platform motions, which affect the aerodynamics and control actions. It is important to consider advanced modeling methods to capture the dynamic performances of the floating systems. The mooring cable modeling method introduced in
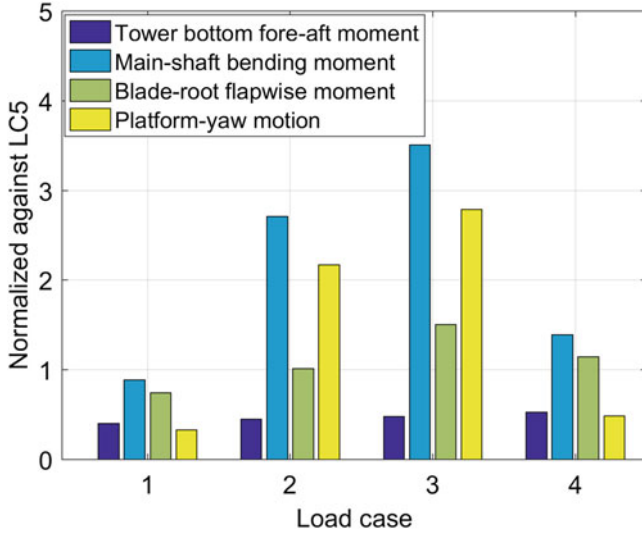
Fig. 9.22 Normalized extreme responses in load cases 1–4 against the reference case (LC5), spar-type wind turbine

this chapter can be applied to various mooring systems of floating wind turbines. For a floating wind turbine in operation, the mechanism of pitch fault and shutdown and the effect on dynamic responses are presented in this chapter. The fault can excite strong dynamic response of the system. The platform-pitch and platform-yaw resonant responses of the spar-type wind turbine are observed. Significant responses, sometimes more than twice those of the extreme wind speed case, can be found in the main-shaft bending moment and tower-top bending moment. For the blade-root flapwise bending moment, the pitch controller fault and shutdown should raise concern at the design stage.

9.5.2 Future Recommendations

Because of the terrestrial constraints on the seabed, the layout of the mooring system may not be symmetrical, and the impact between the cable and the seabed generate unbalanced loads on the fairlead. Future study should focus on the dynamic behavior of the wind turbines considering unbalanced loads from the mooring system.

Faults should be immediately diagnosed and detected upon occurrence for the safety of wind turbines. Therefore, machine learning models, such as the support vector machines, may be applied in the condition monitoring of wind turbine systems. For minor faults such as biased pitch sensor output, it is not economically viable to shut down the wind turbine after detection, and advanced control strategies are needed to continue power production. These interesting research topics can be pursued in the future.

References

Agarwal A, Jain A (2003) Dynamic behavior of offshore spar platforms under regular sea waves. Ocean Eng 30(4):487–516

Statoil AS (2017) Statoil to build the world's first floating wind farm: Hywind Scotland. https://www.statoil.com/en/news/hywindscotland.html

Bachynski EE, Etemaddar M, Kvittem MI, Luan C, Moan T (2013) Dynamic analysis of floating wind turbines during pitch actuator fault, grid loss, and shutdown. Energy Procedia 35:210–222

Bauchau OA (2010) Flexible multibody dynamics, vol 176. Springer Science & Business Media, Dordrecht

Bossanyi EA (2009) GH Bladed user manual. Garrad Hassan and Partners Limited, Bristol, England

Buckham BJ (2003) Dynamics modelling of low-tension tethers for submerged remotely operated vehicles. University of Victoria, British Columbia, Canada

Buckham B, Nahon M, Cote G (2000) Validation of a finite element model for slack ROV tethers. In: OCEANS 2000 MTS/IEEE Conference and Exhibition, IEEE pp 1129–1136

Buckham B, Nahon M, Seto M, Zhao X, Lambert C (2003) Dynamics and control of a towed underwater vehicle system, part I: model development. Ocean Eng 30(4):453–470

Burton T, Jenkins N, Sharpe D, Bossanyi E (2011) Wind energy handbook. Wiley, Hoboken

Butterfield S, Musial W, Jonkman J, Sclavounos P (2007) Engineering challenges for floating offshore wind turbines. In. National Renewable Energy Laboratory (NREL), Golden, USA

Chen W, Ding SX, Haghani A, Naik A, Khan AQ, Yin S (2011) Observer-based FDI schemes for wind turbine benchmark. IFAC Proc 44(1):7073–7078

Det Norske Veritas (2010a) Environmental conditions and environmental loads. Recommended Practice DNV-RP-C205, Oslo, Norway

Det Norske Veritas (2010b) Position mooring. Offshore Standard DNV-OS-E301, Oslo, Norway

Dong J, Verhaegen M (2011) Data driven fault detection and isolation of a wind turbine benchmark. IFAC Proc 44(1):7086–7091

Engineering BH (2017) Marine engineering sea star platform. http://www.brighthubengineering.com/marine-engines-machinery/30775-different-types-of-offshore-production-platforms-for-oil-extraction/

Esbensen T, Sloth C (2009) Fault diagnosis and fault-tolerant control of wind turbines. Master thesis, Aalborg University, Aalborg, Denmark

Gobat JI, Grosenbaugh MA (2001) A simple model for heave-induced dynamic tension in catenary moorings. Appl Ocean Res 23(3):159–174

Greenwood DT (1988) Principles of dynamics. Prentice-Hall, Englewood Cliffs

Hall M (2015) MoorDyn users guide. Department of Mechanical Engineering, University of Maine, Orono

Hansen MH, Gaunaa M, Madsen HA (2004) A Beddoes-Leishman type dynamic stall model in state-space and indicial formulations. Technical University of Denmark, Roskilde, Denmark

Huang S (1994) Dynamic analysis of three-dimensional marine cables. Ocean Eng 21(6):587–605

International Electrotechnical Commission (2007) IEC 61400–1: wind turbines part 1: design requirements. Geneva, Switzerland

International Electrotechnical Commission (2009) Part 3: design requirements for offshore wind turbines. Geneva, Switzerland

Ireson WG, Coombs CF, Moss RY (1996) Handbook of reliability engineering and management. McGraw-Hill Professional, New York

Jiang Z, Karimirad M, Moan T (2013a) Response analysis of parked spar-type wind turbine considering blade-pitch mechanism fault. Int J Offshore Polar Eng 23(02)

Jiang Z, Moan T, Gao Z, Karimirad M (2013b) Effect of shut-down procedures on dynamic responses of a spar-type floating wind turbine. ASME 2013 32nd International Conference on Ocean, Offshore and Arctic Engineering, Pages V008T09A011–V008T09A011, Nantes, France

Jiang Z, Moan T, Gao Z (2015) A comparative study of shutdown procedures on the dynamic responses of wind turbines. J Offshore Mechan Arctic Eng 137(1):011904

Johannessen K, Meling TS, Hayer S (2001) Joint distribution for wind and waves in the northern north sea. In: The 11th international offshore and Polar Engineering conference. International Society of Offshore and Polar Engineers. Stavanger, Norway

Johnson KE, Fleming PA (2011) Development, implementation, and testing of fault detection strategies on the national wind technology center's controls advanced research turbines. Mechatronics 21(4):728–736

Jonkman JM (2007) Dynamics modeling and loads analysis of an offshore floating wind turbine. Doctoral Thesis, University of Colorado Boulder, Boulder, USA

Jonkman JM (2010) Definition of the floating system for phase IV of OC3. National Renewable Energy Laboratory, Golden, USA

Jonkman JM, Matha D (2010) A quantitative comparison of the responses of three floating platforms. National Renewable Energy Laboratory, Golden, USA

Jonkman JM, Butterfield S, Musial W, Scott G (2009) Definition of a 5-MW reference wind turbine for offshore system development. National Renewable Energy Laboratory, Golden, USA

Journèe JM, Massie W (2001) Offshore hydrodynamics. Delft Univers Technol 4:38

Kim K-W, Lee J-W, Yoo W-S (2012) The motion and deformation rate of a flexible hose connected to a mother ship. J Mech Sci Technol 26(3):703–710

Kim BW, Sung HG, Kim JH, Hong SY (2013) Comparison of linear spring and nonlinear FEM methods in dynamic coupled analysis of floating structure and mooring system. J Fluids Struct 42:205–227

Laouti N, Sheibat-Othman N, Othman S (2011) Support vector machines for fault detection in wind turbines. IFAC Proceedings 44(1):7067–7072

Larsen T (2009) How 2 HAWC2, the user's manual, ver. 3–7. RisøNational Laboratory, Technical University of Denmark, Copenhagen

Larsen TJ, Hanson TD (2007) A method to avoid negative damped low frequent tower vibrations for a floating, pitch controlled wind turbine. In: Journal of Physics: Conference Series, vol. 1, IOP Publishing, p 012073

Luan C, Gao Z, Moan T (2016) Design and analysis of a braceless steel 5-MW semi-submersible wind turbine. In: ASME 2016 35th international conference on ocean, Offshore and Arctic Engineering, American Society of Mechanical Engineers pp V006T009A052–V006T009A052. Busan, Republic of Korea

Masciola M, Jonkman J, Robertson A (2013) Implementation of a multisegmented, quasi-static cable model. In: The Twenty-third international offshore and polar engineering conference. International Society of Offshore and Polar Engineers. Anchorage, Alaska, USA

Masciola M, Jonkman J, Robertson A (2014) Extending the capabilities of the mooring analysis program: A survey of dynamic mooring line theories for integration into FAST. In: ASME 33rd international conference on Ocean, Offshore and Arctic Engineering 2014, American Society of Mechanical Engineers pp V09AT09A032–V009AT009A032. San Francisco, California, USA

Matha D (2010) Model development and loads analysis of an offshore wind turbine on a tension leg platform with a comparison to other floating turbine concepts: April 2009. In. National Renewable Energy Laboratory (NREL), Golden, USA

Milinazzo F, Wilkie M, Latchman S (1987) An efficient algorithm for simulating the dynamics of towed cable systems. Ocean Eng 14(6):513–526

Mohammed G, Aboelyazied M (2007) Effect of dust on the performance of wind turbines. Desalination 209(1–3):209–220

Myhr A, Maus KJ, Nygaard TA (2011) Experimental and computational comparisons of the OC3-HYWIND and Tension-Leg-Buoy (TLB) floating wind turbine conceptual designs. In: The 21th international offshore and polar engineering conference. International Society of Offshore and Polar Engineers. Maui, Hawaii, USA

Nejad AR, Jiang Z, Gao Z, Moan T (2016) Drivetrain load effects in a 5-MW bottom-fixed wind turbine under blade-pitch fault condition and emergency shutdown. In: Journal of physics: conference series, vol. 11, IOP Publishing p 112011

Nexans (2017) Nexans enables ROV cables to work harder and longer. https://www.nexans.no/eservice/Norway-no_NO/navigatepub_167348_-32474/Nexans_enables_ROV_cables_to_work_harder_and_longe.html

Nikravesh PE (1988) Computer-aided analysis of mechanical systems, vol 186. Prentice-hall, Englewood Cliffs

Offshore: Spar-shaped drilling unit designed for 8,000-10,000 ft depth corridor (2017). https://www.offshore-mag.com/articles/print/volume-56/issue-11/departments/drilling-production/spar-shaped-drilling-unit-designed-for-8000-10000-ft-depth-corridor.html

Roddier D, Cermelli C, Aubault A, Weinstein A (2010) WindFloat: a floating foundation for offshore wind turbines. J Renew Sustain Energy 2(3):033104

Sclavounos P, Lee S, DiPietro J, Potenza G, Caramuscio P, De Michele G (2010) Floating offshore wind turbines: tension leg platform and taught leg buoy concepts supporting 3–5 MW wind turbines. In: European wind energy conference EWEC, pp 20–23. Warsaw, Poland

Shabana AA (2013) Dynamics of multibody systems. Cambridge University Press, Cambridge

Skaare B, Nielsen FG, Hanson TD, Yttervik R, Havmøller O, Rekdal A (2015) Analysis of measurements and simulations from the Hywind Demo floating wind turbine. Wind Energy 18(6):1105–1122

Stamatis DH (2003) Failure mode and effect analysis: FMEA from theory to execution. ASQ Quality Press, Milwaukee

Tahar A, Kim M (2008) Coupled-dynamic analysis of floating structures with polyester mooring lines. Ocean Eng 35(17):1676–1685

Tavner P (2012) Offshore wind turbines: reliability. Availability and maintenance. The Institution of Engineering and Technology, London

Umar A, Datta T (2003) Nonlinear response of a moored buoy. Ocean Eng 30(13):1625–1646

Wendt FF, Andersen MT, Robertson AN, Jonkman JM (2016) Verification and validation of the new dynamic mooring modules available in FAST v8. In: The 26th international ocean and polar engineering conference. International Society of Offshore and Polar Engineers. Rhodes, Greece

Wikipedia: Offshore wind power (2016) https://en.wikipedia.org/wiki/Offshore_wind_power

Xu L, Chen J (2014) Advantages of polyester mooring for deepwater floaters. In: ASME 2014 33rd international conference on Ocean, Offshore and Arctic Engineering, American Society of Mechanical Engineers, pp V01BT01A009–V001BT001A009. San Francisco, California, USA

Zhu X, Yoo W-S (2015) Numerical modeling of a spar platform tethered by a mooring cable. Chinese Journal of Mechanical Engineering 28(4):785–792

Zhu X, Yoo W-S (2016a) Flexible dynamic analysis of an offshore wind turbine installed on a floating spar platform. Adv Mech Eng 8(6):1–11

Zhu X, Yoo WS (2016b) Dynamic analysis of a floating spherical buoy fastened by mooring cables. Ocean Eng 121:462–471

Zhu X, Yoo W-S (2016c) Numerical modeling of a spherical buoy moored by a cable in three dimensions. Chinese J Mechan Eng 29(3):588–597

Zhu XQ, Yoo W-S. (2016d) Verification of a numerical simulation code for underwater chain mooring. Archive of Mechanical Engineering 63(2):231–244

Zhu X, Yoo W-S (2017) Suggested new element reference frame for dynamic analysis of marine cables. Nonlinear Dyn 87(1):489–501

Chapter 10
Advanced Wind Turbine Control

Na Wang

10.1 Introduction

Wind energy is one of the fastest growing sources of electrical energy in the world, with an average increase in installed capacity of nearly 25% per year from 23.9 GW in 2001 to 486.79 GW in 2016 (GWEC 2017). In the USA, the cumulative installed wind power capacity reached 82.184 GW by the end of 2016 (GWEC 2017), and the electricity produced from wind power amounted to 6% of all electrical energy (U. S. D. of Energy 2017). By 2016, in the European Union (EU), a total of 163.33 GW was installed and supplied 10.4% of the EU's electricity consumption (European 2017). With global climate changing, people have become much more interested in renewable energy, and wind energy is one of the most cost-competitive of renewable electricity systems. Therefore, it is reasonable to assume that the wind energy industry will continue to grow in the next few decades. In Europe, 230 GW of wind capacity are expected to be installed by 2020, which will produce up to 17% of the EU's electricity (Taylor 2010). The US Department of Energy (DOE) has also published a report outlining the steps required to achieve 20% wind energy in the USA by 2030; one of the factors in the report is advanced turbine control (U. S. D. of Energy 2012).

Advanced control, which is one of many disciplines that can contribute to a decrease in wind's cost of energy, is becoming more critical due to the increased flexibility of and coupling between structural modes in the wind turbines (Laks et al. 2009). Wind turbines have grown in size significantly over the past decades for many reasons, including advances in research and development and economies of scale. The diameter of the rotor of a commercial wind turbine with rated power of 5 MW is about 126 m (Jonkman et al. 2009). Compared to their smaller counterparts, large

N. Wang (✉)
Siemens Wind Energy, Boulder, CO, USA

modern wind turbines are exposed to higher and more complex loads. The alleviated structural and fatigue loads will significantly decrease the turbine cost by lessening the maintenance requirements and improving overall turbine reliability. In addition, the power capture efficiency is another concern in the wind industry. The improved power capture efficiency will help the turbine to produce more electrical energy throughout its lifetime.

Implementing sophisticated load and rotor power control techniques could assure safe and optimal operation in terms of load mitigation and power enhancement under a range of atmospheric conditions. Therefore, compared with upgrading the mechanical system to extend the lifetime of turbines, modern control systems are more attractive and cheaper cost-reducing strategies (Wright 2004). Using advanced control strategies to make more reliable turbines and upgrade their performance could increase the efficiency of the power generation and reduce the downtime and the operation and maintenance costs (Johnson et al. 2008).

In recent years, LIDAR systems able to provide wind speed measurements upstream of the turbine have been studied for incorporation into wind energy. This technology opens new control concepts such as feedforward control to increase wind energy production and to reduce wind turbine fatigue loads. Advanced feedback controllers can also be combined with feedforward control strategies to further improve turbine performances. This chapter first provides the basics of wind turbine control, then offers a comprehensive literature survey on wind turbine control, and finally focuses on LIDAR-assisted combined feedforward and feedback controllers that use the knowledge of incoming wind speed to reduce the fatigue loads of wind turbines and to increase the energy production.

10.2 Wind Turbine Control Basics

The power available in the wind with velocity u is given by

$$P_{wind} = \frac{1}{2} \rho \pi R_a^2 u^3, \qquad (10.1)$$

where ρ is the air density and R_a is the rotor radius. According to the Betz Limit, no turbine can extract more than 59.3% of the kinetic energy from the wind. C_p is the power coefficient and is given by the ratio of the power captured by the rotor to the power available in the wind, or

$$C_p = \frac{P_{rotor}}{P_{wind}}. \qquad (10.2)$$

C_p is shown as a function of the tip-speed ratio (TSR) λ and blade pitch angle β in Fig. 10.1. TSR is defined as
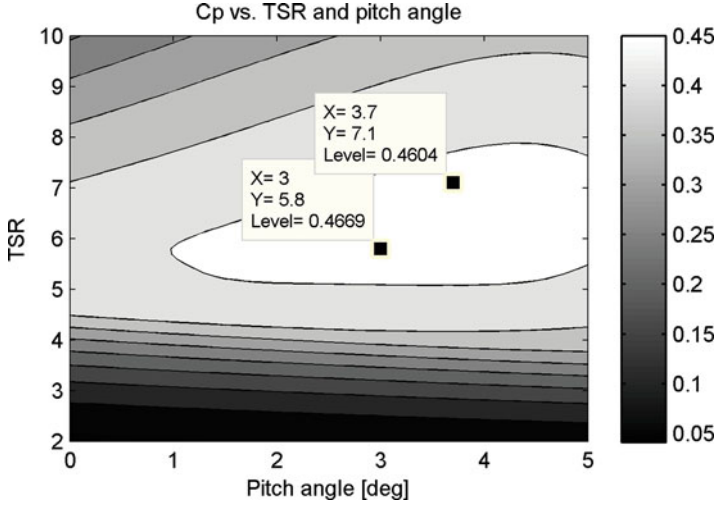
Fig. 10.1 C_p versus TSR and blade pitch angle for the CART3. CART3's C_p-TSR-Pitch surface is fairly flat close to its peak at a TSR of 5.8. The marked points indicate its peak and a sub-optimal design point with TSR of 7.1

$$\lambda = \frac{\Omega}{u} R_a, \tag{10.3}$$

where Ω is the rotor speed.

The aerodynamic torque τ_{aero} exerted on a turbine's rotor is given by

$$\tau_{aero} = \frac{1}{2} \rho \pi R_a^3 \frac{C_p}{\lambda} u^2. \tag{10.4}$$

For a turbine to operate at a constant rotor speed Ω, the generator torque τ_c must be equal to the aerodynamic torque τ_{aero}. When $\tau_{aero} > \tau_c$, the turbine will accelerate and vice versa according to

$$J_T \dot{\Omega} = \tau_{aero} - \tau_c, \tag{10.5}$$

where J_T is the equivalent combined moment inertia of the rotor, the gear box, the low-speed shaft (LSS), and the high-speed shaft (HSS).

Three operating regions are defined in Fig. 10.2 (Pao and Johnson 2009). In Region 1, the wind speed is so low that starting up the turbine is not worthwhile. Once the wind speed reaches a turbine-specific minimum, which is often between 3–5 m/s, the machine will start up. In Region 2, the wind speed is below rated, which is the value at which the turbine first reaches its maximum power output and is usually in the vicinity of 12 m/s. In this region, the wind turbine is designed to capture as much power as possible by adjusting the generator torque to optimize power

Fig. 10.2 Power curve and
generator torque curve for the
CART3
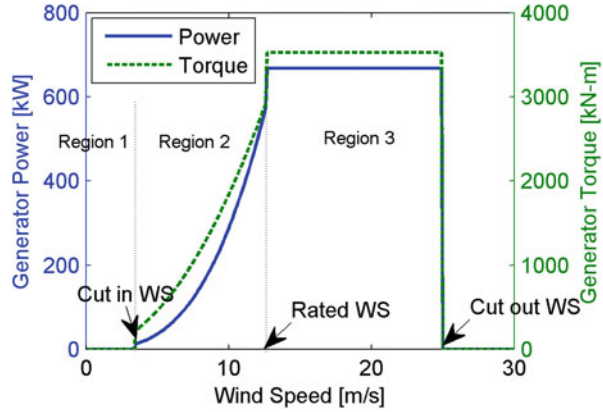
coefficient. Since rotor power is given by the product of available power (10.1) and
power coefficient (10.2), the generated power increases according to a cubic law
with wind speed assuming no energy loss in neither the gearbox nor generator.
In Region 2, pitch angle is often controlled to the constant value that gives
maximum C_p.

In Region 3, as shown in Fig. 10.2, the wind speed is above rated. The rotor speed
and generator power should be limited to their rated values to avoid mechanical and
electrical component damage. Generator torque is often held at rated, and blade
pitch angle is used to limit aerodynamic power by regulating turbine speed to the
rated speed. Load mitigation on the blades and tower should be considered in this
region.

A control system consists of sensors, actuators, and compensators. The control
objectives are defined according to the turbine's operating regions. The basic
structure of the wind turbine control loops is shown in Fig. 10.3.

Current commercial wind turbine pitch control algorithms are typically feedback
only. Though the details of modern utility-scale turbine control algorithms are pro-
prietary and closely protected by industry, until recently most feedback controllers
have been fairly straightforward proportional-integral (PI)-based collective blade
pitch controllers. These controllers typically operate on an input signal such as the
error in rotor speed (or power) in Region 3 wind conditions. In this research, a
PI collective blade pitch controller shown in Fig. 10.4 was selected as the baseline
controller.

Based on (10.5), a generator torque control algorithm can be defined by

$$\tau_c = k\Omega^2, \tag{10.6}$$

where k is the torque coefficient, which is derived to make $\tau_c = \tau_{aero}$ at the optimal
TSR λ_* and is given by
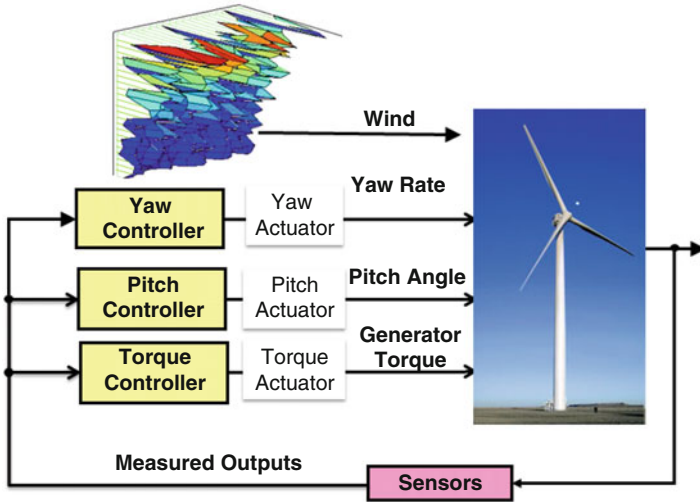
Fig. 10.3 A wind turbine control block diagram. In this configuration, measured turbine speed is used in the pitch and torque feedback loops, while yaw error obtained from a wind direction sensor is utilized for the yaw control loop. (Adapted from a figure in Pao and Johnson 2009.)
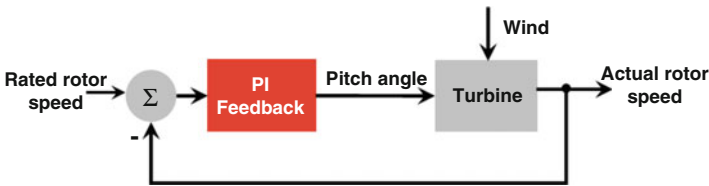
Fig. 10.4 A PI collective blade pitch control configuration in above rate wind speed condition

$$k = \frac{1}{2}\rho\pi R_a^5 \frac{C_{pmax}}{\lambda_*^3}. \tag{10.7}$$

The torque controller (10.6) and (10.7) is designed to maximize C_p (Johnson et al. 2006) and λ_* and β_* are the optimal TSR and blade pitch angle, respectively, at which the maximum C_p ($C_{pmax} = C_p(\lambda_*, \beta_*)$) occurs. Generally, the pitch angle is kept constant at β_*, which is also known as the fine pitch angle, below rated wind. The generator torque algorithm (10.6) and (10.7) was taken as the baseline torque controller for CART3 in this research.

Yaw control is used to adjust the wind turbine to be aligned with the wind direction (Ragheb 2009). In this research, yaw is assumed to operate acceptably, and the novel turbine control methods developed are focused on advanced blade pitch and torque controllers.

10.3 Literature Review

Numerous advanced control techniques for wind turbine fatigue load alleviation have been developed over the past few years.

10.3.1 Speed Control

Classical PI control is typically used in the industry for blade pitch controllers to regulate turbine speed with varying wind conditions. Desired closed-loop characteristics can be achieved by selecting proper PI gains. A PI pitch controller designed using the root locus method for a fixed speed wind turbine is described in Jaucha et al. (2007). Optimal algorithms formulated to design the PI parameters are presented in Ghadimi (2011). Further discussions on methods of choosing the PI gains are summarized in Hand (1999). Generally, in the absence of knowledge of the wind disturbance, PI pitch control strategies are the easiest-to-implement methods for regulating turbine speed in Region 3.

In addition to the PI control strategies, other linear feedback control techniques that have been investigated include full-state feedback control, disturbance-accommodating control (DAC), and linear quadratic regulators (LQRs). Full-state feedback and DAC methods have been applied to reduce blade loads by rejecting the wind disturbances modeled as a step or sinusoids (Wright 2004; Stol and Balas 2003; Hand et al. 2004). Time-varying LQR techniques for a two-bladed teetering hub turbine operating in Region 3 are discussed in Stol (2003).

Most of these linear time-invariant (LTI) controllers are designed for one specific operating point, so performance may degrade when the wind turbine operates away from that operating point and may be limited by the highly nonlinear characteristics of the wind turbine. Gain-scheduling techniques such as those described in Stergaar et al. (2007) and Bianchi et al. (2005) can improve operation over a range of operating points. A gain-scheduled linear quadratic controller with a state and disturbance estimation algorithm is designed in Stergaar et al. (2007) by linearizing the nonlinear plant model along a trajectory of operating points scheduled on the effective wind speed. The controller gains are interpolated linearly to get a control law for the entire operating region. Improved performance in terms of fatigue damage is addressed at the cost of slow variations in the active power. In Bianchi et al. (2005), a linear parameter-varying (LPV) gain-scheduling strategy formulated as a convex optimization problem with linear matrix inequities (LMIs) is proposed for maximizing conversion efficiency, safe operation, resonant mode damping, and robust stability. The LPV controller has better tracking and more damping of resonant modes, but the robust stability performance is hard to achieve.

An adaptive pitch controller designed using an extension of the direct model reference adaptive control approach to regulate turbine rotational speed and to accommodate step disturbances is proposed in Frost et al. (2009), where robustness

to modeling errors and changes in system parameters are demonstrated. A fuzzy logic pitch angle controller is developed to reduce fatigue loads in Sedighizadeh and Rezazadeh (2008). The fuzzy logic controller can compensate for the nonlinearities and reduce fatigue loads, even without knowledge of the system and the mean wind speed. These nonlinear pitch controllers are robust to the nonlinearities and uncertainties of the system model, resulting in improved performance for turbine speed regulation. The downsides in the nonlinear control schemes are that, due to the nature of online learning, computational requirements may be unacceptably high for the wind energy application.

Wind turbines with larger rotor size tend to experience asymmetric loading of the rotor blades due to wind speed variations across the rotor disc (Bossanyi and Hassan 2003). Modern commercial turbines have individual pitch actuators for each rotor blade for implementation of individual pitch control (IPC). The work presented in Bossanyi and Hassan (2003) presents a IPC design based on linear quadratic Gaussian (LQG) control design methods, which reduces the operational load significantly, but the design process is not straightforward, and the resulting algorithm is somewhat cumbersome. Another LQG-based multivariable control technique with feedforward disturbance rejection for reducing the once-per-revolution (1P) loading of the rotor blades due to wind shear, tower shadow, and skew inflow is demonstrated in Selvam (2007).

Sophisticated control strategies for wind turbine extreme load alleviation have been addressed as well. For example, an extreme event recognition and extreme event control (EEC) algorithm for extreme wind gusts with direction change in wind turbines have been proposed in Kanev and Engelen (2008). The EEC algorithm is used to prevent the rotor speed from exceeding the overspeed limit by fast collective blade pitching and to reduce 1P blade loads by means of an individual pitch control algorithm, designed in an H_∞ optimal control setting. An extreme event controller designed to prevent rotor overspeed in response to incoming wind gusts can be found in Pace and Johnson (2013), where LIDAR is used in conjunction with a cumulative summation (CUSUM) test to detect an oncoming gust.

10.3.2 Power Control

Using advanced controllers to maximize power capture for variable-speed wind turbines in Region 2 where the wind speed is below rated has been well addressed by researchers in the past decades as well. Different control methodologies using generator torque control, blade pitch control, or a combination of both are proposed and applied. Most of the control strategies use generator torque to maximize the power capture, while the blades are kept at constant values giving the maximum aerodynamic efficiency. The advanced control strategies for increasing power can be classified into linear and nonlinear control methods.

The linear control methods as presented in Balas et al. (1998) and Malinga et al. (2003) assume a priori knowledge of the optimal operating point, which is

usually not practical because of large uncertainties in the system. Also, the optimal operating point is difficult to determine and varies from turbine to turbine. Balas et al. proposed disturbance tracking control (DTC) to control rotor speed via wind speed estimation with the goal of maintaining a constant optimal TSR (Balas et al. 1998). DTC assumes the optimal TSR is known.

Nonlinear control strategies have the potential to overcome some of the drawbacks of linear strategies. The optimally tracking rotor (OTR) control scheme proposed by Fingersh and Carlin in (1998) and further described in Johnson et al. (2006) can assist the turbine in regaining its optimal TSR using the generator torque to assist acceleration and deceleration. Johnson et al. proposed an adaptive controller that seeks the gain that maximizes power capture despite aerodynamic uncertainty and turbulent effects (Johnson et al. 2006). A nonlinear feedback controller with wind speed estimator for maximizing the energy extracted from the wind while reducing mechanical loads is described in Boukhezzar and Siguerdidjane (2005). Good performance can be achieved because dynamic aspects of the wind and the turbine are taken into account. Additionally, combining pitch control techniques with torque control methodologies is a promising research area. In Hawkins and White (2010), a robust control scheme to optimize the power capture of a wind turbine is proposed. The set points, consisting of the rotor speed and the turbine blade pitch, are adapted by a Lyapunov-based approach to account for unknown aerodynamic properties. Other power optimization and control strategies for grid-coupled wind energy conversion systems have been studied in Aho et al. (2012), Pozo et al. (2013) and Ghaffari et al. (2013).

10.3.3 LIDAR-Assisted Speed and Power Control

Recent advances in LIDAR systems have shown promise for providing real-time measurements of wind speed or direction inputs local to individual wind turbines (Harris et al. 2006; Mikkelsen et al. 2010), opening a new area of research in feedforward wind turbine control.

As presented in Schlipf and Kühn (2008), nacelle- or hub-based LIDAR systems can provide preview information about the wind inflow in front of wind turbines, which can be used to improve speed regulation via a look-ahead update to the collective pitch control. A detailed analysis of the LIDAR-assisted collective pitch control is presented in Schlipf et al. (2010a,b), where, compared to an advanced feedback controller, the best load reduction can be observed for high turbulence and high wind speed. The proposed look-ahead controller uses a realistic LIDAR simulator. In Laks et al. (2010), assuming both a highly idealized wind measurement obtained from a rotating LIDAR and also a stationary measurement with a more realistic LIDAR model, preview-based disturbance feedforward control both with and without the use of multiblade coordinate-based controllers shows excellent performance in load mitigation. However, using the realistic wind measurement could cancel the advantage obtained from preview-based feedforward techniques

unless further optimization is performed. In Laks et al. (2011), a model predictive controller (MPC) is developed in order to recover some of the performance loss due to the measurement error in the LIDAR system. Another LIDAR plus MPC strategy is applied to wind turbine control (Schlipf et al. 2011) for both fatigue and extreme load reduction over the full turbine operational region. Optimal filters derived in both time domain and frequency domain for reducing the mean square rotor speed error have been investigated in Simley and Pao (2013).

In other LIDAR-enabled control research, baseline feedback controllers have been augmented with various collective and individual pitch feedforward controllers using gain-scheduled model-inverse or gain-scheduled shaped compensators, showing promising results in turbine fatigue load alleviation (Dunne et al. 2010, 2011). LIDAR-assisted optimal C_p tracking control is investigated in Wang et al. (2012), but the benefits over conventional methods are less clear. In Kragh et al. (2011), a method for yaw error estimation based on measurements from a spinner-based LIDAR is developed for improved yaw control of horizontal axis wind turbines operating in turbulent flow. A further field test study shown in Kragh and Fleming (2012) indicates that applying a correction scheme to improve yaw alignment increases the power capture by 1–5% in the below-rated domain.

10.4   LIDAR-Assisted Controller Design for Load Mitigation for CART3

In this section, a nonadaptive feedforward controller based on a zero-phase-error-tracking-control (ZPETC) technique and an adaptive feedforward controller based on a filtered-x recursive least square (FX-RLS) algorithm have been investigated for the CART3. Both of the feedforward controllers augment the same collective pitch PI feedback controller, which regulates rotor speed above rated wind speed. The feedforward controllers provide further speed regulation capability in addition to load reduction. The research presented in this section has appeared in Wang et al. (2011).

10.4.1   Model-Inverse-Based Feedforward Control Strategy

ZPETC Masayoshi (1987) is a model-inverse-based strategy for designing feedforward controllers. ZPETC results in a zero phase shift over the whole frequency spectrum and an attenuated gain at high frequencies.

The first step for the ZPETC-based feedforward controller design was to obtain a linear model of CART3 around a specific operating point, which was selected at a wind speed $u_0 = 18$ m/s, rotor speed $\Omega_0 = 41.7$ rpm, and pitch angle $\beta_0 = 12.8°$. The wind turbine was linearized with five DOFs enabled, including the first flapwise blade mode for all three blades, the drive train mode, and the generator mode.
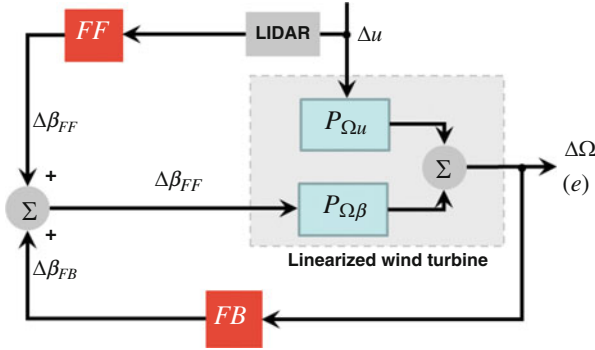
Fig. 10.5 Combined collective feedback and model-inverse-based feedforward control with linearized wind turbine model. $P_{\Omega\beta}$ maps blade pitch angle β to rotor speed Ω. $P_{\Omega u}$ maps wind disturbance u to rotor speed Ω. Δu, $\Delta\beta$ and $\Delta\Omega$ are the deviations from the selected operating point. e denotes the rotor speed error and $\Delta\Omega = e$ in Region 3

Transfer functions were obtained to represent the linearized relationships between the pitch angle β and rotor speed Ω ($P_{\Omega\beta}$) and between the wind speed u and Ω ($P_{\Omega u}$), as shown in Fig. 10.5. The signals Δu, $\Delta\beta$, and $\Delta\Omega$ are the deviations of each signal from its value at the operating point. Note that the ZPETC-based feedforward controller designed in this section did not include pitch actuator dynamics, that is, $\beta = \beta_c$.

In Fig. 10.5, a discrete-time PI feedback controller FB is used to regulate the rotor speed Ω at its rated value and is given by

$$\Delta\beta_{FB}(n) = k_p e(n) + k_i \delta \sum_{j=0}^{n-1} e(j), \tag{10.8}$$

where n is the discrete-time step, k_p and k_i are the proportional and integral gains, and δ is the sampling time, which is selected at 0.01 in this research. The linear model-inverse feedforward controller FF in Fig. 10.5 is used to cancel the effect from the turbulence in wind speed u on the rotor speed error e. According to Fig. 10.5, the error is given by

$$Z\{e(n)\} = \frac{P_{\Omega\beta} \cdot FF \cdot Z\{\Delta u\} + P_{\Omega u} \cdot Z\{\Delta u\}}{1 - P_{\Omega\beta} \cdot FB}, \tag{10.9}$$

where $Z\{\cdot\}$ is the expression for z-transformation. Since the desired rotor speed error is

$$e_{desired} = 0,$$

the feedforward controller FF can be solved for by setting the numerator of (10.9) equal to zero, or

$$P_{\Omega\beta} \cdot FF \cdot Z\{\Delta u\} + P_{\Omega u} \cdot Z\{\Delta u\} = 0,$$

which gives

$$FF = -P_{\Omega\beta}^{-1} \cdot P_{\Omega u}. \tag{10.10}$$

If $P_{\Omega\beta}$ contains non-minimum phase zeros, the resulting FF is unstable. To avoid this situation, a stable model-inverse approximation is used instead. In this research, the ZPETC model-inverse technique was applied to get a stable substitute for the true inverse that was used in the feedforward controller. According to Masayoshi (1987) and Ko et al. (1999), the ZPETC can be expressed as

$$P(z) = \frac{U^-(z)U^+(z)}{V(z)},$$

$$FF_{ZPETC}(z) = \frac{U^-(z^{-1})V(z)}{U^-(1)^2 U^+(z)}, \tag{10.11}$$

where $P(z)$ is the discrete transfer function containing non-minimum phase zeros that need to be inverted, and $FF_{ZPETC}(z)$ is the ZPETC-based stable inverse of $P(z)$. $U^-(z)$ and $U^+(z)$ represent the un-cancelable and cancelable portions of $P(z)$, respectively.

The two transfer functions $P_{\Omega\beta}$ and $P_{\Omega u}$ can be obtained from FAST's linearization routine, and the ZPETC-based model-inverse nonadaptive feedforward controller FF for the research can then be found using (10.10) and (10.11). The Bode plots of $P_{\Omega\beta}$, $P_{\Omega u}$, and FF_{ZPETC} are shown in Fig. 10.6, where a 100 Hz sample rate was used.

Making the ZPETC controller FF_{ZPETC} causal required an additional delay of z^{-1} or one sample period. Thus, the LIDAR code must provide one sample period preview to cancel this delay, making the phase of this controller match the ideal case exactly.

10.4.2   Adaptive Feedforward Control Strategy

Both the FX-RLS and the filtered-x least mean squares (FX-LMS) feedforward algorithms have proven useful in achieving disturbance rejection for vibration (Kashani and Sutherland 1996; Na and Park 1997; Tan and Jiang 2009). The FX-LMS algorithm is used frequently by the vibration and noise control community, in part because it has less computational complexity than the FX-RLS algorithm.
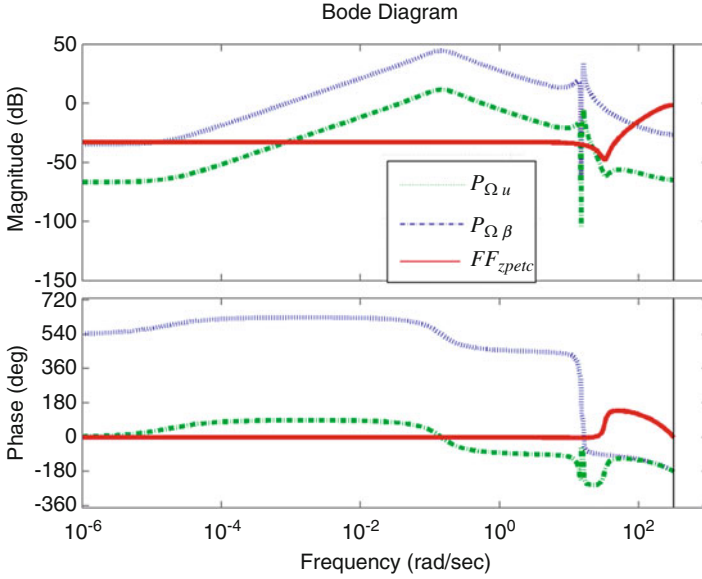
Fig. 10.6 Bode plots of transfer functions $P_{\Omega\beta}$, $P_{\Omega u}$, and ZPETC-based feedforward controller FF_{ZPETC}

However, the FX-RLS algorithm can provide faster convergence and smaller steady-state error than the FX-LMS algorithm (Beerer et al. 2009; Eweda and Macchi 1987), which makes the FX-RLS algorithm more appealing for the adaptive controller design. The LIDAR sensor enables online adjustments to the control law at every time step, and the FX-RLS algorithm has been selected as the structure for a controller to provide load alleviation and rotor speed regulation when the wind turbine is operating above rated wind speed.

In Fig. 10.7, assume that a perfect wind speed measurement x can be obtained via the LIDAR beam sensor, and Δx denotes the deviation from the operating point; that is, $\Delta x = \Delta u$. The rotor speed error $e(n, \vec{\theta})$ is a function of the discrete-time step n and adaptive feedforward controller parameters $\vec{\theta}$ and can be expressed by

$$e(n, \vec{\theta}) = g(n) + d(n, \vec{\theta}), \tag{10.12}$$

where $d(n, \vec{\theta})$ can be obtained from

$$Z\{d(n, \vec{\theta})\} = P_{\Omega_e\beta} \cdot [FF(n, \vec{\theta}) \cdot Z\{\Delta x(n)\} + FB \cdot Z\{e(n, \vec{\theta})\}],$$
$$= FF(n, \vec{\theta}) \cdot P_{\Omega_e\beta} \cdot Z\{\Delta x(n)\} + P_{\Omega_e\beta} \cdot FB \cdot Z\{e(n, \vec{\theta})\},$$

where FB is the PI feedback collective controller given in (10.8).
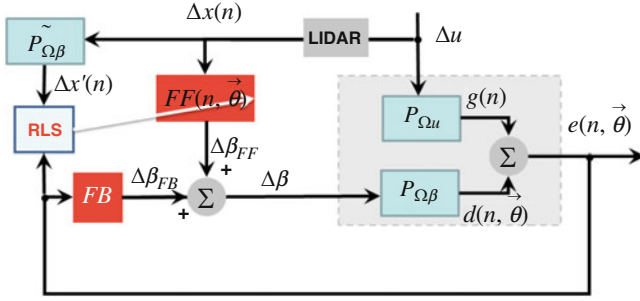
Fig. 10.7 Combined collective feedback and FX-RLS feedforward control strategy. The linearized turbine is indicated by the gray dashed box. $FF(n, \vec{\theta})$ denotes the adaptive feedforward controller. The measured wind speed obtained by the LIDAR sensor is convolved with an approximation of $P_{\Omega\beta}$ ($\tilde{P_{\Omega\beta}}$) in the feedforward path to provide the signal $\Delta x'(n)$

As with the ZPETC feedforward controller design, the FX-RLS feedforward controller design did not consider pitch actuator dynamics, either. Following the procedure in Zeng and Moulin (2010), let

$$Z\{\Delta x'(n)\} := \tilde{P_{\Omega\beta}} \cdot Z\{\Delta x(n)\},$$

where $\tilde{P_{\Omega\beta}}$ is an approximation of $P_{\Omega\beta}$. Thus, the error (10.12) can be approximated by

$$Z\{e(n, \vec{\theta})\} \approx \frac{Z\{g(n)\} + FF(n, \vec{\theta}) \cdot Z\{\Delta x'(n)\}}{1 - P_{\Omega\beta} \cdot FB}. \tag{10.13}$$

The primary control goal is to minimize the rotor speed error signal $e(n, \vec{\theta})$ when the wind turbine operating above rated wind speed, that is to find the minimized rotor speed error by adapting the parameters $\vec{\theta}$ of the feedforward controller, which is accomplished using

$$J = \min_{\vec{\theta}} \frac{1}{N} \sum_{n=1}^{N} e^2(n, \vec{\theta}). \tag{10.14}$$

The denominator of the error (10.13) is not a function of $\vec{\theta}$ or n, so the feedback control loop does not affect the optimization problem (10.14) that determines the adaptive feedforward controller $FF(n, \vec{\theta})$. Let

$$Z\{e'(n, \vec{\theta})\} := Z\{g(n)\} + FF(n, \vec{\theta}) \cdot Z\{\Delta x'(n)\}.$$

Thus, (10.14) becomes

$$J = \min_{\vec{\theta}} \frac{1}{N} \sum_{n=1}^{N} e'^2(n, \vec{\theta}).$$

A finite impulse response (FIR) filter was selected for $FF(n, \vec{\theta})$ because of its inherent stability, which is particularly useful for an adaptive control approach (Vipperman and Burdisso 1995). The RLS algorithm, based on Zeng and Moulin (2010), was used to compute the coefficients $\vec{\theta}(n)$ of the FIR adaptive feedforward controller at each time step n, as given by

$$\vec{\theta}(n) = \vec{\theta}(n-1) + K(n)e'(n, \vec{\theta}), \tag{10.15}$$

$$K(n) = \frac{P_{RLS}(n-1)\Delta x'(n)}{\lambda_{RLS}(n) + \Delta x'(n)^T P_{RLS}(n-1)\Delta x'(n)}, \tag{10.16}$$

$$P(n) = \frac{P_{RLS}(n-1) - K(n)\Delta x'(n)P_{RLS}(n-1)}{\lambda_{RLS}(n)}. \tag{10.17}$$

10.5 Future Work

Although a LIDAR system that can provide the required preview wind information in front of the turbine enables these novel controllers, further research should be conducted to assess the sensitivity of the controllers to measurement uncertainty.

Future work might also include gain scheduling the various linear control strategies. The gain-scheduled controllers can be obtained from interpolating or switching local LTI controllers. LPV control, which is a methodology that resembles classical gain scheduling, enables a systematic way of designing the gain-scheduled controller.

Finally, H_2 (Scherer and Weiland 1999) performance criterion or a mixed H_2/H_∞ (Østergaard 2008) should be considered to develop the controllers, since the wind speed as the main disturbance is most accurately described by a stochastic process, which indicates that the energy-like H_2 methodology is best suited for the tracking problem of generator speed and power references across a wider frequency range.

References

Aho J, Buckspan A, Laks J, Jeong Y, Dunne F, Pao L, Fleming P, Churchfield M, Johnson K (2012) Tutorial of wind turbine control for supporting grid frequency through active power control. National Renewable Energy Laboratory, Golden

Balas M, Lee YJ, Kendall L (1998) Disturbance tracking control theory with application to horizontal axis wind turbines. In: Proceedings of 17th ASME wind energy symposium

Beerer MJ, Yoon H, Agrawal BN (2009) Adaptive filter techniques for optical beam jitter control. In: Proceedings of acquisition, tracking, pointing, and laser systems technologies XXIII

Bianchi FD, Mantz RJ, Christiansen CF (2005) Gain scheduling control of variable-speed wind energy conversion systems using quasi-LPV models. Control Eng Pract 13(2):247–255

Bossanyi EA, Hassan G (2003) Individual blade pitch control for load reduction. Wind Energy 6:119–128

Boukhezzar B, Siguerdidjane H (2005) Nonlinear control of variable speed wind turbines without wind speed measurement. In: Proceedings of the 44th IEEE conference on decision and control, and the European control conference

Dunne F, Pao L, Wright AD, Jonkman B, Kelley N (2010) Combining standard feedback controllers with feedforward blade pitch control for load mitigation in wind turbines. In: Proceedings of American institute of aeronautics and astronautics

Dunne F, Pao L, Wright AD, Jonkman B, Kelley N, Simley E (2011) Adding feedforward blade pitch control for load mitigation in wind turbines: non-causal series expansion, preview control, and optimized FIR filter methods. In: Proceedings of American institute of aeronautics and astronautics

European W (2017) Wind in power 2016 European statistics. European Wind Energy Association (EWEA), pp 1–24

Eweda E, Macchi O (1987) Convergence of the RLS and LMS adaptive filters. IEEE Trans Circuits Syst 34(7):799–803

Fingersh LJ, Carlin PW (1998) Results from the NREL variable speed test bed. In: Proceedings of 17th ASME wind energy symposium, pp 233–237

Frost SA, Balas M, Wright AD (2009) Direct adaptive control of a utility-scale wind turbine for speed regulation. Int J Robust Nonlinear Control 19(1):59–71

Ghadimi N (2011) Genetically adjusting of PID controllers coefficients for wind energy conversion system with doubly fed induction generator. World Appl Sci J 15(5):702–707

Ghaffari A, Krstić M, Seshagiri S (2013) Power optimization and control in wind energy conversion systems using extremum seeking. In: Proceedings of American control conference

GWEC (2017) Global wind statistics 2016. Global Wind Energy Council, pp 1–4

Hand M (1999) Variable-speed wind turbine controller systematic design methodology: a comparison of non-linear and linear model-based designs. National Renewable Energy Laboratory, Golden

Hand M, Johnson KE, Fingersh LJ, Wright AD (2004) Advanced control design and field testing for wind turbines at the national renewable energy laboratory. National Renewable Energy Laboratory, Golden

Harris M, Hand M, Wright AD (2006) LIDAR for turbine control. National Renewable Energy Laboratory, Golden

Hawkins T, White WN (2010) Wind turbine power capture control with robust estimation. In: Proceedings of the ASME 2010 dynamic systems and control conference

Jaucha C, Islamb SM, Orensena PS (2007) Design of a wind turbine pitch angle controller for power system stabilisation. Renew Energy 32:2334–2349

Johnson KE, Pao L, Balas M, Fingersh LJ (2006) Control of variable-speed wind turbines: standard and adaptive techniques for maximizing energy capture. IEEE Control Syst Mag 26(3):70–81

Johnson SJ, Dam CP, Berg DE (2008) Active load control techniques for wind turbines. Sandia National Laboratories, Albuquerque

Jonkman J, Butterfield S, Musial W, Scott G (2009) Definition of a 5-MW reference wind turbine
    for offshore system development. National Renewable Energy Laboratory, Golden
Kanev S, Engelen TV (2008) Wind turbine extreme gust control. Energy Research Center of the
    Netherlands
Kashani AR, Sutherland JW (1996) Adaptive feedforward control for periodic disturbance
    rejection with application to machining processes. In: Proceedings of the 24th North American
    manufacturing research conference
Ko RC, Good MC, Halgamuge SK (1999) Feedforward control strategies for high-speed contour-
    ing machine tools. In: Proceedings of the Australian conference on robotics and automation,
    pp 196–201
Kragh K, Fleming PA (2012) Rotor speed dependent yaw control of wind turbines based on
    empirical data. In: Proceedings of American institute of aeronautics and astronautics
Kragh K, Hansen M, Mikkelsen T (2011) Improving yaw alignment using spinner based LIDAR.
    In: Proceedings of American institute of aeronautics and astronautics
Laks JH, Pao LY, Wright AD (2009) Control of wind turbines: past, present, and future. In:
    Proceedings of American control conference, pp 2096–2103
Laks J, Pao L, Wright AD, Kelley N, Jonkman B (2010) Blade pitch control with preview wind
    measurements. In: Proceedings of American institute of aeronautics and astronautics
Laks J, Pao L, Wright AD, Kelley N, Jonkman B (2011) Model predictive control using
    preview measurements from LIDAR. In: Proceedings of American institute of aeronautics and
    astronautics
Malinga B, Sneckenberger J, Feliachi J (2003) Modeling and control of a wind turbine as a
    distributed resource. In: Proceedings of 35th Southeastern symposium on system theory
Masayoshi T (1987) Zero phase error tracking algorithm for digital control. J Dyn Syst Meas
    Control 109(1):65–68
Mikkelsen T, Hansen K, Angelou N, Sjoholm M, Harris M, Hadley P, Scullion R, Ellis G (2010)
    LIDAR wind speed measurements from a rotating spinner. In: Proceedings of European wind
    energy conference and exhibition
Na H, Park Y (1997) An adaptive feedforward controller for rejection of periodic disturbances. J
    Sound Vib 201(4):427–435
Øtergaard KZ (2008) Robust, gain-scheduled control of wind turbines. PhD thesis, Aalborg
    University
Pace A, Johnson KE (2013) LIDAR-based extreme event control to prevent wind turbine
    overspeed. In: Proceedings of the AIAA aerospace sciences meeting and exhibit
Pao L, Johnson K (2009) A tutorial on the dynamics and control of wind turbines and wind farms.
    In: Proceedings of American control conference, pp 1–47
Pozo F, Vidal Y, Acho L, Luo N, Zapateiro M (2013) Power regulation of wind turbines using
    torque and pitch control. In: Proceedings of American control conference
Ragheb M (2009) Wind power systems lecture notes: control of wind turbines
Scherer CW, Weiland S (1999) Lecture notes: linear matrix inequalities in control. The Nether-
    lands: Dutch institute for systems and control (DISC)
Schlipf D, Kühn M (2008) Prospects of a collective pitch control by means of predictive
    disturbance compensation assisted by wind speed measurements. In: Proceedings of German
    wind energy conference (DEWEK), pp 1–4
Schlipf D, Fischer T, Carcangiu CE, Rossetti M, Bossanyi E (2010a) Load analysis of look-ahead
    collective pitch control using LIDAR. In: Proceedings of German wind energy conference
    (DEWEK), pp 1–4
Schlipf D, Schuler S, Grau P, Allgöwer F, Kühn M (2010b) Look-ahead cyclic pitch control using
    LIDAR. In: Proceedings of European academy of wind energy (EAWE) 3rd conference, pp 1–7
Schlipf D, Schlipf DJ, Kühn M (2011) Nonlinear model predictive control of wind turbines using
    LIDAR. In: Proceedings of American wind energy association wind power conference and
    exhibition, pp 1–18

Sedighizadeh M, Rezazadeh A (2008) Adaptive PID controller based on reinforcement learning for wind turbine control. In: Proceedings of world academy of science, engineering and technology, vol 27

Selvam K (2007) Individual pitch control for large scale wind turbines. Energy Research Center of the Netherlands

Simley E, Pao L (2013) Reducing LIDAR wind speed measurement error with optimal filtering. In: Proceedings of American control conference

Stol K (2003) Disturbance tracking and blade load mitigation for variable speed wind turbines. J Sol Energy Eng 125(4):396–401

Stol K, Balas M (2003) Periodic disturbance accommodating control for blade load mitigation in wind turbines. J Sol Energy Eng 125(4):379–385

Stergaar KZØ, Brath P, Stoustrup J (2007) Gain-scheduled linear quadratic control of wind turbines operating at high wind speed. In: Proceedings of IEEE international conference on control applications, pp 276–281

Tan L, Jiang J (2009) Active noise control using the filtered-x RLS algorithm with sequential updates. J Commun Comput 6(5):9–14

Taylor H (2010) Large majorities in U.S. and five largest European countries favor more wind farms. The Harris Poll, Harris Interactive

U. S. D. of Energy (2012) Strengthening America's energy security with offshore wind. Energy Efficiency and Renewable Energy, U.S. Department of Energy

U. S. D. of Energy (2017) Electricity in the United States. U. S. Energy Information Administration, p 1

Vipperman JS, Burdisso RA (1995) Adaptive feedforward control of non-minimum phase structural systems. J Sound Vib 183(3):369–382

Wang N, Johnson KE, Wright AD (2011) FX-RLS-based feedforward control for LIDAR-enabled wind turbine load mitigation. IEEE Trans Control Syst Technol 20(5):1212–1222

Wang N, Johnson KE, Wright AD (2012) Pulsed LIDAR-assisted controllers for turbine power capture enhancement and fatigue load mitigation below rated. In: Proceedings of 50th AIAA aerospace sciences meeting, pp 1–11

Wright AD (2004) Modern control design for flexible wind turbines. National Renewable Energy Laboratory, Golden

Zeng J, Moulin B (2010) Adaptive feedforward control for gust load alleviation. J Guid Control Dyn 33(3):862–872

Chapter 11
Wind Power and Ramp Forecasting for Grid Integration

Cong Feng and Jie Zhang

11.1 Introduction

Wind energy is a sustainable alternative to the conventional energy in relieving global warming and fuel energy shortage. Notable progress has been made in increasing the wind energy capacity. However, the uncertain and variable characteristics of the wind resource present challenges to wind integration, especially at large penetrations. Accurately forecasting the wind power generation and the extreme wind power changes would greatly help power system operators make better operation schedules, thereby improving the system economic and reliability performance.

Wind forecasting consists of wind speed forecasting and wind power forecasting (Ren et al. 2015). Significant improvements of the wind forecasting have been achieved by developing various forecasting models in the past decades. The wind forecasting models can be classified by different criteria. Based on the algorithm principles, they are generally divided into physical models, statistical models, and hybrid physical and statistical models (Feng et al. 2017a). Based on the forecasting horizons, wind forecasting models are grouped into very short-term models (intra-hour), short-term models (1-h to 6-h-ahead), midterm models (6-h to 1-week-ahead), and long-term models (over 1 week) (Chang 2014).

Different types of statistical models have been applied in the wind forecasting, including conventional time series models, machine learning models, and deep learning models. Conventional time series models include the autoregressive (AR) model (Poggi et al. 2003), the autoregressive moving average (ARMA) model (Erdem and Shi 2011), and the autoregressive integrated moving average (ARIMA)

C. Feng · J. Zhang (✉)
Department of Mechanical Engineering, The University of Texas at Dallas, Richardson, TX, USA
e-mail: jiezhang@utdallas.edu

model (Liu et al. 2015). The most popular machine learning algorithms are artificial neural networks (ANNs) (Li and Shi 2010), support vector machine (SVM) (Chen and Yu 2014), random forest (RF) (Feng et al. 2017a), and gradient boosting machine (GBM) (Nagy et al. 2016). Compared with shallow machine learning models, deep learning models are able to capture the hidden invariant structures in the wind speed. The deep belief network algorithm (Wang et al. 2016) and the deep convolutional neural network (Wang et al. 2017) are also employed in the short-term wind forecasting.

Among many wind integration challenges, severe fluctuation incidents with large magnitudes and short durations, so-called ramping events, are a major concern of power system operators. Wind power ramping events (WPREs) are usually caused by complicated physical processes and atmospheric phenomena, such as thunderstorms, wind gusts, cyclones, and low-level jets (Freedman et al. 2008). The research on WPREs can be generally classified into three directions: WPRE detection, WPRE forecasting, and WPRE application. The WPRE detection uses a mathematical algorithm and wind power ramping definitions to extract all the wind power ramps from actual or forecasted wind power data. The WPRE detection method can be directly applied to historical measured wind power data to extract all historical ramping events. Statistical and machine learning methods can then be developed based on the historical ramping events to directly forecast WPREs. The accuracy of WPRE forecasting highly depends on the accuracy of WPRE detection.

This chapter reviews and discusses different types of models for short-term wind forecasting and ramp forecasting, including both individual and ensemble machine learning models and a recently developed optimized swinging door algorithm.

11.2 Wind Forecasting

The most popular short-term wind forecasting models include ANN, SVM, GBM, and RF machine learning models, which provide accurate forecasts with relatively low computational cost. The ensemble of individual machine learning models is another efficient way to improve the wind forecasting accuracy. Both individual and hybrid machine learning models are reviewed and discussed in this section.

11.2.1 Single Machine Learning Algorithm Models

ANN is a popular algorithm in speech recognition, target tracking, signal analysis, and nonlinear regression problems (such as time series forecasting). ANN mimics the structure of the human brain that consists interconnected neurons. Each neuron is a weighted sum of its inputs and is connected to the neurons in the next layer. The ANN architecture contains one input layer, one or more hidden layer(s), and one output layer. The configuration of the ANN model needs to be well designed to avoid

over-fitting issues. ANN can be classified into different types based on different activation functions and learning algorithms. Deep learning is also a configuration of ANN. The mathematical description of the ANN is expressed as:

$$y_i^{(n)} = f\left(\sum_{j=1}^{N} w_{ij}^{(n,n-1)} y_j^{(n-1)} + \theta_i^n\right) \tag{11.1}$$

where i is a neuron of the nth layer, w_{ij} is the weight from the neuron j in the layer $(n-1)$ to the neuron i in layer n, and θ_i^n is the threshold of the neuron i in layer n.

SVM is originally a supervised linear classifier proposed by Vapnik (1995). As one of the most popular classification methods, SVM has been applied in text categorization, image classification, and other recognition tasks. When dealing with linearly inseparable data, nonlinear mapping-based kernel methods, $K(x) : \mathbb{R}^n \longrightarrow \mathbb{R}^{n_h}$, are used to map the nonlinear data into the high-dimensional feature space. Then, a linear hyperplane is found by maximizing the distance between support vectors and the hyperplane. The SVM algorithm can also be applied in regression problems, which is called support vector regression (SVR). The performance of the SVR was reported to be better than other algorithms (e.g., ANN) in the literature. However, the compute and storage requirements increase significantly with the data dimension. The hyperplane function, also called the SVR function, is described as (Feng et al. 2017b):

$$f(x) = \omega^T K(x) + b \tag{11.2}$$

where ω and b are variables solved by minimizing the empirical risk, which is given by:

$$R(f) = \frac{1}{n}\sum_{i=1}^{n} \Theta(y_i, f(x)) \tag{11.3}$$

where $\Theta_\varepsilon(y_i, f)$ is the ε-insensitive loss function, expressed as:

$$\Theta_\varepsilon(y_i, f) = \begin{cases} \|f - y\| - \varepsilon, \text{ if } \|f - y\| \geq \varepsilon \\ 0, \text{ otherwise} \end{cases} \tag{11.4}$$

Then the optimal hyperplane is found by solving the inequality-constrained quadratic optimization problem.

GBM is a highly customizable learning algorithm widely used in the regression and classification fields. A GBM model relies on the combination of "weak learners" to create an accurate learner therefore, is able to generate both deterministic and probabilistic results in the time series forecasting. The combination is achieved by adding the weighted base learner to the previous model iteratively (Kaur et al. 2014).

The principle of GBM is illustrated by the pseudo-code in Algorithm 11.1. In each iteration, the negative gradient of the chosen loss function is calculated and used to estimate the split variables a by Eqs. (11.5) and (11.6). Then the multiplier β is optimized by Eq. (11.7). The weak learner βh(x; a) is added to the previous model, where h(x; a) is a learning function.

Algorithm 11.1 Gradient boosting machine (GBM)

1   Initialize $f_0(x)$ to be a constant, $f_0(x) = \arg \min_\rho \sum_{i=1}^{n} \Psi(y_i, \rho)$

2   for $i = 1$ to M do

3   Compute the negative gradient of the loss function:

$$\overline{y_i} = -\left[\frac{\partial \Psi(y_i, F(x_i))}{\partial F(x_i)}\right]_{f(x)} = f_{i-1}(x), i = \{1, 2, \ldots, n\} \tag{11.5}$$

4   Fit a model to $\overline{y}$ by least-squares to get a_t:

$$a_t = \arg \min_{\alpha, \beta} \sum_{i=1}^{n} \left[\overline{y_i} - \beta h(x_i, a)\right]^2 \tag{11.6}$$

5   Calculate β_t by:

$$\beta_t = \arg \min_\beta \sum_{i=1}^{n} \Psi(y_i, f_{t-1}(x_i) + \beta h(x_i, a_t)) \tag{11.7}$$

6   Update the model by:

$$f_t(x) = f_{t-1}(x) + \beta_t h(x; a_t) \tag{11.8}$$

7   end for

8   Output $\widehat{f}(x) = f_T(x)$

RF is another supervised ensemble learning method that consists of many single classification and regression trees (CARTs):

$$T = \left\{t\left(X, s_{\Lambda_1}\right), t\left(X, s_{\Lambda_2}\right), \ldots, t\left(X, s_{\Lambda_n}\right)\right\} \tag{11.9}$$

where T is a set of CARTs, t is a single CART, X is the input to the RF model, and s_{Λ_i} is a random vector to extract bootstrap samples which are determined by the bagging algorithm. The robustness of RF models is enhanced by randomness of the bagging algorithm and the best split search process. Since RF is a combination of various different regressions, the model is generally free from over-fitting (Ibarra-Berastegi et al. 2015).

11.2.2 Hybrid Machine Learning Models

Due to the nonlinear and nonstationary characteristics of wind speed, it is challenging to develop a generic model based on a single machine learning algorithm that can produce the best forecasts at different spatial and temporal scales. Hybriding several single machine learning models can make the forecasting more robust. A hybrid example is described in this section as shown in Fig. 11.1. This hybrid model
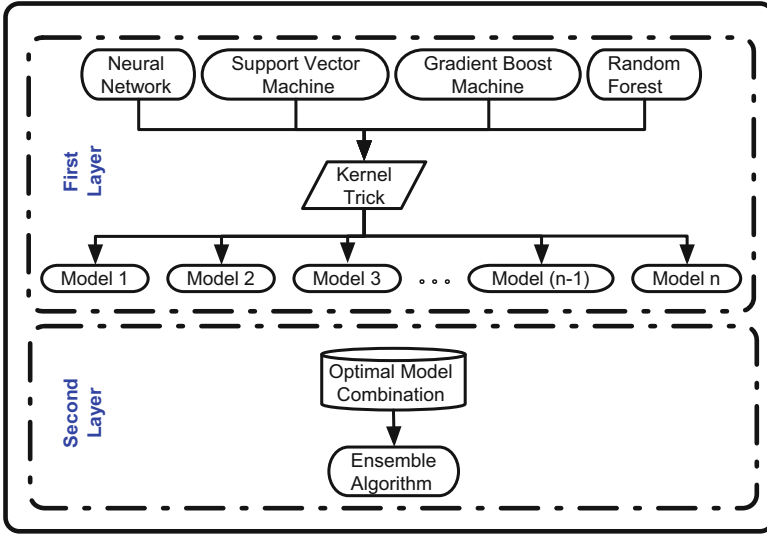
Fig. 11.1   Overall framework of the ensemble forecasting model

has a two-layer forecasting structure (Feng et al. 2017a). The first layer machine learning models are built based on the inputs, such as historical data. These models forecast wind speed or wind power as the output. A blending model is developed in the second layer to combine the forecasts produced by different algorithms from the first layer and to generate both deterministic and probabilistic forecasts. This blending model is expected to integrate the advantages of different algorithms by canceling or smoothing the local forecasting errors. The mathematical description is shown as:

$$y_i = f_i \left(x_1, x_2, \ldots, x_p \right) \tag{11.10}$$

$$\widehat{y} = \Phi \left(y_1, y_2, \ldots, y_m \right) \tag{11.11}$$

where $f_i(_*)$ is the ith algorithm and y_i is the wind speed forecasted by $f_i(_*)$. $\Phi(_*)$ is the second-layer blending algorithm.

11.2.3   Deterministic Results of the Multi-model Forecasting

The performance of the single-algorithm and hybrid machine learning models is evaluated in this section. Two evaluation metrics are utilized to evaluate the forecasting accuracy (Feng et al. 2017a): the normalized mean absolute error
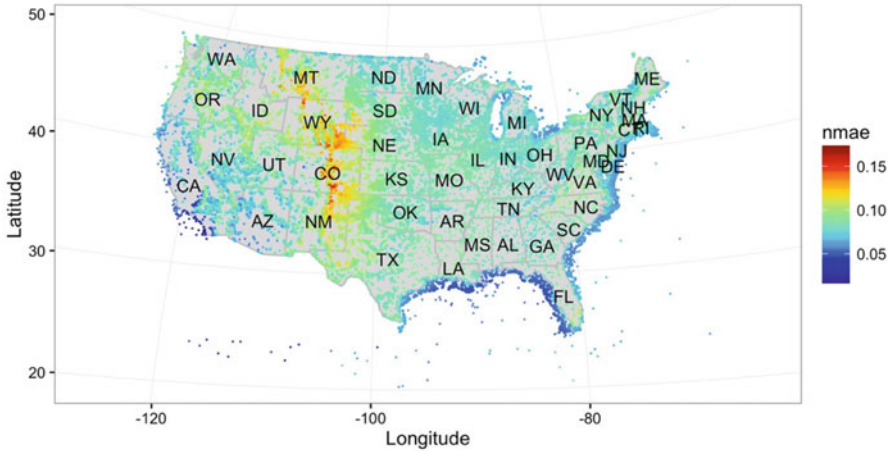
Fig. 11.2 The GBM forecasting nMAE across the United States
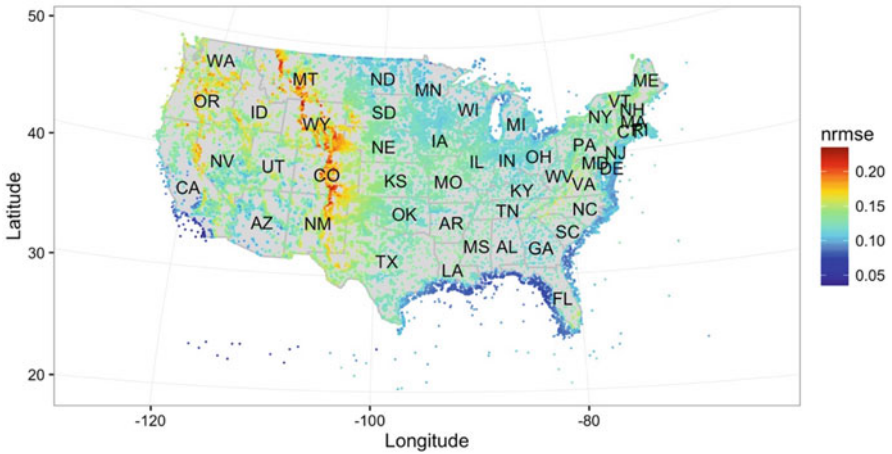
Fig. 11.3 The GBM forecasting nRMSE across the United States

(nMAE) and the normalized root mean square error (nRMSE). The wind forecasting results provided by the GBM models (selected for the robustness and free of preprocessing) of more than 126,000 wind farms over the entire United States are shown in Figs. 11.2 and 11.3. The Wind Integration National Dataset (WIND) Toolkit. Toolkit (Draxl et al. 2015) data was used for the wind forecasting. It is seen from Figs. 11.2 and 11.3 that, the offshore locations, such as the Gulf of Mexico and the East Coast, present relatively high forecasting accuracy; the mountain areas, such as Colorado and New Mexico, have relatively low forecasting accuracy. By comparing Figs. 11.2 and 11.3, regions such as Washington and Oregon present small nMAE but large nRMSE. The variation in the forecasting accuracy across the

Table 11.1 SURFRAD locations

Name	State	Lat.	Long.	Elev. (m)
Bondville (BND)	IL	40.05	−88.37	230
Boulder (TBL)	CO	40.12	−105.24	1689
Desert Rock (DRA)	NV	36.62	−116.02	1007
Fort Peck (FPK)	MT	48.31	−105.24	634
Goodwin Creek (GCM)	MS	34.25	−89.87	98
Penn. State Univ. (PSU)	PA	40.72	−77.93	375
Sioux Falls (SXF)	SD	43.73	−96.62	473

Table 11.2 The nMAE of 1-h-ahead forecasts

Models		BND	TBL	DRA	FPK	GCM	PSU	SXF
SAM	P	4.05	4.27	5.25	4.28	4.13	5.78	3.91
	SVR_li	5.26	5.04	6.65	5.18	5.42	7.13	4.93
	SVR_poly	5.04	4.90	6.17	4.93	5.06	6.86	4.86
	ANN	5.35	5.96	6.23	5.29	5.65	6.90	4.73
	GBM_g	4.95	4.82	6.02	4.80	4.82	6.68	4.78
	GBM_l	5.01	4.80	6.23	4.94	4.96	6.67	4.93
	RF	5.32	4.93	6.51	5.31	5.58	7.51	5.25
MMF	SVR_li	4.32	5.28	5.44	4.45	6.04	6.03	4.05
	SVR_poly	4.20	4.54	5.36	4.31	5.14	5.84	4.01
	GBM	4.26	4.58	5.49	4.37	5.81	6.11	4.19
	RF	4.26	4.60	5.66	4.33	5.34	6.09	4.22

United States is affected by a number of factors. For example, the terrain roughness and the climatic characteristics of the states like Washington and Oregon make wind series more chaotic and less forecastable.

Both the single-algorithm models (SAM) and hybrid multi-model framework (MMF) are applied to the data collected from the Surface Radiation Network (SURFRAD), which includes seven stations (as shown in Table 11.1) with diverse climates. Tables 11.2 and 11.3 list the nMAE and nRMSE, respectively. The multi-model framework includes multiple individual models in the first layer and also several models in the second layer. Different algorithms are tested in both layers, which include SVR with the linear (SVR_li) and polynomial (SVR_poly) kernels, ANN with feed-forward back-propagation learning function and the sigmoid activation function, the GBM models with Gaussian (GBM_g) and Laplacian (GBM_l) loss functions, and the random forest (RF).

As shown in Tables 11.2 and 11.3, none of the SAM models performs better than the persistence method (which assumes that the conditions at the time of the forecast will not change). Without considering the persistence model, no SAM model is always most accurate at all seven locations. Comparing SAM models and MMF models, the MMF with different blending algorithms outperforms the SAM models. The two-layer models have improved the accuracy of the component models by up to 23.8% based on nMAE and 25.6% based on nRMSE. For the blending algorithms,

Table 11.3 The nRMSE of 1-h-ahead forecasts

Models		BND	TBL	DRA	FPK	GCM	PSU	SXF
SAM	P	5.65	6.60	7.36	5.91	5.68	8.27	5.42
	SVR_li	7.76	8.37	9.88	7.92	8.09	9.90	6.95
	SVR_poly	7.05	7.62	8.58	6.81	6.72	9.33	6.51
	ANN	7.27	8.09	8.47	6.94	7.05	9.37	6.30
	GBM_g	6.78	7.77	8.06	6.59	7.01	9.24	6.37
	GBM_l	6.79	7.71	8.86	6.68	6.67	9.42	6.52
	RF	7.36	7.21	9.10	7.35	7.46	10.04	7.11
MMF	SVR_li	6.20	8.96	7.51	6.29	9.21	8.52	5.61
	SVR_poly	5.77	7.22	7.36	6.05	7.08	8.16	5.49
	GBM	5.95	7.29	7.58	6.00	8.23	8.48	5.72
	RF	5.85	7.52	7.63	5.92	7.53	8.46	5.74

the models with nonlinear blending algorithms have better performance than the models with linear blending algorithms. This shows that the forecasts produced from the first-layer models exhibit a nonlinear relationship with the actual wind speed. The model with the polynomial-kernel SVM algorithm is the most accurate model among all the MMF models.

11.2.4 Probabilistic Results of the Multi-model Forecasting

In addition to deterministic forecasts, the multi-model methodology can also produce probabilistic forecasts. Figure 11.4 provides an example of the deterministic forecasts along with the confidence intervals in the form of fan chart, at BND. The confidence bands are calculated based on the component models. The colors of the intervals fade with the increasing confidence level, ranging from 10% to 90% in a 10% increment. The intervals are symmetric around the deterministic forecasting curves with a changing width. When the wind speed fluctuates within a small range, the confidence bands are narrow, as shown by hours 0–10. When there is a significant ramp, the uncertainty of the forecasts is increased and the bands tend to be broader, as shown by hours 150–170. This further proves the necessity of probabilistic forecasting.

11.2.5 The Value of Wind Forecasting

The accurate deterministic and probabilistic wind forecasting could benefit power system operators, energy traders, and wind plant owners by (i) assisting utilities to reduce the backup, therefore achieving savings; (ii) minimizing the production costs by optimizing the slow- and quick-start unit capacity; (iii) providing schedules for
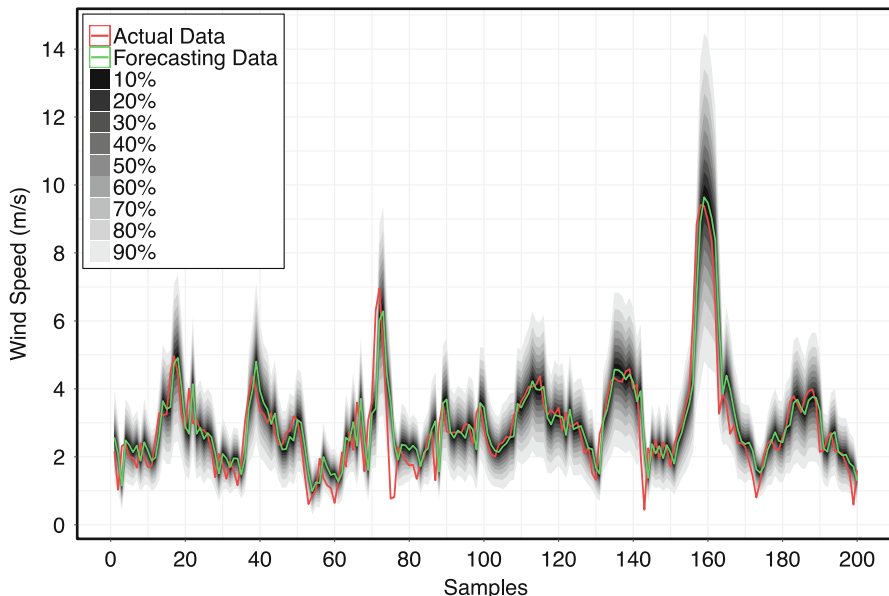
Fig. 11.4 Deterministic forecasting from the MMF_FS with confidence intervals at BND

wind turbine starting up/shutting down in the response to fluctuations; (iv) helping wind farm operators, especially offshore wind farm operators, to better schedule wind turbine maintenance; and (v) reducing curtailment of the wind generation. Overall, the improved wind forecasts could be helpful in reducing the operation costs and increasing the system reliability. The forecasts can also be used to determine the charge and discharge schedule of energy storage in a micro-grid system with distributed wind generators and energy storage.

11.3   Wind Power Ramp Event Detection

Wind power ramps significantly affect the regulation of traditional generators for better managing and dispatching the wind power. Therefore, better detecting and forecasting ramp events are very helpful for power system operators to make operational decisions. Regarding wind power ramp detection, Sevlian and Rajagopal (2012, 2013) proposed an optimal detection technique to identify all WPREs by defining a family of scoring functions associated with any ramping rules and using recursive dynamic programming. Zhang et al. (2014) adopted the swinging door algorithm (SDA) to extract ramp events from actual and forecasted wind power time series. Cui et al. (2016) developed an optimized swinging door algorithm (OpSDA) to improve ramp detection performance, by segregating wind power time series with

the SDA and merging all ramps with a dynamic programming algorithm. Kamath (2010, 2011) used feature selection techniques from data mining to determine ramps in wind power generation.

A number of statistical and machine learning methods have been developed in the literature to forecast wind power ramps at multiple forecasting horizons. For example, Cui et al. (2016, 2017) modeled the wind power generation as a stochastic process by using a neural network and a genetic algorithm and then forecasted the probability distributions of three WPRE properties. Cutler et al. (2007) compared the efficiency of the Wind Power Prediction Tool (WPPT) and the Mesoscale Limited Area Prediction System (MesoLAPS) for WPRE forecasting. Zareipour et al. (2011) mined historical data and predicted the class of WPREs using support vector machines. Greaves et al. (2009) calculated temporal uncertainty to provide an indication of the likely timing of WPREs.

This chapter reviews and discusses a recently developed wind power ramp detection method, the optimized swinging door algorithm (OpSDA). The OpSDA (Cui et al. 2015) is a two-stage process method. The first stage is a data segregation process based on SDA. SDA is used to segregate wind power signals according to the user-specified definition of a ramp. The second stage is an optimization process based on a dynamic programming algorithm. Dynamic programming is used to merge adjacent segments that are segregated with the same ramp changing direction in the first stage.

11.3.1 Swinging Door Algorithm (SDA)

The SDA algorithm (Bristol 1990; Barr 1994) is based on the concept of a "swinging door" with a "hinge" or "pivot point" whenever the next point in the time series causes any intermediate point to fall outside the area partitioned by the up and down segment bounds. The segment bounds are defined by the door width, $\pm\varepsilon$, which is the only tunable parameter in the SDA. More detailed descriptions of the SDA can be found in Florita et al. (2013) and Makarov et al. (2009). After segregating the wind power signal by SDA, wind power ramping events (WPREs) are extracted according to the user-specified definition of a significant ramp.

11.3.2 Optimized Swinging Door Algorithm (OpSDA)

The objective of the optimization in the SDA is to minimize the number of individual ramps whereas still approximating the wind power signal as a ramp. Therefore, adjacent segments that have the same slope (e.g., up-ramps) can be merged into one segment. Toward this end, an optimization process is applied to the original segments (from the SDA) using a dynamic programming algorithm. Dynamic programming is a method for solving a complex problem by breaking it down into

a collection of simpler subproblems. Every subinterval (subproblem) of the ramp detection problem complies with the same ramp rules. First, the subintervals that satisfy the ramp rules are rewarded by a score function; otherwise, their score is set to zero. Next, the current subinterval is retested as above after being combined with the next subinterval. This process is performed recursively to the end of the dataset. Finally, the significant ramp with the maximum score is extracted. More detailed formulations of the dynamic programming algorithm used in this work are shown in Eqs. (11.12), (11.13), and (11.14).

In this chapter, an increasing length score function, S, is designed based on the length of the interval segregated by the SDA. The optimization problem seeks to maximize the length score function, which corresponds to a ramp event. Given a time interval, (i, j), of all discrete time points and an objective function, J, of the dynamic programming algorithm, a WPRE is detected by maximizing the objective function:

$$J\,(i,\,j) = \max_{i<k\leq j} \left[S\,(i,\,k) + J\,(k,\,j) \right], \;\; i < j \tag{11.12}$$

subject to:

$$S\,(i,\,j) > S\,(i,\,k) + S\,(k+1,\,j)\,, \;\; \forall i < k < j \tag{11.13}$$

$$S\,(i,\,j) = (j-i)^2 \times R\,(i,\,j) \tag{11.14}$$

where J(i, j) can be computed as the maximum over (j−i) subproblems. The term of S(i, k) is a positive score value corresponding to the interval, (i, k), which conforms to a super-additivity property in Eq. (11.13). There is a family of score functions satisfying Eq. (11.13), and the score function presented in (Sevlian and Rajagopal 2013) is adopted in this research, expressed as Eq. (11.14). R(i, j) represents a ramp within the time interval (i, j). Significant wind power ramps can be defined based on the power change magnitude, direction, and duration. Three definitions proposed in (Zhang et al. 2014) are investigated in this research:

  (i) Significant ramp definition 1—the change in wind power output is greater than 20% of the installed wind capacity without constraining the ramping duration.
 (ii) Significant ramp definition 2—the change in wind power output is greater than 20% of the installed wind capacity within a time span of 4 h or less.
(iii) Significant ramp definition 3—a significant up-ramp is defined as the change in wind power output greater than 20% of wind capacity within a time span of 4 h or less; a significant down-ramp is defined as the change in wind power output greater than 15% of the installed wind power capacity within a time span of 4 h or less.

If R(i, j) conforms to the threshold of ramp definitions, R(i, j) is 1; otherwise, R(i, j) is 0. Since the process of detecting down-ramps is the opposite process of

detecting up-ramps, note that up-ramp detection is taken as an example to illustrate the specific detecting process.

When optimizing ramps, one of the more interesting findings was the presence of small ramps (non-WPREs), which are termed "bumps" in this paper and set as B(i, j) in the formulations below. The key characteristic of a bump is the changing direction (e.g., a down-bump between two up-ramps or an up-bump between two down-ramps), which makes the iteration of the dynamic programming to break abruptly due to the strict super-additivity property in Eq. (11.13). When a bump occurs, it breaks one integrated WPRE into two discrete ramps, which affects the performance of WPRE detection. To address this issue, the dynamic programming process is improved so that it can also merge ramps and bumps with different changing directions. If B(i, j) conforms to the threshold of bump definitions, B(i, j) is assigned to be 1; otherwise, B(i, j) is assigned to be 0. During the recursion, bumps are also considered and merged into the WPRE.

11.3.3 Experimental Results

In this section, the OpSDA is applied to two case studies. We present various statistics to analyze the detected WPREs and parameterize the WPRE process. The total wind power generation is taken from a balancing area in the northwestern region of the United States. The dataset contains 7,884,012 samples sampled every 4 s spanning from October 1, 2012, to September 30, 2013. In this case, we use the maximum power output, 123 MW, as the base benchmark capacity. The 4-s dataset is averaged to obtain wind power data at different timescales: 1-min, 5-min, 15-min, 30-min, 1-h, and 2-h. A total of 2,089 ramps within 1-min timescale (1,941 ramps within 5-min timescale, 1,701 ramps within 15-min timescale, 1,340 ramps within 30-min timescale, 1,009 ramps within 1-h timescale, and 705 ramps within 2-h timescale) are detected and utilized to generate the probability density distributions. Figure 11.5 shows the ramp feature statistics and seasonal ramp counts of each timescale over the course of a whole year.

Figure 11.5a indicates that along with the increasing timescale (from 1-min to 2-h), for ramp durations, the peak duration value and probability density rise from 50 min with 0.03–400 min with 0.17. For the distribution of ramp change rate in Fig. 11.5b, the peak change rate value decreases from 0.004 p.u./min to 0.001 p.u./min, whereas the corresponding probability density rises from 80 to 820. For the distribution of ramp magnitude in Fig. 11.5c, the peak magnitude value rises from 0.21 p.u. to 0.33 p.u., whereas the corresponding probability density decreases from 9 to 2. Figure 11.5d illustrates that the seasonal ramp counts also decrease along with the increasing timescale in each season. There are relatively fewer ramp events occurring in winter and spring, whereas there are relatively more ramp events occurring in summer and fall. This can be partially attributed to the higher wind generation in summer and fall as shown in Fig. 11.5e. It is seen from Figs. 11.5d and 11.5e that seasonal ramp counts increase along with the increasing wind generation.
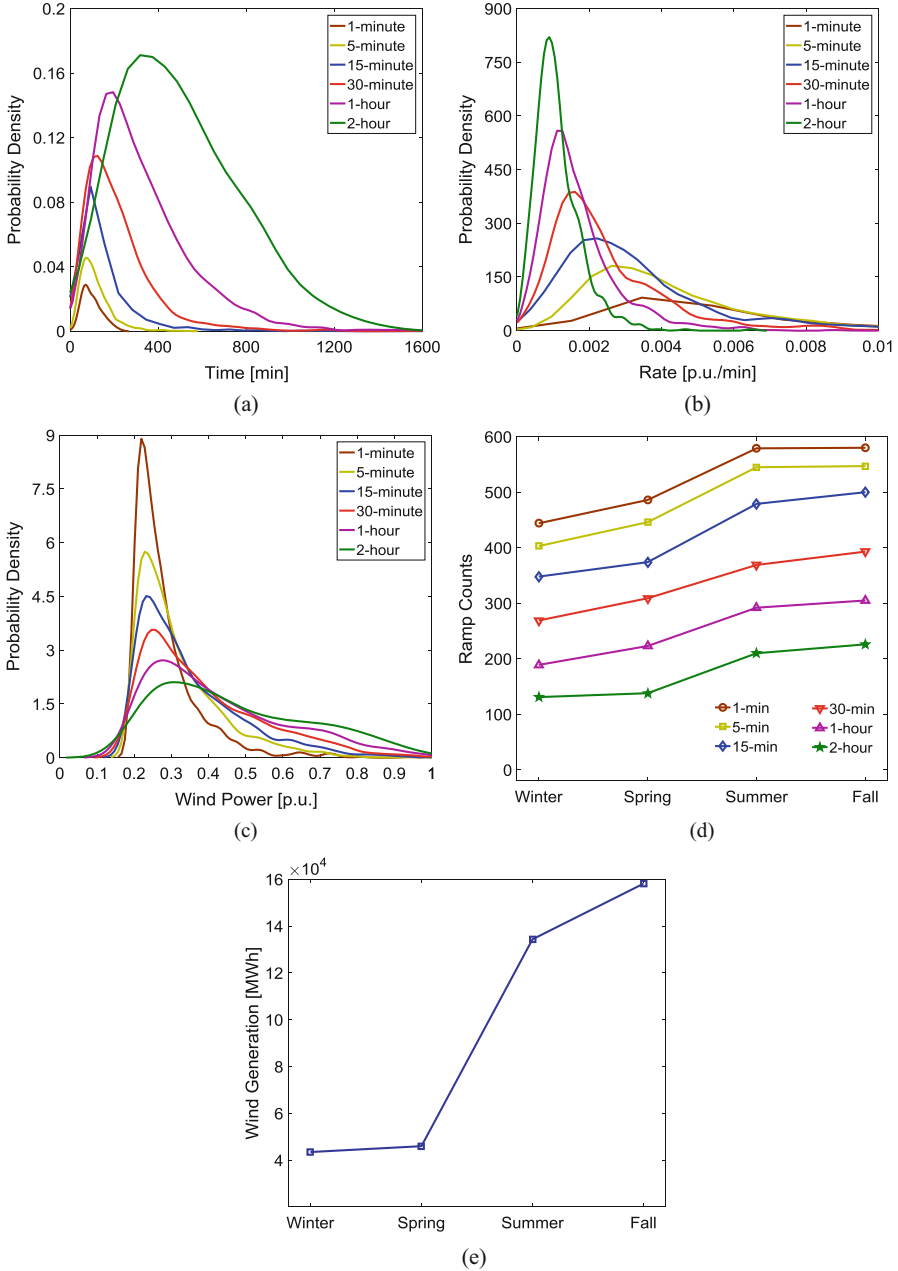
Fig. 11.5 Probability density distributions of ramp features of six timescales (1-min, 5-min, 15-min, 30-min, 1-h, and 2-h) and seasonal ramp counts over a whole year for Case II. (**a**) Ramp duration. (**b**) Ramp change rate. (**c**) Ramp magnitude. (**d**) Seasonal ramp counts. (**e**) Seasonal wind generation

11.4 Multi-timescale Power System Operations with Variable Wind Generation

11.4.1 Multi-timescale Scheduling Models

Wind power ramps usually show different characteristics in the multi-timescale power system operations, including ramping starts, ramping magnitudes, and ramping durations. To study the impact of wind power ramps on power system operations, multi-timescale scheduling models as illustrated in Fig. 11.6 could be used. A multi-timescale steady-state power system operation simulation tool consists of different sub-models, such as day-ahead security-constrained unit commitment (DASCUC), real-time security-constrained unit commitment (RTSCUC), real-time security-constrained economic dispatch (RTSCED), and automatic generation control (AGC).
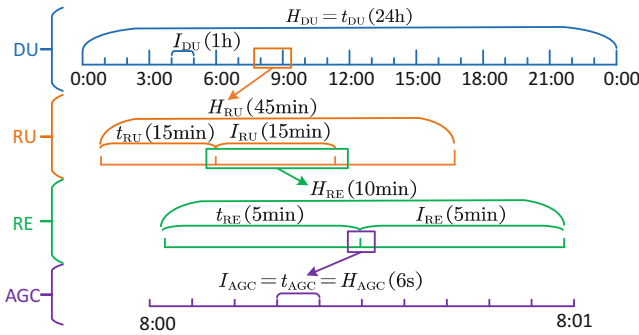
Fig. 11.6 Timeframes of multi-timescale scheduling models
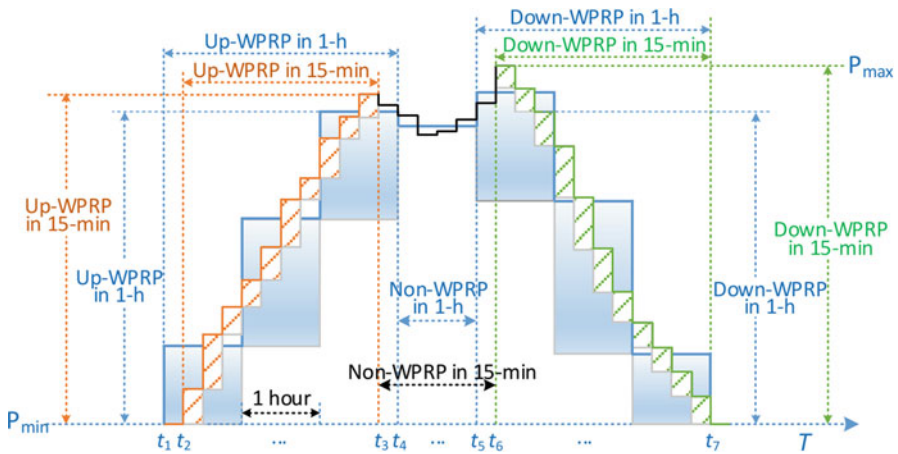
Fig. 11.7 WPRP performance in the multi-timescale operations using the stairstep graph

Figure 11.7 exhibits an example of multi-timescale wind power ramping product (WPRP) detection. The rectangle represents the ramping product that can be provided by wind power at the current time. The first three blue rectangles consist of one up-WPRP with the ramping start time t1 and ramping end time t4 in the 1-h timescale. The up-WPRP in the 15-minute-timescale model starts at time t2 (=t1 + 15 min) and terminates at time t3 (=t4-15 min). Moreover, the ramping capacity in the 15-min-timescale model is much less than that in the 1-h-timescale model, according to the areas of blue and yellow rectangles. The same phenomenon can also be found in the down-WPRP (time t5 t7 and time t6 t7). Under this circumstance, it is essential to characterize and consider WPRP features in a multi-timescale fashion.

11.5   Conclusions

In this chapter, several widely used models for the short-term wind forecasting and ramp forecasting were reviewed and discussed. The 1-h-ahead wind power forecasts at over 126,000 wind sites in the United States were generated using a gradient boosting machine model. We also found that the ensemble machine learning models have improved the wind forecasting accuracy, compared with the single-algorithm models. A recently developed wind power ramp detection method was introduced in this chapter. The results showed that the OpSDA successfully identified wind power ramps and performed significantly better than the SDA. The accurate wind power forecasts and ramp detection could benefit power system operators, energy traders, and wind plant owners.

References

Barr DC (1994) The use of a data historian to extend plant life. In Proceedings of international conference life management of power plants, Heriot-Watt University, Dec. 12–14. Edinburgh, UK

Bristol EH (1990) Swinging door trending: adaptive trend recording? In Proceedings of ISA national conference, pp 749–756

Chang WY (2014) A literature review of wind forecasting methods. *Journal of Power and Energy*. Engineering 2(04):161

Chen K, Yu J (2014) Short-term wind speed prediction using an unscented Kalman filter based state-space support vector regression approach. Appl Energy 113:690–705

Cortes C, Vapnik V (1995) Support-vector networks. Mach Learn 20(3):273–297

Cui M, Zhang J, Florita AR, Hodge BM, Ke D, Sun Y (2015) An optimized swinging door algorithm for wind power ramp event detection. IEEE Power Energy Society General Meeting, Denver

Cui M, Zhang J, Florita AR, Hodge BM, Ke D, Sun Y (2016) An optimized swinging door algorithm for identifying wind ramping events. IEEE Trans Sustainable Energy 7(1):150–162

Cui MJ, Zhang J, Feng C, Florita AR, Sun YZ, Hodge BM (2017) (2017). Characterizing and analyzing ramping events in wind power, solar power, load, and netload. Renew Energy 111:227–244

Cutler N, Kay M, Jacka K, Nielsen TS (2007) Detecting categorizing and forecasting large ramps in wind farm power output using meteorological observations and WPPT. Wind Energy 10(5):453–470

Draxl C, Clifton A, Hodge B-M, McCaa J (2015) The WIND integration national dataset (WIND) toolkit. Appl Energy 151:355–366

Erdem E, Shi J (2011) ARMA based approaches for forecasting the tuple of wind speed and direction. Appl Energy 88(4):1405–1414

Feng C, Cui M, Hodge BM, Zhang J (2017a) A data-driven multi-model methodology with deep feature selection for short-term wind forecasting. Appl Energy 190:1245–1257

Feng C, Cui MJ, Lee M, Zhang J, Hodge BM, Lu SY, Hamann HF (2017b) Short-term global horizontal irradiance forecasting based on sky imaging and pattern recognition. IEEE Power Energy Society General Meeting, Chicago

Florita A, Hodge BM, Orwig K Identifying wind and solar ramping events. in Proceedings of IEEE 5th Green Technologies Conference, Denver, CO, 4–5, 2013

Freedman J, Markus M, Penc R (2008, Jan. 28) Analysis of West Texas Wind Plant Ramp-Up and Ramp-Down Events [Online]. Available: http://interchange.puc.state.tx.us/WebApp/Interchange/Docu ments/33672_1014_580034.pdf

Greaves B, Collins J, Parkes J, Tindal A (2009) Temporal forecast uncertainty for ramp events. Wind Eng 33(4):309–320

Ibarra-Berastegi G, Saénz J, Esnaola G, Ezcurra A, Ulazia A (2015) Short-term forecasting of the wave energy flux: analogues, random forests, and physics-based models. Ocean Eng 104:530–539

Kamath C (2010) Understanding wind ramp events through analysis of historical data. Proceedings transmission and distribution conference exposition. New Orleans, LA

Kamath C (2011) Associating weather conditions with ramp events in wind power generation. Proceedings transmission and distribution conference exposition. Phoenix, AZ

Kaur A, Pedro HT, Coimbra CF (2014) Ensemble re-forecasting methods for enhanced power load prediction. Energy Convers Manag 80:582–590

Li G, Shi J (2010) On comparing three artificial neural networks for wind speed forecasting. Appl Energy 87(7):2313–2320

Liu H, Tian HQ, Li YF (2015) An EMD-recursive ARIMA method to predict wind speed for railway strong wind warning system. J Wind Eng Ind Aerodyn 141:27–38

Makarov YV, Loutan C, Ma J, Mello P (2009) Operational impacts of wind generation on California power systems. IEEE Trans Power Syst 24(2):1039–1050

Nagy GI, Barta G, Kazi S, Borbély G, Simon G (2016) GEFCom2014: probabilistic solar and wind power forecasting using a generalized additive tree ensemble approach. Int J Forecast 32(3):1087–1093

Poggi P, Muselli M, Notton G, Cristofari C, Louche A (2003) Forecasting and simulating wind speed in Corsica by using an autoregressive model. Energy Convers Manag 44(20):3177–3196

Ren Y, Suganthan PN, Srikanth N (2015) Ensemble methods for wind and solar power forecasting—a state-of-the-art review. Renew Sust Energ Rev 50:82–91

Sevlian R, Rajagopal R (2012) Wind power ramps: detection and statistics. IEEE Power Energy Society General Meeting, San Diego

Sevlian R, Rajagopal R (2013) Detection and statistics of wind power ramps. IEEE Trans Power Syst 28(4):3610–3620

Wang HZ, Wang GB, Li GQ, Peng JC, Liu YT (2016) Deep belief network based deterministic and probabilistic wind speed forecasting approach. Appl Energy 182:80–93

Wang HZ, Li GQ, Wang GB, Peng JC, Jiang H, Liu YT (2017) Deep learning based ensemble
  approach for probabilistic wind power forecasting. Appl Energy 188:56–70
Zareipour H, Huang D, Rosehart W (2011) Wind power ramp events classification and forecasting:
  a data mining approach. IEEE Power Energy Society Generation Meeting, San Diego
Zhang J, Florita AR, Hodge BM, Freedman J (2014) Ramp forecasting performance from improved
  short-term wind power forecasting. In: ASME International Design Engineering Technical
  Conference & Computers and information in engineering conference (IDETC/CIE 2014),
  Buffalo

Chapter 12
Emerging Technologies for Next-Generation Wind Turbines

Weifei Hu

12.1 Wind Turbines with Permanent Magnetic Direct Drive

12.1.1 Comparison of Different Wind Turbine Concepts

During the last two decades, various horizontal-axis wind turbine (HAWT) concepts have been developed to harvest wind energy. When considering different generator systems, HAWTs can be categorized into two major groups, gearbox-operated wind turbines and direct-drive wind turbines. The former type uses rotor blades to drive the main shaft that is connected through a gearbox to the generator. The gearbox converts the low rotational speed of the rotor system (e.g., 15–20 rotations per minute (rpm) for a megawatt (MW)-scale turbine) into high rotational speed (e.g., 1800 rpm) that the generator needs to generate electricity. This large rotational speed transition requires multiple gears and bearings and causes tremendous stress and fatigue issues in the gearbox due to wind turbulence, which makes the gearbox one of the highest-maintenance components of a wind turbine (Faulstich et al. 2011). A direct-drive wind turbine directly drives the generator without using a gearbox, one of the most complicated part of the first type machine, therefore improving the performance and reliability. The absence of a gearbox also reduces the noise level. However, direct-drive wind turbines with synchronous generators can be expected to have a low-speed, high-torque, and large-diameter generators and fully rated converters which could cause heavy weight and high cost of the machines. Recently developed wind turbines with permanent magnet direct drive (PMDD) are more superior in terms of reliability, operation and maintenance cost, energy yield, and manufacturing cost than the aforementioned wind turbine concepts (Semken et al.

W. Hu (✉)
Sibley School of Mechanical and Aerospace Engineering and Department of Earth and Atmospheric Sciences, Cornell University, Ithaca, NY, USA
e-mail: wh348@cornell.edu

2012). These advantages have attracted a number of wind turbine manufacturers toward this technology which represents 20% of the sold wind turbine worldwide (Mueller and Zavvos 2013). As a demonstration, Fig. 12.1 provides a photo of a Goldwind 1.5 MW PMDD wind turbine deployed in a wind farm and a schematic of subassemblies of the wind turbine in which the generator is directly connected to the hub. As the rotational speed ω of wind turbine rotor is low, the torque T applied on the PMDD generator must be increased in order to scale up the power P of the wind turbines, as expressed in Eq. (12.1):

$$P = T \cdot \omega \tag{12.1}$$

The generator power P can be also defined as a function of the tangential force density F_d, the air gap diameter D_g, the axial length l_s, and the rotational speed ω as expressed in Eq. (12.2):

$$P = \frac{\pi}{2} F_d \cdot D_g^2 \cdot l_s \cdot \omega \tag{12.2}$$

Equation (12.2) shows that the power is proportional to the square of the air gap diameter. Thus, the PMDD generator often has a large diameter to produce high torque and power. The high torque also demands high tangential force applied on the generator. Both the large diameter and high torque result in the mass increase to ensure the air gap in a proper deflection against static and dynamic loads between the rotor and stator, eventually increasing the cost. Thus, the direct-drive wind turbines are usually designed with a large diameter and small pole pitch to increase the efficiency, reduce the active material, and keep the end winding losses small (Bang et al. 2008a). Different configurations of commercial PMDD wind turbines are produced or proposed (Friedrich and Lukas 2017). The following subsections 12.1.2–12.1.4 provide concise introductions of different permanent magnet (PM) generators used in modern wind turbines.

12.1.2 Stator-PM Generator

Traditional PM generators often have magnets on the rotor, which may rise temperature in the magnets due to poor thermal dissipation and cause irreversible demagnetization ultimately limiting the power density of the generator. In contrast, the stator-PM generators have magnets on the stator, which makes the temperature control easier and reduces the magnet protection sleeves in the rotor-PM machines (Cheng et al. 2011). There are three types of stator-PM generators: double salient PM generator, flux-reversal PM generator, and flux-switching PM generator as shown in Fig. 12.2. It can be seen that both the PMs and windings are placed on the stator, which results in easy temperature control of the magnets. Low copper

a

b

Generator Stator

Rotor Blade

Hub

Pitch System

Wind Measurement
Equipment

Auxiliary Crane

Base Frame

Generator PM Rotor

Tower
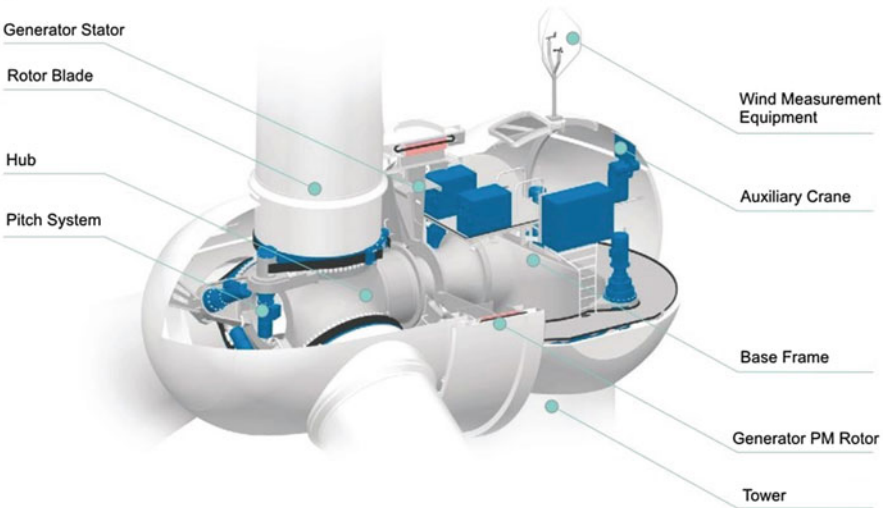
Fig. 12.1 (**a**) Goldwind 1.5 MW PMDD wind turbine (Photo taken by Weifei Hu); (**b**) a schematic of subassemblies of the wind turbine. (Origin: Goldwind brochure (Goldwind 2017))
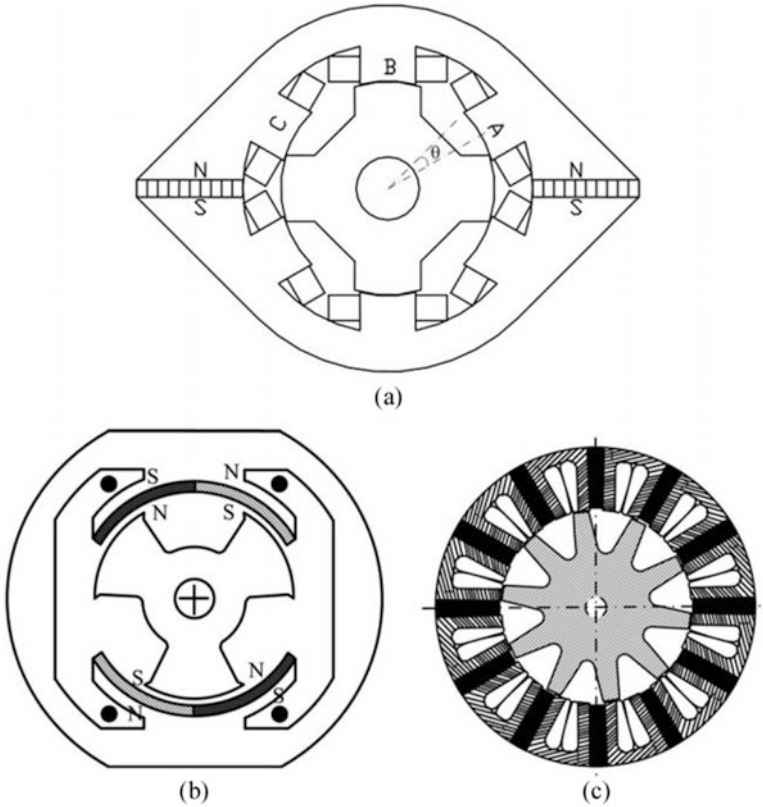
Fig. 12.2 Schematic of three types of stator-PM generators: (**a**) double salient PM generator, (**b**) flux-reversal PM generator, and (**c**) flux-switching PM generator (Cheng et al. 2011)

consumption and winding resistance are produced by employing concentrated windings with shorter end parts, and the rotor made of iron without windings or magnets becomes mechanically robust comparing with the counterparts in rotor-PM generators. The distinguished operation principle and electromagnetic performance of these three types of PM generators are explained in detail by (Cheng et al. 2011).

12.1.3   Magnetic-Geared PM Generator

The basic principle of a magnetic-geared PM generator is that the magnetic fields produced by the PMs on a rotor are modulated by a flux modulator, which generates a harmonic magnetic field with the same number of poles as the magnetic rotor. A typical design of magnetic-geared PM generator includes a stator, a rotor, a stationary ring between the stator and the rotor, and permanent magnets as
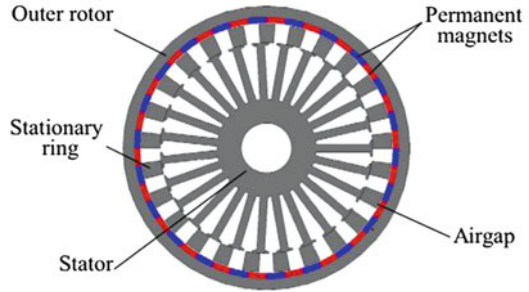
shown in Fig. 12.3. The stationary ring is used to modulate the rotor magnetic field from low speed in the rotor to high speed in the stator in which the armature windings are designed based on high speed magnetic field (Cheng and Zhu 2014). The outer rotor can be coupled with wind turbine rotor which directly provides the torque to the generator. The significant advantages of the magnetic-geared PM generator include reduced acoustic noise, vibration, and maintenance, improved reliability, inherent overload protection, and physical isolation between the input and output shafts.

12.1.4 *PM Generators Classified by Magnetic Flux Path*

The PM generators can also be classified into three categories by the flux path: radial flux PM generators, axial flux PM generators, and transverse flux PM generators, which produce the magnetic flux in the radial direction, axial direction, and perpendicular to the direction of the rotor rotation. A detailed survey of these three types of PM generators has been carried out by Bang et al. (2008b).

12.2 3D Printing for Wind Turbines

12.2.1 *Additive Manufacturing*

Additive manufacturing, also known as 3D printing, is a manufacturing technology which creates a three-dimensional object through the buildup of layers of a base material under computer control. Early development of additive manufacturing technology began in the later 1970s when Wyn Kelly Swainson was granted a patent for a process where a three-dimensional object was created through the buildup of photopolymer material (Bassett et al. 2015; Swainson 1977). The term additive manufacturing started to gain its wide popularity in the 2000s (Google Ngram Viewer 2017). Traditional subtractive manufacturing processes,

e.g., computer-controlled single and multiaxes CNC machines, lathes, laser, and water jet cutting tables, remove material from a stock piece of base substrate to create a component. While a variety of three-dimensional shapes can be created through subtractive process, these traditional technologies suffer from three main drawbacks: (1) additional effort is needed to recycle the removed materials which, otherwise, may be wasted; (2) it is difficult and expensive to create certain complex hollow and shell components by subtractive approaches; and (3) conventional subtractive machining methods (e.g., mechanical cutting and drilling) have other disadvantages such as high tool wear due to mechanical or thermal loads and high costs for tool and processing. In contrast to the subtractive manufacturing, additive manufacturing can cost-effectively utilize the base material, easily create complex hollows and shells by designing a proper deposition path such that the extruder does not pass through the same point in space more than once (Bassett et al. 2015), and avoid high costs for tool replacement.

12.2.2 Applications for Wind Turbine Design and Manufacturing

The primary application of 3D printing for wind turbines has been started from rapid prototyping which promptly creates a part model for engineers and designers to test the component properties before the massive production. 3D rapid prototyping has been successfully applied in areas such as rapid prototyping aerodynamic research models (Shun and Ahmed 2012) and a hydroturbine model (Anagnostopoulos et al. 2012). In wind energy field, this technology is typically used for design of small-scaled wind turbines. For example, Howey et al. utilized the rapid prototyping to form a centimeter-scale shrouded wind turbine rotor assembled from a central hub, an annular rim, and a variable number of blades (Howey et al. 2011). A small-scale vertical axis wind turbine is printed in parts and assembled together without any adhesives or external fasteners, even though the model is just an aesthetic demonstration produced by a commercial company (Ultimaker 2017). The 3D printing can contribute in small-scale wind turbine manufacturing instantly available without requirement of a large investment, create complex and precise shapes of wind turbine components, and print a fully hollow wind turbine that is as light as possible while ensuring the structural reliability.

With the emergence of affordable large-scale 3D printing technology for large wind turbine design, this technology presents new opportunities for decreasing cost when designing new industrial-level wind turbines. A team of US government and industry partners is using 3D printing to make wind turbine blade molds to demonstrate the utility of large-scale additive manufacturing as a platform technology for renewable energy systems (Zayas and Johnson 2016). This technology will speed

Fig. 12.4 3D printing of wind turbine blade molds using the Big Area Additive Manufacturing machine (US Department of Energy 2016)

up the designing process of novel wind turbine blades and reduce costs and time associated with creating blade molds. The blade mold is created using the Big Area Additive Manufacturing (BAAM) machine, which is located at the Manufacturing Demonstration Facility at Oak Ridge National Laboratory (Fig. 12.4). The BAAM is 500–1000 times faster and capable of printing polymer components more than 10 times larger than traditional industrial additive machines (Zayas and Johnson 2016). The basic steps of 3D printing for the wind turbine mold are summarized as follows:

1. The BAAM melts carbon fiber composite pellets, which are used to print the blade mold, and squeezes the molten material through the printing nozzle.
2. The material is layered into the mold shape based on the computer-aided design. The mold is printed in segments 1.8 m long, and each mold segment takes about 8 h to print.
3. The mold segment is then laminated with a layer of fiberglass. Excess is trimmed off to achieve an exact shape and smoothness.
4. Finally, the mold segments are joined together with fiberglass to ensure a smooth, vacuum-tight surface.

Applying 3D printing to create the blade mold, which in turn is used to fabricate the carbon/glass fiber wind turbine blades, can significantly reduce the labor cost, decrease the manufacturing time, and provide researchers additional time and freedom to design new blades thus improving the design flexibility. Although the current 3D printing focuses on small-scale wind turbine manufacturing and large-scale blade mold prototyping, it could also potentially benefit the rapid design and production of other wind turbine components, e.g., hub and tower, which brings the wind energy cost further lower.

12.3 Wind Turbine Icing and Anti-icing and Deicing Techniques

12.3.1 Wind Turbine Icing Effects

Wind turbines installed in cold-climate areas, e.g., high altitude and latitude areas, often face icing conditions over their lifetime, especially during winter periods. Despite of many icing effects as explained below, there exists increasing interest in installing wind turbines in the cold-climate areas. One of the reasons is that wind power is proportional to air density which is larger at lower temperature. For instance, air at -30 °C is 26.7% denser than at 35 °C based on the equation of state for an ideal gas (Dalili et al. 2009). Ice accretion on wind turbine blades, as illustrated in Fig. 12.5, can not only be detrimental to the performance and reliability of wind turbines themselves but also cause safety issues of people and animals (e.g., livestock) nearby operating iced wind turbines. These detrimental icing effects are further described as follows:

- *Performance degradation*. Ice accretion could introduce measurement errors from sensors deployed on wind turbines. For example, wind speed errors measured in icing conditions can be as high as 30–40% for an ice-free anemometer and 60% for a standard anemometer (Laakso et al. 2003; Fortin et al. 2005). More importantly, ice accretion changes the shape and roughness of the blade surface, which consequently affects the aerodynamic performance. Small amounts of ice on the leading edge of airfoils significantly reduce aerodynamic properties of the blade, and the resulting power loss may vary from 0.005% to 50% of the annual production depending on icing intensity and its duration on the site, wind turbine models, and the evaluation methodology (Botta et al. 1998; Laakso et al. 2005; Tammelin et al. 2005; Parent and Ilinca 2011).

Fig. 12.5 Illustration of icing blades (Muñoz et al. 2016)

- *Reliability reduction*. This detrimental consequence due to the ice accretion could be further divided into mechanical failure and electrical failure. The former is caused by the increased load due to the ice accretion on blades and tower, which may produce high vibrations and/or resonance as well as mass imbalance between blades, while the latter is likely due to ice/snow infiltration in nacelle leading to condensation in the electronics (Parent and Ilinca 2011; Laakso et al. 2003).
- *Safety risks*. Threat of ice thrown from rotating blades has been a serious safety issue, particularly when the wind power plant is closed to roads, housing, power lines, and shipping routes. Research shows that large icing accumulation on blades can be thrown at a distance of up to 1.5 times the combined height of the turbine and the rotor diameter (Tammelin et al. 2000).

12.3.2   Ice Accretion on Wind Turbines

Before addressing the icing issues, it is important to first understand basic physics of three types of atmospheric icing related to wind turbines, i.e., in-cloud icing, precipitation icing, and frost icing (Parent and Ilinca 2011; Boluk 1996; Fikke et al. 2006; ISO-12494 2001; Richert 1996).

In-cloud icing happens when supercooled water droplets hit a surface below 0 °C and freeze upon impact. Ice accretions of this type have different sizes, shapes, and properties depending on the number of droplets in the air (i.e., liquid water content (LWC)) and their size (i.e., median volume diameter (MVD)), the temperature, the wind speed, the duration, the chord length of the blade, and the collection efficiency. The in-cloud icing can be further divided into three subcategories, soft rime, hard rime, and glaze. The soft rime is a white ice deposition with needles and flakes. It often appears when temperature is well below 0 °C and the MVD and LWC are small. The resulting accretion has low density and little adhesion. The higher MVD and LWC will cause hard rime with higher accretion density, which is more difficult to remove. Glaze happens when a portion of the droplet does not freeze upon impact, but runs back on the surface and freezes later, resulting in strong ice density and adhesion. Precipitation icing can be caused by freezing rain and wet snow and have the accretion rate much higher than that of in-cloud icing. Freezing rain is a type of rain precipitation that freezes on contact on surfaces with temperature below 0 °C. Ice density and adhesion are high when freezing rain occurs. Wet snow happens when snow is slightly liquid at air temperature between 0 and −3 °C and sticks to the surface. It is easy to remove at first but can be difficult if it freezes on the surface. Frost icing appears when water vapor solidifies directly on a cool surface often occurring during low winds.

12.3.3 Anti-icing and Deicing Techniques for Wind Turbines

Anti-icing prevents ice to accrete on the object, while deicing removes the ice layer from the surface. Both approaches can be divided into two subcategories: passive and active. Passive methods take advantage of the physical properties of the blade surface to eliminate or prevent ice, while active methods use external systems and require an energy supply that is either thermal, chemical, or pneumatic (Dalili et al. 2009; Parent and Ilinca 2011). Anti-icing and deicing approaches from aerospace industry are often transferred to the wind energy after scaling adjustment has to be done in the new application field (Richert 1996). A comprehensive survey of anti-icing and deicing strategies has been carried out by Parent and Ilinca (Parent and Ilinca 2011). These strategies are concisely summarized in the Table 12.1.

12.4 Data-Mining Techniques for Wind Energy

12.4.1 Overview of Data-Mining Techniques for Wind Energy

As the big data are collected by wind turbine manufacturers, wind farm operators, and other sectors from the wind energy industry, the data-mining techniques have been dramatically developed/adopted from other industrial fields over the past decade and become more applicable and beneficial in a wide range of wind energy systems (e.g., prediction and diagnosis of wind turbine faults (Kusiak and Li 2011), wind power optimization (Park and Law 2016), wind power prediction (Negnevitsky et al. 2009), placement of wind turbines (Grady et al. 2005), wind energy storage management (Blonbou et al. 2011), just to name a few) than ever before. The core of data-based techniques is to take full advantage of the huge amounts of available data, acquire useful information within, and eventually lower the wind energy cost. Without recourse to complex physical models, the interested wind energy performance (e.g., wind farm power and wind turbine responses) could be revealed via available historical measurements or forecasted values from numerical models. Through the deep insights of the data-mining techniques, wind energy system characteristics and regularity can be dug out for optimal modeling and decision making. Many approaches, methods, and algorithms have been developed in the field of data mining which could be classified into the following categories based on the functionalities (Colak et al. 2012):

- *Characterization* used for summarizing the general characteristics of any dataset.
- *Discrimination* utilized for determining the diversities among different datasets.
- *Classification* used for determining the class of a new observation utilizing available classes of the observations in training set. Examples of the classification techniques include decision trees, regression analysis, artificial neural network, support vector machines, naïve Bayes algorithm, k-nearest algorithm, and genetic algorithm (Liao and Triantaphyllou 2008).

Table 12.1 Anti-icing and deicing techniques for wind turbines

Type	Name	Description	Advantage	Disadvantage
Passive anti-icing	Special coating	Create ice-phobic coatings that prevent ice from sticking to the surface or super-hydrophobic coatings that do not allow water to remain on the surface, e.g., nanocomposite coatings	Low cost, no special lightning protection needed, easy blade maintenance	Icing occurred on coated surfaces, not truly ice-phobic, ice throw, and becomes porous and loses its ability to repel ice
	Black paint	Allow blade heating during daylight	Show immediate and noticeable improvement; be sufficient in sites where icing is slight, infrequent and winter solar intensity is high	Not sufficient to prevent icing; blade surface temperature may affect the properties of composite materials
	Chemicals	Lower the water's freezing by applying on blade surface	Well used in aerospace industry, e.g., use chemicals during aircraft take-off	It is a pollutant and needs special application and maintenance; cannot remain on the blade surface for a long period
Passive deicing	Flexible blades	Loose the ice by flexing blade	Without external deicing equipment	Limited test and validation
	Active pitching	Use start/stop cycles to orient iced blades into the sun	It may work in slight icing environments	Limited test and validation
Active anti-icing	Thermal	Use heating resistance and warm air for anti-icing	No ice accumulates on blades; save power production	Need addition energy to warm air; may damage blade epoxies and resins at high temperature
	Air layer	Consist of an air flow originating inside the blade and pushed through rows of small holes near the blade leading and trailing edges to generate the air layer	Would deflect the majority of water droplets in the air and melt the few droplets that managed to hit the surface	Limited test and validation
	Microwave	Heat the blade material with microwaves to prevent ice formation	It has been tested by LM Glasfiber on a LM19.1 blade with a 6 kW power	Has yet to be successfully implemented in the field

Table 12.1 (continued)

Type	Name	Description	Advantage	Disadvantage
Active deicing	Heating resistance	Consist of electrical heating element embedded inside the membrane or laminated on the surface	Simple method in both aerospace and wind industry; require small heating energy	The technology is still at the prototype level due to limited market; may cause rotor imbalance if one heater fails; heating elements can attract lightning
	Warm air and radiator	Consist of blowing warm air into the rotor blade	Allow low temperature of the blade surface; no effects on blade aerodynamics and lightning protection system	Consume a lot of power at high wind speed and low temperature; low thermal efficiency
	Flexible pneumatic boots	Inflate to break ice after the ice is built up of generally 6–13 mm on the blade surface	Have equivalent ice shedding and residual ice performance as conventional aircraft deicers; low energy consumption	It has yet to be field-tested and may disturb the aerodynamics by increasing draft and cause more noise. Require intensive maintenance
	Electro impulsive/ expulsive	Consist of very rapid electromagnetically induced vibration pulses in cycles that flex a metal abrasion shield and crack the ice	It has been certified in aerospace industry. The system is efficient and environmentally friendly and has low energy consumption	It has not yet been tested on wind turbines

Summarized based on Parent and Ilinca (2011)

- *Cluster analysis* used for clustering similar data structures, e.g., hierarchical methods, partitioning methods, density-based methods, grid-based methods, and heuristic methods (Tan et al. 2006).
- *Association analysis* used to discover relationships among observations and determine which observations can be realized together.
- *Outlier analysis* used in the stage of analyzing the observations that differ from the data distribution model of available dataset.
- *Evolution analysis* to reveal time-varying tendencies of the observations within the dataset.

Although data-mining techniques have been implemented in various wind energy applications, this section aims to provide an overview of two most widely investi-

gated wind energy areas using data-mining techniques: (1) wind power prediction and (2) wind turbine condition monitoring.

12.4.2   Wind Power Predication

The balance of different power systems is maintained by continuously adjusting generation capacity and by controlling demand. Among various power systems, wind power has larger intermittent structure and variability than traditional thermal power systems do, due to the inherent large uncertainty of wind. A traditional generator is often described as "dispatchable," whereas wind generation is usually referred to as "non-dispatchable." Reducing the error in wind power prediction can benefit the electricity markets trade with more certainty. Research shows that contract errors as a function of time in electricity markets can be as high as 39% for a forecasting lead time of 4 h (Bathurst and Strbac 2003). Accurate wind power prediction is therefore of critical importance for dispatching, scheduling, and unit commitment of thermal generators, hydro plant, and energy storage plant, as well as more competitive market trading as wind power ramps up and down (Foley et al. 2012). According to the predicted time horizons, data-mining techniques for wind power prediction could be categorized into very short-term (few seconds – 30 min), short-term (30 min – 6 h), medium-term (6 h – 1 day), and long-term time scales (1 day – 1 week). A comprehensive literature survey of data-mining techniques for each time scale has been carried out by Colak et al. (2012) and is concisely summarized in Table 12.2.

12.4.3   Wind Turbine Condition Monitoring

Wind turbine condition monitoring (WTCM) is key to reduce the wind turbine operation and maintenance (O&M) costs, which may account for 10–20% of the total cost of energy for a wind project and reach 35% for a wind turbine at the end of life (Tchakoua et al. 2014). Comparing with traditional condition monitoring techniques, data-mining techniques provide attractive advantages to WTCM, as listed below:

- Do not require massive deployment of additional sensors for wind turbine subassemblies.
- Reduce the costs and hardware complexity for WTCM.
- Can be used online and offline with nonintrusive, low-cost, and reliable features.

According to different types of data collected from wind turbines, data-mining techniques could be used for (1) wind turbine performance monitoring, (2) power signal analysis, (3) signature analysis, and (4) supervisory control and data acquisition (SCADA) data analysis (Tchakoua et al. 2014).

Table 12.2 Data-mining techniques categorized based on different prediction time scales (Colak et al. 2012)

Predicted time scale	Usage	Input data	Recording intervals	Prediction intervals	Data-mining model	Reference
Very short-term (few seconds – 30 min)	Wind turbine control and load tracking	Wind power, wind speed, wind direction	10-min	10-min	First-order artificial neural network model	Li et al. (2001)
		Total wind farm power	1-min	5-min	Adaptive neuro-fuzzy inference system	Johnson et al. (2007), Negnevitsky and Johnson (2008)
		Wind power	10-min	10-min	Markov-switching autoregressive model	Pinson and Madsen (2008)
		Wind power, wind speed	10-min	10-min	Combination of k-nearest neighbor algorithm and principal component analysis	Kusiak et al. (2009a)
		Wind power	10-min	10-min	Second-order Markov chain model	Carpinone et al. (2010)
		Wind power, wind speed, wind generator speed, voltage and current in all phases	1-s	15-min	Focus time-delay neural network model	Vargas et al. (2010)
		Wind power, wind speed, wind direction, rotor speed, generator torque, blade pitch angle	10-s	10-s	Neural network model	Kusiak and Zhang (2010)
		Wind power, wind speed	1-s	5-min	Artificial neural network model along with adaptive Bayesian learning and Gaussian process approximation	Blonbou (2011)

		Wind power	15-min	15-min	Combination of particle swarm optimization and adaptive–network–based fuzzy inference system	Catalão et al. (2009, 2011)
		Wind power	10-min	10-min	Combination of wavelet transform, weighted one-rank local-region method, and first-order one-variable gray differential equation model	An et al. (2011)
Short-term (30 min – 6 h)	Preload sharing	Wind power	1-h	6-h	Combination of neuro-fuzzy and artificial neural network model	Katsigiannis et al. (2006)
		Weather data, wind power	1-h	1-h	Artificial neural network based on particle swarm optimization	Jursa and Rohrig (2008)
		Wind power	1-h	3-h	Artificial neural network model based on wavelet transform	Wang et al. (2009)
		Wind speed, wind power	1-h	1-h	Multilayer perceptron	Kusiak et al. (2009b)
		Wind speed, wind power	1-h	1-h	Cascaded multilayer feed-forward neural network models trained by SPSA	Hong et al. (2010)
		Wind speed, wind power	1-h	3-h	Piecewise support vector machine model based on genetic algorithm	Shi et al. (2010)

(continued)

Table 12.2 (continued)

Predicted time scale	Usage	Input data	Recording intervals	Prediction intervals	Data-mining model	Reference
		Wind speed	10-min	3-h	Genetic back propagation neural network model	Xin et al. (2010)
		Wind speed, wind power	10-min	1-h	Adaptive neuro-fuzzy inference system	Wu et al. (2010)
		Wind speed, wind power	1-h	5-h	Improved time series model based on the wind turbine	Liu et al. (2010)
		Wind speed, wind power	1-h	6-h	Multilayer perceptron	De Giorgi et al. (2011)
Medium-term (6 h – 1 day) and long-term time scales (1 day – 1 week)	Power system management and energy trading (medium-term); maintenance and repair of wind turbines (long-term)	Wind power	1-h	12-h, 18-h, 24-h	Combination of neuro-fuzzy and artificial neural network model	Katsigiannis et al. (2006)
		Wind power, wind speed	10-min	1-day	Adaptive neuro-fuzzy inference system	Wu et al. (2010)
		Wind power, wind speed	1-h	12-h, 24-h	Multilayer perceptron, Elman back propagation network model	De Giorgi et al. (2011)

Wind speed	1-day/3-day	1-day, 3-day	Recurrent neural network model	Senjyu et al. (2006)
Wind power, wind speed, wind direction	1-h	72-h	Infinite impulse response multilayer perceptron	Barbounis et al. (2006)
Wind power, wind speed, wind direction, air density, potential temperature	1-h	9-h, 10-h, 11-h, 12-h, 42-h, 51-h, 63-h, 84-h	Multilayer perceptron	Kusiak et al. (2009c)
Wind power, wind speed, wind direction, air pressure, temperature, humidity	0.5-h	1-day	Neuro-fuzzy network models	Xia et al. (2010)

- In wind turbine performance monitoring, time series of various measured data, e.g., plant capacity factors, power, turbine rotor speed, and blade angle, are compared with the values in operator manuals or manufacturer performance specifications to determine whether the system is performing at optimum efficiency.
- In power signal analysis, significant variations in the wind turbine drivetrain torque are generally signs of abnormalities. A torsional oscillation or shift in the ratio between shaft torque and rotational speed could be caused by faults in the drivetrain. By monitoring the online/offline time series of this ratio, certain fault conditions can be detected. For example, blade or rotor imbalance condition can be detected by monitoring the torque oscillations (Gong 2012; Wilkinson et al. 2007).
- Signature analysis uses different signals, i.e., voltages, power, and currents, to detect various faults, i.e., broken rotor bars, bearing failures, air gap eccentricity, and unbalanced rotors and blades (Popa et al. 2003; Yazidi et al. 2005).
- SCADA data analysis is a cost-effective and reliable way for wind turbine condition monitoring because sensors and data collection networks have already been installed in modern wind turbines. Traditional time series analysis and fast Fourier transform (FFT) can be readily used to analyze SCADA data for monitoring turbine health. Neural network and fuzzy logic methods are also widely used for SCADA data analysis.

Existing data-mining techniques for WTCM can also be classified into techniques that are already used by commercial WTCM and those that are still in research (Yang et al. 2014). The former type can be further grouped into time domain analysis and frequency domain analysis. The time domain analysis sets a warning threshold and plots the data trends against time, load, or rotational speed. When a trend reaches a predefined threshold, the system triggers an alarm. The frequency domain analysis methods, e.g., envelope analysis (Hatch 2004; Hatch et al. 2010), cepstrum analysis (Caselitz et al. 1997), and spectral Kurtosis(Antoni and Randall 2006), are based on FFT and used to extract faulty features from time series of specific wind turbine components, e.g., gearbox and bearing vibration signals. Due to the varying speeds and loads and the negative influences of the environment on wind turbine control, the FFT may not be an idea tool for processing WTCM signals that are nonlinear and nonstationary (Yang et al. 2014). Hence, a number of advanced data-mining techniques have been researched to overcome the drawbacks of conventional time and frequency domain analyses for WTCM. Considering four aspects (advantages, disadvantages, online condition monitoring capability, fault diagnosis capability), Yang et al. reviewed some typical advanced data-mining techniques including high spectrum, continuous wavelet transform, discrete wavelet transform, empirical mode decomposition, energy tracking, Wigner-Ville distribution, neural network, and genetic programming (Yang et al. 2014).

12.4.4   Future Work

Future work on the data-mining techniques for wind energy is still needed to the following aspects:

- Improve the data sharing. Although tremendous amount of data are collected by manufacturers, operators, and utility companies in wind energy industry, many of the big data are archived quietly and have not been fully utilized due to confidentiality. Improving the data sharing among various sectors in wind energy will definitely further promote the development of wind energy.
- Validate current data-mining techniques in research and provide industry-proven data-mining techniques for wind energy.
- Create reliable and flexible data-mining techniques that can be readily applied to existing data collection systems, e.g., SCADA, and facilitate wind turbine power prediction, control, and performance and condition monitoring.
- Combine existing data-mining techniques with other physical-based models, e.g., finite element analysis of wind turbines, to create accurate and efficient data-mining- and physical-based hybrid approaches.
- Develop advanced data-mining techniques that can accurately and rapidly handle nonlinear and nonstationary data from wind turbines and wind farms.

References

An X, Jiang D, Liu C, Zhao M (2011) Wind farm power prediction based on wavelet decomposition and chaotic time series. Expert Syst Appl 38(9):11280–11285

Anagnostopoulos JS, Koukouvinis PK, Stamatelos FG (2012) Papantonis DE optimal design and experimental validation of a Turgo model hydro turbine. In: ASME 2012 11th biennial conference on engineering systems design and analysis, ASME paper no. ESDA2012–82565, Nantes, France, 2–4 July 2012

Antoni J, Randall R (2006) The spectral kurtosis: application to the vibratory surveillance and diagnostics of rotating machines. Mech Syst Signal Process 20(2):308–331

Bang D-j, Polinder H, Shrestha G, Abraham Ferreira J (2008a) Promising direct-drive generator system for large wind turbines. EPE J 18(3):7–13

Bang D, Polinder H, Shrestha G, Ferreira JA (2008b) Review of generator systems for direct-drive wind turbines. In: European wind energy conference & exhibition, Belgium

Barbounis TG, Theocharis JB, Alexiadis MC, Dokopoulos PS (2006) Long-term wind speed and power forecasting using local recurrent neural network models. IEEE Trans Energy Convers 21(1):273–284

Bassett K, Carriveau R, Ting D-K (2015) 3D printed wind turbines part 1: design considerations and rapid manufacture potential. Sustainable Energy Technol Assess 11:186–193

Bathurst G, Strbac G (2003) Value of combining energy storage and wind in short-term energy and balancing markets. Electr Power Syst Res 67(1):1–8

Blonbou R (2011) Very short-term wind power forecasting with neural networks and adaptive Bayesian learning. Renew Energy 36(3):1118–1124

Blonbou R, Monjoly S, Dorville J-F (2011) An adaptive short-term prediction scheme for wind energy storage management. Energy Convers Manag 52(6):2412–2416

Boluk Y (1996) Adhesion of freezing precipitates to aircraft surfaces, Optima Speciality Chemicals & Technology Inc., Montreal, Quebec

Botta G, Cavaliere M, Holttinen H (1998) Ice accretion at acqua spruzza and its effects on wind turbine operation and loss of energy production. BOREAS IV FMI, Hetta, pp 77–86

Carpinone A, Langella R, Testa A, Giorgio M (2010) Very short-term probabilistic wind power forecasting based on Markov chain models. In: 2010 IEEE 11th International Conference on Probabilistic Methods Applied to Power Systems (PMAPS), Singapore. IEEE, pp 107–112, 14–17 June 2010

Caselitz P, Giebhardt J, Mevenkamp M, Reichardt M (1997) Application of condition monitoring systems in wind energy converters. In: EWEC-conference. Bookshop for Scientific Publications, Dublin, Ireland, pp 579–582, October, 1997

Catalão JPdS, Pousinho HMI, Mendes VMF (2009) An artificial neural network approach for short-term wind power forecasting in Portugal. In: Intelligent system applications to power systems, 2009. ISAP'09. 15th international conference on, 2009. IEEE, pp 1–5

Catalão JPS, Pousinho HMI, Mendes VMF (2011) Short-term wind power forecasting in Portugal by neural networks and wavelet transform. Renew Energy 36(4):1245–1251

Cheng M, Hua W, Zhang J, Zhao W (2011) Overview of stator-permanent magnet brushless machines. IEEE Trans Ind Electron 58(11):5087–5101

Cheng M, Zhu Y (2014) The state of the art of wind energy conversion systems and technologies: a review. Energy Convers Manag 88:332–347

Colak I, Sagiroglu S, Yesilbudak M (2012) Data mining and wind power prediction: a literature review. Renew Energy 46:241–247

Dalili N, Edrisy A, Carriveau R (2009) A review of surface engineering issues critical to wind turbine performance. Renew Sust Energ Rev 13(2):428–438

De Giorgi MG, Ficarella A, Tarantino M (2011) Error analysis of short term wind power prediction models. Appl Energy 88(4):1298–1311

Faulstich S, Hahn B, Tavner PJ (2011) Wind turbine downtime and its importance for offshore deployment. Wind Energy 14(3):327–337

Fikke SM, Ronsten G, Heimo A, Kunz S, Ostrozlik M, Persson P, Sabata J, Wareing B, Wichura B, Chum J (2006) COST 727: atmospheric icing on structures: measurements and data collection on icing: state of the art. Meteo Schweiz, Zurich, Switzerland

Foley AM, Leahy PG, Marvuglia A, McKeogh EJ (2012) Current methods and advances in forecasting of wind power generation. Renew Energy 37(1):1–8

Fortin G, Perron J, Ilinca A (2005) Behaviour and modeling of cup anemometers under Icing conditions. IWAIS XI, Montréal, p 6

Friedrich K, Lukas M (2017) State-of-the-art and new technologies of direct drive wind turbines. In: Uyar TS (ed) Towards 100% renewable energy techniques, costs and regional case-studies. Springer International Publishing, Cham, pp 33–50

Goldwind (2017) 1.5 MW PMDD wind turbine. http://www.goldwindamericas.com/sites/default/files/Goldwind-Brochure-1.5-Web.pdf. Accessed 28 Aug 2017

Gong X (2012) Online nonintrusive condition monitoring and fault detection for wind turbines. The University of Nebraska-Lincoln, Lincoln

Google Ngram Viewer 2017 (2017) Additive manufacturing. Google. https://books.google.com/ngrams/. Accessed 12 Nov 2017

Grady S, Hussaini M, Abdullah MM (2005) Placement of wind turbines using genetic algorithms. Renew Energy 30(2):259–270

Hatch C (2004) Improved wind turbine condition monitoring using acceleration enveloping. Orbit 61:58–61

Hatch C, Weiss A, Kalb M (2010) Cracked bearing race detection in wind turbine gearboxes. Orbit 30(1):40–47

Hong Y-Y, Chang H-L, Chiu C-S (2010) Hour-ahead wind power and speed forecasting using simultaneous perturbation stochastic approximation (SPSA) algorithm and neural network with fuzzy inputs. Energy 35(9):3870–3876

Howey DA, Bansal A, Holmes AS (2011) Design and performance of a centimetre-scale shrouded wind turbine for energy harvesting. Smart Mater Struct 20(8):085021

ISO-12494 (2001) Atmospheric icing of structures. ISO Copyright Office, Geneva

Johnson PL, Negnevitsky M, Muttaqi KM (2007) Short term wind power forecasting using adaptive neuro-fuzzy inference systems. In: Power engineering conference, 2007. AUPEC 2007. Australasian Universities. Perth, Australia. IEEE pp 1–6, 9–12 Dec 2007

Jursa R, Rohrig K (2008) Short-term wind power forecasting using evolutionary algorithms for the automated specification of artificial intelligence models. Int J Forecast 24(4):694–709

Katsigiannis Y, Tsikalakis A, Georgilakis P, Hatziargyriou N (2006) Improved wind power forecasting using a combined neuro-fuzzy and artificial neural network model. Advances in Artificial Intelligence, Proceedings of 4th Helenic Conference on AI, SETN 2006, Heraklion, Crete, Greece, pp. 105–115, 18–21 May 2006

Kusiak A, Li W (2011) The prediction and diagnosis of wind turbine faults. Renew Energy 36(1):16–23

Kusiak A, Zhang Z (2010) Short-horizon prediction of wind power: a data-driven approach. IEEE Trans Energy Convers 25(4):1112–1122

Kusiak A, Zheng H, Song Z (2009a) Models for monitoring wind farm power. Renew Energy 34(3):583–590

Kusiak A, Zheng H, Song Z (2009b) Short-term prediction of wind farm power: a data mining approach. IEEE Trans Energy Convers 24(1):125–136

Kusiak A, Zheng H, Song Z (2009c) Wind farm power prediction: a data-mining approach. Wind Energy 12(3):275–293

Laakso T, Holttinen H, Ronsten G, Tallhaug L, Horbaty R, Baring-Gould I, Lacroix A, Peltola E, Tammelin B (2003) State-of-the-art of wind energy in cold climates. IEA Annex XIX 24:53

Laakso T, Talhaug L, Ronsten G, Horbaty R, Baring-Gould I, Lacroix A, Peltola E (2005) Wind energy projects in cold climates. Int Energy Agency 36:21–24

Li S, Wunsch DC, O'Hair E, Giesselmann MG (2001) Comparative analysis of regression and artificial neural network models for wind turbine power curve estimation. J Sol Energy Eng 123(4):327–332

Liao TW, Triantaphyllou E (2008) Recent advances in data mining of enterprise data: algorithms and applications, vol 6. World Scientific, Singapore

Liu H, Tian H-Q, Chen C, Li Y-f (2010) A hybrid statistical method to predict wind speed and wind power. Renew Energy 35(8):1857–1861

Mueller M, Zavvos A (2013) Electrical generators for direct drive systems: a technology over. In: Mueller M, Polinder H (eds) Electrical drives for direct drive renewable energy systems. Woodhead Publishing, Oxford

Muñoz CQG, Márquez FPG, Tomás JMS (2016) Ice detection using thermal infrared radiometry on wind turbine blades. Measurement 93:157–163

Negnevitsky M, Johnson P (2008) Very short term wind power prediction: a data mining approach. In: Power and energy society general meeting-conversion and delivery of electrical energy in the 21st century, 2008 IEEE, 2008. IEEE, pp 1–3

Negnevitsky M, Mandal P, Srivastava AK (2009) Machine learning applications for load, price and wind power prediction in power systems. In: 2009 15th International Conference on Intelligent System Applications to Power Systems (ISAP), Curitiba, Brazil. IEEE pp 1–6, 8–12 Nov 2009

Parent O, Ilinca A (2011) Anti-icing and de-icing techniques for wind turbines: critical review. Cold Reg Sci Technol 65(1):88–96

Park J, Law KH (2016) A data-driven, cooperative wind farm control to maximize the total power production. Appl Energy 165:151–165

Pinson P, Madsen H (2008) Probabilistic forecasting of wind power at the minute time-scale with markov-switching autoregressive models. In: Proceedings of the 10th International Conference on Probablistic Methods Applied to Power Systems, 2008, Rincon, PR, USA . IEEE, pp 1–8, 25–29 May 2008

Popa LM, Jensen B-B, Ritchie E, Boldea I (2003) Condition monitoring of wind generators. In: 38th IAS Annual Meeting on Conference Record of the Industry Applications Conference, 2003, Salt Lake City, UT, USA. IEEE pp 1839–1846, 12–16 October 2003

Richert F (1996) Is rotorcraft icing knowledge transferable to wind turbines. BOREAS III FMI, Saariselkä, pp 366–380

Semken RS, Polikarpova M, Röyttä P, Alexandrova J, Pyrhönen J, Nerg J, Mikkola A, Backman J (2012) Direct-drive permanent magnet generators for high-power wind turbines: benefits and limiting factors. IET Renewable Power Generation 6(1):1–8

Senjyu T, Yona A, Urasaki N, Funabashi T (2006) Application of recurrent neural network to long-term-ahead generating power forecasting for wind power generator. In: Power systems conference and exposition, 2006. PSCE'06. 2006 IEEE PES, 2006, Atlanta, GA, USA. IEEE pp 1260–1265, 29 Oct–1 Nov 2006

Shi J, Yang Y, Wang P, Liu Y, Han S (2010) Genetic algorithm-piecewise support vector machine model for short term wind power prediction. In: Intelligent control and automation (WCICA), 2010 8th world congress on, 2010. IEEE, pp 2254–2258

Shun S, Ahmed NA (2012) Rapid prototyping of aerodynamics research models. In: Applied mechanics and materials. Trans Tech Publications, Switzerland, pp 2016–2025

Swainson WK (1977) Method, medium and apparatus for producing three-dimensional figure product. Google Patents

Tammelin B, Holttinen H, Morgan C, Richert F, Seifert H, Säntti K, Vølund P (2000) Wind energy production in cold climate. Finnish Meteorological Institute, Helsinki

Tammelin B, Säntti K, Dobech H, Durstewich M, Ganander H, Kury G, Laakso T, Peltola E, Ronsten R (2005) Wind turbines in icing environment: improvement of tools for siting, certification and operation-NEW ICETOOLS. Finnish Meteorological Institute, Finland

Tan PN, Steinbach M, Kumar V (2006) Introduction to data mining. Addison-Wesley, Boston

Tchakoua P, Wamkeue R, Ouhrouche M, Slaoui-Hasnaoui F, Tameghe TA, Ekemb G (2014) Wind turbine condition monitoring: state-of-the-art review, new trends, and future challenges. Energies 7(4):2595–2630

U.S. Department of Energy (2016) Transforming wind turbine blade mold manufacturing with 3D printing. https://www.youtube.com/watch?time_continue=241&v=tRiULaXzRNo. Accessed 24 Nov 2017

Ultimaker (2017) Vertical axis wind turbine model. https://ultimaker.com/en/resources/19639-vertical-axis-wind-turbine. Accessed 12 Nov 2017

Vargas L, Paredes G, Bustos G (2010) Data mining techniques for very short term prediction of wind power. In: Bulk power system dynamics and control (iREP)-VIII (iREP), 2010 iREP symposium, 2010. IEEE, pp 1–7

Wang L, Dong L, Hao Y, Liao X (2009) Wind power prediction using wavelet transform and chaotic characteristics. In: World non-grid-connected wind power and energy conference, 2009. WNWEC 2009, Nanjing, China, IEEE, pp 1–5, 24–26 Sept 2009

Wilkinson MR, Spinato F, Tavner PJ (2007) Condition monitoring of generators & other subassemblies in wind turbine drive trains. In: 2007 IEEE International Symposium on Diagnostics for Electric Machines, Power Electronics and Drives, Cracow, Poland. IEEE pp 388–392, 6–8 Sept 2007

Wu Y-K, Lee C-Y, Tsai S-H, Yu S-N (2010) Actual experience on the short-term wind power forecasting at Penghu—from an island perspective. In: 2010 International Conference on Power System Technology, Hangzhou, China. IEEE, pp 1–8, 24–28 Oct 2010

Xia J, Zhao P, Dai Y (2010) Neuro-fuzzy networks for short-term wind power forecasting. In: 2010 International Conference on Power System Technology, Hangzhou, China. IEEE pp 1–5, 24–28 Oct 2010

Xin W, Liu Y, Li X (2010) Short-term forecasting of wind turbine power generation based on genetic neural network. In: Intelligent control and automation (WCICA), 2010 8th world congress on, 2010. IEEE, pp 5943–5946

Yang W, Tavner PJ, Crabtree CJ, Feng Y, Qiu Y (2014) Wind turbine condition monitoring: technical and commercial challenges. Wind Energy 17(5):673–693

Yazidi A, Henao H, Capolino G, Artioli M, Filippetti F, Casadei D (2005) Flux signature analysis:
     an alternative method for the fault diagnosis of induction machines. In: Power tech, 2005 IEEE
     Russia. IEEE, pp 1–6
Zayas J, Johnson M (2016) Transforming wind turbine blade mold manufacturing with 3D printing.
     U.S. DOE's Office of Energy Efficiency and Renewable Energy (EERE), USA

Index